UNIVERSITY OF BIRMINGHAM

Exploiting Dopant Characteristics to Enhance the Performance of Lithium Garnet Solid Electrolytes

By

Mark Stockham

Supervisors: Prof. Peter R. Slater, Prof. Yulong Ding and Prof. Yongliang Li

A thesis submitted to The University of Birmingham

for the degree of Doctor of Philosophy

The School of Chemistry
College of Engineering and Physical Sciences
The University of Birmingham
March 2022

Abstract

Lithium garnet materials are promising candidates as inorganic solid state electrolytes for use in all solid state batteries, owing to their high ionic conductivity, wide electrochemical window and high safety. However, garnets suffer from energy demanding synthesis, rapid proton exchange and high interfacial resistance. Furthermore, even the most promising lithium garnet material ($Ga_xLi_{7-3x}La_3Zr_2O_{12}$) requires specialised handling and has not reached the conductivity of current solvent-based electrolytes. In this work alternative dopant strategies into the lithium garnet system are investigated to unlock new approaches to solid state batteries.

Firstly, the flexibility of the Pr dopant was explored, with primary aims to increase the Li conductivity in $Li_5La_3Nb_2O_{12}$ based systems. Here, Pr was doped onto the Nb and La site with $Li_{5+x}La_3Nb_{2-x}Pr_xO_{12}$ and $Li_5La_{3-x}Pr_xNb_2O_{12}$ prepared respectively. The $Li_{5.8}La_3Nb_{1.2}Pr_{0.8}O_{12}$ system had a room temperature conductivity of 0.41 mS cm^{-1}, the highest reported for a lithium garnet with < 6 Li per formula unit.

Secondly, Hf based garnets have been reported to potentially offer increased electrochemical stability compared to the Zr analogue. Therefore, $Ga_xLi_{7-3x}La_3Hf_2O_{12}$ was synthesised for the first time and its electrochemical properties assessed, with results indicating increased critical current density compared to $Ga_xLi_{7-3x}La_3Zr_2O_{12}$. This work also tackled the energy demanding synthesis of garnet materials and proposed a new lower temperature water-based route.

Amongst the best performing lithium garnet materials are the Li substituted $M_xLi_{7-3x}La_3Zr_2O_{12}$ (M = Ga, Al) systems, however both dopants exsolve to the grain boundary when heated to the high temperatures required for densification. This phenomenon, although posing some potential problems, has not been explored as a method to reduce garnet/Li metal resistance v*ia* Ga/Al alloying. In this work, the Ga dopant was deliberately destabilised by substitution of the smaller Nd for La to form $Ga_xLi_{7-3x}Nd_2Zr_2O_{12}$. The Li/garnet interfacial resistance in these systems was determined to be 67 Ω cm^2, compared to 949 Ω cm^2 for the undoped $Li_7Nd_3Zr_2O_{12}$, with results indicating significant Ga exsolution after Li metal contact. A range of Nd garnets were also studied for the first time.

Much work has been conducted on the cubic lithium garnets, but comparatively little on the tetragonal systems due to their poorer ionic mobility. These systems, however, transition to a highly conductive cubic phase at high temperature, thought to be driven by entropic factors and increased unit cell size. It would, therefore, be ideal if this transition was reduced to room temperature, but this first requires a greater understanding of the tetragonal-cubic transition. To that end, a series of nine tetragonal

garnets were made; $A_3B_2Li_7O_{12}$ (A=La, Pr, Nd) (B=Zr, Hf), $La_3Zr_{1.75}Ce_{0.25}Li_7O_{12}$ and $LaSr_2B_2Li_7O_{12}$ (B=Nb, Ta). It was shown that a dependence on lattice parameters alone is inaccurate, however the B site dopant plays a critical role.

Next, the compositional flexibility of the lithium garnet materials was tested with two high entropy garnet systems; $Ga_{0.2}Li_{5.75}La_{2.5}Nd_{0.5}Nb_{0.65}Ce_{0.1}Zr_1Ti_{0.25}O_{12}$ and $Ga_{0.2}Li_{5.75}La_{2.5}Nd_{0.5}Nb_{0.35}Ta_{0.3}Ce_{0.1}Zr_{0.75}Hf_{0.25}Ti_{0.25}O_{12}$. Here, not only were high performing membranes obtained, especially with such low Li content, numerous dopant properties were exploited simultaneously and both systems (outside of stoichiometric weighing) proved very simple to form.

Finally, additional work not yet published, concentrates upon prior reports which indicate doping tetragonal LLZO with Ce reduces Li metal interfacial resistance. Here, a new co-doped $Li_{6.5}La_3Nb_{0.5}Zr_1Ti_{0.25}Ce_{0.25}O_{12}$ system was made to assess if the favourable interfacial properties are maintained, but also if the increased lattice parameters (in a cubic cell) enable better performance. Curiously, not only is this found true, but this system also shows extremely rapid, and simultaneous, sintering and densification (<1h at 1100°C at 100 °C min^{-1}). This garnet was also shown to be synthetically scalable (>15g) and to react, and remove, short circuits caused by lithium dendrites after short rest periods.

Acknowledgments

First and foremost, I thank Peter R. Slater, who embodies my childhood idea of a scientist, constantly formulating and trying new ideas. His enthusiasm, encouragement and support at every stage has been essential. He has been an inspiration both throughout my time at Birmingham and beyond. I would like to thank Bo Dong, who was not only instrumental in the teaching of many areas, but somehow maintained patience with his explanations. An enormous amount of thanks is afforded to Emma Kendrick, who has not only offered help and support from a supervisory standpoint, but (even though I am not one of her students) gave me the chance to use the facilities in the school of metallurgy and materials, which became key in my later work. I also thank Yulong Ding and Yongliang Li for their support and the chance to work in collaboration with the school of chemical engineering.

I would like to thank my mother, Amy Walker. This thesis, its entire contents and who I am now could not have been possible without her. She has stood by me through every difficult moment and made it seem as seamless as the easy ones now. She is now, and will forever stand, as my hero. I also want to thank Elinor Matthews, who somehow managed to stand by me during what was a more tumultuous time than I initially thought, surviving, and continuing to deal with imposter syndrome is very difficult but somehow she stood by me.

I have also been incredibly lucky to be in a vibrant and academically fulfilling environment, where people never hesitate to offer advice and were never scared to ask questions. This has helped me grow and gave me the chance to help in many other areas of energy storage. Therefore, I thank everyone on floor 5 and 6, but especially (in no particular order) Rosie, Bea, Jaime, Abbey, Matt, Dan, Laura, Josh, Harry, Paul, Javi, Abu and Chris. I would also like to thank Joshua Makepeace and Jeremy Lowen for giving me the chance to work with other solid state ionic conductors and learn so much more in the process.

"the most elementary and valuable statement in science, the beginning of wisdom, is, 'I do not know.'" – Commander Data, Star Trek: The Next Generation.

Abbreviations

Al-LLHO	$Al_xLi_{7-3x}La_3Hf_2O_{12}$
Al-LLZO	$Al_xLi_{7-3x}La_3Zr_2O_{12}$
Al-NLZO	$Al_xLi_{7-3x}Nd_3Zr_2O_{12}$
ASD	A-Site Deficient Perovskite
ASR	Area Specific Resistance
BSE	Back Scattered Electron
CCD	Critical Current Density
Ce-LLZO	$Li_7La_3Zr_{2-x}Ce_xO_{12}$
CI	Conductive Interface
c-LLZO	General term for Cubic $Li_7La_3Zr_2O_{12}$
CPE	Constant Phase Element
CV	Cyclic Voltammetry
DMC	Dimethyl Carbonate
EC	Ethylene Carbonate
EDX	Energy Dispersive X-ray Spectroscopy
EIS	Electrochemical Impedance Spectroscopy
ESI	Electronic Supplementary Information
EXFAS	Extended X-ray Absorption Fine Structure
Ga-LLHO	$Ga_xLi_{7-3x}La_3Hf_2O_{12}$
Ga-LLZO	$Ga_xLi_{7-3x}La_3Zr_2O_{12}$
Ga-NLZO	$Ga_xLi_{7-3x}Nd_3Zr_2O_{12}$
HEG	High Entropy Garnet

HEG1	$Ga_{0.2}Li_{5.75}La_{2.5}Nd_{0.5}Nb_{0.65}Ce_{0.1}Zr_1Ti_{0.25}O_{12}$
HEG2	$Ga_{0.2}Li_{5.75}La_{2.5}Nd_{0.5}Nb_{0.35}Ta_{0.3}Ce_{0.1}Zr_{0.75}Hf_{0.25}Ti_{0.25}O_{12}$
HOMO	Highest Occupied Molecular Orbital
IS	Impedance Spectroscopy
LCO	Li_xCoO_2
LDP	Lithium Double Perovskite
LIB	Lithium-ion Battery
LIPON	Lithium Phosphorus Oxynitride
LIRAP	Lithium Rich Anti-perovskite
LISICON	Lithium Super Ionic CONductor
LLHO	$Li_7La_3Hf_2O_{12}$
LLNO	$Li_5La_3Nb_2O_{12}$
LLZO	$Li_7La_3Zr_2O_{12}$
LMO	Li_xMnO_2
LNO	Li_xNiO_2
LTC	$Li_{6.5}La_3Zr_1Nb_{0.5}Ti_{0.25}Ce_{0.25}O_{12}$
LUMO	Lowest Unoccupied Molecular Orbital
NAISICON	Sodium Super Ionic CONductor
NLZO	$Li_7Nd_3Zr_2O_{12}$
NMR	Nuclear Magnetic Resonance
ND	Neutron Powder Diffraction
PC	Propylene Carbonate
pfu	Per Formula Unit
Pr-LLNO	General term for Praseodymium doped $Li_5La_3Nb_2O_{12}$

R	Resistance
SE	Secondary Electron
SEI	Solid Electrolyte Interphase
SEM	Scanning Electron Microscopy
SI	Supporting Information
SSB/ASSB	All Solid-State Battery
SSE	Solid State Electrolyte
Ta-LLZCO	$Li_{6.5}La_3Zr_{1.25}Ce_{0.25}Ta_{0.5}O_{12}$
Ta-LLZO	$Li_{7-x}La_3Zr_{2-x}Ta_xO_{12}$
Thio-LISCON	Sulphur LISICON
t-LLZO	Tetragonal $Li_7La_3Zr_2O_{12}$
XANES	X-ray Near Edge Spectroscopy
XAS	X-ray Absorption Spectroscopy
XRD	X-Ray Diffraction
σ	Conductivity

Table of Contents

1. Introduction

1.1. Background and Motivation

Technological advancement brings consistent innovation, exemplified in recent years by the improvements in portable electronic devices, electric vehicles and renewable energy. However, a major challenge has yet to be overcome: energy storage[1-3]. Considering a zero-emission society is reliant upon effective storage of captured energy, this challenge is of the utmost importance[1, 4].

Batteries are convenient and self-contained devices that can address this challenge, however, currently lack sufficient energy density, power density and have numerous safety concerns (where energy density is the amount of energy stored per unit mass or volume and power density is the amount of energy delivered per unit mass/area/volume per unit time)[1, 5-8]. Batteries rely upon electrochemical reactions which convert chemical energy into electrical energy through reduction-oxidation reactions (redox) and can either be single use (primary) or rechargeable (secondary)[9, 10].

Primary batteries create power by an irreversible chemical reaction which prevents recharge, therefore are disposed of once depleted. Primary batteries lack the need for a reversible and stable long-term reaction, as seen with secondary batteries (which are more complex). This enables higher energy density anode materials (for example lithium metal)[11]. Primary batteries are more commonly orientated toward non-consumer applications, such as medical implants, but can also be found in some consumer orientated devices, such as watches. These are not the subject of this work and will not be discussed further[8-10].

Secondary batteries operate *via* reversible redox reactions, whereupon a charge carrier is shuttled back and forth between electrodes. This enables the battery to be recharged and so reused[8]. Secondary batteries have found use in a broad variety of devices, ranging from mobile telephony to electric vehicles and grid energy storage[8, 9]. However, an optimal secondary energy storage device with high energy/power density, high safety, low self-discharge and excellent thermal stability has yet to be found[7-9, 12, 13]. Although intense work is underway to improve current technology, secondary batteries often find performance and stability improvements are incremental, rather than monumental[5, 6, 12-16]. This is exemplified well by the rapid progression of microelectronic based circuitry and the advancements it has brought to the computational power and portability of many devices, whereas the energy storage required to power these devices is lagging much further behind[5, 6].

The subject of this thesis is secondary, rechargeable, lithium ion batteries (LIBs). This work focuses upon replacement of the hazardous, performance limiting electrolyte in LIBs (often $LiPF_6$ in ethylene carbonate (EC) and dimethyl carbonate (DMC)) with a solid inorganic crystalline equivalent, which is discussed in more depth in the succeeding sections[5, 6, 8, 10, 16, 17].

1.2. Lithium-ion Batteries

Secondary, rechargeable, LIBs are ideal candidates to address the energy storage challenge. Lithium, being the lightest metal, facilitates theoretical design of high energy density batteries that are lightweight and compact. LIBs also have low self-discharge, minimal maintenance requirements, long cycle life, design flexibility and higher cell voltage (≈3.6 V) than competing secondary battery technologies, such as nickel cadmium (1.2 V), nickel metal hydride (1.2 V) and lead acid (2 V)[6]. Therefore, LIBs are commonplace in a wide array of portable electronics and electric vehicles. However, they require significant improvements to meet modern societal demands.

A primary performance challenge is to enable Li metal anodes, which have a high gravimetric and volumetric capacity (3860 mAh g^{-1} and 2061 mAh cm^{-3}) and a very low electrochemical potential (-3.04 V *vs* the standard hydrogen electrode (SHE))[6, 18, 19]. This would enable a monumental leap in LIB energy storage[6, 12, 18, 20]. Current LIBs cannot use Li metal anodes as the electrolyte is both chemically and mechanically unstable, as the low potential of Li metal degrades the electrolyte by reduction (which also decreases Li^+ concentration) and the liquid/polymer medium enables easy lithium dendrite growth during cell operation (leading to serious safety concerns). Therefore, LIBs are restricted to lesser performing anode materials, such as graphite (theoretical capacity of 372 mAh g^{-1}, or 850 mA cm^{-3}, for the end LiC_6 compound).

However, practical cell capacity is based upon the cathode material, and oxide-based insertion cathodes have reached a limit ≈250 mAh g^{-1} in current experimental LIBs (see section 1.4), therefore underutilising graphite. Commercial LIB cathodes are even lower, for example $LiCoO_2$ (LCO) and $LiNi_{0.6}Mn_{0.2}Co_{0.2}O_2$ have experimental capacities of ≈140 mAh g^{-1} and 176 mAh g^{-1} respectively. The use of higher voltage cathode materials has, thus far, been restricted by the available electrolyte systems (often 1 M $LiPF_6$ in EC/DMC), which currently limit LIB cell voltage to ≈4 V (*vs* Li/Li^+). As it is the electrolyte that determines the electrochemical window and electrode choice, further electrolyte development is essential.

Outside these performance restrictions, current LIBs also have limited thermal windows, numerous safety concerns, toxicity issues, are flammable and have questionable mining practices[5, 6, 10, 16-18, 21, 22]. These concerns, again, largely arise from current electrolytes which often have low flashpoint solvents (for example EC/DMC) with toxic Li salts dissolved within (such as $LiPF_6$). Therefore, improved safety, voltage and capacity depends heavily upon the development of advanced electrolyte materials[22-25]. A solid-state electrolyte (SSE) is one such solution.

SSEs will enable solid state batteries (SSB). These are envisioned to have superior safety, cyclability, thermal stability and wider electrochemical windows compared to current LIBs[26-30] and are hoped to enable Li metal anodes[27-29, 31, 32], which is discussed in depth throughout chapter 2. Unfortunately, the discovery of an ideal SSE has been elusive. This forms the basis of this work, where improving the applicability of the lithium garnet electrolyte system by new doping strategies is investigated[26, 30, 31].

1.3. Operating Principles of a Lithium-Ion Battery

LIBs convert chemical energy to electrical energy *via* redox reactions. A LIB cell is comprised of a cathode and anode material coated onto a metal current collector, often Al and Cu, respectively, see figure 1.1 (the term cathode and anode in LIBs is somewhat of a misnomer, as this definition is dependent upon the state of charge. Although the anode is referred to as the negative electrode, and the cathode as the positive electrode, this is only strictly accurate during discharging of the cell). With LIBs, generally, the cathode refers to a transition metal oxide material (where reduction occurs during discharge) and a graphite anode (where Li oxidation occurs during discharge). Situated between the electrodes is an ionically conductive and electronically insulating electrolyte. A porous separator is also present between the electrodes to prevent a short circuit. A common LIB cell example would be cathodic $LiCoO_2$, anodic graphite, an electrolyte composed of $LiPF_6$ dissolved in EC/DMC and a polyolefin-based separator, see figure 1.1.

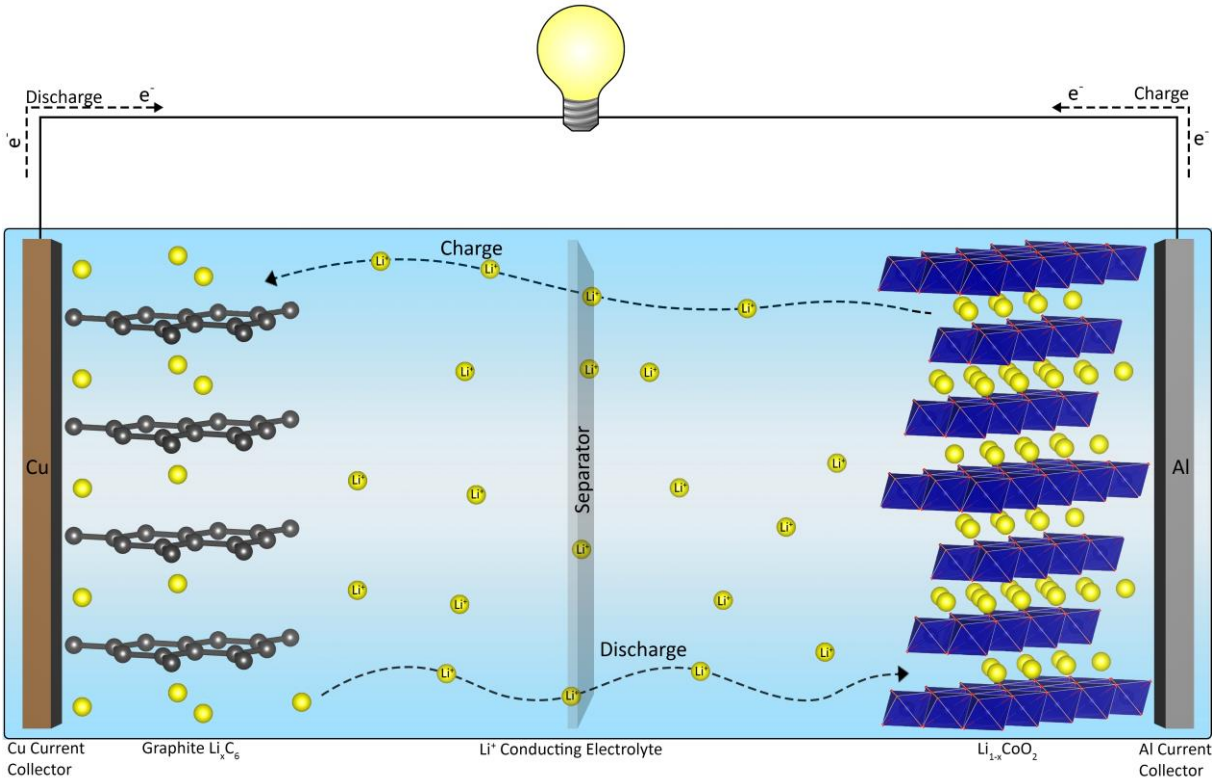

Figure 1.1 Operating principles of a lithium-ion battery, based upon the "rocking chair" model, using a graphite anode, $LiCoO_2$ cathode and a Li^+ conducting electrolyte.

As a LIB discharges, Li^+ moves from the negative electrode (with higher chemical potential) to the positive electrode (with lower chemical potential), the reverse being true during charge. During discharge, there is an excess of electrons at the anode (graphite in this example) which are released once an external wire is connected. This also oxidises lithium to Li^+. The released electron travels into

the external circuit, perturbing the free electron drift velocity within the external conductive wire toward the cathode, aided by the potential difference between the electrodes and the electronically insulating electrolyte. This results in current flow and powering of any connected electronic device. Simultaneously, Li^+ is removed from the anode and released into the electrolyte, see figure 1.1. This perturbs the ionic equilibrium in the electrolyte, causing an Li^+ ion elsewhere in the electrolyte to intercalate into the cathode, which reduces the cathode *via* the addition of an electron from the external circuit). The electrolyte ensures the ionic and electronic contributions remain separate. When the battery is recharged, these reactions are reversed. This forms the LIB rocking chair model, as Li "rocks" back and forth between the electrodes. During cell operation Li^+ would, ideally, be transferred completely between electrodes, with no loss during cycling from side reactions, but perfect Li^+ transport is not observed in practice.

The cell potential, E_{cell}, under non-standard conditions can be calculated by the Nernst equation. This equation links the reversible potential of an electrode to the standard cell potential, E^0_{cell}, and accounts for the relationship between the electrode potential and concentration of the oxidised species, *Ox*, (at the anode during discharge) and the reduced species, *Red* (at the cathode during discharge) (and at different temperatures and pressures)[33]. This is shown in equation 1.1.

$$E_{cell} = E^0_{cell} + \frac{RT}{nF} l\,n\left(\frac{[Ox]}{[Red]}\right) \qquad 1.1$$

where *n* is the number of electrons transferred, *R* is the gas constant, *T* is the temperature and *F* is the Faraday constant (96485.3 C mol^{-1}). *E* is calculated in volts (V). The standard cell potential, E^0_{cell}, is when the concentrations of the oxidised and reduced species have equal contributions under standard conditions *vs* the standard hydrogen electrode (SHE). E^0_{cell} is related to the Gibbs free energy thus:

$$\Delta G^0 = -nFE^0_{cell} \qquad 1.2i$$

Where:

$$E^0_{cell} = E^0_{reduction} - E^0_{oxidation} \qquad 1.2ii$$

where $E^0_{reduction}$ and $E^0_{oxidation}$ are determined from the respective standard electrode potentials, E^0, for each half reaction. The potential between the cathode and anode when electrons are prevented from flowing is the open circuit voltage, V_{oc}. V_{oc}, assuming equilibrium conditions, is the equilibrium potential and can be calculated *via* equation 1.2ii , whereas the Nernst equation describes how V_{oc}

changes under non-standard conditions. V_{oc} depends upon all cell components but is limited by the electrolyte (see section 1.5.)

To charge the battery and force electrons back to the anode an electric potential greater than the equilibrium potential is required, which can be determined as per equation 1.3[10, 34-38].

$$\bar{\mu} = \mu + zF\Phi \qquad 1.3$$

where μ is the chemical potential and $\bar{\mu}$ electrochemical potential of the lithium atoms (assuming a LIB example), where $\mu = \bar{\mu}$ in the absence of any applied voltage. z is the ionic charge and Φ is the potential.

Assuming a cell with a $LiCoO_2$ and graphite electrodes, the overall electrochemical reactions are given by the half-cell equations from the electrode materials, see table 1.1[1].

Table 1.1 Redox half equations for $Li_{1-x}CoO_2$ and graphite-based LIB, with overall cell equation during discharge.

Equation	***Potential (vs SHE)***	***Cell component***
$Li_xC_6 \leftrightharpoons 6C + xLi^+ + xe^-$	E^0 = -2.90 V	Anode
$Li_{1-x}CoO_2 + xLi^+ + xe^- \leftrightharpoons LiCoO_2$	E^0 = 1.20 V	Cathode
$Li_xC_6 + Li_{1-x}CoO_2 \leftrightharpoons C_6 + LiCoO_2$	E^0_{cell} = 4.10 V	Total

1.4. Lithium-ion Battery Development

M. Stanley Whittingham first experimentally demonstrated LIBs in the 1970s, with metal dichalcogenides as the intercalation cathode compound (e.g. TiS_2), Li metal anodes and lithium perchlorate in dioxolane as the electrolyte[5, 6, 13, 39-41]. These LIBs showed excellent promise, but Li metal reactivity enabled explosive side reactions and lithium dendrite growth. Later, an Al-Li alloy was used as the anode to mitigate the metal instabilities; but this significantly limited the cycling performance due to extreme volume changes during operation[42]. Sulphide-based cathodes also generate H_2S gas in contact with moisture, have costly synthesis and require sealed conditions[43]. Therefore, these batteries saw little commercial use and research was discontinued by Exxon.

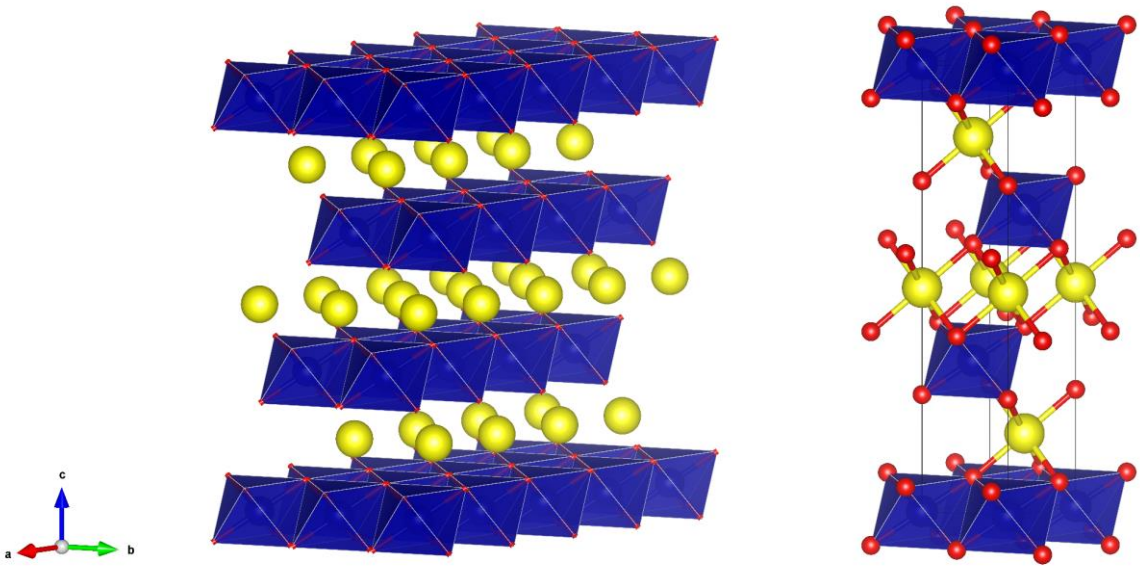

Figure 1.2. $LiCoO_2$ crystal structure, showing the layered trigonal $R\bar{3}m$ structure which enables Li^+ (yellow) intercalation[33,34].

Although Bell Labs, in the United States, were also making significant oxide cathode material advances around this time[44], it was not until the seminal work from Goodenough in 1980, which proposed the Li_xMO_2 series of cathode materials (M = Co, Ni, Mn), that the potential of LIBs began to be realised. $LiCoO_2$ (LCO) in particular led to the first commercial LIB and still remains a popular choice of cathode material to this day[45-48]. The Li_xMO_2 cathodes were paired with lithium metal anodes initially (which progressed to a $Li_{0.1}V_2O_5$ cathode due to Li metal instabilities, one of the few cathode materials available at the time) and an electrolyte composed of 1M $LiBF_4$ solution in propylene carbonate (PC).

LCO is trigonal (space group $R\bar{3}m$) and crystallises in a layered structure that accommodates Li^+ intercalation between the atomic planes, with three CoO_2 per unit cell (stacking order ABCABC) that

facilitate a two-dimensional Li^+ migration channel, see figure 1.2. LCO has a high practical energy density of 150-200 Wh kg^{-1}, a reasonable open circuit voltage (4 V *vs* Li/Li^+), low self-discharge and good electronic conductivity (from the edge shared octahedral array of CoO_6 units)[47, 49, 50]. LCO has a theoretical capacity of 274 mAh g^{-1}, however this assumes one mole of Li can be extracted as per $LiCoO_2$, but in practice < 0.5 moles can be removed before structural collapse. This arises from the physical and chemical instabilities of the $Co^{3+/4+}$ redox couple, whereby the $Co^{3+/4+}$ t_{2g} and O^{2-} : 2p orbital overlap. This limits the experimental capacity of LCO to 140 mAh g^{-1}, see figure 1.3. The Li extraction restrictions stem from LCO, in the Co^{3+}:$3d^6$ configuration, having a filled t_{2g} band and an empty e_g band. However, as lithium is extracted during charge (where Co^{3+} is oxidised to Co^{4+}) the t_{2g} band electrons are removed. As the t_{2g} band overlaps the O^{2-}:2p band, deeper lithium extraction (≈> 0.5) removes O^{2-}:2p band electrons and gives O^{2-} oxidation. This removes lattice oxygens from LCO and enables unfavourable phase transitions which limit the amount of extractable Li to ≈0.5 per formula unit (*pfu*)[51].

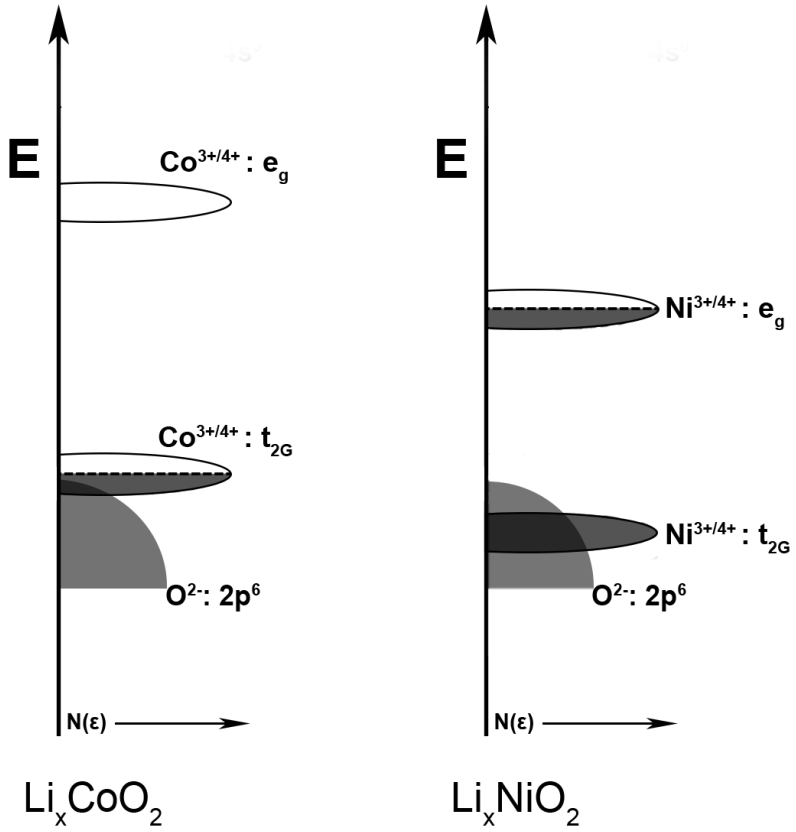

Figure 1.3. Density of states diagram of LCO illustrating the overlap of the $Co^{3+/4+}$ redox couple with the O^{2-}:2p orbital, thus reducing theoretical capacity from 274 mA h g^{-1} to 140 mA h g^{-1}. LNO is also shown, whereby oxidation of Ni involves only the e_g band, therefore minimising the theoretical and experimental capacity difference[36].

Conversely, Ni oxidation in $LiNiO_2$ (LNO) (isostructural with LCO) involves only the e_g band -- which lies above the O^{2-}:2p band. Therefore, this should minimise oxygen lattice changes during Ni oxidation at deep Li intercalation levels. Hence, LNO maintains a real capacity (≈220 mA hg^{-1}) closer to the

theoretical (275 mA hg^{-1})[52]. However, LNO presents separate challenges. LNO is difficult to prepare, as Ni^{3+} is unstable above 250 °C and thus problematic at the high temperatures required for synthesis. As such, Ni^{2+} precursors are used, but this invariably gives some Ni^{2+} in LNO. This Ni^{2+} substitutes onto the Li site, giving poor Li^+ mobility and poor rate capability. LNO, even assuming phase purity, also lacks the structural stability of LCO and undergoes a significant series of phase transitions dependent upon lithium intercalation states. This gives severe capacity fading when $0.5 < Li < 0.75$ (compared to LCO). These increasingly deintercalated phases enable accelerated electrolyte degradation (from O_2 evolution) and exothermic oxidation of the electrolyte as the Li_xNiO_2 structure collapses (from destabilisation of Ni^{4+} to Ni^{2+} at elevated temperatures)[6, 52, 53]. Therefore, LNO has thermal instabilities and safety concerns.

$LiMnO_2$ (LMO) is an attractive alternative to LCO and LNO. LMO has considerable separation between the O^{2-}:2p bands and a high theoretical capacity (285 mA h g^{-1}). However, LMO is not isostructural with LCO/LNO and crystallises in an orthorhombic phase (space group *Pmmm*). Therefore, LMO does not benefit from the same structural stability on lithium deintercalation, instead undergoing a structural breakdown upon even a small amount of lithium removal. This forms a spinel type $LiMn_2O_4$ phase with poor cycle life[54].

However, despite the discovery of Li_xMO_2 cathodes the issues with Li metal anodes remained and other counter electrodes, although giving interesting results, considerably reduced cell voltage. For example, the first LCO cell had a voltage of 4 V (with lithium metal) reduced to 1.5 V, as only $Li_{0.1}V_2O_5$ was available to test *vs* LCO. Therefore, the full modern-day LIB was not complete until the switch away from Li metal to anodic carbonaceous materials. This was first reported by Yazami and Tauzin in solid polymer electrolytes, whereby reversible Li^+ intercalation into graphite was shown but sustained only briefly before cell failure[55]. Later, in 1986, Yoshino patented and fabricated a fully operational LIB cell using petroleum coke[56]. Although the amorphous nature of petroleum coke limits capacity ($\approx Li_{0.5}C_6$) compared with the ideal end graphite compound (LiC_6), this was the first commercialised battery (*via* Sony) owing to its cycling stability. The move to graphitic anodes (to enable LiC_6 and thus increased capacity) remained unrealised until the mid 1990s[57-59], as the initial attempts of reversible Li^+ intercalation into graphite failed due to co-intercalation and electrolyte decomposition (Li^+ salt in PC). PC also resulted in graphite exfoliation from the current collector and battery failure[15, 60, 61]. However, in 1990, Fong *et al.* showed Li intercalation reversibility in graphite could be enabled with ethylene carbonate (EC) based electrolytes, due to formation of a protective passivating solid electrolyte interphase (SEI) layer on the graphite surface[62]. EC was also shown to improve ionic mobility, enable

greater stability with 4 V (*vs* Li/Li^+) cathodes and have suitable electrode wettability. However, the high viscosity of EC alone made it unsuitable for immediate use in LIBs.

Despite the lack of an appropriate electrolyte, Sony commercialised LIBs in 1991 based upon Yoshino's patent with a PC based electrolyte and a coke anode, but research continued to find a suitable electrolyte composition to fully enable graphite anodes. This, ultimately, led to the use of $LiPF_6$ dissolved in EC and DMC, as reported by Guyomard and Tarascon in 1994[63]. DMC diluted the highly viscous EC and increased cell performance, but still prevented graphite exfoliation. $LiPF_6$ in EC/DMC enabled the modern-day LIB and remains the commercial electrolyte of choice in cells with graphite electrodes, however, it is not ideal. This is discussed in the succeeding sections.

1.5. ELECTROLYTE

Electrode materials have seen impressive progress in recent years, with various metal oxides and polyanionic compounds being discovered[6, 64-71]. Conversely, the electrolyte system has seen less progress, despite considerable efforts. The electrolyte determines the battery current (power density), time stability, electrochemical stability window and battery safety (whereas the electrodes determine energy density and cyclability). As intimate contact is made at the electrolyte/electrode interface (and throughout the cell), chemical stability issues will arise if an electrolyte is incorrectly tailored to the electrodes (such as electrolyte degradation by undesirable oxidation/reduction). Therefore, stable cell operating potentials depend upon the stability window of the electrolyte, which restricts electrode choice[72].

Electrolytes are often based upon lithium salts dissolved in organic solvents. This has primarily been the case since the discovery of $LiPF_6$ in EC/DMC in 1994[63], with this electrolyte system still being commonplace in LIBs[72, 73]. Electrolytes in this category are flammable, toxic, non-renewable, have limited thermal stability windows and narrow electrochemical windows ($V_0 \approx 4$ V *vs* Li/Li^+) that make the use of high voltage cathode materials (such as $LiNi_{0.8}Co_{0.15}Al_{0.05}O_2$ and $LiNi_{0.8}Co_{0.1}Mn_{0.1}O_2$) difficult. Polymer electrolytes (which host Li salts in a polymer matrix) or ionic liquids can overcome some toxicity and stability issues, however, these have separate concerns (such as poorer ionic mobility than organic electrolytes, higher operating temperatures or increased cost)[74, 75]. However, even if the drawbacks of these electrolytes were addressed, the liquid/polymer medium will not tolerate use of Li metal anodes (see below). As Li metal is the ideal anode material for LIBs (and can act as its own current collector) it is considered a primary goal for next generation energy storage[5, 6, 10, 16-19, 21-25, 76-78].

Li metal anodes alter the rocking chair model, as they involve generation of a mobile Li^+ species at the anode during discharge and subsequent reformation of Li metal during charge, rather than intercalating as seen with graphite. This presents numerous mechanical issues with respect to the liquid or polymer medium of current electrolytes, as Li stripping and plating during cell operation gives uneven Li deposition. This enables lithium dendrite growth which worsens with repeated cycling and ultimately, extends between electrodes and short circuits the cell. Although smaller short circuits can result only in performance degradation, larger dendrites enable quick discharge between electrodes and can give battery temperatures exceeding 500 °C, enabling device ignition and thermal runaway[5, 6, 10, 16-18, 21, 22]. Assuming these mechanical instabilities could be addressed, the exceptionally low potential of Li metal also reacts rapidly with current electrolyte materials. This degrades the electrolyte, giving safety concerns, “dead Li” and severe capacity fading[77]. Dendritic growth is also not

solely confined to Li metal, as the lower the potential the more likely Li metal plating can occur on the anode. This can arise with graphite from over lithiation due to loss of active material on the negative electrode from high charging rates, solid electrolyte interphase issues/destruction, electrolyte solvent reactions or low temperature operation[79-86].

An ideal LIB electrolyte consists of[26, 87-91];

- Li^+ ion transference number close to one
- high ionic mobility
- negligible electrolyte-electrode resistance, good interfacial stability and charge transfer
- lithium metal anode stability
- electrochemical stability ≥ 4 V *vs* Li^+/Li
- wide thermal stability window
- negligible electronic conductivity
- inert to other cell components
- minimal toxicity/environmental hazards

Presently, no material has all the required properties, but not all are required simultaneously for a functioning energy storage device. Current LIB electrolytes are commercially acceptable when $\sigma_{rt} \geq 10^{-3}$ S cm^{-1}, are stable in an operating voltage window ≈3.2-3.6 V (*vs* Li/Li^+) and have low electronic mobility. The remaining issues have yet to be fully addressed[26, 31, 87]. LIB electrolytes are classified into liquid electrolytes, ionic liquids, polymer electrolytes and solid-state electrolytes (SSE), only the latter of which is discussed in this work.

1.5.1. Electrolytes - Electrochemical Considerations

LIB electrode choice depends upon tailoring electrode chemical potentials to the lowest unoccupied molecular orbital (LUMO) and the highest occupied molecular orbital (HOMO) of the electrolyte; the electrodes must be chemically stable in the window between the electrolyte energy bands. Within LIB research the most used model of electrolyte stability considers electron transfer with respect to the electronic levels in the electrode. Figure 1.4 shows the relative band energies of the cathode, anode and electrolyte. The anode and cathode are electronic conductors, with chemical potentials of μ_a and μ_c respectively. When the μ_a is above the electrolyte LUMO, the electrolyte will be reduced. Correspondingly, when the μ_c is below the HOMO the cathode will oxidise the electrolyte. These reactions degrade the electrolyte, which should remain inert and only facilitate ionic movement and charge transfer favourably at the interface during cell operation; it should neither be reduced or oxidised. Therefore, the μ_a and μ_c must be below and above the electrolyte LUMO and HOMO respectively throughout cell operation. Accordingly, the separation between the electrolyte HOMO and LUMO is the electrochemical window in which the electrolyte is considered stable.

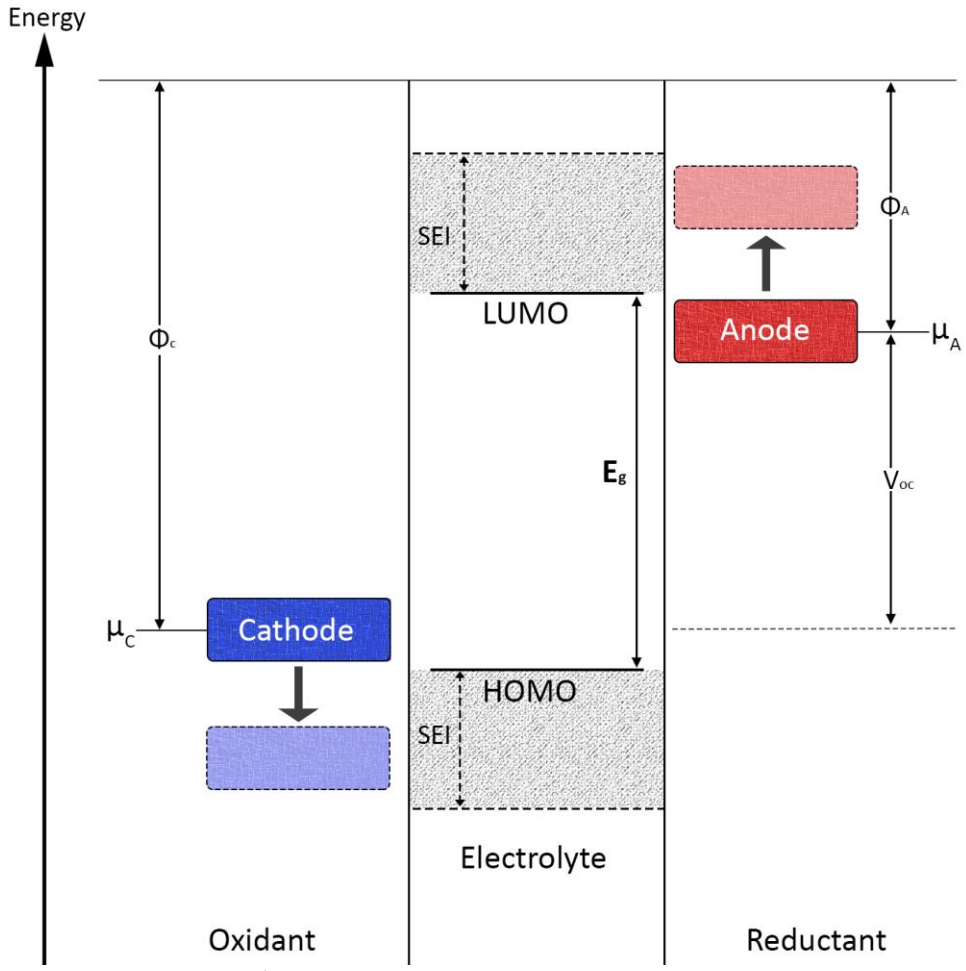

Figure 1.4. Diagram illustrating HOMO/LUMO considerations of electrolytes with respect to electrode materials. Additionally shown is the effect of the SEI layer, and the corresponding alteration of the molecular orbital energy levels, that enable cell stability.

Therefore, thermodynamic stability requires locating the electrode electrochemical potentials within the window of the electrolyte, which is a major challenge, see figure 1.4. This constrains the open circuit potential (V_{oc}) of the battery to equation 1.4.

$$eV_{oc} = \mu_a - \mu_c \leq E_g \qquad 1.4$$

where *e* is the electron charge magnitude and E_g is the energy gap between the HOMO and LUMO. The HOMO/LUMO levels of an electrolyte can be estimated from the first adiabatic electron transfer to and from the bulk of the electrolyte. Despite incorrect tailoring of the electrodes to the HOMO/LUMO of the electrolyte causing degradation, those electrolytes/electrodes with only slightly mismatched energy levels have been shown to form a solid electrolyte interphase (SEI) layer. These SEI layers passivate the electrodes and are ionically conductive but electronically insulating, therefore protecting from further electrolyte degradation. This enables cell operation at the cost of significant initial capacity fade. The SEI effectively alters the electrolyte energy levels with respect to the electrodes to enable cell stability.

The most well-known SEI example is graphite, which has a low potential of 0.2 V *vs* Li/Li^+, this results in $\mu_a >$ LUMO but not excessively so. Therefore $LiPF_6$ (in EC/DMC) is initially unstable with graphite and reduces during cycling. This forms an SEI layer (which can take a few cycles to be optimum) that protects the electrolyte from further reduction (although SEI growth continues throughout battery cycling). This is essential to battery operation, but at the cost of a large initial loss of energy and power density (≈15%), due to the reaction of Li in the cathode and electrolyte to form the SEI[19, 73, 85]. SEI formation is attributed to ethylene carbonate, the electrolyte solvent, which is why it is present in almost all non-aqueous electrolytes, thinned with other carbonates[6]. Reports have also suggested a similarly protective layer forms over the cathode[6, 92, 93], but neither SEI is fully understood.

The electrolyte HOMO/LUMO model is designed more to assess simple electrochemical systems, such as those using H^+ aqueous electrolytes, as it presents only outer sphere charge transfer not the solvation effects (or any other interactions) between species within the electrolyte. Therefore, in LIBs, where lithium salts are dissolved in non-aqueous solvents or polymers, an accurate estimation of electrolyte stability windows needs to consider both the salt and the solvent. This is much more complex. More sophisticated approaches using free energy calculations[94-96] or surface-induced reactions[72, 91, 97-100] are required. An in-depth analysis of this lies outside the scope of this work, however this electrolyte stability model is the most common reported in the literature[90, 100, 101], despite presenting some potential misconceptions (arising from outer sphere charge transfer assumptions)[100].

1.6. Ionic Conduction in Solids

This work primarily discusses inorganic solid-state electrolytes (based on the garnet structure), so ionic conduction within a crystal framework must be discussed. Ionic conduction in solids requires ion mobility within the crystal framework. Ionic movement in many solids is very restricted until high temperature, however some solids have tunnels and/or channels which facilitate ionic migration. Ionic movement is temperature dependent, as increased temperature gives increased atomic vibrations and thus mobility.

In a perfect crystal (at 0 K) all ions are arranged in a regular periodic array and rested on their ideal lattice positions, stacked in closely packed form. Any temperature > 0 K and crystals are imperfect – for example at > 0 K atoms vibrate which in itself may be considered a form of defect[102]. In a perfect crystal the free energy is dominated by the potential energy, with the atomic arrangements at 0 K minimising the total potential energy. When the temperature is increased, so too are the entropic contributions to free energy. At > 0 K the system is attempting to minimise the additional free energy *via* increased entropy. This leads to defect formation. Therefore, crystals are invariably imperfect – as a certain defect concentration will lead to a reduction in the free energy. It is these defects which facilitate ionic movement. Real world systems have more pronounced defects – as atoms are not perfectly present throughout the framework and are inevitably misplaced within the crystal structure. Defect concentrations vary between crystal systems. In some, such as quartz, this can be very minimal but in others this can be much higher[103].

Defects can be intrinsic, whereby the crystal structure is unchanged, or extrinsic *via* doping with aliovalent ions. Intrinsic defects have two major categories: line defects and point defects. Line defects, or dislocations, are spatially extensive and disturb the lattice periodicity. Point defects, which are more relevant for ionic conductivity and this work, arise when unexpected vacant sites occur or when atoms occupy the space between their normal sites (interstitials).

1.6.1. Intrinsic Defects - Point Defects

Intrinsic point defects can be discussed in terms of “Schottky" and “Frenkel” defects. These are generated at any temperature > 0K (due to disorder). These form the basis of the vacancy and interstitial ionic conduction mechanisms, respectively.

Schottky defects describe the removal of charge balanced numbers of oppositely charged ions which have left their corresponding lattice sites. This creates vacancy-based defects, see figure 1.5. As both anion and cation sites are vacant local electroneutrality is maintained, although the removed atoms are still present somewhere in the overall crystal framework (local density reduces due to the vacancies). Schottky defects may be distributed randomly within the crystal or may be associated into pairs and/or larger clusters, therefore are far more complex than represented in figure 1.5. Schottky defects are more common in solids where the anion and cation are of similar size, such as KBr and NaCl.

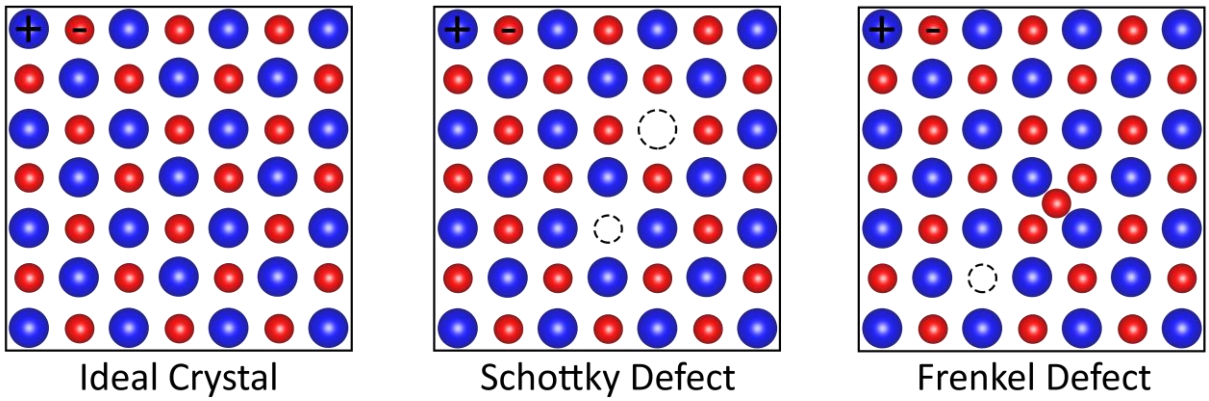

Figure 1.5. Schematic representation of an ideal crystal structure, with Schottky (middle) and Frenkel defects (right). Blue atoms are cations, while red are anions.

Frenkel defects involve an atom displaced off its lattice site into a vacant interstitial, see figure 1.5. These defects more commonly describe a single ion (usually cation) which can effectively “wander” due to electrostatic attraction between the oppositely charged interstitial sites. This forms an ionic pair and enables ionic movement. This is a direct interstitial, whereby an atom moves between one interstitial site to another. Frenkel defects are more common in ionic solids where the anion is substantially larger than the cation, such as in the garnet system with Li^{+} and O^{2-}. However, anion-Frenkel defects are possible in some systems, such as CaF_2.

Using the garnet system as an example, whereby ionic mobility is dominated by an interstitial mechanism, the Kroger-Vink notation (which is a set of conventions for describing point defects in crystals) would correspond to equation 1.5.

$$Null = V_{Li}^{'} + Li_{i}^{\bullet} \qquad 1.5$$

where Null $Li_i^{\bullet}$ he defect creation from the perfect crystal, $V_{Li}^{'}$ is the lithium vacancy with a formal +1 charge and is the Li^+ interstitial[102, 104].

1.6.2. Extrinsic Defects

Extrinsic defects arise upon doping of the pure crystal with aliovalent ions. These can arise unintentionally but is more often by design to enhance certain properties. This can be done *via* processing under specific atmosphere or by altering the starting materials intentionally. For example, the most studied garnet is $Li_7La_3Zr_2O_{12}$, which is tetragonal. However, this can be readily doped with Ta to form a $Li_{6.5}La_3Zr_{1.5}Ta_{0.5}O_{12}$ system, which changes the system to be highly conductive and cubic. In this scenario Ta^{5+} is the donor atom, as it has a higher charge than Zr^{4+}, which introduces lithium vacancies to maintain charge neutrality. If the valences were reversed and the dopant was of a lower charge, it would be an acceptor atom. This system corresponds to the Kroger-Vink:

$$Ta_2O_5 + 2Zr_{Zr}^{x} + 2Li_{Li}^{x} \rightleftharpoons 2V_{Li}^{/} + 2Ta_{Zr}^{\bullet} + Li_2O + 2ZrO_2 \qquad 1.6$$

Vegard's Law states that, within a crystal structure with a deliberately increased dopant concentration, that the unit cell parameters should change linearly with the solid solution composition[105]. This is, however, only approximately obeyed as measuring the actual (instead of intended) stoichiometry of intentionally doped atoms in the bulk material is difficult, especially with techniques such as X-ray diffraction. Vegard's law implicitly assumes that unit cell parameters are governed purely by the relative sizes of the dopant atoms/ions in the solid solution, hence implying atomic replacement is a simple substitution mechanism and thus creating a linear dependence[102].

1.6.3. Ionic Conductivity

In most ionic solids, and most assuredly in an ideal crystal, atoms lack the thermal energy to move easily and are trapped on their lattice sites, although they vibrate continuously. Solid electrolytes, however, have ions which are not bound to lattice sites – this enables a structural component to move throughout the crystal framework, often *via* channels or open tunnels within the structure. This is a thermally activated process, as atomic oscillations and defect concentration are increased above 0 K. Upon reaching a certain critical temperature ionic mobility becomes possible, hence ionic conductivity (σ) ensues *via* vacancy (Schottky) and/or interstitial (Frenkel) type mechanisms, see figure 1.5[102]. Ions can move within these structures *via* ionic diffusion or conductivity. Ionic conductivity is driven by the application of an externally applied electric field (electrochemical potential gradient), whereas diffusion is dependent upon a negative chemical potential gradient[106]. These terms are, however, commonly used interchangeably in the literature as it is often difficult to separate both contributions in real world systems, but this thesis corresponds to ionic mobility under an applied electric field.

Long range transport in solid electrolytes, by definition, occurs *via* cations or anions (as opposed to electron mobility). SSEs can be considered to adhere to liquid like movement in a molten state, thus partial conductivity (σ_i) can be expressed by equation 1.7[102, 107, 108].

$$\sigma_i = n_i q \mu_i \tag{1.7}$$

where n_i is the mobile ion concentration of type "*i*", q is the elementary charge and μ_i is ionic mobility ($m^2\ s^{-1}\ V^{-1}$). These factors are temperature dependent and follow Arrhenius-type behaviour. n_i and μ_i are highly dependent upon defect concentration and atmosphere. σ is expressed in Siemens (reciprocal of an Ω) per cm ($S\ cm^{-1}$), where one Siemen is the conductance which allows a current of one ampere across a potential drop of one volt (one ampere per volt). The total conductivity (σ) in a ceramic material is hence given by the sum of the partial conductivities (σ_i) associated with each charge carrier as per equation 1.8[106].

$$\sigma = \sum_i \sigma_i \tag{1.8}$$

The relation of partial conductivity (σ_i) to the total conductivity (σ) is the transference (or transport) number (τ_i), which should ideally be close to unity at the desired operating temperature/pressure. The form in equation 1.9 considers only a single non-interacting charge carrier[106]:

$$\tau_i = \frac{\sigma_i}{\sigma} \tag{1.9}$$

Current solvent-based LIB electrolytes have a $\tau_i < 0.5$[109, 110]. The low τ_i in conventional LIBs indicates large portions of the current relate to anion motion. This arises due to strong preferential solvation of Li^+ over its counterion within the electrolyte, which results in a bulky solvation shell around Li^+ that limits the τ_i[110]. Polymer electrolytes also suffer from low τ_i as Li^+ is tightly bound within the polymer. As no solvent/polymer matrix is needed with SSEs, their τ_i is close to unity.

The conductivity of an SSE is related to the diffusivity of the mobile ions[108]. This is expressed *via* the Nernst-Einstein equation which gives the relation between the random diffusion coefficient (D_i) and charge carrier mobility[108, 111]. Here k_b is the Boltzmann constant, z is the charge number, q is the elementary charge and T is temperature[102, 112].

$$D_i = \frac{\sigma_i k_B T}{n_i z_i^2 q^2} \qquad 1.10$$

Often, due to considerable differences in size between ions in solid conductors, a single charge carrier dominates (such as Li^+ in the lithium garnet materials), with ionic conductivity influenced by charge carrier concentration, temperature, and the availability of vacant accessible sites (controlled by defect concentration). For ionic conduction to occur in solids some, but ideally all, the following conditions should be satisfied[102]:

- Large number of mobile ions
- Large number of vacant and/or interstitial sites for the mobile ions to migrate into
- A highly polarisable anion framework
- Empty and occupied sites with similar potential energies that have a low, and consistent, activation energy for site migration
- A structural framework with open channels and/or tunnels to allow ionic migration

Upon application of a sufficient external electric field to a solid conductor which meets some (or all) of these requirements (at a certain temperature) ionic conduction ensues. This enables ions to move between crystal lattice sites with a superimposed drift velocity that corresponds to the electric field, resulting in current flow, whereby the mobile ion hops along a pathway which offers the lowest energy, see figure 1.6. This forms the “hopping” model of conduction, where an ion hops between sites. In the absence of an electric field no net charge transport is observed (assuming no chemical potential

gradient for diffusion), as hopping motions are restricted to the ionic free drift velocity and is, thus, random with activation energies equal in all directions.

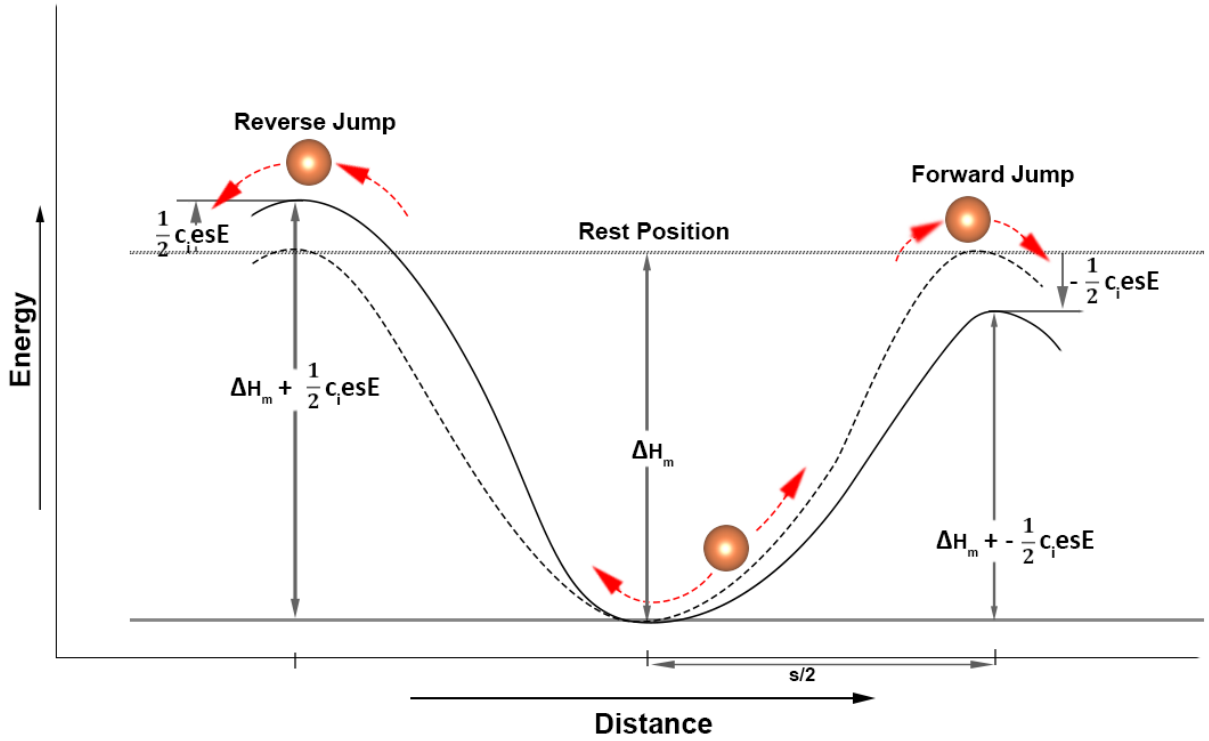

Figure 1.6. The effect of an electric field on the migration of a charged species in an ideal, homogenous crystal. Here ΔH_m is the activation energy when no electric field (E) is present and c_ie is the force exerted on a charged particle of type i over distance s. A charged particle, on application of an electric field, has decreased activation in the forward direction by $\frac{1}{2}c_iesE$ but has increased activation energy in the reverse direction by the same amount, thereby enabling directional current flow. Adapted from[95]

On application of the electric field the "hopping" jump frequency is increased, with a corresponding decrease in the negative direction. Therefore, activation energies are changed. In the forward direction the activation energy is reduced and in the reverse direction it is increased. See figure 1.6. The net flux density is, hence, the difference in the number of jumps in the forward and reverse directions[106]. The energetic barrier which must be overcome to enable hopping is thermally activated and follows Arrhenius type behaviour, see equation 1.11:

$$\sigma = Aexp^{\left(\frac{-E_a}{RT}\right)} \qquad 1.11$$

A, the pre-exponential factor, contains several terms including the vibrational frequency of the mobile ions, the distance the ion moves and the size of the external field. A plot of $Log_e\sigma$ against T^{-1} should give a straight line with a slope of $-E_a/R$ as per appendix 1. Where E_a is the activation energy to enable ionic movement over the analysed temperature range. This is commonly expressed in electron volts (eV), the derivation is in appendix 1.

1.7. REFERENCES

1. K. Amine, R. Kanno and Y. Tzeng, *MRS Bull.*, 2014, **39**, 395-401.
2. R. Gross, M. Leach and A. Bauen, *Environ. Int.*, 2003, **29**, 105-122.
3. A. Evans, V. Strezov and T. J. Evans, *Renewable Sustainable Energy Rev.*, 2012, **16**, 4141-4147.
4. I. Dincer, *Renewable Sustainable Energy Rev.*, 2000, **4**, 157-175.
5. M. Armand and J. M. Tarascon, *Nature*, 2008, **451**, 652.
6. J. M. Tarascon and M. Armand, *Nature*, 2001, **414**, 359.
7. J. Ma, Y. Li, N. S. Grundish, J. B. Goodenough, Y. Chen, L. Guo, Z. Peng, X. Qi, F. Yang, L. Qie, C.-A. Wang, B. Huang, Z. Huang, L. Chen, D. Su, G. Wang, X. Peng, Z. Chen, J. Yang, S. He, X. Zhang, H. Yu, C. Fu, M. Jiang, W. Deng, C.-F. Sun, Q. Pan, Y. Tang, X. Li, X. Ji, F. Wan, Z. Niu, F. Lian, C. Wang, G. G. Wallace, M. Fan, Q. Meng, S. Xin, Y.-G. Guo and L.-J. Wan, *J. Phys. D: Appl. Phys.*, 2021, **54**, 183001.
8. D. Linden and T. Reddy, *Handbook of Batteries*, McGraw-Hill Education, 2001.
9. R. M. Dell, *Solid State Ionics*, 2000, **134**, 139-158.
10. M. Winter and R. J. Brodd, *Chem. Rev.*, 2004, **104**, 4245-4270.
11. D. Lisbona and T. Snee, *Process Saf. Environ. Prot.*, 2011, **89**, 434-442.
12. V. Etacheri, R. Marom, R. Elazari, G. Salitra and D. Aurbach, *Energy Environ. Sci.*, 2011, **4**, 3243-3262.
13. M. S. Whittingham, *Chem. Rev.*, 2004, **104**, 4271-4302.
14. J. G. Kim, B. Son, S. Mukherjee, N. Schuppert, A. Bates, O. Kwon, M. J. Choi, H. Y. Chung and S. Park, *J. Power Sources*, 2015, **282**, 299-322.
15. J. Asenbauer, T. Eisenmann, M. Kuenzel, A. Kazzazi, Z. Chen and D. Bresser, *Sustainable Energy Fuels*, 2020, **4**, 5387-5416.
16. N. Nitta, F. Wu, J. T. Lee and G. Yushin, *Mater. Today*, 2015, **18**, 252-264.
17. B. Scrosati, J. Hassoun and Y. Sun, *Lithium-ion batteries. A look into the future*, 2011.
18. C.-X. Zu and H. Li, *Energy Environ. Sci.*, 2011, **4**, 2614-2624.
19. J. B. Goodenough and K.-S. Park, *J. Am. Chem. Soc.*, 2013, **135**, 1167-1176.
20. Z. J. Zhang and P. Ramadass, *Lithium-Ion Battery Separators*, Springer New York, New York, NY, 2009.
21. V. A. Agubra and J. W. Fergus, *J. Power Sources*, 2014, **268**, 153-162.
22. D. Lin, Y. Liu and Y. Cui, *Nat. Nanotechnol.*, 2017, **12**, 194.
23. H. Yang, C. Guo, A. Naveed, J. Lei, J. Yang, Y. Nuli and J. Wang, *Energy Stor. Mater.*, 2018, **14**, 199-221.
24. J. Lang, L. Qi, Y. Luo and H. Wu, *Energy Stor. Mater.*, 2017, **7**, 115-129.
25. L. Wang, Z. Zhou, X. Yan, F. Hou, L. Wen, W. Luo, J. Liang and S. X. Dou, *Energy Stor. Mater.*, 2018, **14**, 22-48.
26. Q. Liu, Z. Geng, C. Han, Y. Fu, S. Li, Y.-b. He, F. Kang and B. Li, *J. Power Sources*, 2018, **389**, 120-134.
27. A. C. Luntz, J. Voss and K. Reuter, *J. Phys. Chem. Lett.*, 2015, **6**, 4599-4604.
28. J. Li, C. Ma, M. Chi, C. Liang and N. J. Dudney, *Adv. Energy Mater.*, 2015, **5**, 1401408.
29. K. Fu, Y. Gong, B. Liu, Y. Zhu, S. Xu, Y. Yao, W. Luo, C. Wang, S. D. Lacey, J. Dai, Y. Chen, Y. Mo, E. Wachsman and L. Hu, *Sci. Adv.*, 2017, **3**.
30. Y. Kato, S. Hori, T. Saito, K. Suzuki, M. Hirayama, A. Mitsui, M. Yonemura, H. Iba and R. Kanno, *Nat. Energy*, 2016, **1**, 16030.
31. Y. Wang, W. D. Richards, S. P. Ong, L. J. Miara, J. C. Kim, Y. Mo and G. Ceder, *Nat. Mater.*, 2015, **14**, 1026.
32. K. Fu, Y. Gong, J. Dai, A. Gong, X. Han, Y. Yao, C. Wang, Y. Wang, Y. Chen, C. Yan, Y. Li, E. D. Wachsman and L. Hu, *Proc. Natl. Acad. Sci. U. S. A.*, 2016, **113**, 7094.

33. A. J. Bard and L. R. Faulkner, *Electrochemical Methods: Fundamentals and Applications, 2nd Edition*, John Wiley & Sons, Incorporated, 2000.
34. C. Julien, A. Mauger, A. Vijh and K. Zaghib, *Lithium Batteries: Science and Technology*, Springer International Publishing, 2015.
35. M. Park, X. Zhang, M. Chung, G. B. Less and A. M. Sastry, *J. Power Sources*, 2010, **195**, 7904-7929.
36. D. Halliday, R. Resnick and J. Walker, *Fundamentals of Physics Extended, 10th Edition*, Wiley, 2013.
37. A. Väyrynen and J. Salminen, *J. Chem. Thermodyn.*, 2012, **46**, 80-85.
38. R. H. Brugge, PhD thesis, Imperial College London, 2018.
39. M. S. Whittingham, *Science*, 1976, **192**, 1126-1127.
40. M. S. Whittingham, *J. Electrochem. Soc.*, 1976, **123**, 315-320.
41. M. S. Whittingham and L. B. Ebert, in *Intercalated Layered Materials*, ed. F. Lévy, Springer Netherlands, Dordrecht, 1979, DOI: 10.1007/978-94-009-9415-7_10, pp. 533-562.
42. B. M. L. Rao, R. W. Francis and H. A. Christopher, *J. Electrochem. Soc.*, 1977, **124**, 1490-1492.
43. M. S. Whittingham, *Prog. Solid State Chem.*, 1978, **12**, 41-99.
44. D. W. Murphy and P. A. Christian, *Science*, 1979, **205**, 651-656.
45. W. D. Johnston, R. R. Heikes and D. Sestrich, *J. Phys. Chem. Solids*, 1958, **7**, 1-13.
46. E. Shinova, T. Mandzhukova, E. Grigorova, M. Hristov, R. Stoyanova, D. Nihtianova and E. Zhecheva, *Solid State Ionics*, 2011, **187**, 43-49.
47. K. Mizushima, P. C. Jones, P. J. Wiseman and J. B. Goodenough, *Mater. Res. Bull.*, 1980, **15**, 783-789.
48. M. M. Thackeray, W. I. F. David, P. G. Bruce and J. B. Goodenough, *Mater. Res. Bull.*, 1983, **18**, 461-472.
49. P. G. Bruce, *Chem. Commun.*, 1997, DOI: 10.1039/A608551B, 1817-1824.
50. K. Ozawa, *Solid State Ionics*, 1994, **69**, 212-221.
51. R. V. Chebiam, F. Prado and A. Manthiram, *Chem. Mater.*, 2001, **13**, 2951-2957.
52. M. Bianchini, M. Roca-Ayats, P. Hartmann, T. Brezesinski and J. Janek, *Angew. Chem. Int. Ed.*, 2019, **58**, 10434-10458.
53. J. R. Dahn, E. W. Fuller, M. Obrovac and U. von Sacken, *Solid State Ionics*, 1994, **69**, 265-270.
54. G. Vitins and K. West, *J. Electrochem. Soc.*, 1997, **144**, 2587-2592.
55. R. Yazami and P. Touzain, *J. Power Sources*, 1983, **9**, 365-371.
56. A. Yoshino, K. Sanechika and T. Nakajima, *JP Patent 1989293*, 1985.
57. D. Guerard and A. Herold, *Carbon*, 1975, **13**, 337-345.
58. M. Zanini, S. Basu and J. E. Fischer, *Carbon*, 1978, **16**, 211-212.
59. S. Basu, C. Zeller, P. J. Flanders, C. D. Fuerst, W. D. Johnson and J. E. Fischer, *Mater. Sci. Eng.*, 1979, **38**, 275-283.
60. A. N. Dey and B. P. Sullivan, *J. Electrochem. Soc.*, 1970, **117**, 222.
61. J. O. Besenhard, *Carbon*, 1976, **14**, 111-115.
62. R. Fong, U. von Sacken and J. R. Dahn, *J. Electrochem. Soc.*, 1990, **137**, 2009-2013.
63. D. Guyomard and J. M. Tarascon, *J. Electrochem. Soc.*, 1993, **140**, 3071-3081.
64. P. Roy and S. K. Srivastava, *J. Mater. Chem. A*, 2015, **3**, 2454-2484.
65. B. L. Ellis, K. T. Lee and L. F. Nazar, *Chem. Mater.*, 2010, **22**, 691-714.
66. X. Fan, E. Hu, X. Ji, Y. Zhu, F. Han, S. Hwang, J. Liu, S. Bak, Z. Ma, T. Gao, S.-C. Liou, J. Bai, X.-Q. Yang, Y. Mo, K. Xu, D. Su and C. Wang, *Nat. Commun.*, 2018, **9**, 2324.
67. W. Li, E. M. Erickson and A. Manthiram, *Nat. Energy*, 2020, **5**, 26-34.
68. J. Li and A. Manthiram, *Adv. Energy Mater.*, 2019, **9**, 1902731.
69. Z. Lun, B. Ouyang, D.-H. Kwon, Y. Ha, E. E. Foley, T.-Y. Huang, Z. Cai, H. Kim, M. Balasubramanian, Y. Sun, J. Huang, Y. Tian, H. Kim, B. D. McCloskey, W. Yang, R. J. Clément, H. Ji and G. Ceder, *Nat. Mater.*, 2021, **20**, 214-221.

70. Q. Wang, A. Sarkar, D. Wang, L. Velasco, R. Azmi, S. S. Bhattacharya, T. Bergfeldt, A. Düvel, P. Heitjans, T. Brezesinski, H. Hahn and B. Breitung, *Energy Environ. Sci.*, 2019, **12**, 2433-2442.
71. A. Manthiram, *Nat. Commun.*, 2020, **11**, 1550.
72. Q. Li, J. Chen, L. Fan, X. Kong and Y. Lu, *Green Energy Environ.*, 2016, **1**, 18-42.
73. K. Xu, *Chem. Rev.*, 2004, **104**, 4303-4418.
74. M. Armand, F. Endres, D. R. MacFarlane, H. Ohno and B. Scrosati, *Nat. Mater.*, 2009, **8**, 621-629.
75. J. W. Fergus, *J. Power Sources*, 2010, **195**, 4554-4569.
76. W. Xu, J. Wang, F. Ding, X. Chen, E. Nasybulin, Y. Zhang and J.-G. Zhang, *Energy Environ. Sci.*, 2014, **7**, 513-537.
77. Q. Wang, B. Liu, Y. Shen, J. Wu, Z. Zhao, C. Zhong and W. Hu, *Adv. Sci.*, 2021, **8**, 2101111.
78. J. Kalhoff, G. G. Eshetu, D. Bresser and S. Passerini, *ChemSusChem*, 2015, **8**, 2154-2175.
79. T. Waldmann, B.-I. Hogg and M. Wohlfahrt-Mehrens, *J. Power Sources*, 2018, **384**, 107-124.
80. D. Anseán, M. Dubarry, A. Devie, B. Y. Liaw, V. M. García, J. C. Viera and M. González, *J. Power Sources*, 2017, **356**, 36-46.
81. Q. Liu, C. Du, B. Shen, P. Zuo, X. Cheng, Y. Ma, G. Yin and Y. Gao, *RSC Adv.*, 2016, **6**, 88683-88700.
82. J. Luo, C.-E. Wu, L.-Y. Su, S.-S. Huang, C.-C. Fang, Y.-S. Wu, J. Chou and N.-L. Wu, *J. Power Sources*, 2018, **406**, 63-69.
83. Z. Li, J. Huang, B. Yann Liaw, V. Metzler and J. Zhang, *J. Power Sources*, 2014, **254**, 168-182.
84. A. Mauger, M. Armand, C. M. Julien and K. Zaghib, *J. Power Sources*, 2017, **353**, 333-342.
85. A. Patil, V. Patil, D. Wook Shin, J.-W. Choi, D.-S. Paik and S.-J. Yoon, *Mater. Res. Bull.*, 2008, **43**, 1913-1942.
86. C. Shen, G. Hu, L.-Z. Cheong, S. Huang, J.-G. Zhang and D. Wang, *Small Methods*, 2018, **2**, 1700298.
87. V. Thangadurai, S. Narayanan and D. Pinzaru, *Chem. Soc. Rev.*, 2014, **43**, 4714-4727.
88. A. D. Robertson, A. R. West and A. G. Ritchie, *Solid State Ionics*, 1997, **104**, 1-11.
89. S. Liang, W. Yan, X. Wu, Y. Zhang, Y. Zhu, H. Wang and Y. Wu, *Solid State Ionics*, 2018, **318**, 2-18.
90. J. B. Goodenough and Y. Kim, *Chem. Mater.*, 2010, **22**, 587-603.
91. M. Gauthier, T. J. Carney, A. Grimaud, L. Giordano, N. Pour, H.-H. Chang, D. P. Fenning, S. F. Lux, O. Paschos, C. Bauer, F. Maglia, S. Lupart, P. Lamp and Y. Shao-Horn, *J. Phys. Chem. Lett.*, 2015, **6**, 4653-4672.
92. Y. Wu, X. Liu, L. Wang, X. Feng, D. Ren, Y. Li, X. Rui, Y. Wang, X. Han, G.-L. Xu, H. Wang, L. Lu, X. He, K. Amine and M. Ouyang, *Energy Stor. Mater.*, 2021, **37**, 77-86.
93. Z. Zhang, J. Yang, W. Huang, H. Wang, W. Zhou, Y. Li, Y. Li, J. Xu, W. Huang, W. Chiu and Y. Cui, *Matter*, 2021, **4**, 302-312.
94. L. Xing, W. Li, C. Wang, F. Gu, M. Xu, C. Tan and J. Yi, *J. Phys. Chem. B*, 2009, **113**, 16596-16602.
95. H. Zhang, I. M. Ritchie and S. R. La Brooy, *J. Electrochem. Soc.*, 2001, **148**, D146.
96. O. Borodin, W. Behl and T. R. Jow, *J. Phys. Chem. C*, 2013, **117**, 8661-8682.
97. R. Hausbrand, *J. Chem. Phys.*, 2020, **152**, 180902.
98. D. Choi, J. Kang, J. Park and B. Han, *Phys. Chem. Chem. Phys.*, 2018, **20**, 11592-11597.
99. T. Tamura, M. Kohyama and S. Ogata, *Phys. Rev. B*, 2017, **96**, 035107.
100. P. Peljo and H. H. Girault, *Energy Environ. Sci.*, 2018, **11**, 2306-2309.
101. S. J. An, J. Li, C. Daniel, D. Mohanty, S. Nagpure and D. L. Wood, *Carbon*, 2016, **105**, 52-76.
102. A. R. West, *Solid State Chemistry and its Applications*, John Wiley & Sons, 2014.
103. P. P. Kumar and S. Yashonath, *J. Chem. Sci.*, 2006, **118**, 135-154.
104. M. W. Barsoum, *Fundamentals of Ceramics*, McGraw-Hill Education, 2001.
105. L. Vegard, *Z. Phys.*, 1921, **5**, 17-26.

106. P. Kofstad and T. Norby, Defects and Transport in Crystalline Solids. [Online], Available: https://www.uio.no/studier/emner/matnat/kjemi/KJM5120/v09/undervisningsmateriale/, (accessed 05/11/2021).
107. R. Murugan and W. Weppner, *Solid Electrolytes for Advanced Applications*, Springer, 2019.
108. E. D. Tsagarakis and W. Weppner, *Ionics*, 2005, **11**, 240-247.
109. M. Doyle, T. F. Fuller and J. Newman, *Electrochim. Acta*, 1994, **39**, 2073-2081.
110. K. M. Diederichsen, E. J. McShane and B. D. McCloskey, *ACS Energy Lett.*, 2017, **2**, 2563-2575.
111. W. Weppner and R. A. Huggins, *Annu. Rev. Mater. Sci.*, 1978, **8**, 269-311.
112. R. Murugan and W. Weppner, *Solid electrolytes for advanced applications: Garnets and competitors*, Springer International Publishing, 2019.

2. Literature review – Solid State Electrolytes

SSEs, and by extension SSBs, are a relatively experimental class of materials, however, are expected (once commercialised) to yield a new age of energy storage. These devices replace the conventional electrolytes in LIBs with a solid, be that a solid which exhibits long range order or one which is amorphous. These materials are expected to fulfil most, if not all, of the ideal electrolyte properties outlined in section 1.5. However, all components in a LIB are currently solid it is only the electrolyte that remains to be replaced, but a suitable SSE has yet to be found.

The first solid crystalline material reported with charge transport properties was by Michael Faraday in 1883, whereupon Ag_2S and PbF_2 were observed to increase in conductivity with increased temperature[1]. However, this work exclusively considers Li^+ SSEs, and it was not until the 1990s that $Li_qPO_YN_Z$ (LIPON) was discovered, which remains the only solid state ionic Li^+ conductor to be commercialised (owing largely to its ability to be used as a thin film material). LIPON is an amorphous glass with short range order and was first prepared by Oak Ridge national laboratory by partial N substitution into amorphous Li_3PO_4 *via* N_2 gas synthesis with γ-Li_3PO_4[2]. More recent work has investigated alternate thin film deposition techniques, such as radio frequency magnetron sputtering[3-6], atomic layer deposition[7, 8] and chemical vapor deposition[9, 10] but these remain quite expensive by comparison[4, 9, 11-13].

LiPON SSEs have a wide electrochemical window (≈5.5 V *vs* Li/Li^+), high cyclability (>10000), very low electronic conductivity (≈10^{-12} - 10^{-15} S cm^{-1}), and good electrochemical stability toward anodic lithium metal[2, 4, 14, 15]. LIPON, however, has poor ionic mobility, with a peak of $\sigma_{25°C}$ of 3 x 10^{-6} S cm^{-1} for thin film $Li_{2.9}PO_{3.3}N_{0.46}$, which worsens in bulk samples to $\sigma_{25°C} \approx 10^{-7}$ S cm^{-1} [2, 3, 9, 15-18]. This is relatively low compared to other SSEs, and too poor to be used in anything but more specialised applications. LIPON is also amongst the only SSE to have worse performance when analysed in bulk powder in pellet form compared to thin films.

Polymer electrolytes, which are generally composed of polymer salt complexes formed between polymers and alkali metal salts (such as $LiPF_6$/$LiCF_3SO_3$), use a polymer as a solid solvent to host Li^+ for ionic transport. Polymer electrolytes are flexible, resilient, commercially scalable, have low flammability, easy processability, increased vibration/shock tolerance, good mechanical deformation (compared with conventional LIBs), good electrolyte/electrode contact, can eliminate porous separators and can be formed into thin films to improve energy density[19, 20]. Ionic conductivity here differs from other electrolytes, as polymer electrolytes facilitate ionic movement *via* local relaxation

and segmental motion of the polymer chains above the glass transition temperature, rather than by a liquid medium or crystal framework[20, 21]. However, polymer electrolytes have poor σ_{rt} (10^{-6} – 10^{-4} S cm^{-1}), narrow thermal stability, use toxic Li salts, have limited electrochemical windows (≈4V *vs* Li/Li^+), are unstable with lithium metal and are costly compared to conventional LIBs[20, 22]. Nonetheless, polymer electrolyte batteries have been successfully commercialised.

Numerous oxide and sulphide based SSEs with Li^+ conduction have been reported, such as NASICON-type Li^+ conductors, Lithium Super Ionic CONductors (LISICON/thio-LISICON), sulphides, lithium perovskites/antiperovskites and lithium garnet materials[23-28]. However, despite intense SSE research none have all the desirable electrolyte features. Many of the oxides and sulphides reported either have high electrochemical stability or high ionic conductivity[29-31] and additionally suffer from one, or more, of the following; poor wetting between electrode/electrolyte (hence large interfacial resistance), energy demanding and/or time consuming synthesis (often using solid state methods), ambient stability problems and issues being formed into a thin film[20, 32-46]. These issues in mind, however, do not show the excitement building in the battery community and the phenomenal progress made in recent years.

2.1. NASICON AND LISICON

Sodium Super Ionic CONductors (NASICON) type Li^+ conductors first arose as potential Na^+ based electrolytes, and were first investigated by Kierkegaard in 1968 with $NaA_2^{4+}(PO_4)_3$ (A = Ge, Ti, Zr)[47, 48]. Later, Goodenough *et al.* reported a $\sigma_{300°C}$ of 55 mS cm^{-1} with $Na_{1+x}Zr_2P_{3-x}Si_xO_{12}$ ($0 \leq x \leq 3$)[49]. NASICON SSEs afford a 3D ionic pathway *via a* covalent skeleton of $[A_2P_3O_{12}]$, with charge carriers migrating by two interstitial octahedral positions (MO_6 and $M''O_6$) which corner share with an XO_4 unit. Ions transit from one site to another through bottlenecks, the size of which is dependent on the skeleton and interstitial ion size[47, 50, 51].

Considering the similarities of Li^+ and Na^+, NAISCON-type Li^+ conductors were initially prepared by Li substitution to form $LiZr_2(PO_4)_3$ and then $LiZr_{2-x}Ti_x(PO_4)_3$. These had excellent air stability but poor σ_{rt} (≈ 10^{-8} S cm^{-1}) [52] . Later (1989), Zr substitution with Ti and Al gave $Li_{1.3}Al_{0.3}Ti_{1.7}(PO_4)_3$ (LATP) with a $\sigma_{25°C} \approx 3$ mS cm^{-1}, an exceptionally high value even now[53-55]. This was attributed to the substitution of the smaller Al^{3+} enhancing the bottleneck pathway[56]. However, LATP based materials undergo facile Ti^{4+} reduction in the presence of Li metal. Therefore LTAP has a narrow electrochemical window (2.5 V *vs* Li/Li^+)[57]. Use of Ge rather than Ti, as shown with $Li_{1+x}Al_xGe_{2-x}(PO_3)_4$, enables stability up to 7 V (*vs* Li/Li^+)[58] but the Ge precursors are costly[51].

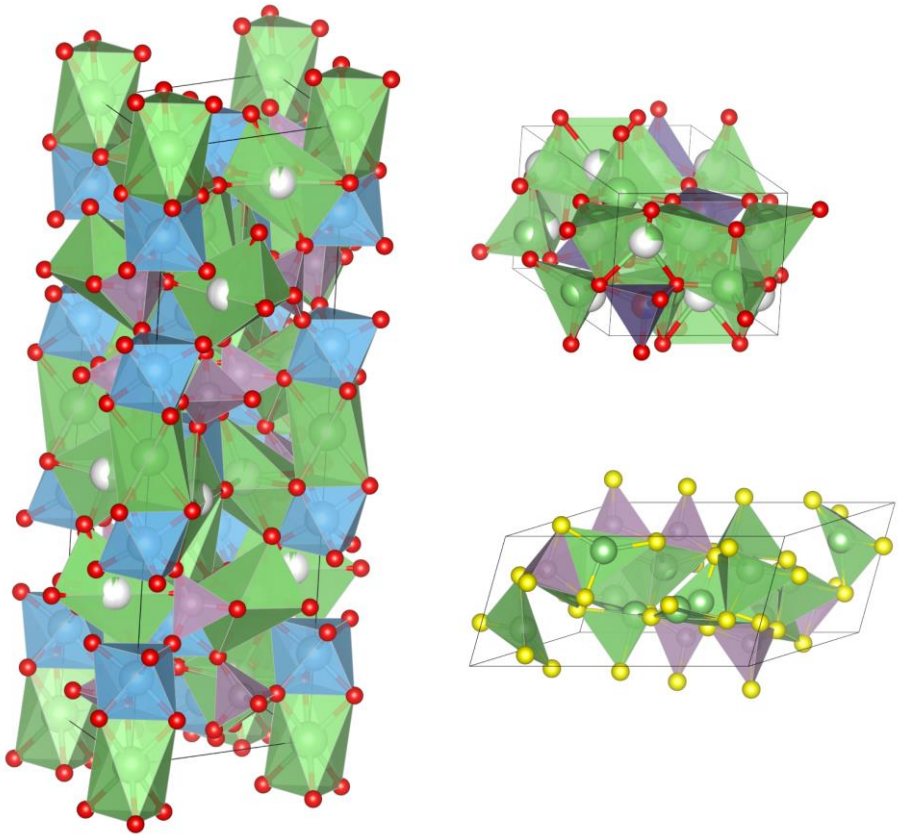

Figure 2.1. Clockwise from left to right, LATP (NASICON) with a trigonal cell (space group $R\bar{3}cH$) $Li_{3.55}Ge_{0.45}Si_{0.10}V_{0.45}O_4$ (LISICON) with an orthorhombic cell (space group Pnma) and $Li_7P_3S_{11}$ (with a triclinic cell (space group P-1))[44, 53, 58].

Lithium Super IONic CONductors (LISICON) were pioneered with $Li_{16-2x}M_x(XO_4)_4$ (M = Mg^{2+}or Zn^{2+}, X = Si^{4+} or Ge^{4+}) by Hong *et al.*, see figure 2.1. LISICONs are structural analogues of γ-Li_3PO_4 and thus differ from NAISCON. $Li_{14}Zn(GeO_4)_4$ had a $\sigma_{33°C}$ of 1.3 x 10^{-6} S cm^{-1}, a high value for 1978[59-61]. Li^+ ionic conduction here is also controlled by the bottleneck size from neighbouring Li^+ sites and between Li^+ and O^{2-}. However, LISICONs have a limited migration pathway as bottlenecks resemble two dimensional parallelograms[59]. Subsequent reports improved ionic conductivity, with $Li_{3.5}Ge_{0.5}VO_4$ and $Li_{3.6}Ge_{0.6}V_{0.4}O_4$ ($\sigma_{18°C}$ ≈ 10^{-5} S cm^{-1})[62], $Li_{3.5}Si_{0.5}P_{0.5}O_4$ ($\sigma_{18°C}$ ≈ 10^{-5} S cm^{-1}) [63] and recently, $Li_{10.42}Si_{1.5}P_{1.5}Cl_{0.08}O_{11.92}$ and $Li_{10.42}Ge_{1.5}P_{1.5}Cl_{0.08}O_{11.92}$ (both $\sigma_{18°C}$ ≈ 10^{-6}) [64]. Computational work has suggested $Li_4Al_{1/3}Si_{1/6}Ge_{1/6}P_{1/3}O_4$ has a $\sigma_{27°C}$ of 9 x10^{-4} S cm^{-1}, however the highest experimental $\sigma_{25°C}$ to date is 5.8 x 10^{-5} S cm^{-1} with $Li_{3.55}Ge_{0.45}Si_{0.10}V_{0.45}O_4$ [65]. Therefore, LISICONS, despite a wide electrochemical stability window (up to 9 V *vs* Li/Li^+) and excellent air stability, lack the ionic mobility required for an SSB[51, 64, 65].

2.2. SULPHIDE ELECTROLYTES

Several sulphide based electrolyte classes have offered promising performance: Thio-LISICON, $Li_{10}MP_2S_{12}$ (M = Ge, Sn, Si) (LMPS), Argyrodite type Li_6PS_5X (X = Cl, Br, I) and $Li_7P_3S_{11}$. All offer high σ_{rt} from ≈1 – 20 mS $^{-1}$. This is competitive with solvent-based electrolytes, such as 1M $LiPF_6$ in EC/DMC ($\sigma_{25°C}$ ≈ 11 mS cm^{-1}). The high ionic conductivity of sulphide SSEs, compared to oxides, stems from the lower electronegativity of S (compared to O). This gives a weaker interaction between S^{2-} with Li^+ and hence the larger (and more polarisable) S enables increased ionic mobility[66-69]. Thio-LISICONs serve as an excellent example, S^{2-} substitution for O^{2-} $Li_{3.25}Ge_{0.25}P_{0.75}S_4$ gave a $\sigma_{25°C}$ of 2.2 mS cm^{-1}, which is considerably higher than the oxide counterpart [70-74]. Sulphide SSEs also benefit, generally, from being much softer than oxide materials, enabling dense membranes by simple compression moulding.

LMPS was first synthesised by Kamaya *et al.* but relates to the initial Thio-LISICON reports[75-77]. Kamaya *et al.* synthesised the $Li_{10}GeP_2S_{12}$ (LGPS) system and reported σ_{rt} of 12 mS cm^{-1}. The LGPS structure is tetragonal (space group $P4_2/nmc$) and consists of PS_4, LiS_4 and $(Ge/P)S_4$ tetrahedra and LiS_6 octahedra. LGPS has four separate Li sites (two in each of the LiS_6 and LiS_4 polyhedra). The two Li sites in LiS_4 form an edge shared tetrahedral chain which affords a one-dimensional Li^+ migration pathway along the *c* axis[78]. This is thought to be the primary pathway at room temperature. The two Li sites in the octahedral LiS_6 are edge shared and enable a less favourable conduction pathway along the *ab* plane[67, 79].

Argyrodite type Li_6PS_5X (X = Cl, Br, I) materials were first synthesised by Deiseroth *et al.* with a reported σ_{rt} > 1mS cm^{-1} (space group $F\bar{4}3m$) [66, 80-82]. Li_6PS_5I was reported with fully ordered S^{2-} and I^-, whereas Li_6PS_5Br has a mixture of ordered and disordered S^{2-}/Br^- sites. Li_6PS_5Cl has a fully disordered S^{2-}/Cl^- arrangement[66, 80]. It has been computationally suggested in Li_6PS_5Cl that three Li sites coexist (Li1(1) 48h site, Li(2) 24g site and the Li(3) 16e site.) Three Li1 and Li2 sites combine to form a hexagon, with four of these hexagons connected by interstitial Li(3) atoms. This forms a pathway cage surrounded by S and Cl anions. Li^+ migration was then suggested to occur by two mechanisms; a 48h-48h tetrahedral jump and a less favourable 48h-24g-48h jump[67, 81-83].

$Li_7P_3S_{11}$ was first reported by Seino *et al.* by heating Li_2S-P_2S_5 glasses to 280°C, see figure 2.1.[73, 81]. This formed a ceramic material with a triclinic cell (space group *P*-1) which comprised P_2S_7 ditetrahedra and PS_4 tetrahedra, with lithium located around these sites surrounded by 3 - 5 S atoms[74]. $Li_7P_3S_{11}$ was reported with a $\sigma_{rt°C}$ of 11 mS cm^{-1}. Computational work from Chang *et al.* reported that Li^+ transport consists of equal contributions along the *a*, *b* and *c* axes, therefore suggesting a three-dimensional migration network *via* mesh like channels[84]. However, the structure and transport mechanisms for

LMPS, Li_6PS_5X and $Li_7P_3S_{11}$ are not well understood, as characterisation by neutron diffraction (ND) or NMR which fully excludes moisture, and thus retain phase stability, is a difficult task.

Sulphide SSEs despite their high ionic mobility, reasonable activation energies (≈ 0.16 - 0.25 eV) and soft nature suffer from several severe instabilities. The most concerning of these is the high susceptibility of sulphide SSEs to hydrolysis which generates toxic H_2S gas and can induce structural changes. Therefore, sulphides require handling in inert atmosphere which limits any potential commercial applications. Secondly, the soft nature of sulphide SSEs causes mechanical instabilities with Li metal, potentially enabling dendrite growth at low current densities. Finally, sulphide SSEs have poor reduction and oxidation resistance compared to oxides which restricts cathode choice. This often arises from the reduction of the P^{5+} cation (present in most sulphides) at ≈2.1 - 2.3 V (*vs* Li/Li^+), but also Ge^{4+} reduction in LGPS and $Li_{3.25}Ge_{0.25}P_{0.75}S_4$ (≈1.6 – 1.7 V *vs* Li/Li^+). This gives a narrow electrochemical window and an SSE which reacts with both Li metal and commonly used cathode materials, such as $Li(Ni,Mn,Co)O_2$.

2.3. PEROVSKITE ELECTROLYTES

A wide variety of perovskite structures have been reported with Li-ion conductivity. A-site deficient perovskites (ASD) were the first, followed by lithium rich anti-perovskites (LIRAP) then lithium double perovskites (LDP).

ASDs are based on an $A^{2+}Ti^{4+}O_3$ parent structure, whereby the A^{2+} cation is substituted for La to form $La^{3+}_{2/3}TiO_3$. This leaves one third of the A site vacant, upon which small amounts of Li can be substituted. Ionic mobility ensues *via* the A sites. These were first reported with $Li_{0.5}La_{0.5}TiO_3$ (LLTO), but subsequently enhanced with $La_{0.67-x}Li_{3x}TiO_3$ (x = 0.06 – 0.15) with a reported $\sigma_{bulk25°C} \approx 1.5$ mS cm^{-1} when x = 0.12[85-89]. Although, reports with (Li, Sr) (B,B')O_3 (B = Zr, Hf, Ti, Sn, Ga, B' = Nb, Ta) and $Li_{3x-y}La_{1-x}Al_{1-y}Ti_yO_3$ have seen similarly high conductivity, ASDs have limited electrochemical windows and are unstable with Li metal (due to Ti^{4+} reduction)[87, 90]. ASDs also undergo Li^+/H^+ exchange in the presence of moisture, which forms LiOH layers. LiOH subsequently reacts with CO_2 and forms insulating Li_2CO_3 layers which passivate the grain surface. This gives increased resistance at the solid-solid interface and inconsistent membrane densification. This compromises σ_{total}, giving ≈10^{-5} S cm^{-1} at 25 °C[91-94].

LiRAPs, such as Li_3OCl, are inverted perovskites and were first synthesised by Zhao and Daemen[26]. The anti-perovskite structure is obtained by replacing the electronegative X site anion (in a perovskite structure adhering to $A^+B^{2+}X^-_3$) with a strongly electropositive cation, such as Li^+. Further substitution with a monovalent A^- and divalent B^{2-} anion and yields the anti-perovskite- structure, with a nominal formula of $A^-B^{2-}X^+_3$. Li_3OCl (and Li_3OBr) had a perovskite cubic cell (*Pm3m)* with Li^+ at the octahedral vertices, O^{2-} at the octahedral centre and Cl^- at the dodecahedral centre[26]. LiRAPs have $\sigma_{rt} \approx 1$ mS cm^{-1}, low activation energies (0.2 - 0.3 eV), negligible electronic conductivity, good cyclability and a wide electrochemical window (0 - 5V *vs* Li/Li$^+$)[26]. However, these structural characteristics and material properties have been difficult to experimentally determine and replicate, as LiRAPs tend to easily form Li_2OHCl in the presence of moisture[95]. This instability is so extreme that decomposition occurs even when stored in a sealed container in a glovebox. Therefore, LiRAPs have yet to progress beyond a few initial studies[95]. Recently, it has been reported that Li_3OCl has good kinetic stability below 400 – 450 K under concentration gradients or with typical cell voltages, which is afforded by the sluggish O^{2-} and Cl^- transport[96].

LDP materials are very much an emerging field, with the pioneering work by Amores *et al.* published in 2020. This work introduced a new class of materials corresponding to $Li_{1.5}La_{1.5}MO_6$ (M = W^{6+}, Te^{6+}) and were synthesised *via* a microwave assisted solid-state approach. These materials demonstrated appreciable room temperature conductivity (0.01 mS cm^{-1}) but had a much larger electrochemical

window (5 V *vs* Li/Li^+) than prior ASD perovskite work, suggesting research into the perovskite electrolyte field is far from exhausted[25].

2.4. LITHIUM GARNETS

SSE work has shifted increasingly toward lithium garnet materials in recent years, and it is this system which forms the basis of this thesis. Lithium garnets ($Li_5La_3M_2O_{12}$, M =Nb, Ta) were first analysed for their ionic conduction properties by Thangadurai *et al.* in 2003, although were discovered many years prior by Mazza[27, 97]. $Li_5La_3M_2O_{12}$ had a $\sigma_{25°C.} \approx 10^{-6}$ S cm^{-1} which, for the time, was very high. However, it was not until the seminal work by Murugan *et al.* in 2007, which showed that $Li_7La_3Zr_2O_{12}$ (LLZO) had $\sigma_{25°C}$ of 0.5 mS cm^{-1}, that lithium garnet materials became exceptionally popular[28]. Several recent reports have shown some lithium garnets, such as $Ga_{0.15}Li_{6.55}La_3Zr_2O_{12}$ (when handled appropriately), have a $\sigma_{25°C} \approx 1$ mS cm^{-1}. This rivals that of some solvent based LIB electrolytes (1 M $LiPF_6$ in EC/DMC, $\sigma_{25°C} \approx 11$ mS cm^{-1})[98]. Therefore, lithium garnets have high electrochemical stability (≈ 6 V *vs* Li/Li$^+$) and fast ionic mobility, which is rare amongst SSE candidates. Furthermore, lithium garnets are chemically stable with lithium metal, non-toxic, air stable (from a safety perspective), non-flammable and have low activation energies.

However, many lithium garnet challenges remain. Firstly, the solid state synthesis methods are time consuming, energy demanding and difficult to scale up, while preparing high density membranes from the sintered powders is very challenging. This, albeit a relatively general problem with solid ionic conductors, needs addressing for industrial scalability. Secondly, most reported lithium garnets have $\sigma_{20°C} \approx 10^{-4}$ S cm^{-1}. The superior $\sigma_{rt} \approx 1$ mS cm^{-1} requires specific handling (such as full synthesis under Ar/O_2) and is, thus, not commercially scalable nor easy to replicate. Furthermore, the reported $\sigma_{rt} \approx 1$ mS cm^{-1} is insufficient at the lower operating temperatures needed for portable electronics/vehicles, whereupon a $\sigma_{rt<10°C} \approx 10^{-4}$ S cm^{-1} (or less) is commonly observed for garnet materials[44, 98-101]. Thirdly, lithium garnets undergo undesirable Li^+/H^+ exchange in the presence of moisture, which makes handling under ambient conditions problematic. Proton exchange in lithium garnets leads to passivating Li_2CO_3 layers that decreases ionic conductivity and gives substantially high electrode/electrolyte interfacial resistance (an already abundant problem at the solid-solid interface, see section 2.5.3.). Finally, lithium garnets lack mechanical stability in the presence of Li metal, as repeated cycling enables dendritic growth along grain boundaries, with some reports even suggesting Li dendrites can penetrate through individual grains[102, 103]. Lithium dendrites can also propagate due to the appearance of voids on repeated lithium plating, which degrades the electrode/electrolyte interface and creates high local current densities (see section 2.5.4.). Therefore, much optimisation is required for lithium garnets to be used in a commercial battery system.

The subject of this thesis is the development of new doping strategies in lithium garnets toward enhancing lithium-ion conductivity, decreasing interfacial resistance, decreasing synthesis time and to aid in general improvements to the understanding of the garnet system. However, first an in depth look into lithium garnet materials is presented. This will concentrate on the structure, ionic conduction mechanisms and development. This is followed by a discussion on the key advantages and disadvantages. Figure 2.2 shows a timeline of the main Li garnet milestones.

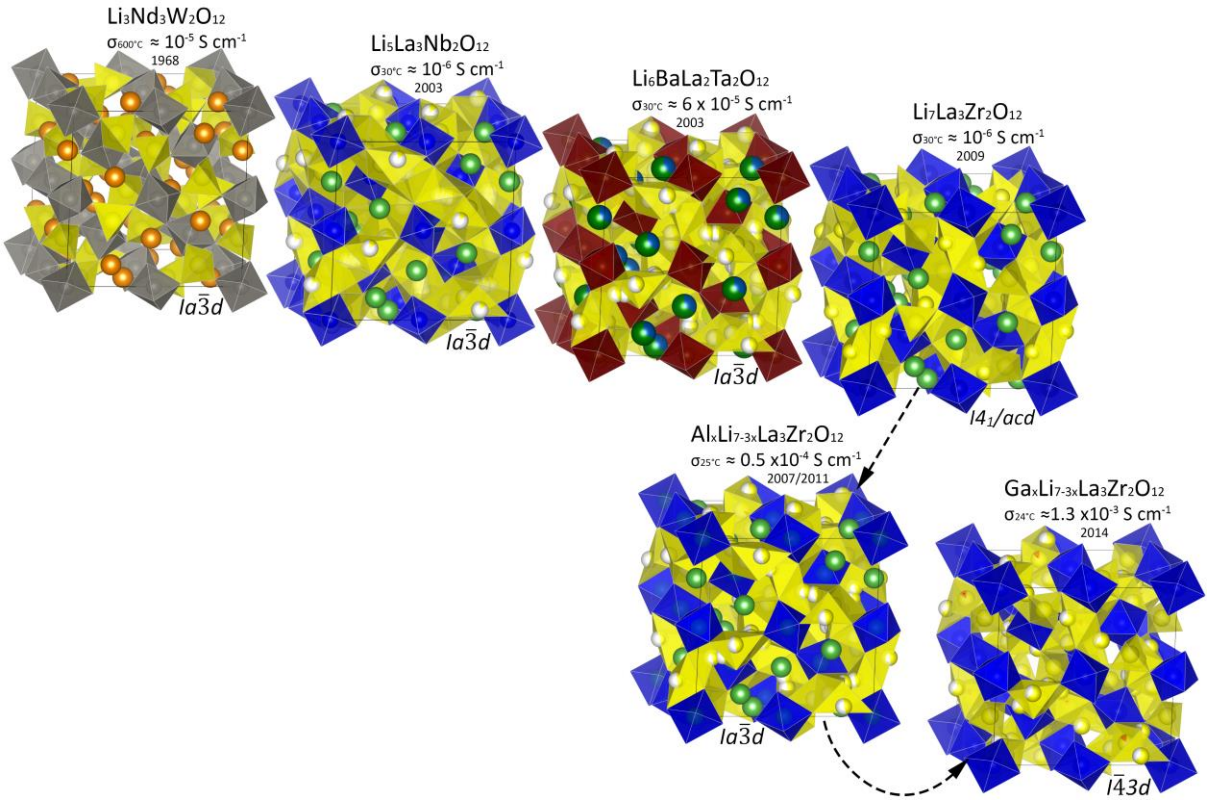

Figure 2.2. Timeline of lithium garnet milestones, which will be discussed in turn in the succeeding sections.

2.4.1. Structure of Lithium Containing Garnet Type Materials

Garnet materials are, traditionally, orthosilicates with the formula $A_3B_2X_3O_{12}$ (e.g. A = Mg, Fe, B = Al, Cr, Fe, and X = Si, Fe, Al, Ga). A, B and X are 8, 6 and 4 oxygen coordinated sites respectively, which have crystallised in a body centred cubic structure with space group $Ia\bar{3}d$ (No. 230) [30, 97, 104]. This ideal garnet structure has linked AO_8, BO_6 and XO_4 polyhedra with a mixture of cations on filled square antiprismatic, octahedral and tetrahedral sites in a 3:2:3 ratio, see figure 2.3[104, 105].

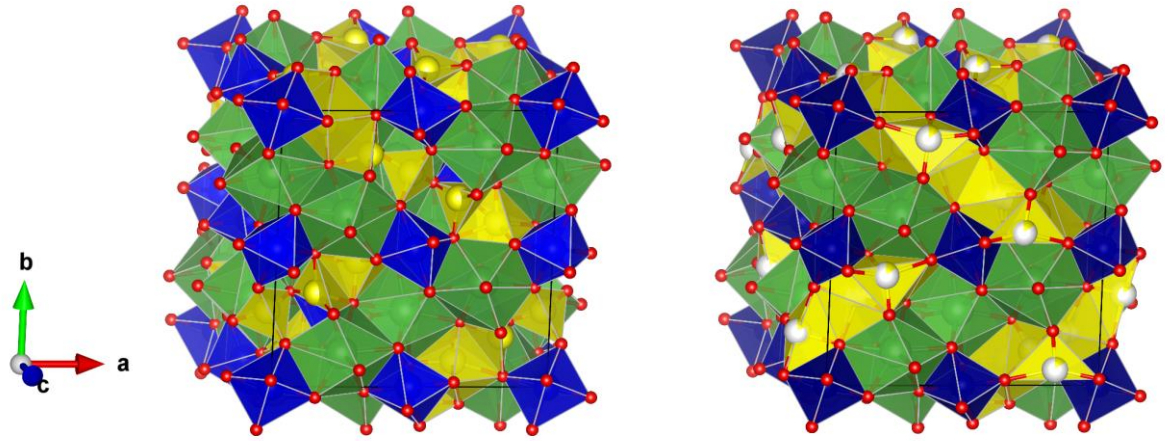

Figure 2.3. Tetragonal LLZO (left) and Cubic LLNO (right), where yellow is Li, Green is La, blue is Zr and dark blue is Nb. Adapted from[109,110].

X site substitution with lithium forms a lithium garnet. This yields an Li_3 system in the form of $Li_3A_3B_2O_{12}$ (A = La, B = W, Te), with lithium fully occupying the 24*d* tetrahedral site[106-108]. Lithium content can be increased further by replacement of the A or B sites with cations in a lower oxidation state, such as Nb^{5+}. This yields $Li_5La_3Nb_2O_{12}$ (LLNO), see figure 2.3. Thus far, lithium garnets have been synthesised with up to Li_7 per formula unit (*pfu*), such as $Li_7La_3Zr_2O_{12}$ (LLZO). These Li_7 systems (thought to be the upper Li limit) crystallise in the tetragonal cell with space group $I4_1/acd$ (no. 142). Tetragonal garnets have fully occupied lithium sites and poor ionic mobility, whereas the cubic $Ia\bar{3}d$ symmetry has partially occupied Li sites and good conductivity[109].

Determination of the lithium positions within the garnet structure is complex, due to the weak X-ray scattering factor of lithium. However, good evidence has been gained from neutron powder diffraction (ND), nuclear magnetic resonance (NMR) and Raman spectroscopy. In the cubic $Ia\bar{3}d$ modification, reports indicate lithium fully occupies the 24*d* tetrahedral site in Li_3 systems. Increasing lithium content further, such as with $Li_5La_3Nb_2O_{12}$ systems (or beyond), gives increased occupation of the distorted 96*h* and 48*g* octahedral sites and decreased occupancy of the 24*d* tetrahedral site, see figure 2.4. Although

some debate persists as to the level of occupation of these sites in higher lithium content cubic phases. This is discussed in more depth in the next section[97, 98, 100, 105, 108, 110-120].

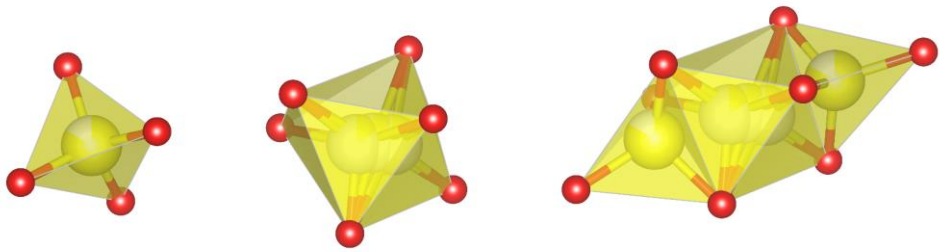

Figure 1. Tetrahedral 24d (left) and the distorted octahedral 48g and 96h Li sites (middle) in the cubic garnet system adhering to $Ia\bar{3}d$ type symmetry. Furthest right is the complete Li site subunit, with two tetrahedral Li sites bridged by a face sharing octahedron.

In Li_7 systems (with a tetragonal cell) the tetrahedral and octahedral Li sites are fully occupied in an ordered manner to prevent short Li-Li distances. This elongates an axis and forms the tetragonal cell with $I4_1/acd$ symmetry. This has poor ionic mobility, as the conduction mechanism in lithium garnets requires Li^+ vacancies and a disordered Li sub-lattice for an effective migration pathway. In $I4_1/acd$ symmetry, Li^+ is thought to occupy the 8*a* tetrahedral site and the distorted 32*g* and 16*f* octahedral sites[109, 121-123].

The poorly conductive tetragonal phases, such as LLZO and $Li_7La_3Sn_2O_{12}$, undergo a reversible phase transition to the cubic cell at high temperature (≈700 °C), which is believed to arise from entropic factors and increased unit cell parameters. Initial studies suggested the transition occurred between 100 - 200 °C in LLZO, but this was later found to be a result of hydration from direct insertion of water into the structure or from Li^+/H^+ exchange[124, 125]. The true phase transition for LLZO is suggested to be 620 – 650 °C[126, 127], with the smaller $Li_7La_3Sn_2O_{12}$ cell transitioning between 750 – 800 °C[121]. Conversely, $Li_7La_3Zr_{1.75}Ce_{0.25}O_{12}$, with a larger cell volume than LLZO arising from Ce^{4+} substitution, had a reported transition temperature of 325 °C[127]. This suggests a direct relation to cell volume – whereby the larger volume gives a reduced transition temperature. Ideally, the transition temperature would be reduced further to yield a true cubic Li_7 type garnet at room temperature. This has yet to be accomplished and only limited reports in the literature are available which investigate the driving factors behind the phase transition, as the tetragonal phase is undesirable due to low conductivity[20, 121, 124-129].

The tetragonal systems can form the cubic cell *via* Li exchange in the form of $M_xLi_{7-3x}La_3Zr_2O_{12}$ (M = Al, Ga)[117, 124, 130]. These maintain the cubic symmetry when Li < ≈ 6.6. When ≈6.6 ≤ Li ≥ 7, the phase homogeneity of the powder is often reported *via* X-ray diffraction to be a mix of cubic and tetragonal

cells, thus meaning the tetragonal component compromises σ_{total}. However, a recent report on $Li_{6.95}La_3Zr_{1.95}Nb_{0.05}O_{12}$ proposed orthorhombic symmetry with space group *Ibca*. This pattern is very similar to the tetragonal $I4_1/acd$ garnet cell but has several additional, very low, intensity reflections which required single crystal XRD to resolve[131].

Li needs to be < 7 *pfu* to prevent a transition to the tetragonal cell, but still maintain a high Li content sufficient to enable a highly disordered Li sublattice and fast ionic movement. Hence, most garnet reports concentrate on Li contents between 6 - 6.6 *pfu*. Dopant strategies, therefore, aim to increase Li content in Li_5 based systems or to remove Li from Li_7 systems. Some examples include $Li_{5+x}La_3B_{2-x}M_xO_{12}$ (B = Nb, Ta, Zr, Hf, M = Ce, Ta, Nb), $Li_{7-3x}A_xLa_3B_2O_{12}$ (A = Al, Ga, B = Zr, Hf, Ti, Sn)[98, 116, 121, 130, 132-134], a selection is available in table 2.1. Compelling evidence has suggested that the $Ga_xLi_{7-3x}La_3Zr_2O_{12}$ system crystallises in a different cubic modification, the acentric $I\bar{4}3d$ space group. This is thought to potentially explain its superior properties. The specific structural aspects for $Ga_xLi_{7-3x}La_3Zr_2O_{12}$ are discussed in section 2.4.2.2.[101].

2.4.1.1. Ionic Conduction Pathway

A full consensus has not been reached regarding the exact Li^+ hopping pathway, as it is difficult to accurately confirm ionic motion under an applied electric field, especially with such a small charge carrier. Some evidence has been obtained *via* ND, computational studies, and NMR. It is generally considered, in the cubic $Ia\bar{3}d$ system, that Li^+ occupies the 24*d* tetrahedral site and the 48*g* and 96*h* octahedral sites[105, 110, 135-137], with the level of occupation in each site being dependent upon overall cell Li^+ concentration. The 96*h*/48*g* octahedra and 24*d* tetrahedra are all interconnected, with each tetrahedron being bridged by a single face sharing octahedron, see figure 2.5 and 2.6.

In a Li_3 type garnet (such as $Li_3Nd_3Te_2O_{12}$), Li^+ is thought to fully occupy the 24*d* interstices with the Li^+ well-ordered on the A sites[108, 112]. It was initially thought, as these systems also have minimal conductivity, that the 24*d* site played little role in the conduction mechanism. This was substantiated by reports from O'Callaghan *et al.* (with $Li_{3+x}Nd_3Te_{2-x}Sb_xO_{12}$) and Cussen ($Li_5La_3M_2O_{12}$, M = Ta, Nb), which both suggested Li movement occurred only *via* the edge sharing octahedra. The reports suggested an energetic barrier too great to overcome for Li^+ migration from the tetrahedron into the octahedron[110, 135, 138]. However, work also indicated that increased octahedral site occupation (when Li > 3 *pfu*) was also accompanied by an increasing number of 24*d* site vacancies[108, 135, 138]. For example,

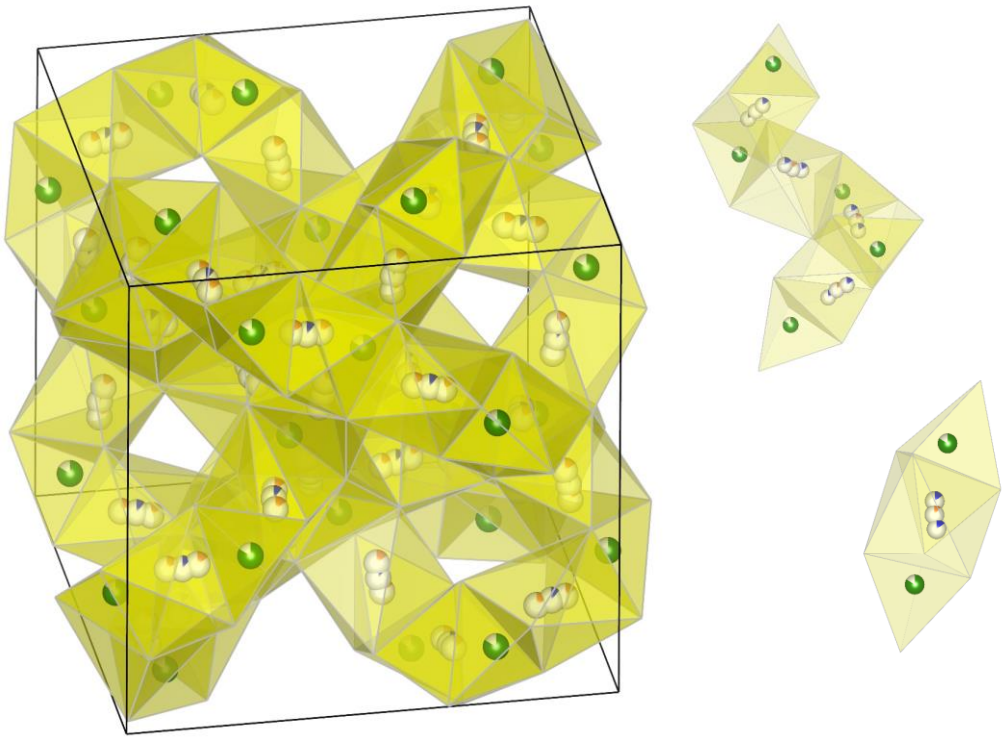

Figure 2.5. Suspected Li^+ conduction pathway in cubic $Ia\bar{3}d$ type lithium garnet systems, shown is $Li_5La_3Nb_2O_{12}$ adapted from[110]. Only Li^+ atoms are shown, individual colours represent partial occupancies of each site. On the right is the Li sub-unit. Green is the 24d site, blue is the 96h site and orange is the 48g site.

with $Li_5La_3M_2O_{12}$ (M= Ta, Nb), Cussen reported that the 24*d* site was 80% occupied, whereas the octahedral sites were 40% occupied[110, 118]. As Li is increased beyond 5 *pfu* and conductivity improves, octahedrally located Li^+ becomes increasingly clustered. This also gives decreased tetrahedral (24*d*) site occupancy[118]. The introduction of vacancies to the 24*d* site are, therefore, now thought to contribute to the ionic hopping pathway[138].

It was the *ab initio* calculations from Xu *et al.* that were the first to indicate the tetrahedral sites could assist in ionic movement, whereupon two possible pathways were calculated: one which bypasses the 24*d* sites and another which incorporates the 24*d* sites[136]. The two pathways were reported with different energetic barriers, with the octahedral-tetrahedral-octahedral jump (0.26 eV) being lower than the octahedral-octahedral jump (0.8 eV), suggesting the former is more favourable. Although these are simulations at 0K and aimed at finding the minimum energy of the Li^+ path, the more favourable (0.26 eV) path has gained experimental evidence. ND and NMR studies from Han *et al.* and Wang *et al.* both suggested a migration pathway consisting of a 3D lithium hopping network along 24*d*-96*h*-48*g*-96*h*-24*d*, thus using the tetrahedral site, see figure 2.6[136, 137]. The work by Wang *et al.,* with ^6Li magic angle spinning and ^7Li pulsed field gradient NMR, showed that the 24*d* site mobility dominates the total ionic conductivity by acting as a bottleneck for diffusion. Wang *et al.* also calculated several activation energies; however, the primary bottleneck (which corresponded to 0.26 eV) was related to the jump between the tetrahedral and octahedral sites. This corresponds to the DFT simulations reported prior by Xu *et al.* on the octahedral-tetrahedral-octahedral jump (0.26 eV).

Assuming a 24*d*-96*h*-48*g*-96*h*-24*d* mechanism, as each 24*d* site face shares with four octahedral Li sites in the garnet structure, there is a displacement of the octahedral Li (due to the repulsive interaction between Li^+- Li^+) away from the 96*h* to the 48*g* site. When Li is in the 24d position the neighbouring Li^+ is either in another tetrahedron (separated by an octahedron, see figure 2.6) or Li^+ is in an adjacent octahedron in the distorted 96*h* position away from the occupied tetrahedron face (hence distorted away from the 48*g* position). Each octahedral site is adjacent to 24*d* sites. Therefore, any additional 24*d*-96*h*-24*d* chains require at least one vacant site. Such an arrangement of Li gives many unoccupied sites, and slightly different migration pathways. Concisely summarising, the most commonly suggested pathway involves Li-Li repulsion at the 24d site. This distorts the 48g site toward 96h which then leaps forward into the tetrahedral site on the opposite face. This, therefore, corresponds to a 3D Li hopping pathway consisting of an interlocking chain of 24*d*-96*h*-48*g*-96*h*-24*d* units[136, 137, 139, 140], see figure 2.5 and 2.6. This pathway, although having good evidence is not confirmed.

This applies only to the cubic $Ia\bar{3}d$ garnets, for the Li site substituted Ga-LLZO, which has been suggested to adopt $I\bar{4}3d$ type symmetry, see section 2.4.2.2..

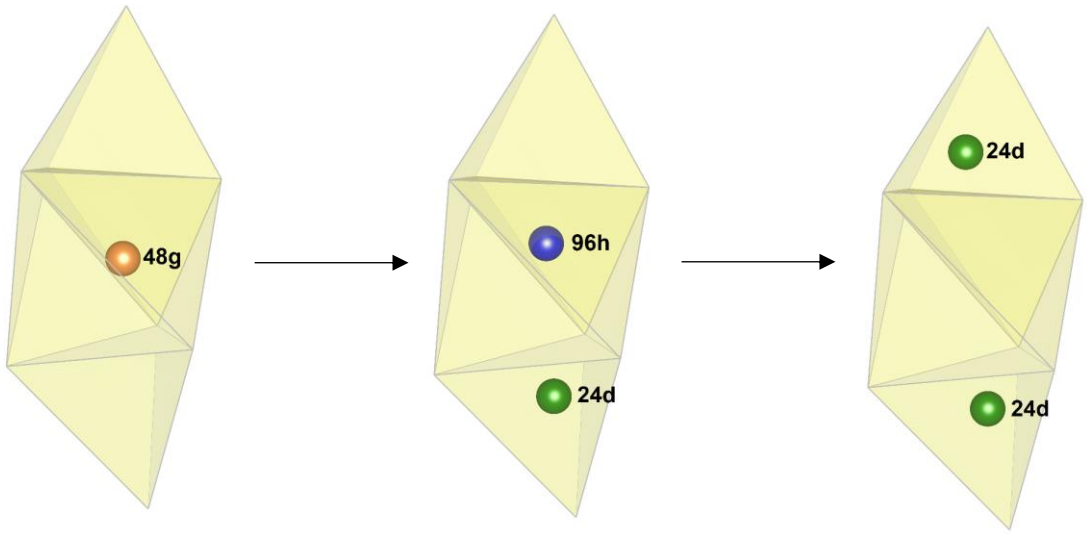

Figure 2.6. Illustration of the potential Li conduction pathway in cubic $Ia\bar{3}d$ type garnets. Illustrating the displacement of Li arising from Li^{+}-Li^{+} repulsion as Li migrates through the pathway.

2.4.2. Development and Doping

Kasper *et al.* first synthesised lithium containing garnets in 1968 with $Li_3Ln_3M_2O_{12}$ (M= Te, W) (Ln= Y, Pr, Nd, Sm, Eu, Gd, Tb, Dy, Ho, Er, Tm, Yb, Lu)[106]. However, the pioneering work by Thangadurai *et al.*, in 2003, on $Li_5La_3M_2O_{12}$ (M = Nb, Ta) was the first to show lithium garnets had good Li^+ ion conduction (≈10^{-6} S cm^{-1}). These were synthesised by heating stoichiometric weights of $La(NO_3)_3{\cdot}6H_2O$, $LiOH{\cdot}H_2O$, and M_2O_5 (M = Nb, Ta) to 950 °C for 24 hours, with an additional 10% $LiOH{\cdot}H_2O$ excess (to account for lithium evaporation at higher temperatures)[27]. This formed $Li_5La_3M_2O_{12}$ with a peak $\sigma_{25°C}$ of 4 x 10^{-6} S cm^{-1}.

Thangadurai and Weppner subsequently increased the lithium content in $Li_6ALa_2Ta_2O_{12}$ (A = Sr, Ba). This improved room temperature conductivity to 4 x 10^{-5} S cm^{-1}. Similar results were also reported with $Li_6ALa_2Nb_2O_{12}$ (A = Sr, Ba, Ca)[141, 142]. Lesser lithium but increased lattice parameters, with $Li_{5.5}La_{2.75}K_{0.25}Nb_2O_{12}$ and $Li_{5.5}La_3Nb_{1.75}In_{0.25}O_{12}$, also marginally improved σ beyond 4 x 10^{-5} S cm^{-1}. This indicated the potential of the garnet system to host numerous dopants, but also found the optimum sintering temperature for $Li_5La_3M_2O_{12}$ (950 °C). This is a temperature commonly found in this work[143].

Later, Percival *et al.* reported Ln site doping from lanthanum to europium in $Li_5Ln_3Sb_2O_{12}$ formed lithium garnet-type materials. This established an upper lanthanoid limit for synthesis, as progression beyond europium, with gadolinium and holmium, formed a perovskite type phase rather than garnet[113]. Percival *et al.* also established that quenching of a sintered $Li_6ALa_2Nb_2O_{12}$ (A = Ca, Sr) pellet from 700 °C improved room temperature conductivity by an order of magnitude (compared to furnace cooling)[144, 145]. It was suggested that quenching effectively froze the high temperature structure, increasing lithium occupancy at the octahedral site, and reduced proton exchange (see section 2.5.2.)[144].

However, it was the seminal work by Murugan *et al.* on $Li_7La_3Zr_2O_{12}$ (LLZO) which ignited the current volume of research into the lithium garnet system. Murugan *et al.* showed a $\sigma_{18°C}$ of 0.4 mS cm^{-1} was possible. This is only an order of magnitude less than conventional solvent-based electrolytes. Murugan *et al.* also showed the garnet system could accommodate seven lithium atoms *pfu*, which has been substantiated by later research but discussed in more depth in section 2.4.2.1.[28, 109, 121, 122]. This work showed a solid ionic conductor which had both high ionic mobility and a wide electrochemical window in addition to Li metal stability, high safety, and relative ease of preparation (although energy demanding)[28, 109, 125, 129].

Significant reports of aliovalent doping of lithium garnets followed, with a variety of differing sintering aids, lithium contents and improvements to conductivity. These were primarily investigated *via*

conventional solid-state synthesis. Some examples include $Li_7La_3Zr_{2-x}M_XO_{12}$ (M = Bi^{5+}, Nb^{5+}, Ta^{5+}, Nb^{5+}, Sb^{5+}), $Li_{7-3x}M_xLa_3B_2O_{12}$ (M = Al, Ga, B = Zr, Hf) and $Ge_xLi_{7-4x}La_3Zr_2O_{12}$[98, 116, 120, 126, 130, 132-134, 146-151]. Conductivities of these systems, however, are often ≈10^{-4} S cm^{-1} and, thus, still inferior to current LIB electrolytes. A selection is summarised in table 2.1.

The solid-state route remains the most common method to form the garnet materials, however, is energy demanding, time-consuming and has difficulties with mixing homogeneity. The high temperature also enables lithium volatility and helps promote Al exchange from the crucible due to formation of Al-Li eutectics (see next section)[152]. Increasingly focus has shifted toward lower temperature/better optimised synthesis routes. Wet chemical techniques, such as sol-gel type methods, involve the mixing of molecular precursors *via* dissolution, therefore overcoming the inhomogeneity of the solid-state route. This enables lower reaction temperatures. Wet chemical methods also yield finer powders with a more uniform size distribution, which are more suitable to form the dense structures required for good SSE performance[153-155]. However, despite the lower sintering temperatures, powder densification still requires high temperature treatments (> 1000°C).

Sol-gel type methods involve dissolving starting materials (generally an alkoxide, nitrate, or chloride) into a solvent followed by addition of reagents (such as tetraethyl orthosilicate). This forms a gel *via* polymerisation which is dried and then sintered. Garnet sol-gel methods often use nitrate precursors (and a variety of gelling agents) and require drying at 350°C in a fume hood prior to sintering, as toxic nitrous oxide gas needs to be removed.

Gao *et al.* was amongst the first to use sol-gel type methods for lithium garnets, and prepared nanocrystalline cubic $Li_5La_3Ta_2O_{12}$ with ethylene glycol as the gelling agent. $Li_5La_3Ta_2O_{12}$ was then formed (after the initial drying step) at 700 °C[156]. This gave ionic conductivities similar to the inaugural work by Thangadurai *et al.,* but decreased the sintering temperature by 250°C. Shimonishi *et al.* increased the lithium content further by synthesising $Li_6La_3Zr_2O_{11.5}$ *via* similar methods, this required sintering at 800°C and gave $\sigma_{25°C}$ of 0.14 mS cm^{-1} and was thus similar to cubic LLZO[154]. Later, Janani *et al.* employed a sol gel process involving citric acid as the organic complexing agent and butan-1-ol or propan-2-ol as the surface-active agent. This gave single phase cubic LLZO (and Al-LLZO) at 700°C which had $\sigma_{25°C}$ of 0.5 mS cm^{-1}, which matches the initial report of LLZO from Murugan *et al.* [28, 155, 157]. Peng *et al.* reported successful synthesis of cubic phase $Li_{6.4}La_{2.3}Na_{0.7}Nb_2O_{12}$, using an unmodified sol-gel process with sintering at 750°C[158] while Li *et al.* reported sol gel synthesis of cubic LLZO *via* initially forming tetragonal LLZO and sintering at 900°C for 6 hours. The powder was then subjected to high energy ball milling to yield cubic LLZO[159].

Rosenkiewitz *et al.* attempted to overcome the toxic nitrous oxide gas by proposing a nitrogen-free route to form Al-LLZO. This involved reacting lithium acetate, lanthanum acetate, zirconium propoxide and aluminium chloride. However, a sintering temperature of 1000°C was required and $\sigma_{25°C}$ was inferior to cubic LLZO at ≈ 10^{-5} S cm^{-1}, potentially due to trace lithium zirconate remaining[160]. Several other reports of similar garnet materials (which differ in temperatures and synthesis conditions) substantiated the favourability of the sol-gel route for garnet production (compared to the solid state route)[141, 153, 161-164]. It was, however, a sol-gel type method that Bernuy-Lopez *et al*., used to synthesise $Ga_{0.15}Li_{6.55}La_3Zr_2O_{12}$. This was the first reported lithium garnet with $\sigma_{24°C}$ of 1.3 mS cm^{-1}, which rivals conventional LIBs (see section 2.4.2.2.)[98].

2.4.2.1. Aluminium Doping

In 2011, doubts arose regarding the true reason for formation of the higher symmetry cubic phase in LLZO, in preference to the more stable tetragonal crystal system reported prior by Awaka *et al.*[109]. Investigations by Geiger *et al.* revealed alumina crucible contamination was responsible for forming cubic LLZO, with identical samples synthesised in platinum crucibles being tetragonal[124]. It was theorised that the formation of the cubic phase was due to exchange of $3Li^+$ with Al^{3+}. Shimonishi *et al.* also reported aluminium content (0.23 mol) in cubic LLZO around this time, *via* inductively coupled plasma spectroscopy, and theorised it was due to the alumina crucibles but it was not discussed further[154]. Al substitution into LLZO is described by Kroger-Vink notation thus[124, 165]:

$$Al_2O_3 + 6Li_{Li}^{x} \rightarrow 2[Al_{Li}^{\bullet\bullet}] + 4V_{Li}^{/} + 3Li_2O \qquad 2.1$$

Cubic phase stabilisation of LLZO by Al substitution has subsequently been substantiated experimentally *via* ND and ^{27}Al NMR[109, 115, 116, 122-124, 127]. It is, therefore, likely that unintentional Al^{3+} doping was a contributing factor in many, if not all, the reports of highly conductive LLZO prior to 2011, especially as many were sintered in alumina crucibles and lacked elemental analysis[109, 121, 124]. Hence, cubic LLZO reports prior to the work by Geiger *et al.* correspond to $Al_xLi_{7-3x}La_3Zr_2O_{12}$ (Al-LLZO) and the term "cubic LLZO" is somewhat of a misnomer, as these systems should be tetragonal.

Structural reports have been somewhat conflicting regarding Al site occupation in the Al-LLZO structure, but all indicate $Ia\bar{3}d$ type symmetry. The works by Geiger *et al.* and Li *et al.* both suggested Al doped onto the 24*d* and 48*g* sites, as determined from ^{27}Al NMR [124, 166]. However, Al was also suggested by Buschmann *et al.* to be confined to the 24*d* site. This was supported by Hubaud *et al.* in later work and substantiated further *via* several ND reports[115, 137, 147, 167]. Düvel *et al.* even reported, *via* ^{7}Li and ^{27}Al NMR, Al could incorporate onto both the La and Zr sites[119]. Later, Rettenwander *et al.* indicated (*via* DFT analysis) that determination of Al site preference in Al-LLZO is a non-trivial task by ^{27}Al NMR, as Al was suggested to have several, slightly different, 4-fold coordination on the 24*d* and 96*h* sites. This leads to broad ^{27}Al NMR resonances which are difficult to interpret, which could explain the conflicting reports. Rettenwander *et al.* also suggested that the 48*g* site may also host Al, therefore further confirming all Li sites had some level of Al occupation. It is, however, generally difficult to ascertain atomic positions from ND and NMR. ND is not a local technique, rather giving an averaged sample view, and NMR (although localised) interpretation is generally a non-trivial task, but especially when broad resonances are present. Nonetheless, these data suggest that Al^{3+} resides on the Li^+ sublattice and, even if Al were fully controlled, could partially block Li^+ movement.

Rangasamy *et al.* investigated the optimal aluminium content to stabilise the cubic $Al_xLi_{7-3x}La_3Zr_2O_{12}$ modification, reporting an Al content of 0.24 mol *pfu* was required for a single cubic phase[168]**.** This coincides with the aluminium ratio originally reported by Shimonishi *et al.*[154]. It was also suggested by Dobretsov *et al.* that lithium excess can facilitate the alumina crucible reaction, further complicating the standard synthesis with Al_2O_3 crucibles[169].

Although Al-LLZO is amongst the most studied and highest performing garnet materials, Al^{3+}/Li^+ exchange is not, by definition, beneficial. The crucible-based reaction is uncontrolled, so Li content can be degraded significantly as Al^{3+} increasingly substitutes onto the Li^+ site[116, 170-172]. Prior work suggested an Al solubility limit of 0.389 mol *pfu* in LLZO (thus a $Al_{0.389}Li_{5.833}La_3Zr_2O_{12}$ system). Beyond this limit, $LaAlO_3$ is formed at the grain boundaries, thus reducing performance. Hence, Al contamination can lead to both low Li content and Li^+ insulating layers on the grain surface (the deterministic factor of total system conductivity) which will degrade performance[168]. Xia *et al.* investigated $Al_{0.25}Li_{6.25}La_3Zr_2O_{12}$ synthesis in different reaction vessels and discovered those synthesised in Pt crucibles were more conductive and had higher relative density (96%), larger grains and increased air stability compared to their alumina crucible counterparts, confirming numerous material properties are degraded by uncontrolled Al_2O_3 crucible synthesis[171]. Al contamination is not exclusive to LLZO and poses a problem with all the Li_7 tetragonal systems and extends to other Li rich garnets (Li_{5+x} phases).

Al-LLZO (and other Al doped garnets) also form Li_2O-Al_2O_3 melts > 1000°C. These Li_2O-Al_2O_3 melts tend to exsolve Al to the grain surface. This aids in densification but decreases Al content in the bulk and gives Li deficient grain boundaries[146, 152, 162, 167, 173]. This makes controlled Al distribution difficult in garnet samples sintered in alumina crucibles, which can be additionally worsened by the Al_2O_3 crucibles creating concentration gradients through a sample[152]. Therefore, garnet synthesis using traditional alumina crucibles constitutes a major problem, but they remain the most popular choice in solid state synthesis due to the low cost. Al contamination can, however, be mitigated by using significant mother powder or by protective ZrO_2 pellets (or crucibles) on to which pellets are placed before sintering/densification.

2.4.2.2. Gallium Doping

Gallium, being directly underneath Aluminium on the periodic table, has similar crystal behaviour and thus Ga^{3+} facilitates Li^{+} exchange in a similar way as Al^{3+} as per $Ga_xLi_{7-3x}La_3Zr_2O_{12}$ (Ga-LLZO). This was first reported by Howard *et al.*[117] and remains amongst the highest ionic conductors within the garnet materials class, with several independent reports of $\sigma_{25°C} \approx 1$ mS cm^{-1} [98, 100, 101]. Ga is introduced to LLZO according to:

$$Ga_2O_3 + 6Li_{Li}^{x} \rightarrow 2[Ga_{Li}^{\bullet\bullet}] + 4V_{Li}^{/} + 3Li_2O \qquad 2.2$$

Bernuy-Lopez *et al.* was among the first to report a $\sigma_{24°C}$ of 1.3 mS cm^{-1} with $Ga_{0.15}Li_{6.55}La_3Zr_2O_{12}$: here the powders were uniaxially pressed and then fully processed in a dry oxygen furnace to alleviate proton exchange (see section 2.5.2.) and to assist in densification. This was the highest conductivity reported at the time and near the theoretical calculated σ_{bulk} limit of 1.6 mS cm^{-1} in LLZO type materials [98, 174]. Wu *et al.* later found a higher conductivity of $\sigma_{25°C}$ of 1.46 mS cm^{-1} in the lesser Li content $Ga_{0.25}Li_{6.25}La_3Zr_2O_{12}$ system[100]. Wu *et al.* used isostatic pressing and densified pellets in air (with significant mother powder) and obtained the same relative density as Bernuy-Lopez *et al.* (ρ_{rel} = 94%). This is contradictory to Bernuy-Lopez *et al.*, who reported that a ρ_{rel} of only 70% could be obtained *via* air densification. Nonetheless, despite the identical 94% ρ_{rel} the system with lesser Li content ($Ga_{0.25}Li_{6.25}La_3Zr_2O_{12}$) outperformed the higher Li content ($Ga_{0.15}Li_{6.55}La_3Zr_2O_{12}$). Rettenwander *et al.*, using the standard solid state route and isostatic pressing, obtained a ρ_{rel} = 84% but still showed a $\sigma_{25°C}$ of 1.32 mS cm^{-1} with $Ga_{0.2}Li_{6.4}La_3Zr_2O_{12}$[175]. Isostatic pressing and O_2 synthesis with a $\sigma_{25°C}$ in the 1 mS cm^{-1} range has also been reported elsewhere[176-178], whereas reports of Ga-doped LLZO *via* hot pressing at > 1000°C[133, 134] and uniaxial pressing[117] are commonly reported in the ≈10^{-4} S cm^{-1} range. This suggests that isostatic pressing of powders and/or O_2 synthesis is the key to high performing Ga-LLZO materials

Ga-LLZO outperforms similarly processed Al-LLZO, despite theoretically substituting for Li^{+} by a similar mechanism. This is a result of both symmetry and dopant size. Ga-LLZO was assumed initially to be $Ia\bar{3}d$, however the larger Ga^{3+} ion (compared to Al^{3+}) in $Ga_xLi_{7-3x}La_3Zr_2O_{12}$ (x > 0.07) distorts the Ga-LLZO lattice away from $Ia\bar{3}d$ to the acentric $I\bar{4}3d$ space group. This was first reported by Wagner *et al.* by single crystal XRD and ND for Ga-LLZO. $I\bar{4}3d$ symmetry had, however, been mentioned prior with $H_xLi_{6-x}CaLa_2Nb_2O_{12}$ and $H_xLi_{7-x}La_3Zr_2O_{12}$, but these were attributed to uneven H^{+} and Li^{+} distribution and thus potentially irrelevant to high Li content garnet electrolytes[179, 180].

The determination of the $I\bar{4}3d$ space group is quite difficult in garnet materials expected to adopt $Ia\bar{3}d$ type symmetry, especially using only X-ray diffraction. $I\bar{4}3d$ presents with three additional, very low intensity, reflections at 2ϑ = 21.5°, 40.3° and 53.4° in the diffraction pattern. These correspond to the (310), (530) and (710) reflections in the $I\bar{4}3d$ space group which are forbidden in $Ia\bar{3}d$ type symmetry. These low intensity peaks were observed by Wagner *et al.* in Ga-LLZO, but with relative intensities of 1.2, 0.4 and 0.3% compared to the strongest reflection at 2ϑ = 30.81. These peaks are essentially lost in XRD and overlap with $LiGaO_2$ impurities at 2ϑ = 21.52°, therefore can be incorrectly assigned. Employing ND and single crystal XRD enabled the structure to be resolved as $I\bar{4}3d$ for Ga-LLZO. Later $Fe_xLi_{7-3x}La_3Zr_2O_{12}$ was also determined to adhere to $I\bar{4}3d$ symmetry [99, 101].

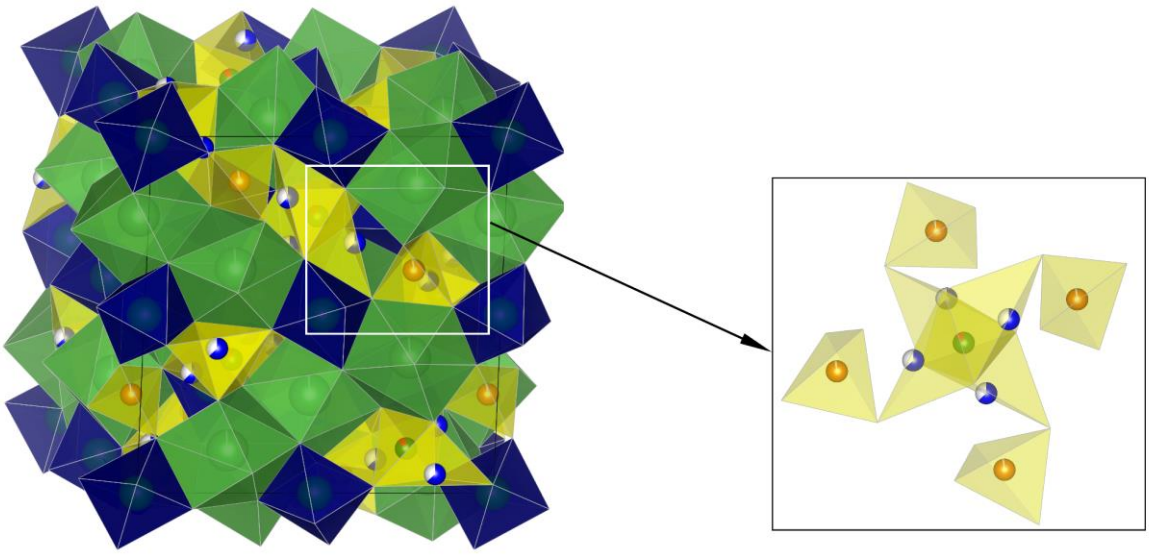

Figure 2.7. Li sites and suspected migration pathway in Ga and Fe substituted lithium garnets adhering $I\bar{4}3d$ type symmetry; all viewable atoms are Li. 12a Li is green, the 12b site is orange, the 48e site is blue and Ga is red. Adapted from reference[99].

Wagner *et al.* determined three Li^+ sites for Ga-LLZO and $Fe_xLi_{7-3x}La_3Zr_2O_{12}$ in the $I\bar{4}3d$ space group, see figure 2.7. Two Li sites correspond to the $Ia\bar{3}d$ tetrahedral 24*d* site but are split over the 12*a* and 12*b* sites. These differ in bond lengths and polyhedral distortions compared to $Ia\bar{3}d$. The third is a partially occupied 48*e* octahedral site[99, 101]. It was also suggested that Fe (and by extension Ga) substitutes preferentially on to the 12*a* site, which initiates the reduction in symmetry from $Ia\bar{3}d$ to $I\bar{4}3d$. The 12b site, conversely, has only minor Fe^{3+}/Ga^{3+} presence. Rettenwander *et al.* subsequently confirmed, *via* numerous compositions based upon $Al_{0.2-x}Ga_xLi_{6.4}La_3Zr_2O_{12}$ ($0 \leq x \leq 0.2$), that a critical concentration of 0.15 Ga *pfu* is required for the full transition to $I\bar{4}3d$[175]. The symmetry transition was shown to correspond to two distinct drops in activation energy between x = 0 (0.31 eV), x = 0.05 (0.28 eV) and x = 0.15 (0.26 eV). The first relates to Ga-Li repulsion, which was suggested to smooth the Li^+ migration

pathway compared to the $Al_{0.2}Li_{6.4}La_3Zr_2O_{12}$ analogue. The second (at Ga = 0.15) corresponds to the change from $Ia\bar{3}d$ to $I\bar{4}3d$ (as determined by DFT). A corresponding increase in conductivity was also observed, from 0.3 mS cm^{-1} at Ga = 0 to ≈1 mS cm^{-1} when Ga = 0.20[175]. Increased ionic mobility was additionally analysed by NMR relaxometry, which indicated these garnets have a different diffusion mechanism and faster Li^+ dynamics, supporting the conclusion of different symmetry[175]. These data explain why Ga-LLZO type garnets perform best when Li content is between 6.4-6.6 Li *pfu* (which is also further discussed generally in section 2.4.1.) and why it offers class leading performance compared to other garnet materials.

Table 2.1. Selection of lithium garnets synthesised by the solid-state route (SS), the sol-gel route (SG) and co-precipitation (CP). All Li_7 garnets have $I4_1/acd$ symmetry; garnets with < 7 Li pfu are reported $Ia\bar{3}d$ except Ga-LLZO which has $I\bar{4}3d$.

System	Synthesis method	Sintering Temp (°C) / Time (hrs)	σ_{bulk} (S cm^{-1}) / Temp (°C)	σ_{total} (S cm^{-1}) / Temp (°C)	Lattice parameter (Å)	Activation energy E_a (eV)	From Ref
$Li_5La_3Nb_2O_{12}$	SS	950/24	~10^{-6} / 25		12.762 (3)	0.43	[27]
$Li_5La_3Ta_2O_{12}$	SS	950/24	1.20 x 10^{-6} / 25	3.40 x 10^{-6} / 25	12.766 (3)	0.56	[27]
$Li_6SrLa_2Ta_2O_{12}$	SS	950/24	8.84 x 10^{-6} / 22	7.00 x 10^{-6} / 22	12.808(2)	0.50	[141]
$Li_6BaLa_2Ta_2O_{12}$	SS	950/24	5.38 x 10^{-5} / 22	4.00 x 10^{-5} / 22	12.946(3)	0.40	[141]
$Li_6CaLa_2Nb_2O_{12}$	SS	950/24	1.60 x 10^{-6} / 22	-	12.697(2)	0.55	[142]
$Li_6SrLa_2Nb_2O_{12}$	SS	950/24	4.20 x 10^{-6} / 22	-	12.811(1)	0.50	[142]
$Li_6BaLa_2Nb_2O_{12}$	SS	950/24	6.00 x 10^{-6} / 22	-	12.868(1)	0.44	[142]
$Li_{5.5}La_3Nb_{1.75}In_{0.25}O_{12}$	SS	950/24	1.80 x 10^{-4} / 50	-	12.821 (2)	0.51	[143]
$Li_{5.5}La_{2.75}K_{0.25}Nb_2O_{12}$	SS	950/24	6.00 x 10^{-5} / 50	-	12.7937(8)	0.49	[143]
$Li_7La_3Zr_2O_{12}$	SS	1230/36	5.11 x 10^{-4} / 25	7.74 x 10^{-4} / 25	12.9682	0.32	[28]
$Li_{6.25}Ba_{1.25}La_{1.75}Ta_2O_{12}$	SS	900/12	5.00 x 10^{-5} / 33	7.40 x 10^{-5} / 33	12.993(4)	0.40	[181]
$Li_6BaLa_2Ta_2O_{11.5}$	SS	900/24	1.81 x 10^{-4} / 50	1.51 x 10^{-4} / 50	12.9755 (4)	0.42	[182]
$Li_7LaSr_2Ta_2O_{12}$	SS	850/12	-	9.41 x 10^{-8} / 150	a. 13.0988(7), c. 12.480 (1)		[122]
$Li_7PrSr_2Ta_2O_{12}$	SS	850/12	-	1.88 x 10^{-5} / 150	a. 13.0289(6), c. 12.439 (1)		[122]
$Li_7NdSr_2Ta_2O_{12}$	SS	850/12	-	1.18 x 10^{-6} / 150	a. 13.0244(3), c. 12.4228(4)		[122]
$Li_7SmSr_2Ta_2O_{12}$	SS	850/12	-	5.29 x 10^{-6} / 150	a. 12.9965(6), c. 12.425 (1)		[122]
$Li_7GdSr_2Ta_2O_{12}$	SS	850/12	-	1.18 x 10^{-6} / 150	a. 12.9206 (1), c. 12.454 (1)		[122]
$Al_{0.24}Li_{6.24}La_3Zr_2O_{11.98}$	SS	1000/4	-	4.00 x 10^{-4} / 25	-	0.26	[154]
$Li_7La_3Zr_2O_{12}$ + 0.25 mol Al_2O_3 in alumina crucible	SS	900/24	-	1.81 X 10^{-4} / 25	12.945	0.37	[171]
$Li_7La_3Zr_2O_{12}$ + 0.25 mol Al_2O_3 in Pt Crucible	SS	900/24	-	4.48 x 10^{-4} / 25	12.967	0.32	[171]
$Li_{6.75}La_3Zr_{1.75}Ta_{0.25}O_{12}$	CP, SS	1000/4	-	8.70 x 10^{-4} / 25	12.96	0.22	[134]
$Al_{0.2}Li_{6.15}La_3Zr_{1.75}Ta_{0.25}O_{12}$	CP, SS	1000/4	-	3.70 x 10^{-4} / 25	12.95	0.30	[134]
$Ga_{0.2}Li_{6.15}La_3Zr_{1.75}Ta_{0.25}O_{12}$	CP, SS	1000/4	-	3.70 x 10^{-4} / 25	12.95	0.27	[134]
$Li_{6.5}La_3Zr_{1.75}Mo_{0.25}O_{12}$	SS	1250/4	3.40 x 10^{-4} / 25	-	12.964	0.36	[120]
$Li_{6.5}La_3Nb_{1.25}Y_{0.75}O_{12}$	SS	1100/6	2.70 x 10^{-4} / 25		12.9488(11)	0.36	[183]
$Li_{6.4}La_3Zr_{1.4}Ta_{0.6}O_{12}$	SS	950/12 (x2)	5.00 x 10^{-5} / 33		-	0.44	[151]
$Li_6La_3Zr_2O_{11.5}$	SG	1180/36	5.69 x 10^{-4} / 25	1.39 x 10^{-4} / 25	-	-	[154]
$Li_7La_3Zr_2O_{12}$	SG	700/12					[157]
$Al_{0.28}Li_{6.16}La_3Zr_2O_{12}$	SG	900/12		3.00 x 10^{-7} / 33			[155]
$Li_{6.4}La_{2.3}Na_{0.7}Nb_2O_{12}$	SG	750/6		1.60 x 10^{-4} / 25	12.776	0.41	[158]
$Li_7La_3Zr_2O_{12}$	SG	900/6/12	-	-	13.07793	-	[159]
$Li_5La_3Bi_2O_{12}$	SG	650/5		2.40 x 10^{-5} / 26	13.06 (6)	0.40	[164]
1.2 wt.% Al doped $Li_7La_3Zr_2O_{12}$	SG	1200/6	-	2.00 x 10^{-4} / 25	-	-	[162]
$Li_6BaLa_2Ta_2O_{12}$	SG	800/6	-	2.00 x 10^{-5} / 25	12.995(2)	0.40	[161]
$Ga_{0.15}Li_{6.55}La_3Zr_2O_{12}$	SG	800/6 in O_2		1.30 x 10^{-3} / 24	-	0.30	[98]
$Ga_{0.25}Li_{6.25}La_3Zr_2O_{12}$	SS	900/6, 1100/24		1.46 x 10^{-3} / 25	12.9733(6)	0.28	[100]

2.4.2.3. Defect Chemistry of Lithium Garnets

Aliovalent doping of lithium garnets is the most popular choice to form the room temperature stable cubic phase[41, 167, 171, 184]. This is often assumed to relate to formation of charge compensating lithium defects, see previous sections[28, 124, 130, 184-187]. For example, substitution on the Li site by Al leads to Li vacancies, to maintain charge neutrality, and can be considered as:

$$[Al_{Li}^{\bullet\bullet}] = 2V_{Li}^{/} \qquad 2.3$$

Such Li charge compensation defects have enabled a simplistic view of lithium garnet doping. However, this approach oversimplifies defect formation in general, but especially in complex systems such as lithium garnets[185].

Numerous studies have suggested formation of oxygen vacancies, which could play a significant role in the lithium garnet defect chemistry[146, 188-193]. As oxygen vacancies can act as electronic donors, their presence has been suggested to affect lithium stoichiometries through a charge compensating Schottky pair mechanism, which is thought to arise from Li_2O volatilisation at >600 °C as per:

$$2Li_{Li}^{X} + O_{O}^{X} \rightleftharpoons 2V_{Li}^{/} + V_{O}^{\bullet\bullet} \qquad 2.4$$

Nyman *et al.* was the first to experimentally suggest oxygen vacancies could form during a modified synthesis of $Li_5La_3M_2O_{12}$ (M = Nb, Ta), but lacked suitable oxygen sensitive techniques to confirm[193]. Oxygen vacancies were first observed by Kubicek *et al.*, using isotope exchange 3D depth profiling with ^{18}O, which enabled characterisation of oxygen vacancies and interstitials. Kubicek *et al.* found that (in $Li_{6.25}Al_{0.25}La_3Zr_2O_{12}$, $Li_{6.5}La_3Zr_{1.5}Nb_{0.5}O_{12}$ and $Li_{6.5}La_3Zr_{1.5}Ta_{0.5}O_{12}$) oxygen vacancy levels can be as high as 2.5%, thus impacting lithium ion conductivities *via* reduced Li stoichiometries[189]. Therefore, certain sintering strategies, such as higher temperatures or lower oxygen partial pressures, could enhance oxygen vacancies. Later, Kuganathan *et al.* confirmed, *via* a computational study, that oxygen vacancies did arise from Li_2O volatilisation, thus confirming the prior suggestion from Nyman *et al.*[193, 194].

Oxygen vacancies alone indicate the difficulties in assessing lithium garnet defects by a simple Li charge compensation approach. However, additional native defects are often discussed in minimal detail. Cationic lattice defects, such as Nb, Zr and La vacancies, are assumed to be negligible[191], which is not the case and these are dependent upon synthesis condition[185]. Secondly, oxygen and all common garnet dopants (such as La, Zr, Nb and Ta) are assumed in a singular charged state (such as La^{3+} or Zr^{4+})[190, 195]. As multiple garnet valence states would enable electronic conduction they are, often,

assumed absent, however this is not necessarily so (especially under reducing conditions). Zhu *et al.*, *via* XPS (using an ultra-high vacuum transfer stage and 500 °C annealing step) reported that $Li_{6.25}Al_{0.25}La_3Zr_2O_{12}$ and $Li_{6.5}La_3Zr_{1.5}M_{0.5}O_{12}$ (M = Nb, Ta) had strong Zr^{2+} signals while $Li_{6.5}La_3Zr_{1.5}Nb_{0.5}O_{12}$ had multiple Nb oxidation states which propagated through the bulk, thus reducing cycling stability. Furthermore, Squires *et al.* computationally suggested that oxygen vacancies under highly reducing conditions can exhibit 0, +1 and +2 charge states, and can act as colour centres trapping electrons[185, 188]. Therefore, the assumption of a single charged state is an oversimplification.

Squires *et al.* also suggested, *via* a DFT study, that garnets have numerous lithium and oxygen defects (as previously reported), in addition to a significant number of cation antisite defects. Squires *et al.* reported Li vacancies are not the dominant compensating acceptor defects under all synthesis conditions, finding those conducted under Li-rich/Zr poor conditions are primarily compensated by Li_{Zr} antisites (which extends to other antisites, such as Li_{La}, La_{Zr} and Zr_{Li}, dependent upon conditions). Therefore, lithium stoichiometries were found to deviate significantly from a simplistic Li charge compensating mechanism, however the defect chemistry of lithium garnets is still not well understood.

This, therefore, leads to complex issues during sintering of garnet materials, especially when optimising lithium content and thus, conductivity. As many techniques lack Li sensitivity it is often a non-trivial task to accurately ascertain the Li content within a material. Such complex defect chemistry undoubtedly affects lithium garnets and causes unexpected sintering behaviour (outside of reduced Li stoichiometry), but to what extend remains unclear. Complex defect chemistry prediction requires computational chemistry; however, this remains expensive for regular use and is based upon a zero entropy reference state (perfect ordered lattice) over a relatively small number of atoms, while it remains unknown how to address the Li disorder within the model[185]. Hence, an understanding of defects in real world systems lacks clarity. Therefore, despite great interest in untangling such complex defect chemistry, the simple Li charge compensated defects arising from extrinsic doping remains the most commonly used model.

2.4.2.4. Lithium Garnet Impurities

Lithium garnets commonly follow extrinsic doping techniques based upon the similar crystal chemistry amongst groups, for example both $Li_7La_3M_2O_{12}$ (M = Zr, Hf) and $Li_5La_3M_2O_{12}$ (M = Nb, Ta) are easily formed. However, despite the similar chemistry, Hf and Ta based garnets differ in conductivity compared to their Zr and Nb counterparts[27, 28, 116, 133, 146, 156, 190, 193, 196-203]. Such differences are problematic, as the simplicity of substitution amongst similar elements likely enables bulk integration of extrinsic dopants from precursor impurities.

Oxide/nitrate/hydroxide precursors, currently, cannot be fully purified. Therefore, even elements with high purity, such as semi-conductor grade Si (≥99.99999%), still retain some small impurities[204]. Therefore, all garnet precursors will have some impurities. However, most are available cheaply at battery grade (≥99.95%) purity, such as Al_2O_3, Ga_2O_3 and La_2O_3. This minimises potential impurity concerns and explains the current lack of unintentional extrinsic dopant defect studies within garnet materials, as in a controlled synthesis (for example with no unintentional Al) there will be negligible impact at this stage of lithium garnet development. However, one exception is the Zr and Hf salts, which remain difficult to purify from each other (for example, ZrO_2 is commonly available at >99% purity, metals basis excluding Hf, with HfO_2 ≤2%)[205-207].

Mann *et al.* systematically investigated the effect of Hf impurities with $Li_{6.45}Al_{0.05}La_3Zr_{1.6-x}Hf_xTa_{0.4}O_{12}$ by using high purity ZrO_2 (< 100 ppm Hf), in addition to the ZrO_2 mentioned above. It was reported that ionic conductivity decreased when x = > 0.1, due to the decreased unit cell parameters arising from the smaller ionic radii of Hf (0.71 Å) compared to Zr (0.72 Å)[203]. However, the reported conductivity differences were small, such as 0.6 mS cm^{-1} (x = 0.048) compared to 0.578 mS cm^{-1} (x = 0.4). Mann *et al.* progressively added Hf into $Li_{6.45}Al_{0.05}La_3Zr_{1.6-x}Hf_xTa_{0.4}O_{12}$ yet observed no linear lattice parameter relationship. This disregards Vegard's Law which should yield some form of approximate linear relationship. This indicates unexpected stoichiometries or other unknown factors, especially as linearity was observed by Ladenstein *et al.* with $Li_{7-x}La_3Hf_{2-x}Ta_xO_{12}$ ($0 \leq x \leq 2$). Therefore, the role of Hf impurities remains unclear[203]. Nonetheless, Hf based garnets are inferior in terms of conductivity, as reported elsewhere[116, 199-202], and thus Hf impurities require minimisation if possible.

Similarly, Ta and Nb impurities affect garnet performance. Here Ta is commonly reported to be superior, with both Tong *et al.*[208] and Xiang *et al.*[209] reporting improved performance with $Li_{6.4}La_3Zr_{1.4}Ta_{0.6}O_{12}$ compared to the Nb analogue. Both Nb and Ta precursors are easier to purify than Zr/Hf salts, with Nb_2O_5 and Ta_2O_5 often >99.9% pure for synthesis, but the specific effects of impurities are yet to be studied. However, the sub valence states of Nb and Ta garnets (considered rare under

most circumstances) in the presence of highly reducing Li metal has been reported. Here, XPS was used which, although giving no indication of bulk impurity formation, indicates the complexities arising from hard to detect impurity phases. Zhu *et al.* reported that Ta, Nb and Al dopants in LLZO cause Zr^{4+} reduction to Zr^{2+} [190]. It was reported that Zr reduction led to an oxygen deficient interphase at the Li metal interface, with the quantity increasing on the order of Ta < Nb < Al. However, the Nb doped LLZO additionally formed lower valent Nb species (Nb^{1+}, Nb^{2+}, Nb^{3+} and Nb^{4+}) which were suggested to propagate into the bulk based upon increasing ASR (which was not seen with the Ta and Al dopants). This, possibly, explains why Ta based garnets perform better (especially in contact with Li) and highlights the potentially large detrimental effect of Nb impurities within Ta doped LLZO garnets. However, the work by Zhu *et al*. lacks starting material purities, therefore it is difficult to assess the role of precursor impurities in this work[190, 210].

Overall, the extent of lithium garnet impurities requires further investigation, but studies suggest some performance differences. These impurities are present in very low quantities, hence are often below the limits of many elemental analysis techniques, such as EDX and XRF, instead requiring more sensitive analysis techniques such as inductively coupled plasma mass spectrometry. These are also further compounded by synthesis, whereupon numerous unwanted impurities (based upon starting materials) can form. For example, reaction intermediaries, such as $Li_6Zr_2O_7$ and Li_2ZrO_3 (in LLZO), will form if synthesis time is too short. These are poor Li conductors that segregate to the grain boundaries and block Li transport. Conversely, pyrochlore impurities can form if the reaction time is too great, which have no Li conductivity and greatly impact sinterability, see section 2.5.1.

Further information regarding Al impurities is available in section 2.4.2.1., whereas issues relating to proton exchange are in section 2.5.2. Concerns relating to tetragonal Li garnet impurities were discussed in section 2.4.1, whereas microstructural defects can be found in section 2.5.1.

2.5. Lithium Garnet Disadvantages

The benefits of lithium garnet materials have been discussed above, this includes their wide electrochemical window, high ionic mobility, easy synthesis, non-toxic nature, Li metal stability and high safety. However, numerous issues remain; the high temperature/time consuming synthesis, and ionic conductivity which, although good, is not achievable without specialised equipment and, even if achieved, is insufficient at lower operating temperatures, such as 0 °C. Lithium garnets are also prone to atmospheric H^+/Li^+ exchange (which forms insulating Li_2CO_3 across the grain surface and much increased interfacial resistance) and lithium dendrite formation; these are covered in section 2.5.2. and 2.5.4., respectively.

2.5.1. General Garnet Issues

Lithium garnet materials are ceramics and suffer from the general issues relating to solid state synthesis and ionic conductors; high temperature/energy demanding powder synthesis which requires subsequent densification into pellets/membranes to examine the material properties (with denser membranes leading to higher performing materials due to intimate contact at the grain boundary). Lithium garnets, despite much work to reduce initial sintering temperatures, still require high temperature heat treatments (700 - 1050°C) for long periods of time (12 - 36h) to synthesise. This is then followed by densification, which is generally achieved with further high temperature treatments above the initial sintering temperature for equally long time periods (≈1050 - 1200 °C), which do not guarantee high density samples will be formed. Furthermore, lithium volatility during the high temperature densification treatment becomes increasingly problematic, consuming the excess added during synthesis (*via* Li evaporation from the vessel) and enabling formation of a pyrochlore type phase (for example $La_2Zr_2O_7$ in LLZO). This has no lithium conductivity and disrupts densification of the remaining material (as the pyrochlore content is increased as Li is consumed further)[168, 211, 212]. This is also true of the $LaAlO_3$ impurity in Al doped garnets, see section 2.4.2.1.

Microstructural defects, such as porosities, grain boundaries and flaws, are naturally present during ceramic densification, as the material is processed below the melting point and relies upon grain growth into neighbouring grains to densify. Therefore, densification by high temperature treatments is inherently slow (due to limitations of atomic diffusion in the solid-state) and cannot always be maintained for very long time periods due to phase instabilities (and cost), as is the case with lithium garnets. Microstructural defects can considerably reduce conductivity in lithium garnets (as gaps and voids throughout the SSE are intrinsically insulating) and degrade cell performance (see section 2.5.3

and 2.5.4.). Therefore, much work has been done to mitigate these issues and minimise microstructural defects.

Some garnet reports have used sintering aids, which melt at lower temperatures (such as Li_3BO_3, LiF and LiCl), to increase relative density. These can degrade performance if the grain boundaries are plated with lesser ionic conductors than the garnet material and/or react to form impurity phases[155, 170, 213]. Therefore, the sintering aid approach is a balancing act between higher densification but potentially lesser performance. Cold sintering is another approach and has seen some promising results; however, the best work often uses polymeric compounds (to bind grains together at low temperatures) which are much poorer ionic conductors than pristine garnet materials, which can also induce additional grain boundary impurities[214, 215]. The polymeric suspension of garnet grains also essentially eliminates the Li_2CO_3/LiOH removal methods, which contribute enormously to electrode/electrolyte resistance (see next section). The softer nature of the polymers can also help to reduce the intrinsic solid-solid resistance, however, does so at the cost of easier lithium dendrite penetration[215]. Cold sintering requires specialised equipment, which is not readily compatible for glovebox use, therefore restricting processing under inert gas. Hence to date, cold sintering has not seen the performance of the solid-state route, with relative densities ≈85% being achieved[214-217].

All the above processes usually result in the powders forming circular pellets with a diameter in the centimetre range. Ceramic pellets are inherently brittle, and fracture easily which thus limits minimum thickness to ≈1 mm. However, garnet pellet formation also tends toward rapid H^+/Li^+ exchange (from atmospheric moisture) which forms passivating and insulating Li_2CO_3 layers within minutes. The exchange is so rapid that surface bound LiOH and Li_2CO_3 can from residual moisture and carbon dioxide in a glovebox (< 0.5 ppm H_2O, < 5 ppm CO_2) within 5 minutes (see section 2.5.2.)[218]. The exchange needs to be excluded for high density; therefore, powders require atmosphere-controlled processing and/or significant sacrificial powder.

These pellet sized samples are not applicable for use in full scale batteries. Thin films (≈50 µm) are required to reduce electrolyte mass and volume in commercial cells, and to enable layered battery architectures which give high energy density. This is a developing field but early indications have shown difficulty with fabrication of garnet membranes (usually LLZO based). At the µm level, evidence suggests the 3D network for ionic migration is compromised, reducing $\sigma_{25°C}$ to ≈10^{-7} - 10^{-5} S cm $^{-1}$ [35]. Some recent reports, with commercially expensive techniques, have seen conductivities of ≈ 0.1 mS cm^{-1}, but this remains below the original report of LLZO by Murugan *et al.* at 0.5 mS cm^{-1}. This area is, nonetheless, very exciting but is unrelated to this work directly. No thin films were made in this work;

hence the specific complexities of this area will not be discussed further although required mentioning due to its importance. This work is aimed at exploiting the comprehensive elemental options available to lithium garnets to optimise various properties, but it is hoped this work will provide some benefit to the thin film regime.

However, air stability (proton exchange), interfacial resistance and the mechanical instabilities of lithium metal anodes require discussion.

2.5.2. Air Stability - Proton Exchange

Lithium garnet materials are unstable with respect to moisture. This is a particular problem when handling in standard atmospheric conditions which, inevitably, have some humidity. Hydrogarnets, such as $Ca_3Al_2(OH)_{12}$, $Sr_3Al_2(OH)_{12}$, $Sr_3Ga_2(OH)_{12}$ and $Sr_3Fe_2(OH)_{12}$, have been known for sometime[219], however lithium garnets were initially considered stable toward moisture. It has since been determined this is not the case and is in fact quite the opposite. Lithium garnets undergo proton exchange rapidly in the presence of moisture with H^+ exchanging with Li^+. Lithium is released in the form of LiOH which combines with atmospheric CO_2 to form passivating Li_2CO_3 layers across the grain surface within minutes, as determined by controlled tests using ultrahigh vacuum transfer to an X-ray photoelectron spectrometer[218]. This reaction reduces overall Li concentration in the system, occurs on the grain surface and passivates the grains with ionically insulating Li_2CO_3 impurities (but is harmless from a safety perspective). This degrades total system conductivity, especially as it is the grain boundary characteristics which are key to total system conductivity.

A complete consensus has not been reached on the reaction mechanisms between lithium garnets, CO_2 and H_2O, but was initially thought to correspond to equation 2.5:

$$Li_{56}La_{24}Zr_{16}O_{96} + H_2O_{(g)} \rightarrow Li_{54}La_{24}Zr_{16}O_{95} + 2LiOH \qquad \Delta G = -0.53\ eV \qquad 2.5i$$

$$Li_{56}La_{24}Zr_{16}O_{96} + CO_{2(g)} \rightarrow Li_{54}La_{24}Zr_{16}O_{95} + Li_2CO_3 \qquad \Delta G = -1.99\ eV \qquad 2.5ii$$

This suggests a direct reaction with CO_2 was energetically preferential and it was reported proton exchange in lithium garnets could occur even in dry conditions[43, 128, 220, 221]. Later, Sharifi *et al.* proposed positive ΔG values for equation 2.5*i* and 2.5*ii*, thus indicating an unfavorable protantion route. This also corresponded to the observation of much-reduced Li_2CO_3 formation in dry air[221]. Instead, a two-step reaction was put forward involving formation of LiOH followed by carbonation from CO_2. This corresponded succinctly with experimental results and gave negative ΔG values, as per equation 2.6:

$$Li_{56}La_{24}Zr_{16}O_{96} + H_2O_{(g)} \rightarrow Li_{55}HLa_{24}Zr_{16}O_{96} + LiOH \qquad \Delta G = -0.34\ eV \qquad 2.6i$$

$$LiOH + \frac{1}{2}CO_{2(g)} \rightarrow \frac{1}{2}Li_2CO_3 + \frac{1}{2}H_2O_{(g)} \qquad \Delta G = -0.35\ eV \qquad 2.6ii$$

Li_2CO_3 layers vary in thickness, as proton exchange continues beyond initial surface bound exchange due to Li^+ diffusion from the grain interior[220]. This thickens the exchanged layer as per equation 2.7:

$$LiOH + H_2O_{(g)} \rightarrow LiOH \cdot H_2O_{(g)} \qquad 2.7i$$

$$2LiOH \cdot H_2O + CO_{2(g)} \rightarrow Li_2CO_3 + 3H_2O_{(g)} \qquad 2.7ii$$

Irrespective of the definitive protonation route, it is a prevalent issue amongst garnet research, with Li_2CO_3 passivating layers readily forming on the pellet surface and propagating along grain boundaries, which continually removes Li^+.

Nyman *et al.* first reported Li^+/H^+ exchange with $Li_5La_3M_2O_{12}$ (M = Nb, Ta) when deliberately dispersed in water. This gave a pH rise to 10-11 in aqueous medium, but was undertaken deliberately as part of a synthesis strategy to vacate the octahedral sites, therefore did not elucidate the instability of lithium garnets toward moisture[222]. Galven *et al.* subsequently assessed $Li_7La_3Sn_2O_{12}$ and found spontaneous proton exchange indeed occurs under ambient conditions (as per $Li_{7-x}H_xLa_3Sn_2O_{12}$)[223]. Follow up ND and NMR (^6Li, ^7Li, and ^{119}Sn) studies on both the tetragonal tin system and $Li_5La_3Nb_2O_{12}$ confirmed this exchange can be generalised to all garnets. The exchange was found to enable a phase transition from $I4_1/acd$ to $Ia\bar{3}d$ and from $Ia\bar{3}d$ to $I2_13$ in $Li_7La_3Sn_2O_{12}$ and $Li_5La_3Nb_2O_{12}$ respectively. It was subsequently suggested that proton exchange occurs readily at any garnet stoichiometry when Li > 3 *pfu*[224]. Galven *et al.* also suggested the apparent increase in unit cell dimensions arose from the replacement of Li-O bonds with weaker O-H---H bonds. These form a hydrogen bonding network throughout the crystal framework, thereby expanding the unit cell.

Larraz *et al.* proposed low temperature hydration or ambient ageing of $Li_{7-x}H_xLa_3Zr_2O_{12}$ leads to the $I\bar{4}3d$ space group[179], which was confirmed later by Orera *et al.*, when $Li_{7-x}H_xLa_3Zr_2O_{12}$ ($0 \leq x \leq 5$) was analysed by ND. The symmetry changes were found to be dependent upon proton content and the exchange temperature. Orera *et al.* reported that tetragonal LLZO, aged ambiently for three years, mostly transitioned to the cubic phase, although a clear tetragonal component remained. This complicated an in-depth structural analysis, but nonetheless confirmed proton exchange. Thermal treatment at 150°C led to a single cubic phase, with inductively coupled plasma analysis confirming the formula $Li_{2.2}H_{4.8}La_3Zr_2O_{12}$. ND data suggested this conformed to the $I\bar{4}3d$ space group, with H^+ located in the 48*e* octahedral sites with Li^+ in the 12*a* and 12*b* sites. Orera *et al.* then annealed LLZO > 300 °C; this gave a $H^+ \approx 1.5$ *pfu* but *a*dhered to $Ia\bar{3}d$ symmetry, with H^+ located in the octahedral 96*h* site[225].

Larraz *et al.* investigated this tetragonal-cubic phase transition in LLZO, as other reports had also detailed a transition occurring 100 - 200 °C, rather than the originally reported 650 °C[124, 198]. It was determined the lower temperature transition was due to water molecules, either residing within the garnet framework or due to proton exchange.

Jin *et al.* later confirmed proton exchange readily occurs between humid air and LLZO and does not require significant ageing. This was shown to degrade pellet integrity, ionic conductivity and cell performance compared to those pellets protected from moisture[223, 226]. Ma *et al.*, using a similarly

substituted $Li_{7-x}H_xLa_3Zr_2O_{12}$, measured H^+ content as high as 63.6% but registered no phase change away from $Ia\bar{3}d$ to $I\bar{4}3d$ type symmetry, as reported prior by Orera *et al.* Here, proton exchange preferentially occupied the 96*h* site[227]. Once Li from this site was depleted, H^+/Li^+ exchange then proceeded *via* the 48g site, the 24d site remained wholly occupied by Li^+. This complicates the suggestion of the transition to $I\bar{4}3d$ type symmetry, as this is ascribed to splitting of the 24*d* tetrahedral site into the 12*a* and 12*b* sites, yet no H^+ was reported on the tetrahedral sites to cause the splitting. Later, Yow *et al.* analysed $Li_{6.6}La_3Zr_{1.6}Ta_{0.4}O_{12}$ immersed in either water or 1M LiOH solution for 7 days, finding Li contents of 3 and 5 *pfu* respectively, and found the $Ia\bar{3}d$ space group was retained. This was conducted on both pellets and powder and a total exchange of 53.4% and 8.8% was recorded respectively (via FTIR, pH and TGA), illuminating the uncontrolled nature of proton exchange within Li garnets[228].

Larraz *et al.* further suggested proton exchange occurred preferentially on the octahedral site, as did Li *et al.* with $Li_{6.5}La_3Zr_{1.5}Ta_{0.5}O_{12}$ (48*g*)[229], Galven *et al.* with $Li_{6-x}H_xCaLa_2Nb_2O_{12}$ (48*e*)[180] and Truong *et al.* with $Li_5La_3Nb_2O_{12}$ (96*h*)[230]. Therefore, reports agree that H^+/Li^+ exchange is confined to the more mobile octahedral sites, albeit with discrepancies with respect to the Wyckoff positions. However, only those reports using ND have suggested formation of the $I\bar{4}3d$ space group, with this being additionally confined to high levels of proton exchange. Determination of $I\bar{4}3d$ symmetry is not readily accomplished by other means as discussed in section 2.4.2.2..

Protonated layers have been reported to be 10 - 100 nm thick in lithium garnet materials and up to 1 µm after 6 months[220]. The low $\sigma_{200°C}$ of 10^{-8} S cm^{-1} of Li_2CO_3, and its tendency to passivate the grain surface, gives much decreased total system conductivity, especially as exchange primarily occurs from the more mobile Li^+ octahedral sites[128, 231]. Protons also sit on the Li sites, therefore also hinder the movement of the remaining Li^+. For example, Al-LLZO reduced from 1.81 x 10^{-4} S cm^{-1} to 2.39 x 10^{-5} S cm^{-1} after 3 months of air exposure[171]. The proton exchange mechanism can also induce formation of impurity phases, often $La_2Zr_2O_7$ (in LLZO), and this has also been proposed to enable spontaneous fractures to appear within the electrolyte pellet due to internal stress[232, 233]. These protonated layers subsequently cause high interfacial resistance, which is a substantial issue and is discussed in the succeeding section.

This presents complex handling requirements for garnet materials, as ambient conditions invariably lead to unavoidable proton exchange unless powders are fully processed under a controlled atmosphere. Reports from Zhu *et al.* have shown that proton exchange on pristine garnets reforms surface impurities in as little as 5 minutes when placed in an Ar glovebox with only residual moisture

present. These pellets were analysed by a special ultra-high vacuum transfer system from a glovebox environment which enabled annealing at 500°C before direct analysis by X-ray photoelectron spectroscopy (XPS). Firstly, garnet pellets were polished and transferred to the XPS. This confirmed most of the proton exchange layer had been removed, leaving only LiOH likely from residual moisture in the glovebox. The residual layer was completely removed by transferring *via* the UHV system and annealing at 500°C. Pellets, when placed back into the glove box after the XPS, then started to reform surface contaminants within 5 minutes, with a full return to a similar LiOH content observed post polishing within 3 hours[190].

Hence, the highest performing reported lithium garnets are processed under tightly controlled atmosphere conditions, such as the report by Bernuy-Lopez with $Ga_{0.15}Li_{6.55}La_3Zr_2O_{12}$ with the high $\sigma_{25°C}$ of 1.3 mS cm^{-1} [98]. Recent work has also established class leading results for thin films between 50 – 250 µm giving a $\sigma_{25°C}$ of 0.39 mS cm^{-1} (with $Al_{0.05}Li_{6.45}La_3Zr_{1.6}Ta_{0.4}O_{12}$) in tightly controlled conditions[234].

2.5.3. Interfacial Resistance

SSEs, in general, are hard crystalline or glassy materials which are required to operate in a device with two similarly hard electrode materials, hence there is poor wetting between these surfaces when compared to solvent based electrolytes and therefore a high interfacial resistance. This resistance is so high that it is arguably the primary barrier towards commercialisation of an all-solid state cell, in addition to further refinement of the electrolyte system. The fundamental issues regarding the large interfacial resistance with lithium garnets stems from two fundamental interfacial problems. Firstly, that of Li_2CO_3 formation on the garnet surface and secondly the inability of current technology to create atomically flat surfaces that perfectly align at the solid-solid interface with no gaps or voids. The latter of these is out of reach for current device fabrication strategies but general improvements in interfacial charge transfer and increased charge carrier mobility can mitigate this problem. However, the formation of Li_2CO_3 has seen considerable work to overcome. The cathode/garnet interface does not form the basis of this work, hence only the lithium metal/garnet interface is specifically considered below.

Arguably the most simple way to remove surface bound Li_2CO_3 and LiOH is to reverse the proton exchange, which is readily accomplished by annealing the sample at high temperature, usually > 750°C[235]. This, however, still presents a problem as the material invariably will require handling again in ambient conditions, as if it were possible to form the materials and exclude ambient moisture this would have been done in the first instance. Unfortunately, common laboratory gloveboxes struggle to deal with even small muffle furnaces without additional heat extraction. If the sample were reheated in a tube furnace to reverse the exchange, this would invariably contact with humidity without additional precautionary steps, such as forming of Li deficient layers and burying in significant excess mother powder. Therefore, ideally, heat treatments need to be conducted wholly within a glovebox.

As proton exchange is surface bound, mechanical polishing (either dry or wet) removes Li_2CO_3 and LiOH and is additionally desirable as it creates flat surfaces, which decreases the number of gaps and voids. Dry polishing involves sanding of the garnet pellet with increasingly higher grit abrasive papers (for example from 240 to 4000 grit). Wet polishing firstly involves sanding to a high grit, followed by additional polishing with a cloth and aprotic polishing agents, this can yield a flatter surface. Polishing to a mirror finish, after transferring pellets to an Ar glovebox, can substantially reduce area specific resistance (ASR) between the garnet and Li metal from ≈10000 Ω cm^2 to ≈100 Ω cm^2 [152, 220, 236, 237]. This was first reported by Cheng *et al.*, whereupon interfacial resistance was decreased to 109 Ω cm^2 in polished samples compared to 960 Ω cm^2 for unpolished, suggesting that the high resistance is not an

intrinsic property of lithium garnet electrolytes[220]. Later, it was also systematically shown that higher quantities of Li_2CO_3 lead directly to larger interfacial resistance, as measured by Li metal wetting contact angles, confirming that lithium garnets are not intrinsically lithophobic[221]. Here, unpolished LLZO pellets had Li metal contact angles of 142 - 146°, which is similar to Li_2CO_3 at 142°. However, once LLZO samples were wet polished and heated to 500°C to reverse proton exchange the contact angle reduced to 95°; this gave interfacial resistance of 2 Ω cm^2. DFT calculations actually suggested the contact angle could be as low as 62°, but this is difficult to confirm as eliminating proton exchange is a non-trivial task[238]. Slightly later, Wu *et al.* calcined Ga-LLZO at 900°C for 24h in air to reverse proton exchange and create Li-deficient La-Zr compounds, which protected the garnet interior from proton exchange. This, after sanding in a glovebox, yielded a Li_2CO_3 free surface, as confirmed by XPS and Raman spectroscopy, which gave an improved 56° Li metal contact angle but, curiously, much higher resistance than Sharifi *et al.* at 49 Ω cm^2 (*vs* 2 Ω cm^2) but this required the application of pressure and Wu *et al.* used only a melting process to form the lithium symmetry cell[239]. These reports of the lithophilic nature of garnets were also further substantiated by the same group with $Li_{6.4}Al_{0.2}La_3Zr_2O_{12}$ (65°) and $Li_{6.4}La_3Zr_{1.4}Ta_{0.6}O_{12}$ (59.5°)[239].

Li_2CO_3 and LiOH can be removed *via* surface reactions, for example with acids. These are not only easy but could be argued to a be a requirement in garnet processing, as Li_2CO_3 and LiOH propagate throughout the sample, plating the exposed grain boundaries which are inevitably present at any ρ_{rel} < 100% and scale accordingly as electrolyte porosity increases. However, use in conjunction with mechanical polishing is desirable, as this creates flat surfaces for increased solid-solid contact and ensures any residual proton exchange that occurred since treatment is removed.

Huo *et al.* reported acidic treatment of $Li_{6.5}La_3Zr_{1.5}Ta_{0.5}O_{12}$ pellets with HCl or H_3PO_3 reduced interfacial resistance to 26 and 7 Ω cm^2 respectively[240]. The use of H_3PO_4 was more successful due to creation of the lithophilic Li_3PO_4, which reacted favourably to form an SEI type layer of Li_3P. Such acid treatment of garnets also extends generally to other strong/weak acids such as H_2SO_4[241]. However, acid treatment decreases conductivity due to corrosion and increased porosity, thus compromising the pellet density. Non-acidic routes, such as washing pellets with zinc nitrate solutions, have been proposed. Here, Zhong *et al.* washed $Li_{6.4}La_3Zr_{1.4}Ta_{0.6}O_{12}$ pellets to form an intermediary layer of Zn, $ZnLi_x$ alloys, Li_3N and Li_2O with Li metal to reduce interfacial resistance[242]. This gave high cycling rates (> 4 mA cm^{-2}) and excellent coulombic efficiency (>99.5%). However, proton exchange was not discussed in any depth, despite garnets being processed and polished in air and using a $Zn(NO_3)_2{\cdot}4H_2O$ solution. Furthermore, no impedance spectroscopy was undertaken to assess the interfacial resistance. Recently, trace

amounts of molten Na (0.05%) have been used to remove Li_2CO_3 and thus enhance Li metal wetting, giving interfacial resistance as low as 1 Ω cm^2 and cycling current densities of 1 mA cm^{-2}, however any additional effect of residual Na on charge carrier mobility was not discussed[243].

Artificial interlayers have proven promising to decrease interfacial resistance, while enabling high current densities and lithium dendrite prevention. These strategies present a flexible approach, as they can be accomplished by deliberate introduction of extrinsic defects or *via* subsequent addition of interlayers (such as sputtering or atomic layer deposition). These often focus upon addition of elements which can alloy during the lithium stripping and plating process, such as Au[244], Ag[245], Ge[246], Si[247], Al[248], Zn[249] and Sn[250], with some highly interesting reports on the use of candle soot[251] building on the work of lithiated graphite at the interface[46, 251, 252], all of which have shown interfacial resistance in the tens of ohms. Passivating thin interlayers have been added to the garnet interface which improve Li metal wettability, such as Al_2O_3[41], SnO[250, 253], MoS_2[254], Cu_3N[255] and SiN_4[256] these enable low resistance but remain thin enough so as not to degrade charge carrier mobility. As of yet, no ideal solution to the problem of interfacial resistance has been proposed[29, 44, 257].

However, the issue of incomplete solid-solid contact remains, even with the increased plastic deformation of Li metal. This arises from the intrinsic issues of solid-solid interfaces but is made considerably worse during cell operation, whereupon the chemo-mechanical phenomena which dictate electrochemical behaviour remain limited compared to solid-liquid interfaces. In such circumstances, Li stripping, especially at high current densities and areal capacities, drives loss of contact creating voids which constricts the current. This is now suggested to be the primary cause of cell failure[258-260] and the morphological changes at the Li metal interface are amongst the greatest challenges in achieving fast rate capable SSBs[261]. It is thought that voids form when the flux of Li^+ migration away from the metal/garnet interface exceeds the metallic Li transport. Hence the lost Li^+ is unable to be replenished *via* creep and diffusion from the Li metal[260, 262-267], as per equation 2.8.

$$J_{Li\ diffusion} + J_{Li\ creep} < J_{Li^+ migration} \qquad 2.8$$

As this process is repeated, and/or with increased current density, void formation increases. This enables large cell polarisation and high local current densities which enable dendrite nucleation and growth, thereby restricting charging capability (see next section)[43]. As these migration issues can occur at relatively low current densities, they are currently suggested to be of more concern than the generally discussed garnet critical current density (CCD).

Application of high external stack pressures (on the order of >100 MPa) can prevent void formation and enable negligible interfacial resistance, as the pressure driven creep of lithium metal replenishes the voids at the interface[260, 261]. It has been suggested a "critical stack pressure" is required and that this scales with increasing current density[261]. For example, a critical stack pressure of 2MPa with Li/LLZO was required to achieve 0.4 mA cm^{-2}. However, current LIBs are assembled with stack pressures between 0.1 - 1 MPa and cycling current densities which range ≈1 - 3 mA cm^{-2}, therefore making the high stack pressure approach unfavourable from a commercial perspective[261, 268-270]. Void formation represents an emerging field, as the combination of the limited air stability of Li metal while attempting to measure the contributions of stress, reactivity, contact and the dynamics of Li/Li^+ transport is challenging[102, 271].

2.5.4. Lithium Dendrites

The chemical stability of lithium garnet materials with lithium metal is amongst one of its most promising aspects. However, although garnets are rigid ceramics and have a Li ion transfer number close to unity (which could effectively suppress dendrite growth), lithium metal stability presents numerous mechanical challenges, as Li deposits unevenly during cell cycling. This enables nucleation of lithium dendrites which grow readily along grain boundaries at a certain critical current density (CCD). Reports also indicate dendrites can pierce singular grains. Dendrites eventually grow and connect electrodes, causing a short circuit which presents numerous safety concerns. These dendrite nucleation and growth mechanisms are not well understood as, although these phenomena can be investigated by numerous techniques, characterisation of the electrolyte/electrode interface *in-operando* is exceptionally challenging. Therefore, it remains unclear what properties a lithium garnet requires to supress dendritic growth.

The Monroe-Newman model (used for polymer electrolytes) has previously predicted any electrolyte with a room temperature shear modulus > 8.5 GPA should resist Li dendrite growth. This was initially applied to SSEs and lithium garnets far exceed this predicted value, with a shear modulus of 58 - 60 GPa[272-274]. The reality is more complex. Garnet materials are not easily formed by the single crystal route and synthesis is usually in powder form, of varying morphologies, which is pressed into a pellet. These invariably have grain boundaries, pores and cracks which compromise the structural integrity of the membrane. Additionally, grain boundaries in lithium garnets are also reported softer than the bulk[275]. It is along these imperfections which lithium dendrites propagate and can do so at very low current densities[274, 276, 277]. Therefore, for this reason the Monroe-Newman model is generally not considered valid for garnets and SSEs in general[103, 273, 275, 278].

High density pellets help to reduce dendrite growth; but no powder method results in perfect density (ρ_{rel} = 100%). In practice a ρ_{rel} between 80-95% is observed. However, grains also invariably have defects, such as surface cracks, into which lithium metal can penetrate above a certain CCD. This produces crack tip stresses which drive membrane cracking and dendrite propagation during Li plating[103]. High density/low porosity[276, 279, 280], low Li metal/garnet resistance[187, 221, 265, 281] and high ionic mobility (intrinsically linked with temperature)[44, 187, 236, 282] are all features suggested to suppress dendrite growth. Evidence also suggests dendrite growth relates to fewer boundaries/larger grains/grain orientation[283, 284], grain electrical properties[187, 277, 284-287] and microstructure[288, 289]. Conversely, the increased resistance of grain boundaries, lower shear modulus (up to 50% less than the bulk), higher electronic conductivity [275] and compositional differences (compared to the bulk)[187, 275, 277, 290, 291] have all been reported to drive dendrite growth in lithium garnet materials.

These reports indicate that precise control of grain boundary characteristics will aid in dendrite suppression, however most of the above studies have some form of conflicting reports. Therefore, it is difficult to ascertain the importance of a singular factor. For example, dendrite suppression has both been suggested to occur, and be reduced by, the presence of Al at the grain boundary. Al was suggested by Pesci *et al.* to enable increased electron mobility and a short circuit at 0.1 mA cm^{-2} in Al-LLZO, whereas Sudo *et al.* suggested 0.5 mA cm^{-2} was possible for the same composition prepared similarly[187, 292] (perhaps a result of uncontrollable Al distribution at the grain boundary, see section 2.4.2.1.). The suggestion of high shear modulus has been regarded of both high and low importance[273, 283, 285] and it has been reported that lithium dendrites can penetrate highly polished single crystals (due to surface defects), suggesting garnets cannot intrinsically resist dendrite propagation[102, 103]. However, other reports also suggest single crystal LLZO type garnets are too dense for dendrite formation[293]. It has also been similarly reported that both large and small grain sizes suppress dendrite growth, with the true reasons for dendrite growth suggested to relate to grain boundary defects, which clearly scale with smaller grains[285, 294]. It has also been suggested dendrites nucleate at the interface and propagate through the electrolyte[295, 296] but also that dendrites are nucleated from within the grain boundaries or arise due to void formation on plating (which creates large interfacial resistance)[103, 244, 297].

It could be argued that lithium dendrite nucleation and growth follows no single mechanism and is rather just opportunistic based on the presence of certain interfacial, electrolyte and electrode contributions. This would account for the conflicting reports which rarely have similar synthesis and processing conditions so key aspects, like density or interfacial resistance, are inconsistent variables which makes direct comparisons difficult. Comparative analysis is further complicated once the numerous mechanisms to overcome interfacial resistance (section 2.5.3.) are accounted for. Recently, studies have begun to concentrate upon understanding the electrochemical and morphological concerns of lithium metal, rather than the garnet material, as any dendrite suppression techniques will be far easier to implement to the malleable Li metal rather than the brittle garnet material.

Firstly, Ling *et al.* assessed thermal evaporation of Li metal, with aims to assess natural deposition morphology. It was found by DFT studies that dendrite growth is an intrinsic property of Li metal. It was suggested that when Mg and Li were thermally evaporated, the latter would naturally form clusters rather than a planar geometry, potentially due to the lower Li^+ diffusion barrier along the 1D direction. It was subsequently proposed that Li tends to undergo island like growth during early nucleation, instead of the thin film growth seen with Mg[298, 299]. Although both were computational studies, the suggestion that Li intrinsically deposits with an extruding morphology is not ideal.

Later, Wang *et al.* established *via* the Nernst-Einstein relation, that the self-diffusion limit of Li metal is 5.6 x 10^{-11} cm^2 s^{-1}. The diffusion coefficient in model type cubic-LLZO was calculated as 2.15 x10^{-9} cm^2 s^{-1} and thus the self-diffusion of metallic Li is considerably slower than for LLZO. Therefore, at sufficiently large current densities, Li^+ flux toward the interface (during plating) greatly exceeds the flux of Li^0 away from the interface, so the interface cannot maintain a high enough volume of vacant sites. The lack of vacant sites forces non-planar Li plating, resulting in Li "pile-up" and formation of Li "hot spots". This creates local curvatures on the Li metal surface, which gives increased local electron density, that can act as nucleation sites for Li dendrites[296].

Around the same time Kasemchainan *et al.* (with Li_6PS_5Cl) discussed lithium dendrite formation in SSBs in terms of the heterogeneity of the lithium metal interface during cycling which, as described in the previous section, lends itself to void formation during plating. It was proposed that when the stripping of Li at the interface outpaces the speed at which it can be replenished from the Li metal, voids are increasingly formed. It is within these voids that local current density is increased beyond the CCD during cycling. This leads to non-uniform Li^+ current distribution and facilitates dendrite formation on plating[260]. Work with lithium garnets supports a similar mechanism may occur, with continual lithium plating giving enhanced current density at the void edge, enabling dendrite nucleation.

The application of high stack pressures, such that $J_{creep} > J_{diffusion}$, enable Li to be replenished more readily at the surface (and helps maintain intimate contact between the electrolyte/electrode) thereby preventing dendrite growth[260, 261, 268-271]. However, it has also been reported that stack pressures of 2 MPa are not sufficient to maintain a conformal Li/Garnet interface and even pressures as high as 7 MPa do not ensure long cycle life without microstructure growth (which is near the limit of the garnet material)[300].

Although the high stack pressures can potentially address the above issues, Han *et al.* recently proposed the origin of dendrite growth in LLZO type garnets arises from the electronic conductivity of the garnet electrolyte[297]. It was reported that Li dendrites nucleated and grew inside LLZO during cell cycling (determined by neutron depth profiling) and it was proposed that for Li plating current densities of 1 and 10 mA cm^{-2} the electrolyte required electronic conductivity of 10^{-10} and 10^{-12} S cm^{-1} respectively for dendrite suppression. However, the room temperature electronic conductivity of $Li_{6.4}La_3Zr_{1.4}Ta_{0.6}O_{12}$ is reported as 5.5 x10^{-8} S cm^{-1}, with Al-LLZO being reported as high as 1.1 x 10^{-6} S cm^{-1} during Li plating under applied voltage[301]. These are orders of magnitude away from the calculated values and the higher electronic conductivity in Al-LLZO may also explain other conflicting reports, which indicate short circuits are independent of density and surface reduction of Al-Li glassy phases[244].

This, potentially, explains how LIPON electrolytes, with much poorer σ_{rt} ($\approx 10^{-6}$ S cm^{-1}) but significantly lower electronic conductivity ($\approx 10^{-12}$ -10^{-15} S cm^{-1}), can cycle at higher current densities (> 10 mA cm^{-2}) than lithium garnet materials before dendritic growth.

Aguesse *et al.* suggested electron mobility in Ga-LLZO arises from O^{2-}electrons, although it was noted to potentially be a result of the non-zero electron conductivity generally seen in lithium garnets[178]. Tian *et al.* also proposed a computational model based upon trapping of excess electrons. It was suggested that the interface band gap of LLZO was much less than the bulk, effectively allowing the surface to trap excess electrons[285, 297, 302]. These could reduce Li^+ and thus serve to nucleate dendrites. Han *et al.* stated that cycling of cells at higher temperature does not assist in dendrite suppression, rather it is just a result of improved kinetics, as results indicated a lower driving force is required for dendrite growth at higher temperature and is thus in line with thermally increased electronic conductivity in LLZO[297]. The electronic conductivity of LLZO based materials (and other lithium garnets) therefore could enable internal nucleation and growth of lithium dendrites.

Overall, the mechanisms of lithium dendrite formation in solid state cells are unclear, as interface characterisation during cycling and subsequent understanding of the chemo-mechanical phenomena which drive dendrite formation *in-operando* is extremely complex. Dendrite growth can be considered to relate to poor interfacial contact (be that initially or after repeated cycling) which results in large interfacial resistance and polarisation. Dendrites also relate to grain boundary characteristics, pellet density and surface impurities (such as Li_2CO_3) and higher than desirable electronic conductivity, the latter perhaps being a key problem. The intrinsic limitations of lithium metal are now, however, being assessed more readily. This has led to an emerging consensus that future Li metal anode work needs to focus upon the transport within the metal and the morphological changes it undergoes, as opposed to only the SSE.

2.6. Summary and Project Objectives

Lithium garnet materials hold fantastic prospects for next generation energy storage, owing to their high ionic mobility, wide electrochemical window, high safety, air stability (from a safety perspective) and non-toxic nature. There is fantastic excitement surrounding these materials and this has led to some phenomenal advancements in recent years. However, several key fundamental aspects need to be addressed. Firstly, further development of lithium garnet materials is required as maximal conductivities at room temperature (≈1 mS cm^{-1}) remain inferior when compared to conventional LIBs, and are insufficient in colder climates. Secondly, removal of Li_2CO_3/LiOH in a cost-effective way that does not damage or waste the garnet material is paramount to reducing interfacial resistance, with this ideally being intrinsic to the garnet material rather than requiring additional processing/interlayers. Thirdly, an accurate understanding of lithium dendrite growth and enhancement of the CCD toward > 3 mA cm^{-2}. Hence, there is a pressing need to develop a garnet material which is cost effective and scalable without the need for complete inert conditions. Of late, research within the garnet area has concentrated very succinctly upon LLZO type materials, these are commonly Ga-LLZO or Ta-LLZO, with comparatively little attention paid to exploiting new dopant strategies. Therefore, the objectives of this project are:

- To investigate new, alternate, doping strategies to lithium garnet synthesis to optimise and improve material properties, such as conductivity, reduced interfacial resistance and dendrite growth suppression
- To reduce synthesis/densification times and/or temperatures considerably, and to employ the first objective to find scalable materials which operate > 5g
- Further investigation of the garnet crystal structure, aiming to enhance knowledge specifically around the tetragonal-cubic phase transition
- To enable higher entropy lithium garnet systems which test the very nature of what the garnet crystal framework can accommodate

Initially, this thesis will build upon work by Dong *et al.*, whereby it was found that introduction of Ce into LLZO readily enables reduced interfacial resistance between the garnet and Li metal (388 Ω cm^2)[127]. However, this system maintained the tetragonal structure therefore conductivity remained low. This work will look to increase Li content in the cubic $Li_5La_3Nb_2O_{12}$ system *via* extrinsic Pr doping in the form of $Li_{5+x}La_3Nb_{2-x}Pr_xO_{12}$.

Secondly, it was computationally predicted by Jalem *et al.* and Gupta *et al.* that Hf based garnets have increased electrochemical stability over LLZO, while also experimentally indicating increased stability

with respect to carbon-related decomposition during battery charging[200, 303]. Therefore, for the first time, $Ga_xLi_{7-3x}La_3Hf_2O_{12}$ will be synthesised to compare its electrochemical properties with the, well established, Ga-LLZO system. This will be additionally aimed at generally reducing the synthesis demands of lithium garnets by a water-based approach.

Thirdly, considerable work has also been directed toward understanding the formation of Al-Li eutectics which enable high density, but Li deficient grain boundaries. However, such dopant exsolution has yet to be exploited to enable a reactive interface with Li metal, which could be tailored to form alloys which reduce interfacial resistance. This will be done *via* deliberate destabilisation of a Li site dopant by substitution of La for Nd, thereby reducing lattice parameters and increasing lattice strain.

Fourthly, it is aimed to better understand the tetragonal-cubic phase transition. To this end, nine tetragonal lithium garnets of differing compositions will be synthesised to assess if increased lattice parameters directly relate to lower temperature cubic transitions.

Fifthly, the compositional flexibility of the lithium garnet system will be tested to see if deliberate increases in entropy *via* multiple dopant/multiple site substitution enables better performing garnets, or if such increased entropy will simplify garnet heat treatments. This will be done by first assessing all previous results to pick a selection of elements which have shown beneficial properties, in combination with literature reports.

Finally, a co-doped Ce/Ti system, in the form of $Li_{6.5}La_3Zr_1\ Nb_{0.5}Ce_{0.25}Ti_{0.25}O_{12}$ (LTC), will be developed to assess if Ce can retain its reduced interfacial resistance mentioned above, but also increase conductivity when employed in a cubic garnet system. LTC will not use any Li site substituted dopants to enable greater stability and reduced dopant exsolution.

The works detailed in the subsequent chapters are all published, with the exception of the LTC work which is being prepared for submission and is hence included in appendix 2.

2.7. REFERENCES

1. K. Funke, *Sci. Technol. Adv. Mater.*, 2013, **14**, 043502.
2. J. B. Bates, N. J. Dudney, G. R. Gruzalski, R. A. Zuhr, A. Choudhury, C. F. Luck and J. D. Robertson, *Solid State Ionics*, 1992, **53-56**, 647-654.
3. C. S. Nimisha, K. Y. Rao, G. Venkatesh, G. M. Rao and N. Munichandraiah, *Thin Solid Films*, 2011, **519**, 3401-3406.
4. N. Suzuki, S. Shirai, N. Takahashi, T. Inaba and T. Shiga, *Solid State Ionics*, 2011, **191**, 49-54.
5. C. H. Choi, W. I. Cho, B. W. Cho, H. S. Kim, Y. S. Yoon and Y. S. Tak, *Electrochem. Solid-State Lett.*, 2002, **5**, A14.
6. K.-i. Chung, W.-S. Kim and Y.-K. Choi, *J. Electroanal. Chem.*, 2004, **566**, 263-267.
7. A. C. Kozen, A. J. Pearse, C.-F. Lin, M. Noked and G. W. Rubloff, *Chem. Mater.*, 2015, **27**, 5324-5331.
8. M. Nisula, Y. Shindo, H. Koga and M. Karppinen, *Chem. Mater.*, 2015, **27**, 6987-6993.
9. L. Meda and E. E. Maxie, *Thin Solid Films*, 2012, **520**, 1799-1803.
10. H. T. Kim, T. Mun, C. Park, S. W. Jin and H. Y. Park, *J. Power Sources*, 2013, **244**, 641-645.
11. J. F. Ribeiro, R. Sousa, J. P. Carmo, L. M. Gonçalves, M. F. Silva, M. M. Silva and J. H. Correia, *Thin Solid Films*, 2012, **522**, 85-89.
12. J. D. LaCoste, A. Zakutayev and L. Fei, *J. Phys. Chem. C*, 2021, **125**, 3651-3667.
13. S. Zhao, Z. Fu and Q. Qin, *Thin Solid Films*, 2002, **415**, 108-113.
14. B. Wang, *J. Electrochem. Soc.*, 1996, **143**, 3203.
15. J. B. Bates, N. J. Dudney, G. R. Gruzalski, R. A. Zuhr, A. Choudhury, C. F. Luck and J. D. Robertson, *J. Power Sources*, 1993, **43**, 103-110.
16. J. B. Bates, N. J. Dudney, B. Neudecker, A. Ueda and C. D. Evans, *Solid State Ionics*, 2000, **135**, 33-45.
17. K. Senevirathne, C. S. Day, M. D. Gross, A. Lachgar and N. A. W. Holzwarth, *Solid State Ionics*, 2013, **233**, 95-101.
18. B. Wang, B. S. Kwak, B. C. Sales and J. B. Bates, *J. Non·Cryst. Solids*, 1995, **183**, 297-306.
19. S. Liang, W. Yan, X. Wu, Y. Zhang, Y. Zhu, H. Wang and Y. Wu, *Solid State Ionics*, 2018, **318**, 2-18.
20. S. Ramakumar, C. Deviannapoorani, L. Dhivya, L. S. Shankar and R. Murugan, *Prog. Mater Sci.*, 2017, **88**, 325-411.
21. M. Watanabe and N. Ogata, *Br. Polym. J.*, 1988, **20**, 181-192.
22. D. Zhou, D. Shanmukaraj, A. Tkacheva, M. Armand and G. Wang, *Chem.*, 2019, **5**, 2326-2352.
23. H. El-Shinawi, A. Regoutz, D. J. Payne, E. J. Cussen and S. A. Corr, *J. Mater. Chem. A*, 2018, **6**, 5296-5303.
24. R. Kanno and M. Murayama, *J. Electrochem. Soc.*, 2001, **148**.
25. M. Amores, H. El-Shinawi, I. McClelland, S. R. Yeandel, P. J. Baker, R. I. Smith, H. Y. Playford, P. Goddard, S. A. Corr and E. J. Cussen, *Nat. Commun.*, 2020, **11**, 6392.
26. Y. Zhao and L. L Daemen, *J. Am. Chem. Soc.*, 2012, **134**, 15042-15047.
27. V. Thangadurai, H. Kaack and W. J. F. Weppner, *J. Am. Ceram. Soc.*, 2004, **86**, 437-440.
28. R. Murugan, V. Thangadurai and W. Weppner, *Angew. Chem. Int. Ed.*, 2007, **46**, 7778-7781.
29. W. D. Richards, L. J. Miara, Y. Wang, J. C. Kim and G. Ceder, *Chem. Mater.*, 2016, **28**, 266-273.
30. V. Thangadurai, S. Narayanan and D. Pinzaru, *Chem. Soc. Rev.*, 2014, **43**, 4714-4727.
31. V. Thangadurai and W. Weppner, *Ionics*, 2006, **12**, 81-92.
32. F. Han, Y. Zhu, X. He, Y. Mo and C. Wang, *Adv. Energy Mater.*, 2016, **6**, 1501590.
33. Y. Zhu, X. He and Y. Mo, *J. Mater. Chem. A*, 2016, **4**, 3253-3266.
34. Y. Zhu, X. He and Y. Mo, *ACS Appl. Mater. Interfaces*, 2015, **7**, 23685-23693.
35. A. I. Waidha, V. Vanita and O. Clemens, *Ceramics*, 2021, **4**.

36. C. Loho, R. Djenadic, M. Bruns, O. Clemens and H. Hahn, *J. Electrochem. Soc.*, 2017, **164**, A6131-A6139.
37. S. Lobe, C. Dellen, M. Finsterbusch, H. G. Gehrke, D. Sebold, C. L. Tsai, S. Uhlenbruck and O. Guillon, *J. Power Sources*, 2016, **307**, 684-689.
38. A. Patil, V. Patil, D. Wook Shin, J.-W. Choi, D.-S. Paik and S.-J. Yoon, *Mater. Res. Bull.*, 2008, **43**, 1913-1942.
39. J. Sastre, A. Priebe, M. Döbeli, J. Michler, A. N. Tiwari and Y. E. Romanyuk, *Adv. Mater. Interfaces*, 2020, **7**, 2000425.
40. M. Balaish, J. C. Gonzalez-Rosillo, K. J. Kim, Y. Zhu, Z. D. Hood and J. L. M. Rupp, *Nat. Energy*, 2021, **6**, 227-239.
41. X. Han, Y. Gong, K. Fu, X. He, G. T. Hitz, J. Dai, A. Pearse, B. Liu, H. Wang, G. Rubloff, Y. Mo, V. Thangadurai, E. D. Wachsman and L. Hu, *Nat. Mater.*, 2017, **16**, 572-579.
42. J. Zhu, X. Li, C. Wu, J. Gao, H. Xu, Y. Li, X. Guo, H. Li and W. Zhou, *Angew. Chem. Int. Ed.*, 2021, **60**, 3781-3790.
43. L. Yang, Z. Lu, Y. Qin, C. Wu, C. Fu, Y. Gao, J. Liu, L. Jiang, Z. Du, Z. Xie, Z. Li, F. Kong and G. Yin, *J. Mater. Chem. A*, 2021, **9**, 5952-5979.
44. G. V. Alexander, M. S. Indu and R. Murugan, *Ionics*, 2021, **27**, 4105-4126.
45. F. Flatscher, M. Philipp, S. Ganschow, H. M. R. Wilkening and D. Rettenwander, *J. Mater. Chem. A*, 2020, **8**, 15782-15788.
46. W. Feng, X. Dong, X. Zhang, Z. Lai, P. Li, C. Wang, Y. Wang and Y. Xia, *Angew. Chem. Int. Ed.*, 2020, **59**, 5346-5349.
47. P. K. L.O. Hagman, *Acta Chem. Scand.*, ***1968***, **22**, 1822-1832.
48. P. Knauth, *Solid State Ionics*, 2009, **180**, 911-916.
49. J. B. Goodenough, H. Y. P. Hong and J. A. Kafalas, *Mater. Res. Bull.*, 1976, **11**, 203-220.
50. H. Y. P. Hong, *Mater. Res. Bull.*, 1976, **11**, 173-182.
51. F. Zheng, M. Kotobuki, S. Song, M. O. Lai and L. Lu, *J. Power Sources*, 2018, **389**, 198-213.
52. M. A. Subramanian, R. Subramanian and A. Clearfield, *Solid State Ionics*, 1986, **18-19**, 562-569.
53. H. Aono, E. Sugimoto, Y. Sadaoka, N. Imanaka and G. y. Adachi, *J. Electrochem. Soc.*, 1989, **136**, 590-591.
54. H. Aono, E. Sugimoto, Y. Sadaoka, N. Imanaka and G.-y. Adachi, *Solid State Ionics*, 1991, **47**, 257-264.
55. D. Case, A. J. McSloy, R. Sharpe, S. R. Yeandel, T. Bartlett, J. Cookson, E. Dashjav, F. Tietz, C. M. Naveen Kumar and P. Goddard, *Solid State Ionics*, 2020, **346**, 115192.
56. K. Arbi, J. M. Rojo and J. Sanz, *J. Eur. Ceram. Soc.*, 2007, **27**, 4215-4218.
57. S. Yu, S. Schmohl, Z. Liu, M. Hoffmeyer, N. Schön, F. Hausen, H. Tempel, H. Kungl, H. D. Wiemhöfer and R. A. Eichel, *J. Mater. Chem. A*, 2019, **7**, 3882-3894.
58. J. K. Feng, L. Lu and M. O. Lai, *J. Alloys Compd.*, 2010, **501**, 255-258.
59. H. Y. P. Hong, *Mater. Res. Bull.*, 1978, **13**, 117-124.
60. U. v. Alpen, M. F. Bell, W. Wichelhaus, K. Y. Cheung and G. J. Dudley, *Electrochim. Acta*, 1978, **23**, 1395-1397.
61. I. Abrahams, P. G. Bruce, A. R. West and W. I. F. David, *J. Solid State Chem.*, 1988, **75**, 390-396.
62. J. Kuwano and A. R. West, *Mater. Res. Bull.*, 1980, **15**, 1661-1667.
63. Y. W. Hu, I. D. Raistrick and R. A. Huggins, *J. Electrochem. Soc.*, 1977, **124**, 1240-1242.
64. S. Song, J. Lu, F. Zheng, H. M. Duong and L. Lu, *RSC Adv.*, 2015, **5**, 6588-6594.
65. G. Zhao, K. Suzuki, T. Seki, X. Sun, M. Hirayama and R. Kanno, *J. Solid State Chem.*, 2020, **292**, 121651.
66. K. J. Kim, M. Balaish, M. Wadaguchi, L. Kong and J. L. M. Rupp, *Adv. Energy Mater.*, 2021, **11**, 2002689.
67. T. Yu, B. Ke, H. Li, S. Guo and H. Zhou, *Mater. Chem. Front.*, 2021, **5**, 4892-4911.

68. P.-J. Lian, B.-S. Zhao, L.-Q. Zhang, N. Xu, M.-T. Wu and X.-P. Gao, *J. Mater. Chem. A*, 2019, **7**, 20540-20557.
69. A. Manthiram, X. Yu and S. Wang, *Nat. Rev. Mater.*, 2017, **2**, 16103.
70. R. Kanno and M. Murayama, *J. Electrochem. Soc.*, 2001, **148**, A742.
71. M. Tatsumisago and A. Hayashi, *International Journal of Applied Glass Science*, 2014, **5**, 226-235.
72. X. Yao, D. Liu, C. Wang, P. Long, G. Peng, Y.-S. Hu, H. Li, L. Chen and X. Xu, *Nano Lett.*, 2016, **16**, 7148-7154.
73. Y. Seino, T. Ota, K. Takada, A. Hayashi and M. Tatsumisago, *Energy Environ. Sci.*, 2014, **7**, 627-631.
74. H. Yamane, M. Shibata, Y. Shimane, T. Junke, Y. Seino, S. Adams, K. Minami, A. Hayashi and M. Tatsumisago, *Solid State Ionics*, 2007, **178**, 1163-1167.
75. N. Kamaya, K. Homma, Y. Yamakawa, M. Hirayama, R. Kanno, M. Yonemura, T. Kamiyama, Y. Kato, S. Hama, K. Kawamoto and A. Mitsui, *Nat. Mater.*, 2011, **10**, 682-686.
76. J. M. Whiteley, J. H. Woo, E. Hu, K.-W. Nam and S.-H. Lee, *J. Electrochem. Soc.*, 2014, **161**, A1812-A1817.
77. P. Bron, S. Johansson, K. Zick, J. Schmedt auf der Günne, S. Dehnen and B. Roling, *J. Am. Chem. Soc.*, 2013, **135**, 15694-15697.
78. Y. Kato, S. Hori and R. Kanno, *Adv. Energy Mater.*, 2020, **10**, 2002153.
79. O. Kwon, M. Hirayama, K. Suzuki, Y. Kato, T. Saito, M. Yonemura, T. Kamiyama and R. Kanno, *J. Mater. Chem. A*, 2015, **3**, 438-446.
80. H.-J. Deiseroth, S.-T. Kong, H. Eckert, J. Vannahme, C. Reiner, T. Zaiß and M. Schlosser, *Angew. Chem. Int. Ed.*, 2008, **47**, 755-758.
81. H.-J. Deiseroth, J. Maier, K. Weichert, V. Nickel, S.-T. Kong and C. Reiner, *Z. Anorg. Allg. Chem.*, 2011, **637**, 1287-1294.
82. H. M. Chen, C. Maohua and S. Adams, *Phys. Chem. Chem. Phys.*, 2015, **17**, 16494-16506.
83. R. Schlenker, A.-L. Hansen, A. Senyshyn, T. Zinkevich, M. Knapp, T. Hupfer, H. Ehrenberg and S. Indris, *Chem. Mater.*, 2020, **32**, 8420-8430.
84. D. Chang, K. Oh, S. J. Kim and K. Kang, *Chem. Mater.*, 2018, **30**, 8764-8770.
85. Y. Harada, T. Ishigaki, H. Kawai and J. Kuwano, *Solid State Ionics*, 1998, **108**, 407-413.
86. J. Brous, I. Fankuchen and E. Banks, *Acta Crystallogr.*, 1953, **6**, 67-70.
87. J. Lu and Y. Li, *Journal of Materials Science: Materials in Electronics*, 2021, **32**, 9736-9754.
88. J. Lu, Y. Li and Y. Ding, *Mater. Res. Bull.*, 2021, **133**, 111019.
89. Y. Inaguma, C. Liquan, M. Itoh, T. Nakamura, T. Uchida, H. Ikuta and M. Wakihara, *Solid State Commun.*, 1993, **86**, 689-693.
90. J. Lu, Y. Li and Y. Ding, *Ceram. Int.*, 2020, **46**, 7741-7747.
91. A. Boulant, P. Maury, J. Emery, J.-Y. Buzare and O. Bohnke, *Chem. Mater.*, 2009, **21**, 2209-2217.
92. N. S. P. Bhuvanesh, O. Bohnké, H. Duroy, M. P. Crosnier-Lopez, J. Emery and J. L. Fourquet, *Mater. Res. Bull.*, 1998, **33**, 1681-1691.
93. O. Bohnke, Q. N. Pham, A. Boulant, J. Emery, T. Šalkus and M. Barré, *Solid State Ionics*, 2011, **188**, 144-147.
94. A. Boulant, J. F. Bardeau, A. Jouanneaux, J. Emery, J.-Y. Buzare and O. Bohnke, *Dalton Trans.*, 2010, **39**, 3968-3975.
95. I. Hanghofer, G. J. Redhammer, S. Rohde, I. Hanzu, A. Senyshyn, H. M. R. Wilkening and D. Rettenwander, *Chem. Mater.*, 2018, **30**, 8134-8144.
96. J. A. S. Serejo, J. S. Pereira, R. Mouta and L. G. C. Rego, *Phys. Chem. Chem. Phys.*, 2021, **23**, 6964-6973.
97. D. Mazza, *Mater. Lett.*, 1988, **7**, 205-207.
98. C. Bernuy-Lopez, W. Manalastas, J. M. Lopez del Amo, A. Aguadero, F. Aguesse and J. A. Kilner, *Chem. Mater.*, 2014, **26**, 3610-3617.

99. R. Wagner, G. J. Redhammer, D. Rettenwander, G. Tippelt, A. Welzl, S. Taibl, J. Fleig, A. Franz, W. Lottermoser and G. Amthauer, *Chem. Mater.*, 2016, **28**, 5943-5951.
100. J.-F. Wu, E.-Y. Chen, Y. Yu, L. Liu, Y. Wu, W. K. Pang, V. K. Peterson and X. Guo, *ACS Appl. Mater. Interfaces*, 2017, **9**, 1542-1552.
101. R. Wagner, G. J. Redhammer, D. Rettenwander, A. Senyshyn, W. Schmidt, M. Wilkening and G. Amthauer, *Chem. Mater.*, 2016, **28**, 1861-1871.
102. D. Wang, C. Zhu, Y. Fu, X. Sun and Y. Yang, *Adv. Energy Mater.*, 2020, **10**, 2001318.
103. L. Porz, T. Swamy, B. W. Sheldon, D. Rettenwander, T. Frömling, H. L. Thaman, S. Berendts, R. Uecker, W. C. Carter and Y.-M. Chiang, *Adv. Energy Mater.*, 2017, **7**, 1701003.
104. A. F. Wells, *Structural inorganic chemistry*, Clarendon Press, 1984.
105. E. J. Cussen and T. W. S. Yip, *J. Solid State Chem.*, 2007, **180**, 1832-1839.
106. H. M. Kasper, *Inorg. Chem.*, 1969, **8**, 1000-1002.
107. D. Mazza, *Mater. Lett.*, 1988, **7**, 205-207.
108. M. P. O'Callaghan, D. R. Lynham, E. J. Cussen and G. Z. Chen, *Chem. Mater.*, 2006, **18**, 4681-4689.
109. J. Awaka, N. Kijima, H. Hayakawa and J. Akimoto, *J. Solid State Chem.*, 2009, **182**, 2046-2052.
110. E. J. Cussen, *Chem. Commun.*, 2006, **37**, 412-413.
111. H. Hyooma and K. Hayashi, *Mater. Res. Bull.*, 1988, **23**, 1399-1407.
112. H. Xie, J. A. Alonso, Y. Li, M. T. Fernández-Díaz and J. B. Goodenough, *Chem. Mater.*, 2011, **23**, 3587-3589.
113. J. Percival, E. Kendrick and P. R. Slater, *Solid State Ionics*, 2008, **179**, 1666-1669.
114. J. Percival and P. R. Slater, *Solid State Commun.*, 2007, **142**, 355-357.
115. H. Buschmann, J. Dölle, S. Berendts, A. Kuhn, P. Bottke, M. Wilkening, P. Heitjans, A. Senyshyn, H. Ehrenberg, A. Lotnyk, V. Duppel, L. Kienle and J. Janek, *Phys. Chem. Chem. Phys.*, 2011, **13**, 19378-19392.
116. Y. V. Baklanova, A. P. Tyutyunnik, N. V. Tarakina, A. D. Fortes, L. G. Maksimova, D. V. Korona and T. A. Denisova, *J. Power Sources*, 2018, **391**, 26-33.
117. M. A. Howard, O. Clemens, E. Kendrick, K. S. Knight, D. C. Apperley, P. A. Anderson and P. R. Slater, *Dalton Trans.*, 2012, **41**, 12048-12053.
118. M. P. O'Callaghan and E. J. Cussen, *Chem. Commun.*, 2007, DOI: 10.1039/B700369B, 2048-2050.
119. A. Düvel, A. Kuhn, L. Robben, M. Wilkening and P. Heitjans, *J. Phys. Chem. C*, 2012, **116**, 15192-15202.
120. D. Rettenwander, A. Welzl, L. Cheng, J. Fleig, M. Musso, E. Suard, M. M. Doeff, G. J. Redhammer and G. Amthauer, *Inorg. Chem.*, 2015, **54**, 10440-10449.
121. J. Percival, E. Kendrick, R. I. Smith and P. R. Slater, *Dalton Trans.*, 2009, **26**, 5177-5181.
122. M. A. Howard, O. Clemens, A. S. Parvathy, P. A. Anderson and P. R. Slater, *J. Alloys Compd.*, 2016, **670**, 78-84.
123. J. Awaka, N. Kijima, K. Kataoka, H. Hayakawa, K.-i. Ohshima and J. Akimoto, *J. Solid State Chem.*, 2010, **183**, 180-185.
124. C. A. Geiger, E. Alekseev, B. Lazic, M. Fisch, T. Armbruster, R. Langner, M. Fechtelkord, N. Kim, T. Pettke and W. Weppner, *Inorg. Chem.*, 2011, **50**, 1089-1097.
125. G. Larraz, A. Orera and M. L. Sanjuán, *J. Mater. Chem. A*, 2013, **1**, 11419-11428.
126. N. Bernstein, M. D. Johannes and K. Hoang, *Phys. Rev. Lett.*, 2012, **109**, 205702.
127. B. Dong, S. R. Yeandel, P. Goddard and P. R. Slater, *Chem. Mater.*, 2020, **32**, 215-223.
128. L. Cheng, C. H. Wu, A. Jarry, W. Chen, Y. Ye, J. Zhu, R. Kostecki, K. Persson, J. Guo, M. Salmeron, G. Chen and M. Doeff, *ACS Appl. Mater. Interfaces*, 2015, **7**, 17649-17655.
129. F. Chen, J. Li, Z. Huang, Y. Yang, Q. Shen and L. Zhang, *J. Phys. Chem. C*, 2018, **122**, 1963-1972.
130. R. H. Brugge, J. A. Kilner and A. Aguadero, *Solid State Ionics*, 2019, **337**, 154-160.
131. K. Kataoka and J. Akimoto, *Inorg. Chem.*, 2020, **59**, 14376-14381.

132. F. M. Pesci, A. Bertei, R. H. Brugge, S. P. Emge, A. K. O. Hekselman, L. E. Marbella, C. P. Grey and A. Aguadero, *ACS Appl. Mater. Interfaces*, 2020, **12**, 32806-32816.
133. J. Wolfenstine, J. Ratchford, E. Rangasamy, J. Sakamoto and J. L. Allen, *Mater. Chem. Phys.*, 2012, **134**, 571-575.
134. J. L. Allen, J. Wolfenstine, E. Rangasamy and J. Sakamoto, *J. Power Sources*, 2012, **206**, 315-319.
135. E. J. Cussen, *J. Mater. Chem.*, 2010, **20**, 5167-5173.
136. J. Han, J. Zhu, Y. Li, X. Yu, S. Wang, G. Wu, H. Xie, S. C. Vogel, F. Izumi, K. Momma, Y. Kawamura, Y. Huang, J. B. Goodenough and Y. Zhao, *Chem. Commun.*, 2012, **48**, 9840-9842.
137. D. Wang, G. Zhong, W. K. Pang, Z. Guo, Y. Li, M. J. McDonald, R. Fu, J.-X. Mi and Y. Yang, *Chem. Mater.*, 2015, **27**, 6650-6659.
138. M. P. O'Callaghan, A. S. Powell, J. J. Titman, G. Z. Chen and E. J. Cussen, *Chem. Mater.*, 2008, **20**, 2360-2369.
139. J. Awaka, A. Takashima, K. Kataoka, N. Kijima, Y. Idemoto and J. Akimoto, *Chem. Lett.*, 2010, **40**, 60-62.
140. M. Xu, M. S. Park, J. M. Lee, T. Y. Kim, Y. S. Park and E. Ma, *Phys. Rev. B*, 2012, **85**, 052301.
141. V. Thangadurai and W. Weppner, *Adv. Funct. Mater.*, 2005, **15**, 107-112.
142. V. Thangadurai and W. Weppner, *J. Am. Ceram. Soc.*, 2005, **88**, 411-418.
143. V. Thangadurai and W. Weppner, *J. Solid State Chem.*, 2006, **179**, 974-984.
144. J. Percival, D. Apperley and P. R. Slater, *Solid State Ionics*, 2008, **179**, 1693-1696.
145. H. Peng, Y. Zhang, L. Li and L. Feng, *Solid State Ionics*, 2017, **304**, 71-74.
146. S. Mukhopadhyay, T. Thompson, J. Sakamoto, A. Huq, J. Wolfenstine, J. L. Allen, N. Bernstein, D. A. Stewart and M. D. Johannes, *Chem. Mater.*, 2015, **27**, 3658-3665.
147. W. Gu, M. Ezbiri, R. Prasada Rao, M. Avdeev and S. Adams, *Solid State Ionics*, 2015, **274**, 100-105.
148. R. Wagner, D. Rettenwander, G. J. Redhammer, G. Tippelt, G. Sabathi, M. E. Musso, B. Stanje, M. Wilkening, E. Suard and G. Amthauer, *Inorg. Chem.*, 2016, **55**, 12211-12219.
149. J. Gai, E. Zhao, F. Ma, D. Sun, X. Ma, Y. Jin, Q. Wu and Y. Cui, *J. Eur. Ceram. Soc.*, 2018, **38**, 1673-1678.
150. D. M. Abdel-Basset, S. Mulmi, M. S. El-Bana, S. S. Fouad and V. Thangadurai, *Inorg. Chem.*, 2017, **56**, 8865-8877.
151. X. Huang, T. Xiu, M. E. Badding and Z. Wen, *Ceram. Int.*, 2018, **44**, 5660-5667.
152. R. H. Brugge, F. M. Pesci, A. Cavallaro, C. Sole, M. A. Isaacs, G. Kerherve, R. S. Weatherup and A. Aguadero, *J. Mater. Chem. A*, 2020, **8**, 14265-14276.
153. I. Kokal, M. Somer, P. H. L. Notten and H. T. Hintzen, *Solid State Ionics*, 2011, **185**, 42-46.
154. Y. Shimonishi, A. Toda, T. Zhang, A. Hirano, N. Imanishi, O. Yamamoto and Y. Takeda, *Solid State Ionics*, 2011, **183**, 48-53.
155. N. Janani, C. Deviannapoorani, L. Dhivya and R. Murugan, *RSC Adv.*, 2014, **4**, 51228-51238.
156. Y. X. Gao, X. P. Wang, W. G. Wang and Q. F. Fang, *Solid State Ionics*, 2010, **181**, 33-36.
157. N. Janani, S. Ramakumar, L. Dhivya, C. Deviannapoorani, K. Saranya and R. Murugan, *Ionics*, 2011, **17**, 575.
158. H. Peng, L. Li, L. Feng, Y. Zhang and Y. Zou, *Mater. Res. Bull.*, 2018, **99**, 414-418.
159. J. Li, Z. Liu, W. Ma, H. Dong, K. Zhang and R. Wang, *J. Power Sources*, 2019, **412**, 189-196.
160. N. Rosenkiewitz, J. Schuhmacher, M. Bockmeyer and J. Deubener, *J. Power Sources*, 2015, **278**, 104-108.
161. I. Kokal, K. V. Ramanujachary, P. H. L. Notten and H. T. Hintzen, *Mater. Res. Bull.*, 2012, **47**, 1932-1935.
162. Y. Jin and P. J. McGinn, *J. Power Sources*, 2011, **196**, 8683-8687.

163. L. Dimesso, in *Handbook of Sol-Gel Science and Technology*, eds. L. Klein, M. Aparicio and A. Jitianu, Springer International Publishing, Cham, 2016, DOI: 10.1007/978-3-319-19454-7_123-1, pp. 1-22.
164. Y. X. Gao, X. P. Wang, W. G. Wang, Z. Zhuang, D. M. Zhang and Q. F. Fang, *Solid State Ionics*, 2010, **181**, 1415-1419.
165. E. Rangasamy, J. Wolfenstine, J. Allen and J. Sakamoto, *J. Power Sources*, 2013, **230**, 261-266.
166. Y. Li, J.-T. Han, C.-A. Wang, S. C. Vogel, H. Xie, M. Xu and J. B. Goodenough, *J. Power Sources*, 2012, **209**, 278-281.
167. A. A. Hubaud, D. J. Schroeder, B. Key, B. J. Ingram, F. Dogan and J. T. Vaughey, *J. Mater. Chem. A*, 2013, **1**, 8813-8818.
168. E. Rangasamy, J. Wolfenstine and J. Sakamoto, *Solid State Ionics*, 2012, **206**, 28-32.
169. E. A. Dobretsov, Y. G. Mateyshina and N. F. Uvarov, *Solid State Ionics*, 2017, **299**, 55-59.
170. N. C. Rosero-Navarro, A. Miura, M. Higuchi and K. Tadanaga, *J. Electron. Mater.*, 2017, **46**, 497-501.
171. W. Xia, B. Xu, H. Duan, Y. Guo, H. Kang, H. Li and H. Liu, *ACS Appl. Mater. Interfaces*, 2016, **8**, 5335-5342.
172. Y. Wang, P. Yan, J. Xiao, X. Lu, J.-G. Zhang and V. L. Sprenkle, *Solid State Ionics*, 2016, **294**, 108-115.
173. S. Kumazaki, Y. Iriyama, K.-H. Kim, R. Murugan, K. Tanabe, K. Yamamoto, T. Hirayama and Z. Ogumi, *Electrochem. Commun.*, 2011, **13**, 509-512.
174. R. Jalem, M. J. D. Rushton, W. Manalastas, M. Nakayama, T. Kasuga, J. A. Kilner and R. W. Grimes, *Chem. Mater.*, 2015, **27**, 2821-2831.
175. D. Rettenwander, G. Redhammer, F. Preishuber-Pflügl, L. Cheng, L. Miara, R. Wagner, A. Welzl, E. Suard, M. M. Doeff, M. Wilkening, J. Fleig and G. Amthauer, *Chem. Mater.*, 2016, **28**, 2384-2392.
176. H. El Shinawi and J. Janek, *J. Power Sources*, 2013, **225**, 13-19.
177. Y. Matsuda, A. Sakaida, K. Sugimoto, D. Mori, Y. Takeda, O. Yamamoto and N. Imanishi, *Solid State Ionics*, 2017, **311**, 69-74.
178. F. Aguesse, W. Manalastas, L. Buannic, J. M. Lopez del Amo, G. Singh, A. Llordés and J. Kilner, *ACS Appl. Mater. Interfaces*, 2017, **9**, 3808-3816.
179. G. Larraz, A. Orera, J. Sanz, I. Sobrados, V. Diez-Gómez and M. L. Sanjuán, *J. Mater. Chem. A*, 2015, **3**, 5683-5691.
180. C. Galven, E. Suard, D. Mounier, M.-P. Crosnier-Lopez and F. Le Berre, *J. Mater. Res.*, 2013, **28**, 2147-2153.
181. R. Murugan, V. Thangadurai and W. Weppner, *Ionics*, 2007, **13**, 195-203.
182. R. Murugan, V. Thangadurai and W. Weppner, *Appl. Phys. A*, 2008, **91**, 615-620.
183. S. Narayanan, F. Ramezanipour and V. Thangadurai, *J. Phys. Chem. C*, 2012, **116**, 20154-20162.
184. T. Thompson, J. Wolfenstine, J. L. Allen, M. Johannes, A. Huq, I. N. David and J. Sakamoto, *J. Mater. Chem. A*, 2014, **2**, 13431-13436.
185. A. G. Squires, D. O. Scanlon and B. J. Morgan, *Chem. Mater.*, 2020, **32**, 1876-1886.
186. D. Rettenwander, P. Blaha, R. Laskowski, K. Schwarz, P. Bottke, M. Wilkening, C. A. Geiger and G. Amthauer, *Chem. Mater.*, 2014, **26**, 2617-2623.
187. Federico M. Pesci, R. H. Brugge, A. K. O. Hekselman, A. Cavallaro, R. J. Chater and A. Aguadero, *J. Mater. Chem. A*, 2018, **6**, 19817-19827.
188. J. Wolfenstine, J. L. Allen, J. Read and J. Sakamoto, *J. Mater. Sci.*, 2013, **48**, 5846-5851.
189. M. Kubicek, A. Wachter-Welzl, D. Rettenwander, R. Wagner, S. Berendts, R. Uecker, G. Amthauer, H. Hutter and J. Fleig, *Chem. Mater.*, 2017, **29**, 7189-7196.
190. Y. Zhu, J. G. Connell, S. Tepavcevic, P. Zapol, R. Garcia-Mendez, N. J. Taylor, J. Sakamoto, B. J. Ingram, L. A. Curtiss, J. W. Freeland, D. D. Fong and N. M. Markovic, *Adv. Energy Mater.*, 2019, **9**, 1803440.

191. X. Zhan, S. Lai, M. P. Gobet, S. G. Greenbaum and M. Shirpour, *Phys. Chem. Chem. Phys.*, 2018, **20**, 1447-1459.
192. S. Kc, R. C. Longo, K. Xiong and K. Cho, *Solid State Ionics*, 2014, **261**, 100-105.
193. M. Nyman, T. M. Alam, S. K. McIntyre, G. C. Bleier and D. Ingersoll, *Chem. Mater.*, 2010, **22**, 5401-5410.
194. N. Kuganathan, M. J. D. Rushton, R. W. Grimes, J. A. Kilner, E. I. Gkanas and A. Chroneos, *Sci. Rep.*, 2021, **11**, 451.
195. A. Moradabadi and P. Kaghazchi, *Solid State Ionics*, 2019, **338**, 74-79.
196. L. van Wüllen, T. Echelmeyer, H.-W. Meyer and D. Wilmer, *Phys. Chem. Chem. Phys.*, 2007, **9**, 3298-3303.
197. S. Ohta, T. Kobayashi and T. Asaoka, *J. Power Sources*, 2011, **196**, 3342-3345.
198. S. Adams and R. P. Rao, *J. Mater. Chem.*, 2012, **22**, 1426-1434.
199. T. Zaiß, M. Ortner, R. Murugan and W. Weppner, *Ionics*, 2010, **16**, 855-858.
200. A. Gupta, R. Murugan, M. P. Paranthaman, Z. Bi, C. A. Bridges, M. Nakanishi, A. P. Sokolov, K. S. Han, E. W. Hagaman, H. Xie, C. B. Mullins and J. B. Goodenough, *J. Power Sources*, 2012, **209**, 184-188.
201. N. Hamao, K. Kataoka and J. Akimoto, *J. Ceram. Soc. Jpn.*, 2017, **125**, 272-275.
202. L. Ladenstein, S. Simic, G. Kothleitner, D. Rettenwander and H. M. R. Wilkening, *J. Phys. Chem. C*, 2020, **124**, 16796-16805.
203. M. Mann, M. Küpers, G. Häuschen, M. Finsterbusch, D. Fattakhova-Rohlfing and O. Guillon, *Ionics*, 2022, **28**, 53-62.
204. A. V. Shaverina, A. R. Tsygankova, I. R. Shelpakova and A. I. Saprykin, *Inorg. Mater.*, 2013, **49**, 1283-1287.
205. W. S. Clabaugh and R. Gilchrist, *J. Am. Chem. Soc.*, 1952, **74**, 2104-2105.
206. X. Ma and Y. Li, *Anal. Chim. Acta*, 2006, **579**, 47-52.
207. B. Arnold, *Zirkon, Zirkonium, Zirkonia - ähnliche Namen, verschiedene Materialien*, Springer Berlin Heidelberg, 2019.
208. X. Tong, V. Thangadurai and E. D. Wachsman, *Inorg. Chem.*, 2015, **54**, 3600-3607.
209. X. Xiang, F. Chen, W. Yang, J. Yang, X. Ma, D. Chen, K. Su, Q. Shen and L. Zhang, *J. Am. Ceram. Soc.*, 2020, **103**, 2483-2490.
210. S. T. G. Anderson, R. V. D. Robért and H. N. Farrer, *J. Anal. At. Spectrom.*, 1992, **7**, 1195-1199.
211. M. Huang, T. Liu, Y. Deng, H. Geng, Y. Shen, Y. Lin and C.-W. Nan, *Solid State Ionics*, 2011, **204-205**, 41-45.
212. A. Paolella, W. Zhu, G. Bertoni, S. Savoie, Z. Feng, H. Demers, V. Gariepy, G. Girard, E. Rivard, N. Delaporte, A. Guerfi, H. Lorrmann, C. George and K. Zaghib, *ACS Appl. Energy Mater.*, 2020, **3**, 3415-3424.
213. N. C. Rosero-Navarro, T. Yamashita, A. Miura, M. Higuchi and K. Tadanaga, *Solid State Ionics*, 2016, **285**, 6-12.
214. X. Wang, J. Wang, F. Li, F. Zhu and C. Ma, *Ceram. Int.*, 2020, **46**, 18544-18550.
215. A. I. Waidha, T. Ferber, M. Donzelli, N. Hosseinpourkahvaz, V. Vanita, K. Dirnberger, S. Ludwigs, R. Hausbrand, W. Jaegermann and O. Clemens, *ACS Appl. Mater. Interfaces*, 2021, **13**, 31111-31128.
216. J.-H. Seo, H. Nakaya, Y. Takeuchi, Z. Fan, H. Hikosaka, R. Rajagopalan, E. D. Gomez, M. Iwasaki and C. A. Randall, *J. Eur. Ceram. Soc.*, 2020, **40**, 6241-6248.
217. Y. Liu, Q. Sun, D. Wang, K. Adair, J. Liang and X. Sun, *J. Power Sources*, 2018, **393**, 193-203.
218. H. Yamada, T. Ito, S. P. Kammampata and V. Thangadurai, *ACS Appl. Mater. Interfaces*, 2020, **12**, 36119-36127.
219. P. R. Slater and C. Greaves, *Solid State Ionics*, 1992, **53-56**, 989-992.

220. L. Cheng, E. J. Crumlin, W. Chen, R. Qiao, H. Hou, S. Franz Lux, V. Zorba, R. Russo, R. Kostecki, Z. Liu, K. Persson, W. Yang, J. Cabana, T. Richardson, G. Chen and M. Doeff, *Phys. Chem. Chem. Phys.*, 2014, **16**, 18294-18300.
221. A. Sharafi, S. Yu, M. Naguib, M. Lee, C. Ma, H. M. Meyer, J. Nanda, M. Chi, D. J. Siegel and J. Sakamoto, *J. Mater. Chem. A*, 2017, **5**, 13475-13487.
222. L. Truong and V. Thangadurai, *Inorg. Chem.*, 2012, **51**, 1222-1224.
223. C. Galven, J.-L. Fourquet, M.-P. Crosnier-Lopez and F. Le Berre, *Chem. Mater.*, 2011, **23**, 1892-1900.
224. C. Galven, J. Dittmer, E. Suard, F. Le Berre and M.-P. Crosnier-Lopez, *Chem. Mater.*, 2012, **24**, 3335-3345.
225. A. Orera, G. Larraz, J. A. Rodríguez-Velamazán, J. Campo and M. L. Sanjuán, *Inorg. Chem.*, 2016, **55**, 1324-1332.
226. Y. Jin and P. J. McGinn, *J. Power Sources*, 2013, **239**, 326-331.
227. C. Ma, E. Rangasamy, C. Liang, J. Sakamoto, K. L. More and M. Chi, *Angew. Chem. Int. Ed.*, 2015, **54**, 129-133.
228. Z. F. Yow, Y. L. Oh, W. Gu, R. P. Rao and S. Adams, *Solid State Ionics*, 2016, **292**, 122-129.
229. Y. Li, J.-T. Han, S. C. Vogel and C.-A. Wang, *Solid State Ionics*, 2015, **269**, 57-61.
230. L. Truong, M. Howard, O. Clemens, K. S. Knight, P. R. Slater and V. Thangadurai, *J. Mater. Chem. A*, 2013, **1**, 13469-13475.
231. M. A. K. L. Dissanayake and B. E. Mellander, *Solid State Ionics*, 1986, **21**, 279-285.
232. Amardeep, S. Kobi and A. Mukhopadhyay, *Scripta Mater.*, 2019, **162**, 214-218.
233. S. Kobi and A. Mukhopadhyay, *J. Eur. Ceram. Soc.*, 2018, **38**, 4707-4718.
234. M. Rosen, R. Ye, M. Mann, S. Lobe, M. Finsterbusch, O. Guillon and D. Fattakhova-Rohlfing, *J. Mater. Chem. A*, 2021, **9**, 4831-4840.
235. Y. Li, X. Chen, A. Dolocan, Z. Cui, S. Xin, L. Xue, H. Xu, K. Park and J. B. Goodenough, *J. Am. Chem. Soc.*, 2018, **140**, 6448-6455.
236. A. Sharafi, H. M. Meyer, J. Nanda, J. Wolfenstine and J. Sakamoto, *J. Power Sources*, 2016, **302**, 135-139.
237. G. V. Alexander, S. Patra, S. V. Sobhan Raj, M. K. Sugumar, M. M. Ud Din and R. Murugan, *J. Power Sources*, 2018, **396**, 764-773.
238. A. Sharafi, E. Kazyak, A. L. Davis, S. Yu, T. Thompson, D. J. Siegel, N. P. Dasgupta and J. Sakamoto, *Chem. Mater.*, 2017, **29**, 7961-7968.
239. J.-F. Wu, B.-W. Pu, D. Wang, S.-Q. Shi, N. Zhao, X. Guo and X. Guo, *ACS Appl. Mater. Interfaces*, 2019, **11**, 898-905.
240. H. Huo, Y. Chen, N. Zhao, X. Lin, J. Luo, X. Yang, Y. Liu, X. Guo and X. Sun, *Nano Energy*, 2019, **61**, 119-125.
241. Y. Ruan, Y. Lu, X. Huang, J. Su, C. Sun, J. Jin and Z. Wen, *J. Mater. Chem. A*, 2019, **7**, 14565-14574.
242. Y. Zhong, Y. Xie, S. Hwang, Q. Wang, J. J. Cha, D. Su and H. Wang, *Angew. Chem. Int. Ed.*, 2020, **59**, 14003-14008.
243. X. Fu, T. Wang, W. Shen, M. Jiang, Y. Wang, Q. Dai, D. Wang, Z. Qiu, Y. Zhang, K. Deng, Q. Zeng, N. Zhao, X. Guo, Z. Liu, J. Liu and Z. Peng, *Adv. Mater.*, 2020, **32**, 2000575.
244. C.-L. Tsai, V. Roddatis, C. V. Chandran, Q. Ma, S. Uhlenbruck, M. Bram, P. Heitjans and O. Guillon, *ACS Appl. Mater. Interfaces*, 2016, **8**, 10617-10626.
245. W. Feng, X. Dong, P. Li, Y. Wang and Y. Xia, *J. Power Sources*, 2019, **419**, 91-98.
246. W. Luo, Y. Gong, Y. Zhu, Y. Li, Y. Yao, Y. Zhang, K. Fu, G. Pastel, C.-F. Lin, Y. Mo, E. D. Wachsman and L. Hu, *Adv. Mater.*, 2017, **29**, 1606042.
247. W. Luo, Y. Gong, Y. Zhu, K. K. Fu, J. Dai, S. D. Lacey, C. Wang, B. Liu, X. Han, Y. Mo, E. D. Wachsman and L. Hu, *J. Am. Chem. Soc.*, 2016, **138**, 12258-12262.

248. K. Fu, Y. Gong, B. Liu, Y. Zhu, S. Xu, Y. Yao, W. Luo, C. Wang, S. Lacey, J. Dai, Y. Chen, Y. Mo, E. Wachsman and L. Hu, *Sci. Adv.*, 2017, **3**, e1601659.
249. G. V. Alexander, O. V. Sreejith, M. S. Indu and R. Murugan, *ACS Appl. Energy Mater.*, 2020, **3**, 9010-9017.
250. M. He, Z. Cui, C. Chen, Y. Li and X. Guo, *J. Mater. Chem. A*, 2018, **6**, 11463-11470.
251. Y. Zhang, J. Meng, K. Chen, Q. Wu, X. Wu and C. Li, *ACS Appl. Mater. Interfaces*, 2020, **12**, 33729-33739.
252. Y. Shao, H. Wang, Z. Gong, D. Wang, B. Zheng, J. Zhu, Y. Lu, Y.-S. Hu, X. Guo, H. Li, X. Huang, Y. Yang, C.-W. Nan and L. Chen, *ACS Energy Lett.*, 2018, **3**, 1212-1218.
253. Y. Chen, M. He, N. Zhao, J. Fu, H. Huo, T. Zhang, Y. Li, F. Xu and X. Guo, *J. Power Sources*, 2019, **420**, 15-21.
254. J. Fu, P. Yu, N. Zhang, G. Ren, S. Zheng, W. Huang, X. Long, H. Li and X. Liu, *Energy Environ. Sci.*, 2019, **12**, 1404-1412.
255. H. Huo, Y. Chen, R. Li, N. Zhao, J. Luo, J. G. Pereira da Silva, R. Mücke, P. Kaghazchi, X. Guo and X. Sun, *Energy Environ. Sci.*, 2020, **13**, 127-134.
256. M. Du, Y. Sun, B. Liu, B. Chen, K. Liao, R. Ran, R. Cai, W. Zhou and Z. Shao, *Adv. Funct. Mater.*, 2021, **31**, 2101556.
257. J. Wang, G. Huang and X.-B. Zhang, *Batteries Supercaps*, 2020, **3**, 1006-1015.
258. J. A. Lewis, F. J. Q. Cortes, Y. Liu, J. C. Miers, A. Verma, B. S. Vishnugopi, J. Tippens, D. Prakash, T. S. Marchese, S. Y. Han, C. Lee, P. P. Shetty, H.-W. Lee, P. Shevchenko, F. De Carlo, C. Saldana, P. P. Mukherjee and M. T. McDowell, *Nat. Mater.*, 2021, **20**, 503-510.
259. U. Roy, N. A. Fleck and V. S. Deshpande, *Extreme Mech. Lett.*, 2021, **46**, 101307.
260. J. Kasemchainan, S. Zekoll, D. Spencer Jolly, Z. Ning, G. O. Hartley, J. Marrow and P. G. Bruce, *Nat. Mater.*, 2019, **18**, 1105-1111.
261. M. J. Wang, R. Choudhury and J. Sakamoto, *Joule*, 2019, **3**, 2165-2178.
262. D. Cao, X. Sun, Q. Li, A. Natan, P. Xiang and H. Zhu, *Matter*, 2020, **3**, 57-94.
263. F. Yonemoto, A. Nishimura, M. Motoyama, N. Tsuchimine, S. Kobayashi and Y. Iriyama, *J. Power Sources*, 2017, **343**, 207-215.
264. W. Manalastas, J. Rikarte, R. J. Chater, R. Brugge, A. Aguadero, L. Buannic, A. Llordés, F. Aguesse and J. Kilner, *J. Power Sources*, 2019, **412**, 287-293.
265. R. H. Basappa, T. Ito and H. Yamada, *J. Electrochem. Soc.*, 2017, **164**, A666-A671.
266. R. Koerver, W. Zhang, L. de Biasi, S. Schweidler, A. O. Kondrakov, S. Kolling, T. Brezesinski, P. Hartmann, W. G. Zeier and J. Janek, *Energy Environ. Sci.*, 2018, **11**, 2142-2158.
267. H. Koshikawa, S. Matsuda, K. Kamiya, M. Miyayama, Y. Kubo, K. Uosaki, K. Hashimoto and S. Nakanishi, *J. Power Sources*, 2018, **376**, 147-151.
268. J. Cannarella and C. B. Arnold, *J. Power Sources*, 2014, **245**, 745-751.
269. T. Krauskopf, H. Hartmann, W. G. Zeier and J. Janek, *ACS Appl. Mater. Interfaces*, 2019, **11**, 14463-14477.
270. X. Zhang, Q. Xiang, S. Tang, A. Wang, X. Liu and J. Luo, *Nano Lett.*, 2020, **20**, 2871-2878.
271. H. Yan, K. Tantratian, K. Ellwood, E. T. Harrison, M. Nichols, X. Cui and L. Chen, *Adv. Energy Mater.*, 2021, **12**, 2102283.
272. A. Masias, N. Felten, R. Garcia-Mendez, J. Wolfenstine and J. Sakamoto, *J. Mater. Sci.*, 2019, **54**, 2585-2600.
273. C. Monroe and J. Newman, *J. Electrochem. Soc.*, 2005, **152**, A396.
274. S. Yu, R. D. Schmidt, R. Garcia-Mendez, E. Herbert, N. J. Dudney, J. B. Wolfenstine, J. Sakamoto and D. J. Siegel, *Chem. Mater.*, 2016, **28**, 197-206.
275. S. Yu and D. J. Siegel, *ACS Appl. Mater. Interfaces*, 2018, **10**, 38151-38158.
276. Y. Ren, Y. Shen, Y. Lin and C.-W. Nan, *Electrochem. Commun.*, 2015, **57**, 27-30.
277. R. Raj and J. Wolfenstine, *J. Power Sources*, 2017, **343**, 119-126.
278. C. Monroe and J. Newman, *J. Electrochem. Soc.*, 2003, **150**, A1377.

279. Y. Lu, X. Huang, Y. Ruan, Q. Wang, R. Kun, J. Yang and Z. Wen, *J. Mater. Chem. A*, 2018, **6**, 18853-18858.
280. M. B. Dixit, M. Regala, F. Shen, X. Xiao and K. B. Hatzell, *ACS Appl. Mater. Interfaces*, 2019, **11**, 2022-2030.
281. S. Kim, C. Jung, H. Kim, K. E. Thomas-Alyea, G. Yoon, B. Kim, M. E. Badding, Z. Song, J. Chang, J. Kim, D. Im and K. Kang, *Adv. Energy Mater.*, 2020, **10**, 1903993.
282. N. J. Taylor, S. Stangeland-Molo, C. G. Haslam, A. Sharafi, T. Thompson, M. Wang, R. Garcia-Mendez and J. Sakamoto, *J. Power Sources*, 2018, **396**, 314-318.
283. A. Sharafi, C. G. Haslam, R. D. Kerns, J. Wolfenstine and J. Sakamoto, *J. Mater. Chem. A*, 2017, **5**, 21491-21504.
284. L. Cheng, W. Chen, M. Kunz, K. Persson, N. Tamura, G. Chen and M. Doeff, *ACS Appl. Mater. Interfaces*, 2015, **7**, 2073-2081.
285. H.-K. Tian, Z. Liu, Y. Ji, L.-Q. Chen and Y. Qi, *Chem. Mater.*, 2019, **31**, 7351-7359.
286. M. D. Tikekar, S. Choudhury, Z. Tu and L. A. Archer, *Nat. Energy*, 2016, **1**, 16114.
287. Y. Song, L. Yang, W. Zhao, Z. Wang, Y. Zhao, Z. Wang, Q. Zhao, H. Liu and F. Pan, *Adv. Energy Mater.*, 2019, **9**, 1900671.
288. R. Hongahally Basappa, T. Ito, T. Morimura, R. Bekarevich, K. Mitsuishi and H. Yamada, *J. Power Sources*, 2017, **363**, 145-152.
289. B. Xu, W. Li, H. Duan, H. Wang, Y. Guo, H. Li and H. Liu, *J. Power Sources*, 2017, **354**, 68-73.
290. S. Yu and D. J. Siegel, *Chem. Mater.*, 2017, **29**, 9639-9647.
291. K. Ishiguro, H. Nemori, S. Sunahiro, Y. Nakata, R. Sudo, M. Matsui, Y. Takeda, O. Yamamoto and N. Imanishi, *J. Electrochem. Soc.*, 2014, **161**, A668-A674.
292. R. Sudo, Y. Nakata, K. Ishiguro, M. Matsui, A. Hirano, Y. Takeda, O. Yamamoto and N. Imanishi, *Solid State Ionics*, 2014, **262**, 151-154.
293. K. Kataoka, H. Nagata and J. Akimoto, *Sci. Rep.*, 2018, **8**, 9965.
294. H. Huo, J. Luo, V. Thangadurai, X. Guo, C.-W. Nan and X. Sun, *ACS Energy Lett.*, 2020, **5**, 252-262.
295. E. J. Cheng, A. Sharafi and J. Sakamoto, *Electrochim. Acta*, 2017, **223**, 85-91.
296. M. Wang, J. B. Wolfenstine and J. Sakamoto, *Electrochim. Acta*, 2019, **296**, 842-847.
297. F. Han, A. S. Westover, J. Yue, X. Fan, F. Wang, M. Chi, D. N. Leonard, N. J. Dudney, H. Wang and C. Wang, *Nat. Energy*, 2019, **4**, 187-196.
298. M. Jäckle and A. Groß, *J. Chem. Phys.*, 2014, **141**, 174710.
299. C. Ling, D. Banerjee and M. Matsui, *Electrochim. Acta*, 2012, **76**, 270-274.
300. W. Chang, R. May, M. Wang, G. Thorsteinsson, J. Sakamoto, L. Marbella and D. Steingart, *Nat. Commun.*, 2021, **12**, 6369.
301. Y.-T. Chen, A. Jena, W. K. Pang, V. K. Peterson, H.-S. Sheu, H. Chang and R.-S. Liu, *J. Phys. Chem. C*, 2017, **121**, 15565-15573.
302. H.-K. Tian, B. Xu and Y. Qi, *J. Power Sources*, 2018, **392**, 79-86.
303. R. Jalem, Y. Morishita, T. Okajima, H. Takeda, Y. Kondo, M. Nakayama and T. Kasuga, *J. Mater. Chem. A*, 2016, **4**, 14371-14379.

3. Experimental Techniques

3.1. Solid State Synthesis

This work makes use of high temperature solid state synthesis methods. This is the most common synthesis method for ceramic materials[1-3]. Solid state synthesis is restricted by atomic diffusion limitations, therefore high temperatures and long reaction times are required.

In a typical synthesis, the required elements (usually in oxide form) are stoichiometrically weighed and thoroughly mixed *via* hand grinding or ball milling. These powders are then dried (if a wetting agent was used) and, sometimes, pressed into a pellet. Pellets enable close contact of the particles, which helps to overcome the atomic diffusion limitations and is especially helpful if ball milling is unavailable. The powder/pellet is then heated to a temperature either based on work elsewhere or, if unavailable, to a temperature two thirds the melting point of the lower melting reactant (Tamman's Rule). Most materials in this work were heated ≈5°C min^{-1} for 12 - 24h. These materials were then assessed for phase purity *via* X-ray diffraction (XRD) and reheated as required to obtain phase pure samples.

Lithium garnets present some additional problems. Firstly, Li is volatile at high temperature and is easily lost through evaporation from the reaction vessel. Hence, Li was always used in excess (20 - 40% mol excess) in this work. Secondly, the relative complexity of the garnet system makes the ball milling route somewhat essential. Hence, a typical Li garnet synthesis will involve weighing of the chemicals with additional excess Li, and ball milling with zirconium oxide balls for 1 - 6h at 350 - 500 rpm using hexane. These materials are then heated to 950 – 1050°C (based upon the available literature elsewhere), but these temperatures deviate in this work based upon each research theme. The powders are then removed, hand ground and characterised by XRD. Additional Li may then be added with further ball milling and reheating. Heating rates in this work varied from 2 - 100°C min^{-1}, and sintering times range from 5 minutes to 12 hrs.

As discussed in section 2.4.2., wet chemical techniques are an attractive alternative to the standard solid-state route, whereby precursors are dissolved to form a gel and then sintered. This work made use of a modified sol-gel route using the bio-polymer agar, but this was rapidly changed to only dissolve the precursors in water. This applies only to the work on Hf garnets (see chapter 6).

3.2. POST SINTERING METHODS

After sintering, the Li garnet powders required densification to characterise the material properties. This was done by compressing the powder into a pellet with Specac pellet dies and uniaxially pressing the powders to ≈1 - 3 tonnes. The pellets were then heated under dry N_2 or O_2 or in a dry room. This reduces proton exchange and affords effective grain growth into neighbouring grains to increase density. This is often done 100 - 150°C above the synthesis temperature. Densification was undertaken in this work initially under N_2 or O_2 but progressed to a dry room once facilities became available.

As per section 2.5.2., lithium garnets have considerable issues with proton exchange, which negatively impacts a variety of properties but, primarily, gives high interfacial resistance. In this work, the polishing method was employed under Ar atmosphere to form lithium symmetry cells. This is covered in the cell assembly section (4.6).

Any specific alterations to these methods will be stated in the corresponding research chapters.

4. Characterisation Techniques

4.1. CRYSTALLOGRAPHY

The origin of crystallography can be traced to the desire to study natural minerals based on their appearance, such as fluorite and quartz, which have regular shapes and clearly exhibit symmetry. Modern crystallography, however, considers the idea that materials are built from exceptionally small individual units. These, three-dimensional, solid crystalline materials are composed of atoms, ions or molecules that exhibit long range order and are arranged in a periodic pattern in three-dimensions, with numerous specific symmetry constraints. The periodicity and symmetry therefore define a crystalline solid. Not all solids (macroscopically speaking) exhibit such order, for example amorphous materials have short range order which results in the appearance of a solid material[4]. The important distinction is the emphasis on both the repetition of the atom, ion or molecule and their adherence to certain symmetry constraints, which amorphous materials (such as glass) lack.

Crystalline materials have an effective infinite repetition of structural motifs/components of defined symmetry which cumulatively create the solid material. This is the unit cell, which is defined as the smallest repeating unit from which the overall crystal symmetry can be determined and from which the entire lattice can be built[1, 4]. Unit cells are characterised in terms of their dimensions (cell parameters), angles and symmetry. Unit cell dimensions are defined by three sides (*a*, *b* and *c*) and three angles (*α, β* and *γ*; where α is the angle between sides *b* and *c*, *β* the angle between a and c, *γ* the angle between *a* and *b)*, see figure 4.1. There are seven possible unit cell shapes (or crystal classes) which are defined by the lattice points, angles and cell parameter relationship, see table 4.1. Six of these crystal systems can be derived from distortion of a cubic structure, for example a tetragonal unit cell involves elongation of a single axis. Hexagonal cells, however, are effectively built from individual trigonal sub-units but have a single sixfold axis symmetry (compared to a threefold axis for trigonal)[1, 5-8].

The seven crystal systems are further described *via* four different unit cell types depending upon lattice point arrangements, see table 4.2. These unit cell types are combined with the seven crystal systems to create a set of fourteen Bravais lattices, see table 4.1 and 4.2.

Table 4.1. The seven different crystal systems and respective symmetry constraints.

Crystal System	Defining symmetry	Allowed Lattices
Cubic	$a = b = c, \alpha = \beta = \gamma = 90°$	*P, I, F*
Tetragonal	$a = b \neq c, \alpha = \beta = \gamma = 90°$	*P, I*
Orthorhombic	$a \neq b \neq c, \alpha = \beta = \gamma = 90°$	*P, F, I, A (B or C)*
Hexagonal	$a = b \neq c, \alpha = \beta = 90° \gamma = 120°$	*P*
Trigonal / Rhombohedral	$a = b = c, \alpha = \beta = \gamma \neq 90°$	*P*
Monoclinic	$a \neq b \neq c, \alpha = \gamma = 90° \beta \neq 90$	*P, C*
Triclinic	$a \neq b \neq c, \alpha \neq \beta \neq \gamma \neq 90°$	*P*

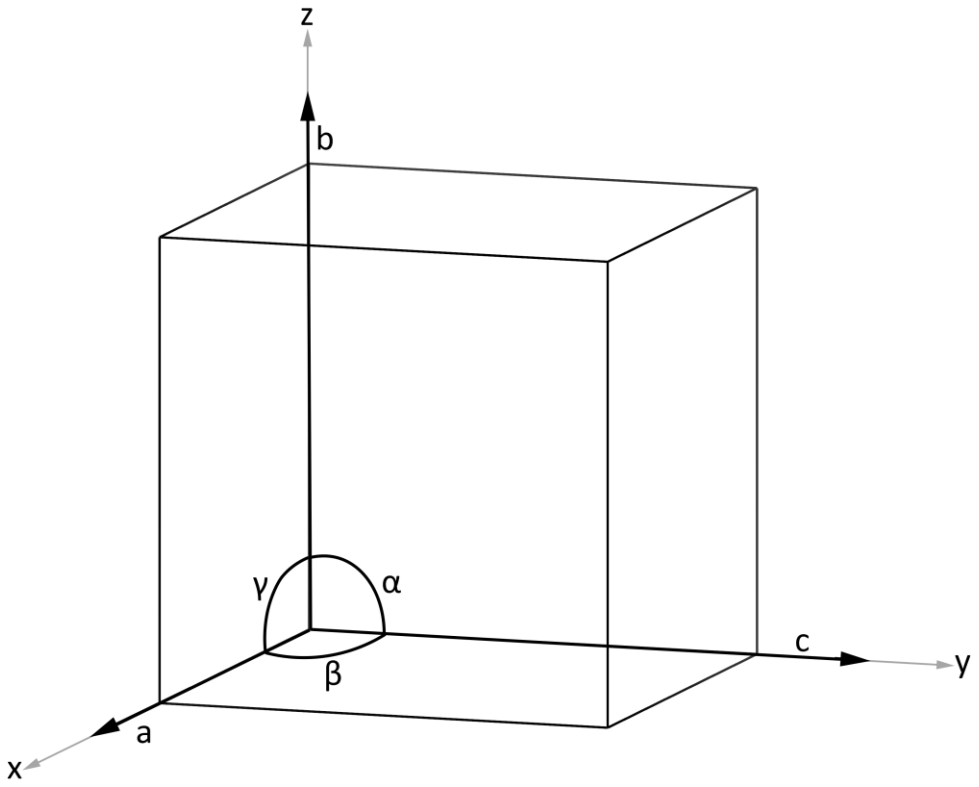

Figure 4.1. Example of a cubic celll showing cell dimensions.

Atomic positions in a lattice are described using a fractional co-ordinate system. Axis position ranges from 0 (the origin) to 1, with 0 conventionally (but not always) taken from the far bottom corner. The fractional coordinates (*x*, *y*, *z*) are combined with the lattice sides (*a*, *b*, *c*) to form *xa*, *yb* and *zc.* For example, fractional coordinates of 0.25, 0.75, 0.5 correspond to an atom a quarter way along the *a* axis, three quarters along the *b* axis and halfway along the *c* axis.

Table 4.2. Unit cell types and lattice point requirement.

Type of Cell	Lattice Point Requirement
Primitive (*P*)	One lattice point at each corner
Body Centred (*I*)	One lattice point in the centre and at each corner
Face centred (*F*)	One lattice point at each corner, one in centre of each face
Base centred (*A*, *B* of *C*)	Lattice points are centred on opposite faces of the cell and the corners of the unit cell. (e.g. the A face is defined by the *b* and *c* axes and so on)

The unit cell can be further broken down into the asymmetric unit cell -- the smallest collection of lattice points to which a symmetry operation can be applied. This cumulatively forms the unit cell. These asymmetric unit cells generate a collection of symmetry operations which, in combination with the fourteen Bravais lattices, gives 230 different space groups. These define the overall symmetry of a unit cell (see next section) and are examined by diffraction techniques, such as X-ray diffraction (section 4.2.3.)[4-6, 8].

4.1.1. Symmetry and Space Groups

Unit cell symmetry in crystalline materials falls into two groups: point and translational symmetry[1, 4, 5, 7, 8]. Point symmetries are those which all pass-through a given point; therefore, the cell does not change with the application of the symmetry operation. These include proper rotation axis, mirror planes, centre of symmetry and rotary inversion axes. Proper rotation involves rotation about an axis by 360°/n. Mirror planes involve reflection of an object. Centre of symmetry is present when any part of the structure can be reflected through this centre (or point) of symmetry and an identical arrangement found on the other side. Rotary inversion axes are a combined symmetry operation which involves rotation and inversion through the centre. Overall, this forms 32-point symmetry operations and can be referred to by the Schönflies notation. This notation, however, applies to finite molecules which demonstrate order but not necessarily the long-range infinite order experienced within crystalline solids. Here, translational symmetry operations need describing to account for the screw axis and glide plane. This requires the Hermann–Mauguin nomenclature, which is used in this work.

Table 4.3. Defining symmetry of a unit cell and associated Hermann–Mauguin symbols.

	Symmetry Element	**Hermann–Mauguin symbols**
Point Symmetry	Mirror Plane	*m*
	Rotation Axis	*n* = 2, 3, 4, 6
	Inversion Axis	$\bar{n}$ = $\bar{1}$, $\bar{2}$, *etc.*
	Alternating Axis	–
	Centre of Symmetry	$\bar{1}$
Space Symmetry	Glide Plane	*a, b, c, d, n*
	Screw Axis	2_1, 3_1, 3_2, 4_1, 4_2, 4_3, 6_1 - 6_5

The screw axis, n_m (see table 4.3) combines rotation and translation. This is best described as an atom/s lying helically about a point/s. Here, the atoms or ions on a screw axis lie helically about these axes. Screw axes are symbolised by n_m, this indicates translation by the fraction of Y/X of the unit cell edge together with the simultaneous rotation by 360/n° about the axis. For example, a 4_1 screw axis parallel to *a* involves translation by 1/4 and rotation by 90°. The glide plane considers translation in combination with reflection. Here, translation is parallel to the unit cell axis (*a*, *b*, *c*), to a face diagonal (*n*) or body diagonal (*d*) with reflection across the plane. The *a*, *b*, *c* and *n* glide planes have a translation step one half the unit cell in those directions. The *d* glide plane has a translation step one quarter of the body diagonal. Both the screw axis and glide plane cause systematic absences within diffraction patterns. This is also true of face and body centred cells (see section 4.2.3.).

The point and translational symmetry groups, when combined with the fourteen Bravais lattices, encompass 230 different space groups. These become increasingly complex to visualise, especially when multiple symmetry elements coexist, and are therefore best visualised by software. This work makes use of Vesta[9] to aid in visualising the three garnet type space groups in this work; $Ia\bar{3}d$, $I\bar{4}3d$ and *I4₁/acd*, see table 4.4.

Table 4.4. Lithium garnet space groups encountered in this work and associated extended space group fully describing the cell symmetry.

Space group	**Extended space group**	**Garnet System**
Ia$\bar{3}$*d*	$I4_1/a\ \bar{3}\ 2d$	Most cubic garnet systems
I$\bar{4}$3*d*	-	Ga-LLZO, Fe-LLZO
*I*4₁/*acd*	$I4_1/a\ 2/c\ 2/d$	Tetragonal garnets

4.2. POWDER X-RAY DIFFRACTION

Powder X-ray Diffraction (PXRD) enables examination of unit cell characteristics, such as dimensions and symmetry. However, phase purity, particle size, and lattice strain (to name but a few), can also be determined. PXRD is used throughout this work (abbreviated only to XRD).

4.2.1. Generation of X-rays

X-rays are generated when high energy charged particles are accelerated through ≈40 kV and collide with matter. The interaction of the charged particles with matter gives emission of an X-ray spectrum composed of monochromatic and white radiation (Bremsstrahlung). The monochromatic radiation is of many fixed wavelengths and is explained below. White radiation (of little importance in XRD) arises from matter collisions which slow and/or stop electrons, resulting in energetic loss in the form of electromagnetic radiation. See figure 4.2 for an example spectrum produced on electron bombardment of Cu.

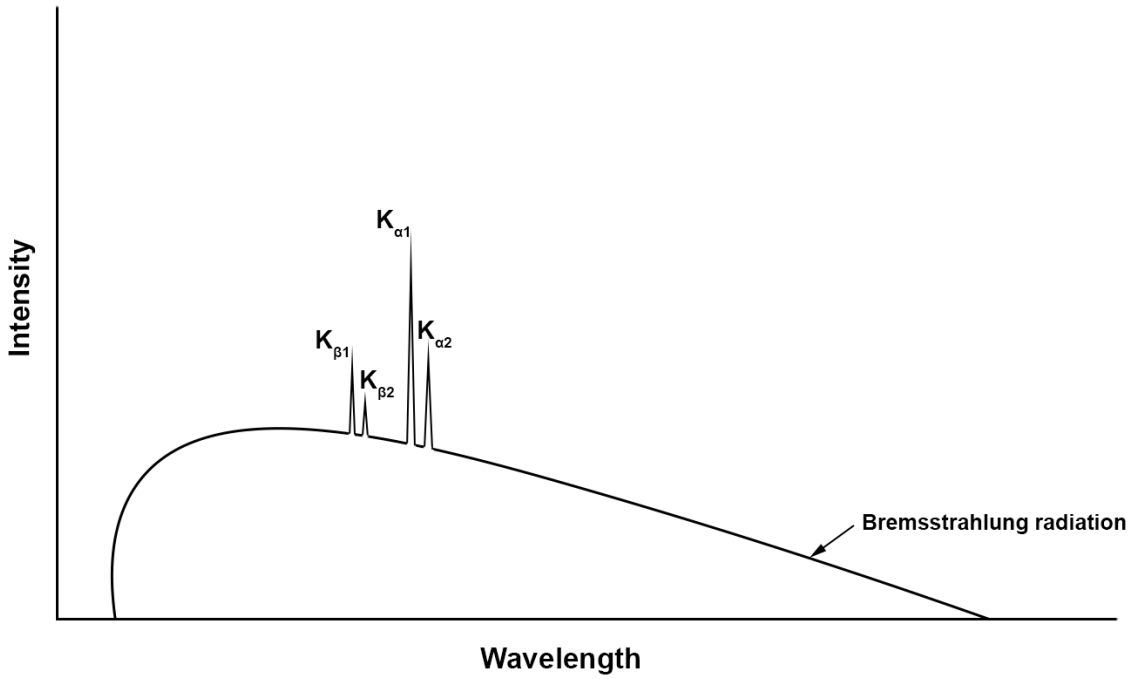

Figure 4.2. Example emission spectrum of Cu after bomdarbment with electrons.

Monochromatic radiation is required for XRD. This is generated (in this work) by first heating a tungsten filament which causes thermionic emission of electrons. The electrons are then accelerated at high voltage (≥ 10kV) at a metal target (Cu in this work), affixed to an anode. Upon electron bombardment, with sufficiently accelerated electrons, the metal target ejects inner core electrons. The inner core vacancies are immediately filled by outer shell electrons, which releases energy in the process in the

form of an X-ray. These transitions create an X-ray spectrum which is dependent upon orbital arrangement and is thus characteristic of the element and the orbital from which the electron originates. These shells are denoted by the Siegbahn notation, therefore the 2p → 1s and the 3p → 1s transition are termed K_α and K_β respectively. Only ≈1% of collisions generate X-rays; the remaining energy is lost by thermal energy. Therefore, the X-ray tube, which houses the filament and target, is constantly cooled (usually with water).

Cu K_α has a weighted average wavelength of 1.5418 Å while K_β is 1.39225 Å. These both correspond to interatomic spacing in crystalline materials, but the K_α transition is more common, and thus higher intensity, so is preferred for diffraction experiments. This requires filtering to obtain a single monochromatic Cu K_α beam. This is done by using Ni foil, as the ionisation energy of Ni K_α corresponds to Cu K_β. Therefore, Cu K_β is absorbed (along with most of the white radiation) while Cu K_α passes through. This gives a reasonably clean beam of Cu K_α. Further filtering *via* crystals, such as quartz or germanium, can increase the beam purity. Here, crystals with known lattice spacing are orientated in a way which diffracts certain wavelengths toward the sample.

Cu K_α radiation is, however, a doublet of $K_{\alpha1}$ (1.54051 Å) and $K_{\alpha2}$ (1.54433 Å) due to the slightly different energies relating to the 2p electron spin states, relative to the spin of the 1s orbital. $K_{\alpha1}$ and $K_{\alpha2}$ are too close in energy to filter out effectively (unless using a crystal monochromator), hence an average of 1.54178 Å is used. This shows as a peak doublet within XRD, which is more well resolved at higher angle. The K_α radiation then leaves the X-ray tube by a Be window, which is effectively invisible due to minimal X-ray scattering arising from its low atomic weight. The beam is then moved between a specific angle range relative to the sample, discussed further in section 4.2.3.

4.2.2. Interaction of X-rays with Atoms

When an electromagnetic wave impinges upon a charged particle (such as an electron) it creates an oscillating motion of the charged particle, which generates a secondary source of radiation that scatters the incident beam. When X-rays are directed at an atom the oscillating electromagnetic field causes each electron in the atom to vibrate. The vibrating electron then emits radiation, which can be coherent with the incident X-ray beam. As X-rays are scattered by the electrons in the atomic shell, each atom is effectively a point scatterer with a scatter strength proportional to the number of electrons (therefore scattering scales with atomic weight). The scattered radiation can either lose or maintain the incident energy. Elastic scattering, or Thompson scattering, has no loss of energy when scattered, therefore is coherent with the incident radiation. Inelastic, or Compton scattering, is the opposite. Elastic scattering forms the basis of XRD.

Figure 4.3 shows an oversimplified view of an atom with several electrons (shown as points) scattering incident radiation. Here, the scattering X-ray photons, shown in grey, across the A-B electrons in the forward direction are in phase (or coherent) across the 22' wavefront. The 2 and 2' waves have travelled the same total distance before and after scattering so no path (or phase) difference arises. The in phase, scattered, waves across wavefront 22' are the sum of both incident radiation amplitudes, therefore a wave with twice the amplitude and the same wavelength results – constructive interference[1, 6, 7]. The scattered waves across wavefront 11' are out of phase, as the path distance is not an integral number of wavelengths (CB-AD), therefore scattered radiation is of a lower amplitude. Complete destructive interference occurs if a wave is 180° out of phase with another and both have the same amplitude[7].

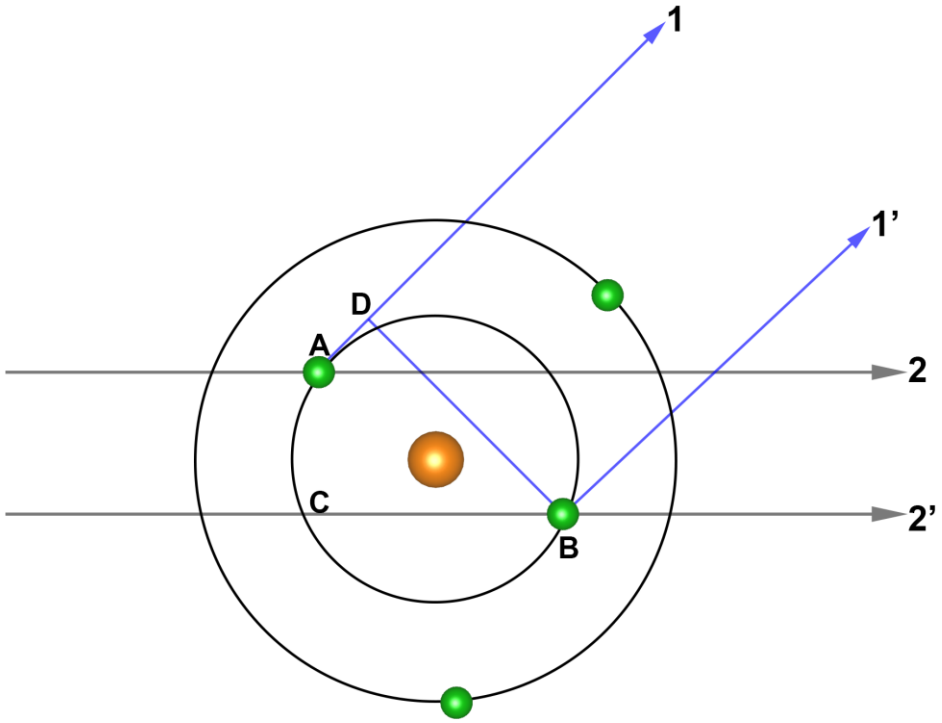

Figure 4.3. Simplified view of an atom showing in phase (22') and out of phase scattering (11') across two wavefronts. Electrons in green.

The atomic scattering factor explains how efficiently an atom scatters in a given direction, and is defined thus[7]:

$$f = \frac{Amplitude\ of\ wave\ scattered\ by\ atom}{Amplitude\ of\ wave\ scattered\ by\ one\ electron} \qquad 4.1$$

4.2.3. X-ray Diffraction

X-rays have wavelengths (0.05 nm to 0.25 nm), similar to the typical interatomic spacing in crystals (≈0.2 nm). Therefore, X-rays can probe crystal structures, first realised by Max von Laue in 1912 with W.L. Bragg and W.H. Bragg devising the technique of XRD shortly after[10, 11]. When discussing XRD principles it is important to remember that crystalline solids may be regarded as effectively being parallel atomic planes separated by a constant distance, *d (d spacing)*. These atomic planes are uniquely described by miller indices (*hkl*), which are the reciprocal of the points at which the plane intersects the *a*, *b* and *c* axis (intercept reciprocal is taken to avoid ∞ which occurs if a plane does not intersect one of the axes). Miller indices are, usually, taken as the plane closest to the origin without passing through it. *h* is the reciprocal of the fractional coordinate at which the plane intercepts the *a* axis of the unit cell, with *k* and *l* the same but relating to the *b* and *c* axis respectively. Therefore, the (210) plane in a cubic cell intercepts the *a* axis at 0.5, *b* at 1 and the *c* axis at ∞, see figure 4.4.

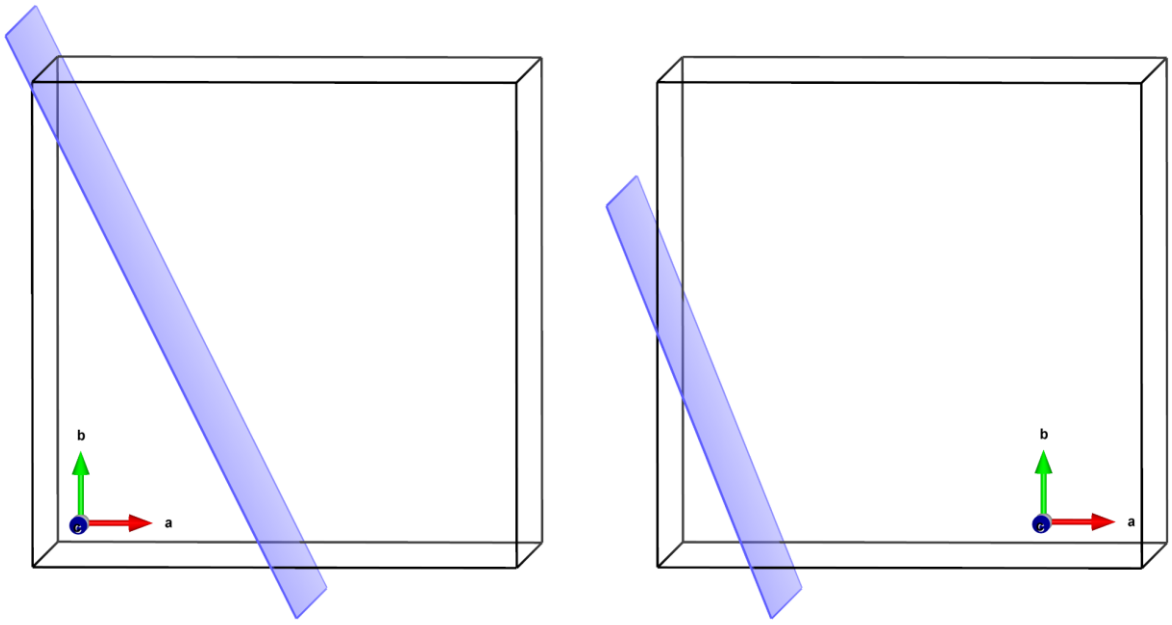

Figure 4.4. Illustration of 210 (left) and 520 (right) lattice planes in a simple cubic cell.

The distance between planes is the d-spacing (d_{hkl}). If a cubic cell is considered, the distance between adjacent planes (*hkl*) is

$$d_{hkl} = \frac{a}{\sqrt{h^2 + k^2 + l^2}} \qquad 4.2$$

Combining miller indices with the discussed concepts of X-ray scattering forms the basis of XRD, as the effectively infinite periodic array of atoms across multiple planes will inevitably allow constructive interference once certain conditions are satisfied. These directions are governed by the nature of the

crystalline sample and the wavelength of the incident radiation. This forms the basis of Bragg's law, which relates the X-ray wavelength (λ) to the d-spacing of the atomic planes[4, 11].

$$n\lambda = 2d_{hkl}\, sin\theta \qquad 4.3$$

In Bragg's law, polycrystalline samples composed of many lattice planes may either be reflected at an angle (θ) equal to the incident radiation or transmitted through the plane to be diffracted by another plane. When the spacing between successive planes provides a path length equal to an integer number of wavelengths, the "reflections" would be in phase and constructively interfere, see figure 4.5. In real crystals, whereupon thousands of planes exist, Braggs law imposes strict conditions upon the angles at which reflection can occur. Hence, if the incident angle is incorrect by more than a few tenths of a degree, beam cancellation is usually complete[1] (although Bragg's law discusses reflection, it is in fact scattering to which it refers).

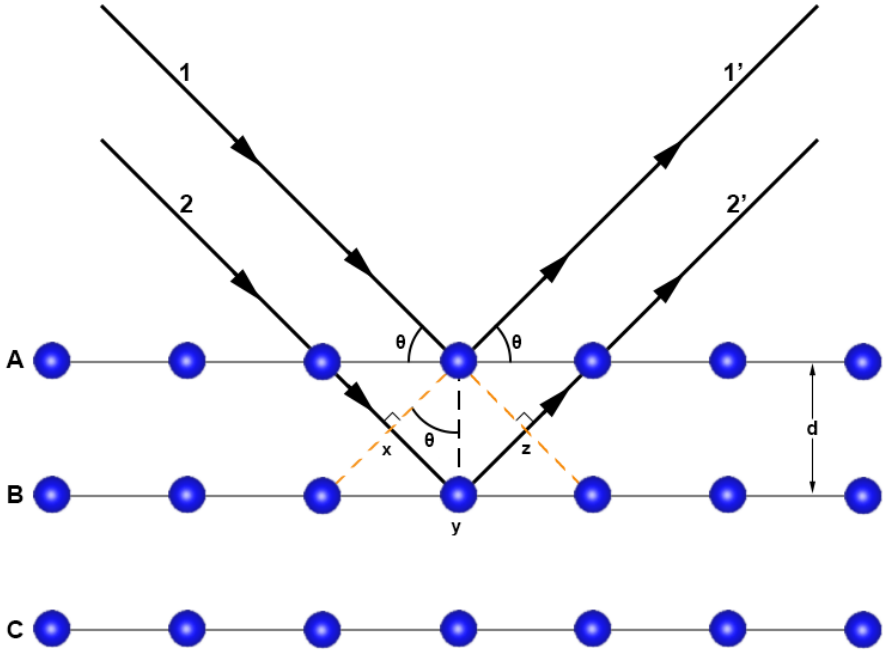

Figure 4.5. Illustration of Bragg's Law, showing atoms (blue) arranged in planes (grey) and constructive interference (black lines).

The interplanar spacing for each lattice plane set can then be determined by varying θ while keeping λ constant. Therefore, to observe the (*hkl*) planes in the diffraction pattern X-rays must constructively interfere, so equation 4.2 and 4.3 can be combined with Bragg's law (for a cubic system) thus,

$$sin^2\theta_{hkl} = \frac{\lambda^2}{4a^2}(h^2 + k^2 + l^2) \qquad 4.4$$

The intensity of the constructive interference is then detected at any given angle, with a plot of intensity *vs* 2θ giving the characteristic pattern for a crystalline material. The atomic scattering factors also dictate the intensity of a Bragg "reflection", which is proportional to the square of the structure factor (see next section), hence illuminating the limitations of XRD with lighter elements. Bragg's law, although robust, is highly simplified when thinking of real-world crystal systems. However, despite the inaccuracies, the same answers are obtained *via* complex mathematical analysis, therefore it is a good way to conceptualise the reality of a very complicated process[1].

When analysing materials which are not primitive cubic, some reflection absences are seen due to additional lattice centering; these are systematic absences. For example, in a face centred cubic cell with (200) and (100) planes, the reflections from the (100) plane will be 180° out of phase with the (200), see figure 4.6. Therefore, these will not be observed in the diffraction pattern. Hence all observed (*hkl*) values for a face centred cubic cell will be either even or odd, similarly for a body centred cell the relationship *h*+*k*+*l* = even must be satisfied. This extends to all crystal classes and can provide vital symmetry information.

Systematic absences also arise from screw axis and glide plane symmetry elements. For example, a 2_1 screw axis has a plane of atoms halfway between the (001) plane, therefore causing destructive interference. This will cause ***I*** to be odd. A glide plane effectively halves the unit cell in the glide direction. Therefore, a glide plane perpendicular to the *b* axis gives a plane which is one half a cell length from the (101) and, thus, a systematic absence. Therefore, only when *h* is even can reflections be observed.

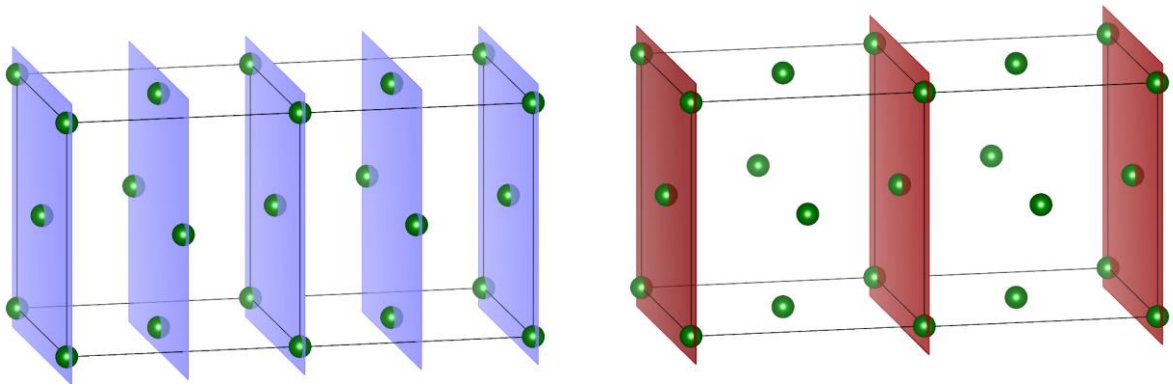

Figure 4.6. Illustration of systematic absences in a face centered cubic cell where blue is the (100) plane and red is the (200) plane.

4.2.4. The X-ray Diffractometer

Powder diffractometers, owing to Bragg's law are fairly standardised. Diffractometers require a source of radiation (discussed in section 4.2.1.), a detector and sample stage. In reflection geometry the X-rays are directed toward the sample stage at the incident angle (θ) and the diffracted beam is the angle between the source and detector, 2θ. This corresponds to reflection or Bragg-Brentano geometry in which the divergent and diffracted beams are focused at a fixed radius from the sample position. A range of angles is scanned, with most diffractors operating from 1 – 140°. The choice of range and scan time depends upon the crystal structure and upon the information which needs to be extracted, for example for known structures only shorter periods may be used, however for unknown structures that need resolving a wide 2θ and with long scan times may be required.

In powder XRD the sample is spread upon a planar substrate which should ideally consist of many similarly sized particles arranged in a random manner, which cover each possible orientation and thus give a good, averaged view of the overall structure. This can be greatly assisted by use of a rotating sample stage. A plot of 2θ against observed intensity then gives a diffraction pattern, see figure 4.7. Within a diffraction pattern information regarding unit cell characteristics, atomic positions, thermal vibrations, phase fractions, crystalline size, and/or preferred orientation can be obtained. Individual peak intensities also give information of the lattice plane multiplicity. It must also be assumed some form of instrumentation contribution to the pattern is present, such as zero-point error.

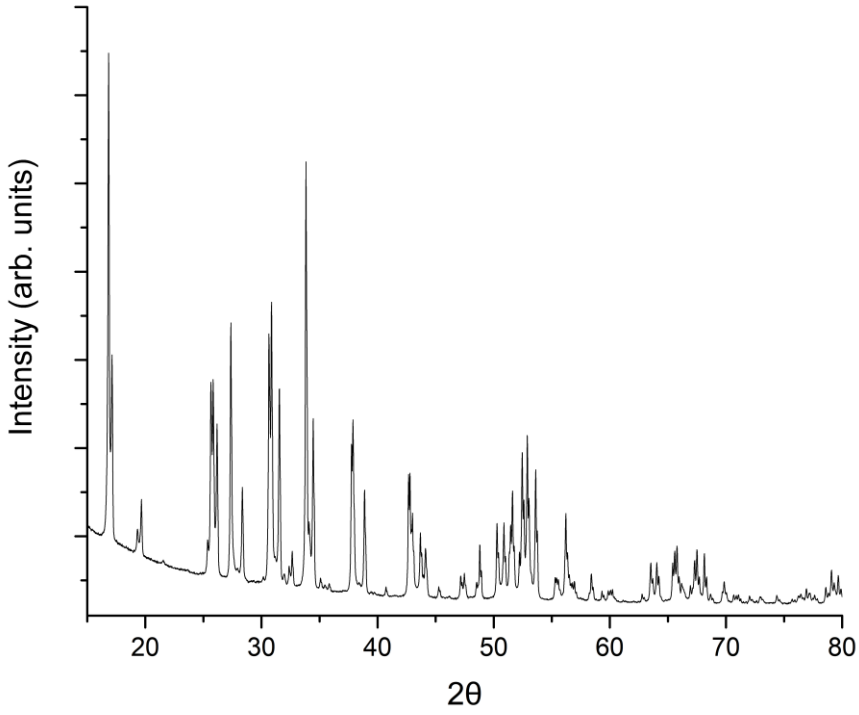

Figure 4.7. Example X-ray pattern obtained from a tetrgonal lithium garnet.

The absolute intensity of a diffraction pattern depends upon experimental parameters, such as the scattering power of the elements and scan duration. Instrumental factors, like radiation source and detector efficiency, will also affect the final pattern. Small particle crystalline samples give broader peaks, which decrease the height of the peak, as too will atomic thermal motion.

Powder XRD is used heavily throughout this work, with this sometimes taking the form of both powders and pellets. XRD was taken on all samples to assess phase purity (which was matched with the PDF2 database). Structure refinement was based upon known structural models to obtain lattice parameters and fractional occupancies (see next section). Sample handling is detailed in the methods sections of each chapter, but generally samples were affixed to low background silicon disc holders. Samples were finely ground and affixed *via* a thin layer of petroleum jelly to the silicon, with powder covering the entirety of the disc. XRD scans were obtained between 15 - 80° 2θ with a 0.02° step size. Scan times varied dependent upon the material, but generally the more complex the system, the longer the scan. A Bruker D8 advance diffractometer in Bragg-Brentano geometry fitted with an Ni filter, a Cu *Kα* X-ray source (λ= 1.5418 Å) and a solid-state LynxEye position sensitive detector was used. The sample was rotated at 15 RPM. Variable temperature measurements were conducted on a similarly equipped D8 but lacked a rotating sample stage.

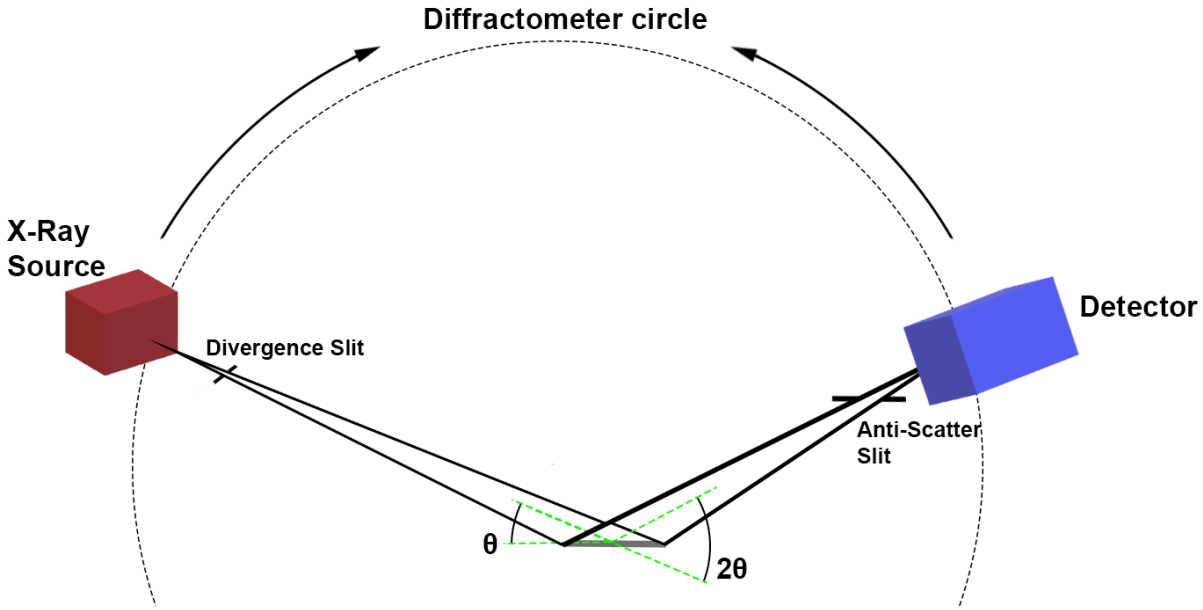

Figure 4.8. Simple diagram of an X-ray diffractormeter

4.2.5. Data Analysis- Rietveld Refinement

Rietveld refinement is used to obtain structural information from XRD patterns[12-18]. The Rietveld method involves fitting a model to experimental data. The model is generated from structural models with enough crystallographic information to calculate an accurate diffraction pattern with the ideal peak intensity. This is then compared to experimental (observed) data to extract numerous structural parameters, such as unit cell size and shape, fractional occupancies and atomic positions. The Rietveld algorithm optimises the model function to minimise the weighted sum of squared differences between the observed and calculated point intensities, with the latter varied using a least squares method until S_y is minimised, as per equation 4.5.

$$S_y = \sum_{i=1}^{n} w_i \, (Y_i^{obs} - Y_i^{calc})^2 \qquad 4.5$$

where Y_i^{obs} is the observed intensity at the *i*th step, w_i is the weight and is equal to $1/Y_i^{obs}$ and Y_i^{calc} is the calculated intensity at the *i*th step and the sum over all data steps[14, 16, 19-21].

Therefore, the accuracy of Rietveld analysis depends very heavily on the quality of the starting model. Several factors must be considered in a diffraction pattern; these include the background, peak profiles, peak positions, and peak intensities. These are discussed in more detail below.

The background cannot be fully removed from an experimental diffraction pattern; its contribution can only be minimised. Although, the data held within the background (diffuse scattering) are useful in other techniques, it is not for standard structural refinement from XRD patterns. Therefore, it must be accounted for so that the remainder of the pattern is modelled accurately. Background functions are modelled by geometric functions, with this work using Chebyshev polynomials in the general structure analysis system (GSAS) II[13]. Further background contributions can arise dependent upon sample holder, see section 4.7.4.

Each analysed experimental diffraction pattern must account for peak shape, as ideal crystalline materials (which show single, sharp, diffraction lines on a pattern) will not be observed. Peak shape also alters due to instrumental influences (such as axial divergence, detector misalignment, X-ray source, slit choice and imperfect monochromatic radiation). XRD peak shapes look similar to the common mathematical descriptions of symmetrical peaks, Gaussian and Lorentzian. However, these are seldom adequate to describe the peak shapes alone. Rather, a combination of Lorentzian and Gaussian factors are used, termed pseudo-Voight[13]. Peak positions can be determined easily from the

diffraction pattern, from which lattice parameters can be derived. Instrumental factors, such as zero-point error, can also affect peak position.

The Bragg peak equation allows calculation of peak intensity, as per equation 4.6:

$$I_{hkl} = K_{(hkl)} F^2_{(hkl)} m_{(hkl)} A_{(hkl)} Lp_{(hkl)} \quad 4.6$$

where $I_{(hkl)}$ is the intensity, $K_{(hkl)}$ is the proportionality constant, $m_{(hkl)}$ is the Bragg reflection multiplicity, $A_{(hkl)}$ the absorption correction factor (dependent upon sample thickness in the diffraction direction) and $Lp_{(hkl)}$ is the Lorentz factor (probability of observing a reflection at a given diffraction angle, and a radiation polarisation factor). $F_{(hkl)}$ is the structure factor, this describes the atomic positions, thermal parameters and site multiplicity as per equation 4.7:

$$F_{(hkl)} = \sum_j f_j \, N_j exp\left[2\pi i\left(hx_j + ky_j + lz_j\right)\right] exp\left[-M_j\right] \quad 4.7$$

f_j is the atomic scattering factor of the *j*th atom type, N_j is the site occupancy of the *j*th atom in the unit cell, x_j, y_j and z_j are the atomic positions of the *j*th atom in the unit cell and M_j accounts for the reduction in scattering power arising from thermal motion. M_j is calculated thus:

$$M_j = 8\pi^2 B_j^2 sin^2\,\theta/_{\lambda^2} \quad 4.8$$

where *Bj* relates to the root square mean thermal displacement of the *j*th atom parallel to the diffracted beam by $1/_{8\pi^2}$.

Within Rietveld refinement, the calculated diffraction pattern intensity for any data point is the sum of all contributions from the overlapping Bragg peaks. This is combined with sample corrections (such as zero-point error or preferred orientation) and the background. These parameters are assessed stepwise within software (this work uses GSAS II) and recalculated after each step. This compares the experimental pattern to its calculated equivalent whereupon the better observed data overlap the calculated (fit), and this determines the quality of the extracted parameters.

R factors are often used to mathematically assess the quality of the fit between the observed and calculated pattern but should not be used alone to assess accuracy. Both R-pattern (see equation 4.9) and R-weighted pattern (see equation 4.10) compare the whole pattern fitting for the observed and calculated diffraction pattern at each data point, with a lower value indicating better fit[13].

$$R_p = \frac{\sum |\, Y_i^{obs} - Y_i^{calc} |}{\sum Y_i^{obs}} \quad 4.9$$

$$R_{wp} = \left[\frac{\sum w_i \, [Y_i^{obs} - Y_i^{calc}]^2}{\sum w_i [Y_i^{obs}]^2}\right]^{\frac{1}{2}} \quad 4.10$$

The optimum R value (assuming a perfect structure model) is R expected (R_{exp}). This takes into consideration the error in the measured intensity and is calculated by equation 4.11.

$$R_{exp} = \left[\frac{N - P - C}{\sum w_i {Y_i^{obs}}^2}\right]^{1/2} \quad 4.11$$

N is the number of observations, *P* the number of refined parameters and *C* the number of constraints used in the refinement process.

However, within Rietveld refinement the most popular quoted term to indicate the quality of the fit is R_{wp}, despite potentially giving false minimums if the selected parameter suite is incorrect (this is also true of other mathematical models). However, R_{wp} suffers from erroneous values if the background is not properly described, if all peaks are not accounted for and/or if a large background is present (giving erroneously high R_{wp}). Accordingly, a background corrected R_{wp} can thus be found in equation 4.12.

$$R_{wp} = \left[\frac{\sum w_i \, [Y_i^{obs} - Y_i^{calc}]^2}{\sum w_i [Y_i^{obs} - Bkg_i]^2}\right]^{1/2} \quad 4.12$$

These numerical data are of high importance, as they describe (albeit not completely) the necessary algorithmic functions to allow for a Rietveld refinement. However, these data alone should not be used, as most refinement software aims to reduce the least squares parameter as much as possible and will thus do so even if an incorrect/impossible set of parameters are selected. The histogram which visually shows the observed and calculated data (difference profile) should also be used (see figure 4.9) in conjunction with R factors to assess data quality, as should a consideration as to whether the final structural model is sensible[12].

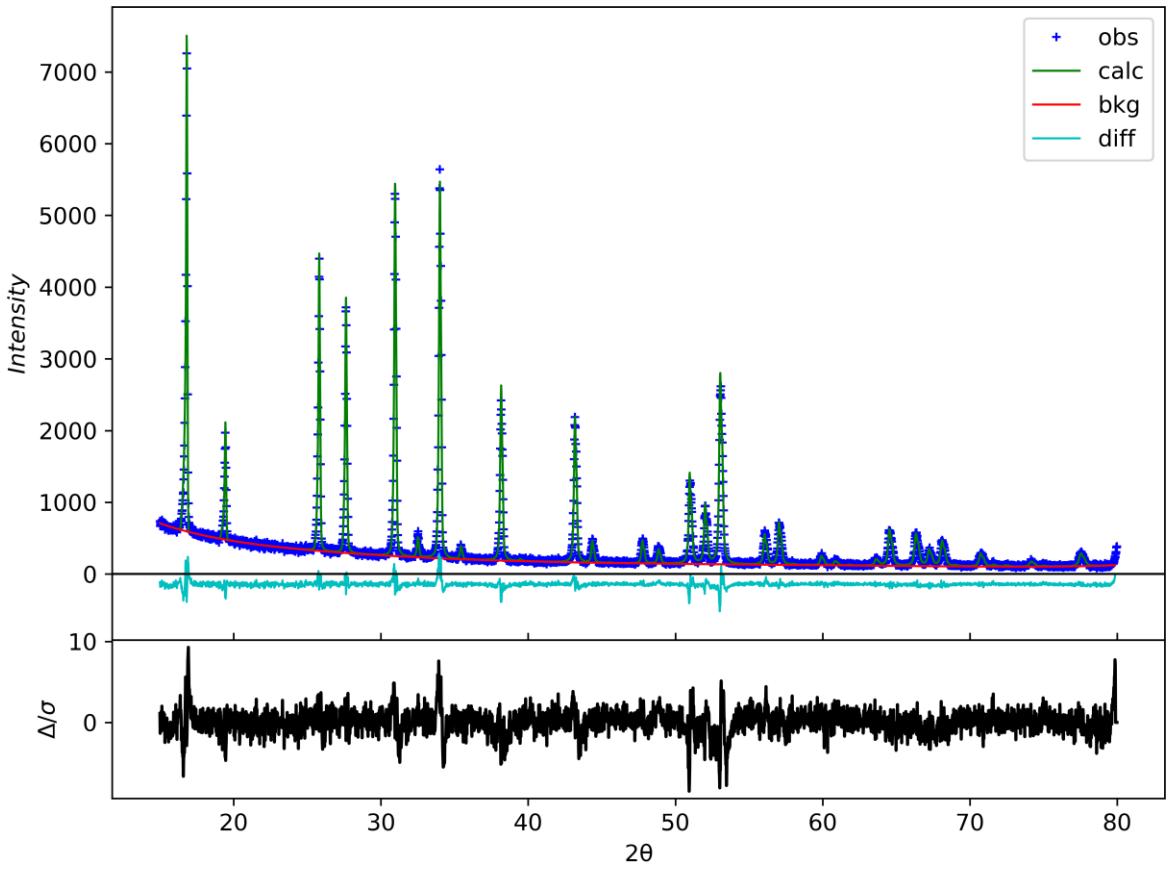

Figure 4.9. Example refinement difference profile of a cubic lithium garnet material, R_{wp} = 7.976%

4.3. X-RAY ABSORPTION SPECTROSCOPY

X-rays can be absorbed by electrons. This forms the basis of X-ray absorption spectroscopy (XAS). Here an incident X-ray beam, which corresponds to the binding energy of a core electron, can promote a core shell electron to an unoccupied orbital (or to a continuum state). This is termed the absorbance edge. The absorbance of an X-ray, and subsequent electron promotion, requires a specific characteristic energy dependent upon atomic orbital arrangement. Therefore, absorbance spectra are characteristic of individual elements and their local environments.

When the incident beam energy matches the binding energy, there is a sharp rise/discontinuity in the linear absorption coefficient of X-rays arising from electronic transitions, the number of which being dependent upon atomic weight. This gives a sharp peak in the transmittance spectra (the edge). This generally describes XAS. X-ray absorption near edge spectroscopy is a subset of XAS where the region around the absorbance edge (≈10 eV below and ≈20 eV above) is studied. This relates to inner shell transitions. As the precise wavelength shape and the absorption edge are very sensitive to the local environment the local structure, such as oxidation state, can be probed (the fine structure). Investigations can also be extended further past the absorption edge to determine bond lengths and coordination environments. This is extended X-ray absorption fine structure (EXAFS), see figure 4.10.

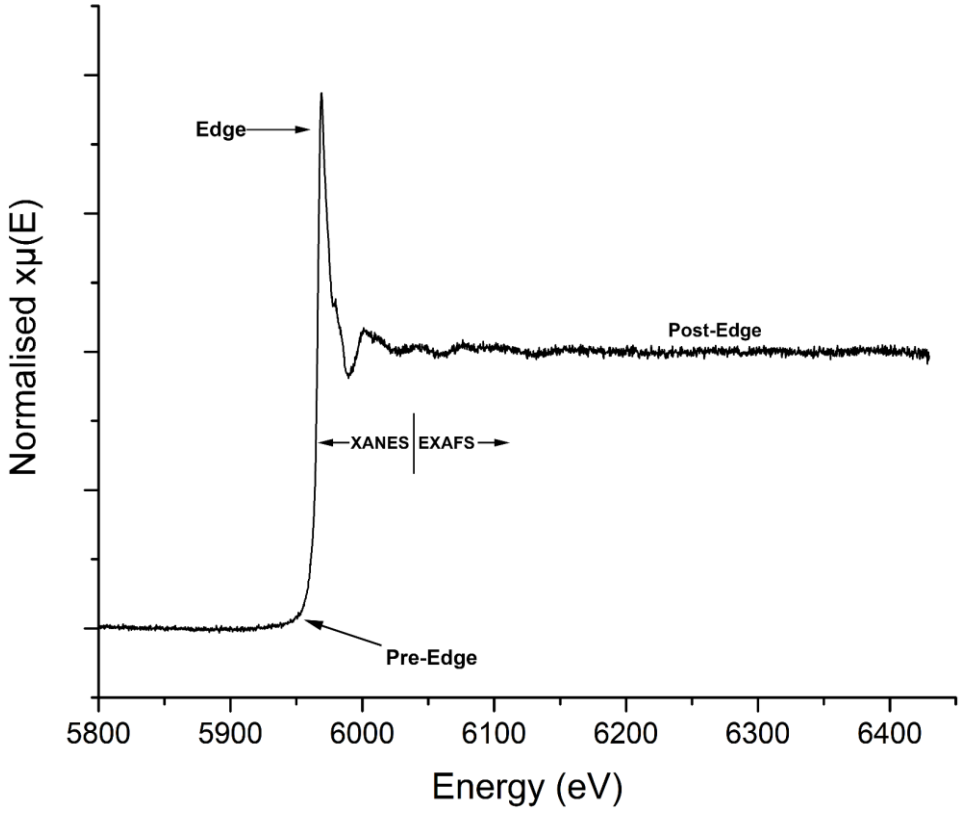

Figure 4.10. Example of X-ray absorbance spectrum obtained from $BaPrO_3$.

An XAS spectrum is split into three regions: the pre-edge, the edge, and the post edge. The pre-edge gives information regarding the coordination environment. The post-edge region allows determination of coordination shells, as the emitted photoelectron scatters off neighbouring atoms (EXAFS). Only the edge is considered in this work, which gives the formal oxidation state of the element. This corresponds to promotion of a core-electron above the continuum (where the absorbance edge is treated as a continuum resonance). As the absorber-scatter interaction (between the nearest neighbour atoms) distance gets shorter, the continuum state energy increases. This corresponds to shorter bond-lengths in samples; therefore, the edge energy increases. Hence, the edges are shifted to higher energies as the sample oxidation state is increased. In this work XANES samples were analysed in pellet form. Here, 7 - 12 mg of powder was mixed with 50 mg of cellulose and uniaxially pressed to 2 tons. Samples were analysed at Diamond Light Source on B18.

The vacancy arising from the promoted, inner shell, electron in XAS is promptly filled by outer shell electrons. This also emits electromagnetic energy in the X-ray region, with an energy equal to the specific energy difference between two quantum states of the electron. These emissions are characteristic of each element and form the basis of X-ray fluorescence spectroscopy (XRF). This was used briefly in this work to confirm Cl presence in the Hf garnets (chapter 6). Here, samples were analysed in powder form under a He atmosphere on a Bruker S8 Tiger XRF.

4.4. A.C. IMPEDANCE SPECTROSCOPY

Impedance spectroscopy (IS) is a commonly used technique to probe a wide variety of systems such as solar cells, photoelectrochemical cells, sensors, biological systems, water splitting and corrosion. This also extends to energy storage, whereupon charge movement and transfer takes place. Slutyers was the first to use IS in energy storage, and it is used heavily throughout this work to investigate the dielectric behaviour and conductivity of the garnet electrolytes[22, 23]. IS is also used to assess the interfacial resistance between the garnet and Li metal in lithium symmetry cells.

4.4.1. A.C. Impedance Overview

A succinct view of A.C. impedance spectroscopy is one where it is considered akin to resistance as per Ohm's law, defined thus,

$$R = \frac{E}{I} \tag{4.13}$$

where R is resistance, E is voltage, and I is current. The equation implies a simplistic view of resistance, with only E and I relating to the ohmic value. Hence, Ohm's law only covers the behaviour of an ideal resistor with a direct current signal, but also assumes that:

- Ohm's law is adhered to at all current and voltage levels
- The resistance value is independent of frequency
- Alternating current and voltage signals through a resistor remain in phase

Therefore, Ohm's law presents an overly simplistic view of resistance, as it does not examine the complex behaviour encountered in all practical systems upon application of a potential. In these real-world systems (even including simple resistance measurements, such as an Au wire) the application of voltage enables charge movement, which arises from ion/electron migration and point defects. This causes an immeasurable number of polarisation events, therefore inducing dipoles/multipoles in the sample. This corresponds to storing energy in either electric or magnetic fields, to which a resistive component is inevitably present as charge does not move freely. Therefore, real world systems fundamentally contain a complex array of resistors, capacitors and inductors connected in parallel and/or series which cannot be accounted for by Ohms law alone[24]. However, IS, not being bound by these properties, gives both a more correct approximation of resistance (real impedance) and can also reflect the ability of a system to store charge (in the imaginary term, see later)[25-29].

4.4.2. A.C. Impedance Theory

A traditional view of an A.C. signal is a sinusoidal waveform, which represents the periodic reversal of the signal (often many times per second), see figure 4.11. In the sine wave, the electrical signal alternates between a maximum and minimum value, with the periodic time between waves being a smooth transition. The time between a full waveform cycle is the periodic time (T) often expressed in Hz, where 1 Hz is one whole periodic cycle per second. With sine waveforms, this periodic time can also be expressed in terms of either degrees or radians, with one full cycle equal to 360° (T = 360°) or 2π (T = 2π). A.C. signals can be discussed in terms of other waveforms, such as square waveforms, but these do not relate to the use of IS in this work.

The measurement of impedance relies upon use of a sinusoidal alternating potential (the term A.C. potential is a misnomer) which, when passed through a sample, maintains its frequency and sinusoidal nature but the alternating current response is phase shifted and the amplitude changed, see figure 4.11. It is this vector quantity which denotes the magnitude of the impedance. It is now relatively simplistic to create a corresponding equation analogous to Ohms law but applicable to A.C. signals. Firstly, the alternating excitation signal is considered and is expressed by equation 4.14:

$$E_t = E_0 sin(\omega t) \tag{4.14}$$

where:

$$\omega = 2\pi f \tag{4.14i}$$

E is the potential at time t, E_0 is the amplitude of the signal and ω is radial frequency (expressed in radians/second) and frequency f (expressed in hertz). A corresponding A.C. response can then be formulated thus:

$$I_t = I_0 sin(\omega t + \Phi) \tag{4.15}$$

where I is current and Φ is the phase shift. Hence an equation analogous to ohms law can be derived whereby:

$$Z = \frac{E_t}{I_t} = \frac{E_0 sin(\omega t)}{I_0 sin(\omega t + \Phi)} = Z_0 = \frac{sin(\omega t)}{sin(\omega t + \Phi)} \tag{4.16}$$

with impedance (Z) being expressed as a vector quantity composed of both magnitude (Z_0) and phase shift (Φ). Hence, $Z = R$.

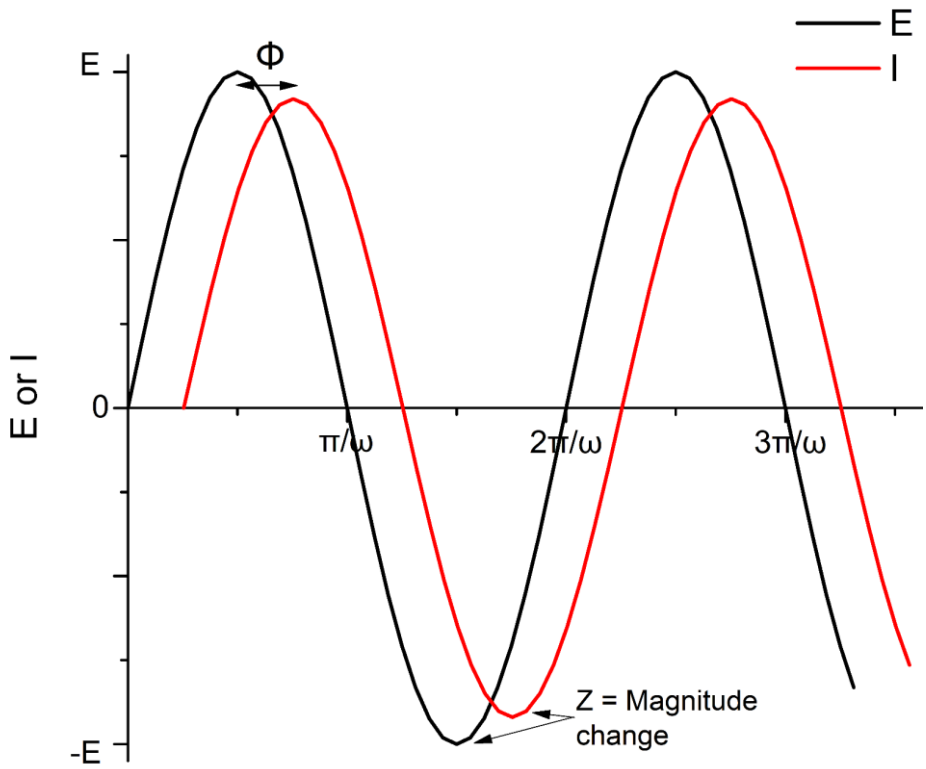

Figure 4.11. Example of IS where alternating potential (black) has a different amplitude compared to the alternating current resonse (red) - (Z, the real component), corresponding to resistance. The current response is also phase shifted (Φ), which reflects a capacitive response and reflects the storing of charge (where an ideal capactior would lag the excitation by 90°).

However, if these values were plotted directly the sinusoidal signal and response is an oval, referred to as a Lissajous Figure (which can also be used to assess the pseudolinearity of the system). This was the traditionally accepted method for data analysis on older oscilloscope-based measurements, prior to the availability of lock-in amplifiers and frequency response analysers. IS data are now analysed more commonly in the form of a complex function, with both real (Z') and imaginary components (Z") by Nyquist and/or Bode plots. However, for these plots, equation 4.16 must be converted to a complex equation. This requires Euler's relationship, which establishes the fundamental relationship between the trigonometric and complex exponential functions with respect to *Φ*:

$$exp^{(j\Phi)} = cos\Phi + jsin\Phi \qquad 4.17i$$

Impedance can then be expressed as a complex function:

$$E_t = E_0 sin(j\omega t) \qquad 4.17ii$$

$$I_t = I_0 sin(j\omega t - \Phi) \qquad 4.17iii$$

Hence equation 4.18 can now be transformed into a complex number as per:

$$\mathrm{Z}(\omega) = \frac{\mathrm{E}}{\mathrm{I}} = \mathrm{Z}_0 \exp^{(\mathrm{J}\Phi)} = \mathrm{Z}_0(\cos\Phi + \mathrm{j}\sin\Phi) = \mathrm{Z}_{\mathrm{real}} + \mathrm{j}\mathrm{Z}_{\mathrm{im}} \qquad 4.18$$

The impedance data can now be represented as a complex number as a combination of "real" or in phase (Z_{real}) and "imaginary" or out of phase jZ_{IM}. This forms the Nyquist and/or Bode plots. The phase shift (Φ) at a chosen radial frequency (ω) is the ratio of the imaginary and the real impedance components, thus:

$$\Phi = tan^{-1}\left(\frac{Z_{im}}{Z_{real}}\right) \qquad 4.19$$

IS is an exceptionally versatile tool and is very useful in the characterisation of ceramic electrolytes, as it allows the electrical properties of the material to be both measured and separated into individual parts. IS involves using a small sinusoidal potential (to keep the system pseudolinear) and measures the current response over a wide frequency range (10MHz – 0.1Hz). Sample features (such as the bulk and grain boundary) undergo polarisation phenomena in different frequency ranges, but also (theoretically) differ by electrical relaxation time (time constants), which can be used to characterise the system components in terms of resistance and capacitance. Sometimes, however, these different time constants, depending on the system under analysis, can overlap and show only a singular response. At high frequency the change in polarisation is rapid, therefore current flows easily whereas at low frequency the amount of charge can reach saturation and give high impedance.

4.4.3. Data Presentation and Interpretation

IS data are commonly interpreted by either Nyquist or Bode plots. Both these plots represent the frequency response; however, Nyquist plots combine Z_{real} and Z_{Im} into one plot in the complex plane and thus lose frequency dependent information. Bode plots, conversely, plot Z_{real} and Z_{im} as a function of frequency response.

In a typical Nyquist plot the real (Z') and imaginary parts of impedance (Z'') are plotted on the X and Y axes respectively, where Z' is the impedance value (akin to resistance) and Z" reflects the reactance of any capacitive (or inductive) components. Nyquist plots are valuable to identify the characteristic features (such as the bulk and grain boundary) exhibited by a system, but all frequency information is inherently lost. This can also complicate interpretation when dealing with a system with a disproportionately large resistive component, which can essentially dwarf a smaller contribution. Conversely, Bode plots plot the impedance magnitude and phase angle against frequency, where magnitude and phase angle are given by equation 4.20 and 4.21.

$$Z = \sqrt{Z_{Re}^2 + Z_{im}^2} \tag{4.20}$$

$$\Phi = tan^{-1}\frac{Z_{im}}{Z_{re}} \tag{4.21}$$

As frequency ranges are commonly quite vast, these plots are logarithmic to allow for easier examination of smaller values.

In this work, lithium-ion conductivity, interfacial resistance in lithium symmetry cells (between garnet/Li metal) and capacitance was evaluated *via* IS. Zview was used exclusively to interpret the data. A typical Nyquist plot is shown in figure 4.12, and this is representative of an ideal SSE response with Li^+ blocking symmetric Au electrodes (Au/SSE/Au), where upon two semi-circles are observed. These relate to the ionic transport within a grain (high frequency) and along the grain boundary (mid-frequency). A spike corresponding to the sample – electrode double layer effect is present at low frequency. This represents the Li-ion transfer resistance between the garnet electrolyte and the Au electrode and arises from the capacitive behaviour of the gold electrodes, which block Li-ion diffusion and thus increasingly charge under an applied alternating potential, as charge movement begins to accumulate and (eventually) reach saturation.

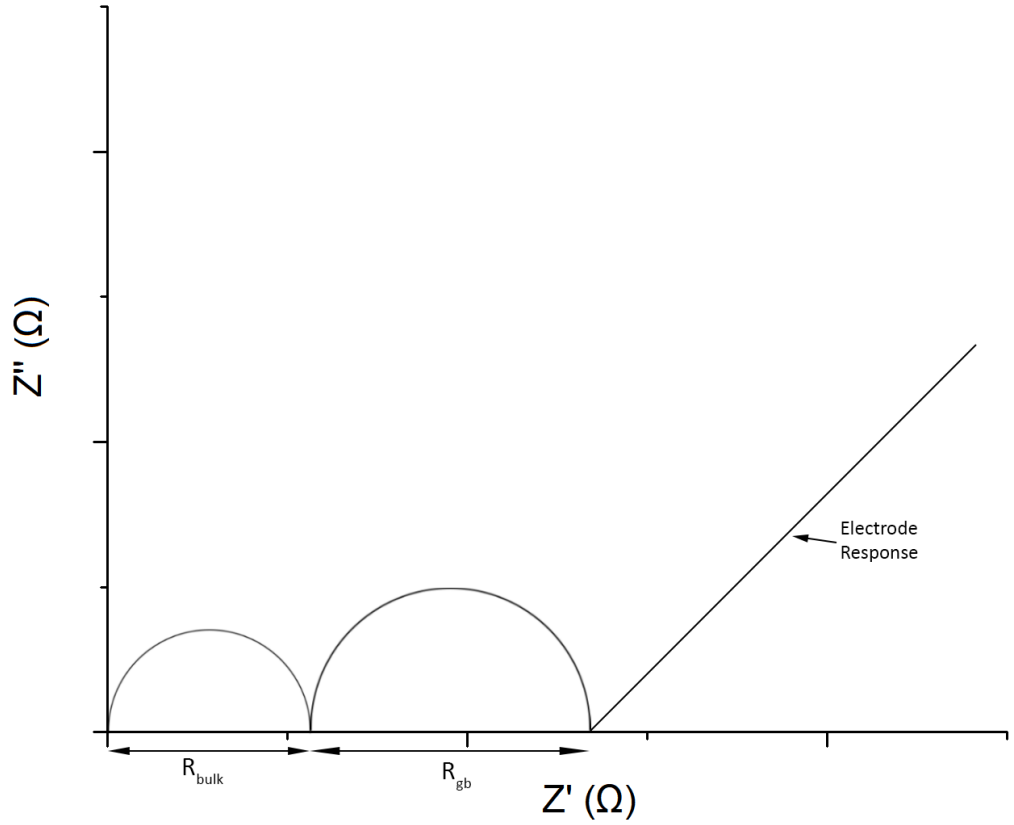

Figure 4.12. Typical Nyquist plot of Au/Lithium garnet/Au, where R_{bulk} is in the high frequency range and R_{gb} is in the mid-frequency range. The low frequency range shows a capacitive spike, corresponding to the charging phenomena encountered at the garnet/Au interface.

Resistance from a Nyquist plot is the high intercept of the semi-circle/s on the real (Z') axis at high frequency. This can directly be converted to conductivity (σ) (the ability of a circuit to allow the flow of current) by equation 4.22.

$$\sigma = \frac{l}{RA} \qquad 4.22$$

where *l* is electrolyte thickness, *A* the contact area between pellet and electrode, and *R* the resistance. The plots in this work are presented in resistivity, with the data scaled in Zview by the geometric factor (pellet-electrode contact area divided by thickness). This allows for presentation of plot axes in Ω cm, the inverse of which is σ (presented in S cm^{-1}).

As IS reflects the ability to characterise real world systems with a variety of resistance (*R*), capacitive (*C*) and /inductive effects (*L*), the data are often interpreted in terms of equivalent real-world circuits. These commonly include R/C elements connected in series or parallel. Here *C* reflects the capacitance arising upon polarisation from the A.C. signal (in this case ionic migration) and *R* the resistance.

An ideal capacitor has parallel, oppositely charged, plates whereupon no current flows (capacitive reactance) and energy is stored in an electric field. This would give a perfect semi-circle and corresponds to:

$$Z = \frac{1}{j\omega C} \tag{4.23}$$

where ω is the angular frequency and $j = \sqrt{-1}$, whereupon Z' = 0 and Z'' = -1 /ωc. C as an EC model is seldomly used – as this indicates an ideal capacitor, where the two plates charge perfectly, and the current lags the voltage by -90°. This angle is not observed in real world samples, where upon poor contact, impurities, defects, sample roughness, tortuosity, conductivity (ionic or electronic), temperature, frequency and/or equipment limitations/setup create a deviation from ideal capacitive charging behaviour. Instead, a constant phase element (CPE) is used, which additionally describes the deviation away from ideality thus

$$Z_{cpe} = \frac{1}{Q(i\omega)^n} \tag{4.24}$$

where *n* is the description of non-ideality, *Q* is the non-ideal capacitance and is equal to 1/Z (where ideal = 1). *C* is then found from Eq. 4.25[30]

$$C = (R^{1-n}\, Q)^{1/n} \tag{4.25}$$

This enables calculation of relative permittivity *via*

$$\varepsilon_r = \frac{C}{\varepsilon_0} \tag{4.26}$$

where ε_0 is vacuum permittivity (8.854 x 10^{-14} F cm^{-1}). Both capacitance and dielectric constants calculated can then be used to characterise the system. In this work values ≈10^{-12} F cm^{-1} and dielectric constants ≈40 - 100 are often seen, as these are typical values for a bulk oxide response[25]. See table 4.5 for assignment of capacitance values to different phenomena[25].

Table 4.5. Typical sample capacitance values obtained from impedance spectroscopy and the phenomena to which they correspond.

Capacitance (F cm^{-1})	Responsible Phenomena
10^{-12}	*Bulk*
10^{-11}	*Minor, second phase*
$10^{-11} – 10^{-8}$	*Grain boundary*
$10^{-10} – 10^{-9}$	*Bulk ferroelectric*
$10^{-9} – 10^{-7}$	*Surface layer*
$10^{-7} – 10^{-5}$	*Sample-electrode interface*
10^{-4}	*Electrochemical reactions*

Energy can also be stored within a magnetic field – an inductor (*L*). The current with inductors leads the voltage by 90°. This is present in this work with highly conductive samples at high (> 5 MHz) frequency and is undesirable. This arises from limitations of the impedance setup, such as wire mismatching (for example different lengths or gauge) which enable generation of a magnetic field. *L* is expressed thus:

$$Z = j\omega L \qquad 4.27$$

The EC elements used in this work are illustrated in figure 4.13.

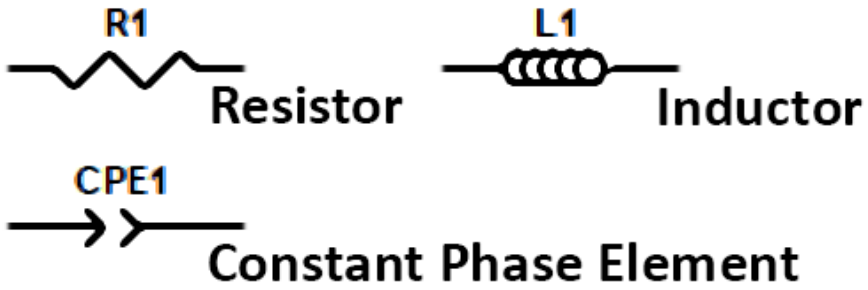

Figure 4.13. Equivalent circuit components used to model the impedance spectra in this work.

Lithium garnets in this work were prepared for IS by pressing the synthesised powders into cylindrical 10 mm pellets by uniaxial pressing. These pellets were then heated to high temperature under N_2, O_2 or in a dry room. Once densified, pellets were weighed, and dimensions measured. The gravimetric density was then calculated and compared to the theoretical density obtained by Rietveld refinements to calculate relative density.

Pellets were sanded to 800 grit (in air) and Au electrodes attached. Au was applied by either sputtering or by painting with Au paste. Au sputtered samples used an Agar automated sputter coater with 40 mA current applied under ≈0.05 mbar for 100 seconds each side. The pellet was protected from a short circuit by Scotch tape. Au sputtered samples were then secured in an MTI split cell and assessed at room temperature and/or at different temperatures manually. Au paste required heating to 800°C for 1hr to cure. This method enabled Au wires to be attached for automated variable temperature measurements to assess activation energy.

Room temperature measurements were carried out on a Solartron 1260 analyser from 10 MHz to 1 Hz or 0.1Hz. Pellets with Au paste were attached to a HP 4192A LF analyser and analysed from 13 MHz to 5 MHz. Potentials between 20 – 100 mV were used. Variable temperature measurements, by using the Arrhenius equation (see section 1.6.3.), plotted log σ *vs* 1000/T (K) to calculate the activation energy over the analysed temperature range. This derivation is available in appendix 1.

Lithium metal symmetry cells were also constructed and analysed on a Solartron 1260 over the same frequency range with an applied potential of 20 mV. Here, plots were scaled to account for the contact area between the electrode/garnet and are, therefore, presented in $\Omega\ cm^2$. The area specific resistance (ASR) is the *R* value corresponding to the semi-circle seen at low frequency and divided by two (to account for two Li metal electrodes). Cell assembly is discussed in section 4.6.

4.5. MICROSCOPY

4.5.1. Scanning Electron Microscopy

Scanning electron microscopy (SEM) has been used throughout this work to image both individual garnet grains and pellets. SEM uses a focused beam of high energy electrons directed at a sample. These produce an image based on sample interactions at varying depths. SEM can provide information on the surface topography, crystalline structure, chemical composition and electrical behaviour originating from, roughly, 1 - 6 µm from the sample surface[31].

In a typical SEM instrument, incident electrons are generated from an electron gun (2 - 40 keV in energies). Several types of electron gun are in use, but this work made use of the tungsten hairpin type. Here, the tungsten filament is heated (*via* current flow) to > 2500°C. This gives thermal emission of electrons. These are accelerated at a specified voltage through an electromagnetic condenser lens, which is then rastered across the selected sample area by scan coils. Electrons penetrate the sample in a teardrop-shaped volume, with dimensions determined by the electron beam energy, sample atomic masses and the incident angle. This interaction produces secondary electrons (SE), back-scattered electrons (BSE), augur electrons and X-rays (white radiation is also created).

SE and BSE images were used in this work. SEs originate near or at the sample surface and are a result of inelastic scattering, whereupon an incident electron excites an electron in the sample. This results in a loss of energy. The excited electron then moves toward the sample surface and is ejected from the sample (assuming sufficient energy), which is detected and forms an image. As only electrons ≈10 Å from the surface are ejected, this enables higher resolution (compared to BSE) and is ideally suited for topographical examinations.

BSEs are generated when incident electrons are reflected (or backscattered) from their original path *via* elastic collisions with the sample. These collisions increase with increased atomic weight, therefore heavier atoms scatter more abundantly. This corresponds to bright/dark spots in the image and can assist in determining sample homogeneity and phase purity, with images well suited toward morphological information. This work made use of a Hitachi TM4000plus instrument with an AZtecOne X-stream2 energy dispersive X-ray spectrometer (EDX) attachment or a Philips XL30 FEG instrument with an Oxford Inca 300 EDX attachment. In all cases samples were secured to an Al stub completely covered in conductive carbon tape, this avoided undesirable Al signals from the EDX (see next section). Any specific alterations to accelerating voltage or sample preparation are discussed in each corresponding section.

4.5.2. Energy Dispersive X-ray spectroscopy

Energy dispersive X-ray Spectroscopy (EDX) is a complementary technique to SEM which utilises the X-rays emitted as a result of the electron bombardment over the selected sample area[32]. These X-rays have characteristic energies related to each element, so can be used to analyse sample composition. Upon bombardment by an electron beam, electrons are ejected from the sample surface. This leaves an inner shell vacancy, which is filled by an electron from a higher shell. This emits energy in the form of an X-ray photon during the process. The energetic emissions, as they are generated from the electron shells, are characteristic of the electronic structure of the element. Numerous emissions can result, dependent on element, and creates a spectrum of energy *vs* the relative counts of the detected X-rays. This gives both quantitative and qualitative information from a sample.

In EDX, the characteristic X-rays are labelled using the Siegbahn notation: K, L, M, N. These are followed by a Greek letter which corresponds to the electron shell that was ionised and filled. The letters have additional subscript numbers that identify the donor shell and sub-shells that filled the vacancy, such as Fe $K\alpha_1$. To ionise inner shell electrons, the incident electrons need sufficient energy. Therefore, electrons below the critical ionisation potential cannot displace a K shell electron but may yield vacancies in higher L or M shells, leading to Lα or Mα emissions, see figure 4.14.

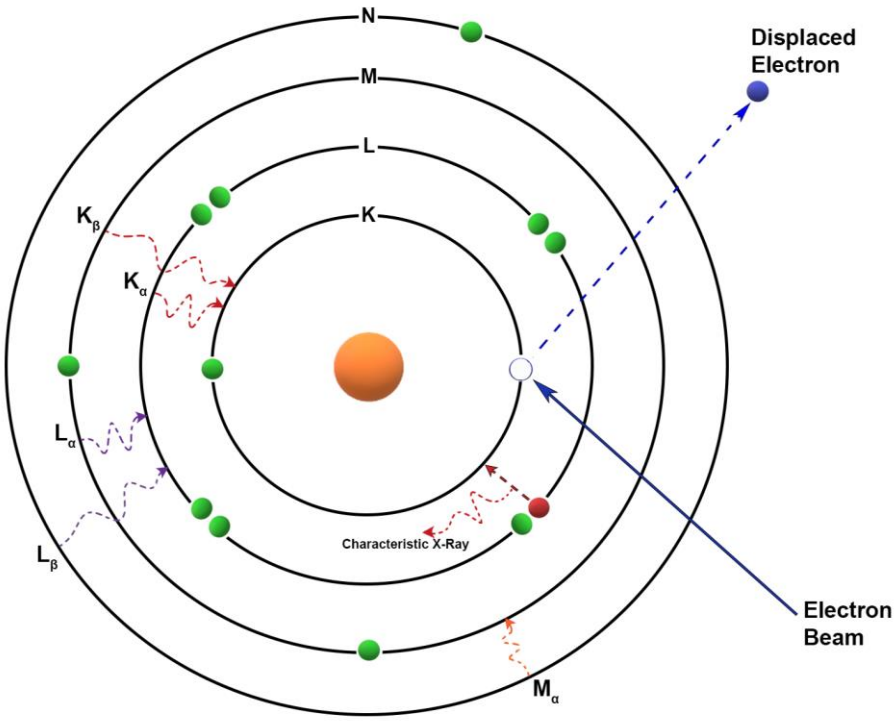

Figure 4.14. Simplified view of an atom (orange) with electrons (green) in K, L, M and N shells. Shows the effect of inner shell ionisation and subsequent emission of a characteristic X-ray when the vacancy is filled from an outer shell electron.

4.6. CELL TESTING

4.6.1. Cyclic Voltammetry

Electrochemistry relates electron transfer processes to chemical changes, which is accompanied by a reduction and/or oxidation within energy storage materials. These redox reactions occur when the HOMO of one material is higher in energy than the LUMO of the other, which enables a thermodynamically favourable route for electron transfer. The energy of these electrons (if not already in favourable energetic positions for electron transfer) can be modulated using an external power source, such as a potentiostat. The output is then analysed for a current response. This is cyclic voltammetry (CV).

CV is a technique which scans the potential of a stationary working electrode using a triangular waveform and measures any current response during the sweep. Any current response relates to faradaic processes (electron transfer) and is shown as peaks in the voltammogram, whereas a flat response indicates non-faradaic type current (such as capacitive)[33, 34]. This allows characterisation of operating electrochemical windows within energy storage materials.

A typical CV experiment has upper and lower voltage limits selected; these increase linearly with time at a set scan rate (for example 1 mV s^{-1}). Upon reaching the set upper value, the scan is reversed, and this can be repeated several times. The measured current response can show a variety of redox reactions within a single material but can also show irreversible change. Here, only an oxidative or reductive peak occurs, which although desirable in some areas indicates the material has degraded within electrochemistry.

This work makes use of CV to assess the electrochemical stability window of the garnet electrolyte materials. In all cases cells were constructed with Au electrodes and Li metal reference/counter electrodes, with a garnet pellet in between. Cells were assembled in an Ar glovebox, whereupon garnet pellets were polished from 240 to 4000 grit until a mirror like finish. Li metal was then added to one side and hand pressed, before being secured in an MTI split cell lined with Au foil. Voltage was then swept either from -0.4 – 5 V or -0.4 - 10V (*vs* Li/Li^+). A 1 mV s^{-1} scan rate was used in all cases. All CVs were undertaken on a Biologic VMP3 or SP50 instrument.

4.6.2. Galvanostatic Cycling

Cells are often cycled under galvanostatic mode but with an imposed potential limitation for both charge and discharge. This work, however, does not relate to any conventional battery charging/discharging and concentrates solely upon Li-Li symmetric cells, which give quantitative evaluation of the Li metal performance without the need to decouple cathodic effects. These symmetric cells were cycled with respect to the contact area between the pellet and Li metal. This differs from the conventional charge/discharge of cells where a constant current is applied per gram (as the electrolyte can wet the electrode, which enables electrochemical reactions and ionic migration throughout the electrode and thus beyond the areal contact encountered at the solid-solid interface).

Analysis of lithium symmetry cells was undertaken with an increasing current density to ascertain the voltage, as a result of the applied current, and to determine at which point lithium dendrites propagated and short circuited the cell. These cycling experiments would either assess long term stability (over several months) or would increase the current after every cycle to assess the critical current density (CCD). The CCD was observed by a voltage drop during cell cycling and by IS.

Typically, a lithium symmetry cell corresponding to Li/Garnet/Li was assembled by polishing the garnet pellet (from 240 to 4000 grit) in an Ar glovebox. Lithium metal foil (with any black impurity layer removed) was then applied to both sides of the pellet and heated to ≈175 °C for ≈1 h under sustained pressure from a hand clamp. These cells were then cooled to room temperature, assembled into an MTI split cell, and analysed *via* IS at room temperature from 10MHz to 0.1 Hz. This assessed the Li/garnet interfacial resistance contribution, which occurs in the low frequency domain, and allowed comparative spectra to be taken to confirm a short circuit had occurred. Cells were then analysed under constant current conditions at different current densities on either a Biologic VMP3 or SP50 instrument.

4.7. Error Analysis

4.7.1. Equipment considerations

Powders and pellets were weighed on analytical balances (Ohaus PA64, Ohaus AX124 or Fisherbrand FAS64) to the 4th decimal place. All balances were readable to 0.1 mg with a linearity of ±0.2mg. Assuming limited drift, values > 0.1mg are unknown and could be rounded up or down. Therefore, the error associated with the balance is half the resolution - ±0.05 mg (0.1 mg / 2) with ±0.2mg arising from drift, which could impact the reported stoichiometries.

Pellet dimensions have errors associated to the digital (Mitutoyo or Duratool) 150 mm calipers, which have a 0.01 mm resolution with a ±0.02 mm error. Therefore, pellet diameters in this work have an error range from ±0.005 - ±0.002 % (derived from the smallest, 4 mm, and the largest, 10 mm, pellet diameter). Pellet thickness was between 0.8 - 3 mm, which gives errors between ±0.025 - ±0.006 %. However, most pellets were ≈1.25 mm thick, therefore an average error of ±0.0116 % can be assumed. This impacts the reported conductivity/ASR values but is considered minimal, as such low errors do not noticeably alter the reported data.

All sample heating and temperature-based measurements used K-type thermocouples, these present a 0.75% error on the stated value (up to 1200 °C). This error relates to all sintering temperatures, ramp rates and variable temperature measurements (XRD and impedance spectroscopy). Room temperatures were monitored by a Fisherbrand™ Traceable™ Thermometer/Clock/Humidity Monitor with an accuracy of ±1 °C.

Reported oxygen and water content was measured *via* the MBraun UniLab pro glovebox sensors. The O_2 sensor, a ZrO_2 semi-conductor, has an approximate error (assuming standard operating parameters) of ±2 % of the displayed ppm value +1 ppm. Moisture was monitored by a dehydrated phosphoric acid layer coated on to a ceramic and, assuming no interference from NH_3 gas, is accurate to ±5 % of the displayed ppm value +1 ppm (between 0 - 10 ppm) or ±20 % of the displayed value (10 - 100 ppm).

4.7.2. Solid State Synthesis

A 10-40 % mol Li excess was used to account for Li volatility at high temperatures. This might alter the Li content per formula unit (*pfu*) during subsequent high temperature steps. This, therefore, introduces potential stoichiometric Li errors in the reported formula. It was not possible to characterise Li content in this thesis - the EDX or S8 Tiger XRF available were insensitive to Li and, irrespectively, cannot give accurate bulk stoichiometries – as both involve X-rays emitted from surface-based interactions. Therefore, phase purity (before and after densification), ionic conductivity and cell performance were relied upon for a qualitative indication of the desired Li content. Here, reduced Li content would be

evident from poorer than expected conductivity and worse cycling performance. Conversely, increased Li (for example > 6.4 *pfu*) would lead to increased detection of the tetragonal cell (*via* XRD) and poor conductivity. All garnet materials in this thesis were synthesised multiple times to the same intended stoichiometry (under the same conditions) - to confirm performance consistency and give increased confidence in the stated formulas.

However, very high purity starting materials were not always available (see table 4.6) and Zr and Hf salts (99 % ≤ 2% Zr or Hf) were used as higher purity options were not available (see section 2.4.2.4.). This introduces a potential 0.1 - 1 % error in the reported stoichiometries and up to 2 % with respect to Zr and/or Hf based salts. This, therefore, impacts the reported structural and elemental data.

Table 4.6. List of all starting materials in this work, including provider and purity.

Chemical	**Supplier**	**Purity (%)**
$Al(NO_3)_3 \cdot 9H_2O$	Sigma	≥ 99
CeO_2	Arcos	99.9
$Cl_2HfO \cdot 8H_2O$	Alfa Aesar	≥ 98 (excluding Zr), Zr < 1.5
$Cl_2ZrO \cdot 8H_2O$	Alfa Aesar	≥ 98 (excluding Hf), Hf < 1.5
$Ga(NO_3)_3 \cdot 8H_2O$	Sigma	99.9
Ga_2O_3	Alfa Aesar	99.999
HfO_2	Sigma	98 (excluding Zr), $ZrO_2 \leq 2$
$La(NO_3)_3$	Sigma	99.99
La_2O_3	Sigma	≥ 99.9
Li_2CO_3	Sigma	≥ 99
$LiNO_3$	Sigma	> 98
Nb_2O_5	Alfa Aesar	99.9
Nd_2O_3	Sigma	99.9
Pr_6O_{11}	Alfa Aesar	99
$SrCO_3$	Sigma	≥ 99.9
Ta_2O_5	Alfa Aesar	99
TiO_2 (anatase)	Alfa Aesar	99.6
ZrO_2	Alfa Aesar	≥ 99 (excluding Hf), $HfO_2 \leq 2$

4.7.3. Powder Densification

Phase pure powders were uniaxially pressed in a 10 mm Specac die (1 - 3 tonnes) on a Specac manual hydraulic pellet press or Specac Autotouch press. The associated pressure error is of little concern, as the aim was to form a pellet without cracks, however, the densification steps require discussion.

Pellets were densified in tube furnaces or in a dry room using a muffle furnace once available (chapter 7 onwards). Tube furnaces had sealed glass ends and allowed for gas flow (N_2, O_2 or 5% H_2/N_2). Standard atmospheric pressure was assumed here, but was unable to be confirmed. Gas flow rate was monitored by sulfuric acid bubblers (for dry gas flow). Densification was optimised until a repeatable maximum, with a small deviation, was reached. After optimisation, maximal variations in pellet relative density from tube furnaces (ρ_{rel}) were 3.5 % (of the same phase), which arise from the largest reported deviation ($Ga_{0.2}Li_{6.4}La_3Hf_2O_{12}$, chapter 6) where ρ_{rel} ranged from 87% - 90.5%. Dry room densification enabled variations of 2% - arising from muffle furnace use with larger heating areas. Therefore, the conductivities reported had slight variations for the same phases. This is discussed in each chapter.

4.7.3.1. Pellet Preparation and Proton Exchange

Proton exchange was unavoidable during the densification process, as full densification in an Ar glovebox was not possible. Tube furnace densification required handling under ambient conditions after heating, as did dry room work (transport and transfer to an Ar glovebox was needed). Furthermore, pellets could not be consistently covered with excessive mother powder (due to sample limitations). Therefore, proton exchange was inevitable. This is especially true for analysis with Au blocking electrodes – which were prepared (pre-dry room availability) in air and assessed under ambient conditions in all cases. This will increase resistance and lead to reduced conductivities compared to a pristine sample. This could not be characterised; however, all pellets were handled similarly so proton exchanged layers should be, largely, equivalent within each succeeding chapter - as should any effect on conductivity or cell performance.

For lithium symmetry cells, all pellets were sanded to a mirror finish by hand in an Ar glovebox (which removes surface bound Li_2CO_3). This invariably lacks consistency, as does the manual pressing of Li foils to form symmetric cells. Therefore, some ASR variations were expected, with these further impacted from symmetric cell construction variations and deviations in glovebox atmosphere. ASR values were assessed for accuracy *via* comparison to other pellets from the same and different batches (of the same garnet phase) and, where available, to reports elsewhere. Once the processes were optimised, ASR values remained mostly consistent. This explains the observed variation in the succeeding chapters, such as with the LTC work (appendix 2) where ASR values varied from 320 - 400 Ω cm^2.

4.7.4. X-ray Diffraction and Structural Refinements

All samples were analysed on low background Si holders, which used a thin layer of petroleum jelly for powder adherence. This invariably results in increased sample displacement error, which was accounted for within Rietveld refinements. The low background Si holder and the petroleum jelly coating (on Si) were scanned for background contributions, see figure 4.15. Additional background contributions are also present in patterns at low 2θ as no knife edge was used.

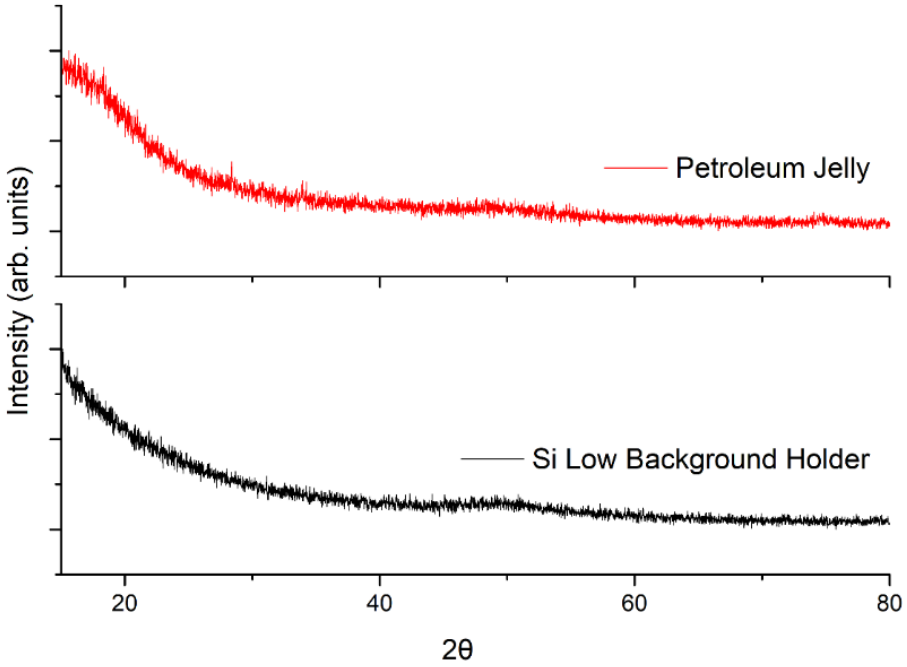

Figure 4.15. XRD patterns of low background silicon holder and petroleum jelly on Si holder

Refinement errors are somewhat related to the estimated errors with the starting materials (0.1 - 2%) (plus any diffractometer contributions to the Pseudo-Voigt function, see section 4.2.5.). However, lattice parameters depend upon the observed peak positions in comparison to the calculated data from the structural model. This therefore minimises, but does not remove, errors surrounding impure starting materials for lattice parameters. Clearly once other sources of error are factored in, such as zero shift and sample displacement, this will rise. Lattice parameters have errors stated in brackets after the number. These numbers primarily fall within single digits for cubic garnets, such as 12.9741(5) Å with $Li_{5.8}La_3Nb_{1.2}Pr_{0.8}O_{12}$. Errors rose with reduced symmetry (the tetragonal cell) and especially in those systems where no high-quality structural model was available, such as $Li_7Pr_3Hf_2O_{12}$ where a = 13.1049(21) Å and c = 12.6474(19) Å. When possible, synthesised garnets were compared to work elsewhere to further verify the reported parameters (discussed in the articles).

However, the precursor impurities will affect the reported fractional occupancies (dependent upon atomic parameters) and can affect peak shape (crystallinity, grain size and defects). This gives a

potential 0.1 - 2 % error for atomic estimations within the unit cell. This impacts fractional occupancies and, thus, theoretical densities. This is especially relevant where fractional occupancies were not refined due to multiple site occupation of similarly scattering atoms (chapters 5, 7, 9 and appendix 2).

As mentioned in section 2.4.2.3, further vacancies are likely present within the lithium garnet structure, such as on the La and/or Zr site. These were investigated *via* Rietveld Refinements in this work, but (if yielding a stable refinement) gave only small changes in occupancy with little (or no) difference in fit or R_{wp}. For example, La occupancy refinement in $Li_{5.5}La_3Nb_{1.5}Pr_{0.5}O_{12}$ increased beyond 1 (indicating an unstable refinement) and gave no R_{wp} (8.209 %) change. Conversely, the fractional occupancy of Nd in $Li_{6.2}Nd_3Zr_{1.2}Nb_{0.8}O_{12}$ reduced from 1 to 0.9981, with no R_{wp} change (5.344%). Hf refinements (in $Ga_{0.2}Li_{6.4}La_3Hf_2O_{12}$) yielded a decrease to 0.9828, with similarly small changes noted for oxygen throughout the reported garnet work. Although some fractional occupancies could be argued as plausible, the lack of additional evidence, the minimal quantitative change, and the little difference in fit or extracted parameters led mostly to the use of structural model occupancies (often 1 for oxygen and larger atoms such as La, Zr, Nb), to simplify the parameter suite - unless otherwise discussed within the articles.

4.7.5. Impedance Spectroscopy

Additional impedance contributions, aside from those stated within the research articles, arise from the spectrometer wiring, which used Pt or oxygen free Cu wires connected to pellets or an MTI split test cell. This gives ≈5 Ω of additional resistance[35]. Further resistance contributions arise from the MTI split test cells, which have stainless steel contact plates and plungers with oxide layers on the contact plates. These oxide layers would show, with conventional LIBs where total cell resistance is usually ≈100 - 200 Ω, as an additional high frequency semi-circle with low resistance (≈10 Ω for 11 mm aluminium coated electrode disc[36]). These oxide layers can be removed by polishing but are indistinguishable from the garnet bulk/grain boundary features (due to high resistance of the garnet pellets), hence was not undertaken. Therefore, the highest estimated resistance error can be calculated using the resistance value (of the semi-circle corresponding to σ_{total}) of the least resistive pellet prior to geometric scaling (at room temperature) and the sum of the resistance encountered from the wires/oxide layers. In this work, this is 743 Ω (LTC pellet at 22 °C) with a total ≈15 Ω additional resistance, Therefore, an error a -2.02 % is indicated. This error reduces as pellet resistance increases (with most sample resistances being > 1000 Ω).

Impedance fitting relied upon sensible equivalent circuit models, extraction of logical values (that correspond well with the physical Nyquist/Bode plot features) and the visual fit, however figure 4.16

shows example errors associated with the fitting of a simple garnet system. These errors increase with increased system complexity. For example, the grain boundary contribution becomes harder to model as density is increased (due to overlap with the bulk time constant), despite the often-clear visual presence. This would require manual fitting based upon the initial least squares regression method. These are explained in the succeeding chapters. Stated capacitance values were derived from the fitted data, but also the spectroscopic C bode plot, and calculated by hand to confirm accuracy.

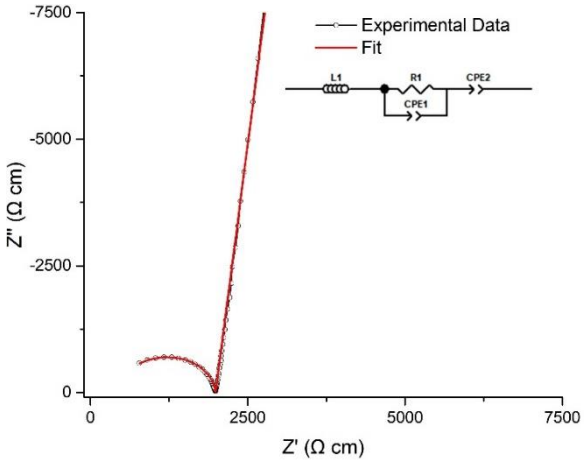

Element	Value	Error	Error (%)
L1	3.8673×10^{-6}	4.951110^{-8}	1.2802
R1	1989	1.09782	0.055163
CPE1-T	$2.106E10^{-11}$	7.555810^{-13}	3.5881
CPE1-P	0.94527	0.0020377	0.21557
CPE2-T	1.130710^{-6}	3.50510^{-9}	0.26979
CPE2-P	0.93384	0.0005008	0.053628

Figure 4.16. Example simple lithium garnet impedance spectrum system showing single, overlapped, bulk/GB response with Au block electrodes. System shown is from chapter 9.

4.7.6. Scanning Electron Microscopy and Energy Dispersive X-ray spectroscopy

Despite the limitations of EDX for stochiometric analysis, it was used in this work to detect Al content. Here an Al stub was used, therefore beam scattering on latent gas within the SEM/EDX chamber would enable generation of erroneous Al K_α signals if not fully covered. Hence the Al stubs were covered with carbon tape. This was assessed by comparison of the bare stub and the same garnet samples with/without tape, with carbon tape showing full removal of Al K_α. Nonetheless, two layers of carbon tape were used to ensure full removal of Al K_α signals. This, therefore, gave increased confidence when stating Al presence. No impurity signals were noted relating to the starting materials, however the EDX used lacks sensitivity for such low impurity content, hence an error of 0.1 – 2 % must be assumed.

4.8. REFERENCES

1. A. R. West, *Solid State Chemistry and its Applications*, John Wiley & Sons, 2014.
2. L. E. Smart and E. A. Moore, *Solid State Chemistry: An Introduction, Fourth Edition*, CRC Press, 2016.
3. B. A. Cheetham, A. K. Cheetham, P. Day and D. R. P. C. P. Day, *Solid State Chemistry: Techniques*, Clarendon Press, 1987.
4. B. D. Cullity, *Elements of X-ray Diffraction*, Addison-Wesley Publishing Company, 1978.
5. C. Hammond, *The Basics of Crystallography and Diffraction*, Oxford University Press, 2015.
6. A. J. Blake, W. Clegg, J. M. Cole, J. S. O. Evans, P. Main, S. Parsons and D. J. Watkin, *Crystal Structure Analysis: Principles and Practice*, OUP Oxford, 2009.
7. C. Suryanarayana and M. G. Norton, *X-Ray Diffraction: A Practical Approach*, Springer US, 1998.
8. Y. Waseda, E. Matsubara and K. Shinoda, *X-Ray Diffraction Crystallography: Introduction, Examples and Solved Problems*, Springer Berlin Heidelberg, 2011.
9. K. Momma and F. Izumi, *J. Appl. Crystallogr.*, 2011, **44**, 1272-1276.
10. M. Laue, *Annalen der Physik*, 1913, **346**, 989-1002.
11. W. L. Bragg, *Proc. Cambridge Philos. Soc.*, 1913, **17**, 43-57.
12. B. H. Toby, *Powder Diffr.*, 2006, **21**, 67-70.
13. B. Toby and R. Dreele, *J. Appl. Crystallogr.*, 2013, **46**, 544-549.
14. H. Rietveld, *J. Appl. Crystallogr.*, 1969, **2**, 65-71.
15. H. Rietveld, *Acta Crystallogr.*, 1967, **22**, 151-152.
16. D. Cox, *J. Appl. Crystallogr.*, 1994, **27**, 440-441.
17. H. M. Rietveld, *An Algol Program for the Refinement of Nuclear and Magnetic Structures by the Profile Method RCN Report*, Netherlands, 1969.
18. A. Coelho, *J. Appl. Crystallogr.*, 2018, **51**, 210-218.
19. M. Howard, PhD thesis, The University of Birmingham, 2015.
20. J. D. Percival, PhD thesis, University of Surrey, 2009.
21. W. I. F. David, *J. Res. Natl. Inst. Stand. Technol.*, 2004, **109**, 107-123.
22. J. H. Sluyters, *Recl. Trav. Chim. Pays-Bas*, 1960, **79**, 1092-1100.
23. J. H. Sluyters and J. J. C. Oomen, *Recl. Trav. Chim. Pays-Bas*, 1960, **79**, 1101-1110.
24. E. N. Kaufmann, *Characterization of Materials*, Wiley-Interscience, 2003.
25. J. T. S. Irvine, D. C. Sinclair and A. R. West, *Adv. Mater.*, 1990, **2**, 132-138.
26. C. H. Chan, C. H. Chia and S. Thomas, *Physical Chemistry of Macromolecules: Macro to Nanoscales*, Apple Academic Press, 2014.
27. V. F. Lvovich, *Impedance Spectroscopy: Applications to Electrochemical and Dielectric Phenomena*, Wiley, 2012.
28. A. Lasia, *Electrochemical Impedance Spectroscopy and its Applications*, Springer New York, 2014.
29. Gamry Instruments, Basics of Electrochemical Impedance Spectroscopy, https://www.gamry.com/application-notes/EIS/basics-of-electrochemical-impedance-spectroscopy/, (accessed 01/11/2021).
30. J. Fleig, *Solid State Ion.*, 2002, **150**, 181-193.
31. J. I. Goldstein, D. E. Newbury, J. R. Michael, N. W. M. Ritchie, J. H. J. Scott and D. C. Joy, *Scanning Electron Microscopy and X-Ray Microanalysis*, Springer New York, 2017.
32. Thermo Scientific White Paper, Wavelength-dispersive (X-ray) Spectroscopy, Available: https://www.thermofisher.com/uk/en/home/global/forms/industrial/wds-essential-knowledge-briefing-booklet.html, (accessed 10/11/2021).
33. N. Elgrishi, K. J. Rountree, B. D. McCarthy, E. S. Rountree, T. T. Eisenhart and J. L. Dempsey, *J. Chem. Educ.*, 2018, **95**, 197-206.

34. A. J. Bard and L. R. Faulkner, *Electrochemical Methods: Fundamentals and Applications, 2nd Edition*, John Wiley & Sons, Incorporated, 2000.
35. R. H. Brugge, J. A. Kilner and A. Aguadero, *Solid State Ionics*, 2019, **337**, 154-160.
36. H. Li, J. Lampkin, Y.-C. Chien, L. Furness, D. Brandell, M. J. Lacey and N. Garcia-Araez, *Electrochim. Acta*, 2022, **403**, 139572.

5. Evaluation of the effect of site substitution of Pr doping in the lithium garnet system $Li_5La_3Nb_2O_{12}$

5.1. PUBLICATION

Evaluation of the effect of site substitution of Pr doping in the lithium garnet system $Li_5La_3Nb_2O_{12}$

Article information : Dalton Transactions, 2012, 41, 12048-12053. Invited front cover article.

Submitted: 23/04/2020

Accepted: 29/05/2020

Author contributions: M. P. Stockham: all experimental and characterisation work, method development, conceptualisation, writing – original draft, formal analysis, investigation. B. Dong: Data curation, investigation, characterisation guidance on impedance spectroscopy and XRD. Y. Ding: Supervision. Y. Li: Supervision. P. R. Slater: Conceptualisation, Lead supervision, characterisation and experimental guidance, writing – review & editing.

Volume 49
Number 30
14 August 2020
Pages 10281-10664

Dalton Transactions

An international journal of inorganic chemistry

rsc.li/dalton

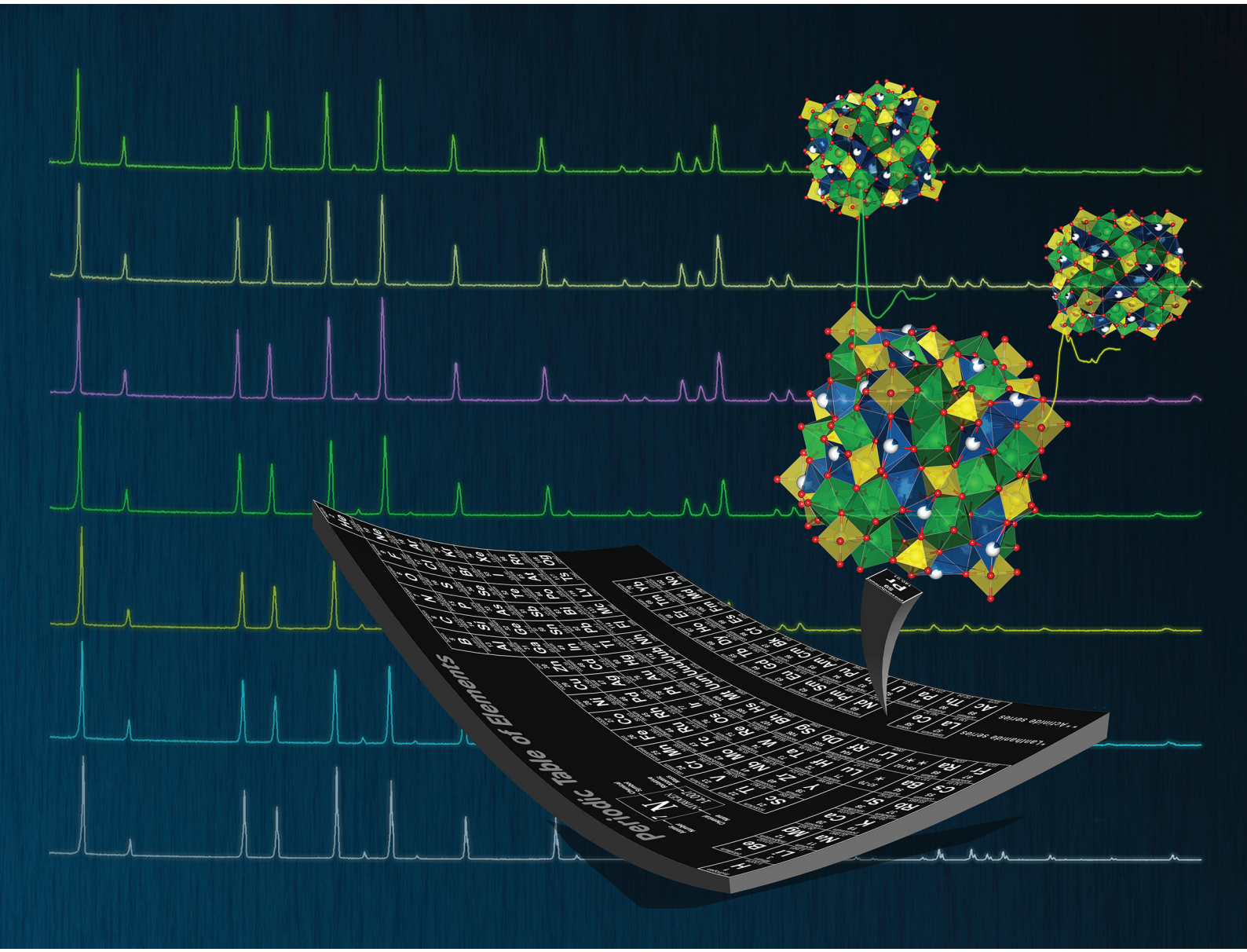

ISSN 1477-9226

ROYAL SOCIETY OF CHEMISTRY

PAPER

M. P. Stockham, P. R. Slater *et al.*
Evaluation of the effect of site substitution of Pr doping in the lithium garnet system $Li_5La_3Nb_2O_{12}$

Dalton Transactions

ROYAL SOCIETY OF CHEMISTRY

PAPER

View Article Online
View Journal | View Issue

Cite this: *Dalton Trans.*, 2020, **49**, 10349

Evaluation of the effect of site substitution of Pr doping in the lithium garnet system $Li_5La_3Nb_2O_{12}$†

M. P. Stockham, *[a] B. Dong,[a] Y. Ding,[b] Y. Li[b] and P. R. Slater *[a]

Received 23rd April 2020,
Accepted 29th May 2020

DOI: 10.1039/d0dt01497d

rsc.li/dalton

Li ion conducting garnets have been attracting considerable interest for use as the electrolyte in all solid-state batteries, due to their high ionic conductivity and wide electrochemical stability window. Consequently, there have been a number of doping studies aimed at optimising the conductivity, focusing on both doping in $Li_7La_3Zr_2O_{12}$ and $Li_5La_3(Nb/Ta)_2O_{12}$ systems. In this paper, we report a detailed study of Pr doping in $Li_5La_3Nb_2O_{12}$, and show that this is a rare example of an ambi-site dopant, being able to be doped onto either the La or Nb site. Interestingly the resultant Pr oxidation state is determined by the site substitution, with oxidation states of 3+ for the La site, and 4+ for the Nb site. While the conductivity is essentially unchanged for the La site substitution, Pr^{4+} substitution on the Nb site leads to a large increase in the conductivity associated with the increase in Li content ($Li_{5+x}La_3Nb_{2-x}Pr_xO_{12}$) up to 0.56 mS cm^{-1} (at 50 °C) for x = 0.8. Overall, this work highlights the flexibility of these garnet materials to doping, and suggests that further consideration of site substitution be considered for other dopants.

Introduction

Increased demand for portable electronic devices, electric vehicles and renewable energy has significantly expanded demand for efficient, safe, low cost and high-power energy storage. Lithium ion batteries (LIB) are principally used for these purposes, due to their high volumetric and gravimetric energy densities.[1] However, current LIBs have a variety of safety, thermal and efficiency issues, which are often attributed to the liquid organic electrolytes used in the cell. These liquid electrolytes also limit the cell potential by preventing the use of lithium metal anodes.[2] These disadvantages, and advantages, are covered in many review articles.[1,3–7] Therefore, the replacement of liquid electrolytes with a solid-state electrolyte (SSE) to give an all solid-state battery (ASSB) remains the key challenge to deliver this next leap in energy storage.[8] Such batteries, when compared to traditional LIBs, offer the potential for increased safety, operate over a wider electrochemical window, have increased thermal stability and are ideally stable against Li metal, hence increasing energy density per cell.[8–12]

As a result, there is considerable interest in the identification and optimisation of new solid state electrolyte materials. However, many of these electrolytes, such as LISICON, sulphides/glass and LiPON, are limited by either low ionic conductivity or a poor electrochemical stability window.[13–15] Of these reports, the lithium containing garnet type systems are one of the few which present with high lithium ion conductivity (reportedly >10^{-4} S cm^{-1} [16]), a wide electrochemical stability window and are chemically stable against Li metal.[9,13,17–19] Hence these systems are attracting considerable interest for use in ASSBs.

However, there still remain challenges for these garnet systems, and so there continues to be interest in new doping studies in these materials. In particular, there is a need to further improve the ionic conductivity, as well as improve the interface between the electrolyte and electrodes.[9,10,13] Traditional garnet materials have the general formula $A_3B_2X_3O_{12}$,[13,20–22] where the A, B, C cations are located in 8, 6, 4 coordinate sites respectively. In the Li containing garnets, excess Li can be accommodated in interstitial sites, such that the general formula of these can be classed as $A_3B_2Li_{3+x}O_{12}$ ($0 \leq x \leq 4$), so that the Li content can be varied between 3 (as in $Li_3Ln_3Te_2O_{12}$), and 7 (as in $Li_7La_3(Zr/Sn/Hf)_2O_{12}$). Those systems with <7 lithium atoms crystallise in a cubic structure which has high Li-ion conductivity. In contrast, the stoichiometric $Li_7La_3(Zr/Sn/Hf)_2O_{12}$ systems crystallise in the less conductive tetragonal phase, although doping to reduce the Li content allows the formation of the cubic cell with enhanced conductivity.

For cubic garnets, such as $Li_5La_3Nb_2O_{12}$ (LLNO), ionic migration pathways have been attributed to two tetrahedral sites bridged by a single face sharing octahedron. As the lithium sites are not fully occupied in these systems, lithium

[a]School of Chemistry, University of Birmingham, Birmingham B15 2TT, UK. E-mail:
[b]School of Chemical Engineering, University of Birmingham, Birmingham B15 2TT, UK

†Electronic supplementary information (ESI) available. See DOI: 10.1039/d0dt01497d

partially occupies the interstitial octahedral sites 48 h and 96 g, in a disordered fashion. This gives a disordered Li sublattice and a migration pathway which leads to high ionic conductivity *via* the Li^+ charge carrier, which is thought to follow the hopping mechanism of 24 d → 96 h → 48 g → 96 h → 24 d, as determined by high temperature neutron diffraction studies.[23]

Of the wide variety of garnet systems, particular attention has been afforded to $Li_7La_3Zr_2O_{12}$ (LLZO). This stoichiometric system is tetragonal at room temperature, with comparatively low conductivity, and changes to a cubic cell at around 750° C; this temperature can be reduced to 350 °C by doping at the Zr site with Ce, leading to an increase in conductivity.[24] Stabilisation of the cubic cell at room temperature (c-LLZO) requires a reduction of the lithium content, often using Al or Ga substitution at the Li site.[16,25,26] Dopants at the Zr site (*e.g.* Nb, Ta[27,28]) also can stabilise c-LLZO.

Although c-LLZO has been reported with conductivities $>10^{-4}$ S cm^{-1}, these often require complex methodologies and/or equipment, such as field assisted sintering, which presents a barrier to commercial scalability.[16,29,30] Consequently, the majority of c-LLZO doping strategies lead to conductivities $\sim10^{-4}$ S cm^{-1}, or lower, and are suboptimal compared with current LIB liquid electrolytes.[31–38] Therefore, it is of interest to investigate alternative doping strategies of other lithium garnet systems, such as $Li_5La_3Nb_2O_{12}$ (LLNO). This system was the first to show fast Li-ion conductivity, and outside of detailed examinations of the lithium migration pathways, has now been superseded by research on c-LLZO.[39,40] However, of the prior reports of doping into the LLNO system, many show room temperature conductivities of $\sim10^{-4}$ S cm^{-1} and are thus similar to c-LLZO.[13,41] Therefore, further doping studies on the LLNO system are warranted. Herein we report an examination of Pr doping in this system. Pr was chosen because of its ability to adopt different oxidation states (3+, 4+), and so potential, based on size considerations, to dope onto either the Nb or the La site according to the following formula $Li_{5+x}La_3Nb_{2-x}Pr_xO_{12}$ (Pr^{4+}) and $Li_5La_{3-x}Pr_xNb_2O_{12}$ (Pr^{3+}). We confirm this ambi-site substitutional ability of Pr, and illustrate in particular that Pr doping on the Nb site leads to samples with high Li ion conductivity.

Methods

Synthesis

$Li_{5+x}La_3Nb_{2-x}Pr_xO_{12}$ garnets were prepared *via* the solid-state route from stochiometric quantities of Li_2CO_3, La_2O_3, Nb_2O_5 and Pr_6O_{11} under air. A 40% mol excess of lithium was added to compensate for lithium loss during high temperature sintering. All powders were ball milled for 1 h (500 rpm) and heated to 950 °C (16 hours). Impure phases ($x > 0.25$) were subsequently ball milled with a 20% lithium mol excess and heated to 950 °C (12 hours). Samples where $x \geq 0.8$ were synthesised in a dry room with a dewpoint between −45 °C to −64 °C (the elimination of humidity was found to be necessary to prepare good quality samples for these high Pr contents: it is known that moisture can be an issue in the synthesis of Li garnet systems).[42–44]

$Li_5La_{3-x}Pr_xNb_2O_{12}$ was also prepared *via* the solid-state route in either air or 5%H_2/N_2. Samples were heated to 950 °C for 16 hours, cooled to room temperature and reheated to 950 °C for 16 hours. After synthesis, all samples were stored in an argon glove box.

Characterisation

Samples were characterised by X-ray diffraction (XRD) using a Bruker D8 diffractometer with Cu Kα radiation. Cell parameters were determined from Rietveld refinement using GSAS II software.[45] In order to evaluate the Pr oxidation states X-ray absorption near edge spectroscopy (XANES) data were recorded at Diamond Light Source on beamline B18 and data interpreted *via* the Athena/Artemis software.[46] Scanning electron microscopy (SEM) was performed using a TM4000plus SEM, with elemental compositions evaluated by the corresponding AZtecOne EDX attachment. The Pr–LLNO garnet powders were placed on carbon tape, attached to the SEM stub and evaluated at 15 kV in back scattered electron mode.

Impedance spectroscopy

Pellets for conductivity measurements were prepared as follows: 10 mm diameter pellets were uniaxially hot pressed with an atlas heating platen to *ca.* 3 tonnes at 300 °C and, subsequently, heated to 1000–1050 °C for 12 hours under dry N_2 to densify the SSE membrane. During N_2 treatment sacrificial powders were used to protect pellets from Li loss and to prevent Al contamination from the Al_2O_3 crucible. Pellets were then polished, painted with gold electrodes and heated to 800 °C for 1 hour in air to cure the Au paste. The pellets were then quenched from 700 °C to limit any H^+/Li^+ on cooling, as has been shown to occur for garnet samples at lower temperatures in air.[26,47] A.C. impedance spectroscopy data were collected during heating over a temperature range of 50 °C to 250 °C (with 16 measurements taken), using a Hewlett Packard 4192A instrument. Data for the most conductive phases ($\sim10^{-4}$ S cm^{-1}) were also measured at room temperature. All measurements were conducted in air.

Results and discussion

Praseodymium doping on the Nb Site: $Li_{5+x}La_3Nb_{2-x}Pr_xO_{12}$

The powder XRD patterns for $Li_{5+x}La_3Nb_{2-x}Pr_xO_{12}$ ($0 \leq x \geq 1$) are shown in Fig. 1, illustrating pure garnet samples across the range. All patterns could be indexed based on a cubic garnet with space group $Ia\bar{3}d$ (no. 230).[22,39,40] Phases where $x > 0.25$ initially demonstrated Pr_2O_3 and La_2O_3 impurity phases which were overcome by addition of 20% excess lithium and reheating. Phases where $x > 0.8$ showed decreased conductivity (see later), hence the synthesis method was not undertaken past $x = 1$. The colour of the samples became increasingly yellow as a function of Pr content, which is attributed to the presence of

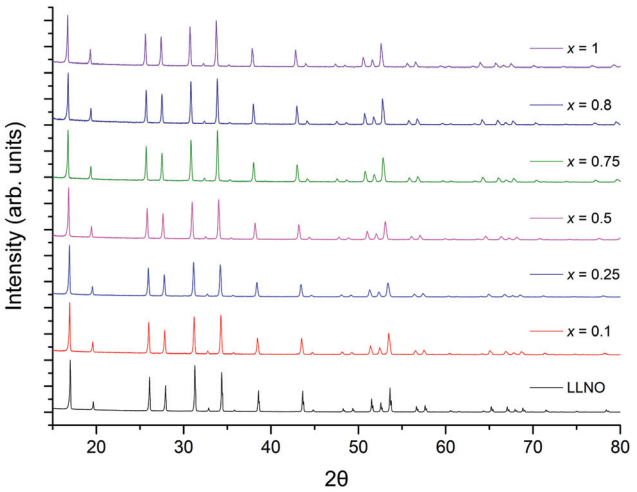

Fig. 1 Powder XRD patterns for $Li_{5+x}La_3Nb_{2-x}Pr_xO_{12}$ ($0 \leq x \geq 1$) synthesised in air, showing the formation of single phase garnet samples across the range.

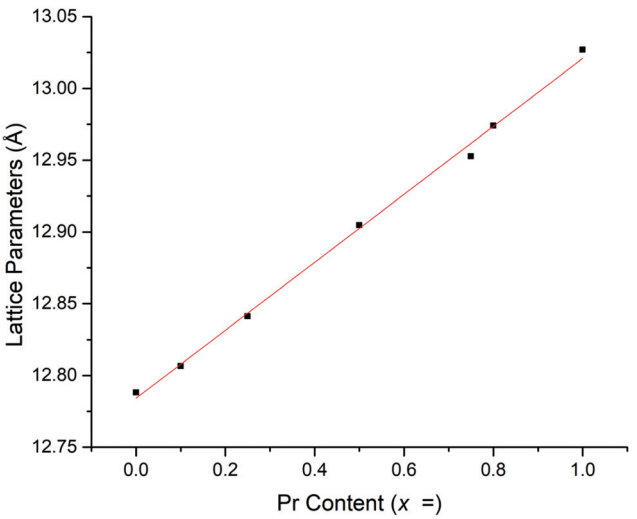

Fig. 2 Cell parameters *vs.* Pr content for $Li_{5+x}La_3Nb_{2-x}Pr_xO_{12}$.

Pr^{4+}, which is commonly believed to be responsible for the colour in the yellow pigment Pr–$ZrSiO_4$ (although some debate persists behind the chemistry of Pr–$ZrSiO_4$).[48–50]

Rietveld refinements, based on the structural model from Cussen[39] showed a linear increase in lattice parameters with increasing Pr content (Fig. 2 and Table 1), in agreement with Vegard's law and so confirming the solid solution range. This increase is due to the larger ionic radius of Pr^{4+} compared to Nb^{5+}.[39,41,51] The refined Pr occupancies on the Nb site were similar to the expected stoichiometric ratio across the series, however, did deviate slightly from the ideal ratio as the Pr content increased, see Table 1.

In order to try to confirm the Pr oxidation state, X-ray absorption near edge spectroscopy (XANES) data were collected for the $Li_{5+x}La_3Nb_{2-x}Pr_xO_{12}$ systems. However, the La L2 edge of La (~5897 eV) interfered with the Pr L3 edge (~5968 eV) to some degree. Nevertheless, when compared to the Pr^{3+} and Pr^{4+} reference (Pr_2O_3 and $BaPrO_3$ respectively), the peaks are qualitatively characteristic of Pr^{4+}, see Fig. 3. These data show a peak at 5973 eV with a shoulder at 5980 eV, which closely matches the Pr^{4+} ($BaPrO_3$) reference (Fig. 3) and can be assigned to Pr^{4+}. Further support for the assignment of Pr^{4+} in the $Li_{5.5}La_3Nb_{1.5}Pr_{0.5}O_{12}$ samples is provided by comparison with $Pr_{0.5}Ce_{0.5}O_2$, a Pr^{4+} reference used elsewhere,[52,53] which shows peaks at 5970 and 5980 eV.

Therefore, considering the XRD, XANES and refinement data, there is compelling evidence that Pr^{4+} has been doped into the LLNO structure at the Nb site (16a).

SEM and EDX

SEM and EDX on a singular grain of $Li_{5.5}La_3Nb_{1.5}Pr_{0.5}O_{12}$ demonstrated uniform Pr presence (in the expected stoichiometric ratio) when compared to La, Nb and O. However, for Pr (x) contents ≥0.5 Al contamination from the Al_2O_3 crucible became increasingly apparent[25] (Fig. 4).

Praseodymium doping on the La site (Pr^{3+}): $Li_5La_{3-x}Pr_xNb_2O_{12}$

The successful synthesis of $Li_5La_{3-x}Pr_xNb_2O_{12}$ garnets in air was limited to samples in the range $0 \leq x \leq 1$. In contrast synthesis under 5%H_2/N_2 permitted a complete solid solution range for the replacement of La with Pr, $0 \leq x \leq 3$. Both XRD patterns for air prepared samples ($0 \leq x \leq 1$) and 5%H_2 prepared samples ($0 \leq x \leq 3$) could be indexed on a cubic garnet cell with space group $Ia\bar{3}d$ (no. 230);[22,39,40] see Fig. 5 and 8 respectively. In some cases, particularly for the air-based synthesis, a small amount of Li_3NbO_4 impurity was observed marked in the respective figures (also see ESI†).

Table 1 Pellet and conductivity data in addition to lattice parameters for $Li_{5+x}La_3Nb_{2-x}Pr_xO_{12}$ samples which were uniaxially hot pressed. The Arrhenius plot $x = 1$ was not linear, hence no activation energy available

Hot pressed samples	Pellet density (g cm^{-1})	Refined density (g cm^{-1})	Relative density (%)	Lattice parameters (Å)	Pr fractional site occupancies on the Nb site	Conductivity (50 °C) (S cm^{-1})	Activation energy (eV)
LLNO reference[39]	—	5.259	—	12.79432		~ $\times 10^{-6}$	
LLNO	4.52	5.248	86	12.7880(3)		4.3×10^{-6}	0.32
$x = 0.1$	4.32	5.284	82	12.8066(3)	0.0649	5.6×10^{-5}	0.28
$x = 0.25$	4.50	5.300	85	12.8410(4)	0.1265	7.3×10^{-5}	0.32
$x = 0.5$	4.33	5.321	81	12.9048(3)	0.2568	1.6×10^{-4}	0.29
$x = 0.75$	4.72	5.361	88	12.9527(3)	0.3876	3.4×10^{-4}	0.37
$x = 0.8$	4.53	5.358	85	12.9741(5)	0.4179	5.6×10^{-4}	0.36
$x = 1$	3.50	5.366	65	13.0269(4)	0.5160	1.9×10^{-4}	—

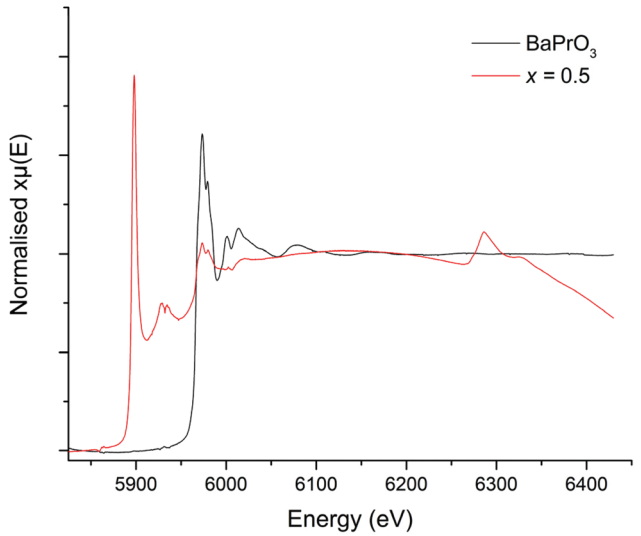

Fig. 3 XANES spectrum for $Li_{5.5}La_3Nb_{1.5}Pr_{0.5}O_{12}$ compared to $BaPrO_3$ (Pr^{4+}) reference.

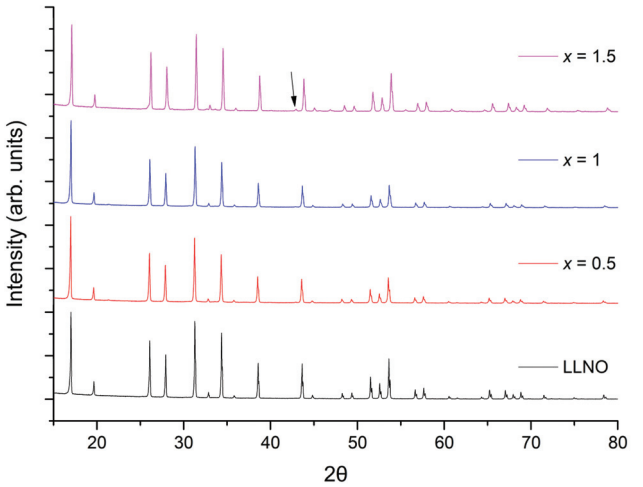

Fig. 5 The powder XRD patterns for $Li_5La_{3-x}Pr_xNb_2O_{12}$ ($0 \leq x \leq 1.5$) synthesised in air. Phase pure samples are shown up to $x = 1$, but all show garnet type symmetry. Li_3NbO_4 impurity marked by arrow. See ESI† for expanded XRD pattern.

$Li_5La_{3-x}Pr_xNb_2O_{12}$ samples prepared in air demonstrated an increasingly straw yellow/brown colour, which was distinctly different from the colour of the $Li_{5+x}La_3Nb_{2-x}Pr_xO_{12}$ samples discussed earlier. Cell parameters determined from Rietveld refinement indicated the expected decrease with increasing Pr content (due to the smaller size of Pr^{3+} *versus* La^{3+}) (Fig. 6) and

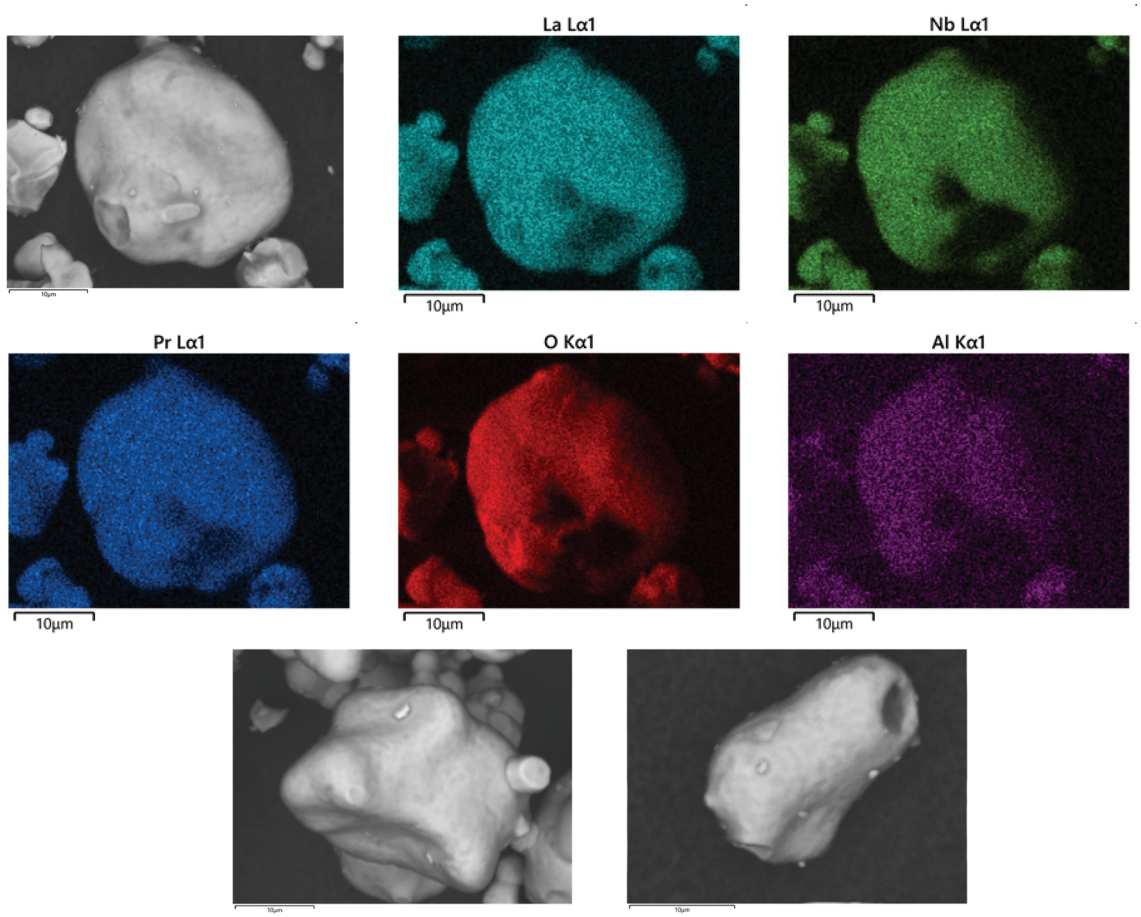

Fig. 4 SEM image and EDX map of elemental distribution in $Li_{5.5}La_3Nb_{1.5}Pr_{0.5}O_{12}$. Scale bar at 10 μm in all images.

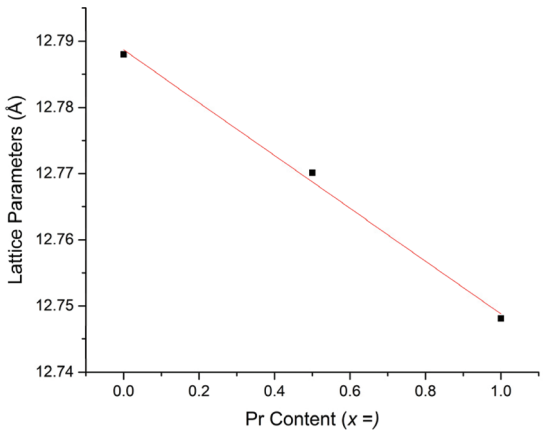

Fig. 6 Cell parameters *vs.* Pr content for air-based synthesis of $Li_5La_{3-x}Pr_xNb_2O_{12}$.

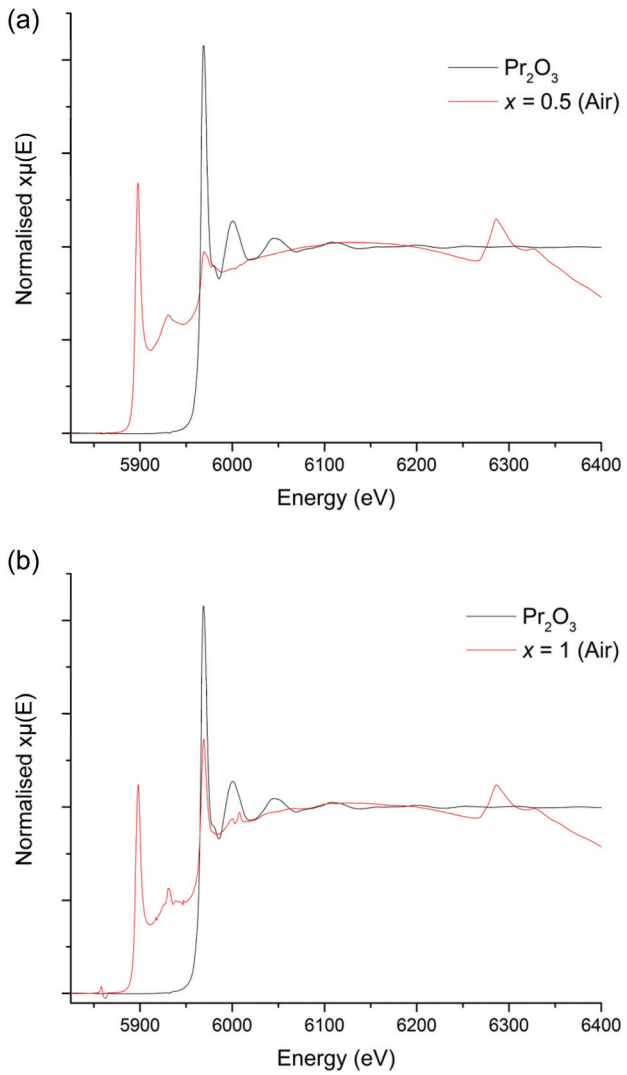

Fig. 7 (a) XANES spectra for $Li_5La_{2.5}Pr_{0.5}Nb_2O_{12}$ (air synthesised) compared to the Pr_2O_3 (Pr^{3+}) reference. (b) XANES spectra for $Li_5La_2Pr_1Nb_2O_{12}$ (air synthesised) compared to the Pr_2O_3 (Pr^{3+}) reference.

were similar to the results for equivalent $Li_5La_{3-x}Pr_xNb_2O_{12}$ phases synthesised under 5%H_2 (discussed below). The presence of the Li_3NbO_4 impurity in the air synthesised samples may suggest Nb site vacancies in the LLNO structure which have been filled by Pr^{4+}, which could account for the yellow powder colour. It could also be the case the Pr^{4+} is located on the La site. Therefore, these data suggest that there may be some partitioning of the Pr over both sites however, more work is needed to confirm whether this is so and to what extent.

In order to confirm the oxidation state of Pr in these samples, XANES data were collected on both x = 0.5 and 1, however, as outlined previously, in all cases the La L2 edge interfered somewhat with the Pr L3 edge. Nevertheless, the

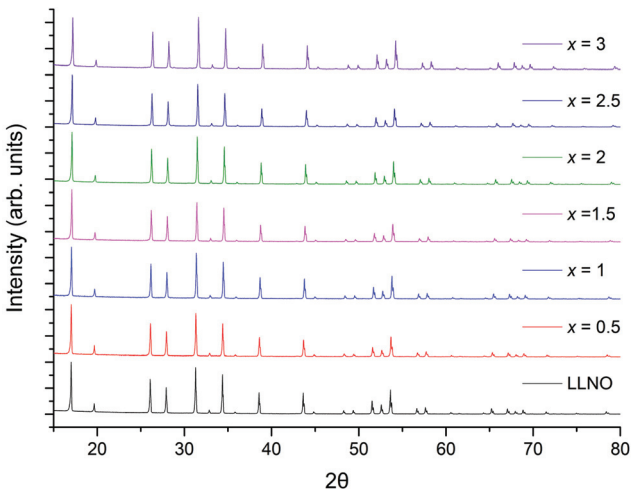

Fig. 8 The powder XRD patterns of $Li_5La_{3-x}Pr_xNb_2O_{12}$ ($0 \leq x \leq 3$) prepared in a reducing atmosphere (5%H_2). Phase pure samples with garnet type symmetry were obtained for all. For the small Li_3NbO_3 impurity see ESI† for expanded XRD pattern.

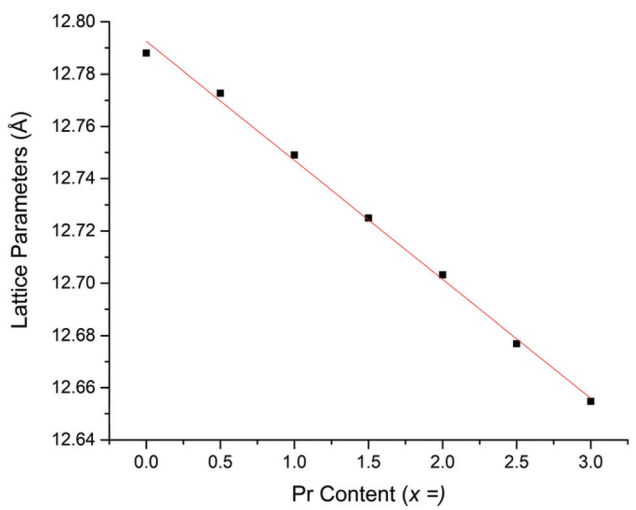

Fig. 9 Cell parameters *vs.* Pr content for 5%H_2 based synthesis of $Li_5La_{3-x}Pr_xNb_2O_{12}$.

XANES spectra of the $Li_5La_{2.5}Pr_{0.5}Nb_2O_{12}$ phase, which was prepared in air, does demonstrate characteristics of the Pr^{4+} reference (which would be consistent with presence of Pr^{4+} on either the Nb or La site), such as the peak broadness and the shoulder noted at 5982 eV, however the main peak appears to be positioned in line with the Pr_2O_3 reference at 5969 eV, consistent with mainly La site substitution, see Fig. 7a. However, the XANES spectra of the higher Pr content phase, $Li_5La_2Pr_1Nb_2O_{12}$, possesses only an absorption peak which is consistent with the Pr^{3+} reference at 5970 eV, Fig. 7b. Therefore, these spectra are somewhat contradictory but indicate, potentially, the presence of Pr in different oxidation states for $x = 0.5$, but not when $x = 1$ where only Pr^{3+} is seen.

The colours of the 5%H_2 synthesised garnets were increasingly vibrant green as the Pr content was increased, which indicates the presence of Pr^{3+}. Cell parameters determined from Rietveld refinement show a linear decrease with increasing Pr content, consistent with the smaller ionic radius of Pr^{3+} compared to La^{3+}, see Fig. 9. Despite the interference from the La L2 edge, the XANES data for these garnets are somewhat clearer than those derived from the $Li_{5+x}La_3Nb_{2-x}Pr_xO_{12}$ phases (Fig. 10a and b). The 5%H_2 prepared samples show a clear correlation with the Pr^{3+} reference (Pr_2O_3) in terms of peak intensity and characteristics, in both $x = 0.5$ and 1. Each phase has a strong absorption peak noted at 5970 eV, characteristic of Pr^{3+}, which matches both the Pr_2O_3 reference and other Pr^{3+} references used elsewhere.[52] When the Pr content is increased to $x = 1$, only increased absorbance occurs, as expected, but the peak characteristics remain unchanged. Hence, the characterisation data support the conclusion that only Pr^{3+} is present, and the different characteristics of the $x = 0.5$ phase prepared in air are unique to the synthesis method, as seen in the XANES data.

The XANES and XRD data for the H_2 synthesised samples therefore support the conclusion that Pr^{3+} has successfully been doped into the LLNO structure at the La site (24c).

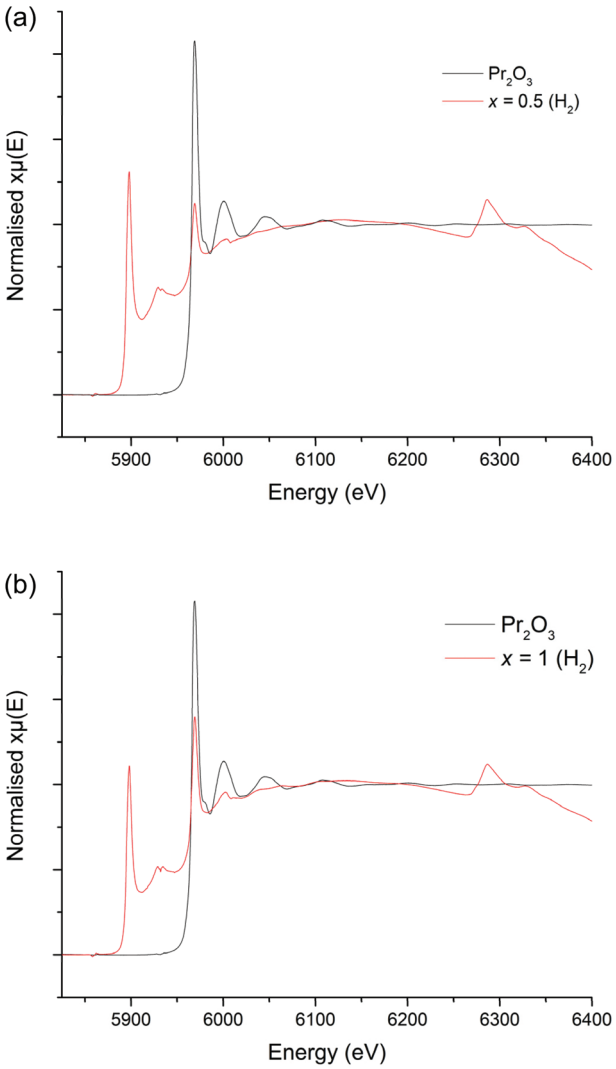

Fig. 10 (a) XANES spectra for $Li_5La_{2.5}Pr_{0.5}Nb_2O_{12}$ (5%H_2) compared to the Pr_2O_3 (Pr^{3+}) reference. (b) XANES spectrum for $Li_5La_2Pr_1Nb_2O_{12}$ (5% H_2) compared to the Pr_2O_3 (Pr^{3+}) reference.

SEM and EDX

SEM/EDX data for $Li_5La_{3-x}Pr_xNb_2O_{12}$ garnets, synthesised in air or H_2, showed uniform elemental distribution throughout the analysed grains, and have similar grain characteristics, see Fig. 11 and 12 respectively. The data for both air and H_2 synthesised samples demonstrated Pr and La present in the expected ratio. Hence EDX data supports the stoichiometric incorporation. However, the air synthesised samples did show some aluminium contamination, see Fig. 11, attributed to a reaction with the Al_2O_3 crucible.

Conductivity data for Nb site substitution: $Li_{5+x}La_3Nb_{2-x}Pr_xO_{12}$

Lithium ion conductivity was evaluated *via* impedance spectroscopy (a typical Nyquist impedance plot is shown in Fig. 13). A single non ideal semicircle was observed. A resistor, R1, in parallel with a constant phase element, CPE1, were used to fit the semicircle, and an inductor, L1, in series with R1/CPE1 was used to account for the inductance effect due to the limitations of the HP impedance spectroscopy equipment.

A characteristic spike relative to the semi-circle is present in all plots. This is attributed to a sample – electrode double layer effect. This spike represents the Li-ion transfer resistance between the garnet electrolyte and the Au electrode and corresponds to the capacitive behaviour of the gold electrodes which block Li-ion diffusion. As the semi-circle and tail were obtained in high and low frequency regions respectively it can be considered that conduction is primarily ionic in nature.[31]

The ionic conductivity of the $Li_{5+x}La_3Nb_{2-x}Pr_xO_{12}$ samples increased in line with increased Pr and hence lithium content (Fig. 14). The highest ionic conductivity of 5.6×10^{-4} S cm^{-1} at 50 °C was observed for $x = 0.8$, with a measured conductivity of 4.1×10^{-4} S cm^{-1} at 21 °C. See Table 1 and Fig. 14. These

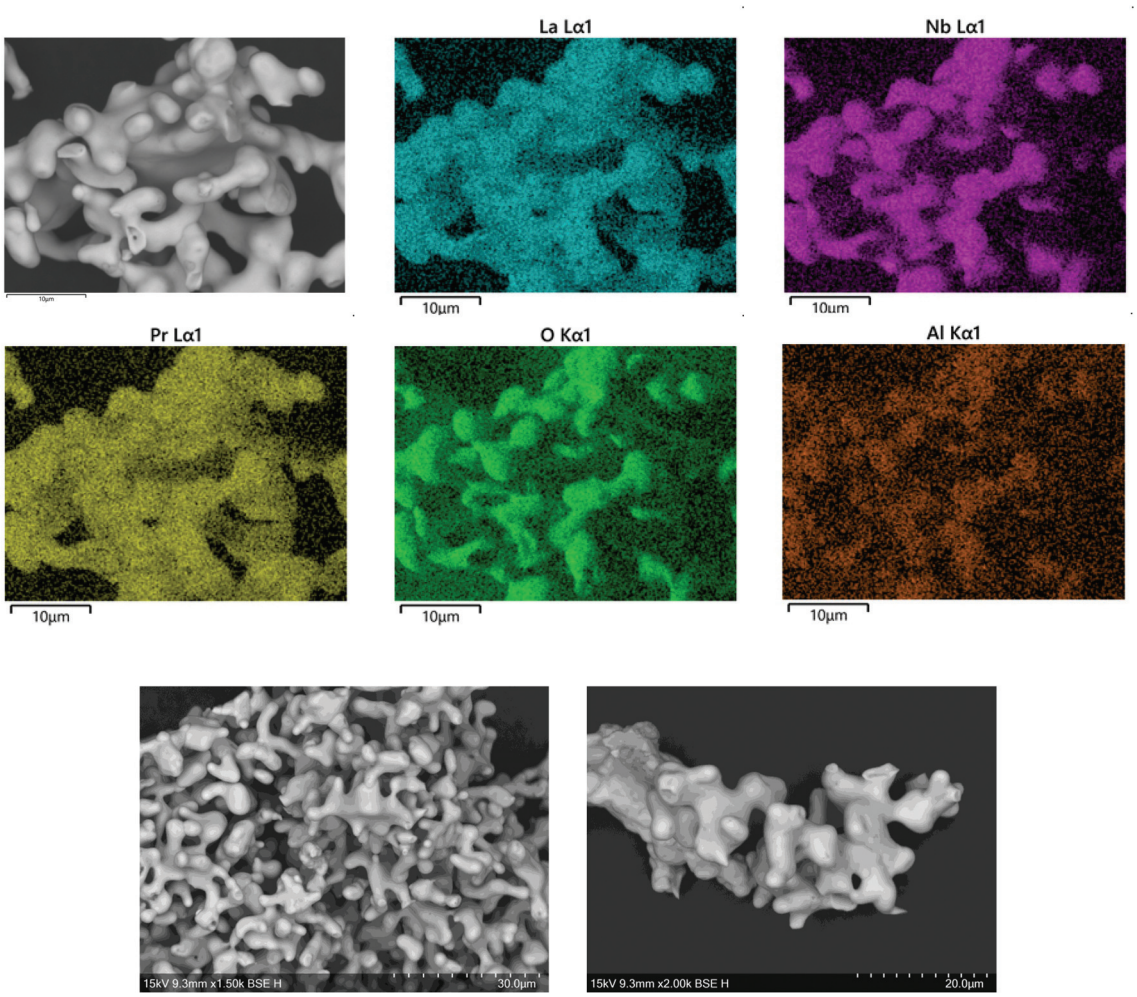

Fig. 11 SEM images and EDX map of elemental distribution in $Li_5La_2Pr_1Nb_2O_{12}$ (air). The presence of Al in this air synthesised sample is attributed to partial substitution onto the Li site. Al incorporation is often apparent in higher lithium content systems, and so this may support the postulation that there is some Pr^{4+} partitioning onto the Nb^{5+} site in the air synthesised $Li_5La_{3-x}Pr_xNb_2O_{12}$ samples. The corresponding H_2 synthesised sample, where only La site substitution is believed to occur, showed no Al contamination.

conductivity values represent some of the highest ever reported for garnets with Li content <6 per formula unit.

Higher content Pr phases ($x > 0.75$) were, however, prone to degradation during the high temperature densification treatment under N_2, resulting in small Pr_2O_3, La_2O_3 and $PrNb_5O_{14}$ impurities. In particular the XRD patterns for the $x = 1$ sample after N_2 sintering showed a more severe phase degradation. This degradation most likely accounts for the low relative pellet density of this sample and the resultant lower conductivity associated with this phase, as well as the non-linear temperature dependence of the Arrhenius plot, see Table 1 and ESI.† Consequently, further studies of samples with higher Pr contents, $x > 1$, were not performed (see ESI† for comparative XRD patterns before and after sintering treatments).

The activation energies for all samples (Fig. 14) ranged between 0.24–0.38 eV, which are similar to reports for other garnets, see Table 1.[51,54]

Conductivity data for La site substitution: $Li_5La_{3-x}Pr_xNb_2O_{12}$

All samples where Pr was doped on the La site showed similar conductivities to LLNO consistent with no change in Li content for this series. A typical Nyquist plot is displayed in Fig. 15a and b for air-based and H_2 synthesis respectively. These plots were fitted to two R/CPE components, representative of overlapping bulk and grain boundary resistance.

It was noted earlier that in the air synthesis samples, there may be some small level of Pr^{4+} substitution on the Nb site, which would be expected to give a small increase in Li content and hence conductivity. This was not observed, however these pellets proved difficult to densify, hence present with much lower relative densities than the corresponding undoped LLNO pellet. The influence of the poorer sintering may therefore mask any increase in conductivity from any Nb site substitution. Activation energies are similar to other reported garnets, see Table 2 and Fig. 16.[51,54]

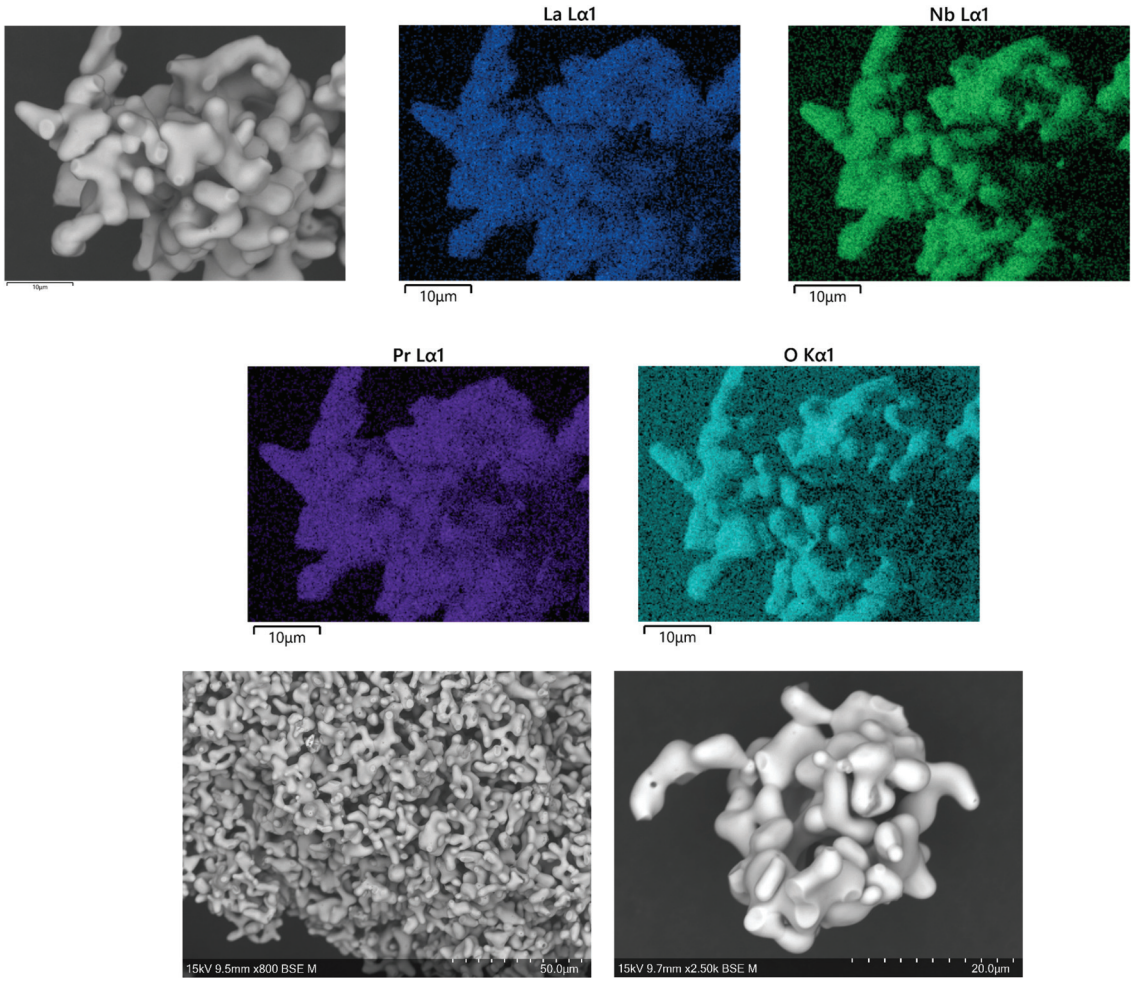

Fig. 12 SEM images and EDX map of elemental distribution in $Li_5La_{1.5}Pr_{1.5}Nb_2O_{12}$ (H_2). Since there is no increased Li content for Pr^{3+} doping on the La^{3+} site, therefore there is a decreased chance of Al exchange, hence no contamination from the alumina crucible is present.

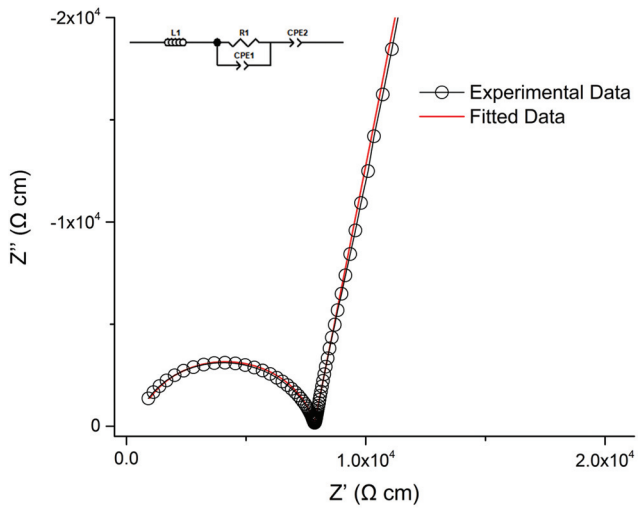

Fig. 13 Nyquist impedance plot for $Li_{5.75}La_3Nb_{1.25}Pr_{0.75}O_{12}$ at 30 °C which was fit the equivalent circuit in the top left.

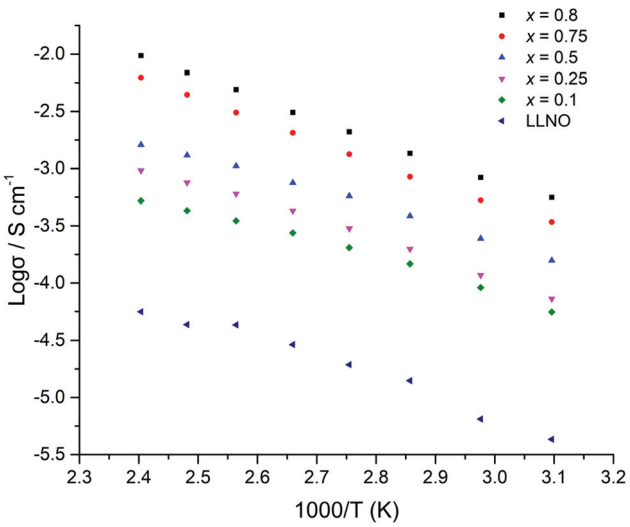

Fig. 14 Arrhenius plots for $Li_{5+x}La_3Nb_{2-x}Pr_xO_{12}$ (x = 0.1–0.8) samples which were hot pressed prior to sintering under N_2.

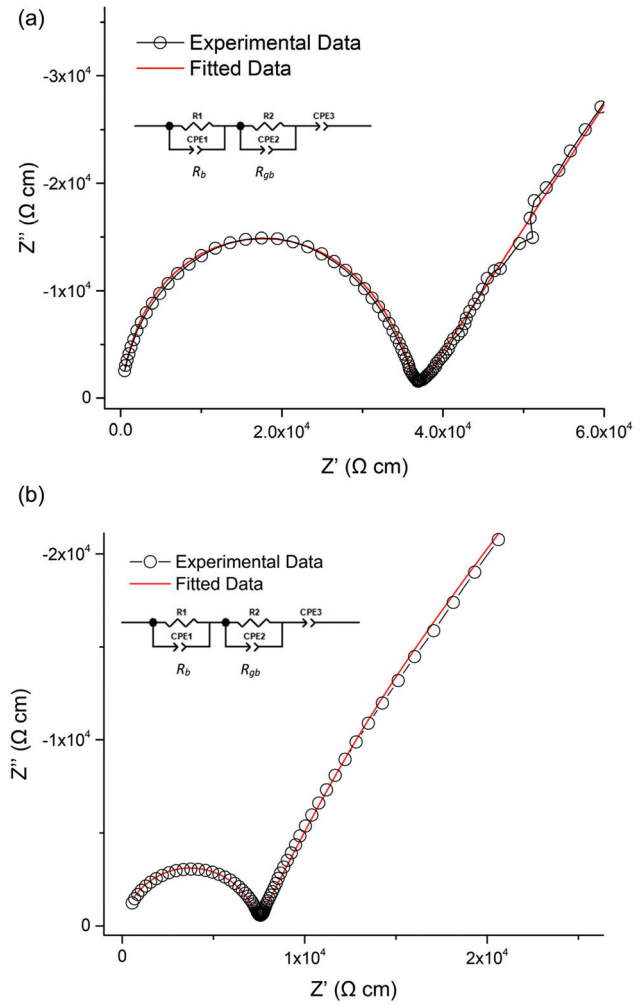

Fig. 15 (a) Nyquist impedance plot for $Li_5La_{3-x}Pr_xNb_2O_{12}$ at 130 °C for air-based synthesis. The fitted equivalent circuit is in the top left. R_b and R_{gb} relate to bulk and grain boundary resistivity respectively. (b) Nyquist impedance plot for $Li_5La_{3-x}Pr_xNb_2O_{12}$ at 130 °C for H_2 synthesis. The fitted equivalent circuit is in the top left. R_b and R_{gb} relate to bulk and grain boundary resistivity respectively.

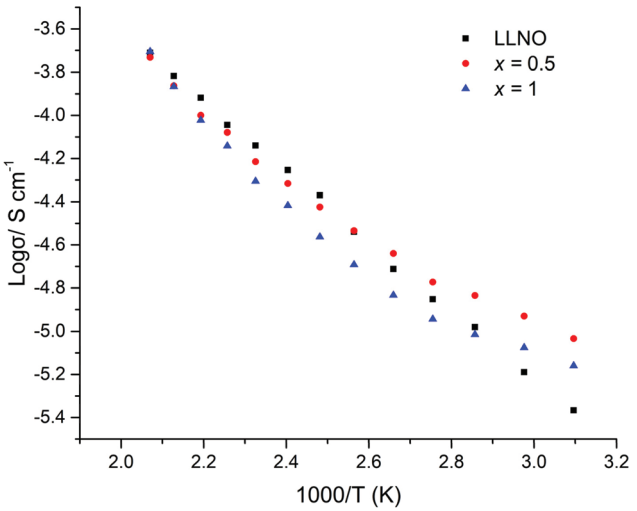

Fig. 16 Arrhenius plots for $Li_5La_{3-x}Pr_xNb_2O_{12}$ samples in air (x = 0–1).

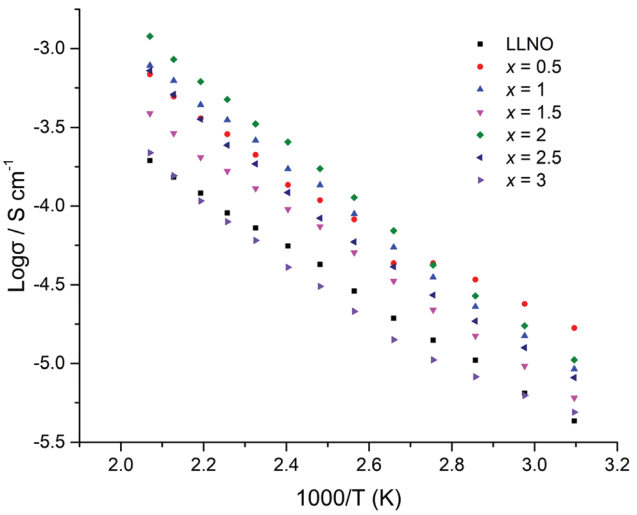

Fig. 17 Arrhenius plots for $Li_5La_{3-x}Pr_xNb_2O_{12}$ samples under H_2 (x = 0–3). The deviation from linearity at lower temperature for the x = 0.5 sample is attributed to partial water incorporation and subsequent loss on heating.

The H_2 synthesised samples showed similar conductivities for all samples, with a small peak in the conductivity of the series (1.7×10^{-5} S cm^{-1} (50 °C)) for x = 0.5, see Fig. 17 for Arrhenius plots. Activation energies fall within the 0.3–0.4 eV range, hence are similar to reports for other garnets, see Table 3.[51,54]

Samples with Pr doping at the La site showed far lower densities than the samples with Pr doping on the Nb site (see Tables 1–3). Hence Pr doping on the Nb site appears to also enhance the sintering compared to Pr doping on the La site, which may be related to the higher lithium content in these $Li_{5+x}La_3Nb_{2-x}Pr_xO_{12}$ systems.

Table 2 Pellet and conductivity data in addition to lattice parameters for $Li_5La_{3-x}Pr_xNb_2O_{12}$ samples synthesised in air

Sample	Pellet density (g cm^{-1})	Refined density (g cm^{-1})	Relative density (%)	Lattice parameters (Å)	Conductivity at 50 °C (S cm^{-1})	Activation energy 50–210 °C (eV)
LLNO	4.52	5.248	86	12.7880(3)	4.3×10^{-6}	0.32
x = 0.5	3.08	5.289	58	12.7701(3)	9.3×10^{-6}	0.25
x = 1	3.21	5.317	60	12.7481(3)	6.9×10^{-6}	0.28

Table 3 Pellet and conductivity data in addition to lattice parameters for $Li_5La_{3-x}Pr_xNb_2O_{12}$ samples synthesised under H_2

Sample	Pellet density (g cm^{-1})	Refined density (g cm^{-1})	Relative density (%)	Lattice parameters (Å)	Conductivity at 50 °C (S cm^{-1})	Activation energy 50–210 °C (eV)
LLNO reference[39]		5.259	—	12.79432	$\sim \times 10^{-6}$	
LLNO synthesized	4.52	5.248	86	12.7880(3)	4.3×10^{-6}	0.32
$x = 0.5$	3.87	5.286	73	12.7727(3)	1.7×10^{-5}	0.31
$x = 1$	3.40	5.316	64	12.7490(2)	9.2×10^{-6}	0.38
$x = 1.5$	3.47	5.346	65	12.7250(5)	6.0×10^{-6}	0.35
$x = 2$	3.91	5.373	73	12.7032(3)	1.1×10^{-5}	0.40
$x = 2.5$	3.72	5.407	69	12.6769(3)	8.1×10^{-6}	0.38
$x = 3$	4.01	5.435	74	12.6548(5)	4.9×10^{-6}	0.32

Conclusions

In summary, we have shown for the first time a dopant (Pr) that can be substituted onto both the La and Nb site in $Li_5La_3Nb_2O_{12}$. Furthermore, the oxidation state of the Pr is dictated by the site substitution; +3 on the La site, and +4 on the Nb site. Due to the resultant increase in Li content for Nb site substitution, a significant increase in conductivity is observed. These $Li_{5+x}La_3Nb_{2-x}Pr_xO_{12}$ samples show some of the highest conductivities for garnets with Li contents less than 6, with values up to 0.56 mS cm^{-1} (at 50 °C) for $x = 0.8$. A final point of note, Pr doped phases at the Nb site ($x \leq 0.25$) were a vibrant yellow, with a vibrant green colour obtained from H_2 based synthesis of $Li_{5+x}La_3Nb_{2-x}Pr_xO_{12}$ garnets when $x \geq 2.5$. Hence the optical properties of these garnets may merit further investigation, especially with respect to potential interest as pigments (see ESI†), however the effect of moisture on the Pr oxidation states, and therefore the sample colour, requires further investigation. It may also be of interest to study the optical properties of these Pr garnets under U.V. light.

Conflicts of interest

There are no conflicts of interest to declare.

Acknowledgements

We would like to thank the University of Birmingham for the studentship funding of Mark Stockham and the EPSRC for funding the GENESIS project (under EP/R024006/1). We thank the Diamond Light Source for the award of beam time as part of the Energy Materials Block Allocation Group SP14239. We would also like to thank Prof. Emma Kendrick for the continued use of the dry room facilities. Raw experimental data can be found at: https://doi.org/10.25500/edata.bham.00000490.

References

1 C.-X. Zu and H. Li, *Energy Environ. Sci.*, 2011, **4**, 2614–2624.
2 Y. Zhu, X. He and Y. Mo, *ACS Appl. Mater. Interfaces*, 2015, **7**, 23685–23693.
3 V. A. Agubra and J. W. Fergus, *J. Power Sources*, 2014, **268**, 153–162.
4 M. Armand and J. M. Tarascon, *Nature*, 2008, **451**, 652.
5 N. Nitta, F. Wu, J. T. Lee and G. Yushin, *Mater. Today*, 2015, **18**, 252–264.
6 M. Winter and R. J. Brodd, *Chem. Rev.*, 2004, **104**, 4245–4270.
7 J. M. Tarascon and M. Armand, *Nature*, 2001, **414**, 359.
8 J. Li, C. Ma, M. Chi, C. Liang and N. J. Dudney, *Adv. Energy Mater.*, 2015, **5**, 1401408.
9 Q. Liu, Z. Geng, C. Han, Y. Fu, S. Li, Y.-B. He, F. Kang and B. Li, *J. Power Sources*, 2018, **389**, 120–134.
10 A. C. Luntz, J. Voss and K. Reuter, *J. Phys. Chem. Lett.*, 2015, **6**, 4599–4604.
11 K. Fu, Y. Gong, B. Liu, Y. Zhu, S. Xu, Y. Yao, W. Luo, C. Wang, S. Lacey, J. Dai, Y. Chen, Y. Mo, E. Wachsman and L. Hu, *Sci. Adv.*, 2017, **3**, e1601659.
12 Y. Kato, S. Hori, T. Saito, K. Suzuki, M. Hirayama, A. Mitsui, M. Yonemura, H. Iba and R. Kanno, *Nat. Energy*, 2016, **1**, 16030.
13 V. Thangadurai, S. Narayanan and D. Pinzaru, *Chem. Soc. Rev.*, 2014, **43**, 4714–4727.
14 W. D. Richards, L. J. Miara, Y. Wang, J. C. Kim and G. Ceder, *Chem. Mater.*, 2016, **28**, 266–273.
15 B. Dong, R. Jarkaneh, S. Hull, N. Reeves-McLaren, J. J. Biendicho and A. R. West, *J. Mater. Chem. A*, 2016, **4**, 1408–1413.
16 C. Bernuy-Lopez, W. Manalastas, J. M. Lopez del Amo, A. Aguadero, F. Aguesse and J. A. Kilner, *Chem. Mater.*, 2014, **26**, 3610–3617.
17 H. Buschmann, J. Dölle, S. Berendts, A. Kuhn, P. Bottke, M. Wilkening, P. Heitjans, A. Senyshyn, H. Ehrenberg, A. Lotnyk, V. Duppel, L. Kienle and J. Janek, *Phys. Chem. Chem. Phys.*, 2011, **13**, 19378–19392.
18 S. Ohta, T. Kobayashi and T. Asaoka, *J. Power Sources*, 2011, **196**, 3342–3345.
19 T. Thompson, S. Yu, L. Williams, R. D. Schmidt, R. Garcia-Mendez, J. Wolfenstine, J. L. Allen, E. Kioupakis, D. J. Siegel and J. Sakamoto, *ACS Energy Lett.*, 2017, **2**, 462–468.
20 A. F. Wells, *Structural inorganic chemistry*, Clarendon Press, 1984.
21 E. J. Cussen and T. W. S. Yip, *J. Solid State Chem.*, 2007, **180**, 1832–1839.

22 D. Mazza, *Mater. Lett.*, 1988, **7**, 205–207.
23 J. Han, J. Zhu, Y. Li, X. Yu, S. Wang, G. Wu, H. Xie, S. C. Vogel, F. Izumi, K. Momma, Y. Kawamura, Y. Huang, J. B. Goodenough and Y. Zhao, *Chem. Commun.*, 2012, **48**, 9840–9842.
24 B. Dong, S. R. Yeandel, P. Goddard and P. R. Slater, *Chem. Mater.*, 2020, **32**, 215–223.
25 C. A. Geiger, E. Alekseev, B. Lazic, M. Fisch, T. Armbruster, R. Langner, M. Fechtelkord, N. Kim, T. Pettke and W. Weppner, *Inorg. Chem.*, 2011, **50**, 1089–1097.
26 M. A. Howard, O. Clemens, E. Kendrick, K. S. Knight, D. C. Apperley, P. A. Anderson and P. R. Slater, *Dalton Trans.*, 2012, **41**, 12048–12053.
27 S. Mukhopadhyay, T. Thompson, J. Sakamoto, A. Huq, J. Wolfenstine, J. L. Allen, N. Bernstein, D. A. Stewart and M. D. Johannes, *Chem. Mater.*, 2015, **27**, 3658–3665.
28 J. L. Allen, J. Wolfenstine, E. Rangasamy and J. Sakamoto, *J. Power Sources*, 2012, **206**, 315–319.
29 S.-W. Baek, J.-M. Lee, T. Y. Kim, M.-S. Song and Y. Park, *J. Power Sources*, 2014, **249**, 197–206.
30 M. Botros, R. Djenadic, O. Clemens, M. Möller and H. Hahn, *J. Power Sources*, 2016, **309**, 108–115.
31 R. Murugan, V. Thangadurai and W. Weppner, *Angew. Chem., Int. Ed.*, 2007, **46**, 7778–7781.
32 R. H. Brugge, J. A. Kilner and A. Aguadero, *Solid State Ionics*, 2019, **337**, 154–160.
33 Y. Jin and P. J. McGinn, *J. Power Sources*, 2011, **196**, 8683–8687.
34 S. Kim, M. Hirayama, S. Taminato and R. Kanno, *Dalton Trans.*, 2013, **42**, 13112–13117.
35 C. Loho, R. Djenadic, M. Bruns, O. Clemens and H. Hahn, *J. Electrochem. Soc.*, 2017, **164**, A6131–A6139.
36 S. Lobe, C. Dellen, M. Finsterbusch, H. G. Gehrke, D. Sebold, C. L. Tsai, S. Uhlenbruck and O. Guillon, *J. Power Sources*, 2016, **307**, 684–689.
37 C.-W. Ahn, J.-J. Choi, J. Ryu, B.-D. Hahn, J.-W. Kim, W.-H. Yoon, J.-H. Choi and D.-S. Park, *J. Electrochem. Soc.*, 2015, **162**, A60–A63.
38 B. Dong, L. L. Driscoll, M. P. Stockham, E. Kendrick and P. R. Slater, *Solid State Ionics*, 2020, **350**, 115317.
39 E. J. Cussen, *Chem. Commun.*, 2006, 412–413, DOI: 10.1039/B514640B.
40 V. Thangadurai, H. Kaack and W. J. F. Weppner, *J. Am. Ceram. Soc.*, 2004, **86**, 437–440.
41 S. Narayanan, F. Ramezanipour and V. Thangadurai, *J. Phys. Chem. C*, 2012, **116**, 20154–20162.
42 R. H. Brugge, A. K. O. Hekselman, A. Cavallaro, F. M. Pesci, R. J. Chater, J. A. Kilner and A. Aguadero, *Chem. Mater.*, 2018, **30**, 3704–3713.
43 G. Larraz, A. Orera and M. L. Sanjuán, *J. Mater. Chem. A*, 2013, **1**, 11419–11428.
44 C. Galven, J. Dittmer, E. Suard, F. Le Berre and M.-P. Crosnier-Lopez, *Chem. Mater.*, 2012, **24**, 3335–3345.
45 B. Toby and R. Dreele, *J. Appl. Crystallogr.*, 2013, **46**, 544–549.
46 B. Ravel and M. Newville, *J. Synchrotron Radiat.*, 2005, **12**, 537–541.
47 J. Percival, D. Apperley and P. R. Slater, *Solid State Ion.*, 2008, **179**, 1693–1696.
48 J. A. Badenes, J. B. Vicent, M. Llusar, M. A. Tena and G. Monr, *J. Mater. Sci.*, 2002, **37**, 1413–1420.
49 G. Del Nero, G. Cappelletti, S. Ardizzone, P. Fermo and S. Gilardoni, *J. Eur. Ceram. Soc.*, 2004, **24**, 3603–3611.
50 M. Shoyama, H. Nasu and K. Kamiya, *Preparation of Rare Earth-Zircon Pigments by the Sol-Gel Method*, 1998.
51 S. Ramakumar, C. Deviannapoorani, L. Dhivya, L. S. Shankar and R. Murugan, *Prog. Mater. Sci.*, 2017, **88**, 325–411.
52 T. Ogier, C. Prestipino, S. Figueroa, F. Mauvy, J. Mougin, J. C. Grenier, A. Demourgues and J. M. Bassat, *Chem. Phys. Lett.*, 2019, **727**, 116–120.
53 R. C. Karnatak, J. M. Esteva, H. Dexpert, M. Gasgnier, P. E. Caro and L. Albert, *Phys. Rev. B: Condens. Matter Mater. Phys.*, 1987, **36**, 1745–1749.
54 J.-F. Wu, E.-Y. Chen, Y. Yu, L. Liu, Y. Wu, W. K. Pang, V. K. Peterson and X. Guo, *ACS Appl. Mater. Interfaces*, 2017, **9**, 1542–1552.

6. Water based synthesis of highly conductive $Ga_xLi_{7-3x}La_3Hf_2O_{12}$ garnets with comparable critical current density to analogous $Ga_xLi_{7-3x}La_3Zr_2O_{12}$ systems

6.1. PUBLICATION

Water based synthesis of highly conductive $Ga_xLi_{7-3x}La_3Hf_2O_{12}$ garnets with comparable critical current density to analogous $Ga_xLi_{7-3x}La_3Zr_2O_{12}$ systems

Article information : M. P. Stockham, B. Dong, M. S. James, Y. Li, Y. Ding and P. R. Slater, Dalton Transactions, 2021, 50, 2364-2374. Invited front cover article.

Submitted: 02/11/2020

Accepted: 16/12/2020

Author contributions: M. P. Stockham: experimental and characterisation work, method development, conceptualisation, writing – original draft, analysis, investigation. B. Dong: Data curation, investigation, guidance on impedance spectroscopy. M.S. James: Data Curation. Y. Ding: Supervision. Y. Li: Supervision. P. R. Slater: Conceptualisation, lead supervision, characterisation and experimental guidance, writing – review & editing.

Volume 50
Number 7
21 February 2021
Pages 2287-2690

Dalton Transactions

An international journal of inorganic chemistry

rsc.li/dalton

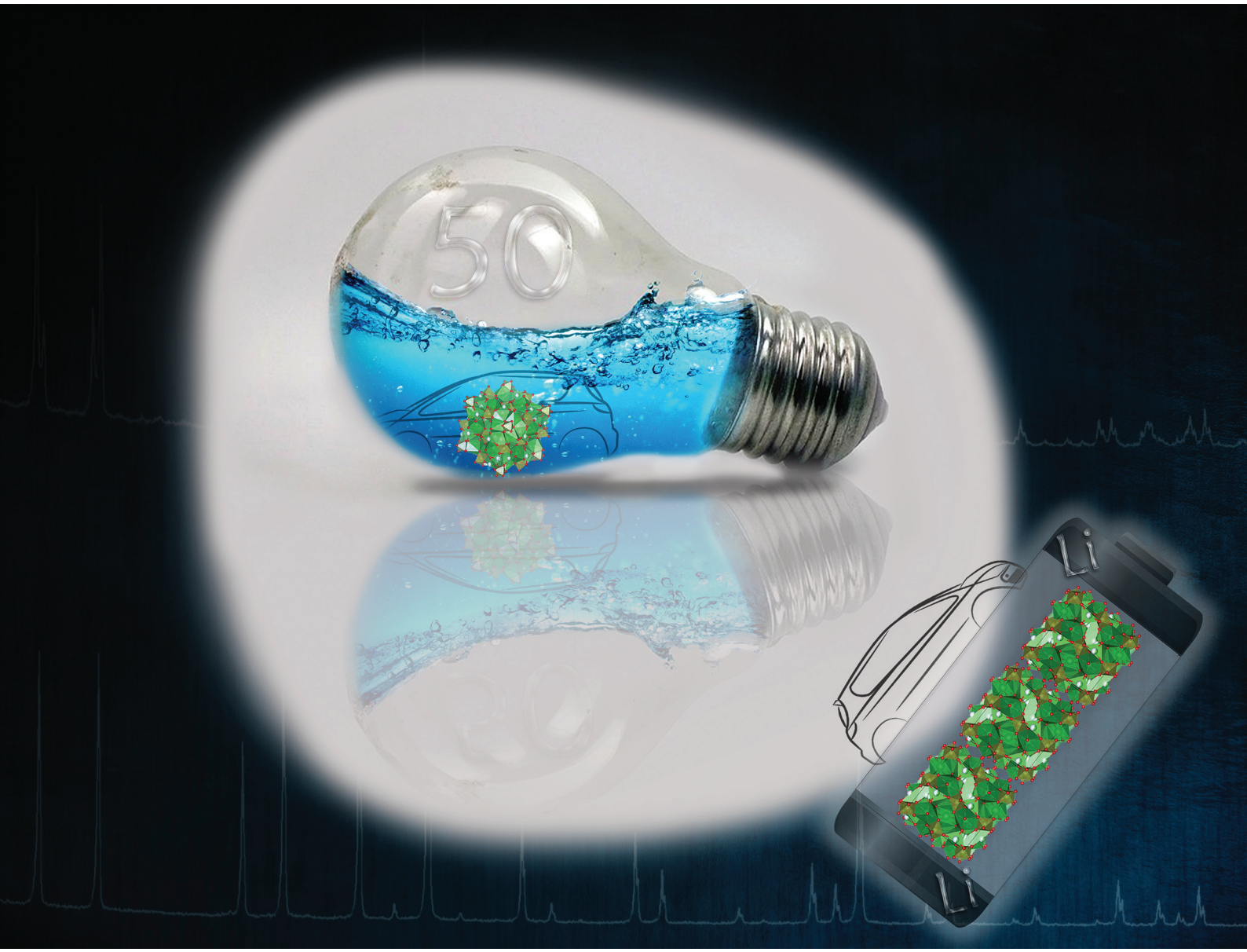

ISSN 1477-9226

PAPER

M. P. Stockham, P. R. Slater *et al.*
Water based synthesis of highly conductive $Ga_xLi_{7-3x}La_3Hf_2O_{12}$ garnets with comparable critical current density to analogous $Ga_xLi_{7-3x}La_3Zr_2O_{12}$ systems

ROYAL SOCIETY OF CHEMISTRY

50 Anniversary Volume

Dalton Transactions

ROYAL SOCIETY OF CHEMISTRY

PAPER

View Article Online
View Journal | View Issue

Cite this: *Dalton Trans.*, 2021, **50**, 2364

Water based synthesis of highly conductive $Ga_xLi_{7-3x}La_3Hf_2O_{12}$ garnets with comparable critical current density to analogous $Ga_xLi_{7-3x}La_3Zr_2O_{12}$ systems†

M. P. Stockham, *[a] B. Dong,[a] M. S. James,[a] Y. Li,[b] Y. Ding[b] and P. R. Slater *[a]

Received 2nd November 2020,
Accepted 16th December 2020

DOI: 10.1039/d0dt03774e

rsc.li/dalton

Next generation lithium ion batteries are envisaged as those which feature an all solid-state architecture. This will enable the higher energy density storage required to meet the demands of modern society, especially for the growing electric vehicle market. Solid state batteries have, however, proved troublesome to implement commercially due to the lack of a suitable solid-state electrolyte, which needs to be highly conductive, have a low interfacial resistance and a suitably wide electrochemical stability window. Garnet materials are potential contenders for these batteries, demonstrating many of the desired properties, although there remain challenges to overcome. Here we report a facile synthesis of $Li_7La_3Hf_2O_{12}$ and $Ga/Al_xLi_{7-3x}La_3Hf_2O_{12}$ garnets, with the synthesis of $Ga_{0.2}Li_{6.4}La_3Hf_2O_{12}$ requiring only dissolution of precursors in water and heating to 700 °C. $Ga_{0.2}Li_{6.4}La_3Hf_2O_{12}$ was shown to display a high room temperature conductivity (0.373 mS cm^{-1} at 28 °C). Moreover, in Li|garnet|Li cells, we observed a comparable critical current density compared to $Ga_{0.2}Lai_{6.4}La_3Zr_2O_{12}$, despite a lower density and higher area specific resistance compared to literature values, suggesting Hf systems may be further engineered to deliver additional improvements for use in future solid state batteries.

Introduction

High energy density secondary lithium ion batteries (LIB) with lithium metal anodes remain the goal of LIB based energy storage research. Li metal has the highest theoretical capacity (3860 mA h g^{-1}) and the lowest electrochemical potential (−3.04 V *vs.* the standard hydrogen electrode) of all possible anode materials.[1,2] However, modern day LIBs use liquid-based electrolytes that enable propagation of lithium dendrites, and so pose significant safety concerns with the use of a Li metal anode.[3] Despite intensive research to prevent dendritic growth,[4–10] a practical solution to eliminate this issue remains elusive. Furthermore, these electrolytes are flammable, toxic, non-renewable and often have a limited electrochemical window (preventing use of high V cathode materials), hence they are not ideal for the high energy demands of modern-day society.[2,11–14]

Overcoming these issues in LIBs can potentially be solved by new battery architectures which negate the need of a liquid electrolyte, such as an all solid-state battery (ASSB). The solid-state electrolyte (SSE) in such batteries in theory should block dendrite growth, and can be non-flammable and non-toxic. Therefore ASSBs are often described as the next major leap in LIB based energy storage.[15]

There have been numerous reports of solid state electrolytes showing Li ion conductivity. However, many of these potential LIB electrolytes, such as LISICON, LiPON and sulphides/glass, are limited by either low ionic conductivity or poor electrochemical stability.[16–19] Of these materials, the lithium garnet type systems have good conductivity (0.1–1 mS cm^{-1}) to approach conventional LIB electrolytes and also have a wide electrochemical stability window. However, these materials do suffer from poor interfacial contact at the solid–solid interface and an issue of dendritic growth along the grain boundaries between particles.[17,20–26] Hence, although garnet materials are promising SSEs for ASSBs, more work is required before they find a practical use as an energy storage system.

A traditional garnet material has the general formula $A_3B_2X_3O_{12}$ (*e.g.* A = Mg, Fe, B = Al, Cr, Fe, and X = Si, Fe, Al, Ga).[17,27–29] Replacement of the X site with Li yields a lithium garnet system such as $Li_3Ln_3W_2O_{12}$, with lithium fully occupying the tetrahedral (24d) site. Further modification by

[a]*School of Chemistry, University of Birmingham, Birmingham B15 2TT, UK.*
E-mail: [redacted]
[b]*School of Chemical Engineering, University of Birmingham, Birmingham B15 2TT, UK*

†Electronic supplementary information (ESI) available. See DOI: 10.1039/d0dt03774e

changing the A, B cations, *e.g.* La (A) and Nb, Zr, Hf (B), enables increased lithium content to maintain charge neutrality, with partial lithium occupation of the octahedral interstitial sites 96h and 48g.[30,31] Garnets with <7 lithium atoms per formula unit (pfu) can be indexed on a cubic cell with space group $Ia\bar{3}d$ (no. 230) or in the case of $Ga_xLi_{7-3x}La_3Zr_2O_{12}$ with <3 La pfu, potentially, $I\bar{4}3d$.[32–34] When the lithium content is increased to 7 atoms pfu, the upper limit, lithium ordering occurs with full occupancy of the octahedral and tetrahedral sites. This cation ordering is necessary to prevent short Li–Li distances and it leads to a reduction of the symmetry from a cubic to a tetragonal cell ($I4_1/acd$, no. 142), which reduces conductivity by two orders of magnitude, as the migration mechanism is based upon the need for vacant interstitial sites.

For cubic garnets, such as $Li_{6.4}Ga_{0.2}La_3Zr_2O_{12}$, ionic migration pathways have been attributed to two tetrahedral sites bridged by a single face sharing octahedron. As lithium partially occupies the interstitial sites, this gives a disordered Li sublattice and a migration pathway which affords ionic conductivity *via* the Li^+ charge carrier, which is thought to follow the hopping mechanism of 24 d → 96 h → 48 g → 96 h → 24 d, as determined by high temperature neutron diffraction and high resolution nuclear magnetic resonance,[35,36] albeit some debate persists as to the exact hopping path.

While highly conducting lithium garnet materials have now been known for some time,[37] current synthesis routes for these highly conducting garnets (ionic conductivity >0.1 mS cm^{-1}) are time consuming, energy demanding and require complex procedures, such as field assisted sintering, to enable high enough densities to give high conductivities, as is the situation for the most conductive system $Ga_{0.15}Li_{6.55}La_3Zr_2O_{12}$ ($Ga_{0.15}$-LLZO).[20,38,39] Hence a need arises to find a more suitable synthesis strategy for industrialisation which reduces the synthesis and sintering temperature. This will reduce the production costs, and will also help prevent Li^+/Al^{3+} exchange from alumina crucibles, which can be detrimental to conductivity if not correctly controlled.[40]

Critical current density (CCD), defined as the current density at which lithium dendrites form and short circuit a cell, is another major concern for solid state batteries. High CCDs are dependent on a SSE achieving a high enough density to resist dendrite formation as well as a low area specific resistance (ASR) at the garnet/Li interface. It has been shown that garnet systems such as $Ga_{0.15}$-LLZO form dendrites at current densities as low as ~0.16 mA cm^{-2} (~95% relative density, ASR of 16.7 Ω cm^2).[21] CCD can be increased to 2.8 mA cm^{-2} when employing single crystal $Ga_{0.2}$-LLZO with an ASR of 13 Ω cm^2, but this was demonstrated to be the natural CCD limit for $Ga_{0.2}$-LLZO, and unfortunately it is impractical to form single crystal garnets on a large scale to be employed in solid state batteries.[41]

CCDs have been further improved with a variety of additional interlayers, high pressures and in mixed SSE systems.[42,43] However, investigations of other systems are required which have increased CCDs intrinsic to their natural form. Of the garnet systems, much attention has been paid to the $Li_{7-3x}M_xLa_3Zr_2O_{12}$ (M = Al/Ga), however less so to the Hf analogue. This is despite computational studies that indicate Hf based garnets may have increased electrochemical stability over LLZO garnets, while also having been experimentally shown to have increased stability with respect to carbon-related decomposition during battery charging.[44–46]

Herein we report the first synthesis of cubic $Li_{6.4}Ga_{0.2}La_3Hf_2O_{12}$ (Ga-LLHO) an attractive alternative to Ga-LLZO. Ga-LLHO is shown to be not only highly conductive but can be synthesised at only 700 °C. Additionally, an investigation into the electrochemical properties of Ga-LLHO is reported with respect to CCD and cycling stability, both of which show promising results in comparison to Ga-LLZO. Conventional SSE densification processes were used with the results demonstrating a total conductivity of 1.04 mS cm^{-1} at 63 °C. The synthesis of tetragonal $Li_7La_3Hf_2O_{12}$ (t-LLHO) and $Al_{0.28}$-LLHO (Al-LLHO) is also reported by the same method, however the conductivity is lower and higher temperatures and increased dopant ratios are required to form the cubic Al-LLHO phase.

Methods

Stoichiometric quantities of $La(NO_3)_3$, $Cl_2HfO{\cdot}8H_2O$, $Ga(NO_3)_3{\cdot}8H_2O$, $Al(NO_3)_3{\cdot}9H_2O$ and $LiNO_3$ were added to ~10 ml of distilled water separately, waiting for each to dissolve before the next powder was added. A 10% mol excess of Li was added to account for lithium volatility. $Ga(NO_3)_3{\cdot}8H_2O$ was assumed octahydrate as based on work here.[47] The water was heated to 80 °C and constantly stirred. After approximately 1 h of stirring, the stirrer bar was removed, and the solution (total volume ~10 ml) heated to 350 °C for 1 hour (0.5 °C min^{-1}) in a fume hood to remove the nitrate content. The product was stored ~100 °C to prevent the atmospheric moisture absorption which occurs once the nitrates are removed; if not stored in this manner the white powder will form a paste like material within 10 min. The product was ground rapidly (to avoid cooling) and placed in a preheated furnace at 100 °C and heated to 700 °C for 12 hours (5 °C min^{-1}). The product was subsequently ball milled (500 rpm, 1 hour, 10 mm ZrO_2 balls) with a further 15–20 wt% Li excess and reheated to 700 °C–950 °C. This yielded phase pure t-LLHO, $Ga_{0.2}Li_{6.4}La_3Hf_2O_{12}$ (Ga-LLHO) and $Al_{0.28}Li_{6.16}La_3Hf_2O_{12}$ (Al-LLHO). Lower Ga contents, *e.g.* $Ga_{0.15}Li_{6.55}La_3Hf_2O_{12}$ ($Ga_{0.15}$-LLHO), were shown not to lead to formation of the desired pure cubic phase, but rather a mixed cubic/tetragonal system with impurities (see ESI†).

Characterisation

All samples were stored in an argon glove box to prevent proton-Li exchange in the garnet.[48] Scanning electron microscopy (SEM) was performed on a Hitachi TM4000plus instrument, with the elemental distribution confirmed by the corresponding AZtecOne energy dispersive X-ray (EDX) attach-

ment. Samples were prepared by applying the powders to a carbon tape and analysed at 15 kV in backscattered electron mode. Pellets were also examined in this manner, which were polished with silicon carbide sandpaper from 800 to 4000 grit to form a flat surface. Elemental composition was also analysed *via* XRF (Bruker Tiger XRF X8), where powders/pellets were placed on mylar film, in a plastic XRF sample cup and examined under He atmosphere. Phase analysis was performed by X-ray diffraction (XRD) using a Bruker D8 diffractometer with Cu source. Experimental pellet densities were determined and compared to theoretical values from Rietveld refinement results (performed using GSAS II software[49]).

Impedance spectroscopy

Samples for Electrochemical impedance spectroscopy (EIS) were prepared as follows: approx. 10 mm diameter pellets were pressed to *ca.* 3 tonnes and, subsequently, heated to 1100 °C for 12 hours under dry N_2 or O_2 (1.6 °C min^{-1}). In both cases sacrificial powders were used to protect pellets from Al contamination *via* the Al_2O_3 crucible and to prevent Li loss (pellets were thermally etched in a similar manner for SEM images). After sintering, the pellets were polished, painted with gold electrodes and heated to 800 °C for 1 hour in air to cure the Au paste. The pellets were then air quenched to room temperature from >700 °C (to limit H/Li exchange).[34,50] A.C. impedance measurements were taken from 5 Hz to 13 MHz using a Hewlett Packard 4192A LF instrument with a 100 mV applied potential from 50–250 °C. Room temperature impedance data were evaluated with a Solartron 1260 impedance analyser from 1 Hz to 10 MHz with a 100 mV potential.

Cell assembly

All cell tests were performed on biologic VMP3 and SP50 instruments. Li|Ga-LLHO|Li symmetric cells were assembled in an Ar glove box. Firstly, the pellets (~1 mm thickness) were polished using silicon carbide sandpaper from 800 to 4000 grit, then lithium metal foil was applied to each side of the pellet. The cell was then heated to 175 °C under a constant pressure for 1 h and secured within a Swagelok cell. Cells were examined *via* impedance spectroscopy before (and after) cell testing from 10 MHz to 0.1 Hz with a 10 mV potential on a Solartron 1260 impedance analyser. These symmetric cells were then cycled under constant current conditions at various current densities to assess cycling stability at room temperature on an open lab bench (between 10–20 °C throughout the day) and at a constant temperature (60 °C). Cells were also cycled with increasing current density, in increments of 10 μA cm^{-2}, until a short circuit formed to assess CCD at room temperature on an open lab bench.

Au|Ga-LLHO|Li cells, for cyclic voltammetry (C.V.), were formed by polishing a Ga-LLHO pellet as above and hand pressing the pellet into Li foil in an Ar glovebox. The cell was placed in a Swagelok cell with Au foil as the working electrode. Cyclic voltammetry was subsequently run from −0.4 to 5 V at a scan rate of 1 mV s^{-1}.

Results and discussion

X-Ray diffraction results

The powder XRD patterns of t-LLHO, Ga-LLHO, and Al-LLHO are shown in Fig. 1. All patterns could be indexed on a tetragonal (I_{41}/acd) and cubic ($Ia\bar{3}d$) garnet cell for t-LLHO and Al/Ga-LLHO respectively. After dissolution of the precursors and completion of the first 700° C heating cycle, a small La_2O_3 impurity was present in addition to an unknown phase, these were overcome by addition of a 15–20 wt% Li excess and a further 700 °C heating cycle. This yielded phase pure t-LLHO and Ga-LLHO. Al-LLHO was prepared similarly, but a higher temperature, further Li excess and increased dopant ratios were needed after the 700 °C stage (950 °C, 14 h) to form the cubic phase, see Table 1. This suggests increased favourability for the formation of the Ga-LLHO and t-LLHO systems in comparison to Al-LLHO. See ESI† for XRD data at different temperatures.

The phase pure XRD patterns of t-LLHO, see Fig. 1, demonstrated peak splitting consistent with the expected reduction in symmetry from a cubic cell to a tetragonal cell. The lattice parameters obtained *via* Rietveld refinements correspond well to the structural model by Awaka *et al.*,[51] see Table 1. The c/a cell ratio of t-LLHO is $c/a = 0.9650$, which is similar to the ratio of tetragonal LLZO (0.9641).[52]

While the facile synthesis of undoped tetragonal LLHO and Ga doped cubic LLHO were readily achieved, synthesis of the corresponding Al doped LLHO proved more challenging, requiring reheating numerous times to higher temperatures (950 °C). For Al-LLHO, $Al_{0.28}$ pfu was required but this still demonstrated broad peaks likely masking a tetragonal component, see ESI† for details on synthesis steps of this phase.

Ga-LLHO has not been investigated prior, hence reference data are not available, however the pattern corresponds well to the cubic doped LLHO patterns reported by Baklanova[46] (Al

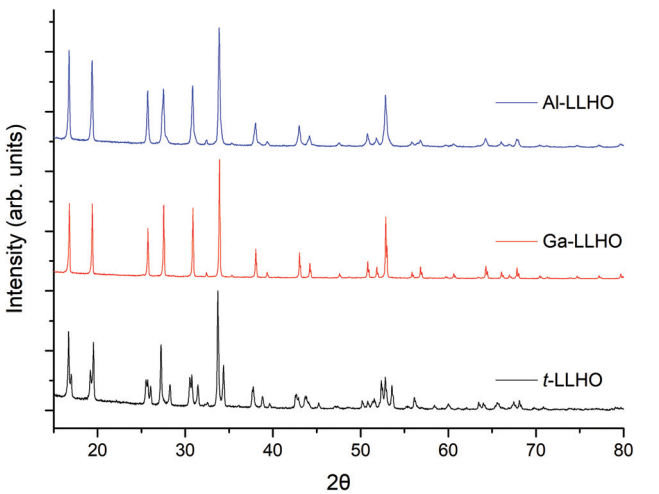

Fig. 1 Powder XRD patterns of $Al_{0.28}Li_{6.16}La_3Hf_2O_{12}$, $Ga_{0.2}Li_{6.4}La_3Hf_2O_{12}$ and $Li_7La_3Hf_2O_{12}$ synthesised by the dissolution method at 700 °C (Ga-LLHO and LLHO) and 950 °C (Al-LLHO).

Table 1 Comparison of LLHO phases and cell parameters; and relative densities of pellets. Example refinement data available in the ESI†

Samples	Quantity of dopant	Lattice parameters (a) (Å)	Lattice parameters (c) (Å)	ρ_{rel} (%)
t-LLHO (Lit)[51]	—	13.1056	12.6303	—
t-LLHO	—	13.1097(13)	12.6513(11)	60
Ga-LLHO	0.2	12.9663(2)		87
Al-LLHO	0.28	12.9820(1)		88

doped) and Hamao[53] (Ta doped). From past work on the analogous Ga-LLZO garnets, two possible cubic space groups have been proposed, with reports that this phase may potentially crystallise with the acentric cubic space group $I\bar{4}3d$ rather than $Ia\bar{3}d$.[32,33] As the XRD patterns do not demonstrate any additional peaks which correspond to the $I\bar{4}3d$ space group it is assumed the Ga-LLHO garnets possess $Ia\bar{3}d$ type symmetry, although more detailed neutron diffraction studies would be required to add further confirmation. Attempts to lower the Ga content and so prepare $Ga_{0.15}$-LLHO were also performed, however this did not yield a pure garnet at any temperature, see ESI,† and so $Ga_{0.2}$-LLHO appears to be the lowest Ga content to stabilise the cubic garnet phase.

The dissolution method was also investigated with co-doping Ga (Li site) and Ce (Hf site), Pr (Hf site) and La replacement with Nd, Eu, Gd and Er, with only Nd-LLHO showing some promise, while all others were either impure or did not form the garnet phase (see ESI†). Therefore, it would appear that the Ga-LLHO phase produced *via* this method is considerably easier to form, with t-LLHO also being formed ~260 °C below prior reports by Awaka *et al.*[51] for the tetragonal modification. The synthesis conditions for Al-LLHO, although requiring higher temperatures using this method, are still ~200 °C below previous reports of doped LLHO and with shorter heating times.[46,54] Furthermore, this method can also be applied to other garnet systems, with $Li_7La_3Zr_2O_{12}$ having been successfully made *via* this route (see ESI†).

XRF, SEM (EDX) results

SEM and EDX images of Ga-LLHO synthesised phases are shown in Fig. 2, with SEM/EDX results for other samples found in the ESI.† All phases demonstrate a uniform distribution of elements across all examined grains, indicative of a phase pure sample. In all cases, a small but notable presence of Cl is detected, while other elements are present in expected quantities. No Al emission signals were detected. To further confirm Cl presence and lack of Al contamination, X-ray fluorescence spectroscopy (XRF) was employed. In accordance with the EDX results, in all LLHO phases <1% Cl content was detected by XRF. Furthermore, no Al content was detected by XRF in LLHO or Ga-LLHO, despite no attempt being made to provide protection from the alumina crucible. This is most likely due to the low temperature synthesis preventing the Li^+/Al^{3+} exchange, demonstrating another benefit of this synthesis route. The presence of Cl in the sample can most likely be explained as being from the hafnium oxychloride starting material.

In order to confirm whether Cl was indeed present in the structure, Cl was added to the oxygen site during Rietveld refinement, and the results suggested a small amount of Cl present after the 700 °C synthesis of t-LLHO. A fractional Cl occupancy of 0.0369 on the 32 g O(1) was present, hence suggesting a Cl content of 0.148 pfu for t-LLHO. The t-LLHO garnets have slightly larger a and c axis dimensions to those reported elsewhere, which is consistent with this small degree of Cl incorporation, see Table 1. Addition of Cl to more than one site did not yield a stable refinement.

Although the addition of Cl to the structure refinements for the Al-LLHO samples gave unstable results, a small amount of Cl was found to be present in Rietveld refinements for the Ga-LLHO phase (Cl occupancy of O site = 0.0163), thus indicating a Cl content of 0.1956 pfu. Further work would be needed to accurately ascertain Cl content and the degree to which this occurs in the structure, as the level of incorporation is uncontrolled during the reaction.

However, analysis *via* XRF and EDX of garnet pellets after densification under N_2 showed Cl was removed, hence Cl incorporation may well be beneficial to formation of the LLHO phases but is unrelated to conductivity or the cell testing data below, see Fig. 3. No Al contamination was detected after pelletisation.

Conductivity measurements

The lithium ion conductivity of the garnets was evaluated *via* impedance spectroscopy. Nyquist impedance plots for t-LLHO and the dopant phases are shown in Fig. 4. A characteristic spike relative to the semi-circle is present in all plots and is attributed to charging of the electrolyte–electrode interface. This spike represents the Li-ion transfer resistance between the garnet electrolyte and the Au electrode and corresponds to the capacitive behaviour of the gold electrodes which block Li-ion diffusion. The observed semi-circles and tail were obtained in high and low frequency regions respectively, therefore it can be considered that conduction is primarily ionic in nature.[55]

For t-LLHO two semi circles are observed which correspond to bulk and grain boundary contributions, the high intercept of the latter relating to total system conductivity. Al-LLHO has overlapping semi-circles indicating combined bulk and grain boundary contributions. Nyquist plots for t-LLHO and Al-LLHO were fit to two R/CPE parallel components in connected in series, illustrative of bulk and grain boundary resistance, and are similar to those plots for LLZO systems elsewhere.[23,42,43,55–60] The Al-LLHO plots demonstrated a small inductive effect, hence an additional inductive component was added. Capacitance values and dielectric constants for the bulk component correspond to values expected for bulk ionic transport within oxide materials,[56,59–61] see Table 2. Conductivity values for t-LLHO and Al-LLHO are similar to those reported elsewhere by Awaka *et al.*[51] and Baklanova

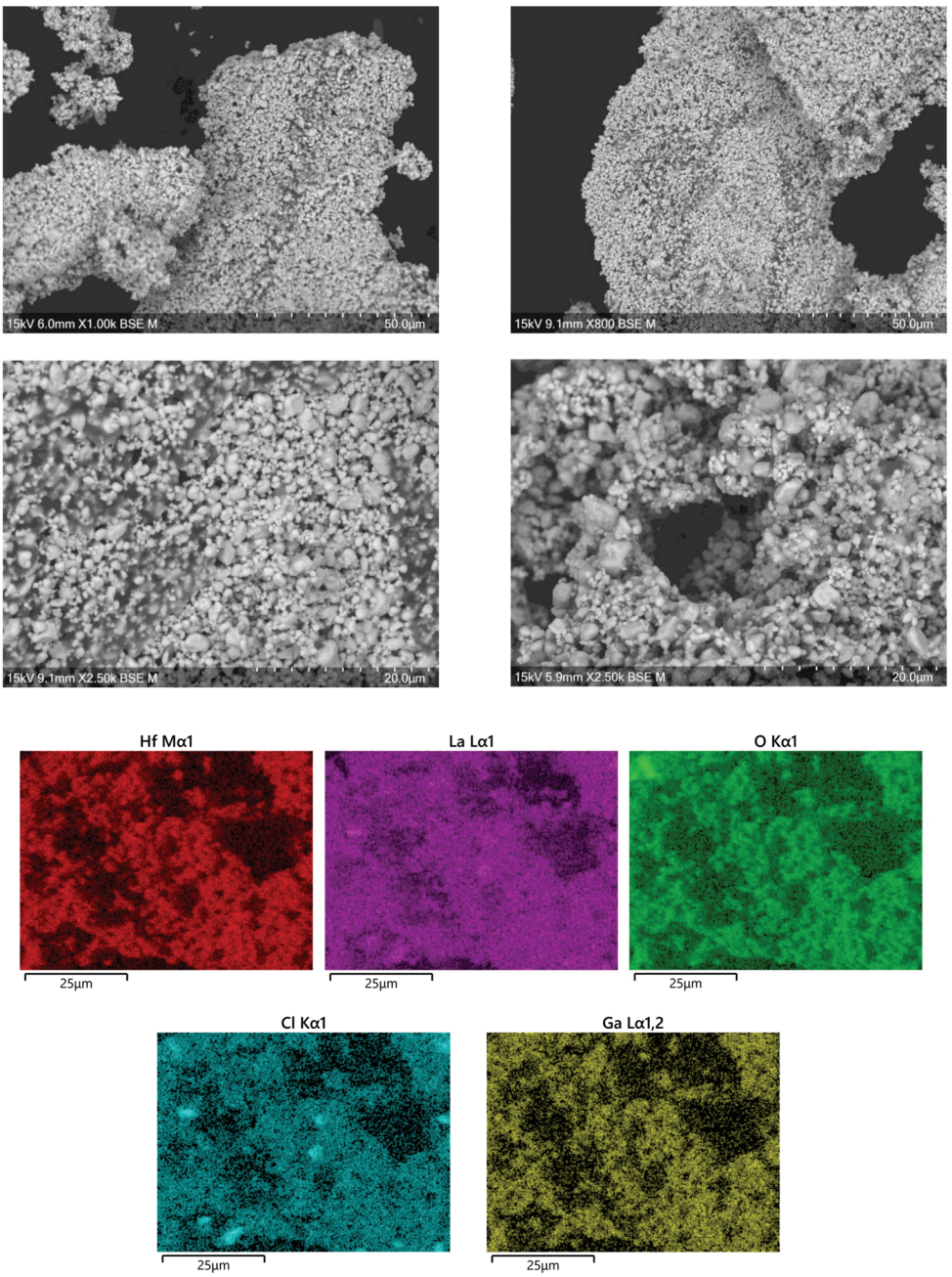

Fig. 2 SEM and EDX images of Ga-LLHO, illustrating homogenous distribution of elements throughout the analysed grains, with a presence of Cl detected. Further SEM and EDX data are available in the ESI.†

et al.[46] respectively, however the Al-LLHO synthesis reported by the latter group required three heating cycles (900–1200 °C) and over 40 hours to form the material.

The Ga-LLHO samples showed higher conductivities and the bulk component in the Nyquist plots was largely masked by an inductive effect at room temperature (and above), see Fig. 4b inlay. In order to see the bulk response, the pellet was cooled to 10 °C and in these low temperature data, we can observe bulk and grain boundary contributions, hence the data were fitted with two R/CPE components in parallel.

Ga-LLHO systems demonstrate high total ionic conductivity of 0.382 mS cm^{-1} at 28 °C, and 1.04 mS cm^{-1} at 63 °C, which represents an impressive value, especially since the pellet only achieved 87% relative density. The conductivity values are in line with many cubic LLZO (and other garnet) phases and are similar to Ga-LLZO values with higher relative densities.[55,56,58,59,62–65] These values therefore represent notably higher conductivities for a doped LLHO garnet compared to the Al, Ta doped samples reported in the literature, while the fact that it has also been synthesised at considerably

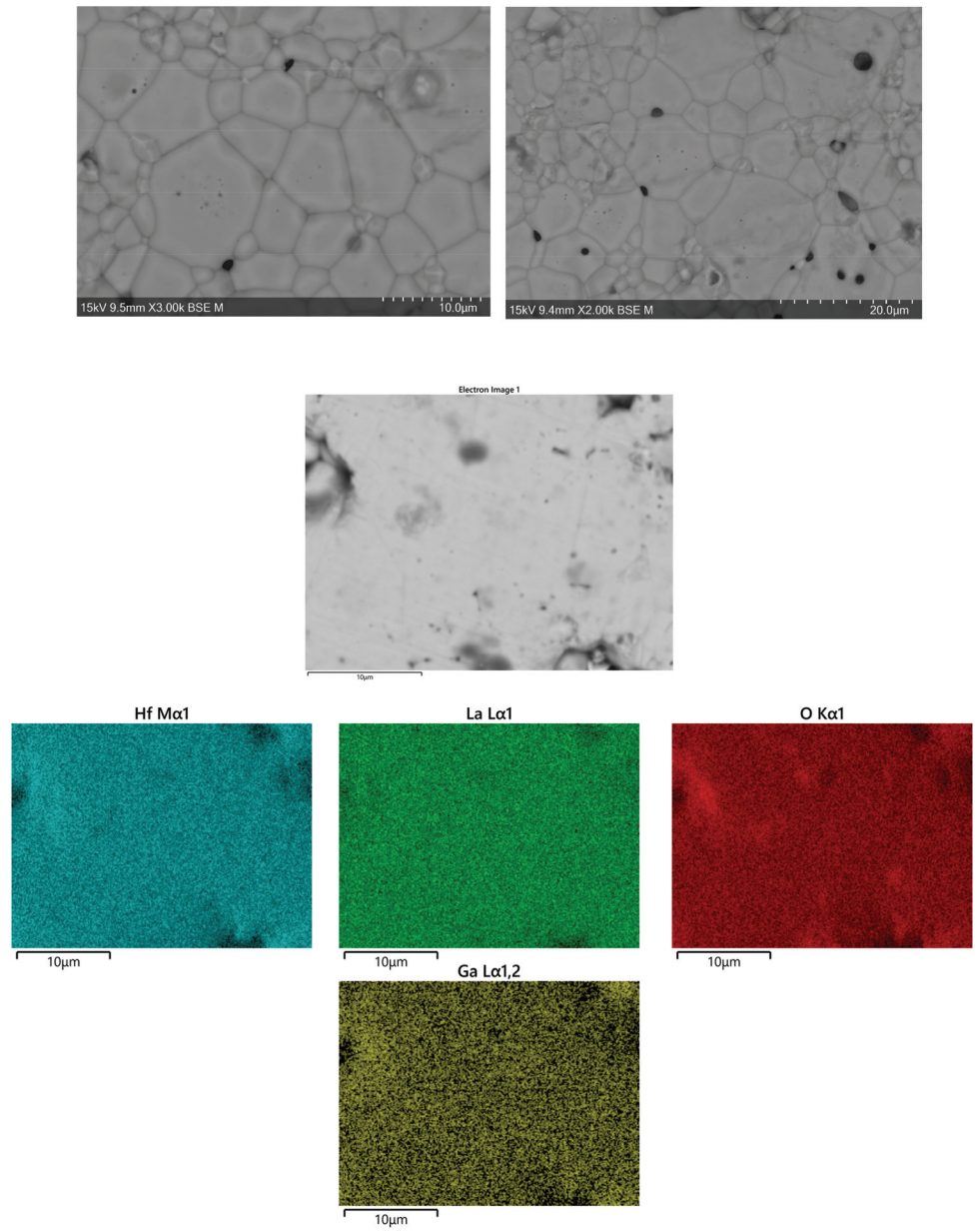

Fig. 3 SEM and EDX images of polished pellet surface after densification, polishing and thermal etching showing close packed grains with some small voids shown in the darker contrast regions. EDX was undertaken on the polished pellet surface prior to thermal etching and showed removal of Cl from the structure and no Al contamination.

lower temperature is also significant.[46,51,53] An examination into sintering of pellets of Ga-LLHO under O_2 at the same temperature led to no difference in relative density or conductivity. Hence N_2 or O_2 sintering can be employed for these garnets (see ESI†).

Arrhenius plots for t-LLHO, Ga-LLHO and Al-LLHO can be found in Fig. 5 and activation energies in Table 2. The deviation from linearity observed with t-LLHO around 100 °C is attributed to water loss (as a result of some H/Li exchange for this sample) which, despite being quenched from >750 °C and measured, is still present. This can be most likely explained by the fact that for t-LLHO the low conductivity enables even a very low amount of H/Li exchange to give a noticeable change in conductivity.

Cell testing

As the Ga-LLHO phase demonstrated the highest conductivity, it represents the most attractive alternative to Ga-LLZO as a potential SSE. Therefore, this Ga-LLHO sample was investigated for cell testing. Li symmetric cells were prepared by hot pressing Li foil onto the pellet surface as described in the experimental section. Impedance spectroscopy was performed prior to cell testing to examine the interfacial resistance properties of the garnet | Li interface after the hot-pressing tech-

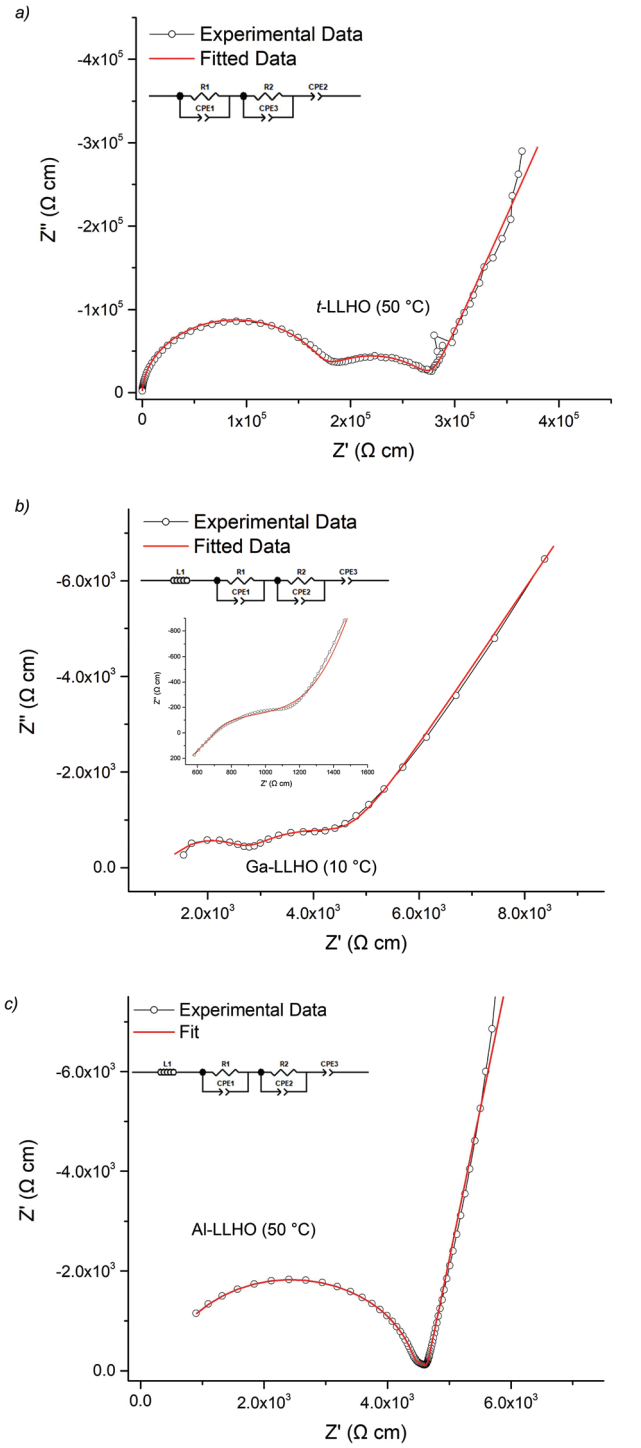

Fig. 4 Impedance spectra of (a) t-LLHO (50° C), (b) Ga-LLHO (10° C) inlay is Ga-LLHO (50° C) fit to the same equivalent circuit, (c) Al-LLHO (50° C). All were fit with two R/CPE parallel components connected in series where R1/CPE1 corresponds to the bulk and R2/CPE2 to the grain boundary contributions.

nique, see Fig. 6a and 7a. The conductivity values obtained from the Nyquist plot for the Ga-LLHO pellet are in agreement with previous results, albeit the values are slightly lower at

Table 2 Conductivity data for LLHO and doped phases. Activation energy is calculated from the Arrhenius plots using the σ_{total} values

	t-LLHO (50 °C)	Ga-LLHO (10 °C)	Al-LLHO (50 °C)
σ_{total} (S cm^{-1})	3.4×10^{-6}	1.7×10^{-4}	6.6×10^{-5}
σ_{bulk} (S cm^{-1})	5.8×10^{-6}	3.6×10^{-4}	2.2×10^{-4}
C_{bulk} (F cm^{-1})	5.08×10^{-12}	5.99×10^{-12}	6.18×10^{-12}
ε_r	57	67	70
Activation energy (eV)	0.52 (50–210 °C)	0.27 (10–90 °C)	0.33 (19–117 °C)

0.175 mS cm^{-1} at 18 °C (compared to 0.270 mS cm^{-1} at the same temperature for the prior conductivity pellet), despite the slightly higher density for the cell test pellet: ρ_{rel} of 90.5%. The slightly lower conductivity values likely arose due to the volatility of lithium during densification; however, the improved sintering has enabled a more well resolved bulk component to be revealed at room temperature. Hence the impedance spectrum was fit with three CPE/R components, representing bulk, grain boundary and Li|garnet interface contributions.

CCD was evaluated at room temperature as shown in Fig. 6b. The symmetric cell was cycled at room temperature, on an open lab bench, with increasing current densities from 10 μA cm^{-2} to 300 μA cm^{-2}. The cell had an ASR value of 464 Ω cm^2. The Li|Ga-LLHO|Li symmetric cell demonstrated ohmic current–voltage behaviour up to 120 μA cm^{-2} with some overpotentials observed above 40 μA cm^{-2}. These overpotentials increase in line with increased current densities until a large voltage drop occurred at 120 μA cm^{-2}, indicating cell short circuit and propagation of Li dendrites, with this confirmed by impedance spectroscopy in Fig. 6a. When the cell is cycled at 60 °C, see Fig. 7c, a voltage drop is noted at 300 μA cm^{-2} which indicates a higher CCD of the Ga-LLHO cell at 60 °C.

CCDs of the lithium garnet systems are thought to depend primarily upon the density of the pellet (which should be as high as possible), grain boundary characteristics, conductivity and the ASR (which should be as low as possible).[21,41,42,66–69] The dependency of CCDs on ASR was systematically evaluated by Flatscher *et al.* with $Ga_{0.2}Li_{6.4}La_3Zr_2O_{12}$ ($Ga_{0.2}$-LLZO) using single crystals (hence relative density is 100%). As this system is analogous to Ga-LLHO comparisons can be drawn. Flatscher *et al.* demonstrated that a $Ga_{0.2}$-LLZO cell with 100% relative density and an ASR of 253 Ω cm^2 would form a short circuit at 120 μA cm^{-2}; this is the same CCD observed for the Ga-LLHO cell which has considerably lower density (90.5%), a higher ASR (464 Ω cm^2) and decreased conductivity (0.175 mS cm^{-1} *vs.* 1 mS cm^{-1}).[41]

Work by Pesci *et al.* found that with high density (>95%), high conductivity (0.74 mS cm^{-1}) and low ASR (16.7 Ω cm^2) pellets of $Li_{6.55}Ga_{0.15}La_3Zr_2O_{12}$ had a CCD of 0.16 mA cm^{-2}. This CCD is slightly higher than the reported CCD of Ga-LLHO, but is nonetheless comparable, despite lower Li content, lower density and a much higher ASR.[21] Hence the Ga-LLHO system suggests an increased CCD over the Ga-LLZO

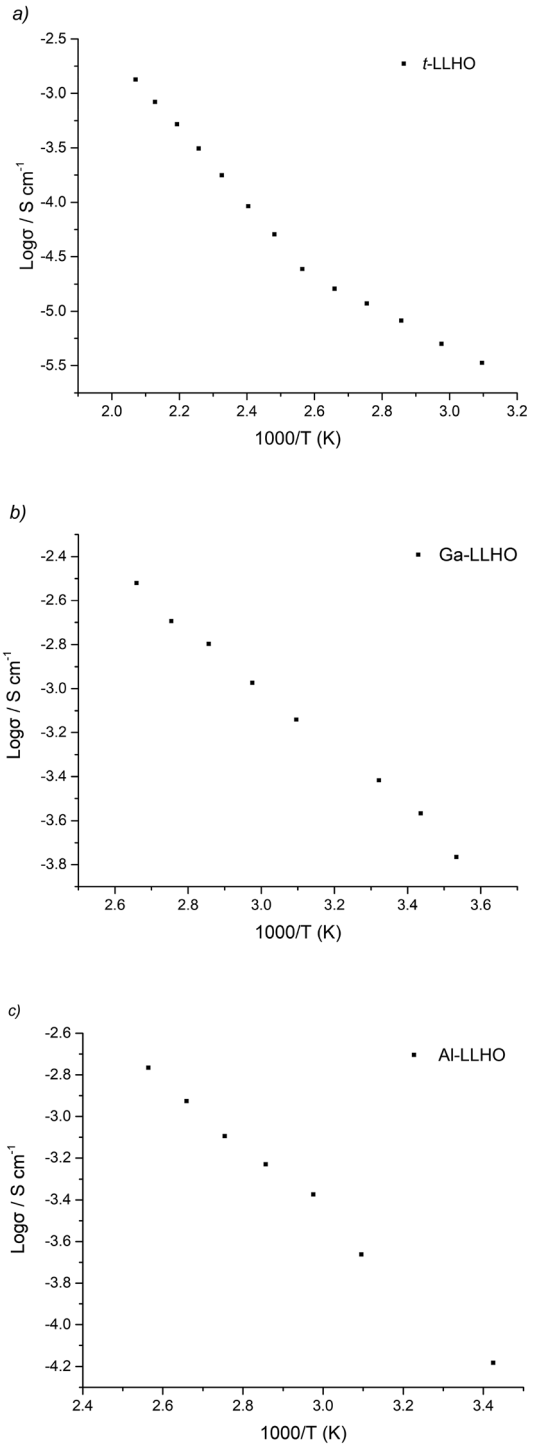

Fig. 5 Arrhenius plots for (a) t-LLHO, (b) Ga-LLHO, (c) Al-LLHO.

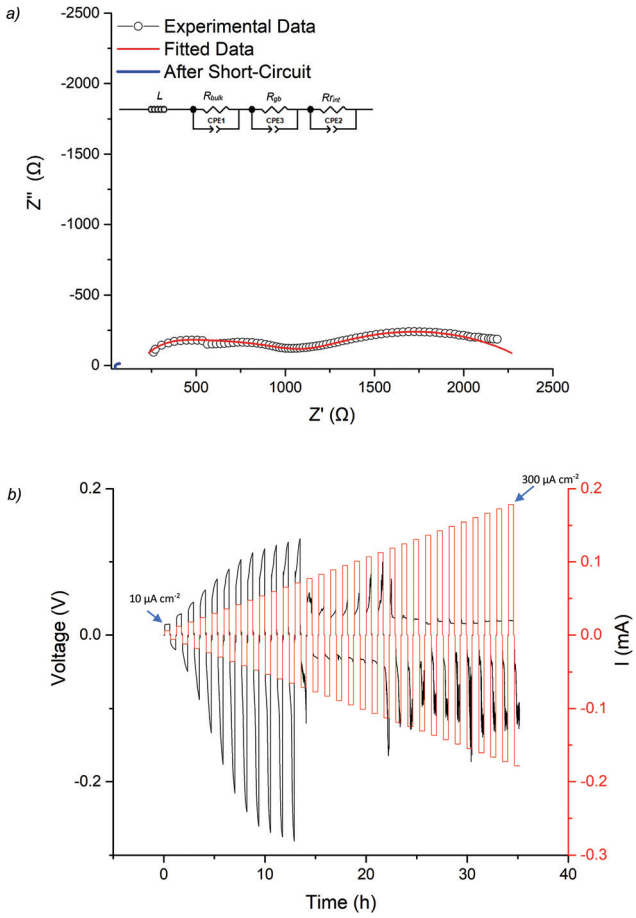

Fig. 6 (a) The impedance spectrum of the Li symmetry cell before and after CCD testing of Ga-LLHO at 21 °C, the fit at higher frequencies is representative of slightly overlapping bulk and grain components, hence was fit with two R/CPE components (b) CCD testing starting at 10 μA cm^{-2} and increasing in increments of 10 μA cm^{-2} until 300 μA cm^{-2}, with a large drop in voltage at 120 μA cm^{-2} indicating cell short circuit and lithium dendrite growth.

phase, however more comparative work is needed to confirm. Although the work by Flatscher *et al.* and Pesci *et al.* is amongst the most exhaustive when considering Ga-LLZO CCDs, it should also be noted that irrespective of density, ASR and conductivity the CCD values of Ga-LLHO are often higher, or at least very similar, to those reported for Al doped LLZO phases synthesised by conventional methods (*e.g.* without hot pressing and using alumina crucibles).[21,66,70,71] As of yet no CCD studies have been performed on LLHO garnets, hence a direct comparison is not possible. Nevertheless, we propose that these Ga doped LLHO systems offer significant promise if improvements to the sintering and reductions in the interfacial resistance can be made.

To assess cycling and interface stability, a Li|Ga-LLHO|Li symmetry cell was examined under constant current conditions while galvanostatically plating and stripping Li metal. Fig. 7b and c shows the time dependant voltage profile where Li|Ga-LLHO|Li symmetric cells were cycled at room temperature (between 10 and 19 °C) and at 60 °C at various current densities. Positive voltage indicates Li stripping, whereas negative indicates Li plating.[72] Cells were cycled for 30 minutes for each charge/discharge cycle for a total of 310 hours at room temperature. The repeating fluctuation in the voltage profile for the room temperature data is ascribed to temperature variations during cell cycling, as the cell was left on an open

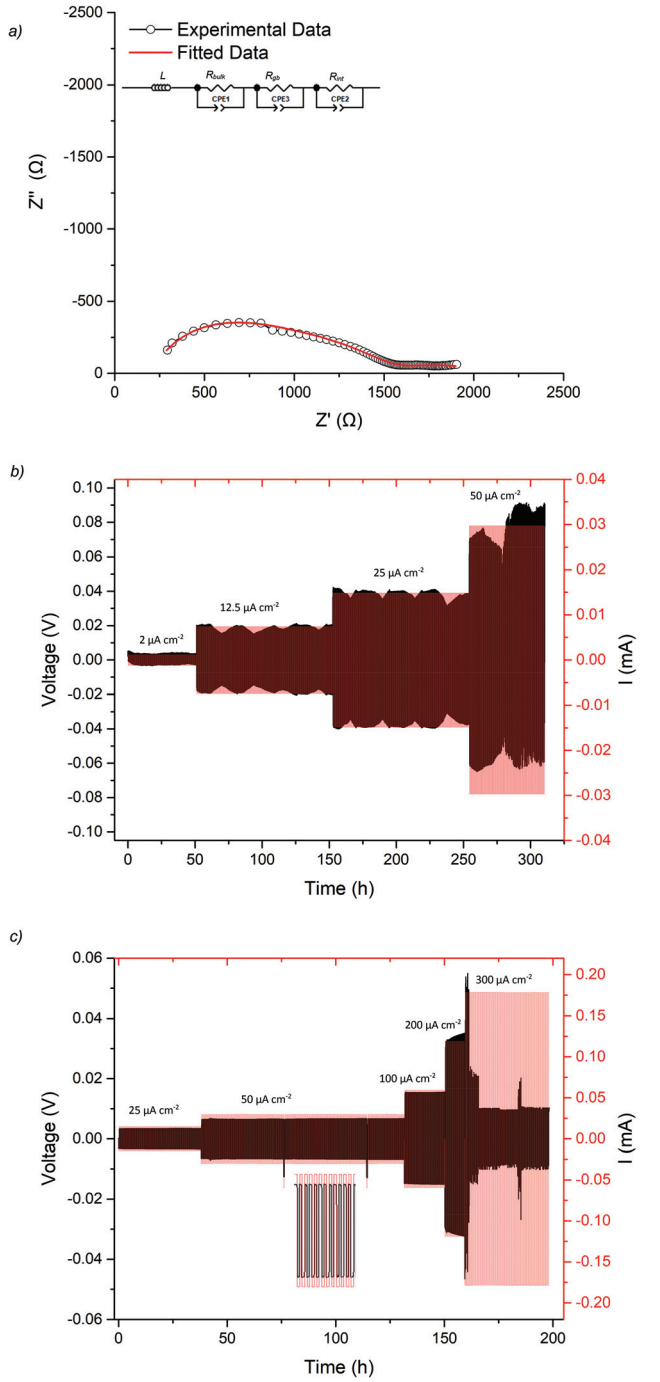

Fig. 7 Li|Ga-LLHO|Li symmetry cell testing where (a) shows the impedance spectrum of the symmetry cell before cycling (at 21 °C) with overlapping bulk and grain boundary components (b) cycling of the cell at various current densities at the fluctuating room temperature experienced on an open lab bench (10–20 °C), (c) cycling data at 60 °C. The spike in current/voltage on the 50 μA cm^{-2} plateau is due to a programming error during cell testing. The large drop in voltage at 300 μA cm^{-2} is attributed to cell short circuit and propagation of lithium dendrites, therefore is the CCD of the Ga-LLHO phase at 60 °C.

bench in a non-air-conditioned lab to approximate general temperature alterations found in real world use. This is confirmed as the peaks in voltage occurred overnight, whereas

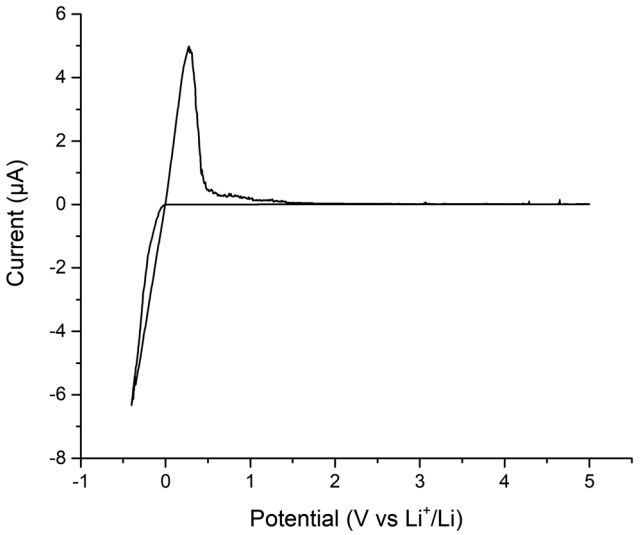

Fig. 8 Cyclic voltammetry of Au|Ga-LLHO|Li cell, showing Li stripping and plating peaks at ~0.3 V and ~−0.4 V respectively, with peaks at lower potentials indicative of Au/Li alloying.

lower voltage troughs occurred in the daytime, corresponding to warmer temperatures and increased conductivity. Cycling stability improves considerably at 60 °C with mostly flat voltage profiles observed when the cell was cycled at the varying current densities (Fig. 7c).

Finally, cyclic voltammetry was performed to assess the electrochemical stability of the Ga-LLHO phase from −0.4 to 5 V, see Fig. 8. As can be seen, clear peaks are present at ~0.3 V and ~−0.4 which indicate Li stripping and Li plating respectively. The small peaks on the tail of ~0.3 V peak are indicative of alloying between Au and Li. Outside of this, the voltage profile remains mostly flat throughout the scan with an absence of clear redox peaks, indicating stability of the Ga-LLHO phase across this range in the presence of Li metal.

Conclusion

In this work we have shown a low temperature (700 °C) route to a variety of LLHO garnets which eliminates Al contamination from the alumina crucible. Of particular interest was to illustrate a potential attractive alternative to Ga-LLZO which has garnered significant attention over recent years. In doing so we have found that Ga-LLHO is relatively simple to prepare and it appears that this particular phase is far easier to form than other variations of the LLHO system. Furthermore, a high CCD is demonstrated compared to the comparable $Ga_{0.2}$-LLZO system, in addition to room temperature stable cycling and excellent cycling stability at 60 °C. We have also demonstrated that Al-LLHO can also be synthesised *via* this route, albeit at a higher temperature. Furthermore, this synthesis method could likely be applied to a wide range of garnet materials, in particular those which have a dichloride octahydrate precursor.

Conflicts of interest

There are no conflicts of interest to declare.

Acknowledgements

We would like to thank the University of Birmingham for the studentship funding of Mark Stockham and Matthew James and the EPSRC for funding the GENESIS project (under EP/R024006/1). Raw experimental data can be found at: https://doi.org/10.25500/edata.bham.00000576

References

1 M. Armand and J. M. Tarascon, *Nature*, 2008, **451**, 652.
2 J. M. Tarascon and M. Armand, *Nature*, 2001, **414**, 359.
3 Y. Zhu, X. He and Y. Mo, *ACS Appl. Mater. Interfaces*, 2015, **7**, 23685–23693.
4 C. Yang, K. Fu, Y. Zhang, E. Hitz and L. Hu, *Adv. Mater.*, 2017, **29**, 1701169.
5 H. Yang, C. Guo, A. Naveed, J. Lei, J. Yang, Y. Nuli and J. Wang, *Energy Storage Mater.*, 2018, **14**, 199–221.
6 H. Yuan, J. Nai, H. Tian, Z. Ju, W. Zhang, Y. Liu, X. Tao and X. W. Lou, *Sci. Adv.*, 2020, **6**, eaaz3112.
7 N.-W. Li, Y.-X. Yin, C.-P. Yang and Y.-G. Guo, *Adv. Mater.*, 2016, **28**, 1853–1858.
8 L. Wang, Z. Zhou, X. Yan, F. Hou, L. Wen, W. Luo, J. Liang and S. X. Dou, *Energy Storage Mater.*, 2018, **14**, 22–48.
9 H. Dai, X. Gu, J. Dong, C. Wang, C. Lai and S. Sun, *Nat. Commun.*, 2020, **11**, 643.
10 S. Liang, Y. Shi, T. Ma, W. Yan, S. Qin, Y. Wang, Y. Zhu, H. Wang and Y. Wu, *ChemElectroChem*, 2019, **6**, 5413–5419.
11 C.-X. Zu and H. Li, *Energy Environ. Sci.*, 2011, **4**, 2614–2624.
12 V. A. Agubra and J. W. Fergus, *J. Power Sources*, 2014, **268**, 153–162.
13 N. Nitta, F. Wu, J. T. Lee and G. Yushin, *Mater. Today*, 2015, **18**, 252–264.
14 M. Winter and R. J. Brodd, *Chem. Rev.*, 2004, **104**, 4245–4270.
15 J. Li, C. Ma, M. Chi, C. Liang and N. J. Dudney, *Adv. Energy Mater.*, 2015, **5**, 1401408.
16 B. Dong, J. Yan, B. Walkley, K. K. Inglis, F. Blanc, S. Hull and A. R. West, *Solid State Ionics*, 2018, **327**, 64–70.
17 V. Thangadurai, S. Narayanan and D. Pinzaru, *Chem. Soc. Rev.*, 2014, **43**, 4714–4727.
18 W. D. Richards, L. J. Miara, Y. Wang, J. C. Kim and G. Ceder, *Chem. Mater.*, 2016, **28**, 266–273.
19 Y. G. Kim and H. N. G. Wadley, *J. Power Sources*, 2011, **196**, 1371–1377.
20 C. Bernuy-Lopez, W. Manalastas, J. M. Lopez del Amo, A. Aguadero, F. Aguesse and J. A. Kilner, *Chem. Mater.*, 2014, **26**, 3610–3617.
21 F. M. Pesci, R. H. Brugge, A. K. O. Hekselman, A. Cavallaro, R. J. Chater and A. Aguadero, *J. Mater. Chem. A*, 2018, **6**, 19817–19827.
22 Q. Liu, Z. Geng, C. Han, Y. Fu, S. Li, Y.-b. He, F. Kang and B. Li, *J. Power Sources*, 2018, **389**, 120–134.
23 H. Buschmann, J. Dölle, S. Berendts, A. Kuhn, P. Bottke, M. Wilkening, P. Heitjans, A. Senyshyn, H. Ehrenberg, A. Lotnyk, V. Duppel, L. Kienle and J. Janek, *Phys. Chem. Chem. Phys.*, 2011, **13**, 19378–19392.
24 S. Ohta, T. Kobayashi and T. Asaoka, *J. Power Sources*, 2011, **196**, 3342–3345.
25 T. Thompson, J. Wolfenstine, J. L. Allen, M. Johannes, A. Huq, I. N. David and J. Sakamoto, *J. Mater. Chem. A*, 2014, **2**, 13431–13436.
26 X. Xiong, Q. Zhou, Y. Zhu, Y. Chen, L. Fu, L. Liu, N. Yu, Y. Wu and T. van Ree, *Energy Fuels*, 2020, **34**, 10503–10512.
27 A. F. Wells, *Structural inorganic chemistry*, Clarendon Press, 1984.
28 E. J. Cussen and T. W. S. Yip, *J. Solid State Chem.*, 2007, **180**, 1832–1839.
29 D. Mazza, *Mater. Lett.*, 1988, **7**, 205–207.
30 J. Percival, E. Kendrick, R. I. Smith and P. R. Slater, *Dalton Trans.*, 2009, 5177–5181, DOI: 10.1039/b907331k.
31 J. Percival and P. R. Slater, *Solid State Commun.*, 2007, **142**, 355–357.
32 R. Wagner, G. J. Redhammer, D. Rettenwander, A. Senyshyn, W. Schmidt, M. Wilkening and G. Amthauer, *Chem. Mater.*, 2016, **28**, 1861–1871.
33 L. Robben, E. Merzlyakova, P. Heitjans and T. M. Gesing, *Acta Crystallogr., Sect. E*, 2016, **72**(3), 287–289.
34 J. Percival, D. Apperley and P. Slater, *Solid State Ionics*, 2008, **179**, 1693–1696.
35 J. Han, J. Zhu, Y. Li, X. Yu, S. Wang, G. Wu, H. Xie, S. C. Vogel, F. Izumi, K. Momma, Y. Kawamura, Y. Huang, J. B. Goodenough and Y. Zhao, *Chem. Commun.*, 2012, **48**, 9840–9842.
36 D. Wang, G. Zhong, W. K. Pang, Z. Guo, Y. Li, M. J. McDonald, R. Fu, J.-X. Mi and Y. Yang, *Chem. Mater.*, 2015, **27**, 6650–6659.
37 V. Thangadurai, H. Kaack and W. J. F. Weppner, *J. Am. Ceram. Soc.*, 2004, **86**, 437–440.
38 M. Botros, R. Djenadic, O. Clemens, M. Möller and H. Hahn, *J. Power Sources*, 2016, **309**, 108–115.
39 C. Loho, R. Djenadic, M. Bruns, O. Clemens and H. Hahn, *J. Electrochem. Soc.*, 2017, **164**, A6131–A6139.
40 C. A. Geiger, E. Alekseev, B. Lazic, M. Fisch, T. Armbruster, R. Langner, M. Fechtelkord, N. Kim, T. Pettke and W. Weppner, *Inorg. Chem.*, 2011, **50**, 1089–1097.
41 F. Flatscher, M. Philipp, S. Ganschow, H. M. R. Wilkening and D. Rettenwander, *J. Mater. Chem. A*, 2020, **8**, 15782–15788.
42 N. J. Taylor, S. Stangeland-Molo, C. G. Haslam, A. Sharafi, T. Thompson, M. Wang, R. Garcia-Mendez and J. Sakamoto, *J. Power Sources*, 2018, **396**, 314–318.

43 T. Deng, X. Ji, Y. Zhao, L. Cao, S. Li, S. Hwang, C. Luo, P. Wang, H. Jia, X. Fan, X. Lu, D. Su, X. Sun, C. Wang and J.-G. Zhang, *Adv. Mater.*, 2020, **32**, 2000030.
44 R. Jalem, Y. Morishita, T. Okajima, H. Takeda, Y. Kondo, M. Nakayama and T. Kasuga, *J. Mater. Chem. A*, 2016, **4**, 14371–14379.
45 A. Gupta, R. Murugan, M. P. Paranthaman, Z. Bi, C. A. Bridges, M. Nakanishi, A. P. Sokolov, K. S. Han, E. W. Hagaman, H. Xie, C. B. Mullins and J. B. Goodenough, *J. Power Sources*, 2012, **209**, 184–188.
46 Y. V. Baklanova, A. P. Tyutyunnik, N. V. Tarakina, A. D. Fortes, L. G. Maksimova, D. V. Korona and T. A. Denisova, *J. Power Sources*, 2018, **391**, 26–33.
47 V. Berbenni, C. Milanese, G. Bruni and A. Marini, *J. Therm. Anal. Calorim.*, 2005, **82**, 401–407.
48 J. Percival, D. Apperley and P. R. Slater, *Solid State Ionics*, 2008, **179**, 1693–1696.
49 B. Toby and R. Dreele, *J. Appl. Crystallogr.*, 2013, **46**, 544–549.
50 M. A. Howard, O. Clemens, E. Kendrick, K. S. Knight, D. C. Apperley, P. A. Anderson and P. R. Slater, *Dalton Trans.*, 2012, **41**, 12048–12053.
51 J. Awaka, N. Kijima, K. Kataoka, H. Hayakawa, K.-i. Ohshima and J. Akimoto, *J. Solid State Chem.*, 2010, **183**, 180–185.
52 J. Awaka, N. Kijima, H. Hayakawa and J. Akimoto, *J. Solid State Chem.*, 2009, **182**, 2046–2052.
53 N. Hamao, K. Kataoka and J. Akimoto, *Li-ion conductivity and crystal structure of garnet-type Li6.5La3M1.5Ta0.5O12 (M = Hf, Sn) oxides*, 2017.
54 L. Ladenstein, S. Simic, G. Kothleitner, D. Rettenwander and H. M. R. Wilkening, *J. Phys. Chem. C*, 2020, **124**, 16796–16805.
55 R. Murugan, V. Thangadurai and W. Weppner, *Angew. Chem., Int. Ed.*, 2007, **46**, 7778–7781.
56 R. H. Brugge, J. A. Kilner and A. Aguadero, *Solid State Ionics*, 2019, **337**, 154–160.
57 S. Song, B. Chen, Y. Ruan, J. Sun, L. Yu, Y. Wang and J. Thokchom, *Electrochim. Acta*, 2018, **270**, 501–508.
58 J. L. Allen, J. Wolfenstine, E. Rangasamy and J. Sakamoto, *J. Power Sources*, 2012, **206**, 315–319.
59 B. Dong, L. L. Driscoll, M. P. Stockham, E. Kendrick and P. R. Slater, *Solid State Ionics*, 2020, **350**, 115317.
60 B. Dong, S. R. Yeandel, P. Goddard and P. R. Slater, *Chem. Mater.*, 2020, **32**, 215–223.
61 R. H. Brugge, A. K. O. Hekselman, A. Cavallaro, F. M. Pesci, R. J. Chater, J. A. Kilner and A. Aguadero, *Chem. Mater.*, 2018, **30**, 3704–3713.
62 M. P. Stockham, B. Dong, Y. Ding, Y. Li and P. R. Slater, *Dalton Trans.*, 2020, **49**(30), 10349–10359.
63 J. Wolfenstine, J. Ratchford, E. Rangasamy, J. Sakamoto and J. L. Allen, *Mater. Chem. Phys.*, 2012, **134**, 571–575.
64 D. Rettenwander, G. Redhammer, F. Preishuber-Pflügl, L. Cheng, L. Miara, R. Wagner, A. Welzl, E. Suard, M. M. Doeff, M. Wilkening, J. Fleig and G. Amthauer, *Chem. Mater.*, 2016, **28**, 2384–2392.
65 B. Dong, M. P. Stockham, P. A. Chater and P. R. Slater, *Dalton Trans.*, 2020, **49**, 11727–11735.
66 A. Sharafi, H. M. Meyer, J. Nanda, J. Wolfenstine and J. Sakamoto, *J. Power Sources*, 2016, **302**, 135–139.
67 X. Huang, Y. Lu, H. Guo, Z. Song, T. Xiu, M. E. Badding and Z. Wen, *ACS Appl. Energy Mater.*, 2018, **1**, 5355–5365.
68 R. Hongahally Basappa, T. Ito, T. Morimura, R. Bekarevich, K. Mitsuishi and H. Yamada, *J. Power Sources*, 2017, **363**, 145–152.
69 Y. Song, L. Yang, W. Zhao, Z. Wang, Y. Zhao, Z. Wang, Q. Zhao, H. Liu and F. Pan, *Adv. Energy Mater.*, 2019, **9**, 1900671.
70 L. Cheng, W. Chen, M. Kunz, K. Persson, N. Tamura, G. Chen and M. Doeff, *ACS Appl. Mater. Interfaces*, 2015, **7**, 2073–2081.
71 E. J. Cheng, A. Sharafi and J. Sakamoto, *Electrochim. Acta*, 2017, **223**, 85–91.
72 K. Fu, Y. Gong, G. T. Hitz, D. W. McOwen, Y. Li, S. Xu, Y. Wen, L. Zhang, C. Wang, G. Pastel, J. Dai, B. Liu, H. Xie, Y. Yao, E. D. Wachsman and L. Hu, *Energy Environ. Sci.*, 2017, **10**, 1568–1575.

7. Evaluation of $Ga_{0.2}Li_{6.4}Nd_3Zr_2O_{12}$ garnets: exploiting dopant instability to create a mixed conductive interface to reduce interfacial resistance for all solid state batteries

7.1. PUBLICATION

Evaluation of $Ga_{0.2}Li_{6.4}Nd_3Zr_2O_{12}$ garnets: exploiting dopant instability to create a mixed conductive interface to reduce interfacial resistance for all solid state batteries

Article information : M. P. Stockham, B. Dong, M. S. James, Y. Li, Y. Ding, E. Kendrick and P. R. Slater, Dalton Transactions, 2021, 50, 13786-13800.

Submitted: 26/07/2021

Accepted: 06/09/2021

Author contributions: M. P. Stockham: experimental and characterisation work, conceptualisation, method development, writing – original draft, formal analysis, investigation. B. Dong: Data curation, investigation. M.S. James: Data Curation. Y. Ding: Supervision. Y. Li: Supervision. E. Kendrick: writing – review, use of dry room facilities. P. R. Slater: lead supervision, conceptualisation, writing – review & editing.

Dalton Transactions

ROYAL SOCIETY OF CHEMISTRY

PAPER

View Article Online
View Journal | View Issue

Cite this: *Dalton Trans.*, 2021, **50**, 13786

Evaluation of $Ga_{0.2}Li_{6.4}Nd_3Zr_2O_{12}$ garnets: exploiting dopant instability to create a mixed conductive interface to reduce interfacial resistance for all solid state batteries†

M. P. Stockham, *[a] B. Dong, [a] M. S. James,[a] Y. Li,[b] Y. Ding,[b] E. Kendrick [c] and P. R. Slater *[a]

Received 26th July 2021,
Accepted 6th September 2021

DOI: 10.1039/d1dt02474d

rsc.li/dalton

The next major leap in energy storage is thought to arise from a practical implementation of all solid-state batteries, which remain largely confined to the small scale due to issues in manufacturing and mechanical stability. Lithium batteries are amongst the most sought after, for the high expected energy density and improved safety characteristics, however the challenge of finding a suitable solid-state electrolyte remains. Lithium rich garnets are prime contenders as electrolytes, owing to their high ionic conductivity (>0.1 mS cm^{-1}), wide electrochemical window (0–6 V) and stability with Li metal. However, the high Young's modulus of these materials, poor wetting of Li metal and rapid formation of Li_2CO_3 passivating layers tends to give a detrimentally large resistance at the solid–solid interface, limiting their application in solid state batteries. Most studies have focused on La based systems, with very little work on other lanthanides. Here we report a study of the Nd based garnet $Ga_{0.2}Li_{6.4}Nd_3Zr_2O_{12}$, illustrating substantial differences in the interfacial behaviour. This garnet shows very low interfacial resistance attributed to dopant exsolution which, when combined with moderate heating (175 °C, 1 h) with Li metal, we suggest forms Ga–Li eutectics, which significantly reduces the resistance at the Li/garnet interface to as low as 67 Ω cm^2 (much lower than equivalent La based systems). The material also shows intrinsically high density (93%) and good conductivity (≥0.2 mS cm^{-1}) *via* conventional furnaces in air. It is suggested these garnets are particularly well suited to provide a mixed conductive interface (in combination with other garnets) which could enable future solid-state batteries.

Introduction

Lithium ion batteries (LIBs) are the electrochemical system of choice for many energy storage applications. To further increase energy density the move to lithium metal negative electrodes, or anodes, is required. This is a particular challenge for cells containing liquid based electrolytes due to hazardous dendritic lithium growth and numerous safety implications.[1–3] Liquid electrolytes are also toxic, flammable, and unable to be employed with high V cathode materials due to their relatively narrow electrochemical window.[4–9] Therefore, the replacement of these electrolytes is a pre-requisite for the next major leap in energy storage.[4,10–13]

Solid state batteries (SSB) enable safer, higher energy density and (theoretically, assuming a perfectly dense structure) are able to block Li dendrite growth, however a practical solid state electrolyte (SSE) remains an intense research challenge.[14–16] Most SSEs, based on oxide and sulphide chemistries, often have either a poor electrochemical window or low ionic conductivity, while also requiring time consuming, energy demanding and/or complex synthesis routes.[17–25] Furthermore, many SSEs also suffer from large interfacial resistance due to poor wetting at the solid–solid interface, thus limiting the practical use of many SSBs.[25–28]

Amongst the oxide SSEs, lithium rich garnet materials have seen enormous interest due to their high room temperature conductivity (rivalling liquid electrolytes at >0.1 mS cm^{-1}), a wide electrochemical window (0–6 V) and stability with lithium metal.[18,29–35] This, therefore, positions these garnet materials relatively uniquely amongst other SSEs, making them promising SSB candidates.

[a]School of Chemistry, University of Birmingham, Birmingham B15 2TT, UK.
E-mail:
[b]School of Chemical Engineering, University of Birmingham, Birmingham B15 2TT, UK
[c]School of Metallurgy and Materials, University of Birmingham, Birmingham B15 2TT, UK

†Electronic supplementary information (ESI) available. See DOI: 10.1039/d1dt02474d

Typical garnets have the general formula $A_3B_2X_3O_{12}$ (*e.g.* A = Fe, Mg, B = Al, Cr, Fe, and X = Si, Fe, Al, Ga).[36–39] An example of such a Li_3 based garnet system is $Li_3Nd_3W_2O_{12}$, with lithium fully occupying the 24*d* tetrahedral site, although this garnet shows minimal Li ion mobility.[38,40] Through modifying this system with lower valent cations, increased Li content results in order to maintain charge neutrality. This gives increased conductivity, with lithium occupying additional interstitial octahedral sites.[37,39,41,42] At the upper maximum of 7 Li per formula unit (pfu), Li ordering occurs to reduce short Li–Li distances as all Li sites are fully occupied, which gives an elongation of an axis in the cubic cell. Therefore, Li garnets present with two distinct crystal systems: cubic and tetragonal.[43–47] Tetragonal garnets have 7 Li pfu and poor conductivity with the $I4_1/ACD$ space group (no. 142).[43–46] Conversely cubic garnets have <7 Li pfu and show high conductivity and either $Ia\bar{3}d$ (no. 230) or $I\bar{4}3d$ (no. 220) symmetry.[39,48,49] Lithium garnets are usually most conductive when the Li content is between ~6.2–6.6, as some vacant interstitial sites are required to provide an effective migration pathway.[24,29,32,34,37,41–43,50–63]

One of the garnet systems that has attracted considerable attention is $Li_{7-3x}Ga_xLa_3Zr_2O_{12}$ (Ga-LLZO),[29,55,59,64] however, there are still challenges with this system to achieve the highest conductivity, which typically requires the powder to be fully synthesised/processed under argon or O_2 to enable high densities and minimize atmospheric proton exchange.[29] Similarly complex procedures are often required to reduce the high interfacial resistance encountered at the interface with the Li metal anode, which is currently one of the key limiting factors toward practical garnet battery applications. This issue is compounded by the rapid formation of a Li_2CO_3 passivating layer, with reports suggesting it forms within minutes of air exposure.[65–67] Therefore, a need arises to investigate other potential garnet systems which can offer improved conductivity, densification and, crucially, intrinsically low interfacial resistance.

Several reports have previously discussed the potential instability of Al and Ga doped LLZO, with dopant exsolution shown to plate the grain boundaries in oxide form after densification.[53,68] Although this has been shown to be advantageous for pellet densification, it also creates Li deficient grain boundaries which can impede overall ionic conductivity. Dopant exsolution, however, has yet to be explored as a potential way to decrease interfacial resistance at the Li–garnet interface. This could be accomplished by enhancing dopant exsolution to enable alloying with Li metal, particularly with Ga doped garnets in the form of Ga–Li eutectics. In doing so, this could create a low impedance interface and remove the need for additional coatings/interlayers/complex techniques post SSE membrane formation. Most reports of dopant exsolution relate more to the Al substituted garnets rather than Ga, however the latter is far more favourable to form Li based eutectics at temperatures >28 °C.[69–71]

Therefore, to examine this possibility a Ga doped garnet must be designed which has enhanced dopant site instability (to enable increased exsolution). In this work, we examine whether replacing La by Nd can generate such an effect, as a result of strain created by the reduced lattice parameters associated with the smaller Nd^{3+} ion. As Ga–Li eutectics form above 28 °C, subsequent heating of a Ga doped Nd garnet in the presence of Li metal may enable enhanced site instability (due to reactivity of Li) and favour formation of the eutectic alloy.[69,71]

Herein, we report the synthesis of $Li_{6.4}Ga_{0.2}Nd_3Zr_2O_{12}$ (Ga-NLZO) for the first time, which demonstrates Ga-exsolution which has been considerably enhanced post Li symmetry cell formation, when compared to reports of Ga-LLZO/Ga-LLHO.[32,55] Significantly Ga-NLZO demonstrates exceptionally low interfacial resistance of 67 Ω cm^2 intrinsic to the garnet material and pellets/powder can be prepared in air. Furthermore, sintered Ga-NLZO has high density (93%), good room temperature conductivity (~0.3 mS cm^{-1}), a wide electrochemical window and cycling stability.

To ascertain if Ga–Li alloying occurs we have performed post cycling analysis and investigate the reaction between purchased Ga_2O_3 and Li metal under similar circumstances. Ga-NLZO is shown to have promising applications as a conductive interface (CI) with proof-of-concept lithium garnet "sandwich" type cells constructed in the form of Ga-NLZO/$Li_{6.5}La_3Zr_{1.25}Ce_{0.25}Ta_{0.5}O_{12}$ (Ta-LLZCO)/Ga-NLZO. As there have been few reports of Nd based garnet systems[3,38,72] we also extended this study to structural and impedance evaluation of $Li_{5+x}Nd_3Nb_{2-x}Zr_xO_{12}$ ($0 \leq x \geq 2$) and $Li_{6.4}Al_{0.2}Nd_3Zr_2O_{12}$ (Al-NLZO).

Methods

Synthesis

$Li_{5+x}La_3Nb_{2-x}Zr_xO_{12}$ ($0 \leq x \geq 2$) and $Li_{6.4}Ga_{0.2}/Al_{0.2}Nd_3Zr_2O_{12}$ were prepared *via* the solid-state route from stochiometric quantities of Li_2CO_3, Nd_2O_3, Nb_2O_5, ZrO_2, Al_2O_3 and Ga_2O_3 in air. A 20–40% mol excess of lithium was added to compensate for lithium loss during high temperature sintering. All powders were ball milled for 1 h with ZrO_2 balls (500 rpm) with hexane, pressed into pellets and heated to 1050 °C (6 hours) at 5 °C min^{-1}. Post sintering, pellets were sanded to remove any Al contamination from the Al crucible. Al-NLZO and $Li_{6.4}Nd_3Nb_{0.6}Zr_{1.4}O_{12}$ required a second heat treatment with 20% wt. Li excess to achieve single phase samples. $Li_{6.5}La_3Zr_{1.25}Ce_{0.25}Ta_{0.5}O_{12}$ (Ta-LLZCO) was synthesised similarly (using CeO_2), but at 950 °C (12 h), for use in the layered cells as previous reports suggest Ce assists with low interfacial resistance, hence may assist in the layered structure.[47]

Characterisation

All samples were stored in an argon glove box to prevent proton-Li exchange in the garnet, which is also thought to occur in Nd based garnets.[3,73] Scanning electron microscopy (SEM) was performed on a Hitachi TM4000plus instrument, with the elemental distribution confirmed by the corres-

ponding AZtecOne energy dispersive X-ray (EDX) attachment. Samples were prepared by applying the powders to a carbon tape and analysed at 15 kV in backscattered electron mode. Pellets were also examined in this manner, which were polished with silicon carbide sandpaper from 240 to 4000 grit to form a flat surface. Phase analysis was performed by X-ray diffraction (XRD) using a Bruker D8 diffractometer with a Cu X-ray source. Experimental pellet densities were determined and compared to theoretical values from Rietveld refinement results (performed using GSAS II software).[74]

Impedance spectroscopy

All Nd garnets (for impedance spectroscopy and cell testing) were pelletised and densified in a dry room with a dewpoint between −45 °C to −64 °C (the elimination of humidity was found to be necessary to prepare good quality samples: it is known that moisture can be an issue in the synthesis of Li garnet systems).[75–77] Pellets were prepared as follows: approx. 10 mm diameter pellets were pressed to *ca.* 1.5 tonnes and heated to 1150 °C for 13 hours (1.9 °C min^{-1}). In all cases sacrificial powders were used to protect pellets from Al contamination *via* the Al_2O_3 crucible and to minimize Li loss. In order to examine the potential of Ga-NLZO as a Li metal contact layer, layered Ga-NLZO pellets, in the form of Ga-NLZO/Ta-LLZCO/Ga-NLZO, were prepared in a similar manner, but at 0.4 °C min^{-1}. Post-sintering, the pellets were polished and were sputtered with Au for room temperature impedance spectroscopy measurements, which were performed with a Solartron 1260 impedance analyser from 1 Hz to 10 MHz with a 20 mV potential. Variable temperature measurements were undertaken by painting the polished pellet with Au electrodes, which required heating to 800 °C for 1 hour in air to cure the Au paste. The pellets were then air quenched to room temperature from >700 °C (to limit H/Li exchange[56,78,79]). The variable temperature impedance measurements were measured from 5 Hz to 13 MHz using a Hewlett Packard 4192A LF instrument with a 100 mV applied potential from 50–143 °C.

Cell assembly

All cell tests were performed on a biologic VMP3 or SP50 instrument. Li|Ga-NLZO|Li symmetric cells were assembled in an Ar glove box. Firstly, the pellets (~1.7 mm thickness) were polished using silicon carbide sandpaper from 240 to 4000 grit, then lithium metal foil was applied to each side of the pellet. The cell was then heated to 175 °C under a constant pressure for 1 h using a commercially and readily available steel 3-way G clamp (see ESI†) and were secured under light pressure *via* hand tightening the clamp. The cell was subsequently secured within a Swagelok type cell. Cells were examined *via* impedance spectroscopy before (and after) cell testing from 10 MHz to 0.1 Hz with a 20 mV potential on a Solartron 1260 impedance analyser. These symmetric cells were then cycled under constant current conditions at various current densities to assess cycling stability at room temperature on an open lab bench (between 15–21 °C throughout the day) as well as at a constant temperature (50 °C) in a fire-proof thermal abuse test chamber (MTI). Cells were also cycled with increasing current density, in increments of 10 μA cm^{-2}, until a short circuit formed to assess CCD at room temperature on an open lab bench. The ASR was analysed as a function of temperature *via* impedance measurements for Ga-NLZO. Li/Ga-NLZO/Ta-LLZCO/Ga-NLZO/Li sandwich type cells were assembled similarly, with Li stripping and plating assessed on an open lab bench (15–27 °C) and at 43 °C (to confirm voltage stability).

Au|Ga-NLZO|Li cells, for cyclic voltammetry (C.V.), were formed by polishing a NLZO pellet as above and hand pressing the pellet into Li foil in an Ar glovebox. The cell was placed in a Swagelok cell with Au foil as the working electrode. Cyclic voltammetry was subsequently run from −0.4 to 5 V at a scan rate of 1 mV s^{-1}.

Post cycling analysis

Post cycled Ga-NLZO pellets, which had short circuited, were analysed by SEM and EDX and compared to freshly prepared pellets. For SEM/EDX, pellets were thermally etched in a manner similar to the densification steps above and analysed on the same SEM/EDX instrumentation as above (see ESI† for pellet analysis prior to thermal etching). Cross sectional areas were also analysed *via* SEM/EDX after the pellet was snapped into smaller segments. The pellet surface and re-ground powder were also analysed *via* XRD.

Results and discussion

X-Ray diffraction results

The powder XRD patterns of $Li_{5+x}Nd_3Nb_{2-x}Zr_xO_{12}$ ($0 \leq x \geq 2$), Ga/Al-NLZO and $Li_7Nd_3Zr_2O_{12}$ (NLZO) are shown in Fig. 1. All patterns correspond to the expected garnet symmetry and could be indexed on a cubic $Ia\bar{3}d$ ($Li_{5+x}Nd_3Nb_{2-x}Zr_xO_{12}$/Al-

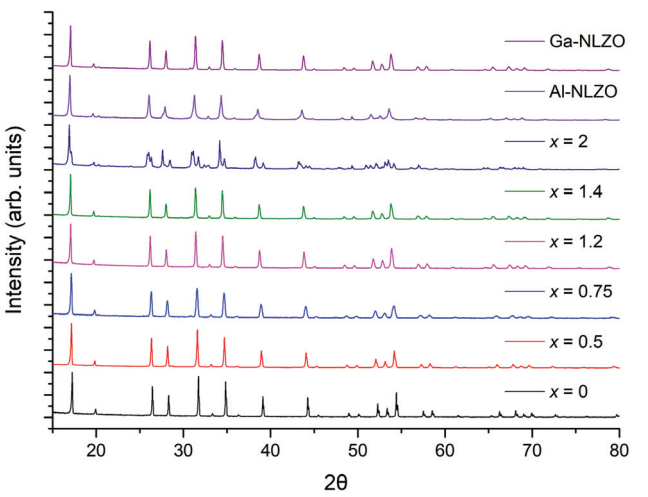

Fig. 1 Powder XRD patterns of $Li_{5+x}Nd_3Nb_{2-x}Zr_xO_{12}$ ($0 \leq x \geq 2$) and $Li_{6.4}Al_{0.2}Nd_3Zr_2O_{12}$ indexed on $Ia\bar{3}d$ type symmetry and $Li_{6.4}Ga_{0.2}Nd_3Zr_2O_{12}$ on $I\bar{4}3d$ symmetry (see ESI† for magnified pattern at ~22 2θ). The small peak ~20 2θ for Al-NLZO and x = 2 is attributed to a small Li_2ZrO_3 impurity.

NLZO) or $I\bar{4}3d$ (Ga-NLZO) cell.[39,44,48] All Nd garnets were blue under artificial lighting but instantly turned neodymium glass purple when placed in sunlight, corresponding to the Alexandrite effect as noted previously.[80]

Rietveld refinements on the $Li_{5+x}Nd_3Nb_{2-x}Zr_xO_{12}$ ($0 \leq x \geq 1.4$) systems were based on the structural model by Cussen[39] and showed a linear increase in lattice parameters (see Fig. 2), in agreement with Vegard's law, thus further confirming the solid solution range. This increase is attributed to the larger ionic radius of Zr^{4+} over Nb^{5+}. Lattice parameters were smaller than the La counterparts reported elsewhere, consistent with the smaller radius of Nd^{3+} *vs.* La^{3+}. Fractional occupancies of Zr and Nb were set to the intended ratio, as the similarities in scattering factors preclude accurate refinement using XRD alone (see ESI† for example refinement). For $x = 1.4$ small Nd/Zr based impurities were present which were unable to be removed. These worsened significantly for samples with $x = 1.6$ and 1.8 (see ESI†).

The Ga-NLZO and Al-NLZO samples had larger lattice parameters compared to $Li_{6.4}Nd_3Zr_{1.4}Nb_{0.6}O_{12}$, see Fig. 1 and 2, with much higher conductivity and improved density for Ga-NLZO (see later). These lattice parameters are still far smaller, however, than Ga-LLZO and Ga-LLHO due to the smaller size of Nd^{3+}.[29,32,55] For Ga-NLZO both the $Ia\bar{3}d$ and $I\bar{4}3d$ space groups were considered. The sample has an additional peak ~22° 2θ which is attributed to the acentric cubic space group $I\bar{4}3d$, therefore it was assumed to adopt this symmetry as per reports for Ga-LLZO (see ESI† for narrow 2θ range XRDs). $I\bar{4}3d$ Ga-LLZO systems are thought to possess a La occupancy <1, however attempts to similarly refine the Nd site occupancy for Ga-NLZO yielded an unstable refinement, hence the Nd occupancy was set to 1. Future work will be needed to ascertain if a fractional occupancy occurs and to what extent. Attempts to reduce the Ga content and so prepare $Ga_{0.15}$NLZO were unsuccessful giving a mixed cubic/tetragonal phase with low conductivity, see ESI.† The Al-NLZO sample did not have any additional peaks, and hence was assumed to have $Ia\bar{3}d$ symmetry, as per the report from Howard *et al.*[3]

The undoped NLZO demonstrated significant peak splitting when compared to the cubic counterparts, consistent with the expected reduction in symmetry from a cubic to a tetragonal cell, hence was indexed on the structural model from Howard *et al.* (space group $I4_1/acd$) giving similar lattice parameters, see Table 1.

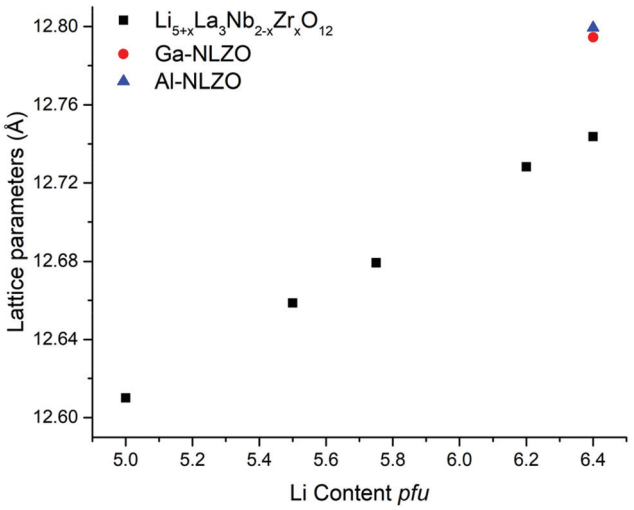

Fig. 2 Lattice parameters *vs.* Li content of $Li_{5+x}La_3Nb_{2-x}Zr_xO_{12}$ ($0 \leq x \geq 1.4$), $Li_{6.4}Al_{0.2}Nd_3Zr_2O_{12}$ and $Li_{6.4}Ga_{0.2}Nd_3Zr_2O_{12}$, as determined from Rietveld refinements.

SEM (EDX)

Fig. 3 displays SEM images and EDX maps of Ga-NLZO powders. Images illustrate similar grain characteristics throughout with no discernible changes in contrast across individual grains, indicating single phase materials. EDX maps show a uniform distribution of the expected elements across the analysed grains, thus confirming elemental composition and a lack of Al contamination from the crucible. Fig. 4 also shows the surface of a Ga-NLZO pellet, showing closely packed grains, indicating high density materials, and similar EDX results as the corresponding powder.

Conductivity measurements

The conductivities of the Nd garnet systems were shown, in general, to increase in line with increased Li content and larger lattice parameters. A typical Nyquist plot with Au blocking electrodes is shown in Fig. 5; these were fit to a single R/CPE component in parallel, illustrative of overlapping bulk and grain boundary contributions. Capacitance values and

Table 1 Lattice parameters, relative density, conductivity, and activation energy of $Li_{5+x}Nd_3Nb_{2-x}Zr_xO_{12}$ ($0 \leq x \geq 2$), Ga/Al-NLZO and NLZO. Ga-NLZO* refer to the second pellet ran in a Swagelok cell

Sample (x =)	Lattice parameters (a) (Å)	Lattice parameters (c) (Å)	ρ_{rel} (%)	σ_{total} (S cm^{-1}) (50 °C)	Activation energy (eV) (20–143 °C)
0	12.6100(1)		71	6.1×10^{-6}	0.53
0.5	12.6587(5)		69	6.9×10^{-6}	0.40
0.75	12.6791(2)		74	2.0×10^{-5}	0.41
1.2	12.7282(1)		91	1.4×10^{-4}	0.38
1.4	12.7437(1)		78	1.2×10^{-4}	0.41
2	12.9221(7)	12.5503(6)	59	6.2×10^{-7}	0.48
$Al_{0.2}$	12.7994(7)		78	8.7×10^{-6}	0.39
Ga-NLZO	12.7945(1)		88	3.1×10^{-4}	0.25
Ga-NLZO*	12.7945(1)		93	6.6×10^{-4}	0.32 (18–73 °C)

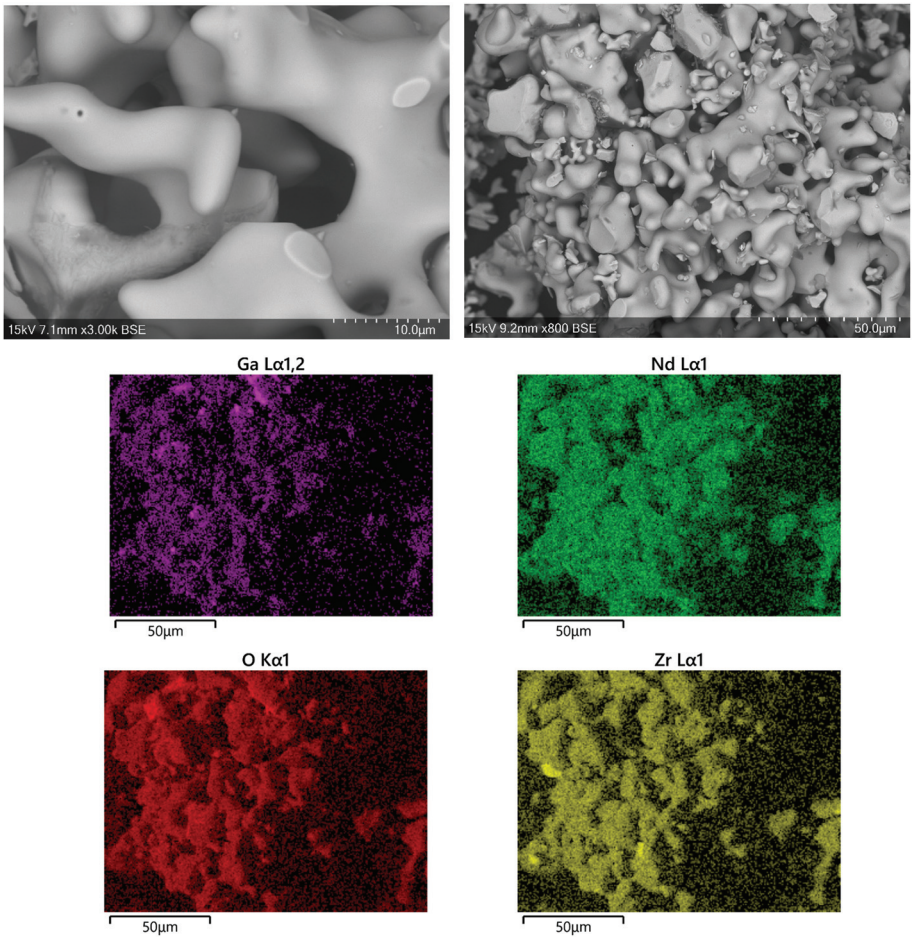

Fig. 3 SEM image and EDX map of elemental distribution in $Ga_{0.2}Li_{6.4}Nd_3Zr_2O_{12}$ in powder form.

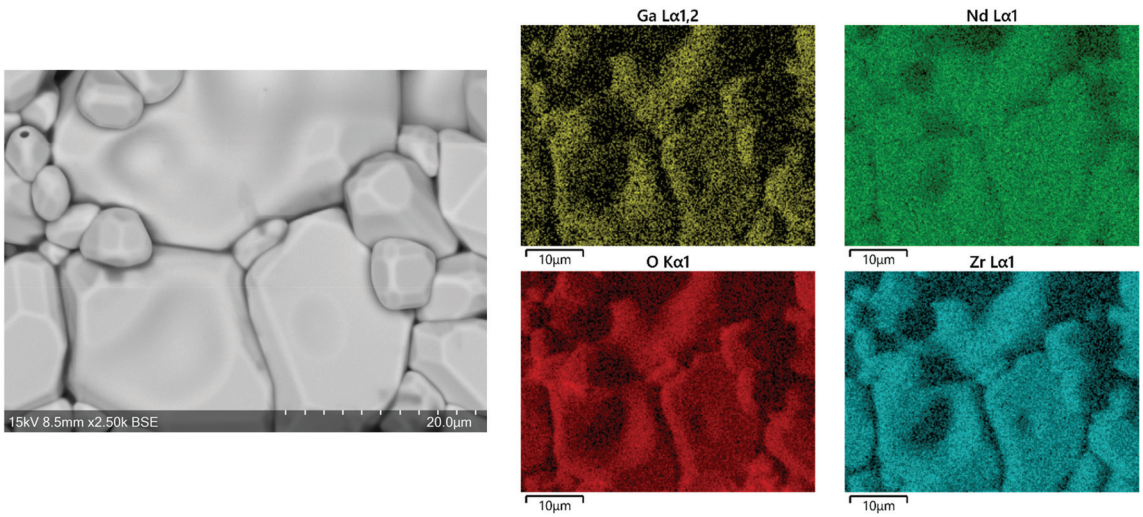

Fig. 4 SEM image and EDX map of elemental distribution in from the pellet surface of $Ga_{0.2}Li_{6.4}Nd_3Zr_2O_{12}$.

dielectric constants fall within the range expected for bulk materials, see ESI.† The measurements for Ga-NLZO at ~20 °C displayed a buried contribution in the double layer capacitance spike relating to the Au electrodes, perhaps relating to a small grain boundary component. However, this was unable to be fitted to the corresponding R/CPE element, see Fig. 5 inlay.

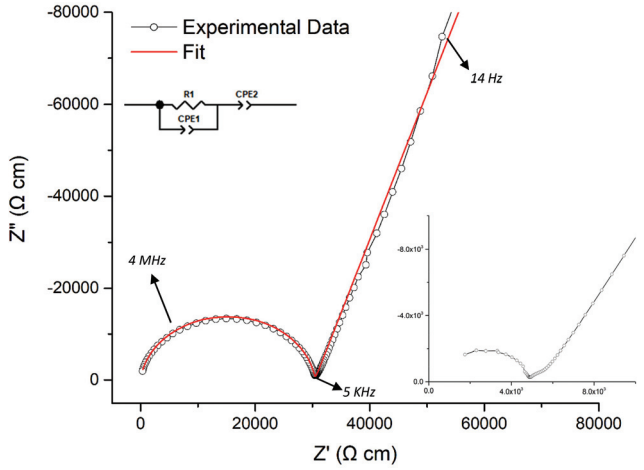

Fig. 5 Typical Nyquist plot of $Li_{5.75}Nd_3Nb_{1.25}Zr_{0.75}O_{12}$ at 63 °C with Au blocking electrodes. The plots were fit to a single R/CPE component, illustrative of overlapping bulk and grain boundary contributions. More conductive plots, such as those in Fig. 8, required the addition of an inductive element. Inlay is Ga-NLZO at 18 °C, demonstrating buried grain boundary contribution in the double layer capacitance spike.

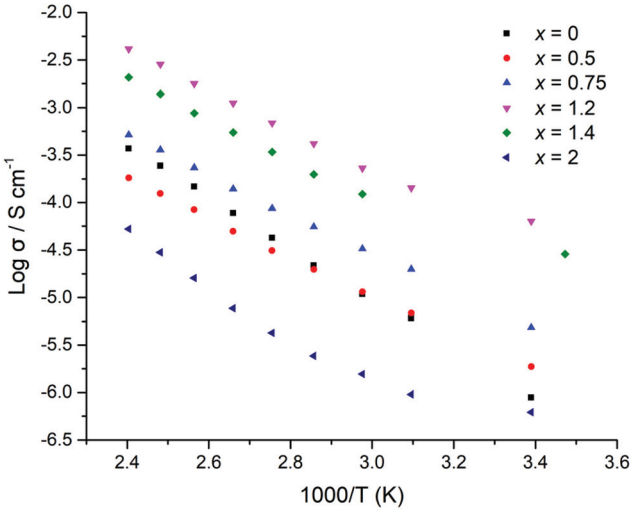

Fig. 6 Arrhenius plots of $Li_{5+x}Nd_3Nb_{2-x}Zr_xO_{12}$ ($0 \leq x \geq 2$). The non-linearity observed is a result of quenching degrading the microstructure. The non-linearity of the tetragonal sample is attributable to water loss, as although samples were stored in a Ar glovebox, it was not possible characterise fully under Ar. The lower temperatures measurement for $Li_{6.4}Nd_3Nb_{0.6}Zr_{1.4}O_{12}$ is due to lower temperature experienced in the Lab. Note – x = 0–0.75 were not Au sputtered first as conductivity was expected to be low, hence linear trend.

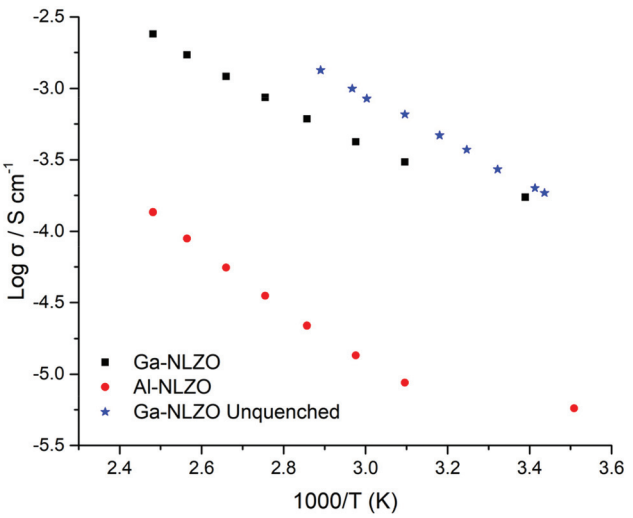

Fig. 7 Arrhenius plots of $Al_{0.2}Li_{6.4}Nd_3Zr_2O_{12}$ and $Ga_{0.2}Li_{6.4}Nd_3Zr_2O_{12}$. As bending of the plots were noted between room temperature and 50 °C, a fresh $Ga_{0.2}Li_{6.4}Nd_3Zr_2O_{12}$ pellet was Au sputtered, secured in a Swagelok cell and measured from 18–73 °C (blue stars), gave a linear plot and confirmed the degradation encountered with Nd garnets when subjected to quenching.

Highly conductive samples, such as Ga-NLZO, demonstrated a high frequency inductance (~10^{-6} H), hence an additional inductive element was included in the equivalent circuit model, see Fig. 8. This corresponds to previous reports and likely arises from the system wiring and/or limitations of the impedance equipment.[34,68,81]

The conductivity of $Li_{5+x}Nd_3Nb_{2-x}Zr_xO_{12}$ garnets reached a maximum of 7×10^{-5} S cm^{-1} (22 °C) for $Li_{6.2}Nd_3Zr_{1.2}Nb_{0.8}O_{12}$ before falling noticeably for $Li_{6.4}Nd_3Zr_{1.4}Nb_{0.6}O_{12}$ attributed to decreased densification of the latter. The conductivity of Al-NLZO was considerably lower at 6×10^{-6} S cm^{-1} (22 °C), however Ga-NLZO showed a much higher conductivity at 2×10^{-4} S cm^{-1} (20 °C), and was the only Nd based garnet to demonstrate room temperature conductivity in the 10^{-4} S cm^{-1} range.

Arrhenius plots, see Fig. 6 and 7, demonstrate a mostly linear trend, with activation energies given in Table 1. NLZO shows some deviation from linearity which is attributed to water loss, as a result of proton-Li exchange. However, non-linearity is present for the high Li content cubic phase Nd garnets between the room temperature measurements and 50 °C, which cannot be explained similarly.

As the room temperature measurements, particularly in the high content Li Nd garnets, were Au sputtered and 50 °C measurements were taken post quenching while curing the Au paste, it can be concluded that the heating step to cure the Au paste (and/or subsequent quenching from >700 °C) may be responsible. Comparative impedance spectra analysis of pre/post quenched Ga-NLZO pellets revealed a newly resolved grain boundary contribution post quenching, which fits to two parallel R/CPE components connected in series rather than one, see Fig. 8. This additional grain boundary contribution reduced the conductivity, with this being so even if the buried contribution in Fig. 5 inlay is considered. As Ga-NLZO is the focus of this work, a pellet was sputtered with Au, cooled naturally and analysed further between 18–73 °C. The Arrhenius plots demonstrate near perfect linearity, thus indicating quenching negatively affects the conductivity of Nd based garnets, see Fig. 7.

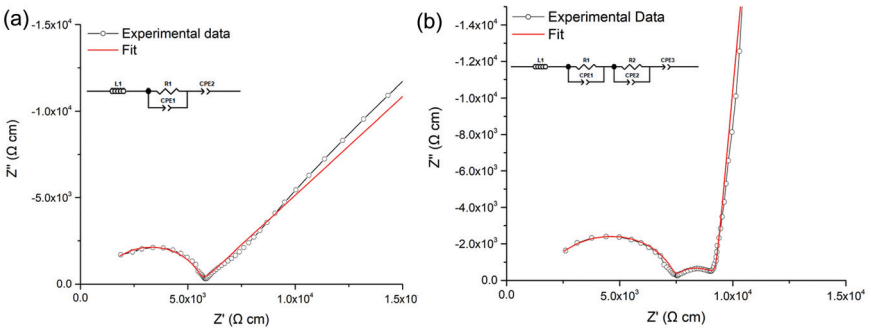

Fig. 8 Nyquist plot of $Ga_{0.2}Li_{6.4}Nd_3Zr_2O_{12}$ at 22 °C where (a) is Au sputtered and fit to a single R/CPE component and (b) is the post quenched plot of the same sample after drying of Au paste, now showing a grain boundary contribution and fitting to two parallel R/CPE components connected in series. The new features in b, which lower total system conductivity, relate to degradation of the pellet microstructure from quenching. This is suspected to relate to thermal shock and shows that Nd based garnets respond less favourably to quenching than other lithium garnets, whereupon increased conductivity is commonly observed.

In order to try to evaluate the origin of this detrimental effect of quenching, fresh Ga-NLZO pellets were quenched for microstructural evaluation, however these violently shattered indicating thermal shock. Hence the results suggest that Nd garnets are degraded by quenching, although more work is needed to confirm the origin of this affect. In contrast, a furnace cooled Ga-NLZO pellet demonstrated an improved 93% relative density and ionic conductivity of 0.3 mS cm^{-1} at 20 °C, (1.34 mS cm^{-1} at 73 °C). See Table 1.

Overall the evaluation of Nd based garnets has revealed that, despite many having rather low room temperature conductivity, the conductivity of Ga-NLZO is similar to other lithium garnets prepared under similar conditions, despite the smaller lattice parameters.[34,42,50,52,55,82–85] The high conductivity observed for Ga-NLZO is likely due, in part, to the good sinterability of this composition leading to higher density (93% theoretical).

The high-density of Ga-NLZO pellets (93%) is notable as it is accomplished relatively simply, and are higher than our previous reports for La based garnets prepared under similar conditions, where densities ≤90% are more commonly observed.[32,53,54,86]

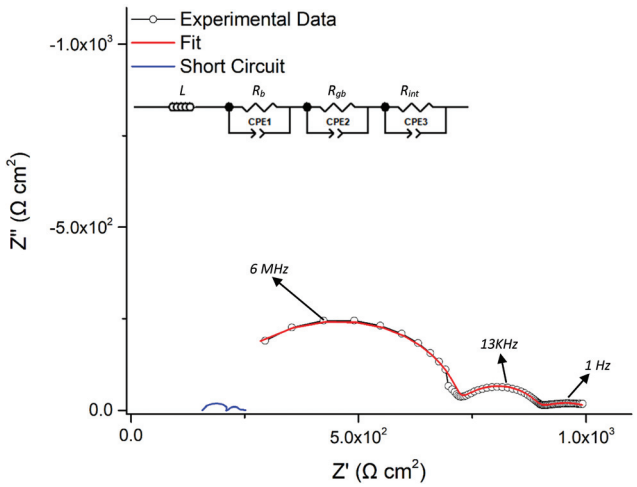

Fig. 9 Li symmetry cell Nyquist plot of $Ga_{0.2}Li_{6.4}Nd_3Zr_2O_{12}$, which was fit to three R/CPE components connect in series, illustrative of bulk, grain and Li/garnet interface contributions. The absence of Au has revealed the entire grain boundary contribution, previously thought buried in the charging spike. Blue line is representative of a cell after short circuit.

Cell testing – interfacial resistance

To assess the ASR in contact with Li metal, a sintered Ga-NLZO pellet was assembled into Li metal symmetric cells. Li stripping and plating was then investigated to assess cycling and ASR stability (see later). Cells were analysed *via* impedance spectroscopy prior to (and after) cell testing. A typical Nyquist impedance plot is shown in Fig. 9. The impedance spectrum was fit to three parallel R/CPE components, with the bulk and grain boundary contribution being present in the high to mid-frequency range, which is now more resolved than the data from the earlier conductivity measurements (Fig. 5 inlay). The conductivity values obtained from this plot are in good agreement with those values obtained prior (~2.5×10^{-4} S cm^{-1}, all pellets ~93% density). Several pellets were analysed, which demonstrated similar characteristics. The semi-circle observed at low frequency in Fig. 9 corresponds to the resistance encountered at the Li metal/garnet interface. The area specific resistance (ASR) is hence determined from this semi-circle.

As a wide variety of potential Ga–Li eutectics can be formed from room temperature to 175 °C, impedance analysis was undertaken after hand pressing the Li foils only (20 °C), using the G clamp pressure (20 °C) and at different temperatures under the clamp pressure (60–175 °C), with ASR values being taken after pressing and cooling to room temperature. These results are shown in Fig. 10a. Hand pressing the Li foil yielded relatively large ASR values, however these were lower than expected at 4175 Ω cm^2 (typically values of ~10 000 Ω cm^2 are found for other garnets analysed similarly).[26,68,87] This fell considerably by applying the force of the clamp but remained quite high at 865 Ω cm^2. Increased temperature reduced the

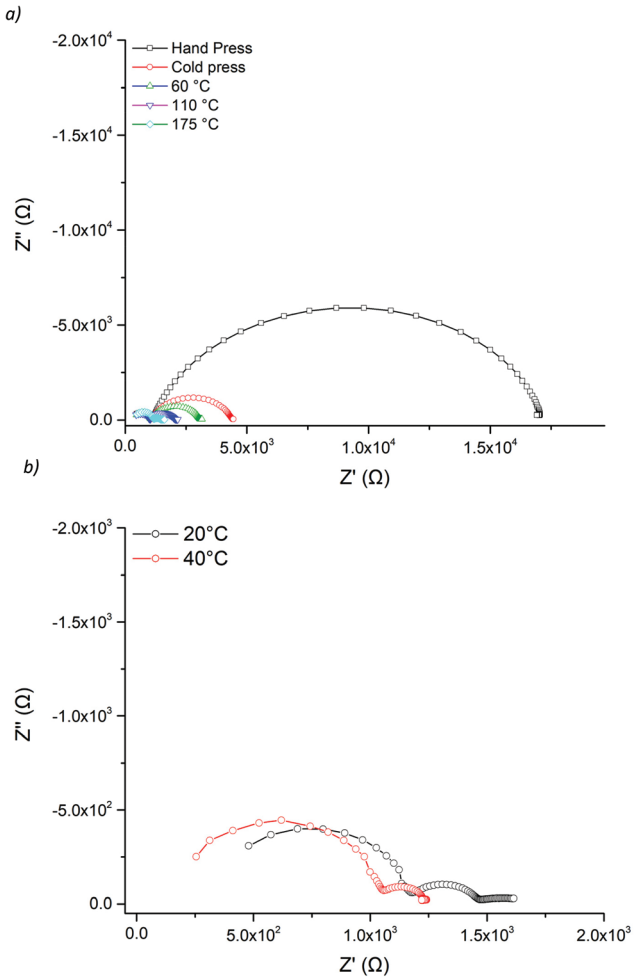

Fig. 10 (a) Impedance spectra demonstrating ASR dependence on heat with the interfacial resistances of 4175 (black, hand pressed), 865 (red, clamp pressure only), 518 (green, 60 °C), 274 (blue (110 °C) and 128 (teal, 175 °C) Ω cm^2. (b) Impedance spectroscopy of Li/Ga-NLZO/Li symmetry cell at room temperature and 40 °C, showing nearly complete removal the Li/garnet interface contribution, indicating minimal interfacial resistance at slightly elevated temperature. The ASR at room temperature was 67 Ω cm^2, and was the lowest recorded in this work. The pellet in (b) had decreased density (91%), hence has also revealed the grain boundary component more clearly.

ASR further, with the ASR after pressing at 110 °C being 274 Ω cm^2 (at 20 °C), which is in the range of many garnet reports which use complex techniques and/or additional coatings. However, heating to 175 °C was required to enable the lowest possible ASR for Ga-NLZO at 67 Ω cm^2, with cells commonly being in the 130–80 Ω cm^2 range due to limitations of the 3-way G-clamp. To confirm the low ASR is due to the presence of Ga, a tetragonal NLZO symmetry cell was assembled and pressed in the same manner. This cell demonstrated a high ASR (~1000 Ω cm^2, see ESI†). Therefore, this result supports the conclusion that the relatively low ASR encountered with Ga-NLZO arises from the Ga dopant, with results indicating additional reactions occur outside of enhanced Li metal plastic deformation at increased temperature. Therefore, all cells were heated to 175 °C under pressure from the G-clamp and left to cool before removing. Impedance was subsequently further analysed on a Li/Ga-NLZO/Li cell at 20 and 40 °C, with the slightly elevated temperature showing almost complete removal of the Li/Ga-NLZO contribution, hence indicating nominal resistance at the interface. See Fig. 10b.

Ga-NLZO cells thus exhibited much decreased ASR values when compared to the Ga-LLHO, Ce-doped LLZO and Ce-doped $Li_{5+x}La_3Nb_{2-x}Ce_xO_{12}$ cells we reported earlier (ASR values ~400 Ω cm^2).[32,47,54] As cells were pressed in a similar manner, this is a considerable reduction in ASR which can only be attributed to an interfacial reaction between Li metal and Ga-NLZO.

Furthermore, these ASR values are lower than those reported for several LLZO based samples processed fully under Ar in a glove box environment. For example, work by Brugge *et al.* (and follow up work by Pesci *et al.*) determined that thermal etching of Ga-LLZO, under controlled conditions (*e.g.* glovebox polishing and transferring *via* vacuum for heating), can reduce ASR values from ~12 372.2 to 148.9 Ω cm^2, with the main difference being Li foils were cold pressed on to the garnet surface and left for 24 h rather than heating to 175 °C for 1 h. This etched value is still higher than that achieved by Ga-NLZO (67 Ω cm^2) and does not require glovebox connected furnaces.[55,68,81] Work by Tsai *et al.* using similar cell making procedures, but employing Au sputtered buffer layers between garnet and Li foil, were also shown to reduce interfacial resistance, however were still significantly higher than Ga-NLZO (380 *vs.* 67 Ω cm^2).[68,88] Many other works also detail interfacial modifications (*e.g.* polymers, pulsed laser deposition)/complex procedures/expensive alloying reactions (*e.g.* Au, Ag) which give higher resistances than the as prepared Ga-NLZO cells[87,89–100] and many others which are similar.[87,101–103] Hence it can be concluded that this Nd based garnet does indeed possess intrinsically lower ASR values than other (La based) garnet materials.

These ASR values could, perhaps, be much improved if the material were able to be processed fully in an Ar glovebox or if the pressure could be accurately controlled/increased to much higher values. However, such low resistances intrinsic to lithium garnets are rare without compromising other desirable qualities, and if Ga-NLZO were used as a conductive interface (CI) layer, it could be co sintered with other SSEs (hence not requiring any additional energy intensive techniques), thus considerably reducing costs.

Cyclic voltammetry

Before analysing the interfacial stability of Ga-NLZO, the electrochemical stability window was assessed *via* cyclic voltammetry, see Fig. 11. Peaks are present at ~0.3 V and ~−0.4 which indicate Li stripping and Li plating respectively, the small peaks ~1–1.5 V is attributed to Li/Au alloying.[34] Outside of this region, the peak profile remains flat with an absence of redox peaks, thus confirming the stability up to 5 V (*vs.* Li/Li$^+$). A negligible current response is present throughout the rest of the voltammogram, indicating low electronic conductivity.

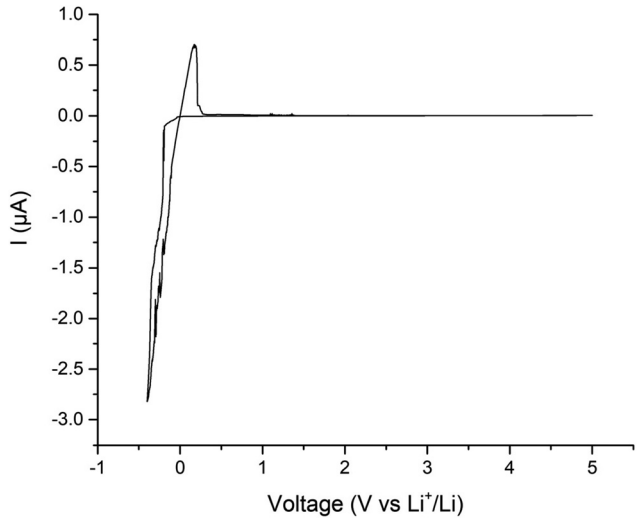

Fig. 11 Cyclic voltammetry between −0.4 to 5 V *vs.* Li_+/Li of Ga-NLZO at 1 mV s^{-1}. Small peaks ~1–1.5 V are attributed to Au/Li alloying.

Cell testing – Li stripping and plating

Li stripping/plating were investigated for the assembled symmetric cells to assess cycling and ASR stability. The cell was left on an open lab bench to approximate real world use, hence small temperature variations were present (between 15–21 °C). The results showed that Ga-NLZO exhibits excellent cycling stability at room temperature at 12.5 and 25 μA cm^{-2}, see Fig. 12. The small fluctuations in the voltage profile relate to the slight alterations in the temperature, with slightly higher voltages occurring overnight and lower voltages during the day. To confirm the voltage stability, a cell was cycled at 50 °C, which shows mostly flat voltage profiles for ~83 hours. Therefore, no interface degradation is apparent and voltage fluctuations are due to real life temperature variations. However, a large voltage drop is present in Fig. 12 when the current density is increased to 50 μA cm^{-2}, which indicates a short circuit due to dendrite propagation. This dendrite propagation at low current densities suggest that the reaction between Li and the Ga dopant must propagate through the pellet.

To confirm the short circuit, critical current density (CCD) analysis was conducted on a fresh cell (where CCD is defined as the maximum current which can be applied to a cell before dendritic lithium propagation and short circuiting occurs). CCDs of the lithium garnet systems are thought to depend primarily upon the pellet density (which should be as high as possible), grain boundary characteristics, conductivity, and the ASR (which should be as low as possible).[26,31,55,104–106] ASR for this cell was calculated at 95 Ω cm^2, pellet density at ~90% and conductivity in the 0.2 mS cm^{-1} range. The cell was left on an open lab bench where temperature fluctuated between 20–22 °C. As shown in Fig. 13, the cell follows ohmic current–voltage behaviour up to 50 μA cm^{-2}, at which point a small voltage drop is noted indicative of a short circuit. The short

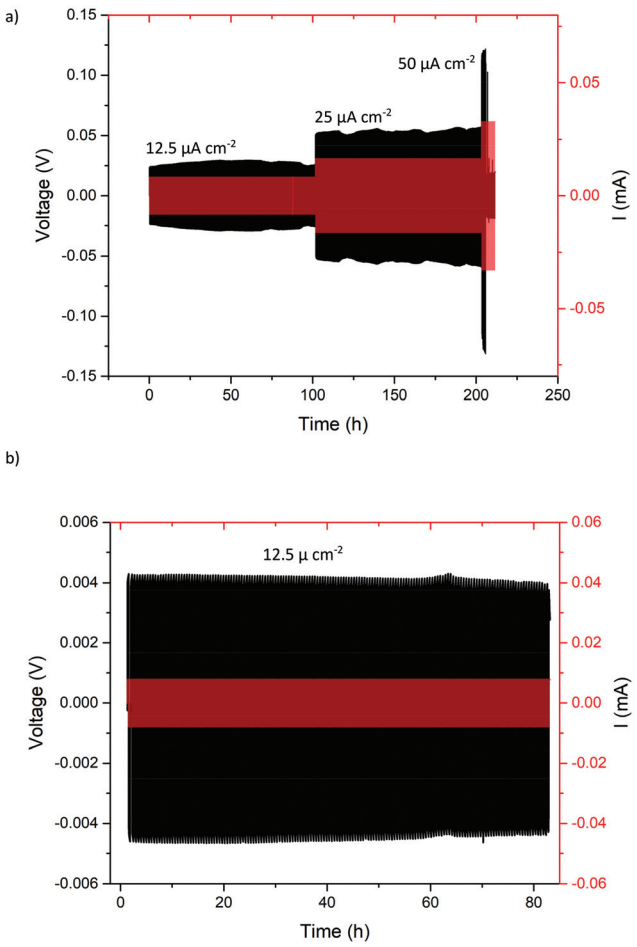

Fig. 12 Lithium stripping and plating of Li/Ga-NLZO/Li cell (a) at different current densities at room temperature on open lab bench (between 15–21 °C throughout the day) and (b) at 50 °C to demonstrate flat voltage profile at controlled temperature.

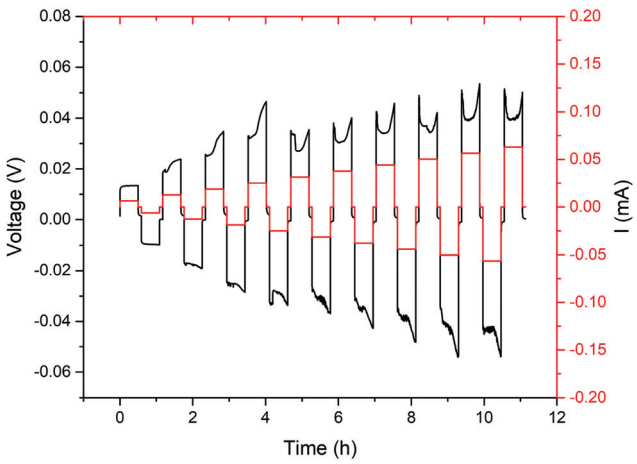

Fig. 13 Critical current density analysis, starting at 10 μA cm^{-2}, and increasing in increments of 10 μA cm^{-2}. A small voltage drop is noted at 50 μA cm^{-2} which corresponded to short circuit. This was confirmed *via* impedance spectroscopy and was analogous the impedance spectrum found in Fig. 9.

circuit was confirmed by impedance spectroscopy, giving a similar Nyquist plot to Fig. 9. Efforts were made to improve this value by ball milling Ga-NLZO powders for 10 h to improve particle size distribution post sintering. This gave the same CCD value. This is indicative of the processes involved in the low ASR values, which we attribute to the formation of a Ga–Li eutectic at the grain boundary, propagating through the SSE during Li stripping and plating. This, therefore suggests that Ga-NLZO cannot be utilized as an electrolyte on its own with Li metal anodes, but may find use as a CI layer in conjunction with another garnet electrolyte.

Therefore, a proof-of-concept Li/Ga-NLZO/Ta-LLZCO/Ga-NLZO/Li layered cell was assembled and can be found in Fig. 14. This pellet was prepared and densified *via* a similar procedure, which resulted in a dense pellet with fused interfaces. The pellet was then analysed *via* impedance spectroscopy with Au electrodes and assembled into symmetric cells, with the latter demonstrating no mechanical interfacial issues while sanding to a mirror finish, see Fig. 14. All Impedance analysis yielded no additional interface contributions, hence indicating well sintered and connected interfaces. This symmetric cell demonstrated a low ASR value of 102 Ω cm^2, similar to Ga-NLZO on its own, with a conductivity at 21 °C of 2.5 × 10^{-4} S cm^{-1}. The layered cells showed extended cycling stability, over multiple current densities (up to at least 100 μA cm^{-2}, ~500 h), significantly beyond the CCD noted solely for the Ga-NLZO garnets. The large voltage drop (indicative of a short circuit) seen for the Ga-NLZO materials in Fig. 12 is absent from the layered cell data, indicating no short circuit over the analysed current densities. Hence Ga-NLZO can be readily co-sintered with other garnets as an interface layer to increase the CCD while maintaining the low ASR values.

Post cycling analysis

In order to gain more information on the short circuited Ga-NLZO cells, a short-circuited symmetric cell was disassembled, and Li metal removed by melting to reveal the pellet surface, which were subsequently analysed by SEM/EDX and compared with a freshly prepared Ga-NLZO pellet. As the polishing procedure does not yield a surface from which SEM/EDX was able to distinguish any unusual features (see ESI†), the short-circuited pellet was thermally etched *via* the densification procedure used for fresh Nd garnet pellets, with the aim of also regenerating the pellet. After this heat treatment, individual grains were well resolved (no mother powder was used). The SEM images of the pellet surface revealed unusual elemental clusters, as distinguished from differences in contrast from the BSE image, with grain boundaries showing clear changes in morphology, see Fig. 15. These features were largely present across the entire pellet surface, but were only sparingly present on fresh pellets prior to cycling, and hence they have dramatically increased post Li metal adhesion and cycling. EDX of these clusters revealed accumulations of Zr, encased by Nd surround by Ga plated grain boundaries, see Fig. 15. This yields evidence of Ga exsolution on the pellet surface, which

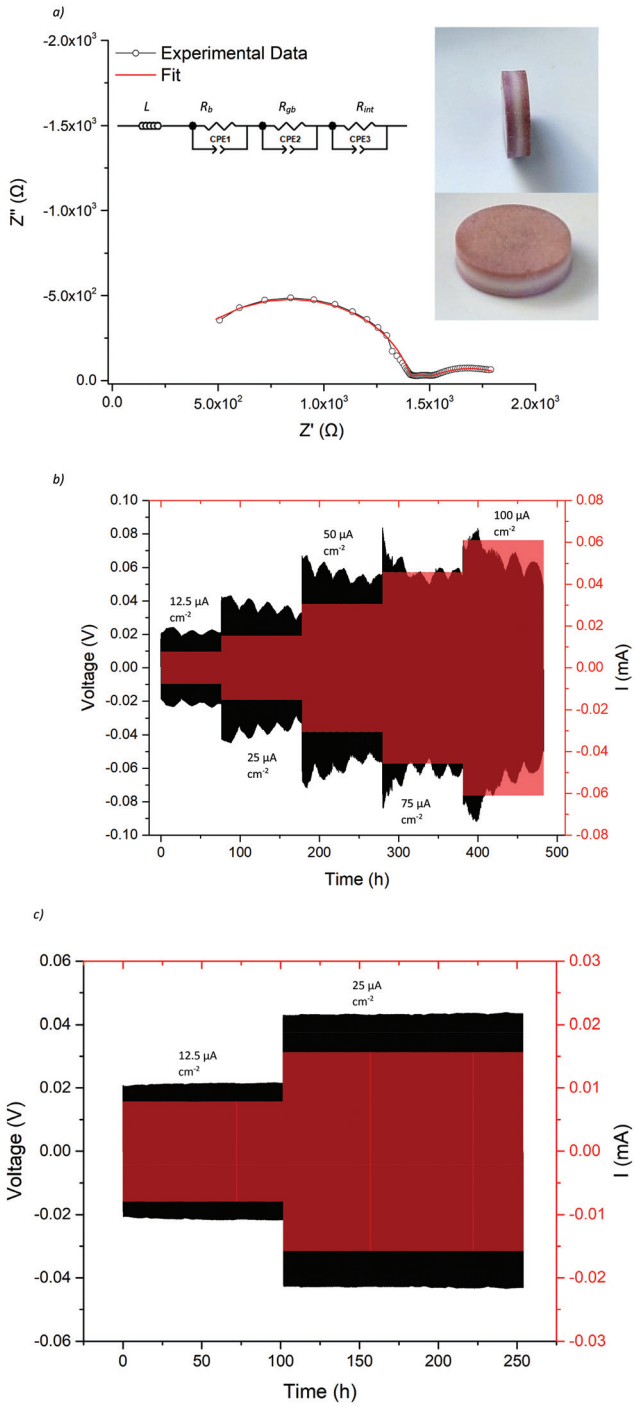

Fig. 14 Li/Ga-NLZO/Ta-LLZCO/Ga-NLZO/Li sandwich cells, where (a) is the impedance spectrum of a symmetry cell, fit to three R/CPE parallel components connected in series. Considering the lack of any additional features in the spectrum only three R/CPE components were used, irrespective of the layered structure. Inlay photographs are of the formed pellet, where purple is Ga-NLZO, and white is Ta-LLZCO. (b) is the Li striping and plating stability of the cell at different current densities. The cell was cycled at room temperature on an open lab bench to approximate real world use during summer (15–27 °C), hence fluctuations in the voltage profile. These are more noticeable compared to Fig. 12 due to larger temperature differential, lower voltage troughs occur overnight, whereas high voltage peaks occur in the day. (c) confirms voltage stability when cycled at a fixed temperature (43 °C).

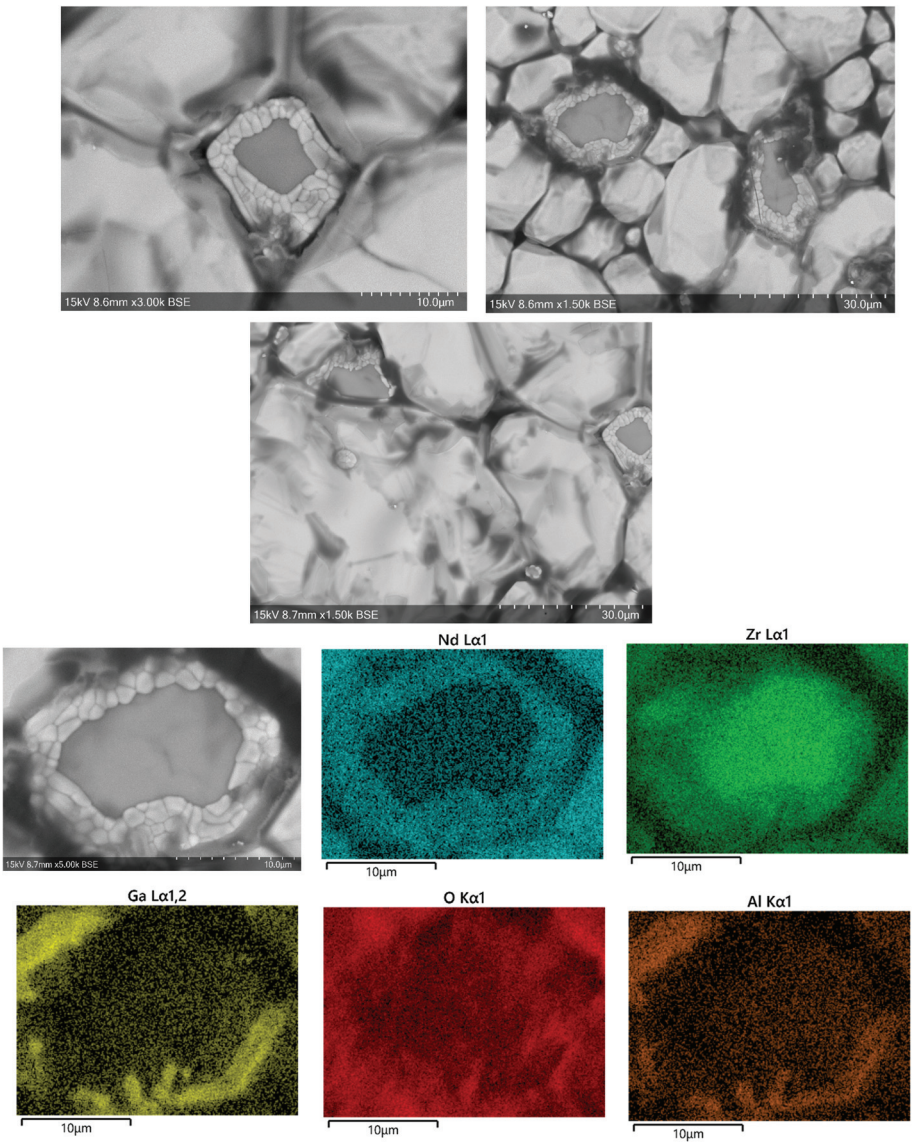

Fig. 15 SEM and EDX images of Ga-NLZO post regeneration, whereby pellet was heated to 1150 °C for 13 hours without protective powder and placed un-polished onto the SEM stub to examine any surface changes compared to Fig. 4. Al signal is thought to arise from Al stub, or perhaps crucible related Al/Li exchange, as this is the same pellet seen in Fig. 3, where no Al signal was detected.

we attribute as contributing to the low CCD by way of Ga–Li eutectic alloys.

A cross section of the pellet was examined and some areas of altering contrast were seen, particularly in Fig. 16, with EDX demonstrating some corresponding evidence of elemental separation in some areas. This indicates these elemental clusters propagate through the pellet and could be related to the observed low CCD. However, further work is needed to provide confirmation.

As large quantities of these surface impurities were present, the pellet was analysed by XRD which showed that it still appeared to be a mostly pure cubic garnet, see Fig. 17. The pellet surface (pre thermal etching) demonstrated some small background peaks corresponding to Ga–Li eutectics, however these peaks are difficult to resolve due to the weak scattering ability of Li/Ga and will require use of Li sensitive techniques, such as time of flight secondary ion mass spectroscopy, for further confirmation.

To provide some confirmation of our hypothesis concerning Li–Ga eutectic formation through Ga exsolution, we examined the effect of placing Li metal discs in contact with a Ga_2O_3 pellet and heating to 175 °C (1 h) and also left a Ga_2O_3 pellet in contact with the metal at room temperature for two days. XRD analysis was subsequently undertaken under inert conditions, with freshly scratched Li metal also analysed for comparison. Both cases indicated a clear reaction with Li metal, with the heated sample fully decomposing Li metal into a black powder. In the heated sample, phases were matched to both Li_2Ga and Li–Ga eutectics (see ESI†). Comparing these data to the XRD of the Ga-NLZO pellet surface shows corres-

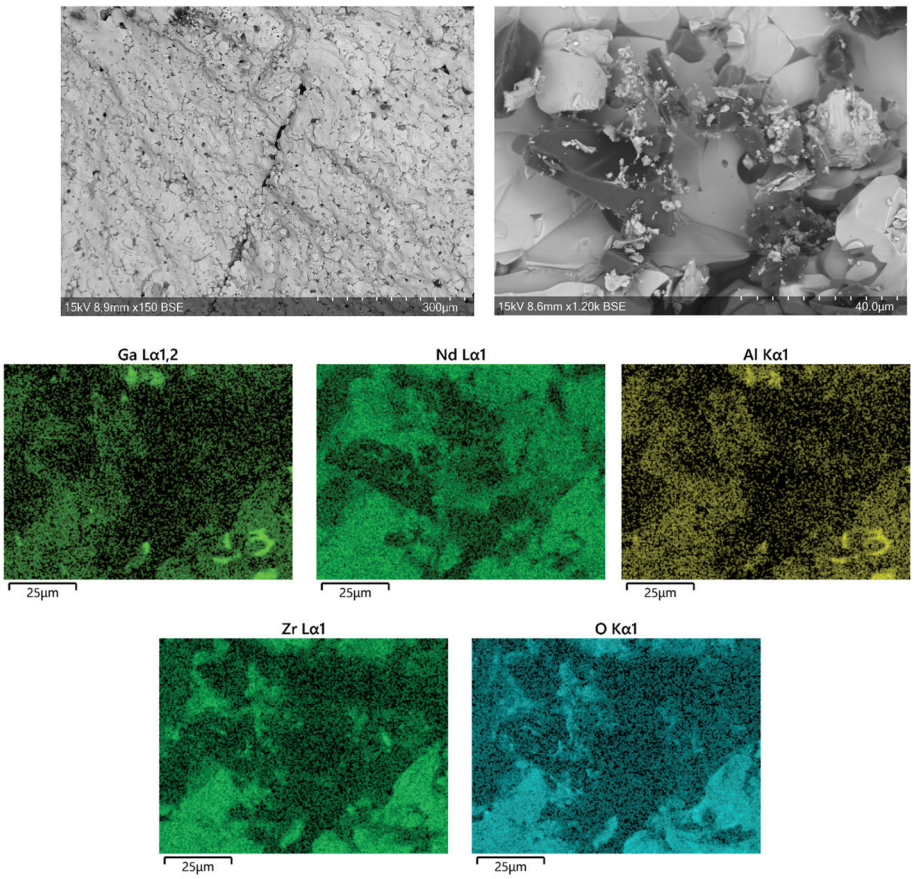

Fig. 16 Side SEM images of Ga-NLZO pellet interior after regeneration. Pellet was measured side on after being broken into fragments. Left image shows potential area where dendrite propagated, and right image (and corresponding EDX) shows some elemental separation as in Fig. 15. Al signal is thought to arise from Al stub, or perhaps Al/Li exchange from crucible, as this is the same pellet as in Fig. 3.

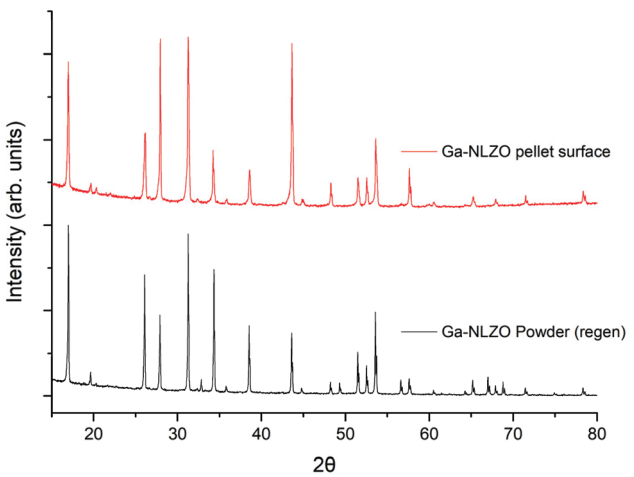

Fig. 17 XRD of Ga-NLZO pellet surface from symmetry cell with Li metal removed (prior to thermal etching), and of the pellet powder taken from re-grinding pellet fragment after regenerating the pellet.

ponding peaks, hence providing some further evidence of a similar reaction occurring at the Ga-NLZO interface. However, some peaks are overlapping with garnet, whereas others are possibly lost in the background, therefore additional work is required to confirm Ga–Li eutectic formation more absolutely. But, nonetheless, it is clear that Ga-NLZO garnets present with

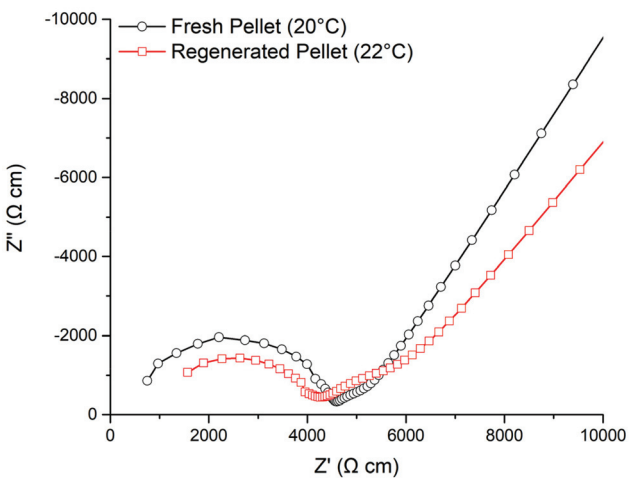

Fig. 18 Impedance spectrum of regeneration pellet (red) overlaid with a fresh pellet (black), illustrating little change outside a small increase in temperature.

exceptionally low ASR values that are intrinsic to the garnet material, a rare feature.

Finally, the regenerated pellet was sputtered with Au and the conductivity remeasured to assess the recoverability of the Ga-NLZO garnet materials after a short circuit event. As shown in Fig. 18, the pellet was mostly regenerated back to its original properties, demonstrating a comparable conductivity of 0.2 mS cm^{-1} (20 °C), with the corresponding XRD of the ground powder displayed in Fig. 17.

Conclusion

In summary, a range of Nd based Li garnet materials have been synthesised for the first time, with Ga-NLZO in particular having room temperature ionic conductivity ($\geq 2 \times 10^{-4}$ S cm^{-1}) similar to La based garnets, despite having significantly smaller lattice parameters. Ga-NLZO also appears relatively straightforward to sinter reproducibly, giving pellets with a high density in lower processing times than equivalent La based garnets. Significantly, we have demonstrated that Ga-NLZO enables very low ASR values in contact with Li metal which remain stable during cell cycling, a feature which is intrinsic to the garnet material itself rather than requiring additional coatings. It is proposed this is due to Ga–Li eutectic formation, which is enhanced by Ga-NLZO due to its much smaller lattice parameters (compared to Ga-LLZO) increasing Ga exsolution when combined with Li metal/heating. Somewhat surprisingly despite the very low ASR value, a comparatively low CCD was observed which requires future work to understand fully, but we propose that it relates to the same Ga exsolution process which enables low ASR values. Despite this issue, the high density and low ASR of Ga-NLZO allows it to be utilized in conjunction with a La based garnet as an interfacial modification to overcome the latter's high Li/electrode interfacial resistance, whereupon Ga-NLZO would act as a CI layer between the Li electrode and the garnet electrolyte.

Raw experimental data

https://doi.org/10.25500/edata.bham.00000716.

Conflicts of interest

There are no conflicts of interest to declare.

Acknowledgements

We would like to thank the University of Birmingham for the studentship funding of Mark Stockham and Matthew James, and the EPSRC for funding the GENESIS project (under EP/R024006/1) and the EPSRC Capital Award for Core Equipment (EP/T02349X/1).

Notes and references

1 S. Wang, K. Rafiz, J. Liu, Y. Jin and J. Y. S. Lin, *Sustainable Energy Fuels*, 2020, **4**, 2342–2351.
2 B. S. Vishnugopi, F. Hao, A. Verma and P. P. Mukherjee, *ACS Appl. Mater. Interfaces*, 2020, **12**, 23931–23938.
3 M. A. Howard, O. Clemens, K. S. Knight, P. A. Anderson, S. Hafiz, P. M. Panchmatia and P. R. Slater, *J. Mater. Chem. A*, 2013, **1**, 14013–14022.
4 J. M. Tarascon and M. Armand, *Nature*, 2001, **414**, 359.
5 C.-X. Zu and H. Li, *Energy Environ. Sci.*, 2011, **4**, 2614–2624.
6 V. A. Agubra and J. W. Fergus, *J. Power Sources*, 2014, **268**, 153–162.
7 N. Nitta, F. Wu, J. T. Lee and G. Yushin, *Mater. Today*, 2015, **18**, 252–264.
8 M. Winter and R. J. Brodd, *Chem. Rev.*, 2004, **104**, 4245–4270.
9 T. Kim, W. Song, D.-Y. Son, L. K. Ono and Y. Qi, *J. Mater. Chem. A*, 2019, **7**, 2942–2964.
10 M. Armand and J. M. Tarascon, *Nature*, 2008, **451**, 652.
11 H. Yang, C. Guo, A. Naveed, J. Lei, J. Yang, Y. Nuli and J. Wang, *Energy Storage Mater.*, 2018, **14**, 199–221.
12 L. Wang, Z. Zhou, X. Yan, F. Hou, L. Wen, W. Luo, J. Liang and S. X. Dou, *Energy Storage Mater.*, 2018, **14**, 22–48.
13 H. Wu, D. Zhuo, D. Kong and Y. Cui, *Nat. Commun.*, 2014, **5**, 5193.
14 Y. Zhu, X. He and Y. Mo, *ACS Appl. Mater. Interfaces*, 2015, **7**, 23685–23693.
15 J. Li, C. Ma, M. Chi, C. Liang and N. J. Dudney, *Adv. Energy Mater.*, 2015, **5**, 1401408.
16 H. Liu, X.-B. Cheng, J.-Q. Huang, H. Yuan, Y. Lu, C. Yan, G.-L. Zhu, R. Xu, C.-Z. Zhao, L.-P. Hou, C. He, S. Kaskel and Q. Zhang, *ACS Energy Lett.*, 2020, **5**, 833–843.
17 B. Dong, J. Yan, B. Walkley, K. K. Inglis, F. Blanc, S. Hull and A. R. West, *Solid State Ionics*, 2018, **327**, 64–70.
18 V. Thangadurai, S. Narayanan and D. Pinzaru, *Chem. Soc. Rev.*, 2014, **43**, 4714–4727.
19 W. D. Richards, L. J. Miara, Y. Wang, J. C. Kim and G. Ceder, *Chem. Mater.*, 2016, **28**, 266–273.
20 Y. G. Kim and H. N. G. Wadley, *J. Power Sources*, 2011, **196**, 1371–1377.
21 Y. Zhao and L. L. Daemen, *Superionic Conductivity in Lithium-Rich Anti-Perovskites*, 2012.
22 Y. Zheng, Y. Yao, J. Ou, M. Li, D. Luo, H. Dou, Z. Li, K. Amine, A. Yu and Z. Chen, *Chem. Soc. Rev.*, 2020, **49**, 8790–8839.
23 Y. Zhang, F. Chen, R. Tu, Q. Shen and L. Zhang, *J. Power Sources*, 2014, **268**, 960–964.
24 M. Botros, R. Djenadic, O. Clemens, M. Möller and H. Hahn, *J. Power Sources*, 2016, **309**, 108–115.
25 E. Kazyak, K.-H. Chen, K. N. Wood, A. L. Davis, T. Thompson, A. R. Bielinski, A. J. Sanchez, X. Wang, C. Wang, J. Sakamoto and N. P. Dasgupta, *Chem. Mater.*, 2017, **29**, 3785–3792.
26 A. Sharafi, H. M. Meyer, J. Nanda, J. Wolfenstine and J. Sakamoto, *J. Power Sources*, 2016, **302**, 135–139.

27 L. Cheng, W. Chen, M. Kunz, K. Persson, N. Tamura, G. Chen and M. Doeff, *ACS Appl. Mater. Interfaces*, 2015, **7**, 2073–2081.
28 L. Cheng, C. H. Wu, A. Jarry, W. Chen, Y. Ye, J. Zhu, R. Kostecki, K. Persson, J. Guo, M. Salmeron, G. Chen and M. Doeff, *ACS Appl. Mater. Interfaces*, 2015, **7**, 17649–17655.
29 C. Bernuy-Lopez, W. Manalastas, J. M. Lopez del Amo, A. Aguadero, F. Aguesse and J. A. Kilner, *Chem. Mater.*, 2014, **26**, 3610–3617.
30 Q. Liu, Z. Geng, C. Han, Y. Fu, S. Li, Y.-b. He, F. Kang and B. Li, *J. Power Sources*, 2018, **389**, 120–134.
31 N. J. Taylor, S. Stangeland-Molo, C. G. Haslam, A. Sharafi, T. Thompson, M. Wang, R. Garcia-Mendez and J. Sakamoto, *J. Power Sources*, 2018, **396**, 314–318.
32 M. P. Stockham, B. Dong, M. S. James, Y. Li, Y. Ding and P. R. Slater, *Dalton Trans.*, 2021, **50**, 2364–2374.
33 Y. Jin and P. J. McGinn, *J. Power Sources*, 2013, **239**, 326–331.
34 R. H. Brugge, J. A. Kilner and A. Aguadero, *Solid State Ionics*, 2019, **337**, 154–160.
35 H. Duan, H. Zheng, Y. Zhou, B. Xu and H. Liu, *Solid State Ionics*, 2018, **318**, 45–53.
36 A. F. Wells, *Structural inorganic chemistry*, Clarendon Press, 1984.
37 V. Thangadurai, S. Adams and W. Weppner, *Chem. Mater.*, 2004, **16**, 2998–3006.
38 E. J. Cussen and T. W. S. Yip, *J. Solid State Chem.*, 2007, **180**, 1832–1839.
39 E. J. Cussen, *Chem. Commun.*, 2006, 412–413, DOI: 10.1039/B514640B.
40 M. P. O'Callaghan, D. R. Lynham, E. J. Cussen and G. Z. Chen, *Chem. Mater.*, 2006, **18**, 4681–4689.
41 V. Thangadurai, H. Kaack and W. J. F. Weppner, *J. Am. Ceram. Soc.*, 2004, **86**, 437–440.
42 R. Murugan, V. Thangadurai and W. Weppner, *Angew. Chem., Int. Ed.*, 2007, **46**, 7778–7781.
43 C. A. Geiger, E. Alekseev, B. Lazic, M. Fisch, T. Armbruster, R. Langner, M. Fechtelkord, N. Kim, T. Pettke and W. Weppner, *Inorg. Chem.*, 2011, **50**, 1089–1097.
44 J. Awaka, N. Kijima, K. Kataoka, H. Hayakawa, K.-i. Ohshima and J. Akimoto, *J. Solid State Chem.*, 2010, **183**, 180–185.
45 J. Awaka, N. Kijima, H. Hayakawa and J. Akimoto, *J. Solid State Chem.*, 2009, **182**, 2046–2052.
46 J. Percival, E. Kendrick, R. I. Smith and P. R. Slater, *Dalton Trans.*, 2009, 5177–5181, DOI: 10.1039/b907331k.
47 B. Dong, S. R. Yeandel, P. Goddard and P. R. Slater, *Chem. Mater.*, 2020, **32**, 215–223.
48 R. Wagner, G. J. Redhammer, D. Rettenwander, A. Senyshyn, W. Schmidt, M. Wilkening and G. Amthauer, *Chem. Mater.*, 2016, **28**, 1861–1871.
49 J. Percival and P. R. Slater, *Solid State Commun.*, 2007, **142**, 355–357.
50 R. Murugan, V. Thangadurai and W. Weppner, *Appl. Phys. A*, 2008, **91**, 615–620.
51 M. A. Howard, O. Clemens, E. Kendrick, K. S. Knight, D. C. Apperley, P. A. Anderson and P. R. Slater, *Dalton Trans.*, 2012, **41**, 12048–12053.
52 J. L. Allen, J. Wolfenstine, E. Rangasamy and J. Sakamoto, *J. Power Sources*, 2012, **206**, 315–319.
53 B. Dong, L. L. Driscoll, M. P. Stockham, E. Kendrick and P. R. Slater, *Solid State Ionics*, 2020, **350**, 115317.
54 B. Dong, M. P. Stockham, P. A. Chater and P. R. Slater, *Dalton Trans.*, 2020, **49**, 11727–11735.
55 F. M. Pesci, R. H. Brugge, A. K. O. Hekselman, A. Cavallaro, R. J. Chater and A. Aguadero, *J. Mater. Chem. A*, 2018, **6**, 19817–19827.
56 M. A. Howard, O. Clemens, E. Kendrick, K. S. Knight, D. C. Apperley, P. A. Anderson and P. R. Slater, *Dalton Trans.*, 2012, **41**, 12048–12053.
57 S. Narayanan and V. Thangadurai, *J. Power Sources*, 2011, **196**, 8085–8090.
58 S. Narayanan, F. Ramezanipour and V. Thangadurai, *J. Phys. Chem. C*, 2012, **116**, 20154–20162.
59 J.-F. Wu, E.-Y. Chen, Y. Yu, L. Liu, Y. Wu, W. K. Pang, V. K. Peterson and X. Guo, *ACS Appl. Mater. Interfaces*, 2017, **9**, 1542–1552.
60 X. Wang, J. Liu, R. Yin, Y. Xu, Y. Cui, L. Zhao and X. Yu, *Mater. Lett.*, 2018, **231**, 43–46.
61 J. Gai, E. Zhao, F. Ma, D. Sun, X. Ma, Y. Jin, Q. Wu and Y. Cui, *J. Eur. Ceram. Soc.*, 2018, **38**, 1673–1678.
62 N. Janani, C. Deviannapoorani, L. Dhivya and R. Murugan, *RSC Adv.*, 2014, **4**, 51228–51238.
63 V. Thangadurai and W. Weppner, *J. Am. Ceram. Soc.*, 2005, **88**, 411–418.
64 L. Robben, E. Merzlyakova, P. Heitjans and T. M. Gesing, *Acta Crystallogr., Sect. E*, 2016, **72**, 287–289.
65 Y. Ren, Y. Shen, Y. Lin and C.-W. Nan, *Electrochem. Commun.*, 2015, **57**, 27–30.
66 D. Wang, K. Peng, Y. Fu, C. Zhu and Y. Yang, *J. Power Sources*, 2021, **487**, 229421.
67 Y. Zhu, J. G. Connell, S. Tepavcevic, P. Zapol, R. Garcia-Mendez, N. J. Taylor, J. Sakamoto, B. J. Ingram, L. A. Curtiss, J. W. Freeland, D. D. Fong and N. M. Markovic, *Adv. Energy Mater.*, 2019, **9**, 1803440.
68 R. H. Brugge, F. M. Pesci, A. Cavallaro, C. Sole, M. A. Isaacs, G. Kerherve, R. S. Weatherup and A. Aguadero, *J. Mater. Chem. A*, 2020, **8**, 14265–14276.
69 J. Saint, M. Morcrette, D. Larcher and J. M. Tarascon, *Solid State Ionics*, 2005, **176**, 189–197.
70 J. Sangster and A. D. Pelton, *J. Phase Equilib.*, 1991, **12**, 33–36.
71 H. Okamoto, *J. Phase Equilib. Diffus.*, 2006, **27**, 200–200.
72 H. Xie, K.-S. Park, J. Song and J. B. Goodenough, *Electrochem. Commun.*, 2012, **19**, 135–137.
73 M. A. Howard, O. Clemens, A. S. Parvathy, P. A. Anderson and P. R. Slater, *J. Alloys Compd.*, 2016, **670**, 78–84.
74 B. Toby and R. Dreele, *J. Appl. Crystallogr.*, 2013, **46**, 544–549.
75 R. H. Brugge, A. K. O. Hekselman, A. Cavallaro, F. M. Pesci, R. J. Chater, J. A. Kilner and A. Aguadero, *Chem. Mater.*, 2018, **30**, 3704–3713.

76 G. Larraz, A. Orera and M. L. Sanjuán, *J. Mater. Chem. A*, 2013, **1**, 11419–11428.
77 C. Galven, J. Dittmer, E. Suard, F. Le Berre and M.-P. Crosnier-Lopez, *Chem. Mater.*, 2012, **24**, 3335–3345.
78 J. Percival, D. Apperley and P. R. Slater, *Solid State Ionics*, 2008, **179**, 1693–1696.
79 H. Peng, Y. Zhang, L. Li and L. Feng, *Solid State Ionics*, 2017, **304**, 71–74.
80 I. P. Roof, M. D. Smith, E. J. Cussen and H.-C. zur Loye, *J. Solid State Chem.*, 2009, **182**, 295–300.
81 F. M. Pesci, A. Bertei, R. H. Brugge, S. P. Emge, A. K. O. Hekselman, L. E. Marbella, C. P. Grey and A. Aguadero, *ACS Appl. Mater. Interfaces*, 2020, **12**, 32806–32816.
82 A. Gupta, R. Murugan, M. P. Paranthaman, Z. Bi, C. A. Bridges, M. Nakanishi, A. P. Sokolov, K. S. Han, E. W. Hagaman, H. Xie, C. B. Mullins and J. B. Goodenough, *J. Power Sources*, 2012, **209**, 184–188.
83 Y. Wang, P. Yan, J. Xiao, X. Lu, J.-G. Zhang and V. L. Sprenkle, *Solid State Ionics*, 2016, **294**, 108–115.
84 M. P. Stockham, B. Dong, Y. Ding, Y. Li and P. R. Slater, *Dalton Trans.*, 2020, **49**, 10349–10359.
85 S. Song, B. Chen, Y. Ruan, J. Sun, L. Yu, Y. Wang and J. Thokchom, *Electrochim. Acta*, 2018, **270**, 501–508.
86 M. P. Stockham, B. Dong, Y. Ding, Y. Li and P. R. Slater, *Dalton Trans.*, 2020, **49**, 10349–10359.
87 G. V. Alexander, S. Patra, S. V. Sobhan Raj, M. K. Sugumar, M. M. Ud Din and R. Murugan, *J. Power Sources*, 2018, **396**, 764–773.
88 C.-L. Tsai, V. Roddatis, C. V. Chandran, Q. Ma, S. Uhlenbruck, M. Bram, P. Heitjans and O. Guillon, *ACS Appl. Mater. Interfaces*, 2016, **8**, 10617–10626.
89 N. C. Rosero-Navarro, R. Kajiura, R. Jalem, Y. Tateyama, A. Miura and K. Tadanaga, *ACS Appl. Energy Mater.*, 2020, **3**, 5533–5541.
90 B. Liu, Y. Gong, K. Fu, X. Han, Y. Yao, G. Pastel, C. Yang, H. Xie, E. D. Wachsman and L. Hu, *ACS Appl. Mater. Interfaces*, 2017, **9**, 18809–18815.
91 W. Zhou, Y. Zhu, N. Grundish, X. Sen, S. Wang, Y. You, N. Wu, J. Gao, Z. Cui, Y. Li and J. B. Goodenough, *Nano Energy*, 2018, **53**, 926–931.
92 B. Xu, W. Li, H. Duan, H. Wang, Y. Guo, H. Li and H. Liu, *J. Power Sources*, 2017, **354**, 68–73.
93 A. Sharafi, E. Kazyak, A. L. Davis, S. Yu, T. Thompson, D. J. Siegel, N. P. Dasgupta and J. Sakamoto, *Chem. Mater.*, 2017, **29**, 7961–7968.
94 Y. Shao, H. Wang, Z. Gong, D. Wang, B. Zheng, J. Zhu, Y. Lu, Y.-S. Hu, X. Guo, H. Li, X. Huang, Y. Yang, C.-W. Nan and L. Chen, *ACS Energy Lett.*, 2018, **3**, 1212–1218.
95 W. Luo, Y. Gong, Y. Zhu, K. K. Fu, J. Dai, S. D. Lacey, C. Wang, B. Liu, X. Han, Y. Mo, E. D. Wachsman and L. Hu, *J. Am. Chem. Soc.*, 2016, **138**, 12258–12262.
96 W. Luo, Y. Gong, Y. Zhu, Y. Li, Y. Yao, Y. Zhang, K. Fu, G. Pastel, C.-F. Lin, Y. Mo, E. D. Wachsman and L. Hu, *Adv. Mater.*, 2017, **29**, 1606042.
97 K. Fu, Y. Gong, B. Liu, Y. Zhu, S. Xu, Y. Yao, W. Luo, C. Wang, S. D. Lacey, J. Dai, Y. Chen, Y. Mo, E. Wachsman and L. Hu, *Sci. Adv.*, 2017, **3**, e1601659.
98 R. Sudo, Y. Nakata, K. Ishiguro, M. Matsui, A. Hirano, Y. Takeda, O. Yamamoto and N. Imanishi, *Solid State Ionics*, 2014, **262**, 151–154.
99 C. Wang, Y. Gong, B. Liu, K. Fu, Y. Yao, E. Hitz, Y. Li, J. Dai, S. Xu, W. Luo, E. D. Wachsman and L. Hu, *Nano Lett.*, 2017, **17**, 565–571.
100 W. Feng, X. Dong, P. Li, Y. Wang and Y. Xia, *J. Power Sources*, 2019, **419**, 91–98.
101 M. He, Z. Cui, C. Chen, Y. Li and X. Guo, *J. Mater. Chem. A*, 2018, **6**, 11463–11470.
102 J.-F. Wu, B.-W. Pu, D. Wang, S.-Q. Shi, N. Zhao, X. Guo and X. Guo, *ACS Appl. Mater. Interfaces*, 2019, **11**, 898–905.
103 Y. Li, X. Chen, A. Dolocan, Z. Cui, S. Xin, L. Xue, H. Xu, K. Park and J. B. Goodenough, *J. Am. Chem. Soc.*, 2018, **140**, 6448–6455.
104 F. Flatscher, M. Philipp, S. Ganschow, H. M. R. Wilkening and D. Rettenwander, *J. Mater. Chem. A*, 2020, **8**, 15782–15788.
105 R. Hongahally Basappa, T. Ito, T. Morimura, R. Bekarevich, K. Mitsuishi and H. Yamada, *J. Power Sources*, 2017, **363**, 145–152.
106 X. Huang, Y. Lu, H. Guo, Z. Song, T. Xiu, M. E. Badding and Z. Wen, *ACS Appl. Energy Mater.*, 2018, **1**, 5355–5365.

8. Assessing the Importance of Cation Size in the Tetragonal-Cubic Phase Transition in Lithium-Garnet Electrolytes

8.1. PUBLICATION

Assessing the Importance of Cation Size in the Tetragonal-Cubic Phase Transition in Lithium-Garnet Electrolytes

Article information : M. P. Stockham, A. Griffiths, B. Dong, P. R. Slater, Chem. Eur. J. 2022, 28, e202103442.

Submitted: 29/09/2021

Accepted: 01/12/2021

Author contributions: M. P. Stockham: experimental and characterisation work, method development, conceptualisation, writing, investigation. A. Griffiths. writing – draft, data curation, analysis. B. Dong: Data curation, investigation, P. R. Slater: Conceptualisation, lead supervision, characterisation and experimental guidance, writing – review & editing.

Chemistry–A European Journal
Full Paper
doi.org/10.1002/chem.202103442
Chemistry Europe
European Chemical Societies Publishing
www.chemeurj.org

Assessing the Importance of Cation Size in the Tetragonal-Cubic Phase Transition in Lithium-Garnet Electrolytes**

Mark P. Stockham,*[a] Alice Griffiths,[a] Bo Dong,[a] and Peter R. Slater*[a]

Abstract: Lithium garnets are promising solid-state electrolytes for next-generation lithium-ion batteries. These materials have high ionic conductivity, a wide electrochemical window and stability with Li metal. However, lithium garnets have a maximum limit of seven lithium atoms per formula unit (e.g., $La_3Zr_2Li_7O_{12}$), before the system transitions from a cubic to a tetragonal phase with poor ionic mobility. This arises from full occupation of the Li sites. Hence, the most conductive lithium garnets have Li between 6–6.55 Li per formula unit, which maintains the cubic symmetry and the disordered Li sublattice.

The tetragonal phase, however, forms the highly conducting cubic phase at higher temperatures, thought to arise from increased cell volume and entropic stabilisation permitting Li disorder. However, little work has been undertaken in understanding the controlling factors of this phase transition, which could enable enhanced dopant strategies to maintain room temperature cubic garnet at higher Li contents.

Here, a series of nine tetragonal garnets were synthesised and analysed by variable temperature XRD to understand the dependence of site substitution on the phase transition temperature. Interestingly the octahedral site cation radius was identified as the key parameter for the transition temperature with larger or smaller dopants altering the transition temperature noticeably. A site substitution was, however, found to make little difference irrespective of significant changes to cell volume.

Introduction

High-energy density, portable and safe energy storage remains one of the most prevalent issues in modern society. Lithium-ion batteries (LIB) are amongst the most promising options but are far from achieving their theoretical performance.[1] Maximal energy density of lithium batteries can only be achieved by use of Li metal anodes, which enable the highest theoretical capacity (3860 mA h g^{-1}) and the lowest electrochemical potential (−3.04 V vs. the standard hydrogen electrode) of all anode materials.[1a,b] However, current LIB electrolytes (usually $LiPF_6$ dissolved in a ethylene carbonate/dimethyl carbonate) are incompatible with Li metal, present with safety concerns and an inability to accommodate high V cathode materials. Hence, electrolyte optimisation, or replacement, is paramount.[1a,b,2]

All solid-state batteries (ASSBs) are natural successors to current LIBs, as they could enable Li metal anodes, wider electrochemical windows and improved safety.[3] However, the development of a suitable solid-state electrolyte (SSE) has proved troublesome. To date many oxide and sulphide SSEs have been studied, but often have a high ionic conductivity or a wide electrochemical window, but rarely both.[2c,3–4] Finding a suitable SSE is, therefore, a key challenge to enable the next generation of energy storage.[3]

Lithium garnets have emerged as contenders for use as an SSE, owing to a wide electrochemical window (0–6 V vs. Li/Li^+), chemical stability with Li metal and (in recent years) high ionic conductivity (> 0.1 mS cm^{-1}).[5] These materials, however, form a poorly conductive tetragonal phase at high Li content (as outlined below) and suffer from atmospheric H^+/Li^+ exchange (which ultimately forms insulating Li_2CO_3 passivating layers due to instability of the Li dopant in high concentrations).[6] This is in addition to the common SSE problems of high interfacial resistance, lithium metal dendrite formation and time-consuming synthesis.[5l,6a,b,7]

An ideal garnet has the formula; $A_3B_2X_3O_{12}$, where A, B and X are eight, six and four coordinated cation sites, respectively, which crystallise in a face-centred cubic structure (e.g., A = Mg, Fe, B = Al, Cr, Fe, and X = Si, Fe, Al, Ga).[5k,8] This structure comprises BO_6 octahedra and XO_4 tetrahedra, arranged in a 3D framework wherein larger A cations occupy dodecahedral positions in the interstices.[9] Lithium ions fully occupy the tetrahedra 24d site, with 3 Li per formula unit (*pfu*). Alteration of A and B sites dopants, such as in $La_3Zr_2Li_7O_{12}$ (LLZO), enables up to 7 Li *pfu* (the upper maximum). However, at this point the system changes from a highly conductive cubic phase ($Ia\bar{3}d$ or $I4\bar{3}d$, Li content ~6.2–6.55 *pfu*), with vacant interstitial sites for ionic mobility, to a system whereby Li sites are fully occupied and have thus ordered (to reduce short Li–Li distances).[10] This gives a reduction in symmetry from a cubic to a tetragonal cell ($I4_1/acd$) with ordered lithium occupying the tetrahedral (8a) and distorted octahedral (16f/32 g) sites.[5q,8b,9b,c,10a,b]

[a] M. P. Stockham, A. Griffiths, Dr. B. Dong, Prof. P. R. Slater
School of Chemistry
University of Birmingham
Birmingham B15 2TT. UK
E-mail:

[**] A previous version of this manuscript has been deposited on a preprint server (https://doi.org/10.33774/chemrxiv-2021-v36v1).

Supporting information for this article is available on the WWW under https://doi.org/10.1002/chem.202103442

However, these tetragonal Li garnets, such as $La_3Zr_2Li_7O_{12}$, $La_3Hf_2Li_7O_{12}$ and $Nd_3Zr_2Li_7O_{12}$, undergo a high temperature Tetragonal-Cubic phase transition (~700 °C), believed to arise from increased unit cell size and entropy factors.[11] It would therefore be of great interest if this transition temperature could be lowered to room temperature, thus forming a cubic Li_7 phase, which should further optimise the conductivity of Li garnets. This requires a greater understanding of the factors which influence the temperature of this phase transition, which is somewhat limited in the literature. Some studies initially thought this transition occurred ~100–200 °C in LLZO but this was determined to arise from hydration, due to either the direct insertion of water molecules or through a H^+/Li^+ exchange mechanism.[10a,12] Therefore, the characteristic, reversible tetragonal-cubic phase transition in LLZO is believed to be 620–650 °C,[4d,5k,12] while the smaller cell volume $La_3Sn_2Li_7O_{12}$ (LLSnO) exhibits a phase transition ~750–800 °C.[9b,10a,11b] This suggests that the cell volume is potentially key to dictating the phase transition.

Dong and co-workers investigated tetragonal garnets of the formula $La_3Zr_{2-x}Li_7Ce_xO_{12}$ ($0 \leq x \geq 0.75$) by XRD studies. This showed a reduction in tetragonality for these Li_7 garnets on Ce doping, attributed to the larger ionic radius of Ce^{4+}. This decreased the Tetragonal-Cubic transition temperature to 325 °C compared to LLZO suggesting further that increased cell volume corresponds to lower transition temperatures.[5k]

However, density functional theory-based calculations by Chen and co-workers, on tantalum doped systems (Ta-doped LLZO) and Li positioning changes in the phase transition, determined the thermodynamic stability of the tetragonal 16f site 'blocked' the formation of cubic LLZO at lower temperatures. Ta^{5+} doping was predicted to give octahedral site Li-ion vacancies which weakened the 'blocking' effect of the tetragonal (16f) sites, allowing for lithium-ion redistribution and thus, lowering the transition temperature.[11b] These data indicate B site substitution could play an important role in the transition temperature, and that the direct relation to cell volume is perhaps too simplistic. Outside of these reports, work on the tetragonal to cubic phase transition is somewhat limited.

Herein, nine tetragonal lithium garnets were synthesised; $A_3B_2Li_7O_{12}$ (A = La, Pr, Nd) (B = Zr, Hf), $La_3Zr_{1.75}Ce_{0.25}Li_7O_{12}$ and $LaSr_2B_2Li_7O_{12}$ (B = Nb, Ta). Both A and B site doping was undertaken to assess the relative importance of each site on the transition temperature. These materials were studied by variable temperature XRD analysis to ascertain if any new insights could be gained regarding the phase transition. Interestingly, we determine that, irrespective of A site substitution it is the B site which is the predominant factor in determining the phase transition temperature. It is shown that a direct relation solely to cell volume is too simplistic, rather it is suggested the sites which dictate the degree of tetragonality, which correspond to the framework polyhedra, are of higher importance than A site cations which reside within. Furthermore, the transition temperatures identified enabled regression analysis to predict the ideal octahedral B site radius for a room temperature stable cubic Li_7 phase.

Experimental

Solid-State Synthesis

$A_3B_2Li_7O_{12}$ (A = La, Pr, Nd) (B = Zr, Hf), $La_3Zr_{1.75}Ce_{0.25}Li_7O_{12}$ and $LaSr_2B_2Li_7O_{12}$ (B = Nb, Ta) were prepared by the solid-state route from stochiometric quantities of Li_2CO_3 (≥99%, Sigma-Aldrich), Nd_2O_3 (99.9% Sigma-Aldrich), La_2O_3 (≥99.9%, Sigma-Aldrich), Pr_6O_{11} (99%, Alfa), $SrCO_3$(≥99.9%, Sigma-Aldrich), ZrO_2 (≥99%, Alfa), HfO_2 (98%, Sigma-Aldrich), Nb_2O_5 (≥99.9%, Alfa), CeO_2(≥99.9%, Acros), Ta_2O_5(≥99%, Alfa). All were synthesised under air except for Pr based garnets which required treatment under 10% H_2 to ensure the formation of Pr^{3+}. A 40% mol excess of lithium was added to compensate for lithium loss during high temperature sintering, this is more than conventional synthesis but was done to ensure tetragonal phase formation. All tetragonal garnets were ball milled for 1 hr with ZrO_2 balls (500 rpm) with hexane. The powders were then pressed into 16 mm pellets. Pr samples were the heated to 950 °C (12 h, 5 °C min^{-1}). LLZO was heated to 1100 °C (12 h, 5 °C min^{-1}) and the Nd garnets were heated to 1050 °C for (6 h, 5 °C min^{-1}). All synthesis was done on an alumina crucible. Sr containing garnets were heated at 700 °C (14 h), 900 °C (14 h) and 800 °C (12 h) (at 5 °C min^{-1}), the latter of which also required a further 20% excess Li, illustrating challenges with the formation of these heavily Sr doped samples. Post sintering, pellets were sanded in an attempt to remove any Al contamination from the Al crucible.

Characterisation

All samples were stored in an argon glove box to prevent proton-Li exchange in the garnet. Phase analysis was performed by X-ray diffraction (XRD) using a Bruker D8 diffractometer with Cu source from 15–80 2θ with a step size of 0.018°. Variable temperature measurements were conducted in a similar manner on a Bruker D8 instrument equipped with an Anton Parr heating stage from 50 °C up to a maximum of 1000 °C in air. Scanning electron microscopy (SEM) was performed on a Hitachi TM4000plus instrument. Elemental analysis was undertaken via an AZtecOne X-stream2 energy dispersive X-ray (EDX) spectrometer. Samples were prepared by applying the powders to a carbon tape and analysed at 15 kV in backscattered electron mode.

Rietveld Refinement

For each garnet synthesised, Rietveld refinements were performed in GSAS-II[13] using room temperature powder X-ray diffraction (XRD) patterns and variable temperature X-ray diffraction (VTXRD) patterns (50 °C to 1000 °C, 50 °C increments). All structural models were obtained from ISCD[10b,c] and atoms altered where required to give an analogous crystal structure. For Ce-doped LLZO, fractional occupancies were set to the intended ratio.

Results and Discussion

X-ray diffraction

All nine Li_7 garnets were first analysed for phase purity at room temperature, and all were indexed on a tetragonal garnet cell ($I4_1/acd$). Variable temperature X-Ray diffraction (VTXRD) data were subsequently collected for these garnets up to 1000 °C. This is beyond the common phase transition temperature (~700 °C) but was required to reach the phase transition

temperature for the Nb/Ta tetragonal phases. This caused some degradation for some systems; hence the complete reversal of the phase transition was not observed. Despite attempts to remove, small amounts of Al contamination remained, see Supporting Information. However, as the tetragonal cell was present at room temperature and the observed transition temperatures are similar to those reports elsewhere, Al is suggested to have limited impact on the observed phase transition trends.[5i,k,12,14]

The tetragonal to cubic phase transition is readily noticeable in the VT-XRD patterns by the coalescence of the split peaks into sharp, singular peaks. Data were collected in 50 °C increments (50 °C–1000 °C), but were plotted every 100 °C for clarity, see Figure 1 for LLZO (the remaining garnets are available in the Supporting Information). Near the phase change temperature patterns were commonly biphasic (cubic and tetragonal phases present) and not used for structure refinements. Rietveld refinements were performed for all other XRD patterns with cell volume, cell parameters and A/B site bond lengths studied. An exemplar refinement (with tabulated data at each temperature) for LLZO is shown in Figure 2 and Table 1. Although these data were collected for all nine Li_7 phases, only LLZO is shown in detail, whereas Table 2 shows the relevant data for the other eight phases only at room temperature and the transition

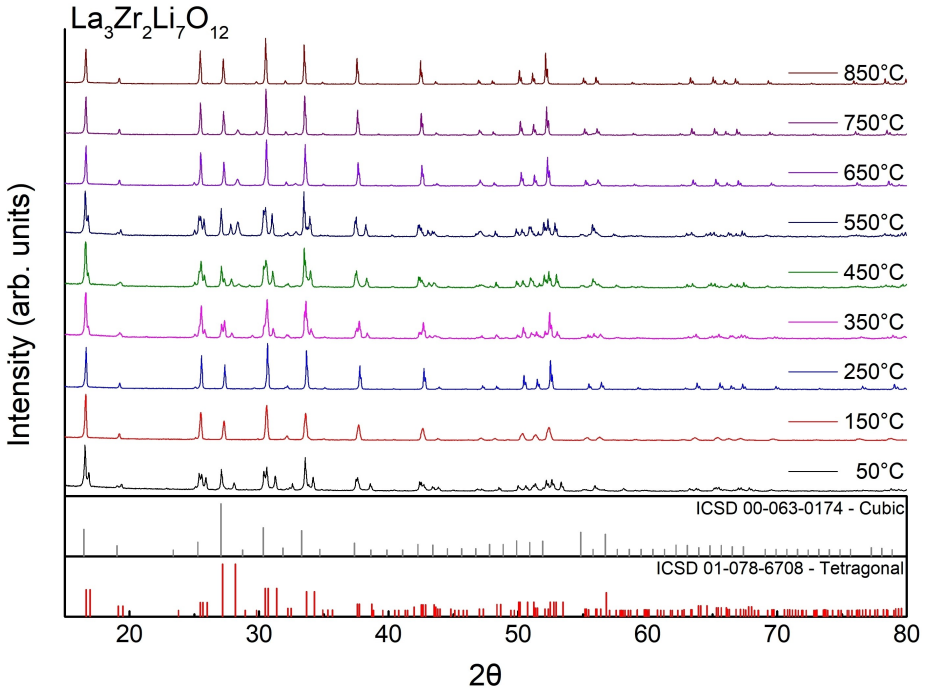

Figure 1. $La_3Zr_2Li_7O_{12}$ stacked XRD patterns. Phase transitions are observed at approximately 150 °C and approximately 650 °C.

Table 1. Refinement data for $La_3Zr_2Li_7O_{12}$. Values in brackets represent standard errors. Degree of tetragonality is calculated as c/a.

T [°C]	Unit-cell parameters a	c	Degree of tetragonality	Cell volume [Å^3]	Phase
50	13.1288(6)	12.6854(6)	0.966	2187.0(25)	Tetragonal
100	*Mixed tet-cubic phase. Transition occurring.*			–	–
150	13.0762(5)	–	–	2235.9(25)	Cubic
200	13.06019(15)	–2	–	2227.7(8)	Cubic
250	13.03577(17)	–	–	2215.2(9)	Cubic
300	*Mixed tet-cubic phase. Transition occurring.*			–	–
350	13.1257(22)	12.8038(21)	0.975	2205.9(10)	Tetragonal
400	13.1383(20)	12.8122(20)	0.975	2211.6(9)	Tetragonal
450	13.1775(7)	12.8206(7)	0.972	2226.3(3)	Tetragonal
500	13.1892(5)	12.8241(6)	0.973	2230.8(24)	Tetragonal
550	13.1942(5)	12.8510(5)	0.974	2237.2(22)	Tetragonal
600	13.1929(5)	12.8887(5)	0.977	2243.3(21)	Tetragonal
650	13.1057(29)	–	–	2251.0(15)	Cubic
700	13.1167(27)	–	–	2256.7(14)	Cubic
750	13.1275(25)	–	–	2262.3(13)	Cubic
800	13.1390(16)	–	–	2269.2(8)	Cubic
850	13.1522(15)	–	–	2275.3(8)	Cubic
900	13.1639(15)	–	–	2281.2(8)	Cubic
950	13.1756(19)	–	–	2287.3(10)	Cubic

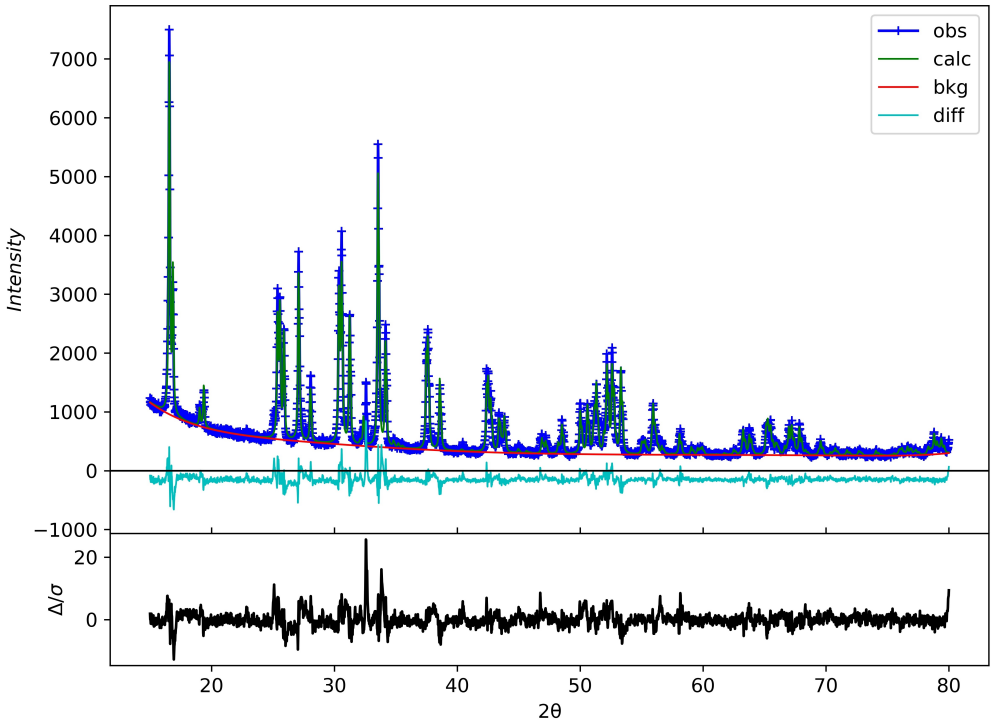

Figure 2. Observed, calculated and difference profiles for $La_3Zr_2Li_7O_{12}$ at 50 °C, tetragonal (space group; $I4_1/acd$), $R_{wp} = 9.95\,\%$.

Table 2. Refinement data for all nine Li7-garnet systems studied. Values within brackets refer to standard deviations. (Note lattice parameters and tetragonality are all based on room temperature XRD data.)

Formula	Unit-cell parameters *a*	*c*	Degree of tetragonality	Cell volume [Å^3]	Transition *T* range [°C]
$La_3Zr_{1.75}Ce_{0.25}Li_7O_{12}$	13.1141(1)	12.7432(1)	0.972	2191.6(10)	325–425
$La_3Zr_2Li_7O_{12}$	13.1242(6)	12.6791(6)	0.966	2183.90(26)	600–650
$Pr_3Zr_2Li_7O_{12}$	12.9783(3)	12.5653(3)	0.968	2116.5(11)	600–650
$Nd_3Zr_2\ Li_7O_{12}$	12.9222(7)	12.5501(7)	0.971	2095.64(29)	600–650
$La_3Hf_2Li_7O_{12}$	13.1049(21)	12.6474(19)	0.965	2172.0(10)	650–700
$Pr_3Hf_2Li_7O_{12}$	12.9700(10)	12.5417(9)	0.967	2109.8(5)	650–700
$Nd_3Hf_2Li_7O_{12}$	12.9101(6)	12.5084(6)	0.969	2085.7(28)	650–700
$LaSr_2Nb_2Li_7O_{12}$	13.0752(16)	12.5091(15)	0.957	2138.6(7)	800–850
$LaSr_2Ta_2Li_7O_{12}$	13.1431(8)	12.5433(8)	0.954	2166.8(3)	850–900

temperature. Tables 3 and 4 show bond lengths of A–O and B–O respectively.

The HTXRD was conducted in air as was the synthesis (except Pr samples), so CO_2 incorporation is possible. This has been reported to stabilise the cubic garnet cell at room temperature by Toda and co-workers, however required 40 h of heating to form the cubic phase, with only minimal CO_2 uptake after 20 h (which also corresponded to increased cell parameters).[15] Therefore, CO_2 incorporation cannot be ruled out. However, as all characterisation and sample handling were conducted similarly (except Pr samples), if CO_2 were present it would be in relatively equal, negligible, amounts. This assumption is evidenced by the available reports elsewhere, regarding phase transition and lattice parameters, being similar to this work.[5i,k,10b,c,14a,b,16] Unfortunately, it was not possible to conduct

Table 3. A site bond length data for all nine Li_7-garnet systems studied. Values within brackets refer to standard deviations. (Note lattice parameters and tetragonality all based on room temperature data.)

Formula	A(1)–O bond length [Å] (average)	A(2)–O bond length [Å] (average)	Transition *T* [°C]
$La_3Zr_{1.75}Ce_{0.25}Li_7O_{12}$	2.628	2.604	325–425
$La_3Zr_2Li_7O_{12}$	2.587	2.543	600–650
$Pr_3Zr_2Li_7O_{12}$	2.535	2.506	600–650
$Nd_3Zr_2Li_7O_{12}$	2.527	2.497	600–650
$La_3Hf_2Li_7O_{12}$	2.583	2.539	650–700
$Pr_3Hf_2Li_7O_{12}$	2.533	2.503	650–700
$Nd_3Hf_2Li_7O_{12}$	2.523	2.493	650–700
$LaSr_2Nb_2Li_7O_{12}$	2.570	2.526	800–850
$LaSr_2Ta_2Li_7O_{12}$	2.581	2.537	850–900

Table 4. B site bond-length data for all nine Li7-garnet systems studied. Values within brackets refer to standard deviations. (Note lattice parameters and tetragonality all based on room temperature data.)

Formula	B(1)–O bond length [Å] (average)	Transition *T* [°C]
$La_3Zr_{1.75}Ce_{0.25}$ Li_7O_{12}	2.117	325–425
$La_3Zr_2Li_7O_{12}$	2.113	600–650
$Pr_3Zr_2Li_7O_{12}$	2.105	600–650
$Nd_3Zr_2Li_7O_{12}$	2.098	600–650
$La_3Hf_2Li_7O_{12}$	2.109	650–700
$Pr_3Hf_2Li_7O_{12}$	2.102	650–700
$Nd_3Hf_2Li_7O_{12}$	2.094	650–700
$LaSr_2Nb_2Li_7O_{12}$	2.107	800–850
$LaSr_2Ta_2Li_7O_{12}$	2.098	850–900

all experiments fully under inert conditions, nor to transfer to the HTXRD without air exposure.

Cell volume increased with temperature (Table 1), as expected, across all the studied Li_7-garnets. This increase in cell volume coupled with the increasing importance of entropic stabilisation helps to promote disorder and drives the phase transition from tetragonal to cubic. Two distinct phase transitions were observed in most studied garnets, one ~100 °C and a second at higher temperature. The phase transition at ~100 °C was attributed to H^+/Li^+ exchange, as it was not possible to completely eliminate moisture. The lower temperature transition was not present in the Pr samples, which were synthesised under H_2, adding further evidence of proton exchange arises from air-based synthesis. The second transition at much higher temperatures is attributed to the true Tetragonal-Cubic phase transition. Most samples, after the low temperature proton exchange transition, had developed a pyrochlore-type phase (e.g., $La_2Zr_2O_7$) impurity, which was removed as the system fully transitioned to the high temperature cubic phase. Although the reason for the temporary development of the pyrochlore phase is not completely clear, it is suggested to relate to the proton exchange (particularly surface bound Li_2CO_3) not being fully reversed until higher temperature, at which point the cubic phase is fully formed.[17] This is further supported by the Pr phases, which did not undergo the low temperature phase transition (due to the H_2 synthesis) and did not have the pyrochlore impurity.

All $A_3Zr_2Li_7O_{12}$ (A = La, Pr, Nd) garnets had comparable phase transition temperatures (~600–650 °C). This was a little surprising given the significant reduction in cell volume across the series from La–Pr–Nd. In addition to little change in transition temperature there was also little change to the degree of tetragonality. Similarly little change was observed for the $A_3Hf_2Li_7O_{12}$ (A = La, Pr, Nd) series, although here the smaller Hf appears to have led to a small increase in the phase transition temperature to ~650–700 °C. Therefore, it appears that doping on the A site has minimal effect on the phase transition, hence suggesting a direct relation to cell volume is too simplistic, as volume considerably reduces across these series of samples.

In contrast, a comparison of the Zr and Hf samples suggest an influence of B site doping, and that this effect requires only a very minimal difference in ionic radius between substituents. Further support for the effect of B site doping is shown by comparing further samples substituted on this site, such as the Ce-doped LLZO and $LaSr_2B_2Li_7O_{12}$ (B = Nb, Ta) phase. These showed clear differences in transition temperature, at ~325–425 °C and 800–900 °C respectively (see Table 2), with the lower transition temperature corresponding to the presence of larger cations in the B site. In line with the transition temperature changes, this corresponded to similar (Ce doped LLZO) and increased ($LaSr_2B_2Li_7O_{12}$, B = Nb, Ta) degrees of tetragonality. A small increase in transition temperature was also observed for $LaSr_2Ta_2Li_7O_{12}$ compared the $LaSr_2Nb_2Li_7O_{12}$ which is similar to the use of Hf over Zr, mentioned above.

Overall the results were in contradiction with the common consensus; that the primary phase transition driving factor is the cell volume alone, as B site substitutions alter the cell volume considerably less than the A site substitutions yet give substantial differences in transition temperature, see Figure 3.[5k,11b] B site substitution in $LaSr_2B_2Li_7O_{12}$ also corresponds to larger increases in tetragonality. This indicates the B site plays a more key structural role in determining tetragonal distortion than the A site.[5k,9b] This is logical given the garnet framework polyhedra of corner linked BO_6 and XO_4 units, as these sites would structurally define the cell more than the interstitial A site. Therefore, B site substitutions would have a greater chance of changing any structure-based transition temperature. This is supported by the results for $LaSr_2B_2Li_7O_{12}$ (B = Nb, Ta) and $La_3Sn_2Li_7O_{12}$ (tetragonality 0.956, transition temperature 750–800 °C[9b]) whereby large differences in tetragonality (compared to A site substitutions) correspond to higher transition temperatures. Hence, the cell volume alone is not the ideal measure of transition temperature, rather the key numerical indicator could be considered the tetragonality which effectively mimics the thermodynamic energy barrier to overcome when transitioning from Li order to disorder.

However, only marginal changes in tetragonality are present for partial B site substitution with Ce-LLZO, yet significant changes in the transition are witnessed yet again. This further indicates the importance of the B site in dictating the temperature. In this respect, although only small changes in tetragonality are noted here, the work by Dong and co-workers (increasing Ce content up to 0.375) does indeed give noticeable changes in tetragonality (~0.980). This further suggests the B site is more responsible for the tetragonal distortion of the framework of the cell than the A site.[5k]

Analysis of bond distances shows the expected reduction in A–O bond lengths with the Zr/Hf samples, which correspond to decreased cell parameters arising from Ln contraction, see Table 3. A–O distances are marginally smaller for the Hf based series which corresponds to a slightly higher transition temperature. The bond distances of $LaSr_2Ta_2Li_7O_{12}$, which are most directly comparable in terms of cell volume with $La_3Hf_2Li_7O_{12}$, show very similar A–O bond lengths despite the addition of Sr, yet show considerable reductions in B–O distances, further indicating the importance of B site substitution on the garnet structure.

Hence, this suggests the degree of tetragonality is a more important indicator for the cell transition temperature, and that

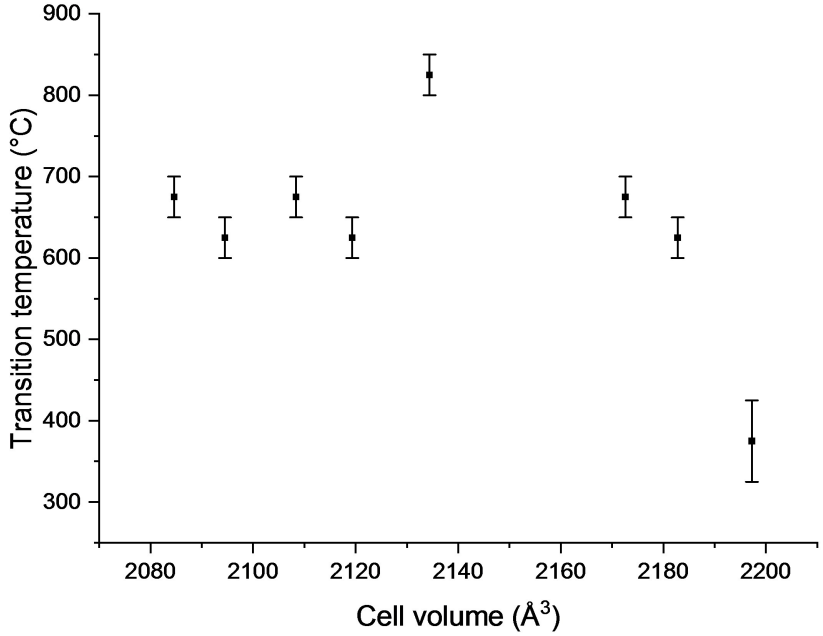

Figure 3. Room-temperature cell volume versus transition-temperature range, illustrating no clear trend.

this is controlled more by the B site composition, as A site substituents have much reduced lattice parameters yet the degree of tetragonality remains similar, as do the transition temperatures.

The temperature differential becomes even clearer when octahedral site ion radii versus the transition temperature range are shown, see Figure 4 and Table 5. This shows considerable difference in B site substituents compared to the A site (most A site doping results are superimposed over each other). Figure 4 shows a clear mathematical relationship as per equation 1, perhaps adding further evidence to octahedral site ion size being a key determining factor. Regression on Figure 4 yields

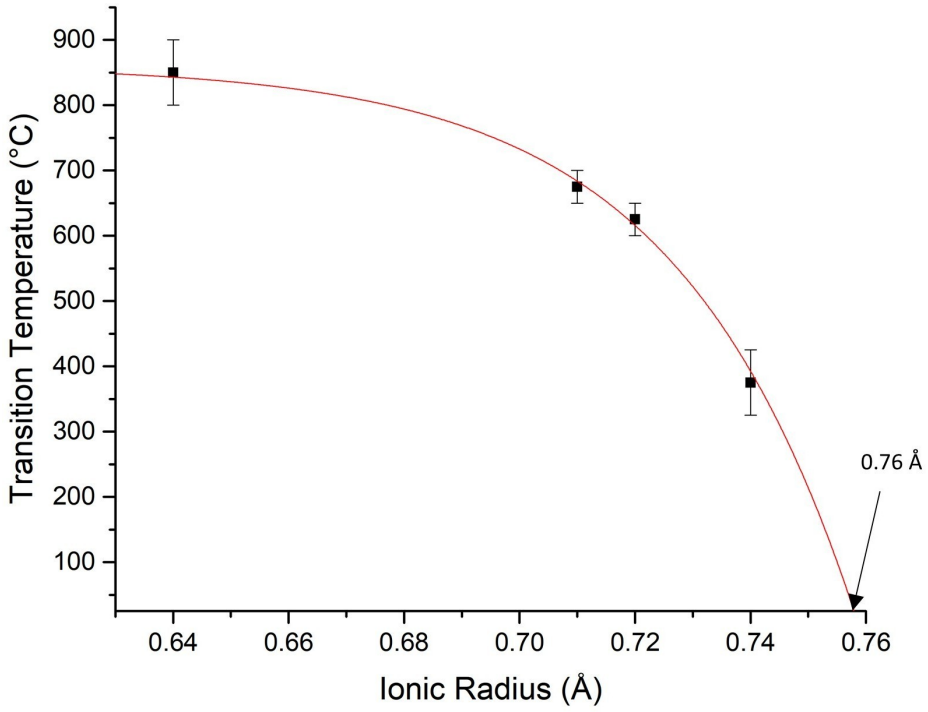

Figure 4. Octahedral site ion radii versus transition-temperature range, several ionic radii are similar and thus superimposed. The data was fit using an exponential function as per Equation (1); data suggests a room temperature cubic phase would require an average octahedral site ionic radius of 0.76 Å.

Table 5. Summary of octahedral site ionic radii for the series of Li_7-garnets studied. (For the Ce-doped garnet, where dual doping on the octahedral site is observed, a weight averaged value is used for the radius).

Garnet formula	Octahedral site ionic radii [Å]	Transition *T* range [°C]
$La_3Zr_{1.75}Ce_{0.25}Li_7O_{12}$	0.74	325–425
$La_3Zr_2Li_7O_{12}$	0.72	600–650
$Pr_3Zr_2Li_7O_{12}$	0.72	600–650
$Nd_3Zr_2Li_7O_{12}$	0.72	600–650
$La_3Hf_2Li_7O_{12}$	0.71	650–700
$Pr_3Hf_2Li_7O_{12}$	0.71	650–700
$Nd_3Hf_2Li_7O_{12}$	0.71	650–700
$LaSr_2Nb_2Li_7O_{12}$	0.64	800–900
$LaSr_2Ta_2Li_7O_{12}$	0.64	800–900

an extrapolated octahedral site radius which could enable room temperature (20 °C) stable cubic lithium garnet phases with the average B cation site size at approximately 0.76 Å.

$$y = y_0 + Ae^{R_0 x} \quad (1)$$

Equation (1). Exponential function with rate constant parameter which was used for fitting the data in Figure 4.

As such, attempts to increase Ce content beyond the 0.25 reported by Dong and co-workers were made, by employing dry room facilities. However, this led to Ce based impurities (see Figure 5), in addition to tetragonal LLZO, similar to the reports in the work.[5k] As employing larger 4+ ions than Ce is not feasible, co-doping strategies (such as Y/Nb or Sc/Nb) need to be considered to reach the octahedral radius of 0.76 Å. For example, a garnet with formula of $La_3YNbLi_7O_{12}$ yields an average octahedral site radius of 0.77 Å[72]. This was attempted by the standard solid-state route. While this did indeed yield a cubic phase, large Nb, Y and La oxide-based impurities were present, see Figure 6.

In terms of future work, a further factor that could be examined to alter the transition temperature is the oxygen site. This determination of the phase transition temperature via O site substitution has yet to be explored, although has been considered as potential room temperature cubic phase stabilisation prior[107]. However, assessment by Cl or F substitution with O on the phase transition temperature is complex, as high temperatures can easily remove the halogen dopant forming more thermodynamically stable by-products. Further correlative evidence could be found by investigating the transition temperature by changing the XO_4 sites, this may yield further confirmation of the controlling factors, but would not necessarily aid in cubic Li_7 phase formation.

Conclusion

It is suggested that the primary factor in the determination of the temperature of the tetragonal–cubic phase transition in the Li_7-garnet systems is the B site, which is suspected to arise from the fact that this cation helps to dictate the garnet framework structure, in contrast to the A site, which occupies the cavities within the framework of corner linked octahedra and tetrahe-

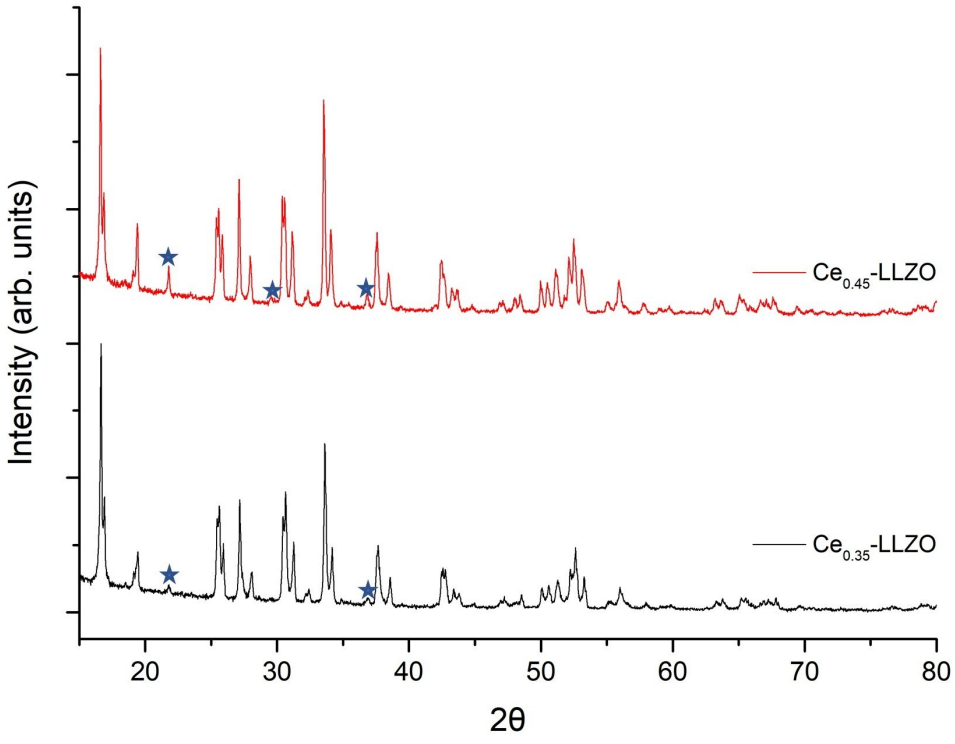

Figure 5. PXRD patterns for $La_3Zr_{2-x}Ce_xLi_7O_{12}$ ($x = 0.35, 0.45$) attempted by the standard solid-state route, leading to impurities for higher Ce levels. Blue stars mark the impurities.

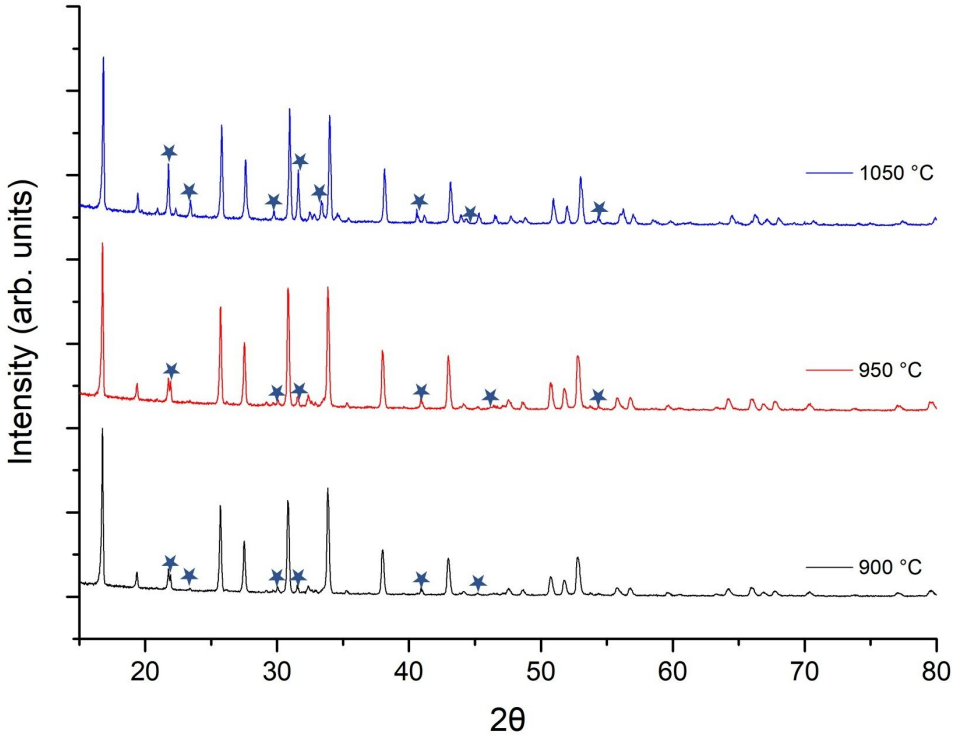

Figure 6. PXRD patterns for $La_3YNbLi_7O_{12}$ attempted by the standard solid-state route between 900–1050 °C showing a cubic garnet phase with additional impurities. Blue stars mark the impurities.

dra. This is illustrated by the fact that octahedral site doping showed significant changes to the transition temperature, whereas negligible changes were observed for A site doping. Changes can be correlated to the degree of tetragonality which appears to be dependent on B site dopant size, rather than the cell volume. This work shows that as the degree of tetragonality of the garnet increases, the transition temperature increases too. Therefore, it is hypothesized that the octahedral site is instrumental in determining the tetragonality of the phase, and hence doping at this site with larger cations is the best method in lowering the transition temperature. A similar affect could also be the case for doping in the XO_4 tetrahedra (which are also part of the garnet framework) and may help to explain the stability of Li site doping by Ga/Al and subsequent formation of the cubic phase.

Further work by neutron diffraction is required to clarify this relationship more accurately, however, once this phase transition is fully understood, it is hoped that Li_7 phases could be cubic at room temperature, thus enabling a higher conductivity SSE.

Acknowledgements

We would like to thank the University of Birmingham for the studentship funding of Mark Stockham.

Conflict of Interest

The authors declare no conflict of interest.

Keywords: lithium · lithium garnets · phase transition · solid-state structures · tetragonal phases

[1] a) M. Armand, J. M. Tarascon, *Nature* **2008**, *451*, 652; b) J. M. Tarascon, M. Armand, *Nature* **2001**, *414*, 359; c) Y. Zhu, X. He, Y. Mo, *ACS Appl. Mater. Interfaces* **2015**, *7*, 23685–23693.
[2] a) C.-X. Zu, H. Li, *Energy Environ. Sci.* **2011**, *4*, 2614–2624; b) V. A. Agubra, J. W. Fergus, *J. Power Sources* **2014**, *268*, 153–162; c) J. G. Kim, B. Son, S. Mukherjee, N. Schuppert, A. Bates, O. Kwon, M. J. Choi, H. Y. Chung, S. Park, *J. Power Sources* **2015**, *282*, 299–322; d) X. Xiong, Q. Zhou, Y. Zhu, Y. Chen, L. Fu, L. Liu, N. Yu, Y. Wu, T. van Ree, *Energy Fuels* **2020**, *34*, 10503–10512; e) V. Etacheri, R. Marom, R. Elazari, G. Salitra, D. Aurbach, *Energy Environ. Sci.* **2011**, *4*, 3243–3262; f) G. Huang, J. Wang, X. Zhang, *ACS Cent. Sci.* **2020**, *6*, 2136–2148.
[3] J. Li, C. Ma, M. Chi, C. Liang, N. J. Dudney, *Adv. Energy Mater.* **2015**, *5*, 1401408.
[4] a) B. Dong, J. Yan, B. Walkley, K. K. Inglis, F. Blanc, S. Hull, A. R. West, *Solid State Ionics* **2018**, *327*, 64–70; b) V. Thangadurai, S. Narayanan, D. Pinzaru, *Chem. Soc. Rev.* **2014**, *43*, 4714–4727; c) W. D. Richards, L. J. Miara, Y. Wang, J. C. Kim, G. Ceder, *Chem. Mater.* **2016**, *28*, 266–273; d) S. Ramakumar, C. Deviannapoorani, L. Dhivya, L. S. Shankar, R. Murugan, *Prog. Mater. Sci.* **2017**, *88*, 325–411; e) Q. Zhao, S. Stalin, C.-Z. Zhao, L. A. Archer, *Nat. Rev. Mater.* **2020**, *5*, 229–252; f) C. Li, Z.-y. Wang, Z.-j. He, Y.-j. Li, J. Mao, K.-h. Dai, C. Yan, J.-c. Zheng, *Sustainable Mater. Technol.* **2021**, *29*, e00297.
[5] a) C. Bernuy-Lopez, W. Manalastas, J. M. Lopez del Amo, A. Aguadero, F. Aguesse, J. A. Kilner, *Chem. Mater.* **2014**, *26*, 3610–3617; b) B. Dong, L. L. Driscoll, M. P. Stockham, E. Kendrick, P. R. Slater, *Solid State Ionics* **2020**, *350*, 115317; c) B. Dong, M. P. Stockham, P. A. Chater, P. R. Slater, *Dalton Trans.* **2020**, *49*, 11727–11735; d) M. P. Stockham, B. Dong, Y. Ding, Y. Li, P. R. Slater, *Dalton Trans.* **2020**; e) M. P. Stockham, B. Dong, M. S. James,

Y. Li, Y. Ding, P. R. Slater, *Dalton Trans.* **2021**, *50*, 2364–2374; f) J. L. Allen, J. Wolfenstine, E. Rangasamy, J. Sakamoto, *J. Power Sources* **2012**, *206*, 315–319; g) S.-W. Baek, J.-M. Lee, T. Y. Kim, M.-S. Song, Y. Park, *J. Power Sources* **2014**, *249*, 197–206; h) H. Buschmann, J. Dölle, S. Berendts, A. Kuhn, P. Bottke, M. Wilkening, P. Heitjans, A. Senyshyn, H. Ehrenberg, A. Lotnyk, V. Duppel, L. Kienle, J. Janek, *Phys. Chem. Chem. Phys.* **2011**, *13*, 19378–19392; i) Y. Chen, E. Rangasamy, C. Liang, K. An, *Chem. Mater.* **2015**, *27*, 5491–5494; j) E. J. Cheng, A. Sharafi, J. Sakamoto, *Electrochim. Acta* **2017**, *223*, 85–91; k) B. Dong, S. R. Yeandel, P. Goddard, P. R. Slater, *Chem. Mater.* **2020**, *32*, 215–223; l) K. Fu, Y. Gong, B. Liu, Y. Zhu, S. Xu, Y. Yao, W. Luo, C. Wang, S. Lacey, J. Dai, Y. Chen, Y. Mo, E. Wachsman, L. Hu, *Sci. Adv.* **2017**, *3*, e1601659; m) C. Galven, J.-L. Fourquet, M.-P. Crosnier-Lopez, F. Le Berre, *Chem. Mater.* **2011**, *23*, 1892–1900; n) Y. X. Gao, X. P. Wang, W. G. Wang, Q. F. Fang, *Solid State Ionics* **2010**, *181*, 33–36; o) M. Huang, A. Dumon, C.-W. Nan, *Electrochem. Commun.* **2012**, *21*, 62–64; p) H. M. Kasper, *Inorg. Chem.* **1969**, *8*, 1000–1002; q) R. Murugan, V. Thangadurai, W. Weppner, *Angew. Chem. Int. Ed.* **2007**, *46*, 7778–7781; *Angew. Chem.* **2007**, *119*, 7925–7928; r) S. Narayanan, F. Ramezanipour, V. Thangadurai, *J. Phys. Chem. C* **2012**, *116*, 20154–20162; s) M. P. O'Callaghan, D. R. Lynham, E. J. Cussen, G. Z. Chen, *Chem. Mater.* **2006**, *18*, 4681–4689; t) J. Percival, D. Apperley, P. R. Slater, *Solid State Ionics* **2008**, *179*, 1693–1696; u) J. Percival, E. Kendrick, P. R. Slater, *Solid State Ionics* **2008**, *179*, 1666–1669; v) F. M. Pesci, A. Bertei, R. H. Brugge, S. P. Emge, A. K. O. Hekselman, L. E. Marbella, C. P. Grey, A. Aguadero, *ACS Appl. Mater. Interfaces* **2020**, *12*, 32806–32816; w) E. Rangasamy, J. Wolfenstine, J. Sakamoto, *Solid State Ionics* **2012**, *206*, 28–32; x) V. Thangadurai, H. Kaack, W. J. F. Weppner, *J. Am. Ceram. Soc.* **2004**, *86*, 437–440; y) R. Wagner, G. J. Redhammer, D. Rettenwander, A. Senyshyn, W. Schmidt, M. Wilkening, G. Amthauer, *Chem. Mater.* **2016**, *28*, 1861–1871.

[6] a) G. V. Alexander, S. Patra, S. V. Sobhan Raj, M. K. Sugumar, M. M. Du Din, R. Murugan, *J. Power Sources* **2018**, *396*, 764–773; b) R. H. Brugge, F. M. Pesci, A. Cavallaro, C. Sole, M. A. Isaacs, G. Kerherve, R. S. Weatherup, A. Aguadero, *J. Mater. Chem. A* **2020**, *8*, 14265–14276; c) L. Cheng, E. J. Crumlin, W. Chen, R. Qiao, H. Hou, S. Franz Lux, V. Zorba, R. Russo, R. Kostecki, Z. Liu, K. Persson, W. Yang, J. Cabana, T. Richardson, G. Chen, M. Doeff, *Phys. Chem. Chem. Phys.* **2014**, *16*, 18294–18300; d) F. Flatscher, M. Philipp, S. Ganschow, H. M. R. Wilkening, D. Rettenwander, *J. Mater. Chem. A* **2020**, *8*, 15782–15788.

[7] a) J. Wang, G. Huang, X.-B. Zhang, *Batteries & Supercaps* **2020**, *3*, 1006–1015; Supercaps **2020**, 3, 1006–1015; b) George V. Alexander, N. C. Rosero-Navarro, A. Miura, K. Tadanaga, R. Murugan, *J. Mater. Chem. A* **2018**, *6*, 21018–21028; c) J. Wang, Y. Yin, T. Liu, X. Yang, Z. Chang, X. Zhang, *Nano Res.* **2018**, *11*, 3434–C3441; d) J. Wang, G. Huang, J.-M. Yan, J.-L. Ma, T. Liu, M.-M. Shi, Y. Yu, M.-M. Zhang, J.-L. Tang, X.-B. Zhang, *Natl. Sci. Rev.* **2021**, *8*; e) J. Wang, G. Huang, K. Chen, X.-B. Zhang, *Angew. Chem. Int. Ed.* **2020**, *59*, 9382–9387; *Angew. Chem.* **2020**, *132*, 9468–9473.

[8] a) A. F. Wells, *Structural Inorganic Chemistry*, Clarendon Press, London, **1984**, p. 189; b) E. J. Cussen, T. W. S. Yip, *J. Solid State Chem.* **2007**, *180*, 1832–1839.

[9] a) D. Mazza, *Mater. Lett.* **1988**, *7*, 205–207; b) J. Percival, E. Kendrick, R. I. Smith, P. R. Slater, *Dalton Trans.* **2009**, 5177–5181; c) E. J. Cussen, *Chem. Commun.* **2006**, 412–413.

[10] a) C. A. Geiger, E. Alekseev, B. Lazic, M. Fisch, T. Armbruster, R. Langner, M. Fechtelkord, N. Kim, T. Pettke, W. Weppner, *Inorg. Chem.* **2011**, *50*, 1089–1097; b) J. Awaka, N. Kijima, H. Hayakawa, J. Akimoto, *J. Solid State Chem.* **2009**, *182*, 2046–2052; c) J. Awaka, N. Kijima, K. Kataoka, H. Hayakawa, K.-i. Ohshima, J. Akimoto, *J. Solid State Chem.* **2010**, *183*, 180–185.

[11] a) N. Bernstein, M. D. Johannes, K. Hoang, *Phys. Rev. Lett.* **2012**, *109*, 205702; b) F. Chen, J. Li, Z. Huang, Y. Yang, Q. Shen, L. Zhang, *J. Phys. Chem. C* **2018**, *122*, 1963–1972.

[12] G. Larraz, A. Orera, M. L. Sanjuán, *J. Mater. Chem. A* **2013**, *1*, 11419–11428.

[13] B. Toby, R. Dreele, *J. Appl. Crystallogr.* **2013**, *46*, 544–549.

[14] a) Y. Wang, W. Lai, *J. Power Sources* **2015**, *275*, 612–620; b) M. Matsui, K. Takahashi, K. Sakamoto, A. Hirano, Y. Takeda, O. Yamamoto, N. Imanishi, *Dalton Trans.* **2014**, *43*, 1019–1024; c) I. Kokal, M. Somer, P. H. L. Notten, H. T. Hintzen, *Solid State Ionics* **2011**, *185*, 42–46.

[15] S. Toda, K. Ishiguro, Y. Shimonishi, A. Hirano, Y. Takeda, O. Yamamoto, N. Imanishi, *Solid State Ionics* **2013**, *233*, 102–106.

[16] M. A. Howard, O. Clemens, K. S. Knight, P. A. Anderson, S. Hafiz, P. M. Panchmatia, P. R. Slater, *J. Mater. Chem. A* **2013**, *1*, 14013–14022.

[17] A. Paolella, W. Zhu, G. Bertoni, S. Savoie, Z. Feng, H. Demers, V. Gariepy, G. Girard, E. Rivard, N. Delaporte, A. Guerfi, H. Lorrmann, C. George, K. Zaghib, *ACS Appl. Energ. Mater.* **2020**, *3*, 3415–3424.

Manuscript received: September 21, 2021
Accepted manuscript online: December 1, 2021
Version of record online: December 16, 2021

9. High entropy lithium garnets – Testing the compositional flexibility of the lithium garnet system

9.1. PUBLICATION

High entropy lithium garnets – Testing the compositional flexibility of the lithium garnet system

Article information : M. P. Stockham, B. Dong and P. R. Slater, *Journal of Solid State Chemistry*, 2022, **308**, 122944.

Submitted: 09/12/2021

Accepted: 25/01/2021

Author contributions: M. P. Stockham: conceptualisation, experimental and characterisation work, method development, writing and review, formal analysis, investigation. B. Dong: Data curation, investigation, P. R. Slater: lead supervision, conceptualisation, writing – review & editing.

Journal of Solid State Chemistry 308 (2022) 122944

Contents lists available at ScienceDirect

Journal of Solid State Chemistry

journal homepage: www.elsevier.com/locate/jssc

High entropy lithium garnets – Testing the compositional flexibility of the lithium garnet system

Mark P. Stockham *, Bo Dong, Peter R. Slater **

School of Chemistry, University of Birmingham, Birmingham, B15 2TT, UK

ARTICLE INFO

Keywords:
Lithium garnet
High entropy
Solid state batteries
Solid state electrolytes

ABSTRACT

There is a pressing need for higher energy density, safer batteries for electric vehicles and grid energy storage. The current consensus is that these batteries need to be replaced with fully solid equivalents, however the discovery of a suitable solid state electrolyte has proven troublesome. Of the promising materials, lithium garnets are popular due to their wide electrochemical window, good ionic mobility (>0.1 mS cm^{-1}) and compatibility with Li metal. However, numerous issues remain relating to interfacial resistance, time consuming and energy demanding synthesis and special handling requirements to ensure the best performing membranes. Of these challenges, little work has been done on the effect of entropy in the cubic lithium garnet systems, for example by addition of multiple elements on multiple sites. Such strategies have given interesting results in other areas (e.g. battery cathodes, metal alloys) and could well enable better performing membranes by increasing the, already high, disorder and take advantage of the numerous dopants reports which often singularly enable favourable properties (such as increased density, higher conductivity, lower interfacial resistance). Herein we test the compositional flexibility of the lithium garnet system with a 9 ($Ga_{0.2}Li_{5.75}La_{2.5}Nd_{0.5}Nb_{0.65}Ce_{0.1}Zr_1Ti_{0.25}O_{12}$) and 11 ($Ga_{0.2}Li_{5.75}La_{2.5}Nd_{0.5}Nb_{0.35}Ta_{0.3}Ce_{0.1}Zr_{0.75}Hf_{0.25}Ti_{0.25}O_{12}$) element system. Surprisingly, we did not find the limit of the garnet system, rather it was shown that (outside of the stoichiometric weighing) these systems were easy to synthesise, had high room temperature conductivity (0.2 mS cm^{-1}), and high density even when processed in air.

1. Introduction

Lithium solid state batteries are considered the holy grail of energy storage, encompassing higher energy densities and increased safety compared with conventional battery systems [1–7]. This, therefore, is thought to enable the ability to meet the power demands of modern society, especially in relation to electric vehicles and effective grid energy storage. Lithium-ion batteries (LIBs) are the energy storage system of choice, however currently they have significant drawbacks relating to electrolyte toxicity and flammability (commonly $LiPF_6$ in carbonate-based solvents). These electrolytes also give narrow electrochemical windows and lead to dendrite growth issues with Li metal anodes [1,2,8–10]. The electrolyte, however, remains the only component left to be replaced with a solid counterpart, and its replacement is the primary challenge in realising the next-generation energy storage [5,11–13].

The replacement of the electrolyte with a solid equivalent has proved exceptionally challenging, and of the available inorganic materials analysed (ranging from sulphides and oxides) most have either poor ionic conductivity or a narrow electrochemical window. Further challenges are also observed amongst these systems, with harder (oxide) materials exhibiting poor solid-solid contact at the electrode/electrolyte interface, while softer (sulphide) materials have better contact but have lower upper voltage stability along with extreme moisture sensitivity. Solid state electrolytes (SSE) also have complex, often non-scalable, synthesis strategies and are commonly analysed in a pellet type form which is of little commercial use. Hence, much work is still required.

Of the available SSEs, lithium garnets have seen high interest within the research community. Lithium garnets offer high conductivity (>0.1 mS cm^{-1}), a wide electrochemical window and chemical compatibility with Li metal. However, garnets are time consuming to synthesise and purify, need special requirements to obtain the highest performing membranes, suffer from high interfacial resistance (a large portion of which relates to Li^+/H^+ exchange) and have had issues transitioning to the thin film regime [14–20]. Of late, there has no reports, to our knowledge, of new high entropy garnets (HEG), which are designed to

* Corresponding author. School of Chemistry, University of Birmingham, Birmingham, B15 2TT, UK.
** Corresponding author. School of Chemistry, University of Birmingham, Birmingham, B15 2TT, UK.
E-mail address: mps846@student.bham.ac.uk (M.P. Stockham).

https://doi.org/10.1016/j.jssc.2022.122944
Received 9 December 2021; Received in revised form 20 January 2022; Accepted 25 January 2022
Available online 29 January 2022

maximise disorder and increase performance, thus opening new engineering approaches to garnet battery challenges.

A typical lithium garnet is cubic with space group Ia $\overline{3}$ d, such as $Li_5La_3Nb_2O_{12}$, with the exception of $Li_{7-x}Ga_xLa_3Zr_2O_{12}$ (Ga-LLZO) which is thought to adopt I4 $\overline{3}$ d type symmetry [21–24]. Li content needs to be > 5 per formula unit (*pfu*) to form a highly conductive garnet system but must remain <7 Li *pfu* to maintain the cubic structure. Those systems with 7 li *pfu*, such as $Li_7La_3Zr_2O_{12}$ (LLZO), form the thermodynamically stable $I4_1/acd$ system which is poorly conductive due to Li ordering reducing charge carrier mobility [21,25,26]. Therefore, most garnet reports concentrate on Li contents between 6 and 6.6 *pfu*, with aims to increase Li content in Li_5 based systems or Li removal with Li_7 systems. This is usually seen in the form of $Li_{5+x}La_3B_{2-x}M_xO_{12}$ (B = Nb, Ta, Zr, Hf, M = Pr, Ce, Ti, Ta, Nb) or $Li_{7-x}M_xLa_3B_2O_{12}$ (M = Al, Ga, Ge, B = Zr, Hf) [14,19,27–34]. Such strategies maintain the disordered Li sublattice and hence high conductivity [21].

Cubic lithium garnet systems, especially those with high Li content, may be considered highly entropic systems due to the Li disorder. It is, therefore, logical to conclude that increased entropy, via multiple dopant addition to several sites, may improve performance. In other areas, there are reports of high entropy alloys (≥ 5 elements), where such strategies can lead to materials with exceptional mechanical, magnetic, and electrical properties [35–44]. Such increasingly complex solid solutions were initially suggested to be stabilised by the entropic contribution to the total free energy and thus overcoming the enthalpic contribution [38], although it is now thought to be somewhat more complex [39]. The high entropy approach has also recently been explored with high entropy cathode materials (batteries and solid oxide fuel cells) which show increased capacity, improved ionic transport and superior rate capability [45–48]. This, therefore, shows the applicability of this approach to the energy storage field which could be, perhaps, quite a harmonious strategy if used with something as disordered as the cubic lithium garnets – whereby the deliberate entropic increases could be considered energetically favourable.

Herein we apply these concepts to lithium garnet materials with the idea that deliberate entropic increases could enable better performing garnet materials. This work aims to test the compositional flexibility of the garnet systems to enable strategic exploitation of numerous favourable dopant properties (e.g. increased density, improved conductivity) simultaneously. We designed two garnet systems based upon the commonly reported dopants elsewhere, with Zr (primary component of most garnet research), Nb and Ta (from the first garnet electrolyte report) [49], and Ti (Li dendrite suppression) [50]. We also encompass our prior work with Ce (increased conductivity, lower interfacial resistance), Ga/Nd (low interfacial resistance, high density) and Hf (possible increased electrochemical stability compared to Zr) [32,51–55]. Ga was also added to promote a symmetry alteration to the acentric I4 $\overline{3}$ d space group, as the exceptional performance of Ga-LLZO has been suggested to arise from the unique symmetry [24]. This, however, reduced Li content to 5.75 *pfu* (efforts to form a $Ga_{0.15}$ system and so prepare a $Li_{6.05}$ system were unsuccessful, see SI). The synthesised formulas were $Ga_{0.2}Li_{5.75}La_{2.5}Nd_{0.5}Nb_{0.65}Ce_{0.1}Zr_1Ti_{0.25}O_{12}$ (HEG1) and $Ga_{0.2}Li_{5.75}La_{2.5}Nd_{0.5}Nb_{0.35}Ta_{0.3}Ce_{0.1}Zr_{0.75}Hf_{0.25}Ti_{0.25}O_{12}$ (HEG2).

These materials, despite their considerable complexity, were easy to synthesise (outside of weighing of the chemicals) and showed good conductivity of ~0.2 mS cm^{-1} at room temperature, an impressive figure for a garnet system with less than 6 Li per formula unit and shows the dopant incorporation is favourable. This shows the tolerance of the garnet system to considerable doping strategies beyond the common single or co-doped route, the latter of which has already been suggested optimal for Li garnet performance due to multiple site disorder [56]. Given the success, there are multiple possible modifications that can be made in the future. It is hoped such strategies will open up new possibilities and enable fresh approaches to the engineering challenges of solid state batteries.

2. Methods

2.1. Synthesis

HEG1 and HEG2 were prepared via the solid-state route from stochiometric quantities of Li_2CO_3, Nd_2O_3, La_2O_3, Nb_2O_5, Ta_2O_5, ZrO_2, HfO_2, TiO_2, CeO_2 and Ga_2O_3 in air. A 40% mol excess of lithium was added to compensate for lithium loss during high temperature sintering. All powders were ball milled for 1 h with ZrO_2 balls (500 rpm) with hexane. The powder was then removed, dried and heated to 950 °C (12 h) at 5 °C min^{-1}.

2.2. Characterisation

Scanning electron microscopy (SEM) was performed on a Hitachi TM4000plus instrument. Elemental analysis was undertaken via an AZtecOne X-stream2 energy dispersive X-ray (EDX) spectrometer. Samples were prepared by applying the powders to a carbon tape and analysed at 15 kV in backscattered electron mode. Phase analysis was performed by X-ray diffraction (XRD) using a Bruker D8 diffractometer with a Cu X-ray source, with a step size of 0.02° and a total scan time of 12h. Experimental pellet densities were determined gravimetrically and compared to theoretical values from Rietveld refinement results (performed using the GSAS II software) [57].

2.3. Impedance spectroscopy

HEG1 and HEG2 were pelletised and densified in a dry room with a dewpoint between −45 °C and −64 °C (the elimination of humidity is known to be beneficial for high quality samples as moisture is an issue with Li garnet systems) [58–60]. Pellets were prepared as follows: approx. 10 mm diameter pellets were pressed to ca. 1.5 tonnes and heated to 1150 °C for 13 h (2 °C min^{-1}). Sacrificial powders were used to protect pellets from Al contamination from the Al_2O_3 crucible. Post-sintering, the pellets were polished and sputtered with Au for room temperature impedance spectroscopy measurements, which were performed with a Solartron 1260 impedance analyser from 1 Hz to 10 MHz with a 20 mV potential. All variable temperature measurements were undertaken from 25 to 117 °C. Variable temperature measurements required painting the pellet with Au electrodes and attaching of Au wires. The pellet was then heated (in air) to 800 °C (1h) to cure the Au paste. The pellets were then air quenched to room temperature from >700 °C (to limit H^+/Li^+ exchange [61–63]).

2.4. Cell assembly

All cell tests were performed on a biologic SP50 instrument. Li|HEG|Li symmetric cells were assembled in an Ar glove box. Pellets (~1 mm thickness) were polished using silicon carbide sandpaper from 240 to 4000 grit, then lithium metal foil was applied to each side of the pellet. The cell was then heated to 175 °C under a constant pressure for 1 h using a steel 3-way G clamp (see SI) and were secured under light pressure via hand tightening the clamp. The cell was subsequently secured in a MTI split test cell. Cells were examined via impedance spectroscopy before cell testing from 10 MHz to 0.1 Hz with a 20 mV potential on a Solartron 1260 impedance analyser. These symmetric cells were then cycled under constant current conditions at various current densities to assess cycling stability at 30 °C in a Genlab classic oven. Each cell cycle was 30 min (15 min each for Li stripping and plating), with a 10 s rest in between. At the lowest current density (12.5 μA cm^{-2}) the cell was cycled 200 times. At all other current densities cells were cycled 300 times. The temperature was monitored additionally via a Fluke 51 II external thermocouple.

3. Results and discussion

3.1. X-ray diffraction

The PXRD patterns of HEG1 and HEG2 are available in Fig. 1 and both were assumed to adopt the Ia $\overline{3}$ d type symmetry, although some small peaks were present in the latter ~22 θ. This peak was not well resolved and absent within HEG1, hence is ascribed to minor amounts of unreacted Li_2CO_3. Therefore, both phases were assumed to be Ia $\overline{3}$ d. Both systems demonstrate near phase pure symmetry, with some very minor background peaks present especially in HEG2, see Fig. 1. These relate to small Li–Ti–O and Li–Nb–O based impurities, however, when the material was heated to densify the pellet, these were readily removed and gave phase pure garnet material. This, therefore, indicates slightly longer sintering times are required for the powder. See Fig. 2.

Rietveld refinements were based upon the structural model from Hamao et al. (Ta-LLZO) [64]. The I4 $\overline{3}$ d model from Wagner et al. was also considered for the HEG2 pattern but the R factors were similar, so in the final refinement the former model was used for both [24]. The similarities in scattering factor on both the Ln site (La, Nd) and, for the most part, the B site (Ti, Zr, Nb, Ta, Hf, Ce) preclude the possibility of refining fractional occupancies. Although Ti and Ce are noticeable exclusions and could be refined, the inability to assess which corresponding B site element changes makes this impractical. Therefore, all elements were set to their intended ratios and not refined further. An example refinement is available in Fig. 3.

Lattice parameters for both systems were smaller than reports of other cubic garnet systems, such as. Ga/Al-LLZO (~13 Å) or Ta-LLZO (~12.94 Å) This corresponds to Ln contraction arising from Nd substitution, see Table 1. HEG2 has an especially high relative density (94%) which is suspected to arise from the Ln contraction and the Ga dopant, as we have shown prior [51]. This, therefore, confirms dopant property exploitation. HEG1, however, is somewhat lower (88%). This could indicate that density has increased with increased entropy, but perhaps is more likely related to the Ta and/or Hf dopants in HEG2. A more accurate understanding of such complex systems will not be a trivial task and will require synchrotron-based techniques and/or neutron diffraction, to more fully understand how substitution to this level affects the local structure.

XRD of HEG2 in pelletised form confirmed annealing removed the small impurities, as marked in Fig. 1. The XRD pattern showed formation of a phase pure product, with Rietveld refinements showing a small increase in lattice parameters to 12.8772(1) Å. Hence the minor background peaks are thought to relate to insufficient sintering time and unreacted Li_2CO_3. This was confirmed when HEG2 was re-synthesised and shown to require 14 h at 950 °C for phase purity, see SI. This is somewhat surprising as even singularly doped garnets (such as Al-LLZO, Ga-LLZO and Ta-LLZO) often suffer from synthesis strategies that require multiple grinding and heat treatment steps. Whereas HEG1 and HEG2 were pure immediately and on the very first synthesis (and remained easy to form upon repeat). It is, therefore, shown that compositional complexity of the garnet system aids in synthesis, however, comes at the cost of arduous weighing of the chemicals. Furthermore, with HEG1, attempts were made to reduce Ga content to 0.15 *pfu* and so prepare $Ga_{0.2}Li_{5.75}La_{2.5}Nd_{0.5}Nb_{0.65}Ce_{0.1}Zr_1Ti_{0.25}O_{12}$ (HEG1A). This was unsuccessful, showing multiple unknown impurities which were unable to be removed by further regrinding and heating, see SI.

3.2. SEM/EDX

The phase pure powder and pellet were subsequently analysed via SEM and EDX to assess elemental composition. Considering the similarities between the two systems only the more complex of the two was analysed, HEG2. The samples were analysed on a carbon tape in secondary electron mode (pellet), see Fig. 4. The EDX shows a mostly homogenous elemental distribution, with all elements detected (excluding Li) across the analysed sample. The EDX data suggests some areas of increased Ga concentration, which is in line with our own work on $Ga_{0.2}Li_{6.4}Nd_3Zr_2O_{12}$ [20,51], indicating further dopant exploitation will be achieved when assessed in symmetry cell format (see later) [52,65]. Outside of this, no Al contamination from the Al_2O_3 crucible was detected, despite no protection during sintering. Back scattered electron

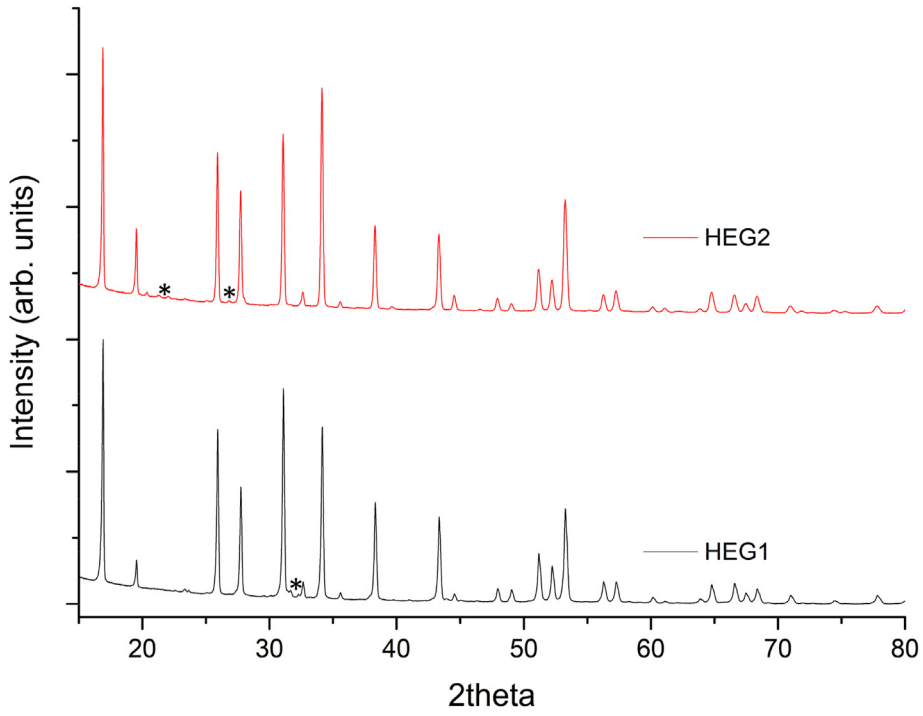

Fig. 1. PXRD patterns of HEG1 and HEG2, minor background impurities marked with stars and relate to Li based impurities which were removed upon annealing or sintering for 14h (rather than 12h). See SI. Both phases were indexed on Ia $\overline{3}$ d type symmetry.

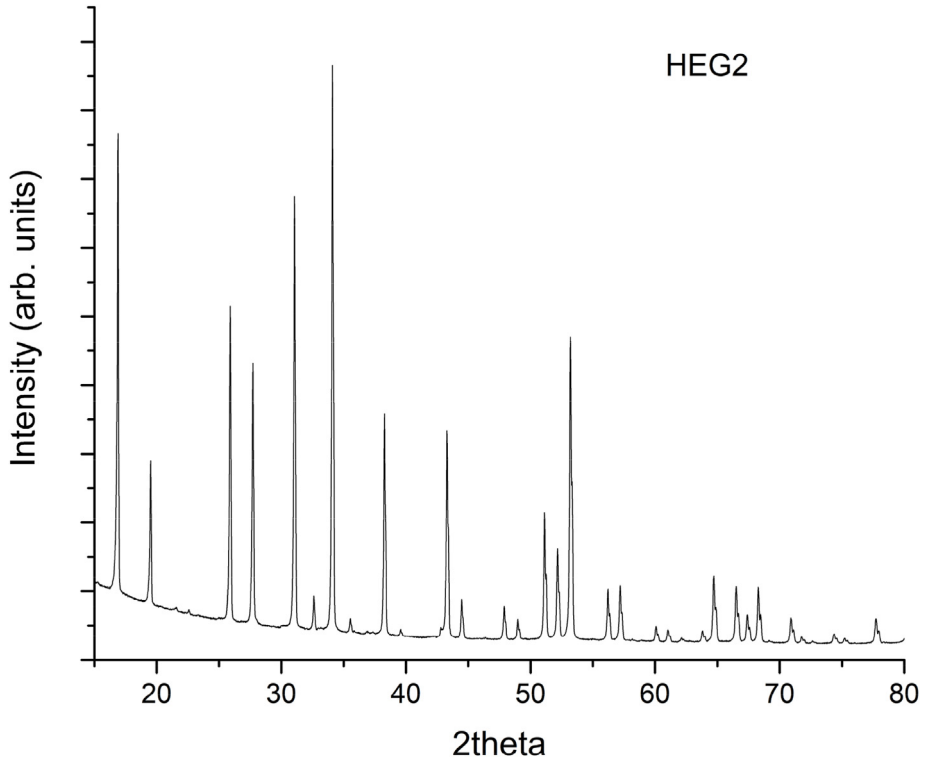

Fig. 2. PXRD pattern HEG2 post pellet densification at 1150 °C, showing removal of minor impurities the phase was indexed on Ia $\bar{3}$ d type symmetry and had a small lattice parameter increase when compared Fig. 1. Although an additional peak remains which could indicate I4 $\bar{3}$ d type symmetry refinements based on either crystal system yield highly similar lattice parameters, hence only Ia$\bar{3}$ d results were tabulated.

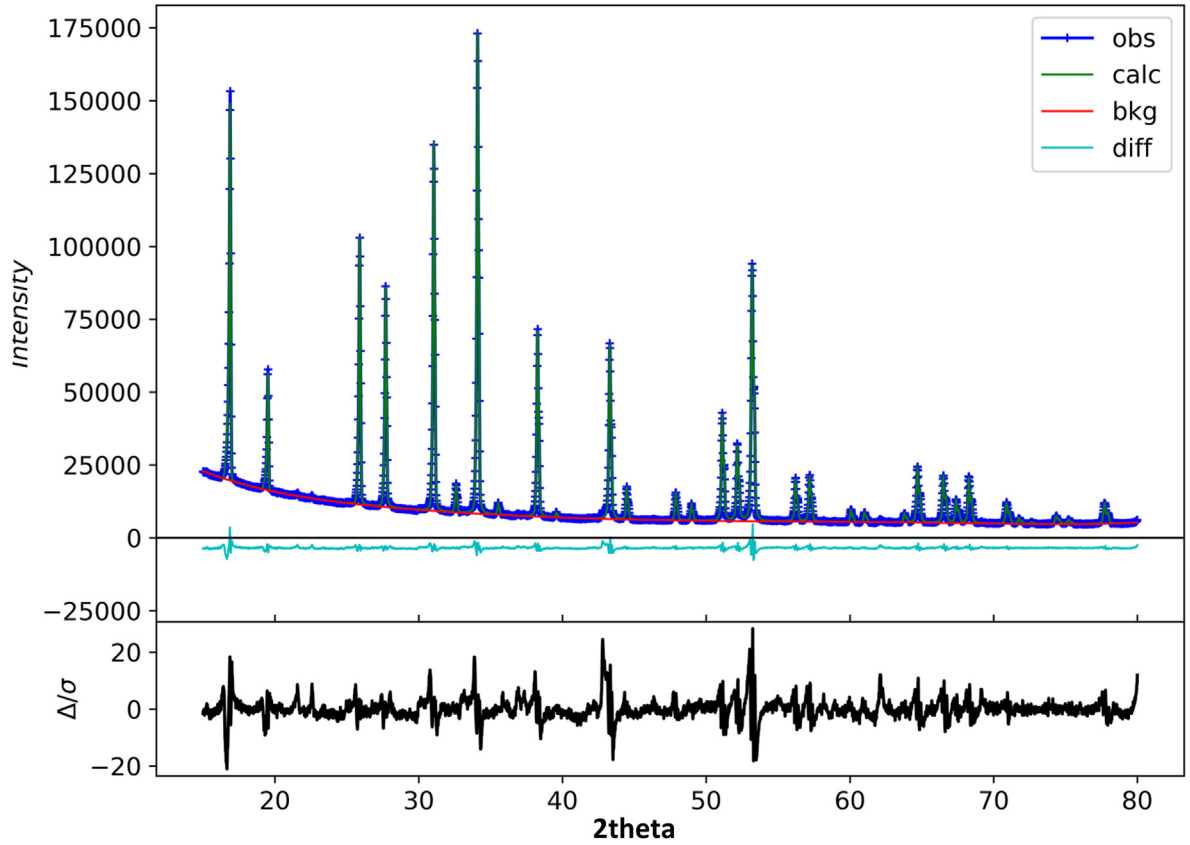

Fig. 3. Example Rietveld refinement of HEG2 based on the structural model of Ta-LLZO from Hamao et al. [64].

Table 1
Rietveld refinement and impedance spectroscopy data. Conductivity values for HEG1 take into consideration the additional grain boundary buried contribution. Further information on the calculation of capacitance and fitted values can be found in the SI.

Sample	Lattice parameters (Å)	σ_{total} (mS cm^{-1})	C_{bulk} (F/cm)	ε_r	C_{gb}(F/cm)	ρ_{rel} (%)
HEG1	12.8624(2)	0.1	5.2×10^{-12}	59	8.5×10^{-8}	88
HEG2	12.8720(3)	0.2	4.7×10^{-12}	53	–	94

images and EDX images of the powder are available in the SI, these show more prominent Ga dopant exsolution.

3.3. Impedance spectroscopy

HEG1 and HEG2 were Au Sputtered and analysed via impedance spectroscopy at room temperature (25 °C) to assess conductivity. Nyquist impedance plots for both samples are shown in Fig. 5a and b. For the less dense HEG1 (Fig. 5a) a clear bulk response is present, however there is a partially buried second response, likely relating to the grain boundary resistance. This is evidenced by the equivalent circuit, which required

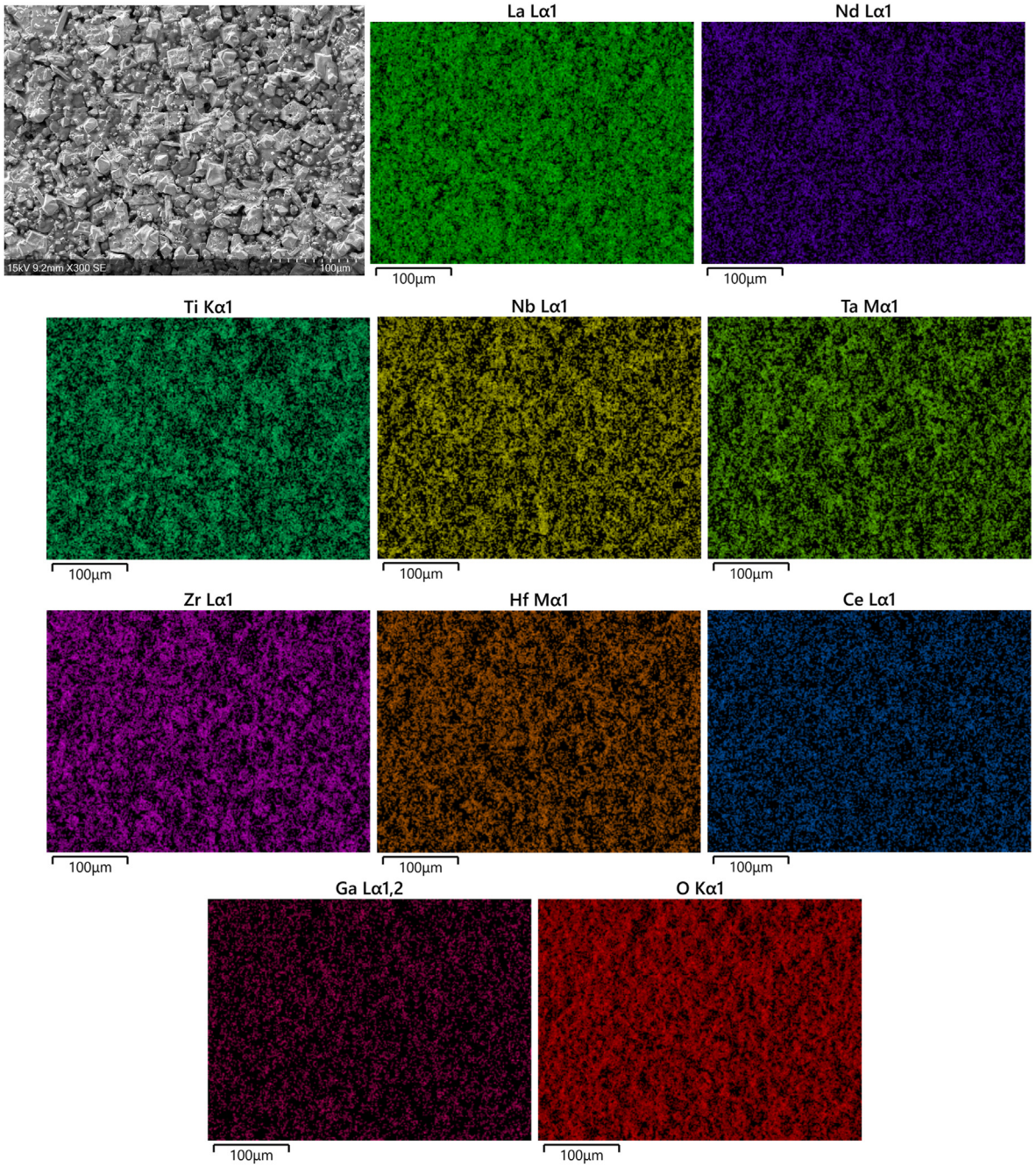

Fig. 4. SEM and EDX of HEG2 pellet surface, showing a relatively homogenous elemental distribution of HEG2 with some areas of higher elemental concentrations, particularly Ga.

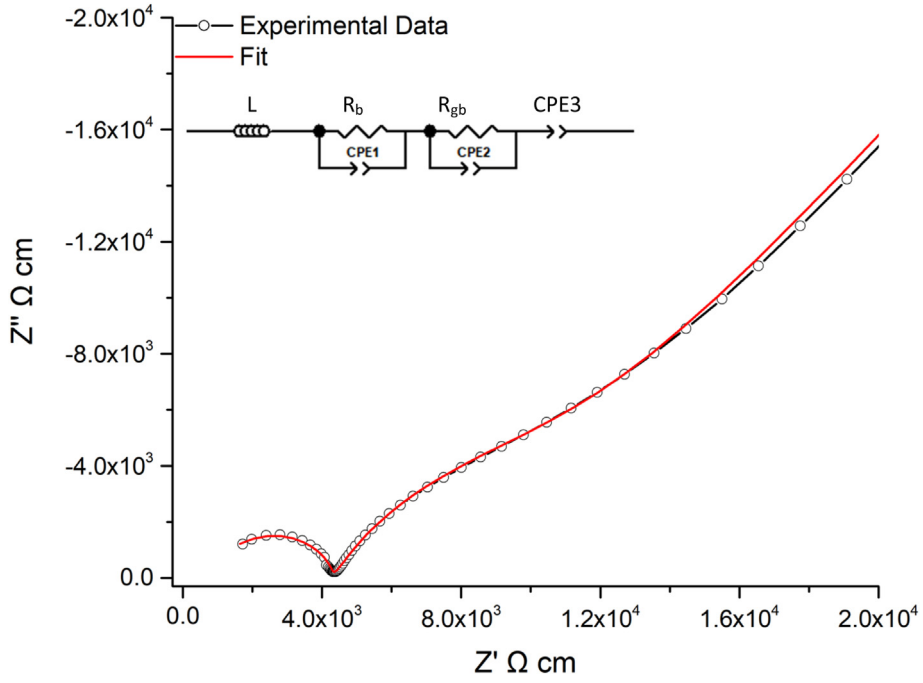

Fig. 5a. HEG1 Nyquist plot at 25 °C demonstrating buried grain boundary contribution. This was fit to the equivalent circuit in the top left.

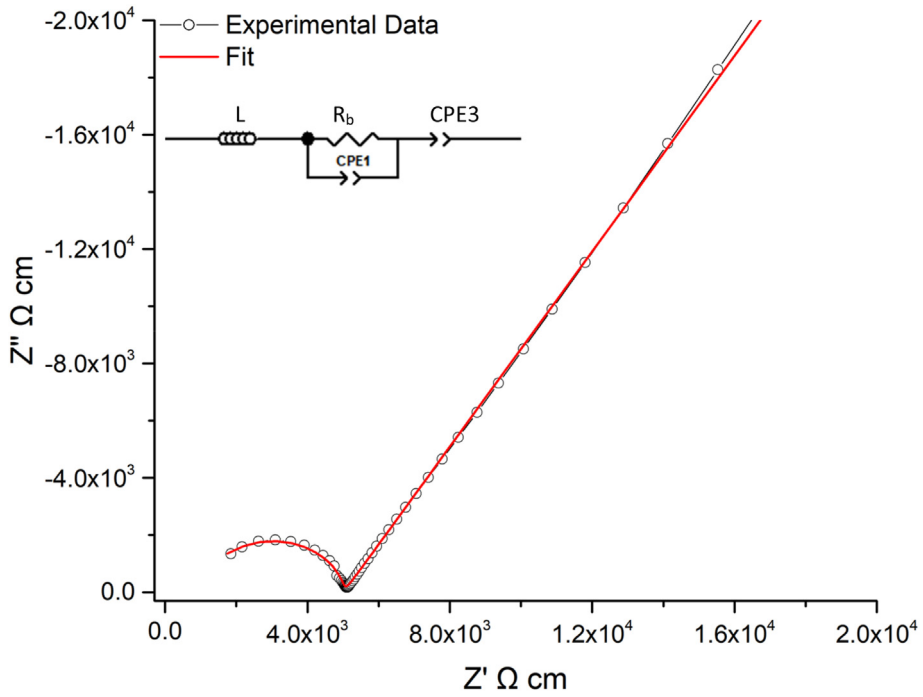

Fig. 5b. HEG2 Nyquist plot at 26 °C demonstrating buried grain boundary contribution. This was fit to the equivalent circuit in the top left and demonstrated overlapping bulk and grain boundary responses.

two parallel R/CPE components (connected in series) to accurately model the system. The denser HEG2 system, by comparison, did not demonstrate any additional contributions, instead fitting to a single R/CPE component in parallel, which corresponds to overlapping bulk/grain boundary contributions, see Fig. 5b. The tail corresponds to the Li transfer resistance at the sample/electrode interface. This arises from the Au which blocks Li diffusion and corresponds to capacitive behaviour due to the formation of space-charge layers. The inductive element is present due to limitations of the setup and has been noted elsewhere in the high frequency range with SSEs [27].

The presence of an additional buried contribution is clearer when the phase angle plots are considered, see Fig. 6a and b. In the high frequency range of both HEG1 and HEG2 a phase angle ~85° is present, which resembles the capacitive behaviour expected within this region (where ideal is 90°). However, a considerably different response is observed in the medium frequency range for HEG1, which has a phase angle of ~65°. This indicates a significant deviance from the expected capacitive behaviour and further indicates a partially buried contribution within the Nyquist plot. These observations are supported further by the spectroscopic C plot. For both phases high frequency plateaus are present with

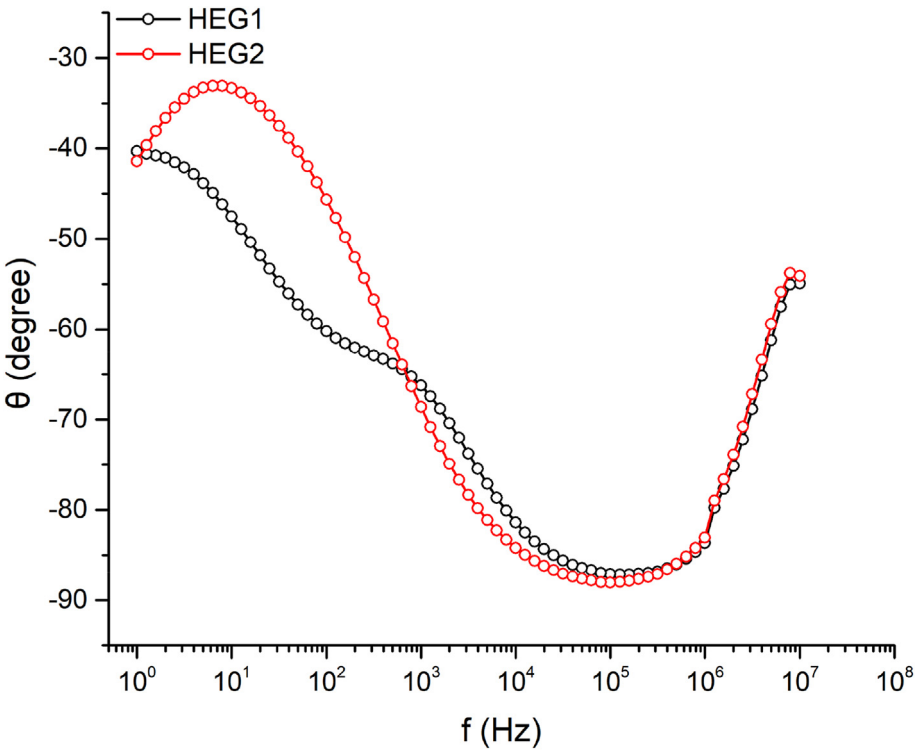

Fig. 6a. Bode plot showing the dependence of phase angle of the two systems, with HEG1 showing considerably difference in the mid-frequency region corresponding to the additional grain boundary response.

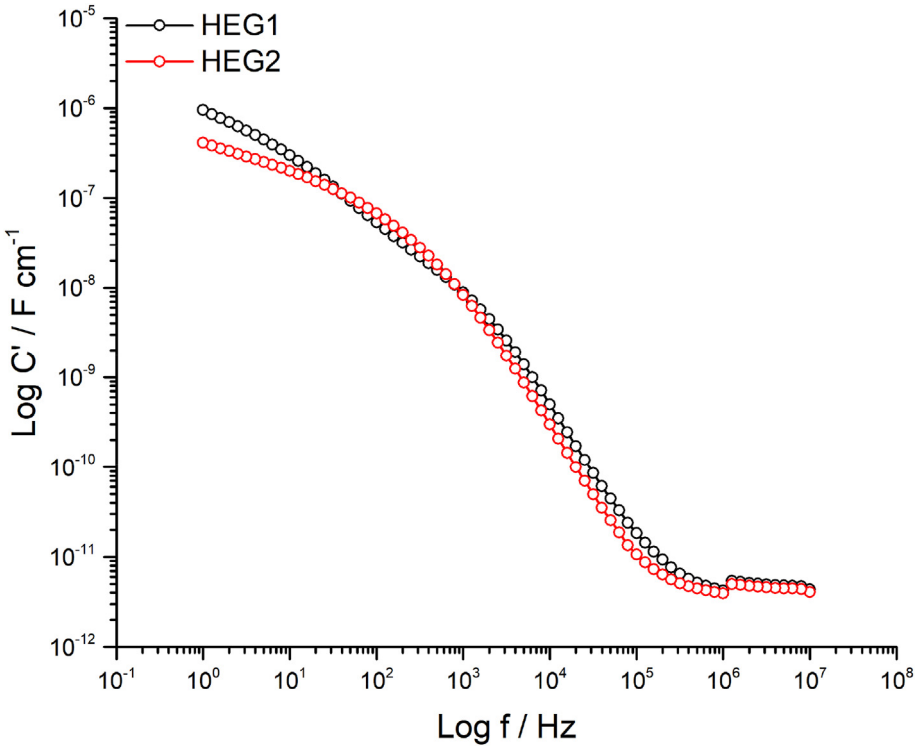

Fig. 6b. Spectroscopic C plot showing high frequency plateaus which in the pF cm^{-1} range which correspond to a bulk oxide response. HEG1 shows additional features ~1000Hz relating the grain boundary component.

capacitance values in the pF cm^{-1} range. This gives dielectric constants between 50 and 60 (based upon the permittivity of free space of 8.854 × 10^{-14} F cm^{-1}). Hence the capacitance values and dielectric constants correspond to the range expected for bulk oxide responses, see Fig. 6 and Table 1 [27,58,66]. HEG1, however, has an additional contribution in the mid frequency region giving capacitance values in ~10^{-8} F cm^{-1} range, indicating a grain boundary response. Therefore, the well resolved semi-circle for HEG1 in Fig. 5a likely corresponds to the bulk response

(0.2 mS cm^{-1}), with the buried contribution being the grain boundary. Therefore, total system conductivity of HEG1 is ~0.1 mS cm^{-1}, see Table 1 and SI for fitted values. The presence of the grain boundary contribution on Fig. 5a is attributed to the decreased density of HEG1 (88%) compared to HEG2 (94%).

The conductivity of both phases falls with ~10^{-4} s cm^{-1}, with HEG2 being slightly better at 0.2 mS cm^{-1}. These are impressive values considering there is only $Li_{5.75}$ *pfu*. Such results are greater than many other, similar, systems and is on par with lithium garnets with larger unit cells and more Li content thus further supporting the favourable properties of increased entropy [27,67–71].

HEG2 was noticeably denser than HEG1, and thus more conductive, hence was analysed further via variable temperature measurements (26–117 °C) to assess activation energy, see Fig. 7. In this case the pellet was painted with Au paste and Au wires attached, as per the methods section. The expected linear dependence was observed and corresponded to a calculated activation energy of 0.33 eV. This is similar to other garnets, therefore indicating the high entropy approach does not alter activation energies. This suggests the hopping pathway is independent of entropic contributions arising from extrinsic defects. Total system conductivity at 103 °C was 3 mS cm^{-1}.

3.4. Symmetrical cell testing

HEG2, being the higher performing system, was subsequently analysed in symmetrical cell form, firstly to analyse the interfacial resistance then to assess galvanostatic lithium plating and stripping stability. Post cell assembly they were analysed via impedance spectroscopy at 20 and 30 °C. The associated Nyquist plot is shown in Fig. 8. The area specific resistance (ASR) for HEG2 was 244 Ω cm^2 at 20 °C (144 Ω cm^2 at 30 °C). These values are lower than our prior reports for Ce-doped LLZO, which suggested partial interfacial Ce reduction led to ASRs of 380 Ω cm^2, but higher than $Ga_{0.2}Li_{6.4}Nd_3Zr_2O_{12}$ (67 Ω cm^2 at room temperature). This may indicate the reduction of ASR with Ce is being enhanced via the Ga and Nd dopants.

The HEG2 symmetric cell was, subsequently, subjected to lithium stripping and plating at 30 °C to assess cycling stability at different current densities, see Fig. 9. HEG2 showed excellent cycling stability with mostly stable voltage profiles over an extended period up to at least 150 μA cm^{-2}. Although some variations in voltage at 150 μA cm^{-2} are present, no large drop in voltage is observed indicative of a short circuit. This shows the HE approach does not compromise the cycling stability of the lithium garnet materials. Furthermore, we reported previously that $Ga_{0.2}Li_{6.4}Nd_3Zr_2O_{12}$ forms a short circuit at 50 μA cm^{-2} but enables low ASR values (67 Ω cm^2) and a high (94%) density. However the strategic use of Ga (0.2 *pfu*) and a smaller amount of Nd (0.5 *pfu*) in HEG2 has enabled much higher current densities while maintaining the favourably high densification and reduction in ASR values previously reported for $Ga_{0.2}Li_{6.4}Nd_3Zr_2O_{12}$, however does so at the cost of Li content due to Li site substitution with Ga and maintaining of charge neutrality [65].

4. Conclusions

In summary, we have shown that lithium garnet materials are very flexible to multi-site dopant strategies, with such dopants enabling relatively easy synthesis despite the elemental complexities involved. We have shown that Li garnet materials can not only handle multiple site substitution simultaneously, but that these sites can also handle several elements at the same time. Although this system is time consuming to weigh out stoichiometrically, the decreased dependency upon a single element could also be economically beneficial. It was also shown that the increased complexity of the garnet system aids in forming of the pure phase, with HEG1 and HEG2 consistently requiring no additional heating steps. It would be of interest to lessen the number of dopants to see if a lower limit can be reached which still enabled such consistency. It would also be of interest to employ more Ln site dopants, such as Ba or Sr to see what properties could be gained from complex Ln site substitution (in addition to increased Li content). An argument arises that Ta and Nb content could be much reduced (therefore increasing Li content) and replaced with increased Ti, as reports suggest dendritic suppression with this dopant [50] whereas use of Fe (on the Li site) has also been shown to alter the garnet symmetry to I4 $\bar{3}$ d. The use of multiple high entropy approaches to produce graded/layered garnet phases, which enable

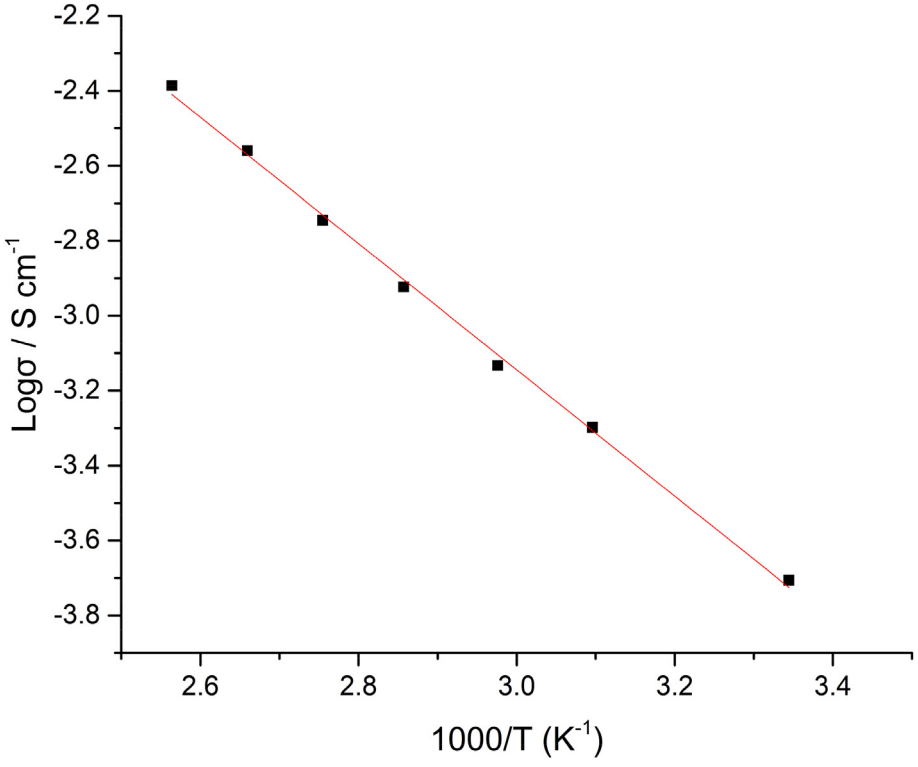

Fig. 7. Arrhenius plot for HEG2 from 26 to 117 °C. Plots show a linear dependence and correspond to an activation energy of 0.33 eV.

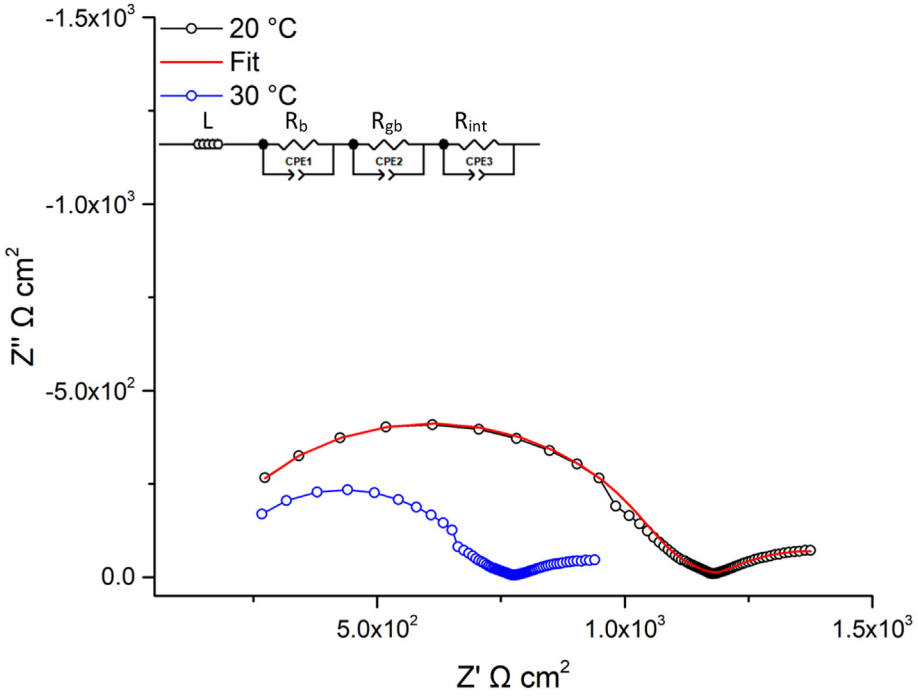

Fig. 8. Li/HEG2/Li symmetrical cell impedance plots at 20 and 30 °C, where the ASR is 224 and 144 Ω cm^2 respectively. Plots are scaled representative the area between the garnet and Li metal, therefore are in ohm cm^2, however conductivity values are similar to what is seen in Fig. 5b.

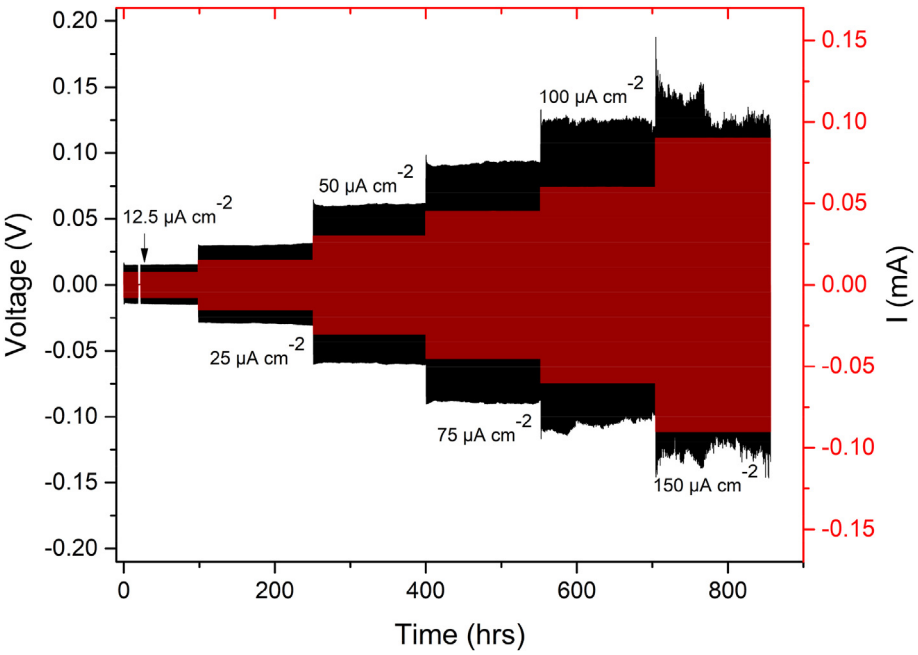

Fig. 9. Li/HEG2/Li symmetrical cell under galvanostatic cycling at 30 °C, indicating mostly flat voltage profiles and excellent cycling stability at several current densities.

different properties at the electrode interface (such as a low ASR) could be a possibility, as would an investigation to see if the high entropy approach is beneficial to use in thin films.

Much work is needed to understand this class of lithium garnets. This cannot be done easily, as the multi-element approach will make distinguishing of structural information a non-trivial task. However, the primary purpose of this work was to demonstrate the possibility of high entropy garnet systems and to push the understanding of the compositional flexibility of these materials. We have additionally shown that these systems show very good conductivity when compared with other garnets with increased Li content and larger lattice parameters. It was also shown that HEGs can exploit a variety of individual dopant properties simultaneously, opening new pathways toward solid state electrolyte engineering.

It is hoped that the exploitation of entropy will enable both better performing materials and provide the basis for more adventurous element combinations. This will allow exploitation of numerous dopants simultaneously, whereupon many are reported to enhance a singular

property (e.g. conductivity, density, interfacial resistance) yet are seldomly used in conjunction. Although the limits of the garnet system have been tested, they have by no means been found. Therefore, there is little reason why further substitution with elements such as Pr, Zn, Ge, Sn, W, Y, Sr and so forth cannot also be considered, with such a strategy possibly being exploited to engineer these materials to achieve optimal performance.

CRediT authorship contribution statement

Mark P. Stockham: Conceptualization, Writing – original draft, Formal analysis, Investigation. **Bo Dong:** Data curation, Investigation. **Peter R. Slater:** Conceptualization, Supervision, Writing – review & editing.

Declaration of competing interest

The authors declare that they have no known competing financial interests or personal relationships that could have appeared to influence the work reported in this paper.

Acknowledgements

We would like to thank the University of Birmingham for the studentship funding of Mark Stockham.

Appendix A. Supplementary data

Supplementary data to this article can be found online at https://doi.org/10.1016/j.jssc.2022.122944.

References

[1] J.M. Tarascon, M. Armand, Issues and challenges facing rechargeable lithium batteries, Nature 414 (2001) 359.
[2] M. Armand, J.M. Tarascon, Building better batteries, Nature 451 (2008) 652.
[3] H. Duan, H. Zheng, Y. Zhou, B. Xu, H. Liu, Stability of garnet-type Li ion conductors: an overview, Solid State Ionics 318 (2018) 45–53.
[4] J.G. Kim, B. Son, S. Mukherjee, N. Schuppert, A. Bates, O. Kwon, M.J. Choi, H.Y. Chung, S. Park, A review of lithium and non-lithium based solid state batteries, J. Power Sources 282 (2015) 299–322.
[5] C. Li, Z.-y. Wang, Z.-j. He, Y.-j. Li, J. Mao, K.-h. Dai, C. Yan, J.-c. Zheng, An advance review of solid-state battery: challenges, progress and prospects, Sustain. Mater. Technol. 29 (2021), e00297.
[6] Q. Liu, Z. Geng, C. Han, Y. Fu, S. Li, Y.-b. He, F. Kang, B. Li, Challenges and perspectives of garnet solid electrolytes for all solid-state lithium batteries, J. Power Sources 389 (2018) 120–134.
[7] Q. Zhao, S. Stalin, C.-Z. Zhao, L.A. Archer, Designing solid-state electrolytes for safe, energy-dense batteries, Nat. Rev. Mater. 5 (3) (2020) 229–252.
[8] C.-X. Zu, H. Li, Thermodynamic analysis on energy densities of batteries, Energy Environ. Sci. 4 (8) (2011) 2614–2624.
[9] N. Nitta, F. Wu, J.T. Lee, G. Yushin, Li-ion battery materials: present and future, Mater. Today 18 (5) (2015) 252–264.
[10] M. Winter, R.J. Brodd, What are batteries, fuel cells, and supercapacitors? Chem. Rev. 104 (10) (2004) 4245–4270.
[11] H. Yang, C. Guo, A. Naveed, J. Lei, J. Yang, Y. Nuli, J. Wang, Recent progress and perspective on lithium metal anode protection, Energy Storage Mater. 14 (2018) 199–221.
[12] Y. Wang, W.D. Richards, S.P. Ong, L.J. Miara, J.C. Kim, Y. Mo, G. Ceder, Design principles for solid-state lithium superionic conductors, Nat. Mater. 14 (2015) 1026.
[13] F. Zheng, M. Kotobuki, S. Song, M.O. Lai, L. Lu, Review on solid electrolytes for all-solid-state lithium-ion batteries, J. Power Sources 389 (2018) 198–213.
[14] C. Bernuy-Lopez, W. Manalastas, J.M. Lopez del Amo, A. Aguadero, F. Aguesse, J.A. Kilner, Atmosphere controlled processing of Ga-substituted garnets for high Li-ion conductivity ceramics, Chem. Mater. 26 (12) (2014) 3610–3617.
[15] F. Flatscher, M. Philipp, S. Ganschow, H.M.R. Wilkening, D. Rettenwander, The natural critical current density limit for Li7La3Zr2O12 garnets, J. Mater. Chem. 8 (31) (2020) 15782–15788.
[16] Y. Zhang, F. Chen, R. Tu, Q. Shen, L. Zhang, Field assisted sintering of dense Al-substituted cubic phase Li7La3Zr2O12 solid electrolytes, J. Power Sources 268 (2014) 960–964.
[17] M. Botros, R. Djenadic, O. Clemens, M. Möller, H. Hahn, Field assisted sintering of fine-grained Li7−3xLa3Zr2AlxO12 solid electrolyte and the influence of the microstructure on the electrochemical performance, J. Power Sources 309 (2016) 108–115.
[18] Federico M. Pesci, R.H. Brugge, A.K.O. Hekselman, A. Cavallaro, R.J. Chater, A. Aguadero, Elucidating the role of dopants in the critical current density for dendrite formation in garnet electrolytes, J. Mater. Chem. 6 (40) (2018) 19817–19827.
[19] F.M. Pesci, A. Bertei, R.H. Brugge, S.P. Emge, A.K.O. Hekselman, L.E. Marbella, C.P. Grey, A. Aguadero, Establishing ultralow activation energies for lithium transport in garnet electrolytes, ACS Appl. Mater. Interfaces 12 (29) (2020) 32806–32816.
[20] R.H. Brugge, F.M. Pesci, A. Cavallaro, C. Sole, M.A. Isaacs, G. Kerherve, R.S. Weatherup, A. Aguadero, The origin of chemical inhomogeneity in garnet electrolytes and its impact on the electrochemical performance, J. Mater. Chem. 8 (28) (2020) 14265–14276.
[21] J. Percival, E. Kendrick, R.I. Smith, P.R. Slater, Cation ordering in Li containing garnets: synthesis and structural characterisation of the tetragonal system, Li7La3Sn2O12, Dalton Trans. (26) (2009) 5177–5181.
[22] E.J. Cussen, T.W.S. Yip, A neutron diffraction study of the d0 and d10 lithium garnets Li3Nd3W2O12 and Li5La3Sb2O12, J. Solid State Chem. 180 (6) (2007) 1832–1839.
[23] E.J. Cussen, The structure of lithium garnets: cation disorder and clustering in a new family of fast Li+ conductors, Chem. Commun. (4) (2006) 412–413.
[24] R. Wagner, G.J. Redhammer, D. Rettenwander, A. Senyshyn, W. Schmidt, M. Wilkening, G. Amthauer, Crystal structure of garnet-related Li-ion conductor Li7−3xGaxLa3Zr2O12: fast Li-ion conduction caused by a different cubic modification? Chem. Mater. 28 (6) (2016) 1861–1871.
[25] J. Awaka, N. Kijima, K. Kataoka, H. Hayakawa, K.-i. Ohshima, J. Akimoto, Neutron powder diffraction study of tetragonal Li7La3Hf2O12 with the garnet-related type structure, J. Solid State Chem. 183 (1) (2010) 180–185.
[26] J. Awaka, N. Kijima, H. Hayakawa, J. Akimoto, Synthesis and structure analysis of tetragonal Li7La3Zr2O12 with the garnet-related type structure, J. Solid State Chem. 182 (8) (2009) 2046–2052.
[27] R.H. Brugge, J.A. Kilner, A. Aguadero, Germanium as a donor dopant in garnet electrolytes, Solid State Ionics 337 (2019) 154–160.
[28] Y.V. Baklanova, A.P. Tyutyunnik, N.V. Tarakina, A.D. Fortes, L.G. Maksimova, D.V. Korona, T.A. Denisova, Stabilization of cubic Li7La3Hf2O12 by Al-doping, J. Power Sources 391 (2018) 26–33.
[29] J. Wolfenstine, J. Ratchford, E. Rangasamy, J. Sakamoto, J.L. Allen, Synthesis and high Li-ion conductivity of Ga-stabilized cubic Li7La3Zr2O12, Mater. Chem. Phys. 134 (2) (2012) 571–575.
[30] B. Dong, M.P. Stockham, P.A. Chater, P.R. Slater, X-ray pair distribution function analysis and electrical and electrochemical properties of cerium doped Li5La3Nb2O12 garnet solid-state electrolyte, Dalton Trans. 49 (33) (2020) 11727–11735.
[31] M.P. Stockham, B. Dong, Y. Ding, Y. Li, P.R. Slater, Evaluation of the effect of site substitution of Pr doping in the lithium garnet system Li5La3Nb2O12, Dalton Trans. (2020).
[32] M.P. Stockham, B. Dong, M.S. James, Y. Li, Y. Ding, P.R. Slater, Water based synthesis of highly conductive GaxLi7−3xLa3Hf2O12 garnets with comparable critical current density to analogous GaxLi7−3xLa3Zr2O12 systems, Dalton Trans. 50 (7) (2021) 2364–2374.
[33] B. Dong, L.L. Driscoll, M.P. Stockham, E. Kendrick, P.R. Slater, Low temperature synthesis of garnet solid state electrolytes: implications on aluminium incorporation in Li7La3Zr2O12, Solid State Ionics 350 (2020) 115317.
[34] J.L. Allen, J. Wolfenstine, E. Rangasamy, J. Sakamoto, Effect of substitution (Ta, Al, Ga) on the conductivity of Li7La3Zr2O12, J. Power Sources 206 (2012) 315–319.
[35] S.W. Xin, M. Zhang, T.T. Yang, Y.Y. Zhao, B.R. Sun, T.D. Shen, Ultrahard bulk nanocrystalline VNbMoTaW high-entropy alloy, J. Alloys Compd. 769 (2018) 597–604.
[36] B. Wu, Z. Xie, J. Huang, J. Lin, Y. Yang, L. Jiang, J. Huang, G. Ye, C. Zhao, S. Yang, B. Sa, Microstructures and thermodynamic properties of high-entropy alloys CoCrCuFeNi, Intermetallics 93 (2018) 40–46.
[37] Naeem, M.; He, H.; Zhang, F.; Huang, H.; Harjo, S.; Kawasaki, T.; Wang, B.; Lan, S.; Wu, Z.; Wang, F.; Wu, Y.; Lu, Z.; Zhang, Z.; Liu Chain, T.; Wang, X.-L., Cooperative deformation in high-entropy alloys at ultralow temperatures. Sci. Adv. 6 (13), eaax4002.
[38] J.W. Yeh, S.K. Chen, S.J. Lin, J.Y. Gan, T.S. Chin, T.T. Shun, C.H. Tsau, S.Y. Chang, Nanostructured high-entropy alloys with multiple principal elements: novel alloy design concepts and outcomes, Adv. Eng. Mater. 6 (5) (2004) 299–303.
[39] E.P. George, D. Raabe, R.O. Ritchie, High-entropy alloys, Nat. Rev. Mater. 4 (8) (2019) 515–534.
[40] J.-W. Yeh, Alloy design strategies and future trends in high-entropy alloys, JOM 65 (12) (2013) 1759–1771.
[41] M.-H. Tsai, J.-W. Yeh, High-entropy alloys: a critical review, Mater. Res. Lett. 2 (3) (2014) 107–123.
[42] Y. Zhang, T.T. Zuo, Z. Tang, M.C. Gao, K.A. Dahmen, P.K. Liaw, Z.P. Lu, Microstructures and properties of high-entropy alloys, Prog. Mater. Sci. 61 (2014) 1–93.
[43] D.J.M. King, S.C. Middleburgh, A.G. McGregor, M.B. Cortie, Predicting the formation and stability of single phase high-entropy alloys, Acta Mater. 104 (2016) 172–179.
[44] M.C. Troparevsky, J.R. Morris, M. Daene, Y. Wang, A.R. Lupini, G.M. Stocks, Beyond atomic sizes and Hume-Rothery rules: understanding and predicting high-entropy alloys, JOM 67 (10) (2015) 2350–2363.
[45] Z. Lun, B. Ouyang, D.-H. Kwon, Y. Ha, E.E. Foley, T.-Y. Huang, Z. Cai, H. Kim, M. Balasubramanian, Y. Sun, J. Huang, Y. Tian, H. Kim, B.D. McCloskey, W. Yang, R.J. Clément, H. Ji, G. Ceder, Cation-disordered rocksalt-type high-entropy cathodes for Li-ion batteries, Nat. Mater. 20 (2) (2021) 214–221.

[46] C. Zhao, F. Ding, Y. Lu, L. Chen, Y.-S. Hu, High-entropy layered oxide cathodes for sodium-ion batteries, Angew. Chem. Int. Ed. 59 (1) (2020) 264–269.
[47] Q. Wang, A. Sarkar, D. Wang, L. Velasco, R. Azmi, S.S. Bhattacharya, T. Bergfeldt, A. Düvel, P. Heitjans, T. Brezesinski, H. Hahn, B. Breitung, Multi-anionic and -cationic compounds: new high entropy materials for advanced Li-ion batteries, Energy Environ. Sci. 12 (8) (2019) 2433–2442.
[48] Shijie, Z.; Na, L.; Liping, S.; Qiang, L.; Lihua, H.; Hui, Z., A novel high-entropy cathode with the A2BO4-type structure for solid oxide fuel cells. J. Alloys Compd. 2021, 162548.
[49] V. Thangadurai, H. Kaack, W.J.F. Weppner, Novel fast lithium ion conduction in garnet-type Li5La3M2O12 (M = Nb, Ta), J. Am. Ceram. Soc. 86 (3) (2004) 437–440.
[50] J. Gao, J. Zhu, X. Li, J. Li, X. Guo, H. Li, W. Zhou, Rational design of mixed electronic-ionic conducting Ti-doping Li7La3Zr2O12 for lithium dendrites suppression, Adv. Funct. Mater. 31 (2) (2021) 2001918.
[51] M.P. Stockham, B. Dong, M.S. James, Y. Li, Y. Ding, E. Kendrick, P.R. Slater, Evaluation of Ga0.2Li6.4Nd3Zr2O12 garnets: exploiting dopant instability to create a mixed conductive interface to reduce interfacial resistance for all solid state batteries, Dalton Trans. 50 (39) (2021) 13786–13800.
[52] B. Dong, S.R. Yeandel, P. Goddard, P.R. Slater, Combined experimental and computational study of Ce-doped La3Zr2Li7O12 garnet solid-state electrolyte, Chem. Mater. 32 (1) (2020) 215–223.
[53] M.C. Troparevsky, J.R. Morris, P.R.C. Kent, A.R. Lupini, G.M. Stocks, Criteria for predicting the formation of single-phase high-entropy alloys, Phys. Rev. X 5 (1) (2015), 011041.
[54] R. Jalem, Y. Morishita, T. Okajima, H. Takeda, Y. Kondo, M. Nakayama, T. Kasuga, Experimental and first-principles DFT study on the electrochemical reactivity of garnet-type solid electrolytes with carbon, J. Mater. Chem. 4 (37) (2016) 14371–14379.
[55] A. Gupta, R. Murugan, M.P. Paranthaman, Z. Bi, C.A. Bridges, M. Nakanishi, A.P. Sokolov, K.S. Han, E.W. Hagaman, H. Xie, C.B. Mullins, J.B. Goodenough, Optimum lithium-ion conductivity in cubic Li7−xLa3Hf2−xTaxO12, J. Power Sources 209 (2012) 184–188.
[56] S. Mukhopadhyay, T. Thompson, J. Sakamoto, A. Huq, J. Wolfenstine, J.L. Allen, N. Bernstein, D.A. Stewart, M.D. Johannes, Structure and stoichiometry in supervalent doped Li7La3Zr2O12, Chem. Mater. 27 (10) (2015) 3658–3665.
[57] B. Toby, R. Dreele, GSAS-II: the genesis of a modern open-source all-purpose crystallography software package, J. Appl. Crystallogr. 46 (2013) 544–549.
[58] R.H. Brugge, A.K.O. Hekselman, A. Cavallaro, F.M. Pesci, R.J. Chater, J.A. Kilner, A. Aguadero, Garnet electrolytes for solid state batteries: visualization of moisture-induced chemical degradation and revealing its impact on the Li-ion dynamics, Chem. Mater. 30 (11) (2018) 3704–3713.
[59] G. Larraz, A. Orera, M.L. Sanjuán, Cubic phases of garnet-type Li7La3Zr2O12: the role of hydration, J. Mater. Chem. 1 (37) (2013) 11419–11428.
[60] C. Galven, J. Dittmer, E. Suard, F. Le Berre, M.-P. Crosnier-Lopez, Instability of lithium garnets against moisture. Structural characterization and dynamics of Li7-xHxLa3Sn2O12 and Li5-xHxLa3Nb2O12, Chem. Mater. 24 (17) (2012) 3335–3345.
[61] J. Percival, D. Apperley, P.R. Slater, Synthesis and structural characterisation of the Li ion conducting garnet-related systems, Li6ALa2Nb2O12 (A=Ca, Sr), Solid State Ionics 179 (27) (2008) 1693–1696.
[62] M.A. Howard, O. Clemens, E. Kendrick, K.S. Knight, D.C. Apperley, P.A. Anderson, P.R. Slater, Effect of Ga incorporation on the structure and Li ion conductivity of La3Zr2Li7O12, Dalton Trans. 41 (39) (2012) 12048–12053.
[63] H. Peng, Y. Zhang, L. Li, L. Feng, Effect of quenching method on Li ion conductivity of Li5La3Bi2O12 solid state electrolyte, Solid State Ionics 304 (2017) 71–74.
[64] N. Hamao, K. Kataoka, J. Akimoto, Li-ion Conductivity and Crystal Structure of Garnet-type Li6.5La3M1.5Ta0.5O12 (M = Hf, Sn) Oxides, 125, 2017, pp. 272–275.
[65] M.P. Stockham, B. Dong, M.S. James, Y. Li, Y. Ding, E. Kendrick, P. Slater, Evaluation of Ga0.2Li6.4Nd3Zr2O12 garnets: exploiting dopant instability to create a mixed conductive interface to reduce interfacial resistance for all solid state batteries, Dalton Trans. (2021).
[66] S. Narayanan, A.K. Baral, V. Thangadurai, Dielectric characteristics of fast Li ion conducting garnet-type Li5+2xLa3Nb2−xYxO12 (x = 0.25, 0.5 and 0.75), Phys. Chem. Chem. Phys. 18 (22) (2016) 15418–15426.
[67] J. Percival, P.R. Slater, Identification of the Li sites in the Li ion conductor, Li6SrLa2Nb2O12, through neutron powder diffraction studies, Solid State Commun. 142 (6) (2007) 355–357.
[68] H. Buschmann, J. Dölle, S. Berendts, A. Kuhn, P. Bottke, M. Wilkening, P. Heitjans, A. Senyshyn, H. Ehrenberg, A. Lotnyk, V. Duppel, L. Kienle, J. Janek, Structure and dynamics of the fast lithium ion conductor “Li7La3Zr2O12”, Phys. Chem. Chem. Phys. 13 (43) (2011) 19378–19392.
[69] M.A. Howard, O. Clemens, K.S. Knight, P.A. Anderson, S. Hafiz, P.M. Panchmatia, P.R. Slater, Synthesis, conductivity and structural aspects of Nd3Zr2Li7−3xAlxO12, J. Mater. Chem. 1 (44) (2013) 14013–14022.
[70] Y. Matsuda, A. Sakaida, K. Sugimoto, D. Mori, Y. Takeda, O. Yamamoto, N. Imanishi, Sintering behavior and electrochemical properties of garnet-like lithium conductor Li6.25M0.25La3Zr2O12 (M: Al3+ and Ga3+), Solid State Ionics 311 (2017) 69–74.
[71] R. Murugan, V. Thangadurai, W. Weppner, Fast lithium ion conduction in garnet-type Li7La3Zr2O12, Angew. Chem. Int. Ed. 46 (41) (2007) 7778–7781.

10. Summary and Conclusions

Considerable efforts have been afforded toward developing an SSB, most of which is dedicated toward the discovery of a suitable SSE. In this thesis lithium garnet materials were studied with respect to dopant properties. Additionally, the tetragonal-cubic phase transition in these systems was studied further.

In Chapter 5, Pr doping into $Li_5La_3Nb_2O_{12}$ was studied with $Li_{5+x}La_3Nb_{2-x}Pr_xO_{12}$ and $Li_5La_{3-x}Pr_xNb_2O_{12}$. For the latter, the larger Pr^{4+} dopant (compared to Nb^{5+}) increased lattice parameters over $Li_5La_3Nb_2O_{12}$, which also increased Li content. $Li_{5.8}La_3Nb_{1.2}Pr_{0.8}O_{12}$ had $\sigma_{21°C}$ of 0.41 mS cm^{-1}. This is the highest reported σ_{rt} of any garnet material with < 6 Li *pfu*. Furthermore, Pr demonstrated ambisite substitution, being hosted on either the La or Nb site in the 3+ and 4+, states respectively**.**

Hf garnets were studied in chapter 6, with the aim of confirming prior modelling predictions of increased electrochemical stability compared to LLZO type systems. Here a water-based approach was used to form LLHO and Ga-LLHO. This enabled a low synthesis temperature of 700°C (also shown applicable to LLZO systems). Al-LLHO was also made by this route, but higher temperatures were required (950°C). Furthermore, results indicated Cl doping of the LLHO system *via* the synthesis process, although this was removed during densification. Ga-LLHO was assessed for electrochemical stability by lithium stripping and plating experiments in lithium symmetry cells. It was suggested that the CCD of Ga-LLHO could exceed Ga-LLZO, although further confirmatory work is required. Therefore, the Hf based (or mixed Zr/Hf) garnets merit further investigation, albeit this presents a commercial challenge due to the higher cost of Hf.

Chapter 7 investigated the Nd based garnets: $Li_{5+x}La_3Nb_{2-x}Zr_xO_{12}$ ($0 \leq x \geq 2$) and $Li_{6.4}Ga_{0.2}/Al_{0.2}Nd_3Zr_2O_{12}$. Focus here concentrated on enhancing Ga dopant instabilities in the garnet system (by increased lattice strain from Nd substitution compared to La) and assessing its effect on interfacial resistance with Li metal. It was found that the Nd garnets were easy to synthesise, however only Ga-NLZO had appreciable performance ($\sigma_{20°C}$ of 0.2 mS cm^{-1}), despite the much-reduced lattice parameters arising from Nd site substitution. This was attributed to the high relative pellet density (93%) achieved for these systems. Ga-NLZO was then examined in Li symmetric cells whereupon a low ASR value of (57 Ω cm^2) was found. This was attributed to a reaction between Li metal and Ga arising from dopant exsolution, which was supported by SEM, EDX and XRD on post-cycled pellets. It was also suggested that the Ga exsolution propagated along the grain boundaries, which gave a low CCD of 50 μA cm^{-2}.

Therefore, a proof-of-concept sandwich cell (Li/Ga-NLZO/Ta-LLZCO/Ga-NLZO/Li) was constructed, which confirmed Ga-NLZO can act as a CI with another garnet system (with a higher CCD). Therefore, Ga-NLZO can possibly be used as an interfacial layer to reduce ASR with Li metal. Li/Ga-NLZO/Li pellets were also shown to be recyclable by reheating.

In chapter 8 the tetragonal-cubic phase transition of lithium garnets was studied, where nine different garnet systems were synthesised. It was shown that a direct relationship between the transition temperature and cell volume (larger volume giving lower temperature) was too simplistic, and the phase transition appeared to be dictated more by the size of the octahedral B site than the dodecahedral A site. The average B site cation size showed a clear relationship to the transition temperature and was modelled mathematically, this predicted the ideal octahedral cation radius to enable a room temperature stable Li_7 garnet phase.

Chapter 9 introduced the concept of high entropy lithium garnet systems, which used numerous beneficial dopants simultaneously in a garnet system. Surprisingly, outside of precursor weighing, these systems were easy to synthesise. Both synthesised garnets showed good performance, however $Ga_{0.2}Li_{5.75}La_{2.5}Nd_{0.5}Nb_{0.35}Ta_{0.3}Ce_{0.1}Zr_{0.75}Hf_{0.25}Ti_{0.25}O_{12}$ demonstrated high conductivity, high density, low ASR and excellent cycling stability. This work was aimed at testing the compositional flexibility of the garnet system, and has shown considerable possibilities are yet to be realised.

11. Future Work

This thesis has shown numerous dopant properties in the lithium garnet system have remained unexplored. Considering the large number of elemental combinations yet to be discovered, many advances into lithium garnets could be forthcoming if the breadth of the periodic table was used. Some more specific areas for future work, based upon this thesis, are discussed below.

The use of a water-based method is highly promising for garnet materials, as other sol-gel type methods require various solvents and polymerisation agents which increases overall cost, production complexity and emissions. Therefore, further investigations seeking temperature reductions and examining scalability are required. It would also be of high interest to process Ga-LLHO in a similar manner to the best performing Ga-LLZO, (fully under Ar). This would allow a more accurate comparative assessment of the CCD between the two phases and confirm if the Hf garnets offer improved electrochemical stability. Furthermore, use of neutron diffraction is required to establish of Ga-LLHO has $Ia\bar{3}d$ type symmetry or if the cell should be indexed on $I\bar{4}3d$, as is the case for Ga-LLZO.

Ideally lithium content in garnets needs to be as high as possible but remain low enough to ensure the cubic symmetry is maintained. It would, however, be ideal if a room temperature lithium garnet could accommodate 7 Li *pfu*. In this work an ideal octahedral cation radius was proposed to enable this, and attempts were made to form such a system with $Li_7La_3Zr_{2-x}Ce_xO_{12}$ (x = 0.35, 0.45) and $La_3YNbLi_7O_{12}$. These were unsuccessful by conventional muffle furnace sintering in air. This warrants further investigation by other dopants to see if a cubic Li_7 system is possible, particularly as the inability to form these materials with any ease potentially indicates more, unknown, factors in the garnet tetragonal-cubic phase transition.

The high entropy garnet systems were a proof-of-concept and primarily aimed at examining the compositional flexibility of the garnet systems. However, this work proved that very complicated lithium garnets can form with ease, while the performance (especially for a system with an Li content of 5.75 *pfu*) was high. Therefore, an investigation into a lower limit of elements could be undertaken to simplify the approach. For example, Ta and Nb could be reduced (therefore increasing Li content) and replaced with increased Ti. Furthermore, much of the HEG work concentrates upon B site elements, yet the Ln site has equal dopant potential with elements such as Ba, Ca or Sr (and many more). Complex La site substitution (in addition to increased Li content) could yield unknown benefits. The use of multiple high entropy approaches to produce graded/layered garnet phases, which enable different properties at the electrode interface (such as a low ASR) could be a possibility, as would an

investigation to see if the high entropy approach is beneficial to use in thin films. An in-depth structural investigation with a range of characterisation techniques (such as XAS, XPS, NMR, neutron diffraction, single crystal XRD and pair distribution function) could reveal the structural effect of site substitution to this level, while also confirming if the Ga dopant had altered the garnet symmetry to $I\bar{4}3d$.

12. Appendix

12.1. Appendix 1 – Arrhenius equation derivation

$$\sigma = Aexp^{\left(\frac{-E_a}{RT}\right)}$$

Hence:

$$Log\sigma = \frac{-E_a}{RT} Log_{10e} + LogA$$

Where:

$$Log_{10e} = \frac{Log_e e}{Log_{e10}} = \frac{1}{2.3026}$$

Therefore:

$$Log\sigma = \left(\frac{-E_a}{2.3026R}\right)\frac{1}{T} + LogA$$

Hence a plot of logσ vs 1/T gives a slope of:

$$\frac{-E_a}{2.3026R} = -slope\ (J\ mol^{-1})$$

However, 1000/T is more commonly used to give the slope in kJ mol^{-1}, hence:

$$E_a = \text{slope x } 2.3026 \text{ x } 8.314 \text{ kJ mol}^{-1}$$

Yet E_a is more commonly quoted in eV, where 1 eV = 96.4869 kJ mol^{-1} (1.602 x10^{-19} J x 6.02 x10^{23} mol^{-1}) so:

$$E_a = Slope\left(\frac{2.3026R}{96.4869}\right)$$

Whereby the bracketed term in the equation above is equal to 0.1984 and is the gas constant (8.314 J mol^{-1} k^{-1}).

12.2. APPENDIX 2 – DRAFT PUBLICATION

12.2.1 Reactive sintering of $Li_{6.5}La_3Zr_1Nb_{0.5}Ce_{0.25}Ti_{0.25}O_{12}$ for high density lithium garnet electrolytes with anti-dendritic healing properties.

Article information : M. P. Stockham, B. Dong, M. S. James, P.Zhu, E. Kendrick and P. R. Slater.

To Be Submitted: 30/04/2021 to Journal of Materials Chemistry A

Author contributions: M. P. Stockham: Conceptualisation, experimental and characterisation work, method development, writing – original draft, formal analysis, investigation. B. Dong: Data curation, investigation. M.S. James: Data Curation. P. Zhu: SEM and EDX. E. Kendrick: writing – review, use of dry room facilities. P. R. Slater: lead supervision, conceptualisation, writing – review & editing.

Reactive sintering of $Li_{6.5}La_3Zr_1Nb_{0.5}Ce_{0.25}Ti_{0.25}O_{12}$ for high density lithium garnet electrolytes with anti-dendritic healing properties.

M. P. Stockham[1*], B. Dong[1,3], M.S. James[1], P. Zhu[2,3], E. Kendrick[2,3], P.R. Slater[1,3]*

[1]School of Chemistry, University of Birmingham, Birmingham B15 2TT. UK

[2]School of Metallurgy and Materials, University of Birmingham, Birmingham B15 2TT. UK

[3]The Faraday Institution, Quad One, Harwell Campus, Didcot OX11 0RA, UK

Correspondence to

M. P. Stockham/P. R. Slater

School of Chemistry, University of Birmingham, Birmingham B15 2TT. UK

Abstract

The next target of energy storage is the all solid state battery, however finding a suitable solid state electrolyte has proven troublesome. Lithium garnet materials are promising solid state electrolytes with high room temperature conductivity, a wide electrochemical window (> 6 V *vs* Li/Li^+), with chemical stability with Li metal and minimal hazards. However, lithium garnets suffer from slow, energy demanding synthesis, rapid proton exchange (leading to high interfacial resistance between the garnet and electrodes), mechanical instabilities with Li metal and require specific handling to achieve the highest performing materials (such as full processing under Ar). Here we report a Ti/Ce co-doped lithium garnet material in the form of $Li_{6.5}La_3Zr_1Nb_{0.5}Ce_{0.25}Ti_{0.25}O_{12}$ which has excellent properties. This material benefits from exceptionally rapid reactive sintering directly from the starting materials, allowing formation of dense pellets in 1hr at 1100°C. $Li_{6.5}La_3Zr_1Nb_{0.5}Ce_{0.25}Ti_{0.25}O_{12}$ has high conductivity (0.5 mS cm^{-1} at 25°C), and is also shown to have unusual dendritic healing properties, which is attributed to the beneficial pairing of Ce and Ti dopants, which enables healing of short circuited pellets in ≈30 mins *via* reduction of Ce.

Introduction

Safe, long-lasting portable energy storage is an elusive goal. Lithium-ion batteries (LIB) are the device of choice for use in secondary, rechargeable, batteries, owing to their high energy density, low self-discharge, long life (compared to other options) and extended cycling stability[1, 2]. Yet LIBs remain far from reaching their theoretical potential, having serious safety concerns and an inability to use Li metal anodes. LIB problems, generally, arise from the liquid based electrolytes, such as $LiPF_6$ in ethylene carbonate and dimethyl carbonate. These electrolytes are flammable, toxic, have limited electrochemical windows and are unstable with Li metal[1, 3-21]. These electrolytes, therefore, require optimisation or replacement for the next leap in energy storage.

Solid state batteries (SSB) are thought to overcome most limitations in current LIBs[5, 22-25]. However, current SSBs remain confined mostly to small scale laboratory work, as finding a suitable solid state electrolyte (SSE) has proved troublesome. The issues primarily relate to either poor ionic mobility or limited electrochemical windows, however are further complicated by long/complex synthesis and poor interfacial contact to the electrodes. This poor interfacial contact leads to a resistance too high for battery operation, abrupt potential changes and increasingly poorer contact due to volume expansion during cell operation[26-33]. Therefore, full SSBs have yet to be deployed commercially.

Of the available SSEs, lithium garnet type materials have received significant attention, owing to their well-established wide electrochemical window and (after considerable work) ionic conductivity rivalling that of current liquid electrolytes at room temperature (0.1 - 1mS cm^{-1})[34-38]. These materials are also chemically stable with Li metal, however despite the high Young's modulus (which gives intrinsically high interfacial resistance), they are susceptible to Li dendrite propagation through grain boundaries, although this can be substantially improved with increased SSE density and low interfacial resistance[39-42]. Lithium garnets, however, often require time consuming synthesis, followed by densification processes, which can take several days. The best performing garnets in the literature involve handling only in an Ar atmosphere to fully prevent atmospheric proton exchange, which arises from thermodynamic instabilities in air associated with the high Li content[34]. Therefore, synthesis often lacks scalability and is usually confined to the ~2-4g level.

Ideal garnets have the general formula $A_3B_2X_3O_{12}$ (e.g. A = Fe, Mg, B = Al, Cr, Fe, and X = Si, Fe, Al, Ga)[43-46]. In Li_3 garnets, e.g. $Li_3La_3Te_2O_{12}$, lithium fully occupies the 24*d* tetrahedral site and shows minimal Li ion mobility[45, 47]. System modifications by addition of lower valent cations permits increased Li content to maintain charge neutrality. This gives increased conductivity with lithium occupying additional interstitial octahedral sites in a disordered fashion[44, 46, 48, 49]. Li garnets can accommodate 7 Li per formula unit (*pfu)* but this results in full Li site occupation and Li ordering (to reduce short Li-Li

distances). This gives an elongation of an axis in the cubic cell forming the thermodynamically stable tetragonal system[50-54]. Tetragonal garnets have 7 Li *pfu* and poor conductivity with the $I4_1/acd$ space group (no. 142)[50-53] whereas cubic garnets have <7 Li *pfu* and show high conductivity commonly with $Ia\bar{3}d$ (no. 230) symmetry, although $I\bar{4}3d$ (no.220) has been proposed for $Ga_xLi_{7-3x}La_3Zr_2O_{12}$ (Ga-LLZO) [46, 55, 56]. Most lithium garnet reports detail systems where Li content is between ~6.2-6.6 *pfu* as this maximises the Li content (and subsequent disorder) while maintaining some vacant interstitial sites for an effective migration pathway[34, 42, 44, 48-50, 57-72].

Much work has focused on single dopant strategies, such as Al/Ga-LLZO, however much less has concentrated on higher entropy lithium garnets, where multiple cations have been substituted onto a single site. Such increased entropic factors could be harmonious with the highly entropic cubic, high Li content garnet systems. This would promote increased disorder which may yield better conductivity, rapid synthesis or a variety of yet unknown benefits.

Prior work from our group has shown that Ce doping in LLZO enables lower interfacial resistance between the Li metal and the garnet (388 Ω cm^2), likely due to partial Ce^{4+} reduction[54]. However, the large Ce^{4+} was investigated in a tetragonal $Li_7La_3Zr_{2-x}Ce_xO_{12}$ system and has yet to be assessed in a cubic garnet system. We also recently reported prior on high entropy garnet systems, and the ease at which they can form. We suggested that, with $Ga_{0.2}Li_{5.75}La_{2.5}Nd_{0.5}Nb_{0.35}Ta_{0.3}Ce_{0.1}Zr_{0.75}Hf_{0.25}Ti_{0.25}O_{12}$, the use of the Ti dopant should be examined further due to prior literature reports of dendrite resistance, high relative density pellets (95%), good ionic conductivity (0.2 mS cm^{-1} at room temperature) and favourable interfacial wetting between the Li metal and Ti doped garnets[73-76]. Therefore, the aim of this work was to build upon prior studies and combine the low interfacial resistance afforded by Ce^{4+} and the favourable performance properties reported for Ti^{4+} doping in a new dual doped garnet system.

Herein, we present an unusually easy to handle Li garnet, in the form of $Li_{6.5}La_3Zr_1Nb_{0.5}Ce_{0.25}Ti_{0.25}O_{12}$ (LTC). LTC enables a scalable and fast approach to a high conductivity garnet, requiring only 1h to form dense pellets directly from the starting materials in a dry room using readily available muffle furnaces. LTC is insensitive to heating rate and forms similar performing SSE membranes when heated at 2°C min^{-1} and at 40°C min^{-1} (furnace limit) and the fast conduction in LTC (1.1 mS cm^{-1} at 45°C, 88% density) does not noticeably degrade if heated for >1h. Mostly pure LTC can form in as little as 5 mins at 1100 °C, whereas powder synthesis can be accomplished at 950 °C/1h (100 °C min^{-1}) in air. The rapid synthesis/densification is also scalable to at least 15g. These results are not mirrored when preparing garnets using Ce or Ti as a single dopant. LTC was also designed to avoid Li site substituted dopants (such as Al/Ga) which exsolve to the grain boundary during heating and are, thus, relatively unstable. LTC shows excellent cycling stability, a wide electrochemical window (up to at least 10 V *vs* Li/Li^+) and has unusual

dendrite healing/prevention behaviour, which is experimentally shown to relate to the combination of Ce and Ti.

Methods

Synthesis

$Li_{6.5}La_3Zr_1\ Nb_{0.5}Ce_{0.25}Ti_{0.25}O_{12}$ (LTC) was prepared via the solid-state route from stochiometric quantities of Li_2CO_3, La_2O_3, Nb_2O_5, ZrO_2, TiO_2 and CeO_2 in air. A 40% mol excess of lithium was added to compensate for lithium loss during high temperature sintering. All powders were ball milled for 1 hr with ZrO_2 balls (350 rpm) with hexane. The powders were heated to 950°C (powder) or pelletised and heated 1100°C (1 h) at the fastest possible ramp rate in air (100°C min^{-1}) and within a dry room (40°C min^{-1}) in Carbolite ELF11/6 or CWF13/3 furnaces respectively. 10 mm pellets were pressed to ~1 ton from the starting materials. The dry room had a dewpoint between -45°C to -64°C (the elimination of humidity is desirable to prepare good quality garnet samples, as it is well established moisture can be an issue in the synthesis of Li garnet systems)[77-79]. Singularly Ce, Ti doped $Li_{6.5}La_3Zr_{1.25}Nb_{0.5}Ce_{0.25}O_{12}$ and $Li_{6.5}La_3Zr_{1.25}Nb_{0.5}Ti_{0.25}O_{12}$ were synthesised in the same manner but required two and four hours respectively to obtain similarly dense pellets.

All samples were stored in an argon glove box to prevent proton-Li exchange[63, 80-83]. Scanning electron microscopy (SEM) was performed on a Philips XL30 FEG instrument, with the elemental distribution confirmed by the corresponding Oxford Inca 300 energy dispersive X-ray (EDX) attachment. Pellets were polished with silicon carbide sandpaper from 800 to 4000 grit to form a flat surface. Phase analysis was performed by X-ray diffraction (XRD) using a Bruker D8 diffractometer with a Cu X-ray source. Experimental pellet densities were determined and compared to theoretical values from Rietveld refinement results (performed using GSAS II software)[84].

Impedance Spectroscopy

Post-sintering, the pellets were polished and were sputtered with Au and secured in a MTI split cell for room temperature impedance spectroscopy measurements, which were performed on Solartron 1260 impedance analyser from 1 Hz to 10 MHz with a 20 mV potential. Variable temperature measurements were undertaken in Genlab Classic oven from 19 – 64 °C, with at least 30-minute rest periods once obtaining the set temperature. Temperature accuracy was confirmed via a Fluke 51 II external thermocouple.

Cell assembly

All cell tests were performed on a biologic VMP3 or SP50 instrument. Li|LTC|Li symmetric cells were assembled in an Ar glove box. Firstly, the pellets (~1 mm thickness) were polished using silicon carbide sandpaper from 240 to 4000 grit, then lithium metal foil was applied to each side of the pellet. The cell was then heated to 175 °C under a constant pressure for 1 h using a commercially and readily available steel 3-way G clamps as reported prior[85] and were secured under light pressure via hand tightening the clamp. The cell was subsequently secured within an MTI split test cell. Cells were

examined *via* impedance spectroscopy before (and after) cell testing from 10 MHz to 0.1 Hz with a 20 mV potential on a Solartron 1260 impedance analyser. These symmetric cells were then cycled under constant current conditions at various current densities to assess cycling stability at room temperature on an open lab bench (between 15–21 °C throughout the day) as well as at a constant temperature in a Genlab classic oven. The temperature was monitored additionally via a Fluke 51 II external thermocouple. Cells were also cycled with increasing current density, in increments of either 10 or 20 μA cm^{-2}, to assess critical current density, at room temperature on an open lab bench.

Au|LTC|Li cells, for cyclic voltammetry (C.V.), were formed by polishing an LTC pellet as above and hand pressing the pellet into Li foil in an Ar glovebox. The cell was placed in a Swagelok cell with Au foil as the working electrode. Cyclic voltammetry was subsequently run from −0.4 to 10 V at a scan rate of 1 mV s^{-1}.

Results and discussion

X-Ray diffraction results

The powder X-ray diffraction (XRD) patterns of the LTC garnet materials at 950°C (powder) and 1100°C (pellet) sintered for 1h are available in figure 1. Both were indexed on the $Ia\bar{3}d$ space group as per other garnet materials without Ga (or Fe) Li site substitution[55, 86]. Rietveld refinements were based upon the structural model from Hamao *et al.*[87]. Considering the scattering similarities between Zr and Nb these were set to the intended ratios. As Zr and Nb could not be refined, Ce and Ti were also set to the intended ratio. See table 1 for determined lattice parameters and the SI for an example refinement. Lattice parameters were 12.9389(6) for the powder sintered at 950°C and 12.9484(3) for the densified pellet at 1100°C (88% relative density). This is in line with other garnets with similarly high Li content on the $Ia\bar{3}d$ type symmetry, and slightly larger than the structural model from Hamao *et al.* with $Li_{6.5}La_3Zr_{1.5}Ta_{0.5}O_{12}$[87].

Considering the rapid speed, additional investigations into the optimum sintering/densification time were undertaken. LTC pellets were prepared and heated to 1100°C for 5, 15, 30, 45 and 60 minutes, see figure 2 and table 1. It was determined that garnet phases form in as little as 5 mins, with lattice parameters of 12.9404(7) being only slightly reduced compared to 1h. However, those phases sintered for 5 min had broad peaks, and were not wholly densified with only a dense inner core that required removal of surrounding loose powders. Such pellets had relative densities of 80%, but were thin and brittle. This is an impressive value nonetheless for only 5 minutes.

Pellets which were heated for ≥ 15 minutes did not require removal of any excess powder and formed denser membranes. These samples showed sharp, highly crystalline, diffraction peaks and gave lattice parameters similar to sintering for 1h. The peaks were mostly garnet related, however some small impurities (relating to mixed Li-Nb-O phases) remained until ≥ 45mins, after which pure garnet type symmetry was observed. Relative densities for pellets sintered for ≥ 15 minutes ranged from 83-88%, the maximum of which was obtained at 1h. Sintering beyond 1h gave little difference in density, therefore subsequent pellets were sintered for 1h. Attempts were made to reduce the Li mol excess to 5, 10 or 20%, however, pellet densification was much reduced by comparison, only giving a partially dense pellet core encapsulated by less dense powders.

Therefore, maximal pellet densities using conventional furnaces is ~88% (similar densities were also achieved under N_2/O_2). This is in line with our previous work conducted under similar experimental procedures for other garnet systems[60-62, 85, 88], however, these reports required sintering the powder for ~12h followed by densification for ~12h in either air or N_2/O_2 (sometimes with densification agents, such as LiF) and were more sensitive to heating rates. The formation and sintering of LTC, however, is

considerably quicker and it is highly conducting compared to similar reports (see later for impedance spectroscopy). LTC was also proven to be scalable to at least 15g (the volume limit of the milling pot) under the same procedure. Increased Li content beyond 6.5 *pfu* was attempted, in the form of $Li_{6.6}La_3Nb_{0.4}Zr_1Ti_{0.35}Ce_{0.25}O_{12}$ and $Li_{6.7}La_3Nb_{0.3}Zr_1Ti_{0.45}Ce_{0.25}O_{12}$. However, this yielded Ce_4O_7 and CeO_2 impurities which were unable to be removed, see SI.

It is not yet completely clear what has enabled such rapid densification, nor why this material is more easily scalable. It could perhaps rely on the increased disorder of the B site, which is host to four separate elements. This could enable greater entropic contributions to the cubic lithium garnet and thus provide the additional contribution driving more rapid synthesis. However, it would appear reactive sintering is crucial, as powder synthesis followed by densification was significantly more troublesome. This required 1200°C for 4-6 hours and gave marginally poorer room temperature ionic conductivity (~0.1 mS cm^{-1}). The beneficial elemental combination in LTC is further confirmed when Ti or Ce is used singularly with $Li_{6.5}La_3Zr_{1.25}Nb_{0.5}M_{0.25}O_{12}$ (M = Ti, Ce), whereupon synthesis was quick, yet densification took several hours, see later.

LTC Sample (mins)	**Lattice Parameters (Å)**	**ρ_{rel} (%)**	**σ (mS cm^{-1})**	**C_{bulk} (F/cm) (pF)**	**ε_r**
Powder	12.9389(6)	-	-	-	-
5	12.9404(7)	80	-	-	-
15	12.9492(6)	84	0.30 (26°C)	4.75	54
30	12.9490(4)	86	0.39 (27°C)	5.57	63
45	12.9507(5)	83	0.35 (24°C)	4.69	53
60	12.9484(3)	88	0.42 (24°C)	5.64	64
180	12.9446(2)	86	0.37 (22°C)	4.29	48
720	12.9539(1)	87	0.38 (22°C)	4.87	55
LT	12.9138(9)	86	0.33 (22°C)	4.77	54
LC	12.9760(14)	84	0.31 (22°C)	5.91	66

Table 1. Lattice parameters, relative density, conductivity, capacitance values and dielectric constants for the analysed materials, where LT and LC correspond to the use of Ti and Ce as single dopants.

SEM/EDX

The sintered pellet (1100°C) was analysed *via* SEM and EDX to assess the microstructural features and to confirm elemental content. The SEM shows a dense pellet structure with an absence of discernible grain boundaries, with the corresponding EDX indicating the expected elemental distribution (see figure 3). Although the pellet has well connected individual grains; clear voids are present. Therefore, magnification was increased to examine these voids more closely. Here, the EDX, while showing a relatively homogenous distribution of elements, shows higher concentrations of Ti around the grain boundary. It is unclear why this is so, however, could relate to some incomplete synthesis which has fallen below the XRD limits.

Conductivity

The room temperature conductivity of LTC was assessed by impedance spectroscopy for each pellet dwell time > 5 mins. Densities of the pellets ranged from 83-88% and were unable to be improved by times > 1h, higher temperature, slower heating rates or under N_2/O_2. A typical Nyquist plot with Au blocking electrodes is shown in figure 4, with the associated capacitance bode plot available in the SI. All LTC materials demonstrated a single resistivity contribution which is attributed to overlapping bulk and grain boundary contributions. Therefore, all plots were fit with a single parallel R/CPE element, see figure 4. The spectroscopic C plot (see SI) shows a high frequency plateau corresponding to capacitance in the pF cm^{-1} range from which dielectric constants of 48-64 were calculated (based on the permittivity of free space of 8.854×10^{-14} F cm^{-1}). This corresponds to the data obtained from the equivalent circuit models and is the expected response for bulk oxide materials[68, 89-91]. The spike observed at low frequency relates to the Au electrode double layer, which blocks Li diffusion giving capacitive behaviour due to space-charge layers.

LTC materials sintered for 1h reached a maximum conductivity of 0.4 mS cm^{-1} at 21°C and 1.1 mS cm^{-1} at 45.5°C. Those sintered between the 15-60 minutes saw marginal changes in conductivity (the 5-minute membrane was too thin to be studied), see table 1. Beyond 1h density was similar, and conductivity degraded only slightly. Therefore, LTC is a robust garnet system that does not require extremely specific handling requirements to form similarly performing membranes. Variable temperature measurements were also taken on pellets sintered for 1h, with the Arrhenius plots displayed in figure 5. These gave an activation energy of 0.34 eV over the temperature range of 19 – 64 °C.

Overall LTC is amongst the most conductive garnet system we have obtained within our laboratory, and compares favourably to other reports of highly conducting systems elsewhere[75, 92], but is far easier to handle and potentially scalable. This, therefore, indicates if this material were able to be synthesised and then sintered fully under Ar (with no intermediate air exposure), which would eliminate any surface Li_2CO_3 as per work here[34, 42], performance could potentially be further improved.

Electrochemical testing

Cyclic Voltammetry

To confirm the electrochemical stability window of the LTC materials, Au/LTC/Li cells were constructed and analysed via cyclic voltammetry, see figure 6. LTC demonstrates an outstanding voltage stability of at least 10 V (*vs* Li/Li^+) (the maximum voltage of the VMP3). A small peak is present at ~ 0.5 V, attributed to Au-Li alloying[68]. Outside of this the current response is flat, which indicates negligible redox activity and no indication of Ti^{4+} reduction in the presence of Li metal. This is higher than previous reports, which indicate stability up to ~6V, further highlighting the potential of LTC materials for use in high voltage cells[93-95].

Symmetry Cell Testing

To assess electrochemical stability and short circuit tolerance, symmetrical Li/LTC/Li cells were assembled and analysed at multiple current densities. Long term cycling was additionally analysed at fixed temperature to confirm voltage stability. In all cases no additional pressure was applied outside of hand tightening of the split cell.

Cells were assembled as per the methods sections and analysed by impedance spectroscopy to assess the area specific resistance (ASR) at the Li/LTC interface, which gave values between 320-400 Ω cm^2. This is similar to our prior reports on Ce doping, hence confirming the strategic use of Ce in low quantities to reduce interfacial resistance[54].

Firstly, the LTC materials were assessed for critical current density (CCD), which is the current at which lithium dendrites can grow and short circuit a cell. Cells were analysed on an open lab bench (non-air conditioned) with small temperature fluctuations between 17-23°C. CCD of lithium garnet materials are thought to depend on several aspects: low interfacial resistance, high ionic conductivity, dense microstructure, chemo-mechanical interfacial phenomena and grain boundary characteristics. LTC demonstrated the expected ohmic current–voltage behaviour up to 140 μA cm^{-2}, with mostly flat voltage profiles, see figure 7a. However, after this a small voltage drop occurs, and voltage profiles become erratic, but do not show the sharp voltage drop expected with a short circuit. At 200 μA cm^{-2} the cell was removed and analysed via impedance spectroscopy and, surprisingly, there were minimal changes in the LTC bulk and grain boundary contributions. However, substantial interfacial changes were present, which reduced ASR from 380 to 250 Ω cm^2 (room temperature), such a reduction would account for reduced voltage during CCD. The CCD analysis was resumed, and the cell was analysed by impedance spectroscopy again after the 300 μA cm^{-2} cycle, whereupon ASR had further reduced to 161 Ω cm^2. This phenomenon continued until 660 μA cm^{-2}, at which point a large voltage spike occurred (to the maximum tester voltage) causing automatic cessation of the cell testing. Complete interfacial breakdown was then confirmed by impedance spectroscopy, whereby the much-reduced ASR as now transformed to an exceptionally large interfacial resistance (> 29000 Ω cm^2), see figure 7c. Analysis at elevated temperature (38°C) also yielded similar results of reduced ASR and dendrite resistance, see figure 8.

It was additionally observed during cell testing that, after short rest periods to run impedance spectroscopy, upon resuming Li stripping and plating the voltage profile briefly returned to more typical ohmic current–voltage behaviour, before resuming the erratic voltage profiles after ~5 minutes. This indicates a potential reversal of the dendritic resistance reaction and is especially well shown in figure 8.

To assess the dendritic behaviour further, symmetrical LTC cells were assembled and galvanostatically cycled at 500 μA cm^{-2} as, according to the CCD, it is around this point that the cell becomes increasingly unstable before ultimately degrading. See figure 9a. These cells, on the first cycle, initially increased in voltage before seeing a slow voltage drop. Immediate impedance analysis, after the first 500 μA cm^{-2} cycle, indicated a short circuit but with higher resistance than expected, see figure 9b. Impedance spectroscopy was then repeated continuously over the course of 1h. This showed a remarkable, and relatively fast, reversal of the short circuit within 32 minutes with the cell healing back to the impedance spectrum of the fresh cell. After ≈1h the impedance spectrum of the pellet stabilised, with the cell having marginally increased resistance.

The cell cycling was then restarted (at 500 μA cm^{-2}) for 36 cycles. This initially demonstrated the same voltage profile as the first galvanostatic cycle (further indicating LTC had chemically reacted with any dendrites), before again dropping to a similar, lower, voltage which remained consistent. Impedance analysis was then conducted after 36 cycles and showed a short circuit in the expected manner (large reduction of the bulk/GB components) and repeated analysis showed only marginal recovery, therefore suggesting limited cyclability of the dendritic healing. However, upon resting the cell for 24hrs the short circuit was removed and the spectrum returned to the original profile prior to restarting cycling, see figure 10.

To assess this behaviour further, the dopants were analysed singularly in the garnet systems $Li_{6.5}La_3Zr_{1.25}Nb_{0.5}Ce_{0.25}O_{12}$ (LC) and $Li_{6.5}La_3Zr_{1.25}Nb_{0.5}Ti_{0.25}O_{12}$ (LT). These were subjected to the same lithium CCD analysis. Both LC and LT were similarly as quick to synthesise in powder form, however, did not demonstrate the same densification properties as LTC. LC required at least two hours to form a dense pellet, whereas LT required four. Both LC and LT were inferior to LTC in terms of density and conductivity, see SI. Interestingly, other reports of Ti doping use much longer sol-gel based techniques, longer sintering times and/or complex pressing methods. These other Ti reports (with similar Li content) are also still less conductive than LTC, even with relative densities ~95% (0.2 mS cm^{-1}), which indicates Ti lacks suitability as a single dopant[62, 75, 92].

Upon CCD testing of LT, it was found that the system did not lend itself to a low ASR value, with results of 1000-2000 Ω cm^2. This is contradictory to other reports, which show Ti based systems enable reduced interfacial resistance. These works, however, employed heating of Li metal beyond 180°C to melt onto the interface in conditions where proton exchange could be more readily controlled[92]. This did not affect the electrochemical testing in this work as, in all cases, irrespective of ASR no CCD was observed, as confirmed by the voltage profile and impedance spectroscopy. Current increased until the upper maximum voltage of the cell tester was reached at 600 μA cm^{-2}, with large voltage spikes

starting from 500 μA cm^{-2}, see SI. This is not present with LTC and indicates large increases in cell resistance, which was confirmed by impedance spectroscopy after the 600 μA cm^{-2} cycle, whereupon complete interfacial breakdown was seen. The interfacial degradation at high current density mimics the behaviour seen in LTC, however LTC was cycled at higher current densities before cell failure. The lack of any voltage reduction during CCD also indicates no reduction in ASR, as observed with LTC.

Upon testing of CCD with LC, an ASR of 328 Ω cm^2 was measured, which is in line with our previous work with Ce garnets (388 Ω cm^2). The LC cell obeyed ohmic current–voltage type behaviour up to 120 μA cm^{-2}, whereupon a voltage drop occurred that mimicked the CCD profile observed with LTC. Cells were analysed *via* impedance spectroscopy at 260, 360 and 600 μA cm^{-2}. The initial ASR of 328 Ω cm^2 fell to 90 Ω cm^2 after the 260 μA cm^{-2} cycle but showed no short-circuit. At 360 μA cm^{-2} the short circuit was present (removal of the bulk/GB resistive component). This was further confirmed at 600 μA cm^{-2}. Impedance analysis showed the short circuit does not recover after the 360 μA cm^{-2} cycle and LC did not undergo interfacial breakdown at high current densities (as seen with LT and LTC). This, therefore, indicates that the unusual behaviour towards dendrites is related to Ce. However, results suggest the pairing of Ti and Ce is required to maintain the healing phenomena at higher current densities, with the Ti dopant being ultimately responsible for Li metal interface degradation (at high current densities), which would prevent dendrite propagation. The synthesis of LC and LT also show the co-doping strategy with LTC is required for the rapid densification, ease of handling and higher performance.

Room and fixed temperature (49°C) long-term cycling of LTC was subsequently undertaken over the course of three months, over a wide degree of current densities, to confirm cycling stability (both before and after the erratic voltage profiles began), see figure 11. LTC had excellent voltage stability up to 150 μA cm^{-2}, at which point the pseudo CCD of LTC is reached and the erratic voltage profile begins (49°C). Past 150 μA cm^{-2}, although the voltage is more erratic, no sign of short circuit is shown and the dendritic resistance appears to be stable for exceptionally long periods of time, lasting several thousand cycles, until degradation occurs at high current density. Deliberate attempts to short circuit cells by melting Li metal with applied pressure or by cycling at current densities ≥ 1mA cm^{-2} were made. This, yet again, demonstrated no short circuit and large interfacial resistance.

As our previous work on Ce-doped LLZO has suggested the presence of interfacial Ce_4O_7, with this being the attributed reason for reduced interfacial resistance and, as the dendritic resistance is catalysed by the presence of Ce (as seen above), it is logical to conclude this is playing a role with LTC. It has been experimentally confirmed in this work that the continued dendritic resistance and the ultimate interfacial breakdown is due to addition of Ti. Therefore, as Ti can obtain same 3+/4+ states

as Ce, it can be theorised that $Ce_2Ti_2O_7$ is being formed, with Ti reduction arising from the Li metal. This, however, is not demonstrated in the C.V.

In order to confirm any oxidation state changes in LTC both freshly prepared and cycled pellets were analysed by X-Ray absorption near edge structure (XANES). Although XANES does not show surface-based phenomena, powder was obtained from the interface and the bulk of the pellet to ascertain if any clear differences were present based upon proximity to Li metal. Ti_2O_3, anatase TiO_2 and CeO_2 references were used for comparison. Data obtained from the Ti K edge in LTC suffered from severe interference from the strong La L3 absorption at 5491 eV. This suppressed the LTC Ti K edge peaks considerably, but a doublet is present at 4987 and 5001 eV across all LTC samples. These peaks are consistent in position and characteristics across the cycled and fresh LTC samples. This doublet corresponds more closely to the position of the Ti K edge peaks in the TiO_2 reference and has a pre-edge peak at 4970 eV (absent in Ti_2O_3), which is similar to reports elsewhere[96-98]. Although this suggests Ti^{4+} presence in LTC it is not conclusive due to the La interference, the difference in peak profiles (compared to the reference) and the comparison to anatase type TiO_2. However, if the spectra are compared to reports of Ti^{4+} orthosilicate garnets, such as schorlomite and andradite, LTC has similar peak profiles, positions and pre-edge characteristics[99, 100]. Irrespective of specific Ti oxidation state the peak positions and characteristics between cycled and fresh LTC samples are highly similar. This indicates no change of Ti during galvanostatic cycling and supports Ti stability during Li stripping and plating.

Examination of the Ce L edges also suffered from La L2 edge interference, however absorption peaks for Ce are much clearer compared to Ti. These show the expected presence of Ce^{4+} within the freshly sintered materials, with a peak doublet at 5731 and 5736 eV. This corresponds to the CeO_2 reference at 5730 and 5737 eV. However, post cycled pellets had these peaks removed, with a new single peak appearing at 5726 eV. This shift to lower energy indicates reduction to a 3+ state. No Ce^{3+} reference was available to test, however, Ce^{3+} reports elsewhere, with compounds such as CeF_3 and $Ce(NO_3)_3{\cdot}6H_2O$, also show a sharp singular peak in this region that is assigned to a trivalent Ce species[101-104]. Therefore, Ce is being reduced during Li stripping and plating beyond a simple grain surface reaction, penetrating into the bulk and throughout the pellet. This confirms the previous work by Dong *et al.*, whereupon Ce reduction was suggested to occur in $Li_7La_3Zr_{2-x}Ce_xO_{12}$ materials[54].

The XANES data, therefore, supports the reduction of Ce in the garnet structure during cycling, with experimental evidence also confirming the anti-dendritic behaviour requires Ce. Therefore, as Ce is reduced from Ce^{4+} to Ce^{3+}, a corresponding Li metal oxidation is likely occurring. This could attack Li metal dendrites and enable formation of Li^+ which, ultimately, combines with the liberated O^{2-} (from

Ce reduction) to form Li_2O. This would remove the short circuit and heal the garnet material at the cost of slightly increased pellet resistance (due to the insulating Li_2O). However, it could also be theorised that when Li^+ is formed, possibly from Ce reduction, it is exchanging with the garnet material as Ce is destabilised from the structure. Therefore Li^+ insertion occurs into the garnet, with this being favourable as LTC does not have the maximal Li content of a lithium garnet. This would also account for the increased resistance in the impedance spectrum, as the system starts to increase Li content toward the poorly conductive tetragonal phase. Irrespectively, this is a rapid reaction and may also enable native protection during cycling at lower current densities and/or during long cycle times (in addition to healing post short circuit). This would require further work to confirm, as does the role which Ti plays in LTC, as it appears crucial to extend the anti-dendrite behaviour beyond a few cycles, yet its contribution remains unclear.

Conclusions

In summary, a new co-doped Ti/Ce garnet material has been synthesised. LTC demonstrated easy synthesis, requiring only 1h to form dense membranes directly from the starting materials. LTC is also shown to be scalable and outperforms other, similarly, doped systems despite having decreased density. If only the powder is required, a similarly rapid synthesis can be achieved at 950°C. LTC was also shown to be very robust, as overall performance does not require specific handling, for example heating rate and/or heating times past 1h yielded similar results. Such absence of specificity in addition to scalability could make LTC ideal for use within a commercial environment. We have also demonstrated that single use of Ce or Ti in these garnets does not generate the same properties, and it is the combination of both which enables the ease of handling in LTC. It was also shown that LTC presents anti-lithium dendrite properties, with short-circuited pellets readily being healed within minutes. Considering how fast this process is, this could also lend itself to dendritic suppression at lower current densities. The healing mechanism was experimentally found to relate to the Ce dopant, with reduction confirmed by XANES. The reduction of Ce^{4+} to Ce^{3+} is then thought to correspond to the oxidation of Li metal to Li^{+}, which could remove the lithium dendrites by ultimate formation of Li_2O or Li^{+} could then insert into the garnet as Ce is destabilised from the structure. This unusual behaviour appears related to Ce, but results also indicate the Ti is required for the effect to be maintained at higher current densities. The effect of the Ti dopant on lithium dendrites remains unclear and requires further work to uncover. This could be investigated by computational modelling or by further analysis by surface sensitive techniques (such as XPS). This would require facilities which can transfer samples under vacuum to avoid proton exchange and to allow assessment of the chemomechanical phenomena.

Conflicts of interest

There are no conflicts of interest to declare.

Acknowledgements

We would like to thank the University of Birmingham for the studentship funding of Mark Stockham and Matthew James, and the EPSRC for funding the GENESIS project (under EP/ R024006/1) and the EPSRC Capital Award for Core Equipment (EP/T02349X/1). This work is supported by the Faraday Institution funded Nextrode (FIRG015) and CATMAT (FIRG016) Projects. We thank the Diamond Light Source for the award of beam time as part of the Energy Materials Block Allocation Group SP14239

Figures:

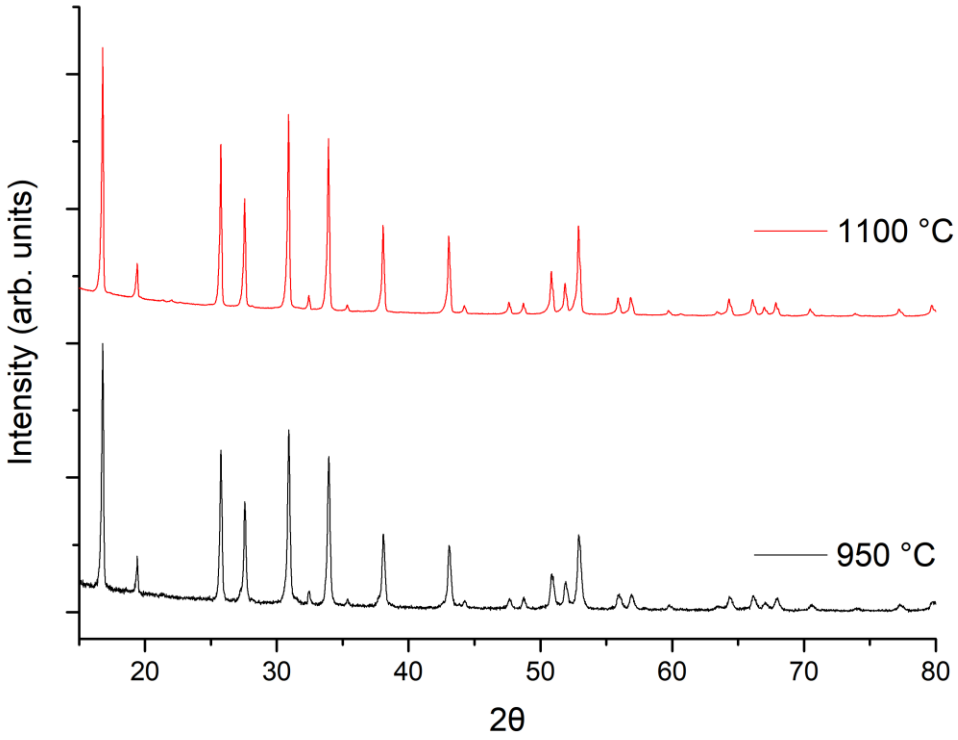

Figure 1. XRD patterns of LTC sintered in powder form (950°C, 100°C min^{-1}) and as a pellet (1100°C, 40°C min^{-1}). Both sintered for 1h and demonstrate pure garnet ($Ia\bar{3}d$) type symmetry

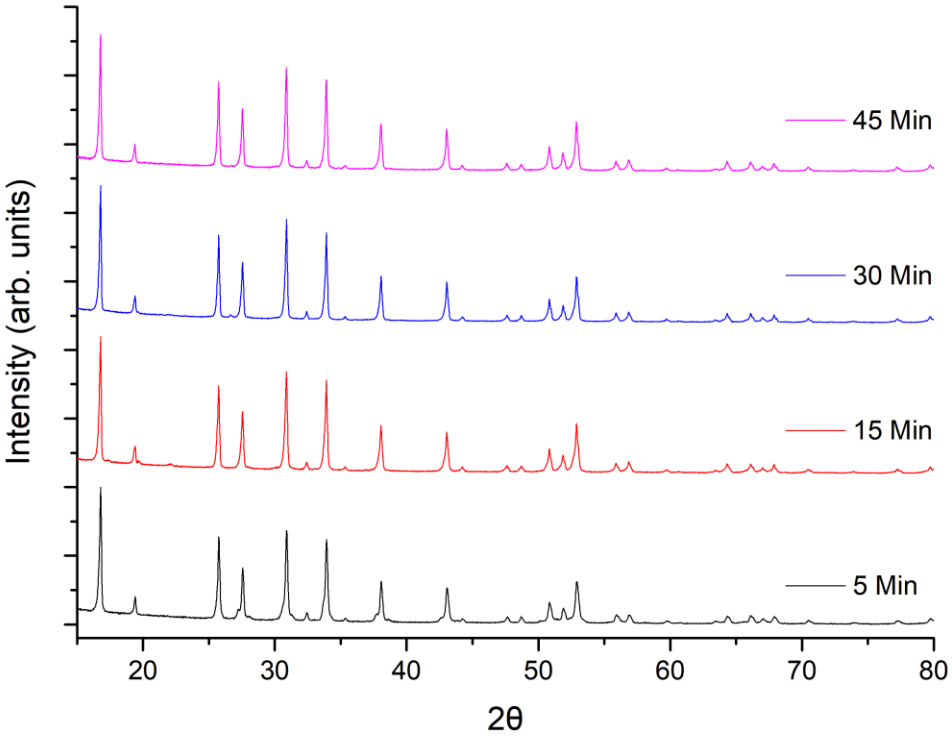

Figure 2. XRD patterns of LTC sintered pellet form at 1100°C different time intervals. All patterns demonstrate garnet type symmetry but sharp, crystalline, peaks only appear ≥ 15 minutes.

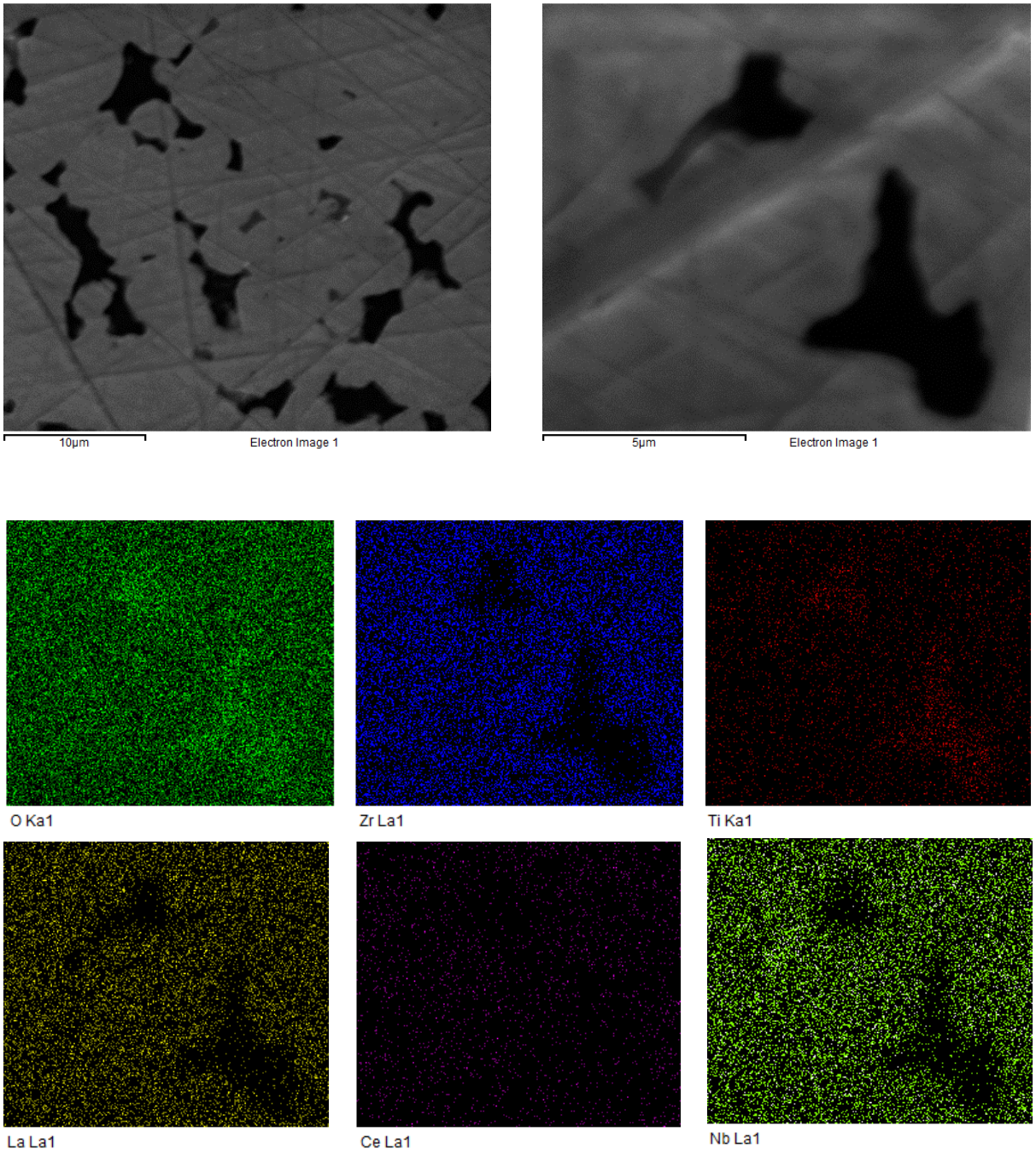

Figure 3. SEM of polished pellet surface at two different magnification levels showing a dense pellet microstructure with no visible grain boundaries, however some voids are present. EDX is also shown, demonstrating concentrated areas of Ti in the pores.

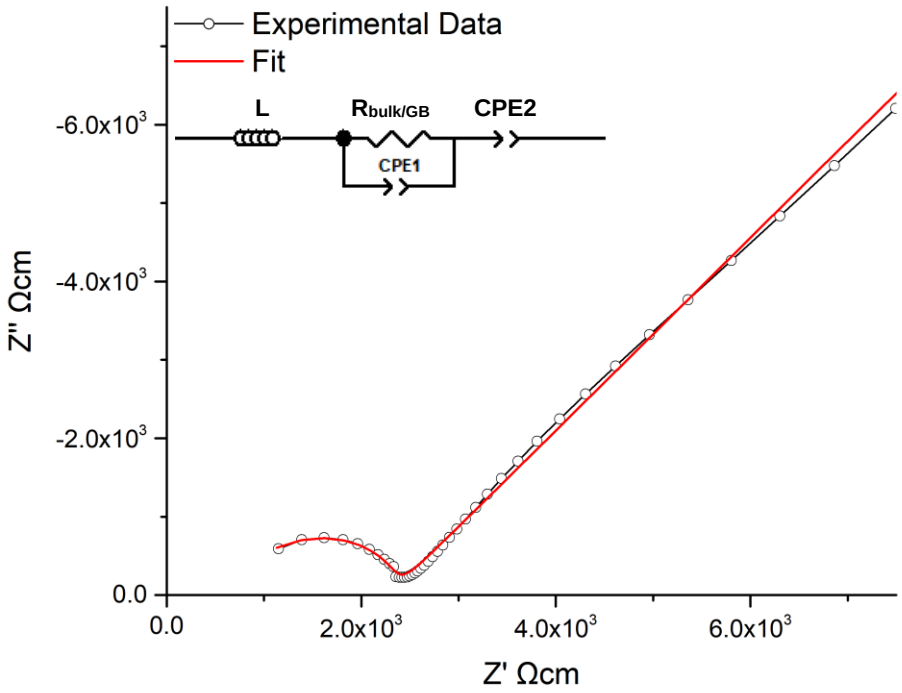

Figure 4. Typical Nyquist impedance plot of LTC, which was fit to the equivalent circuit in the top left.

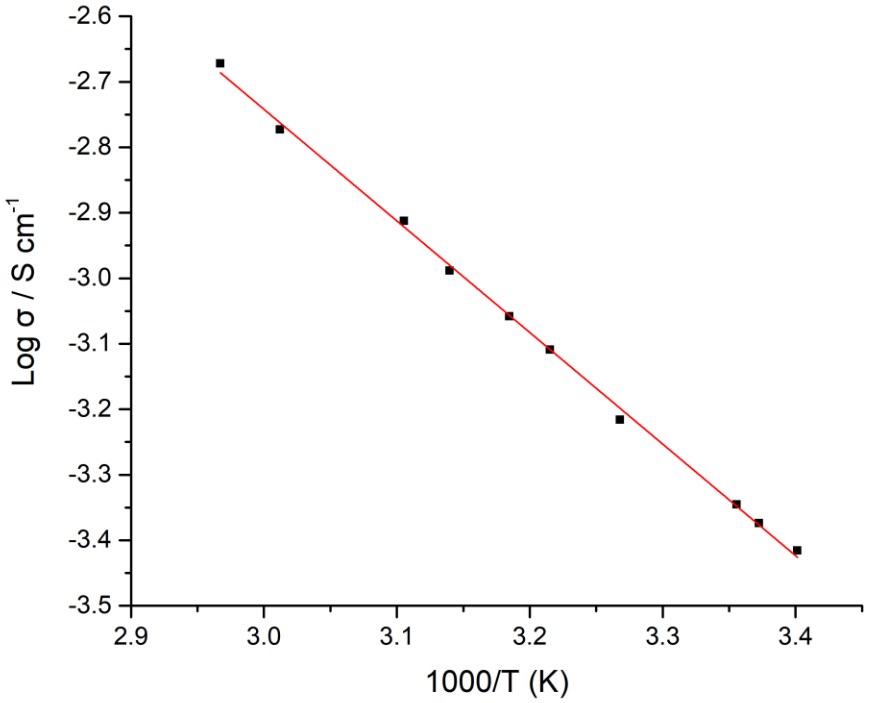

Figure 5. Arrhenius plot of LTC over the temperature range of 19 – 64 °C with an activation energy of 0.34 eV.

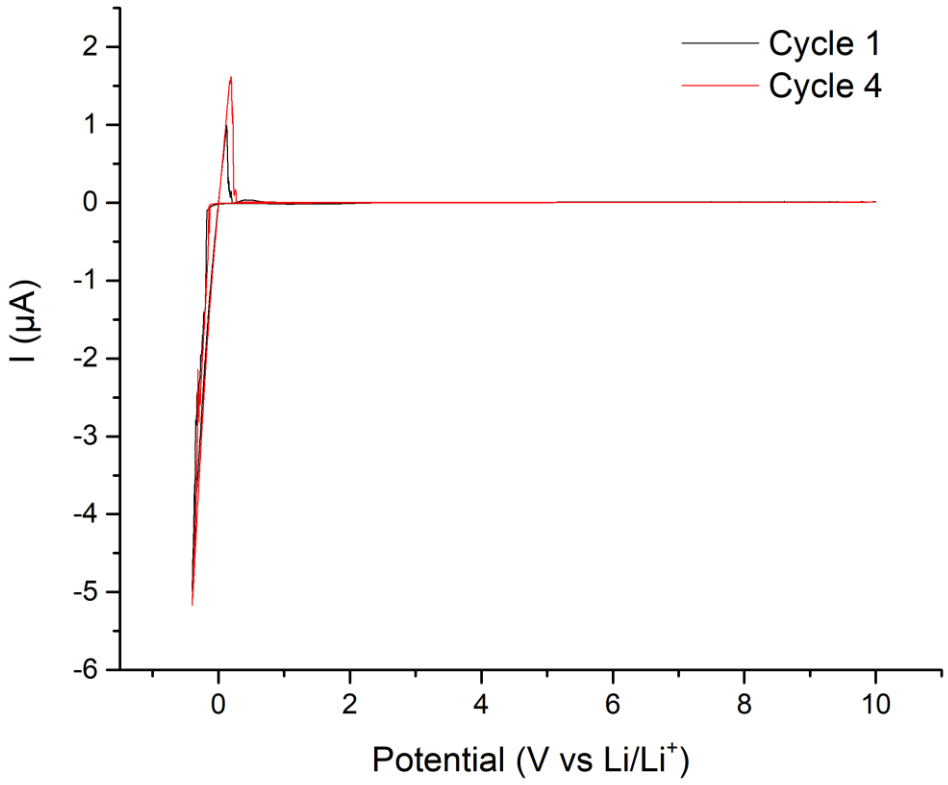

Figure 6. Cyclic voltammetry of LTC at room temperature using a Au/LTC/Li cell.

a)

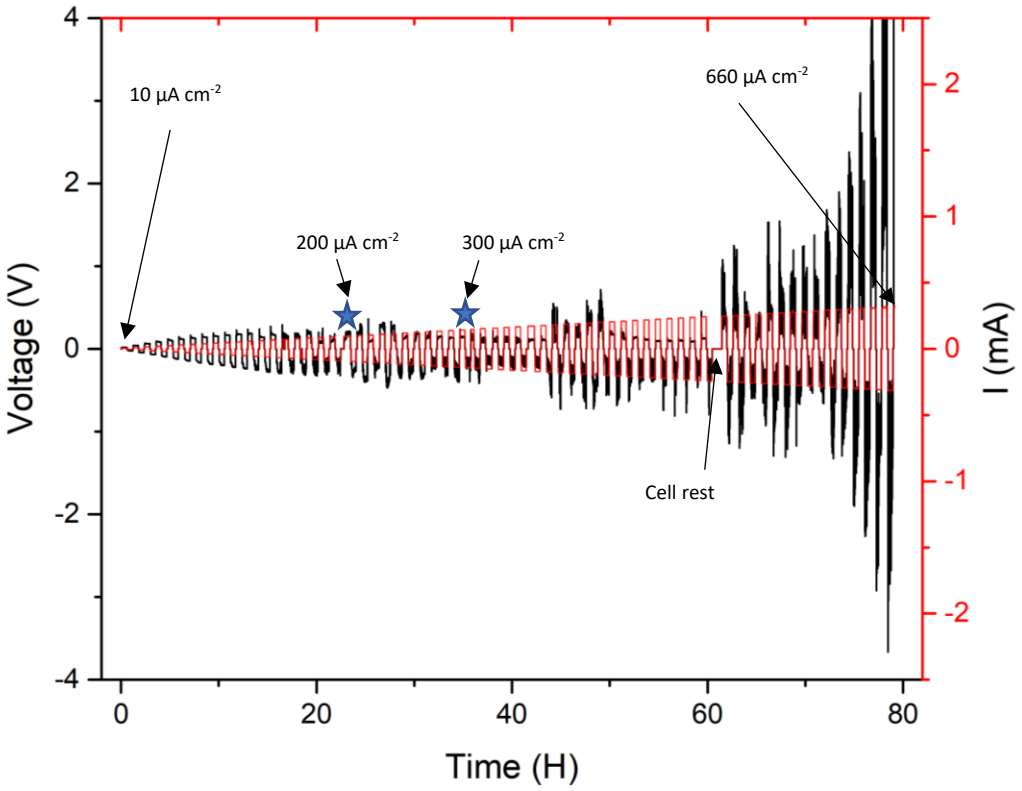
10 µA cm-2
200 µA cm-2
300 µA cm-2
660 µA cm-2
Cell rest
Voltage (V)
I (mA)
Time (H)
4
2
0
-2
-4
0
20
40
60
80
2
1
0
-1
-2

b)

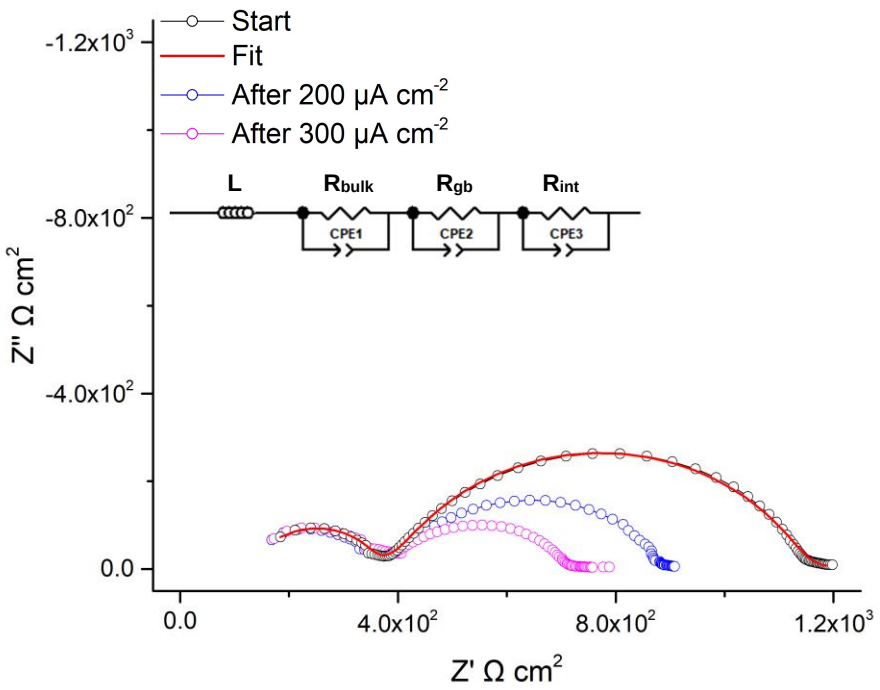
Start
Fit
After 200 µA cm-2
After 300 µA cm-2
L
Rbulk
Rgb
Rint
CPE1
CPE2
CPE3
Z'' Ω cm2
Z' Ω cm2
-1.2x10^3
-8.0x10^2
-4.0x10^2
0.0
0.0
4.0x10^2
8.0x10^2
1.2x10^3

c)

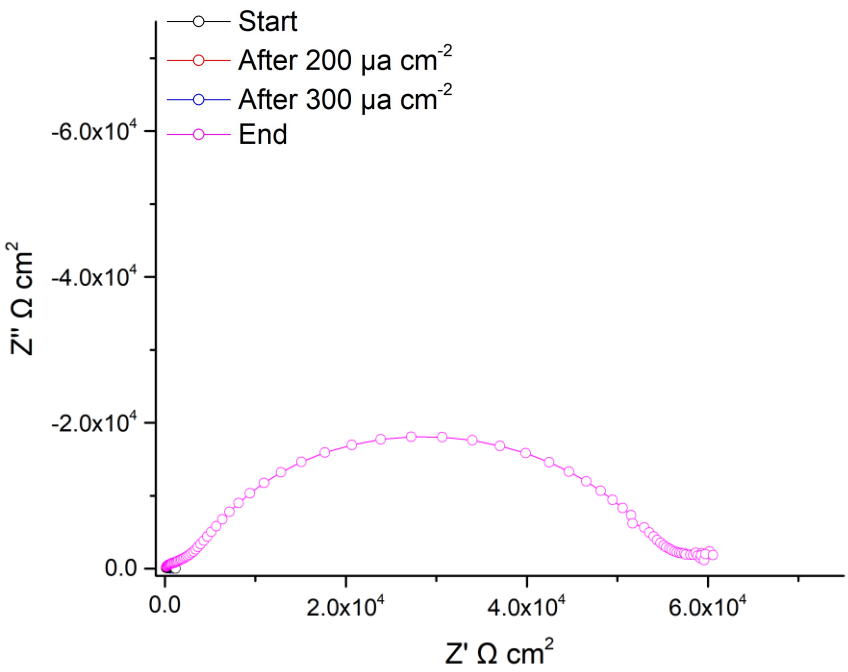

d)

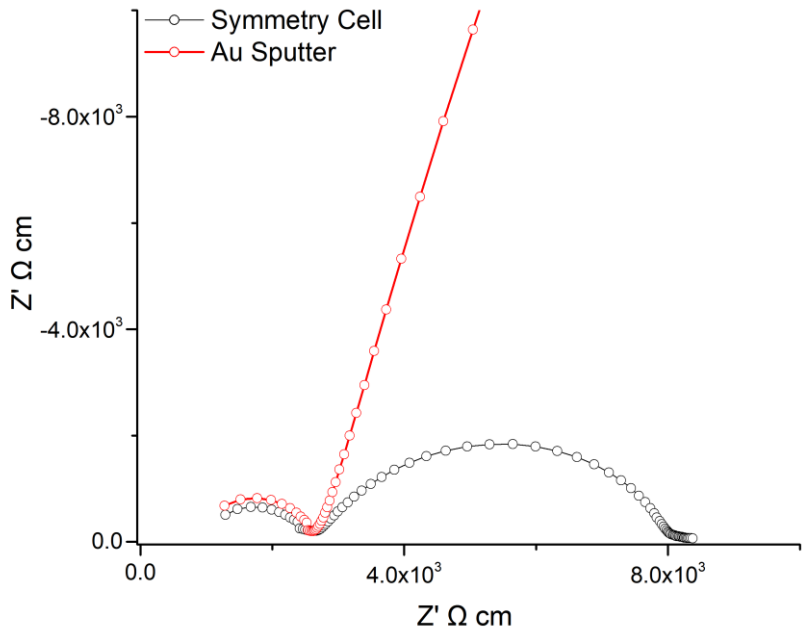

Figure 7. Symmetry cell impedance spectra and CCD density analysis where a) is the CCD analysed in increments of 10 µA cm^{-2}, stars indicate where cell was stopped for impedance analysis. Degradation of the cell occurred at 660 µA cm^{-2}. A short rest at 660 µA cm^{-2} (during CCD analysis) as testing had to be resumed to cycle at high current densities, as additional current steps could not be added during cycling. b) is the overlaid impedance spectrums during the CCD testing at different current densities at room temperature, c) the same as figure 7b but with final impedance spectrum showing interfacial degradation and d) is an overlaid impedance spectrum illustrating the correct assignment of the low frequency semi-circle to Li metal interface

a)

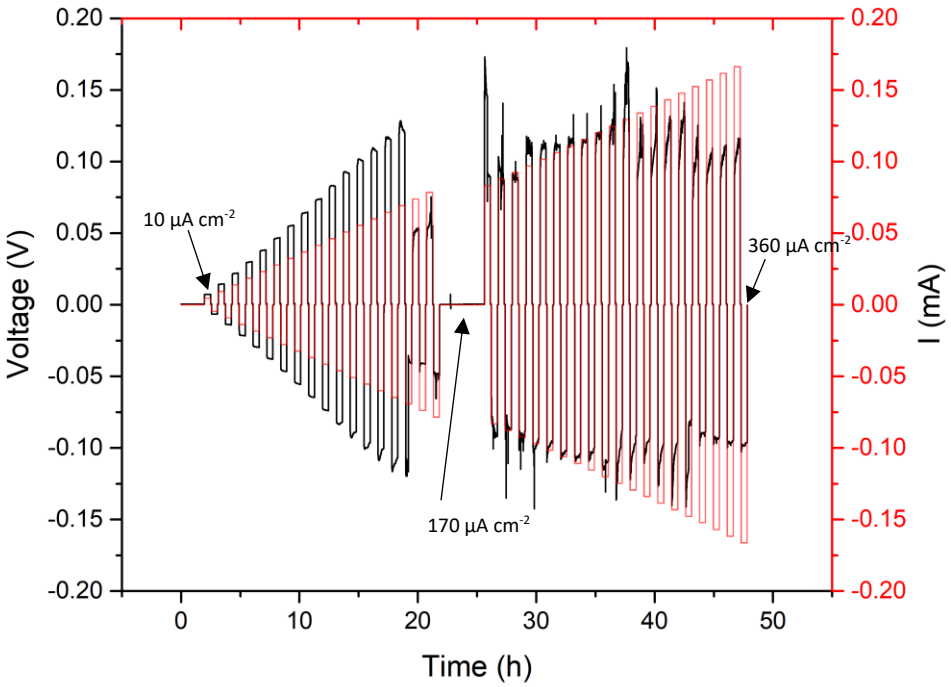

b)

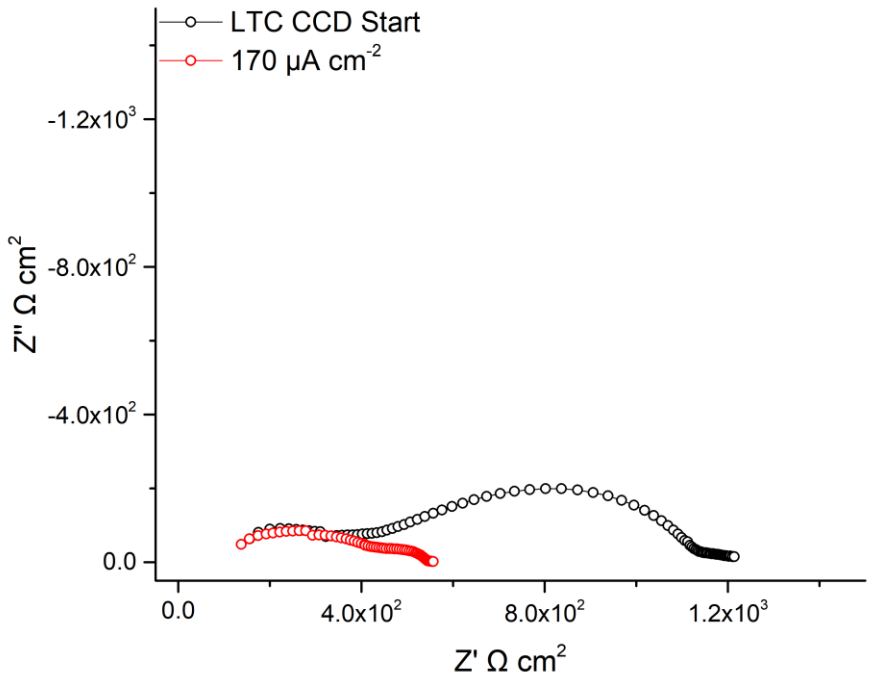

Figure 8. CCD analysis of LTC at 38°C where a) is the CCD analysed in increments of 10 µA cm^{-2} (starting at 10 µA cm^{-2}) the period of rest is where the cell was removed to analyse by impedance spectroscopy at room temperature and subsequently was further rested to stabilise at 38°C and b) is the impedance spectrums (both at 22°C) of the CCD cell at the start and after V drop.

a)

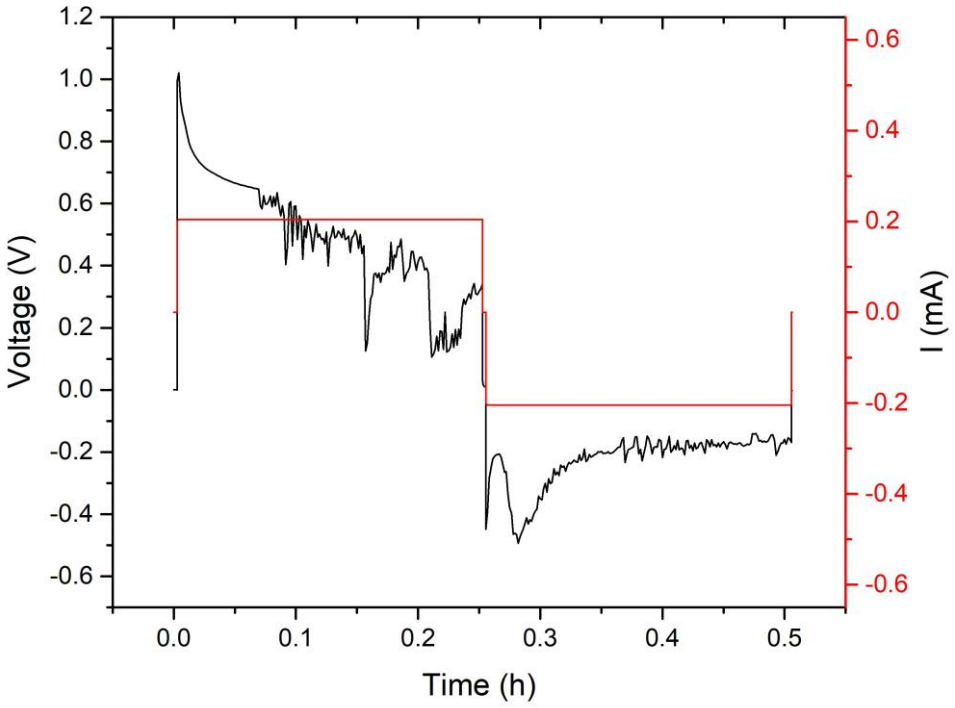

b)

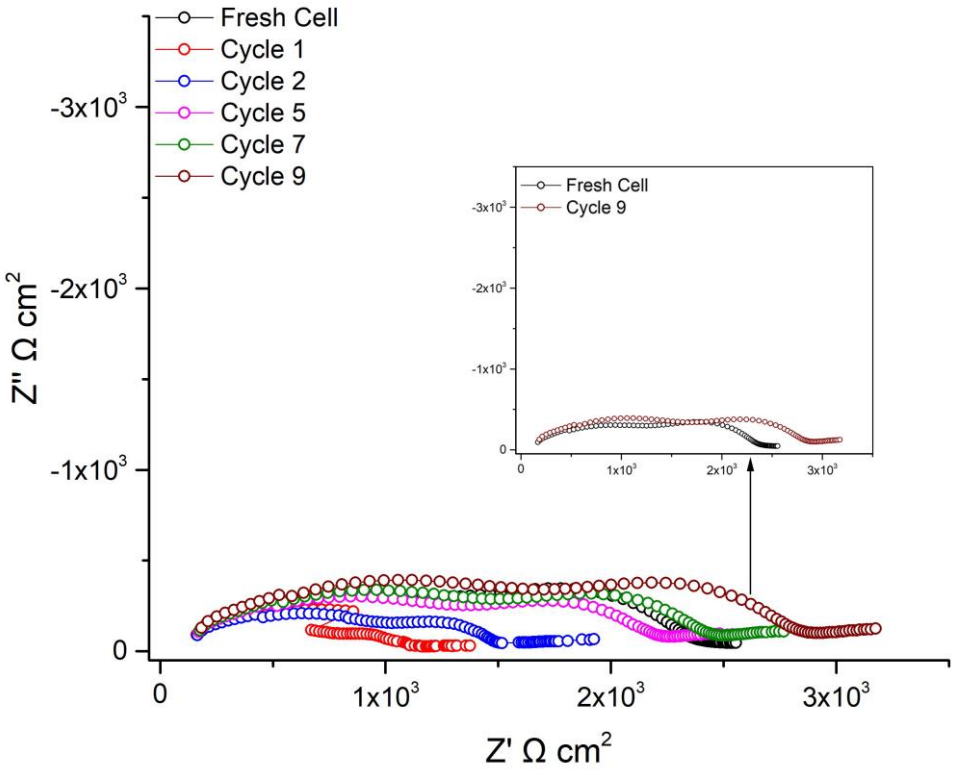

Figure 9. To assess cycling stability directly at high current densities, a fresh LTC cell was galvanostatically cycled at 500 µA cm^{-2} for a) one cycle with the corresponding impedance analysis in b) taken immediately after. Here, an initially large voltage is reduced, shortly after cycling began. Therefore, one cycle was completed before impedance analysis. Time difference between impedance cycles is 3 minutes, which is the length of each scan. Time difference between cycle 7 and 9 is 90 minutes. Inlay is the fresh cell overlaid only with cycle 9.

a)

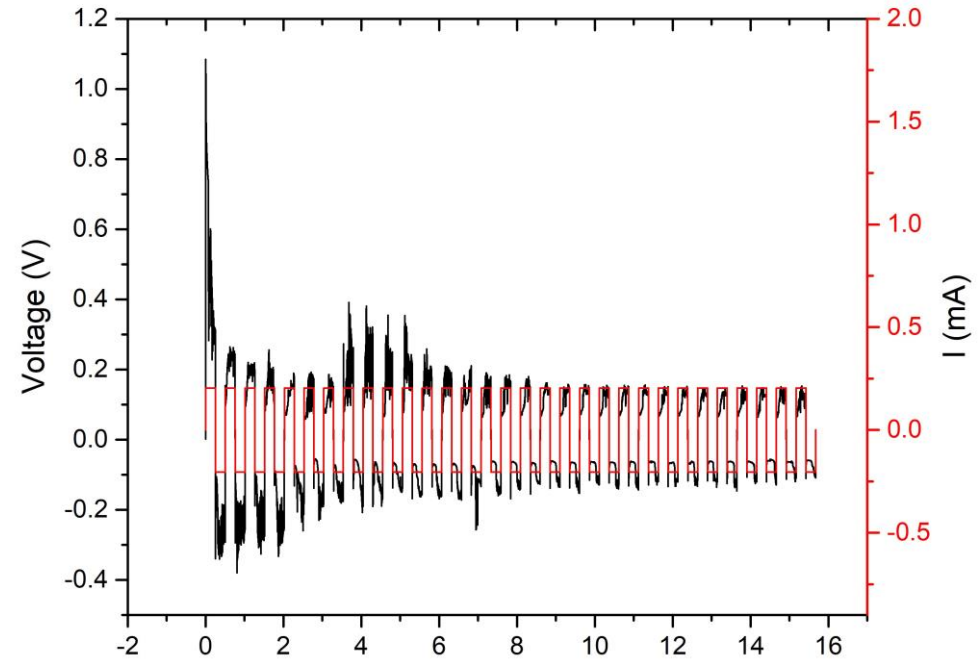

b)

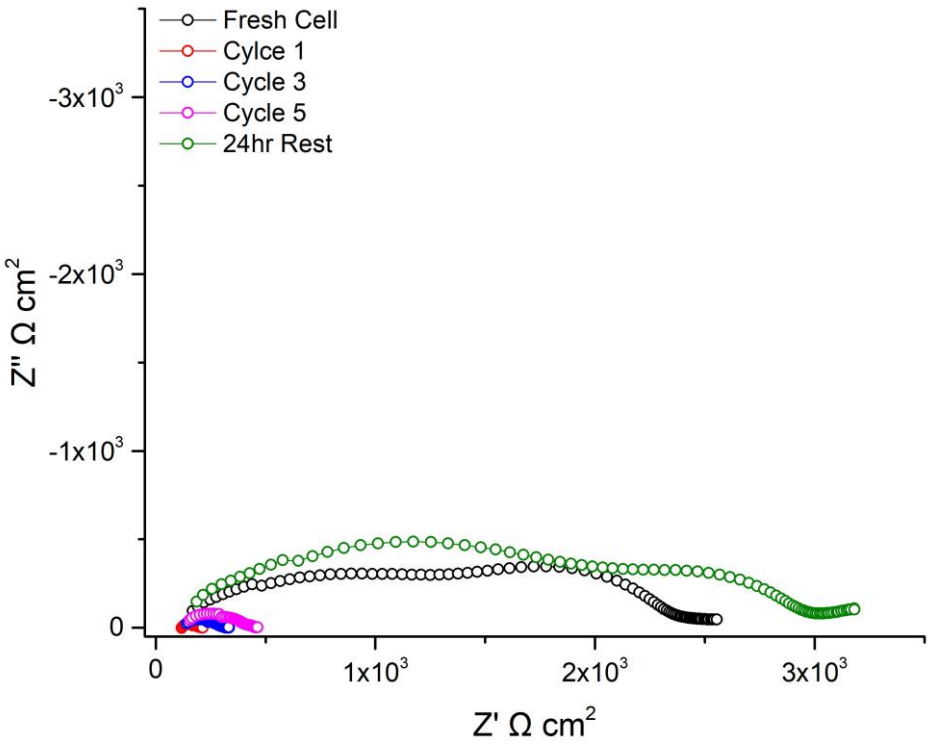

Figure 10. After the first cycle at 500 µA cm^{-2} and the corresponding impedance analysis in figure 9 was complete, LTC cycling was restarted at 500 µA cm^{-2} for a) 36 cycles with the corresponding impedance analysis in b) taken immediately after. Here, the cycling again begins with a high voltage which is similar to the single cycle in figure 9a, and drops in voltage equally as rapidly. This further confirms a change in the LTC pellet. The cell was left running for 36 cycles to assess if the healing phenomena remained, which was analysed by impedance spectroscopy in figure 10b.

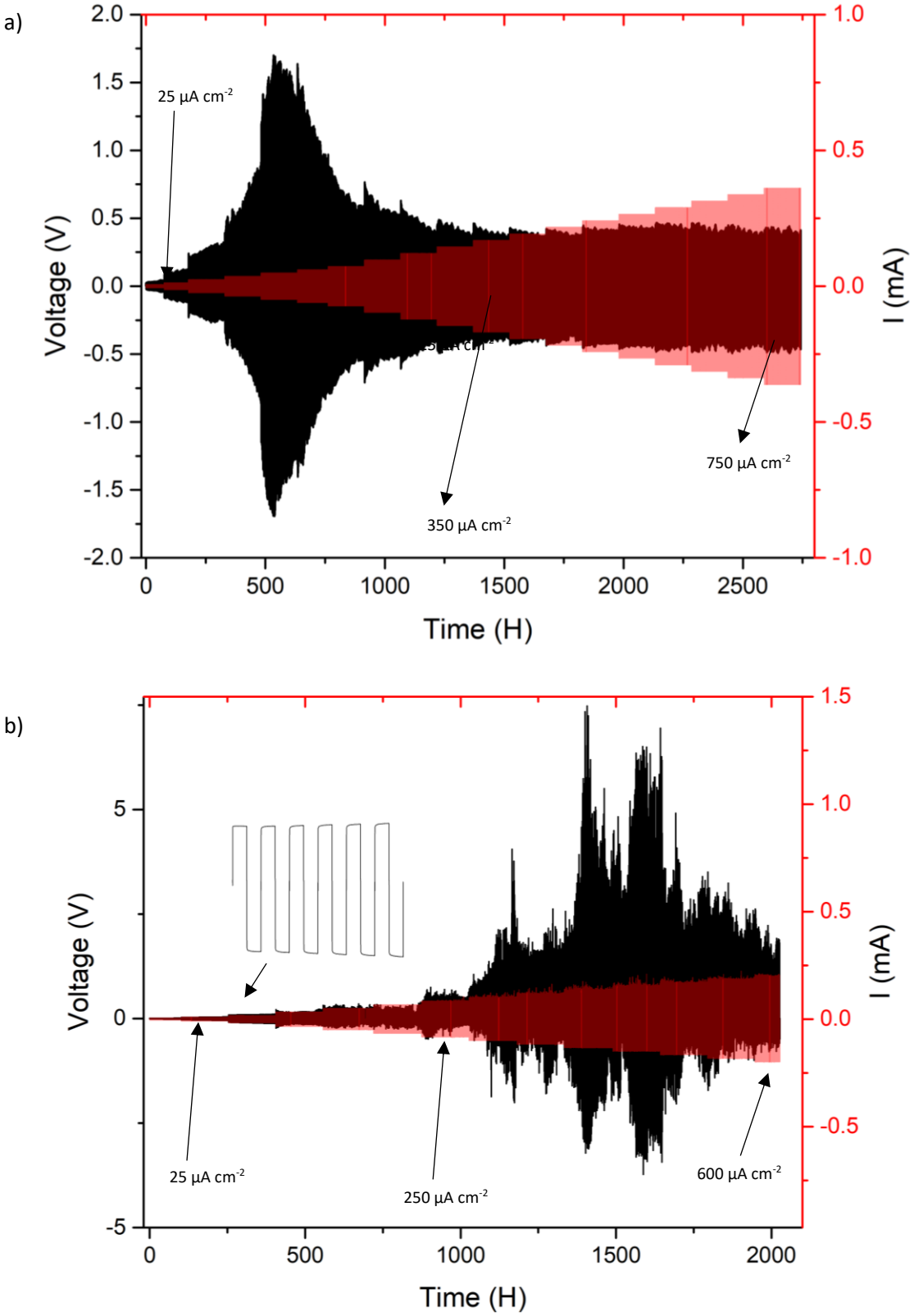

Figure 11. Long term stripping and plating cycling experiments, at differing current densities. Where a) is room temperature, where voltage fluctuates between 12-24°C and b) at 49°C with inlay showing stable voltage profiles until initial V drop occurred. Here, stripping and plating did not reveal typical short circuit behaviour and mirrored the results of the CCD analysis, whereupon the initially stable voltage is decreased but no short circuit is present. Although voltage stability remains far from ideal, the lack of short circuit further confirms the unusual behaviour of LTC over long term cycling. The overlapping red lines arise from impedance measurements, rest periods and from the need to pause the cell while others are attached and, in the case of 11b, time periods to allow to cell to equilibrate back to 49°C after a rest.

a)

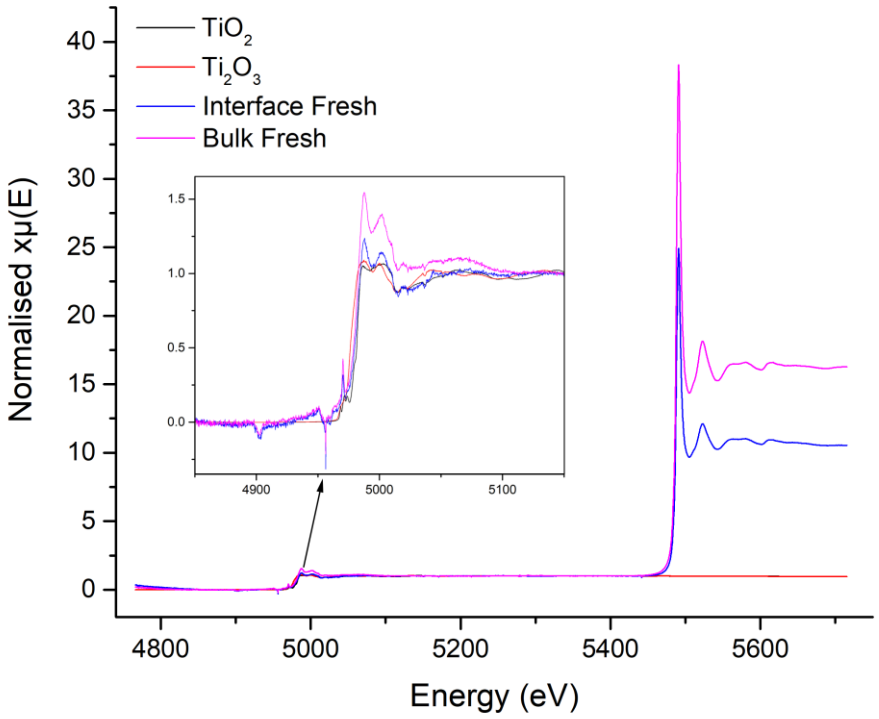

b)

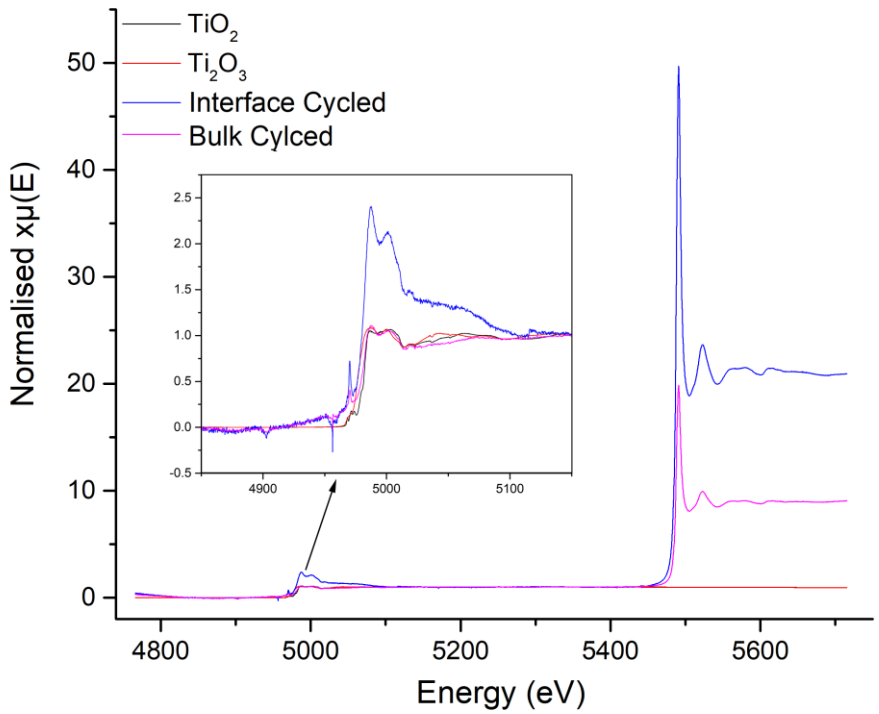

Figure 12. XANES spectra of Ti_2O_3 and anatase TiO_2 compared to LTC where a) is the comparison to freshly sintered and b) the comparison to cycled pellets, with powder taken from both the interface and bulk respectively. All peaks, although lacking intensity, remain similar, indicating no change of Ti oxidation state.

a)

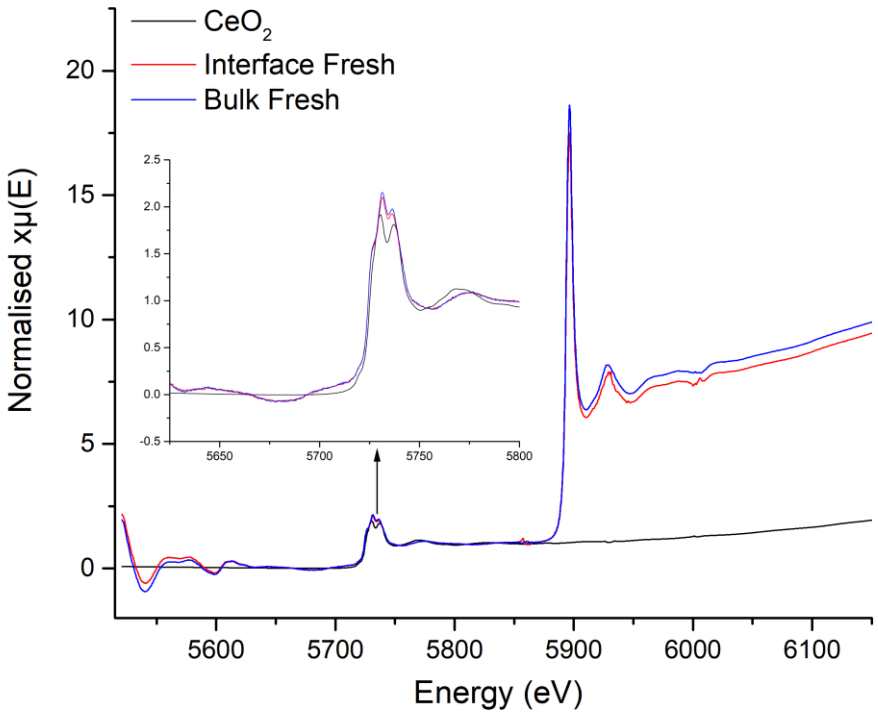

b)

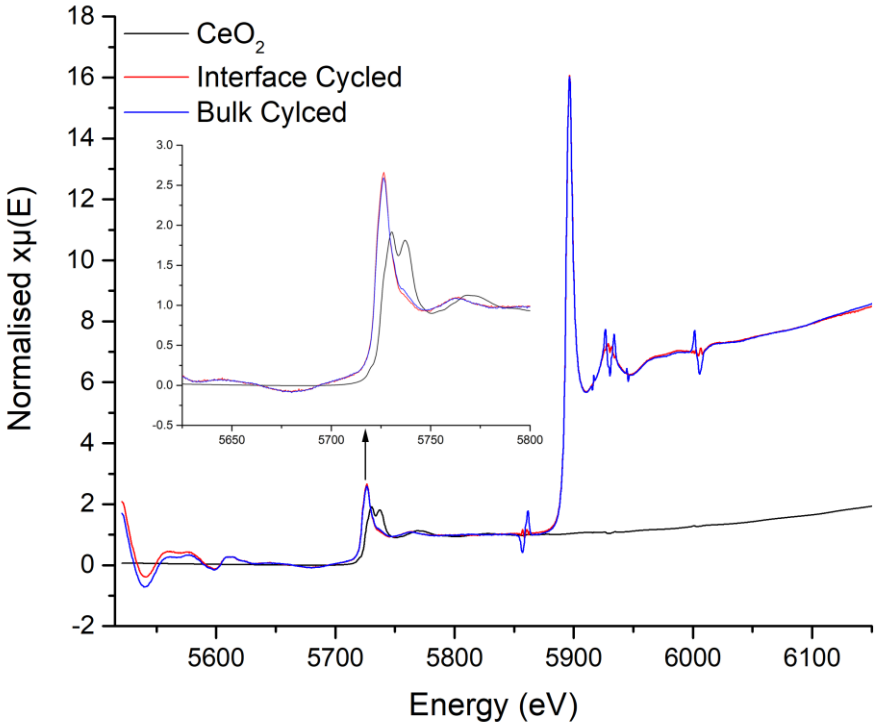

Figure 13. XANES spectra of CeO_2 compared to LTC where a) is the comparison to freshly sintered and b) the comparison to cycled pellets, with powder taken from both the interface and bulk respectively. No change of the Ce L edges is noted across the freshly prepared samples, but a clear change of Ce peaks is present in the cycled cells, whereupon the doublet has coalesced into a singular peak which has shifted to lower energy, this indicates formation of Ce^{3+}.

References

1. J. M. Tarascon and M. Armand, *Nature*, 2001, **414**, 359.
2. M. Armand and J. M. Tarascon, *Nature*, 2008, **451**, 652.
3. C.-X. Zu and H. Li, *Energy Environ. Sci.*, 2011, **4**, 2614-2624.
4. M. Park, X. Zhang, M. Chung, G. B. Less and A. M. Sastry, *J. Power Sources*, 2010, **195**, 7904-7929.
5. V. Thangadurai and W. Weppner, *Ionics*, 2006, **12**, 81-92.
6. H. Yang, C. Guo, A. Naveed, J. Lei, J. Yang, Y. Nuli and J. Wang, *Energy Stor. Mater.*, 2018, **14**, 199-221.
7. C. Yang, K. Fu, Y. Zhang, E. Hitz and L. Hu, *Adv. Mater.*, 2017, **29**, 1701169.
8. T. Kim, W. Song, D.-Y. Son, L. K. Ono and Y. Qi, *J. Mater. Chem. A*, 2019, **7**, 2942-2964.
9. B. Scrosati, J. Hassoun and Y. Sun, *Energy Environ. Sci.*, 2011, **4**, 3287-3295.
10. W. Xu, J. Wang, F. Ding, X. Chen, E. Nasybulin, Y. Zhang and J.-G. Zhang, *Energy Environ. Sci.*, 2014, **7**, 513-537.
11. A. Väyrynen and J. Salminen, *J. Chem. Thermodyn.*, 2012, **46**, 80-85.
12. C. Julien, A. Mauger, A. Vijh and K. Zaghib, *Lithium Batteries: Science and Technology*, Springer International Publishing, 2015.
13. J. B. Goodenough and K.-S. Park, *J. Am. Chem. Soc.*, 2013, **135**, 1167-1176.
14. N. Nitta, F. Wu, J. T. Lee and G. Yushin, *Mater. Today*, 2015, **18**, 252-264.
15. A. Lewandowski and A. Świderska-Mocek, *J. Power Sources*, 2009, **194**, 601-609.
16. H. Wu, D. Zhuo, D. Kong and Y. Cui, *Nat. Commun.*, 2014, **5**, 5193.
17. Y. Kato, S. Hori, T. Saito, K. Suzuki, M. Hirayama, A. Mitsui, M. Yonemura, H. Iba and R. Kanno, *Nat. Energy*, 2016, **1**, 16030.
18. V. A. Agubra and J. W. Fergus, *J. Power Sources*, 2014, **268**, 153-162.
19. L. Wang, Z. Zhou, X. Yan, F. Hou, L. Wen, W. Luo, J. Liang and S. X. Dou, *Energy Stor. Mater.*, 2018, **14**, 22-48.
20. V. Etacheri, R. Marom, R. Elazari, G. Salitra and D. Aurbach, *Energy Environ. Sci.*, 2011, **4**, 3243-3262.
21. X. Shen, H. Liu, X.-B. Cheng, C. Yan and J.-Q. Huang, *Energy Stor. Mater.*, 2018, **12**, 161-175.
22. H. Duan, H. Zheng, Y. Zhou, B. Xu and H. Liu, *Solid State Ionics*, 2018, **318**, 45-53.
23. J. Li, C. Ma, M. Chi, C. Liang and N. J. Dudney, *Adv. Energy Mater.*, 2015, **5**, 1401408.
24. F. Zheng, M. Kotobuki, S. Song, M. O. Lai and L. Lu, *J. Power Sources*, 2018, **389**, 198-213.
25. Y. Zheng, Y. Yao, J. Ou, M. Li, D. Luo, H. Dou, Z. Li, K. Amine, A. Yu and Z. Chen, *Chem. Soc. Rev.*, 2020, **49**, 8790-8839.
26. U. Roy, N. A. Fleck and V. S. Deshpande, *Extreme Mech. Lett.*, 2021, **46**, 101307.
27. J. A. Lewis, F. J. Q. Cortes, Y. Liu, J. C. Miers, A. Verma, B. S. Vishnugopi, J. Tippens, D. Prakash, T. S. Marchese, S. Y. Han, C. Lee, P. P. Shetty, H.-W. Lee, P. Shevchenko, F. De Carlo, C. Saldana, P. P. Mukherjee and M. T. McDowell, *Nat. Mater.*, 2021, **20**, 503-510.
28. J. G. Kim, B. Son, S. Mukherjee, N. Schuppert, A. Bates, O. Kwon, M. J. Choi, H. Y. Chung and S. Park, *J. Power Sources*, 2015, **282**, 299-322.
29. W. Luo, Y. Gong, Y. Zhu, Y. Li, Y. Yao, Y. Zhang, K. Fu, G. Pastel, C.-F. Lin, Y. Mo, E. D. Wachsman and L. Hu, *Adv. Mater.*, 2017, **29**, 1606042.
30. L. Cheng, C. H. Wu, A. Jarry, W. Chen, Y. Ye, J. Zhu, R. Kostecki, K. Persson, J. Guo, M. Salmeron, G. Chen and M. Doeff, *ACS Appl. Mater. Interfaces*, 2015, **7**, 17649-17655.
31. R. Sudo, Y. Nakata, K. Ishiguro, M. Matsui, A. Hirano, Y. Takeda, O. Yamamoto and N. Imanishi, *Solid State Ionics*, 2014, **262**, 151-154.
32. B. Chen, C. Xu and J. Zhou, *J. Electrochem. Soc.*, 2018, **165**, A3946-A3951.
33. Y. Zhu, X. He and Y. Mo, *J. Mater. Chem. A*, 2016, **4**, 3253-3266.
34. C. Bernuy-Lopez, W. Manalastas, J. M. Lopez del Amo, A. Aguadero, F. Aguesse and J. A. Kilner, *Chem. Mater.*, 2014, **26**, 3610-3617.
35. X. Huang, T. Xiu, M. E. Badding and Z. Wen, *Ceram. Int.*, 2018, **44**, 5660-5667.

36. T. Thompson, J. Wolfenstine, J. L. Allen, M. Johannes, A. Huq, I. N. David and J. Sakamoto, *J. Mater. Chem. A*, 2014, **2**, 13431-13436.
37. A. Ramzy and V. Thangadurai, *ACS Appl. Mater. Interfaces*, 2010, **2**, 385-390.
38. S. Hu, Y.-F. Li, R. Yang, Z. Yang and L. Wang, *Ceram. Int.*, 2018, **44**, 6614-6618.
39. Y. Ren, Y. Shen, Y. Lin and C.-W. Nan, *Electrochem. Commun.*, 2015, **57**, 27-30.
40. F. Flatscher, M. Philipp, S. Ganschow, H. M. R. Wilkening and D. Rettenwander, *J. Mater. Chem. A*, 2020, **8**, 15782-15788.
41. R. H. Brugge, F. M. Pesci, A. Cavallaro, C. Sole, M. A. Isaacs, G. Kerherve, R. S. Weatherup and A. Aguadero, *J. Mater. Chem. A*, 2020, **8**, 14265-14276.
42. Federico M. Pesci, R. H. Brugge, A. K. O. Hekselman, A. Cavallaro, R. J. Chater and A. Aguadero, *J. Mater. Chem. A*, 2018, **6**, 19817-19827.
43. A. F. Wells, *Structural inorganic chemistry*, Clarendon Press, 1984.
44. V. Thangadurai, S. Adams and W. Weppner, *Chem. Mater.*, 2004, **16**, 2998-3006.
45. E. J. Cussen and T. W. S. Yip, *J. Solid State Chem.*, 2007, **180**, 1832-1839.
46. E. J. Cussen, *Chem. Commun.*, 2006, **37**, 412-413.
47. M. P. O'Callaghan, D. R. Lynham, E. J. Cussen and G. Z. Chen, *Chem. Mater.*, 2006, **18**, 4681-4689.
48. V. Thangadurai, H. Kaack and W. J. F. Weppner, *J. Am. Ceram. Soc.*, 2004, **86**, 437-440.
49. R. Murugan, V. Thangadurai and W. Weppner, *Angew. Chem. Int. Ed.*, 2007, **46**, 7778-7781.
50. C. A. Geiger, E. Alekseev, B. Lazic, M. Fisch, T. Armbruster, R. Langner, M. Fechtelkord, N. Kim, T. Pettke and W. Weppner, *Inorg. Chem.*, 2011, **50**, 1089-1097.
51. J. Awaka, N. Kijima, K. Kataoka, H. Hayakawa, K.-i. Ohshima and J. Akimoto, *J. Solid State Chem.*, 2010, **183**, 180-185.
52. J. Awaka, N. Kijima, H. Hayakawa and J. Akimoto, *J. Solid State Chem.*, 2009, **182**, 2046-2052.
53. J. Percival, E. Kendrick, R. I. Smith and P. R. Slater, *Dalton Trans.*, 2009, **26**, 5177-5181.
54. B. Dong, S. R. Yeandel, P. Goddard and P. R. Slater, *Chem. Mater.*, 2020, **32**, 215-223.
55. R. Wagner, G. J. Redhammer, D. Rettenwander, A. Senyshyn, W. Schmidt, M. Wilkening and G. Amthauer, *Chem. Mater.*, 2016, **28**, 1861-1871.
56. J. Percival and P. R. Slater, *Solid State Commun.*, 2007, **142**, 355-357.
57. R. Murugan, V. Thangadurai and W. Weppner, *Appl. Phys. A*, 2008, **91**, 615-620.
58. M. A. Howard, O. Clemens, E. Kendrick, K. S. Knight, D. C. Apperley, P. A. Anderson and P. R. Slater, *Dalton Trans*, 2012, **41**, 12048-12053.
59. J. L. Allen, J. Wolfenstine, E. Rangasamy and J. Sakamoto, *J. Power Sources*, 2012, **206**, 315-319.
60. B. Dong, L. L. Driscoll, M. P. Stockham, E. Kendrick and P. R. Slater, *Solid State Ionics*, 2020, **350**, 115317.
61. M. P. Stockham, B. Dong, M. S. James, Y. Li, Y. Ding and P. R. Slater, *Dalton Trans.*, 2021, **50**, 2364-2374.
62. B. Dong, M. P. Stockham, P. A. Chater and P. R. Slater, *Dalton Trans.*, 2020, **49**, 11727-11735.
63. M. A. Howard, O. Clemens, E. Kendrick, K. S. Knight, D. C. Apperley, P. A. Anderson and P. R. Slater, *Dalton Trans.*, 2012, **41**, 12048-12053.
64. S. Narayanan and V. Thangadurai, *J. Power Sources*, 2011, **196**, 8085-8090.
65. S. Narayanan, F. Ramezanipour and V. Thangadurai, *J. Phys. Chem. C*, 2012, **116**, 20154-20162.
66. M. Botros, R. Djenadic, O. Clemens, M. Möller and H. Hahn, *J. Power Sources*, 2016, **309**, 108-115.
67. J.-F. Wu, E.-Y. Chen, Y. Yu, L. Liu, Y. Wu, W. K. Pang, V. K. Peterson and X. Guo, *ACS Appl. Mater. Interfaces*, 2017, **9**, 1542-1552.
68. R. H. Brugge, J. A. Kilner and A. Aguadero, *Solid State Ionics*, 2019, **337**, 154-160.
69. X. Wang, J. Liu, R. Yin, Y. Xu, Y. Cui, L. Zhao and X. Yu, *Mater. Lett.*, 2018, **231**, 43-46.
70. J. Gai, E. Zhao, F. Ma, D. Sun, X. Ma, Y. Jin, Q. Wu and Y. Cui, *J. Eur. Ceram. Soc.*, 2018, **38**, 1673-1678.

71. N. Janani, C. Deviannapoorani, L. Dhivya and R. Murugan, *RSC Adv.*, 2014, **4**, 51228-51238.
72. V. Thangadurai and W. Weppner, *J. Am. Ceram. Soc.*, 2005, **88**, 411-418.
73. Y. Zhang, F. Chen, J. Li, L. Zhang, J. Gu, D. Zhang, K. Saito, Q. Guo, P. Luo and S. Dong, *Electrochim. Acta*, 2018, **261**, 137-142.
74. C. Shao, Z. Yu, H. Liu, Z. Zheng, N. Sun and C. Diao, *Electrochim. Acta*, 2017, **225**, 345-349.
75. J. Gao, J. Zhu, X. Li, J. Li, X. Guo, H. Li and W. Zhou, *Adv. Funct. Mater.*, 2021, **31**, 2001918.
76. M. P. Stockham, B. Dong and P. R. Slater, *J. Solid State Chem.*, 2022, **308**, 122944.
77. R. H. Brugge, A. K. O. Hekselman, A. Cavallaro, F. M. Pesci, R. J. Chater, J. A. Kilner and A. Aguadero, *Chem. Mater.*, 2018, **30**, 3704-3713.
78. G. Larraz, A. Orera and M. L. Sanjuán, *J. Mater. Chem. A*, 2013, **1**, 11419-11428.
79. C. Galven, J. Dittmer, E. Suard, F. Le Berre and M.-P. Crosnier-Lopez, *Chem. Mater.*, 2012, **24**, 3335-3345.
80. M. A. Howard, O. Clemens, K. S. Knight, P. A. Anderson, S. Hafiz, P. M. Panchmatia and P. R. Slater, *J. Mater. Chem. A*, 2013, **1**, 14013-14022.
81. M. A. Howard, O. Clemens, A. S. Parvathy, P. A. Anderson and P. R. Slater, *J. Alloys Compd.*, 2016, **670**, 78-84.
82. J. Percival, D. Apperley and P. R. Slater, *Solid State Ionics*, 2008, **179**, 1693-1696.
83. H. Peng, Y. Zhang, L. Li and L. Feng, *Solid State Ionics*, 2017, **304**, 71-74.
84. B. Toby and R. Dreele, *J. Appl. Crystallogr.*, 2013, **46**, 544-549.
85. M. P. Stockham, B. Dong, M. S. James, Y. Li, Y. Ding, E. Kendrick and P. Slater, *Dalton Trans.*, 2021, **50**, 13786-13800.
86. R. Wagner, G. J. Redhammer, D. Rettenwander, G. Tippelt, A. Welzl, S. Taibl, J. Fleig, A. Franz, W. Lottermoser and G. Amthauer, *Chem. Mater.*, 2016, **28**, 5943-5951.
87. N. Hamao, K. Kataoka and J. Akimoto, *J. Ceram. Soc. Jpn.*, 2017, **125**, 272-275.
88. M. P. Stockham, B. Dong, Y. Ding, Y. Li and P. R. Slater, *Dalton Trans.*, 2020, **49**, 10349-10359.
89. D. Rettenwander, G. Redhammer, F. Preishuber-Pflügl, L. Cheng, L. Miara, R. Wagner, A. Welzl, E. Suard, M. M. Doeff, M. Wilkening, J. Fleig and G. Amthauer, *Chem. Mater.*, 2016, **28**, 2384-2392.
90. A. Wachter-Welzl, J. Kirowitz, R. Wagner, S. Smetaczek, G. C. Brunauer, M. Bonta, D. Rettenwander, S. Taibl, A. Limbeck, G. Amthauer and J. Fleig, *Solid State Ionics*, 2018, **319**, 203-208.
91. S. Narayanan, A. K. Baral and V. Thangadurai, *Phys. Chem. Chem. Phys.*, 2016, **18**, 15418-15426.
92. J. Zhu, X. Li, C. Wu, J. Gao, H. Xu, Y. Li, X. Guo, H. Li and W. Zhou, *Angew. Chem. Int. Ed.*, 2021, **60**, 3781-3790.
93. George V. Alexander, N. C. Rosero-Navarro, A. Miura, K. Tadanaga and R. Murugan, *J. Mater. Chem. A*, 2018, **6**, 21018-21028.
94. S. Ohta, T. Kobayashi and T. Asaoka, *J. Power Sources*, 2011, **196**, 3342-3345.
95. Y. Li, J.-T. Han, C.-A. Wang, H. Xie and J. B. Goodenough, *J. Mater. Chem.*, 2012, **22**, 15357-15361.
96. J. Kanchanawarin, W. Limphirat, P. Promchana, T. Sooknoi, T. Maluangnont, K. Simalaotao, A. Boonchun, P. Reunchan, S. Limpijumnong and J. T-Thienprasert, *J. Appl. Phys.*, 2018, **124**, 155101.
97. D. Mardare, A. Yildiz, R. Apetrei, P. Rambu, D. Florea, N. G. Gheorghe, D. Macovei, C. M. Teodorescu and D. Luca, *J. Mater. Res.*, 2012, **27**, 2271-2277.
98. H. Masai, H. Sakurai, A. Koreeda, Y. Fujii, T. Ohkubo, T. Miyazaki and T. Akai, *Sci. Rep.*, 2020, **10**, 11615.
99. A. J. Berry, A. M. Walker, J. Hermann, H. S. C. O'Neill, G. J. Foran and J. D. Gale, *Chem. Geol.*, 2007, **242**, 176-186.
100. M. R. Ackerson, N. D. Tailby and E. B. Watson, *Am. Mineral.*, 2017, **102**, 173-183.

101. S. Phokha, S. Pinitsoontorn, P. Chirawatkul, Y. Poo-arporn and S. Maensiri, *Nanoscale Res. Lett.*, 2012, **7**, 425.
102. C. H. Booth, M. D. Walter, M. Daniel, W. W. Lukens and R. A. Andersen, *Phys. Rev. Lett.*, 2005, **95**, 267202.
103. M. Tella, M. Auffan, L. Brousset, E. Morel, O. Proux, C. Chanéac, B. Angeletti, C. Pailles, E. Artells, C. Santaella, J. Rose, A. Thiéry and J. Y. Bottero, *Environ. Sci.: Nano*, 2015, **2**, 653-663.
104. W. Yuan, Q. Ma, Y. Liang, C. Sun, K. V. L. V. Narayanachari, M. J. Bedzyk, I. Takeuchi and S. M. Haile, *J. Mater. Chem. A*, 2020, **8**, 9850-9858.

Supplementary Information -- Reactive sintering of $Li_{6.5}La_3Zr_1Nb_{0.5}Ce_{0.25}Ti_{0.25}O_{12}$ for high density lithium garnet electrolytes with anti-dendritic healing properties.

M. P. Stockham[1*], B. Dong[1,3], M.S. James[1], P. Zhu[2,3], E. Kendrick[2,3], P.R. Slater[1,3*]

[1]School of Chemistry, University of Birmingham, Birmingham B15 2TT. UK

[2]School of Metallurgy and Materials, University of Birmingham, Birmingham B15 2TT. UK

[3]The Faraday Institution, Quad One, Harwell Campus, Didcot OX11 0RA, UK

Correspondence to

M. P. Stockham/P. R. Slater

School of Chemistry, University of Birmingham, Birmingham B15 2TT. UK

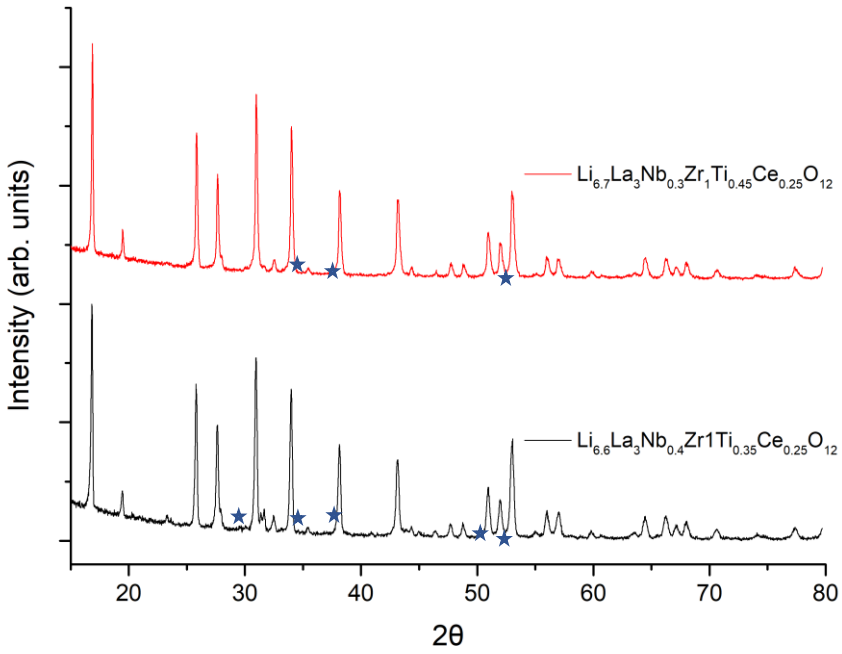

Figure S1 XRD patterns of $Li_{6.6}La_3Nb_{0.4}Zr_1Ti_{0.35}Ce_{0.25}O_{12}$ and $Li_{6.7}La_3Nb_{0.3}Zr_1Ti_{0.45}Ce_{0.25}O_{12}$ showing CeO_2 and Ce_4O_7 impurities marked with blue stars

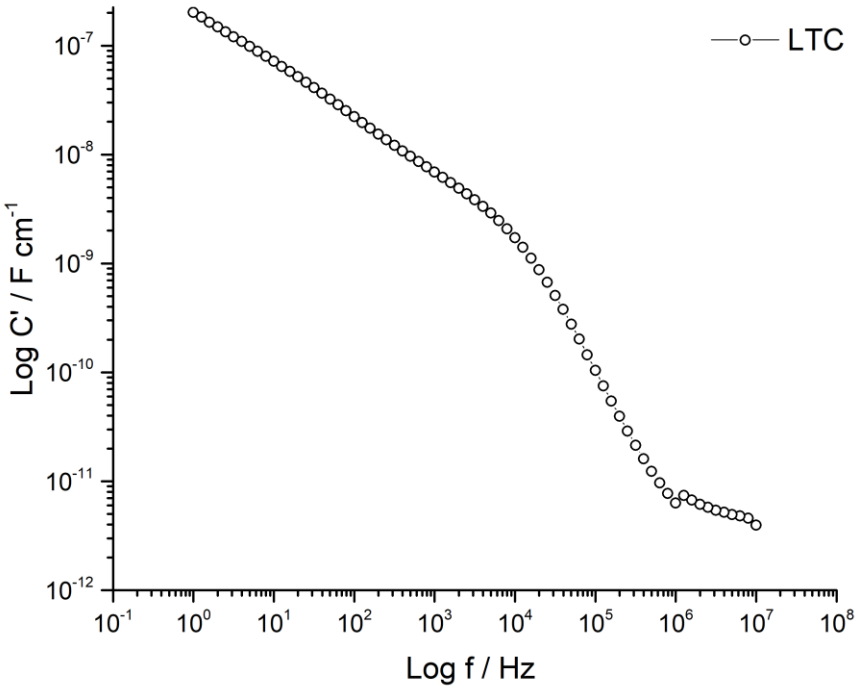

Figure S2. Spectroscopic C plot of LTC at 22°C showing high frequency plateau at 4.79 $x10^{-12}$ F cm^{-1}

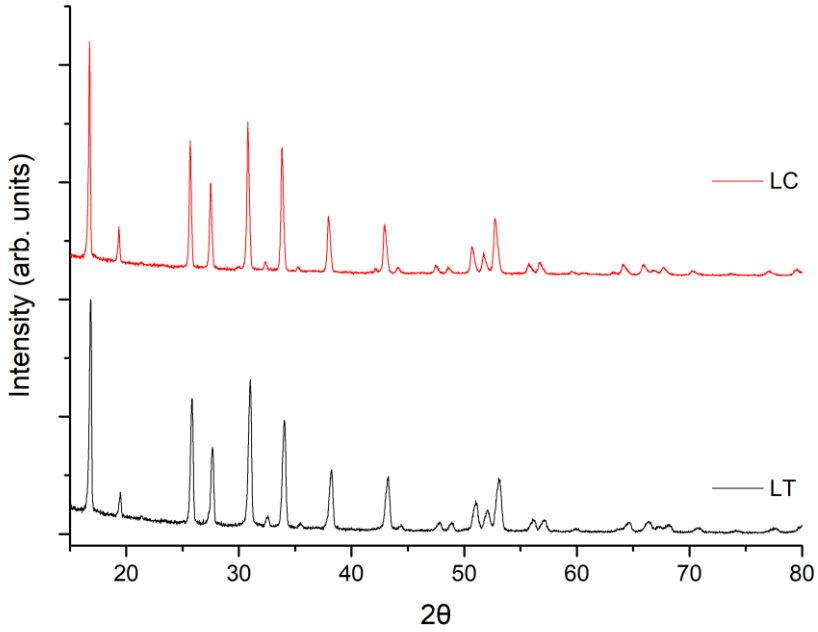

Figure S3. XRD patterns of LT and LC, both showing pure phases indexed on $Ia\bar{3}d$ type symmetry

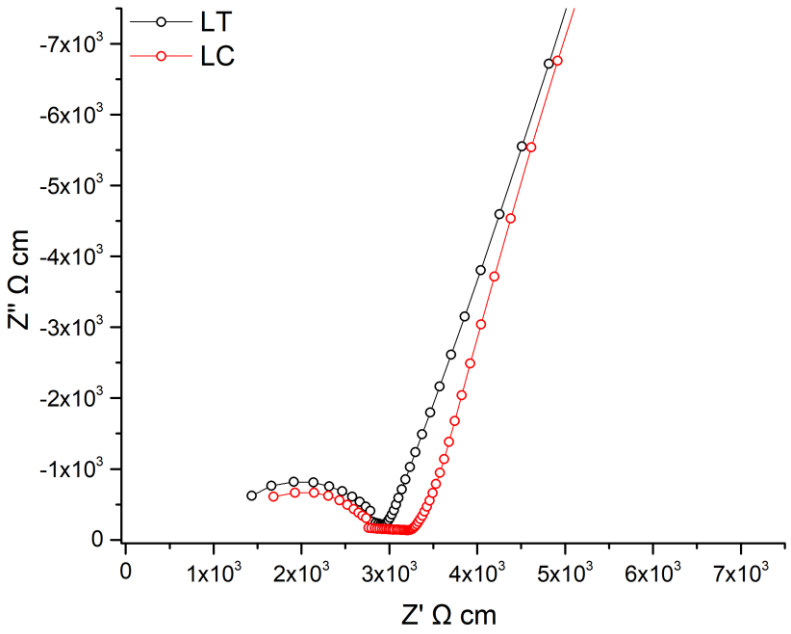

Figure S4. Impedance spectra of LT and LC showing high conductivity. LT is at 22°C and LC at 27°C due to unavoidable temperature differences as the laboratory lacks climate control.

a)

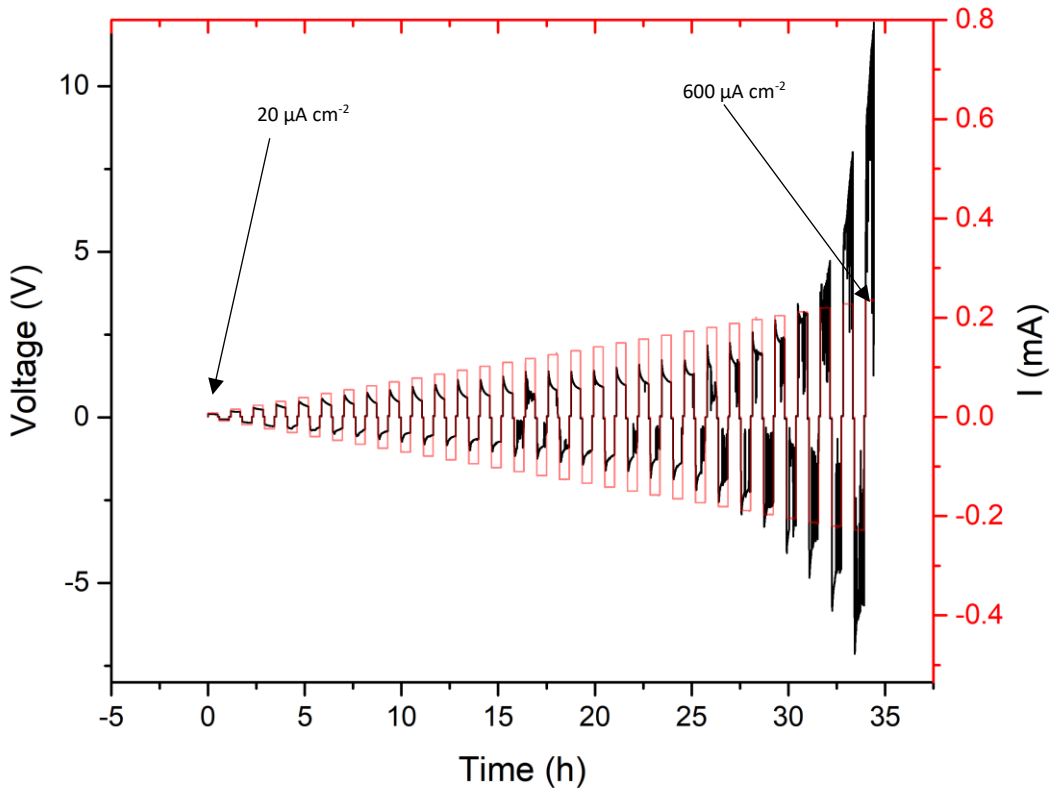

b)

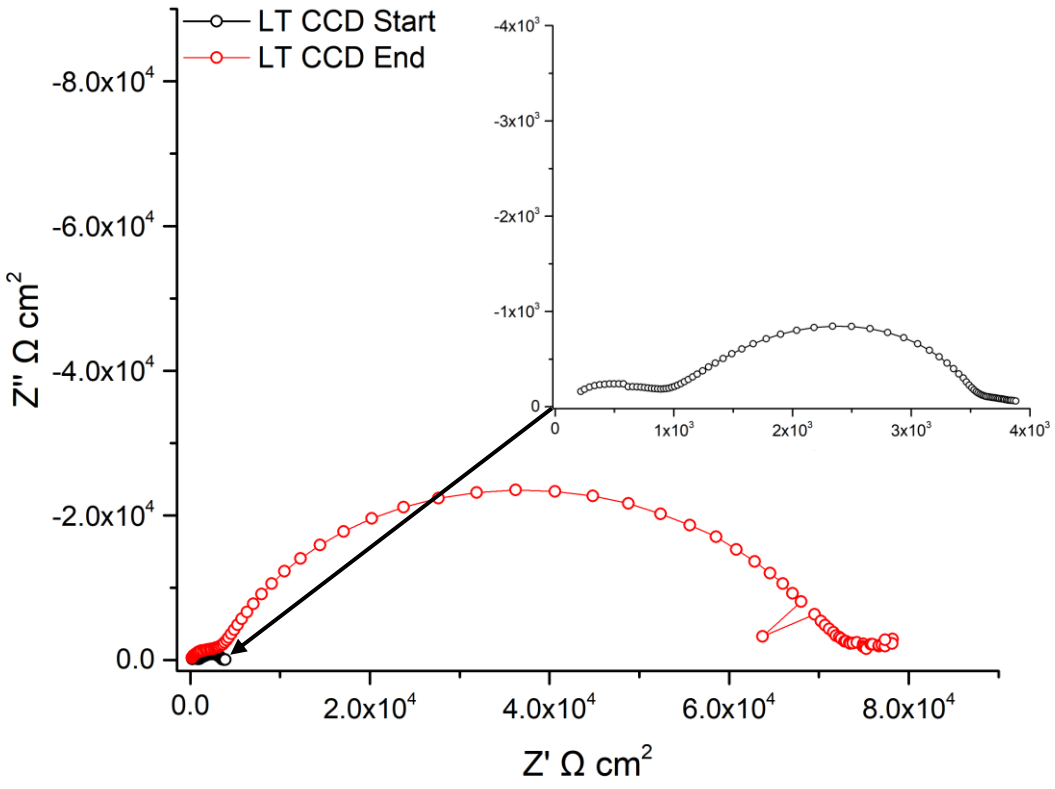

Figure S6. a) CCD analysis of LT garnets in increments of 20 µA cm^{-2} (starting at 20 µA cm^{-2}). b) Impedance spectrums of LTC at the start and upon the voltage spike to 10V, which automatically stopped the tester. Inlay is the original LT spectrum prior to interfacial breakdown.

a)

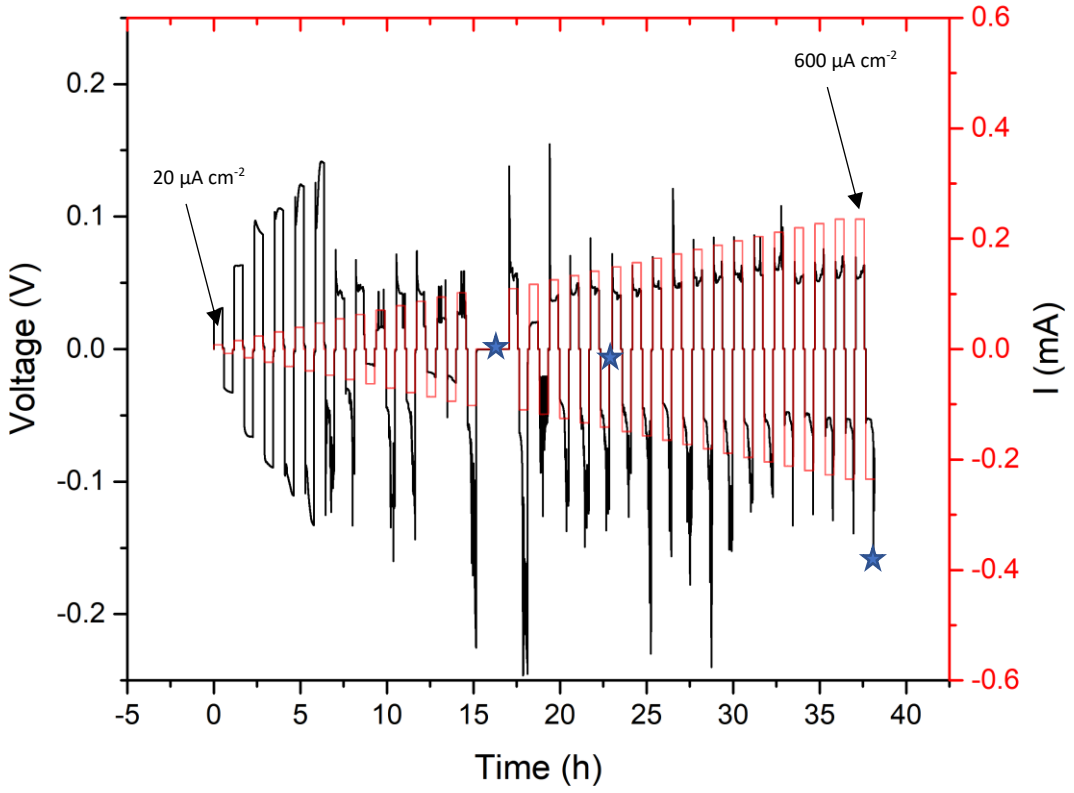

b)

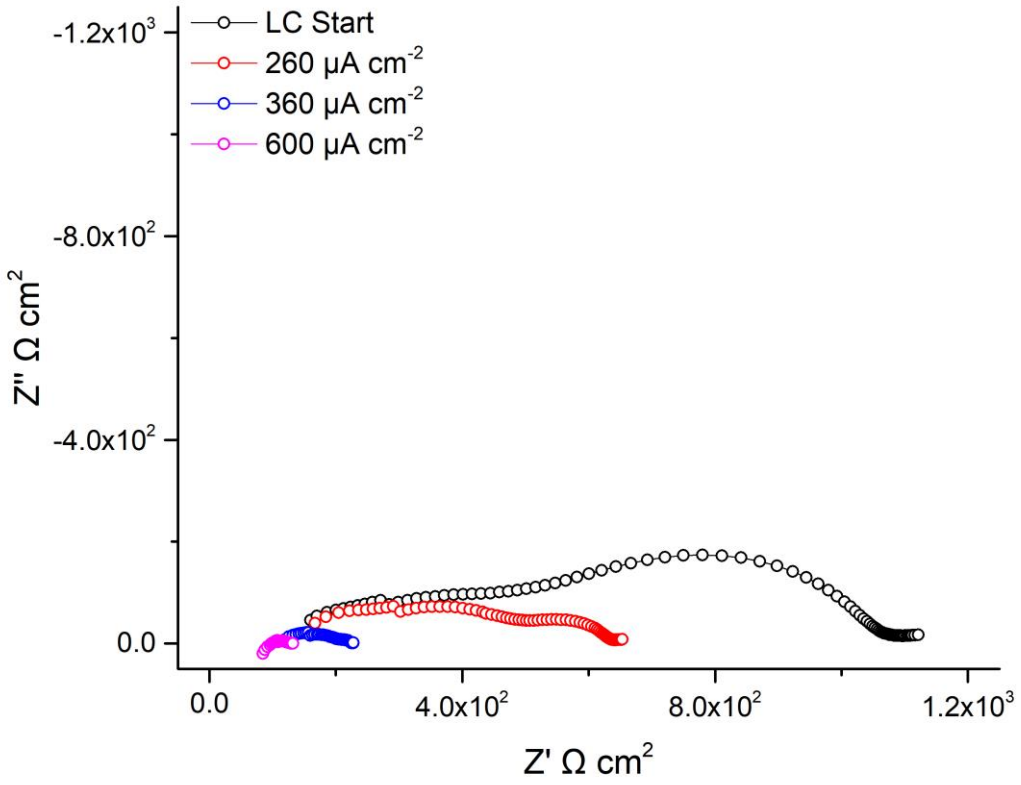

Figure S5. a) CCD analysis of LC garnets in increments of 20 µA cm^{-2} (starting at 20 µA cm^{-2}). Stars indicate where cell was stopped for corresponding impedance measurements seen in b).

12.3. APPENDIX 3 – SUPPLEMENTARY INFORMATION FOR CHAPTER 5.

12.3.1 Evaluation of the effect of site substitution of Pr doping in the lithium garnet system $Li_5La_3Nb_2O_{12}$

M. P. Stockham[1*], B. Dong[1], Y. Ding[2], Y. Li[2], P.R. Slater[1*]

[1]School of Chemistry, University of Birmingham, Birmingham B15 2TT. UK

[2]School of Chemical Engineering, University of Birmingham, Birmingham B15 2TT. UK

Correspondence to

M. P. Stockham/P. R. Slater

School of Chemistry, University of Birmingham, Birmingham B15 2TT. UK

Comparative XRD patterns before and after densification via high temperature N_2 heat treatments, showing increased phase degradation as Pr content increased. Additionally, in figure S1a an XRD pattern is shown after storage in an Ar glove box for 1 week.

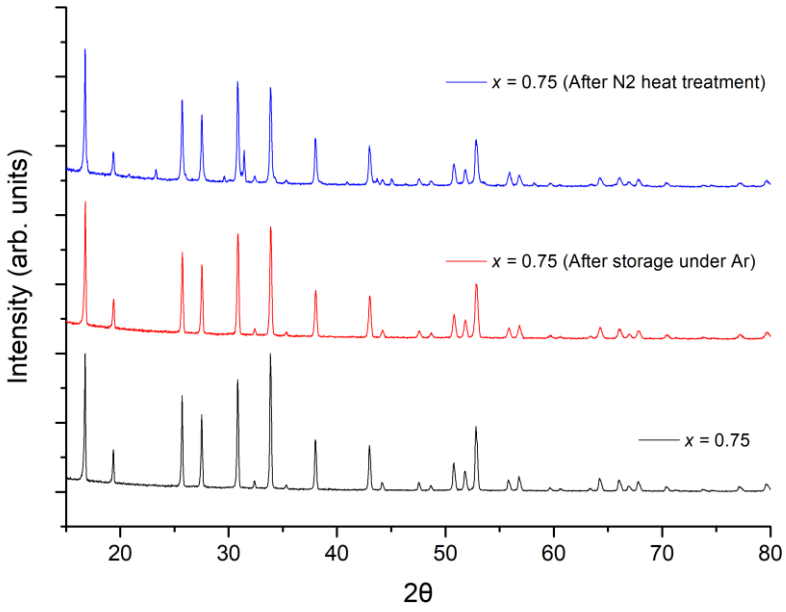

Figure S1a. XRD patterns for $Li_{5.75}La_3Nb_{1.25}Pr_{0.75}O_{12}$ freshly synthesised, after storage in a Ar glove box for 1 week and after the high temperature N_2 treatment, the latter of which shows phase degradation.

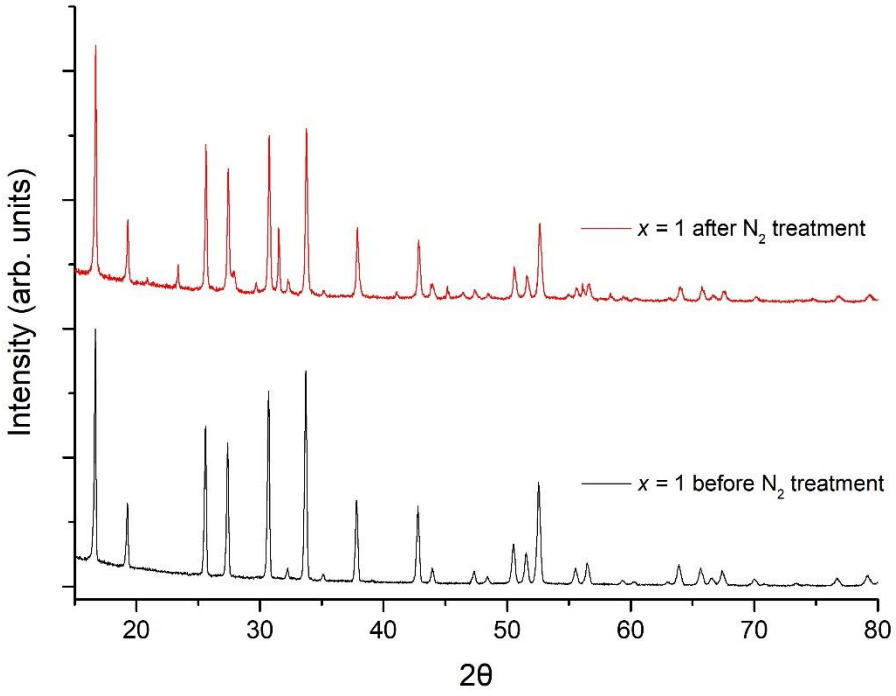

Figure S1b. XRD patterns for $Li_6La_3Nb_1Pr_1O_{12}$ freshly synthesised and after the high temperature N_2 treatment, the latter of which shows more severe phase degradation than x = 0.75

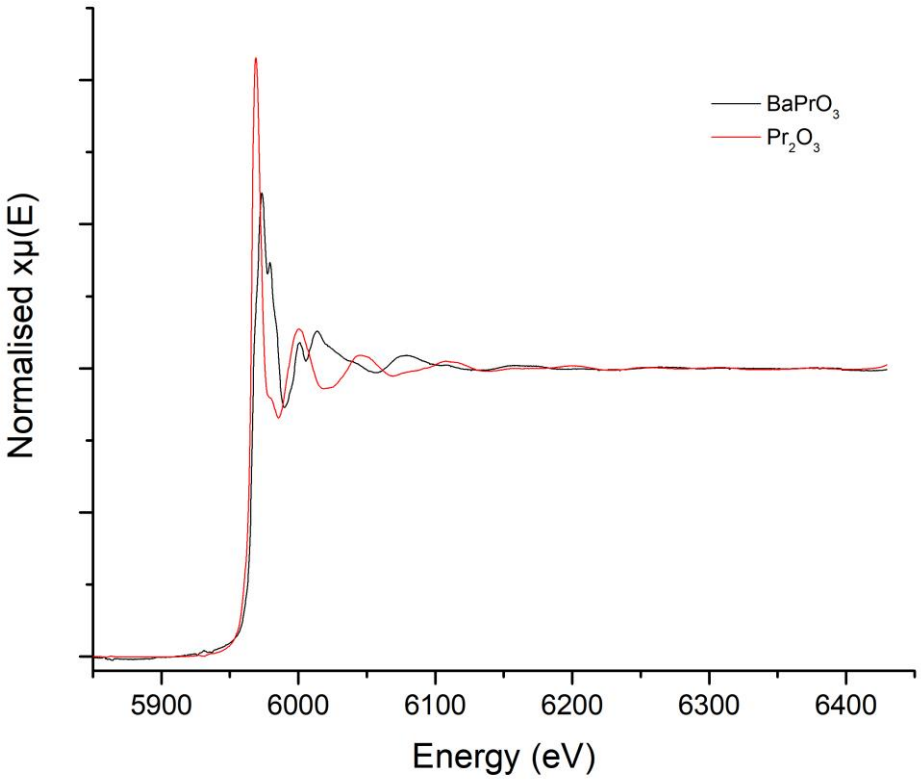

Figure S2. XANES spectra of reference samples Pr_2O_3 and $BaPrO_3$ overlaid.

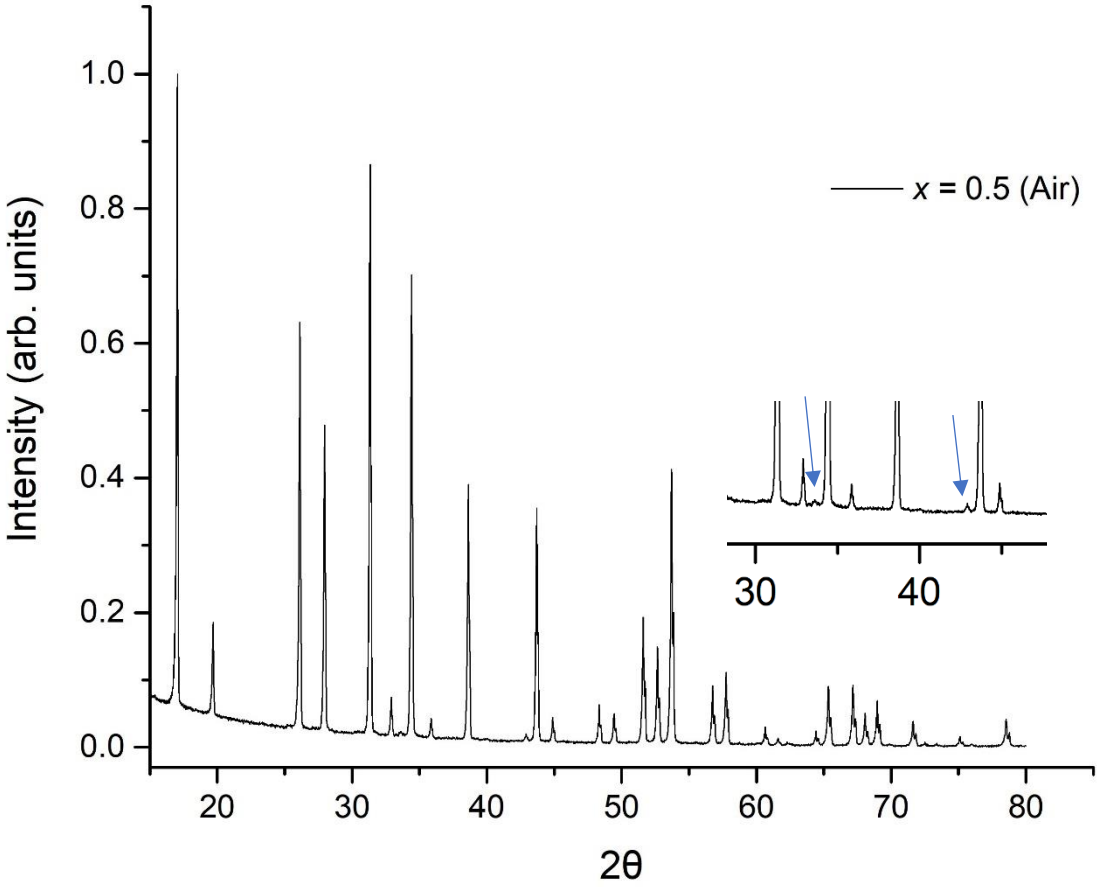

Figure S3. Example XRD of La site doping (x = 0.5 synthesised in air) showing small Li_3NbO_4 impurity, marked additionally with arrows in the magnified inlay. This impurity was noted for all air-based synthesis and in some H_2 synthesised phases.

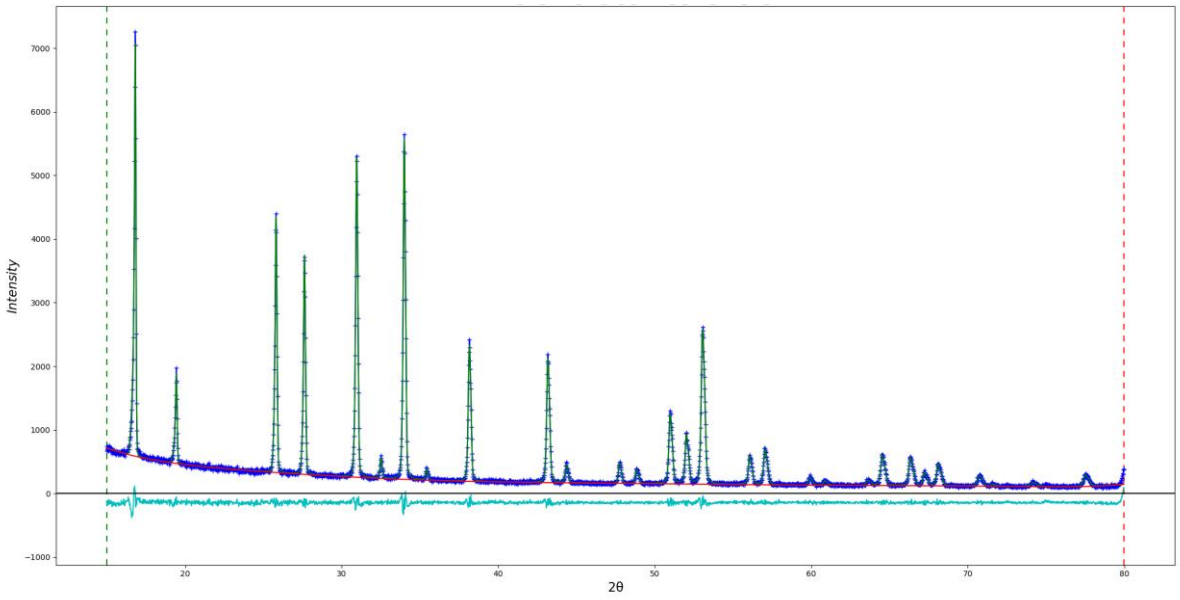

Figure S4. Example Rietveld refinement of Pr LLNO garnet materials. The above example is of $Li_{5.5}La_3Nb_{1.5}Pr_{0.5}O_{12}$

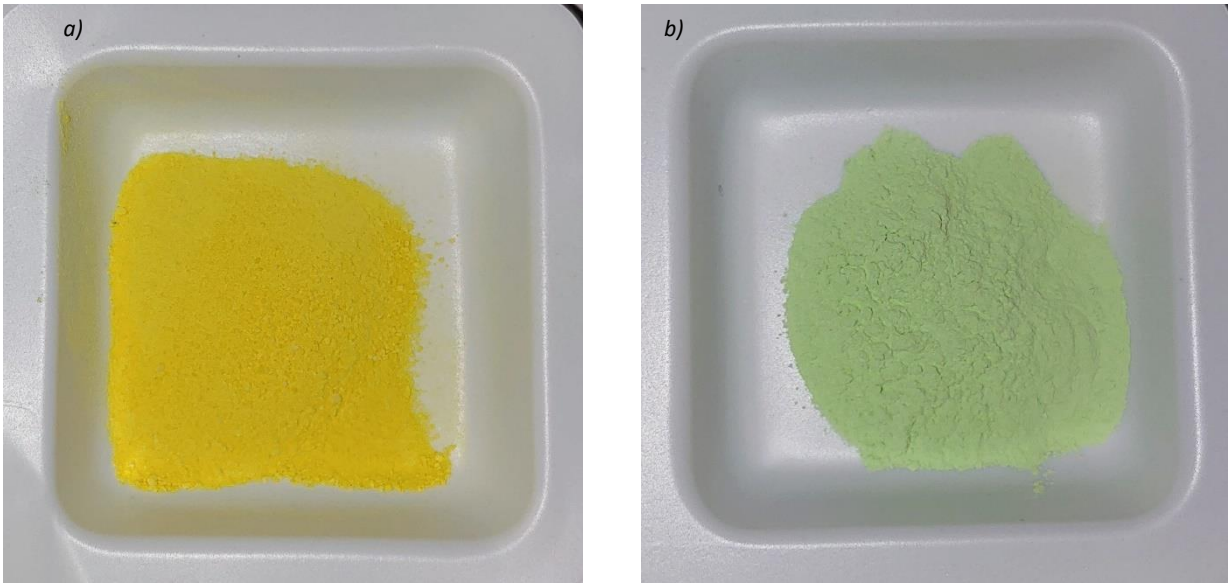

Figure S5. Powder colours of lithium garnet phases where a) is $Li_{5.25}La_3Nb_{1.75}Pr_{0.25}O_{12}$ and b) is $Li_5Pr_{2.5}La_{2.5}Nb_2O_{12}$ synthesised under 5%H_2

12.4. APPENDIX 4 – SUPPLEMENTARY INFORMATION FOR CHAPTER 6.

12.4.1 Water based synthesis of highly conductive $Ga_xLi_{7-3x}La_3Hf_2O_{12}$ garnets with comparable critical current density to analogous $Ga_xLi_{7-3x}La_3Zr_2O_{12}$ systems.

M. P. Stockham[1*], B. Dong[1], M. S. James[1], Y. Ding[2], Y. Li[2], P.R. Slater[1]*

[1]School of Chemistry, University of Birmingham, Birmingham B15 2TT. UK

[2]School of Chemical Engineering, University of Birmingham, Birmingham B15 2TT. UK

Correspondence to

M. P. Stockham/P. R. Slater

School of Chemistry, University of Birmingham, Birmingham B15 2TT. UK

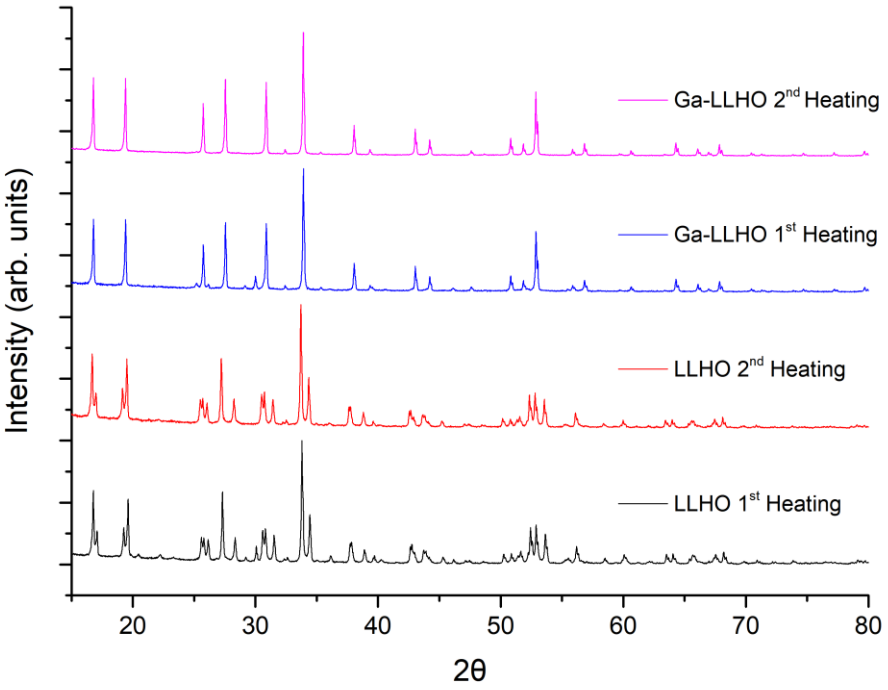

Figure S1. XRD of Ga-LLHO and LLHO during synthesis, all heating steps were 700°C, with a 20% wt. excess of lithium added between steps.

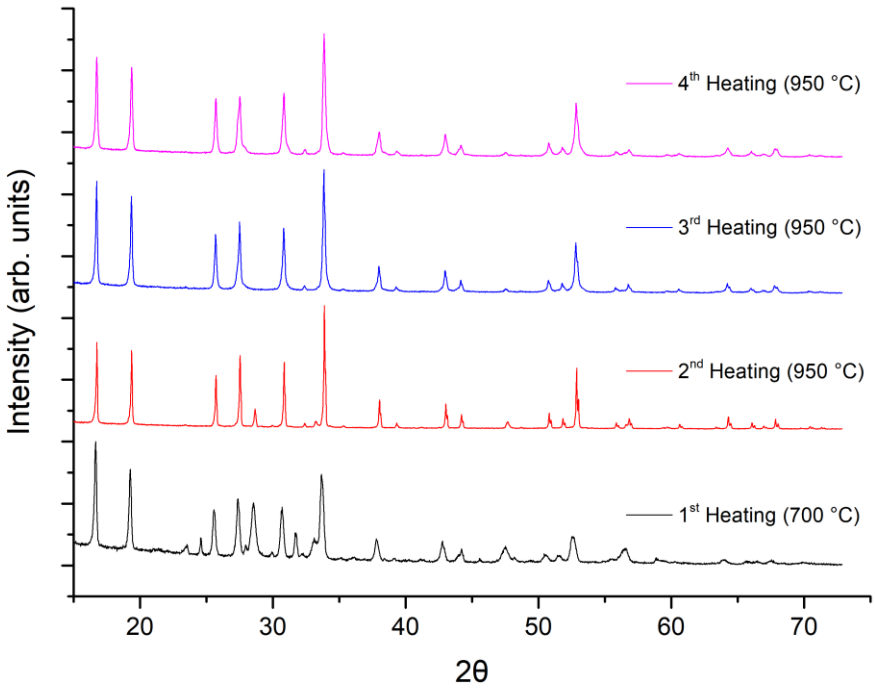

Figure S2. Al-LLHO synthesis steps, with a 20% wt. excess of lithium added between steps, except for the final 950°C heat treatment. A prior synthesis demonstrated no gain in reheating to 700°C, hence the step was removed for this synthesis approach.

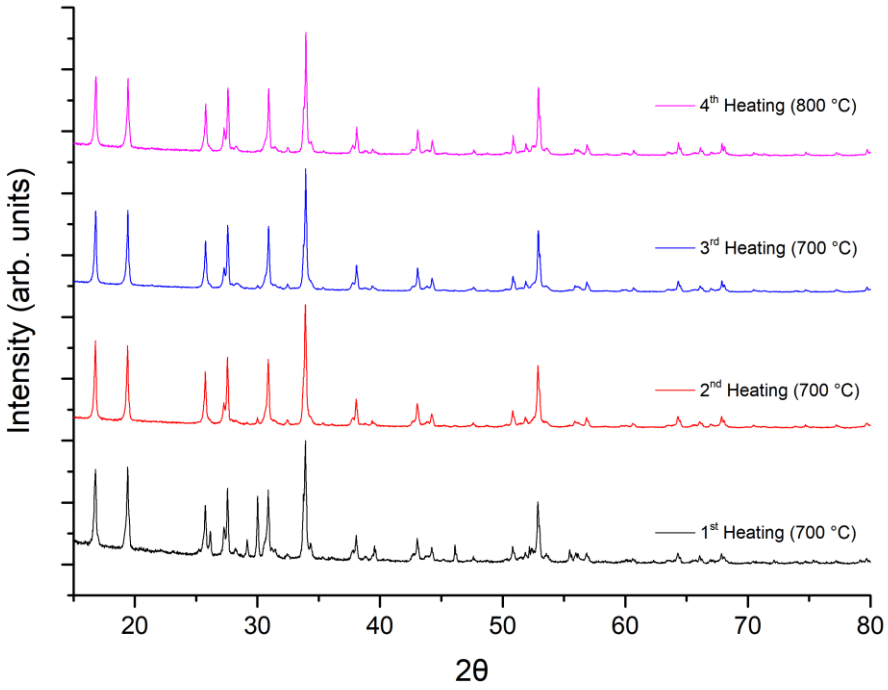

Figure S3. XRD data for $Ga_{0.15}Li_{6.55}La_3Hf_2O_{12}$ during attempted synthesis (showing the presence of a mixed cubic and tetragonal phase), an additional 20% wt. of Lithium was added until the 3rd heating cycle, with no excess added for the heat treatment at 800°C.

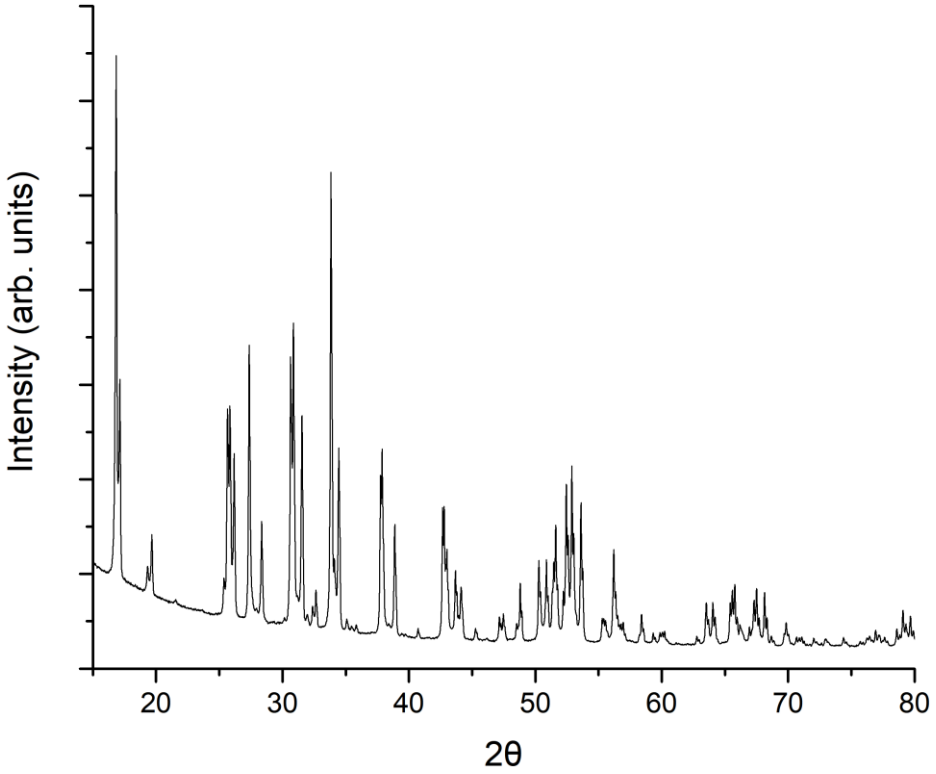

Figure S4. XRD data $Li_7La_3Zr_2O_{12}$ synthesised by the dissolution method, illustrating the expected tetragonal symmetry with space group $I4_1/acd$ (no. 142)

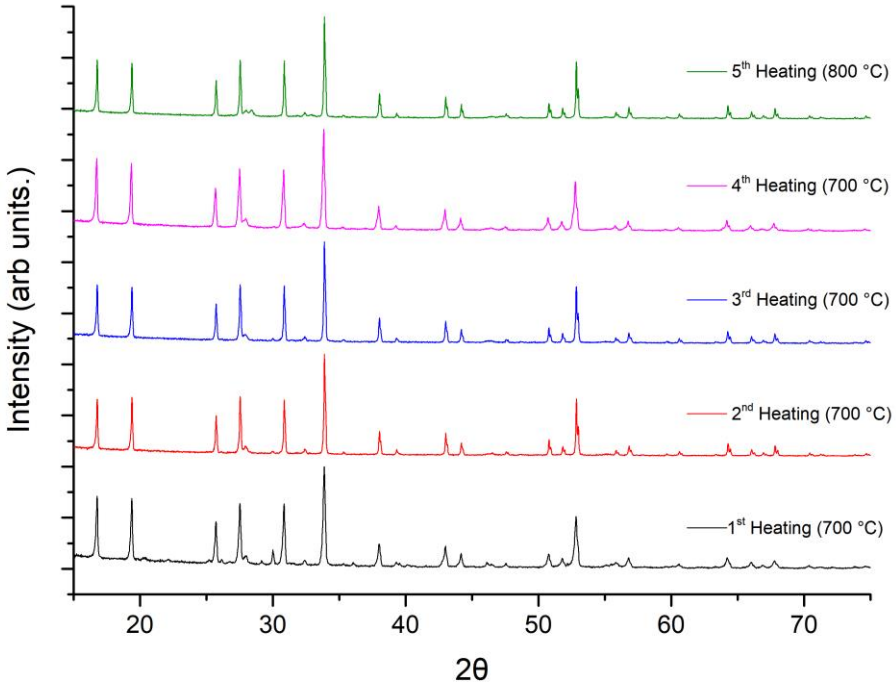

Figure S5. XRD data for attempted co-doping at the Li site with the formula $Ga_{0.2}Li_{6.4}La_3Hf_{1.8}Ce_{0.2}O_{12}$. The system demonstrated similar impurities to the Ga-LLHO synthesis with an addition of Cerium oxide based impurities which were unable to be removed, despite adding 10-20 % wt. lithium and/or addition of 3-5% HfO_2 excess (due to hydration levels of starting Hf salt) during the heating steps.

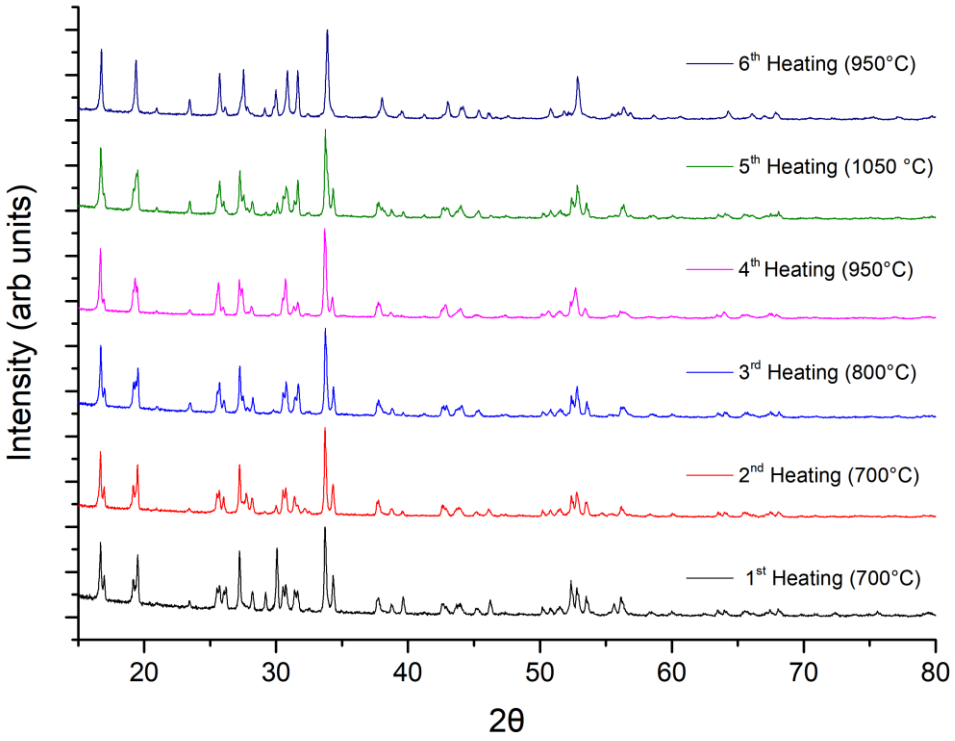

Figure S6. XRD data for attempted Pr doping at the Hf site with the formula $Li_7La_3Hf_{1.5}Pr_{0.5}O_{12}$. The system demonstrated similar impurities to the LLHO synthesis with an addition of Pr_2O_3 impurities which were unable to be removed, despite adding 5-10 % excess Li_2CO_3 and/or addition of 3-5% Hf/La excess (due to hydration levels of starting salts) during the heating steps.

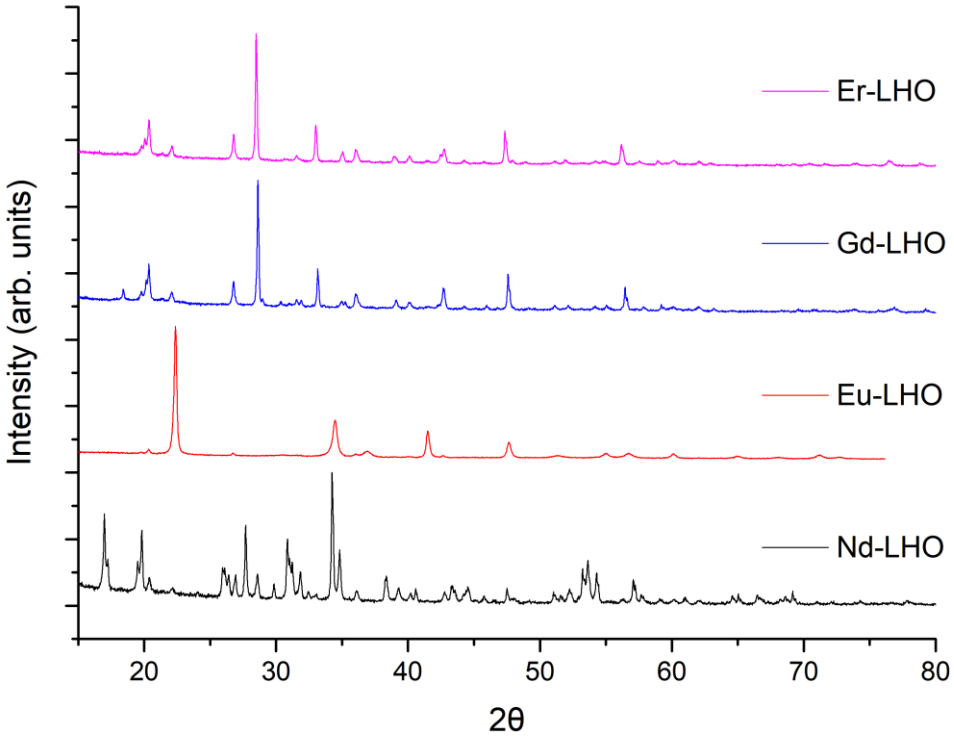

Figure S7. XRD data for attempted La replacement with Nd, Eu, Gd and Er, with only Nd-LHO demonstrating the formation of a garnet type phase. All intended formulas correspond to $Li_7M_3Hf_2O_{12}$ (M = Nd, Eu, Gd, Er).

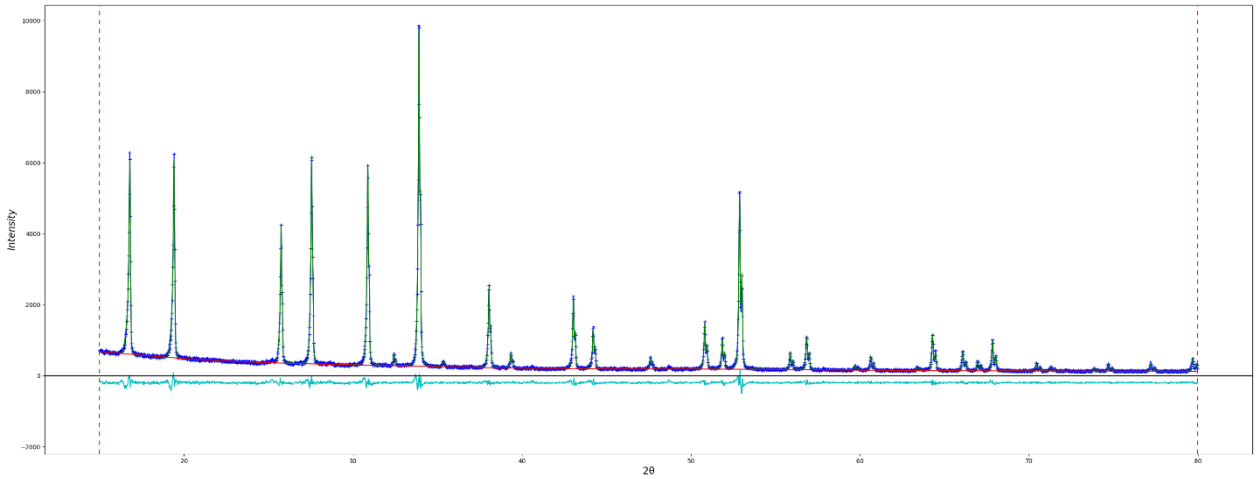

Figure S8. Example Rietveld refinement data for Ga-LLHO.

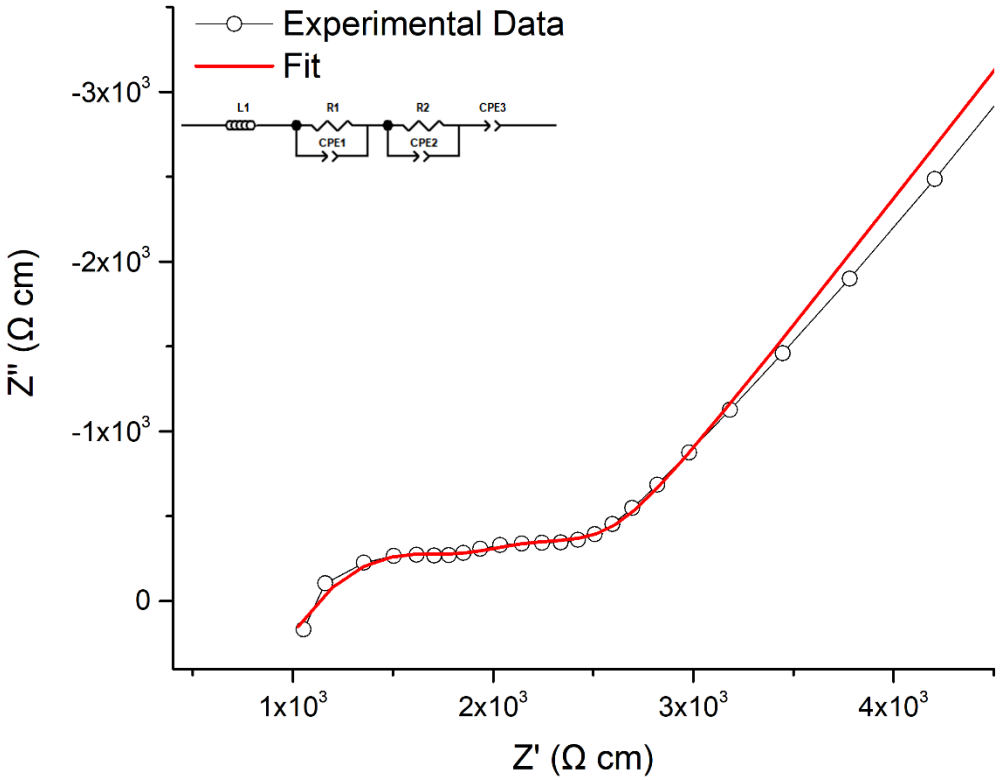

Figure S9. Impedance spectrum of Ga-LLHO at 25°C when densified under O_2. Although the spectrum was fit to two R/CPE components in parallel (where R1/CPE1 corresponds to the bulk and R2/CPE2 to the grain boundary contributions), the errors for the fit were quite large and, considering the similarities in conductivity between O_2 and N_2 densification, this sample was not cooled any further for analysis.

	Ga-LLHO (25°C)
σ_{total} *(S cm^{-1})*	3.7 x10^{-4}
C_{bulk} *(F / cm)*	7.08 x10 $^{-12}$
ε_r	80
ρ_{rel} *(%)*	88

Table S1. Impedance data for Ga-LLHO when densified under O_2

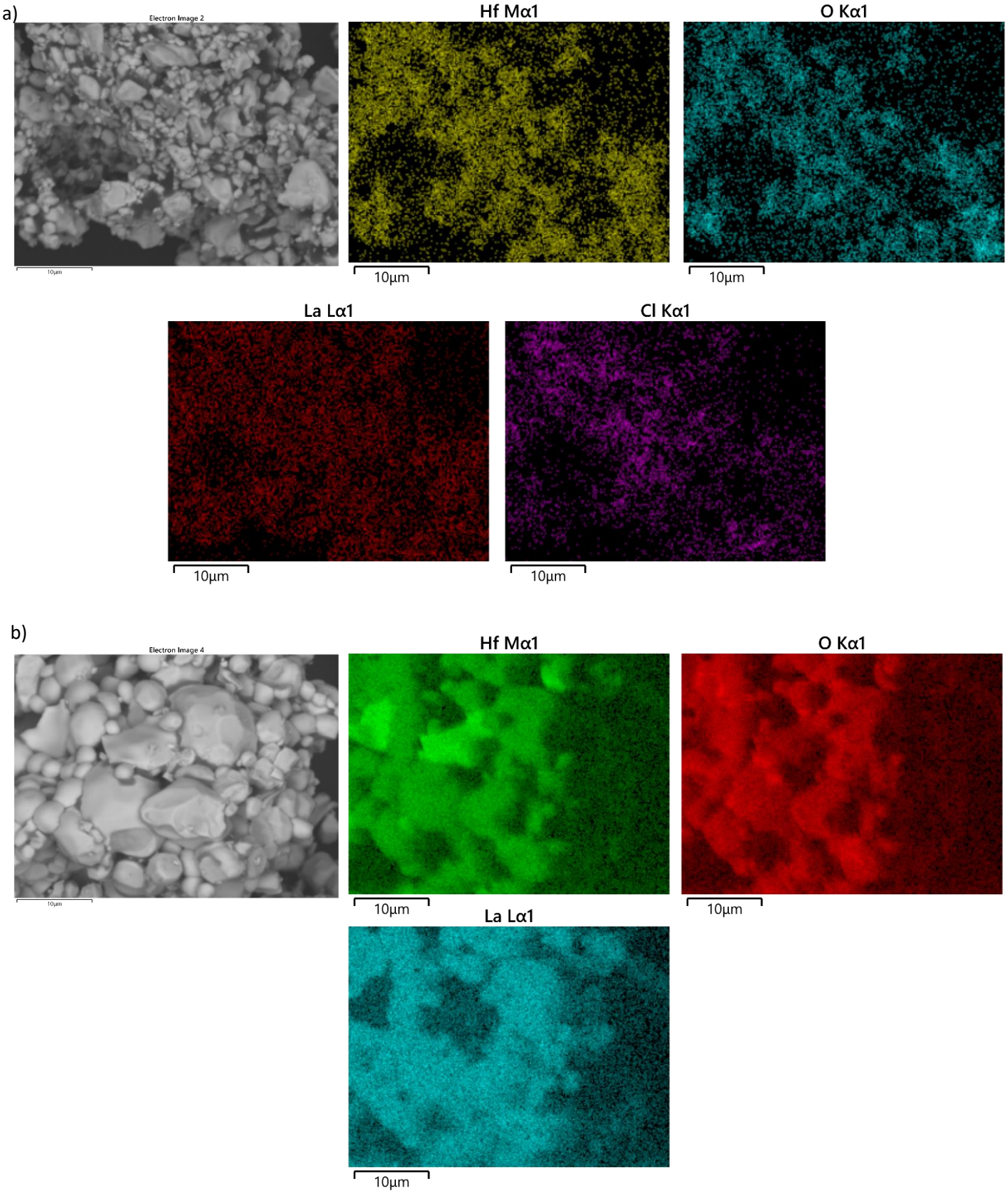

Figure S10. a) *t*-LLHO SEM and EDX map and b) SEM and EDX map of ground powder from densified LLHO pellet. The LLHO pellet was unable to be sanded to examine the pellet surface due to the low relative density.

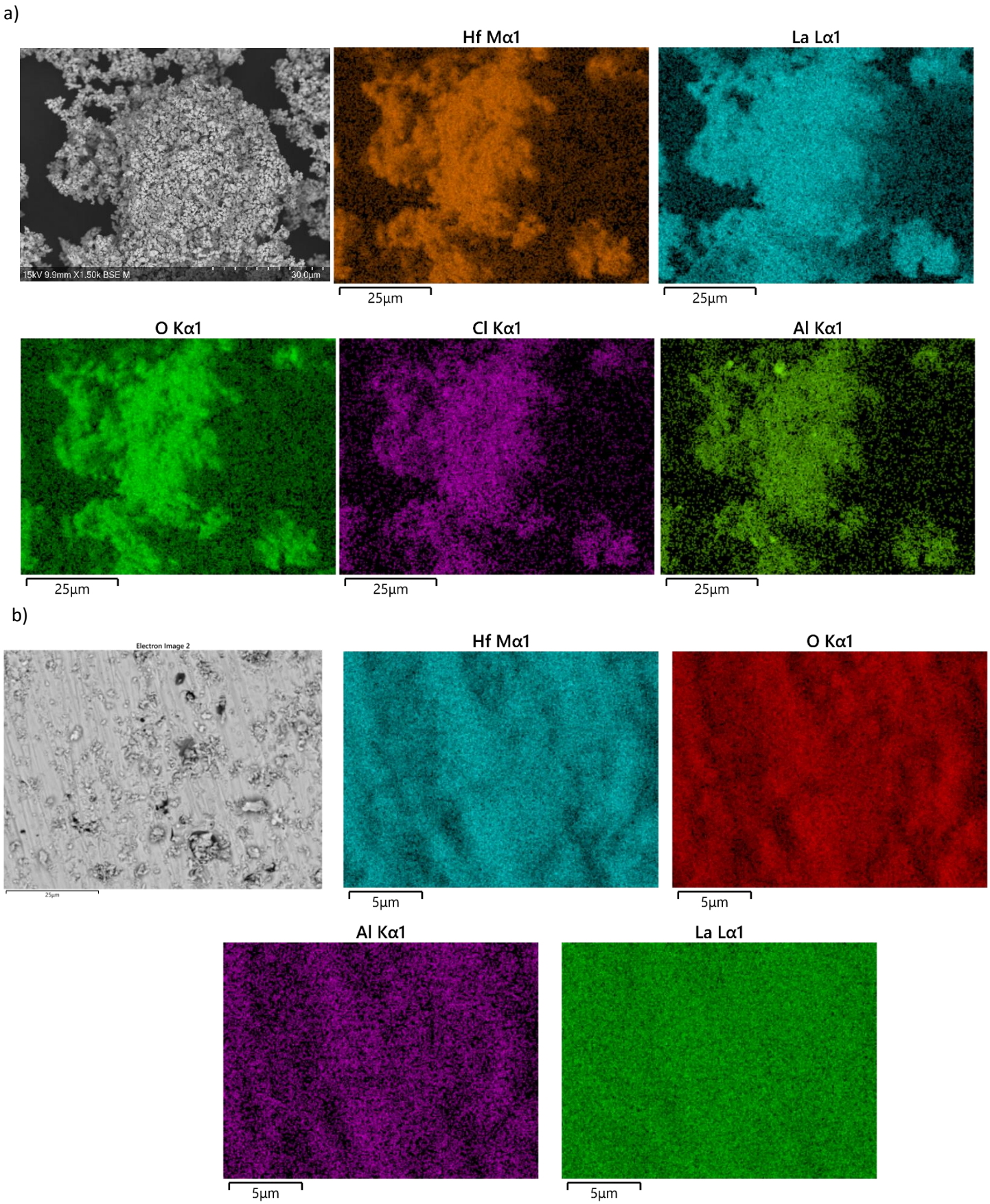

Figure S11. a) Al-LLHO SEM and EDX map and b) SEM and EDX map of polished pellet surface, without thermal etching.

12.5. APPENDIX 5 -- SUPPLEMENTARY INFORMATION FOR CHAPTER 7.

12.5.1 Evaluation of $Ga_{0.2}Li_{6.4}Nd_3Zr_2O_{12}$ garnets: exploiting dopant instability to create a mixed conductive interface to reduce interfacial resistance for all solid state batteries

M. P. Stockham[1*], B. Dong[1], M. S. James[1], Y. Li[2], Y. Ding[2], E. Kendrick[3], P.R. Slater[1*]

[1]School of Chemistry, University of Birmingham, Birmingham B15 2TT. UK

[2]School of Chemical Engineering, University of Birmingham, Birmingham B15 2TT. UK

[3]School of Metallurgy and Materials, University of Birmingham, Birmingham B15 2TT. UK

Correspondence to

M. P. Stockham/P. R. Slater

School of Chemistry, University of Birmingham, Birmingham B15 2TT. UK

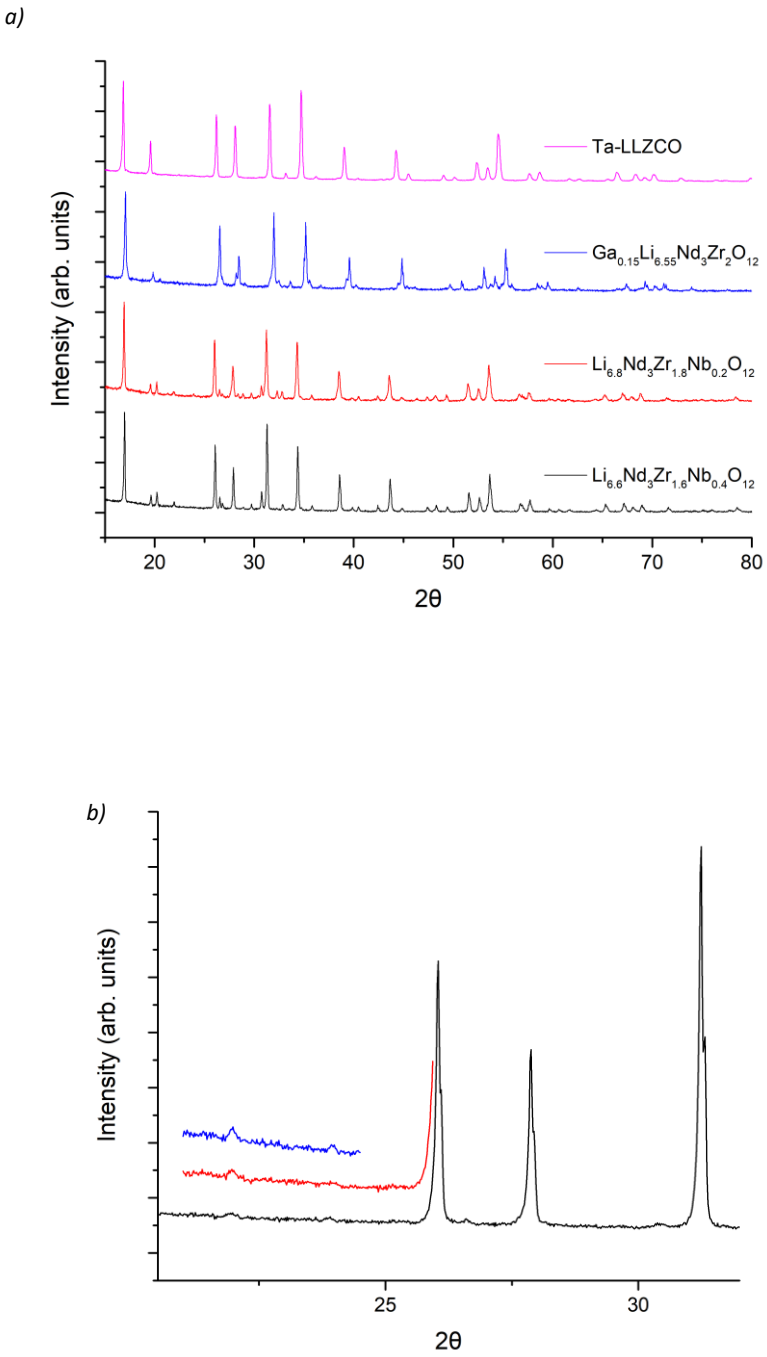

Figure S1. a) Powder XRD patterns of $Li_{6.6}Nd_3Nb_{1.6}Zr_{0.4}O_{12}$, $Li_{6.8}Nd_3Nb_{1.8}Zr_{0.2}O_{12}$ and $Li_{6.55}Ga_{0.15}Nd_3Zr_2O_{12}$. All underwent additional heating cycles and were still impure. $Li_{6.6}Nd_3Nb_{1.6}Zr_{0.4}O_{12}$ and $Li_{6.8}Nd_3Nb_{1.8}Zr_{0.2}O_{12}$ demonstrate Zr and Nb based impurities, whereas $Li_{6.4}Ga_{0.15}Nd_3Zr_2O_{12}$ has a considerable tetragonal component. The PXRD of Ta-LLZCO is also shown. b) narrow 2ϑ scans showing a small peak at ~22 2ϑ in Ga-NLZO, hence suggesting the system has I-43d type symmetry, further work is needed to confirm this.

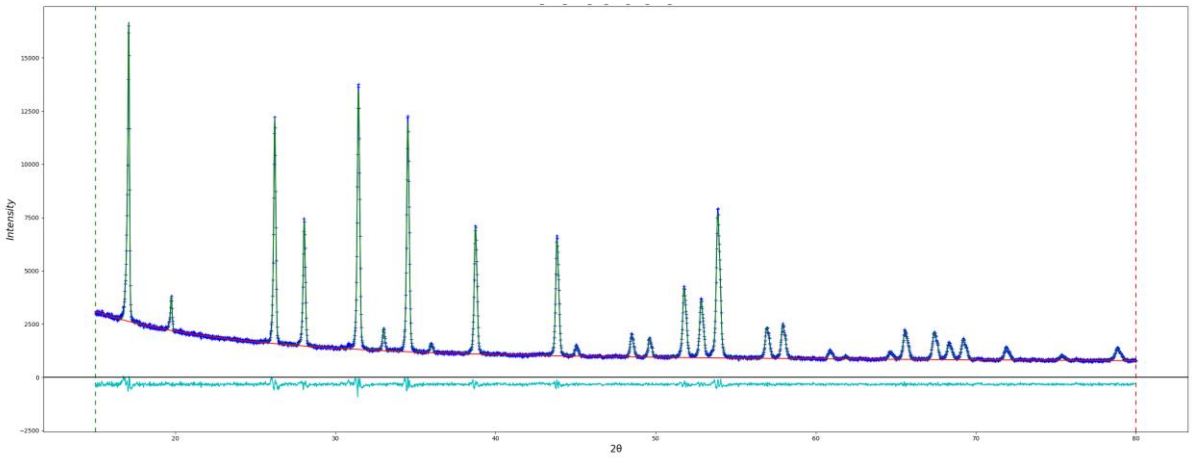

Figure S2. Example refinement of a Nd based lithium garnet; the above example is $Li_{6.2}Nd_3Zr_{1.2}Nb_{0.8}O_{12}$.

Sample (50°C)	C_{Bulk} (F cm^{-1})	ε_r
$Li_5Nd_3Nb_2O_{12}$	9.3×10^{-12}	105
$Li_{5.5}Nd_3Zr_{0.5}Nb_{1.5}O_{12}$	4.2×10^{-12}	47
$Li_{5.75}Nd_3Zr_{0.75}Nb_{1.25}O_{12}$	5.9×10^{-12}	67
$Li_{6.2}Nd_3Zr_{1.2}Nb_{0.8}O_{12}$	7.9×10^{-12}	89
$Li_{6.4}Nd_3Zr_{1.4}Nb_{0.6}O_{12}$	4.55×10^{-12}	51
Al-NLZO	2.1×10^{-11}	239
Ga-NLZO (18°C)	4.6×10^{-12}	52

Table S1. Bulk capacitances and dielectric constants derived from the impedance spectra of the Nd based lithium garnets.

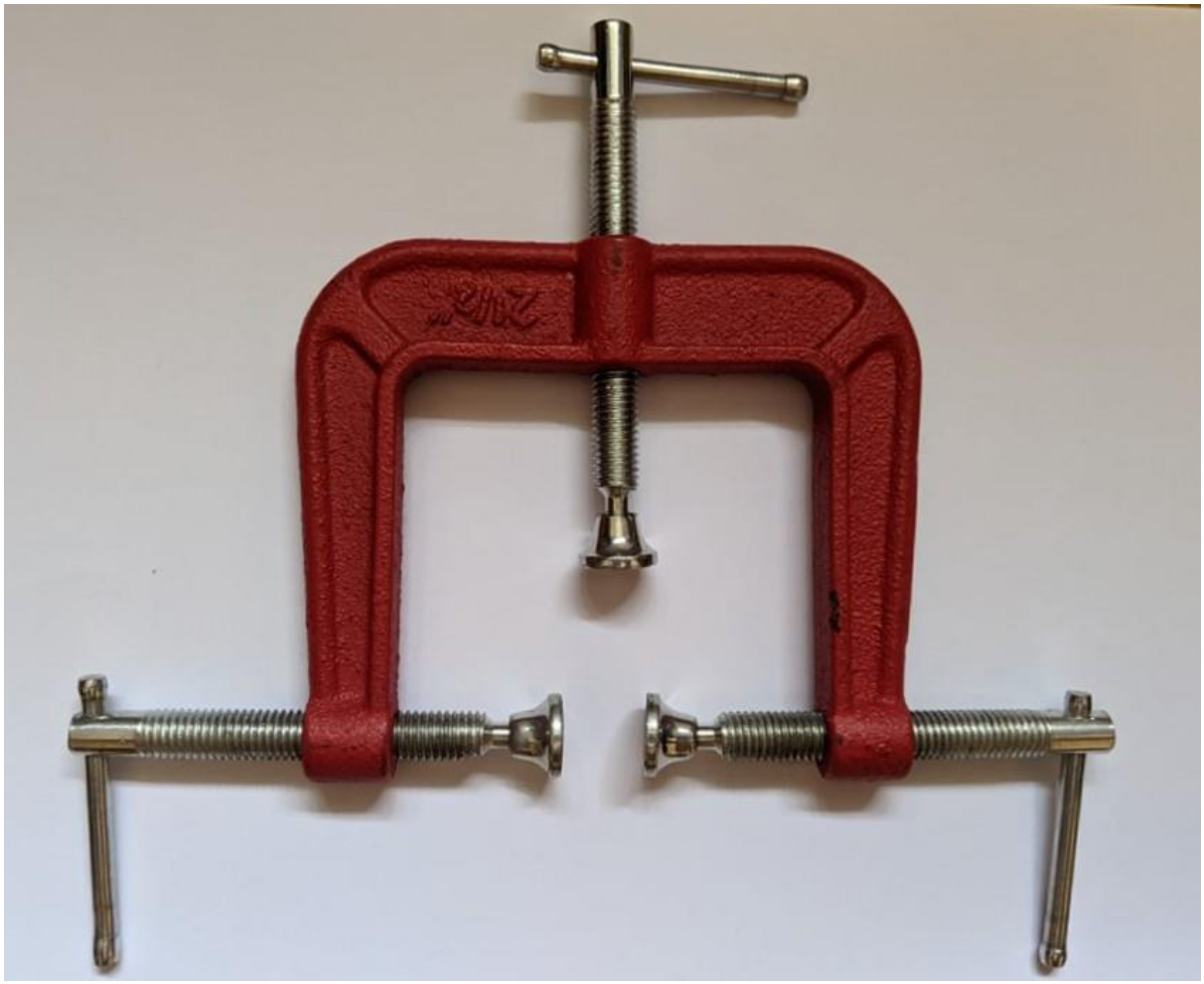

Figure S3. 2½ inch 3-way G-clamp used to form Li symmetry cells (Cu foil was used to cover the contact area to prevent cell adhering to the clamp).

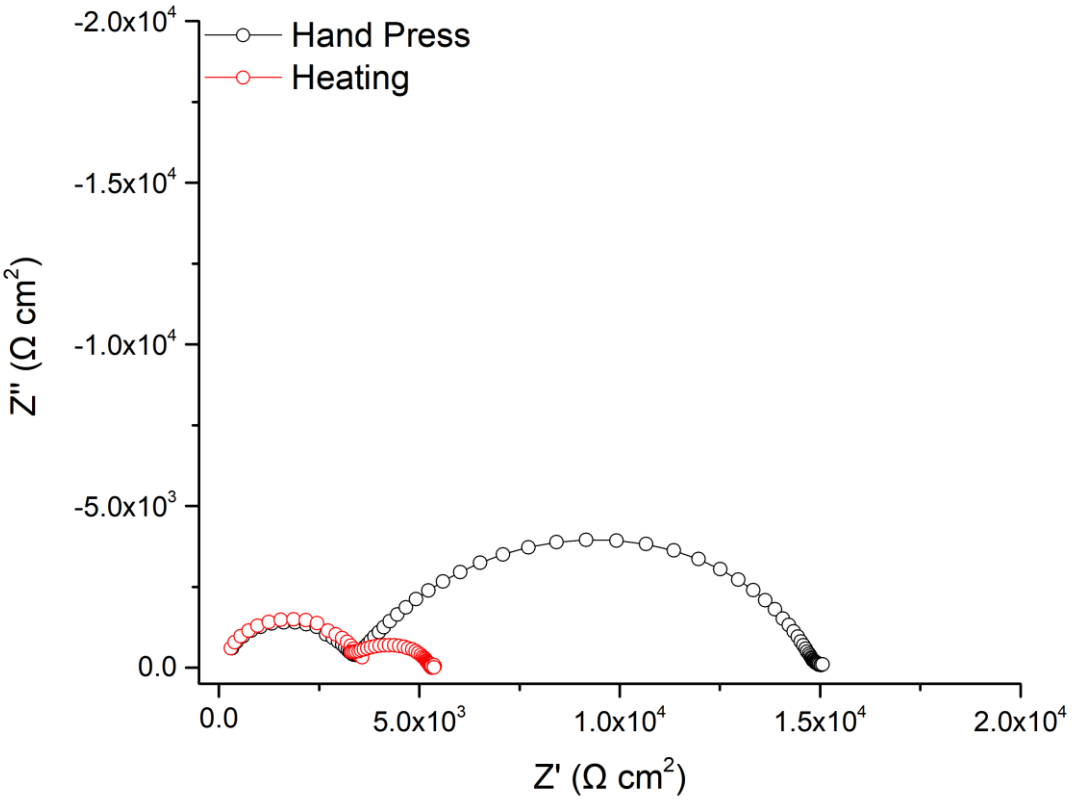

Figure S4. Tetragonal NLZO symmetry cell, pressed via hand and by heating as per the methods section. Both cases illustrate substantially higher Li/Garnet interfacial resistance when compared to Ga-NLZO at 5830 (hand pressed) and 949 (heated) Ω cm^2. This further confirms the low resistance encountered with Ga-NLZO is due to the presence of Ga in the system.

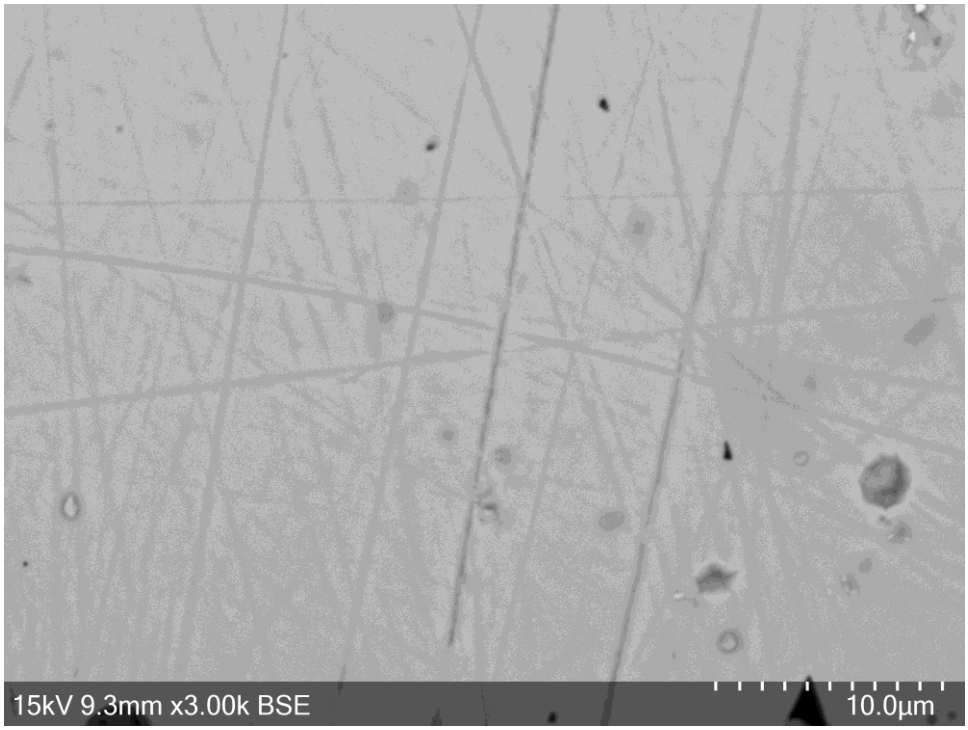

Figure S5. SEM image of post cycled Li/Ga-NLZO/Li before thermal etching, illustrating no discernible features and large scratches due to polishing of the pellets prior to assembling the symmetry cell.

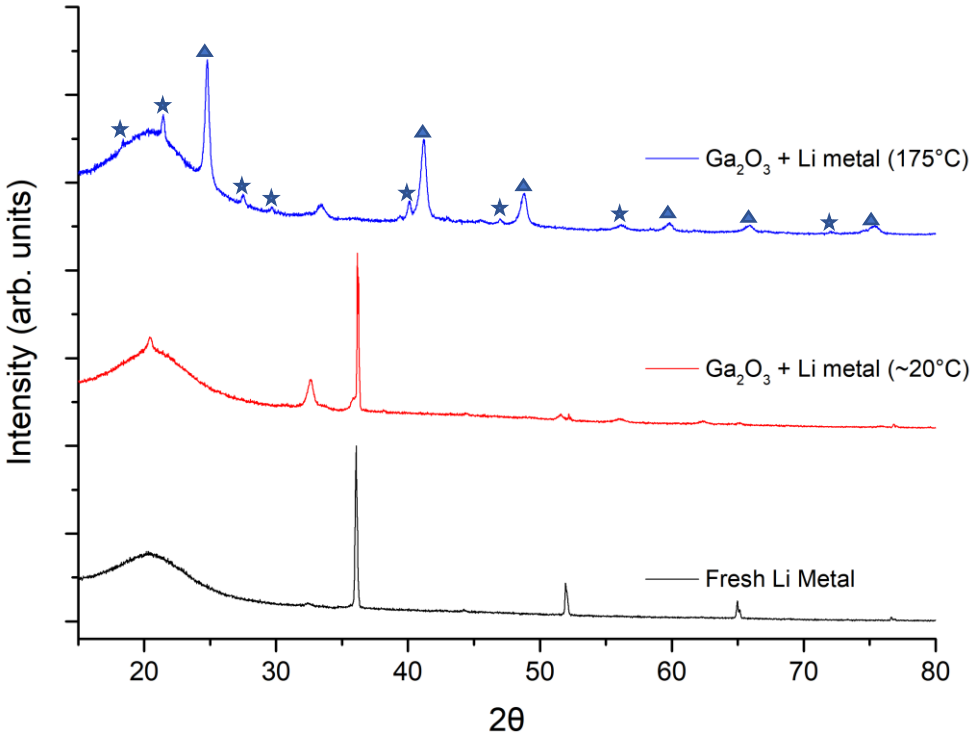

Figure S6. Reaction of Ga_2O_3 with Li metal when heated to 175°C (1h) (blue) and when left in contact with Ga_2O_3 pellet for two days (red). Pellets were uniaxially pressed to ~3 tonnes and placed in contact without any additional pressure. Black line is fresh Li metal for comparison. Ga_2O_3 + Li metal heated to 175°C illustrated evidence of Li_2Ga (stars) and GaLi (triangle) eutectic mixtures, in addition to a small amount of Ga_2O_3 powder residue from the pellet (unmarked).

12.6. APPENDIX 6 -- SUPPLEMENTARY INFORMATION FOR CHAPTER 8.

12.6.1 Assessing the importance of cation size in the tetragonal-cubic phase transition in lithium garnet electrolytes.

M. P. Stockham[1*], A. Griffiths[1], B. Dong[1], P.R. Slater[1*]

[1]School of Chemistry, University of Birmingham, Birmingham B15 2TT. UK

Correspondence to

M. P. Stockham/P. R. Slater

School of Chemistry, University of Birmingham, Birmingham B15 2TT. UK

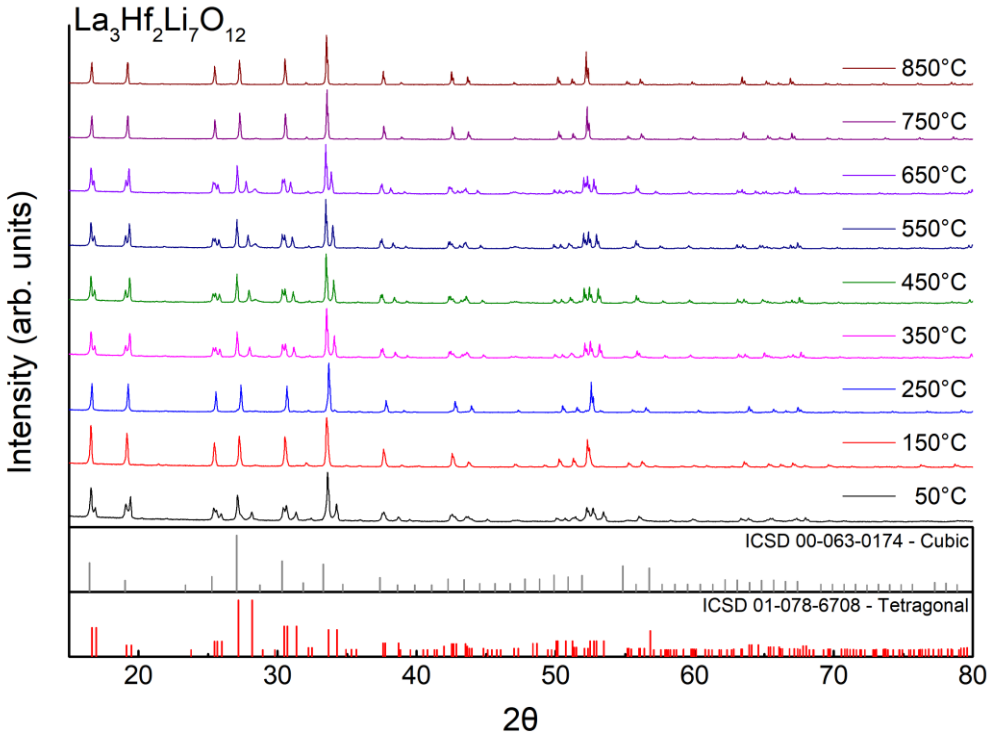

Figure S1. VTPXRD of La based tetragonal garnet $La_3Hf_2Li_7O_{12}$

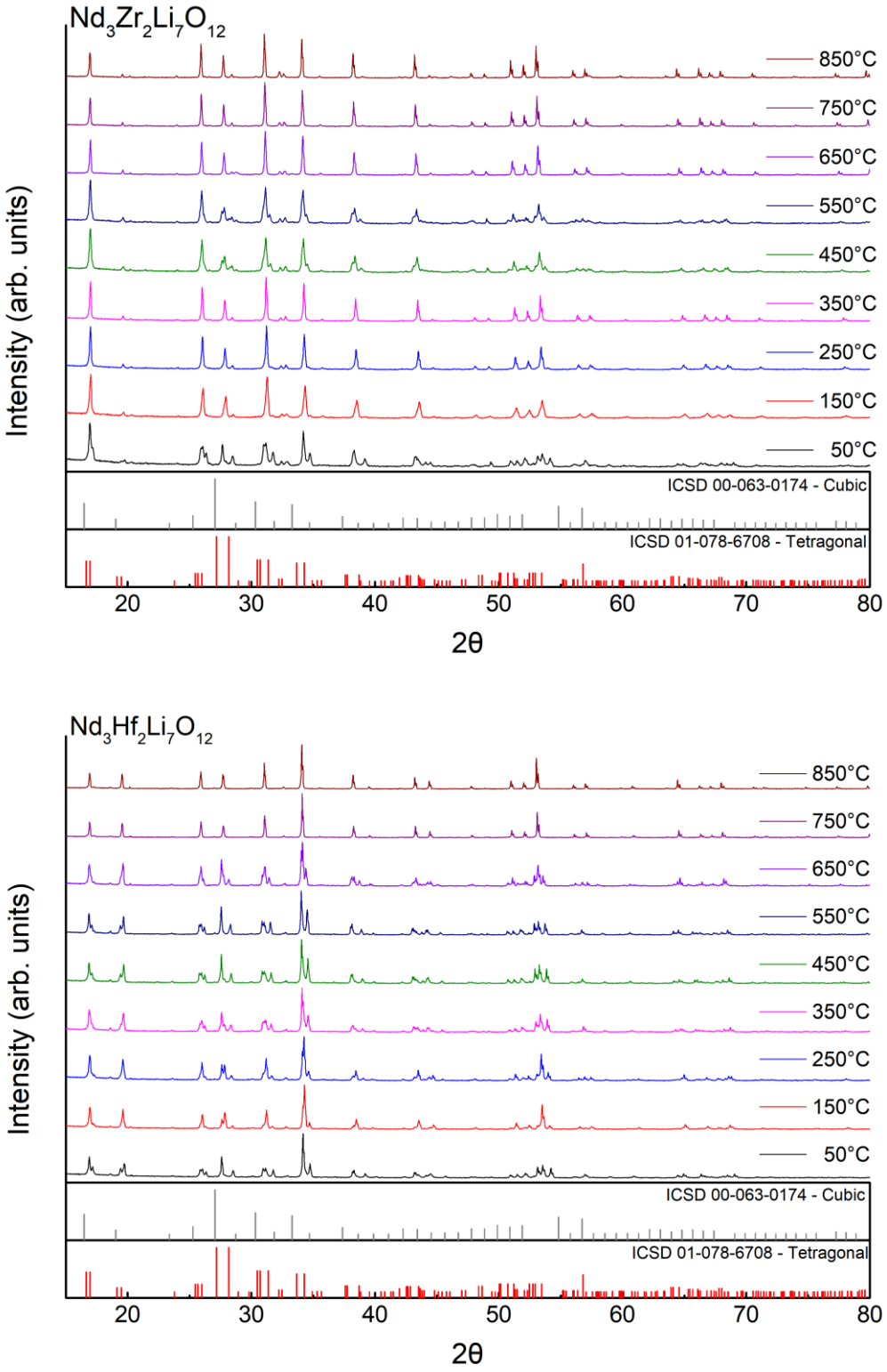

Figure S2. VTPXRD of Nd based tetragonal garnets $Nd_3Zr_2Li_7O_{12}$ and $Nd_3Hf_2Li_7O_{12}$

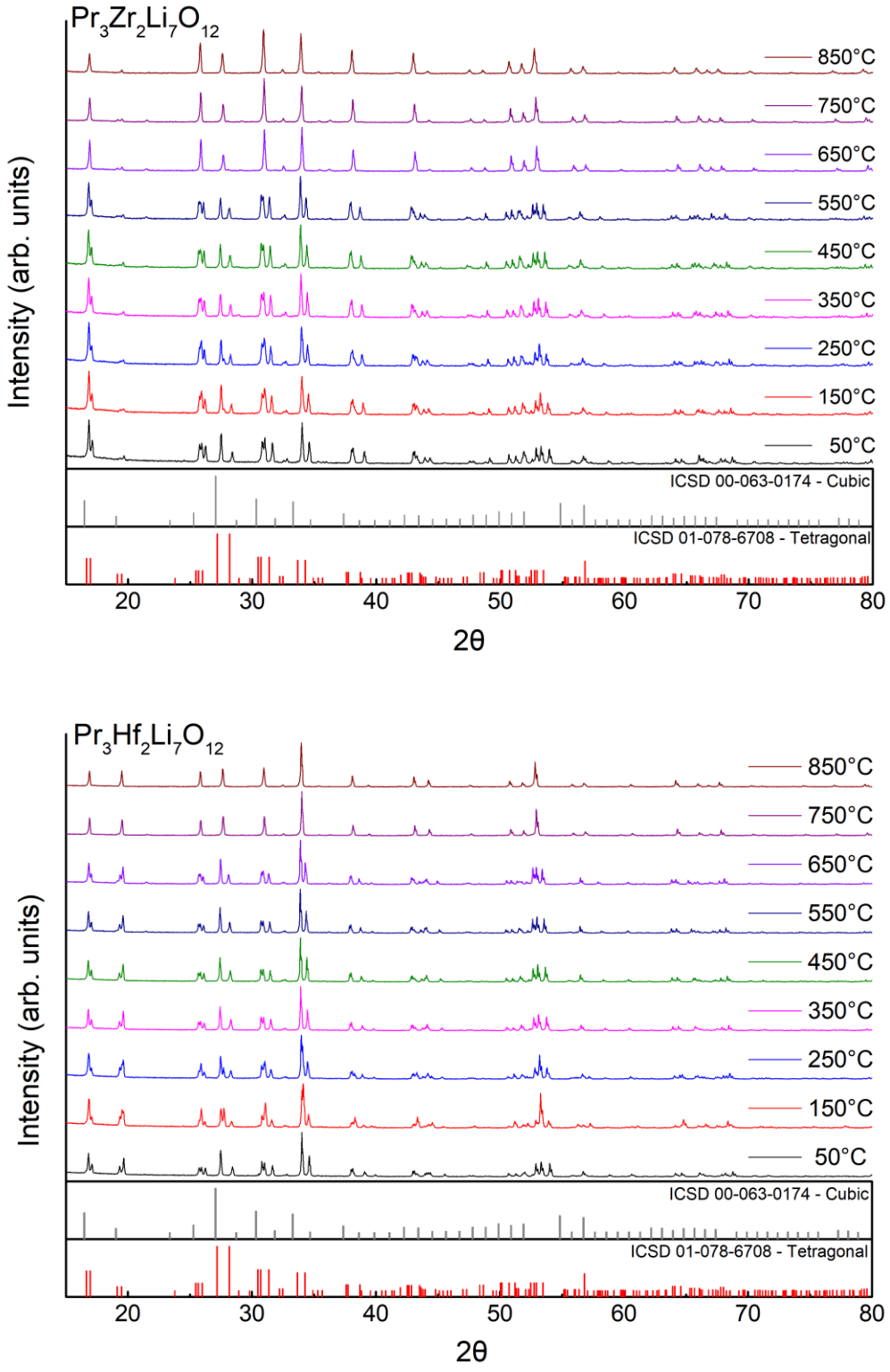

Figure S3. VTPXRD of Pr based tetragonal garnets $Pr_3Zr_2Li_7O_{12}$ and $Pr_3Hf_2Li_7O_{12}$

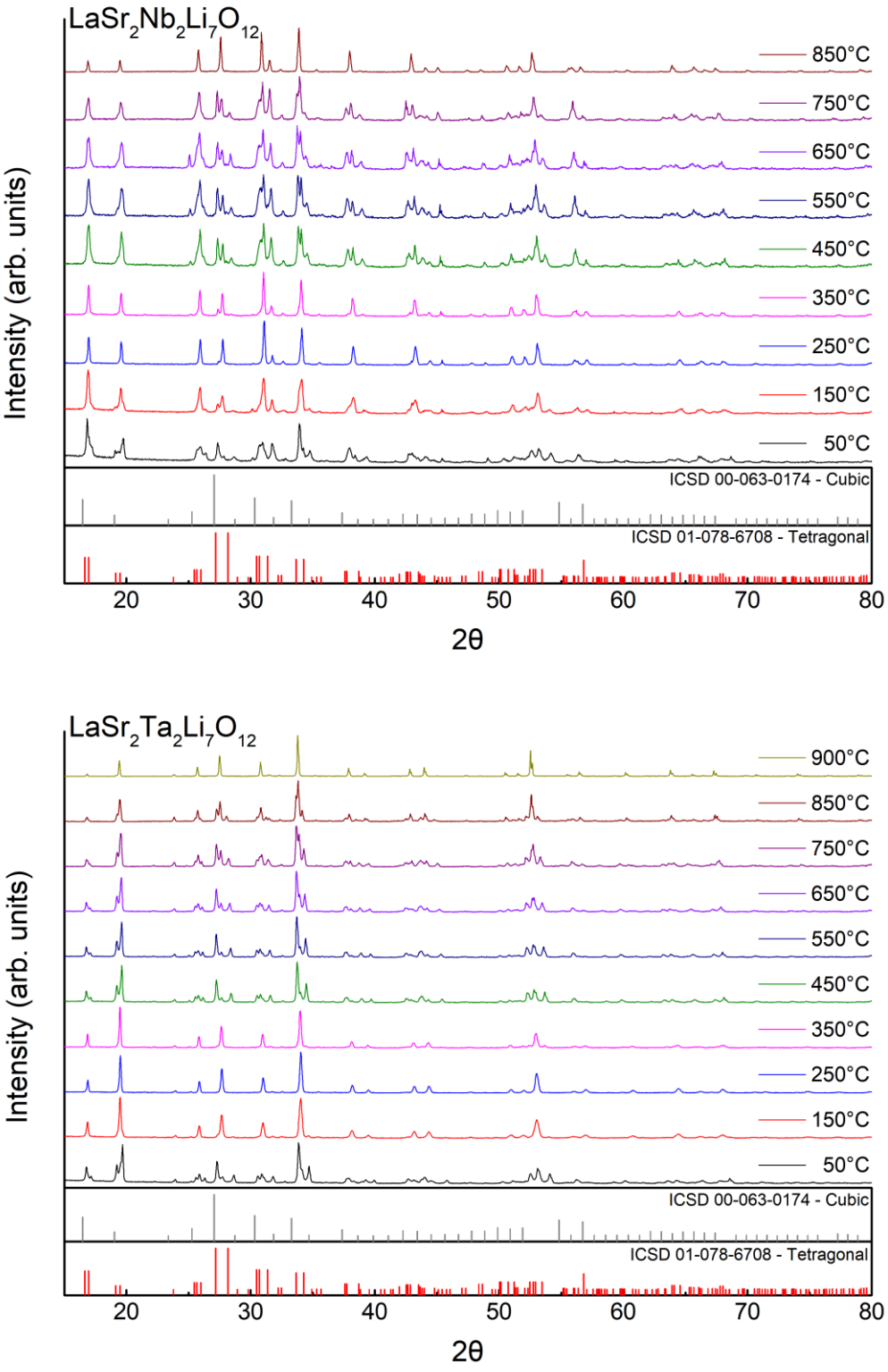

Figure S4. VTPXRD of Sr doped based tetragonal garnets $LaSr_2Nb_2Li_7O_{12}$ and $LaSr_2Ta_2Li_7O_{12}$

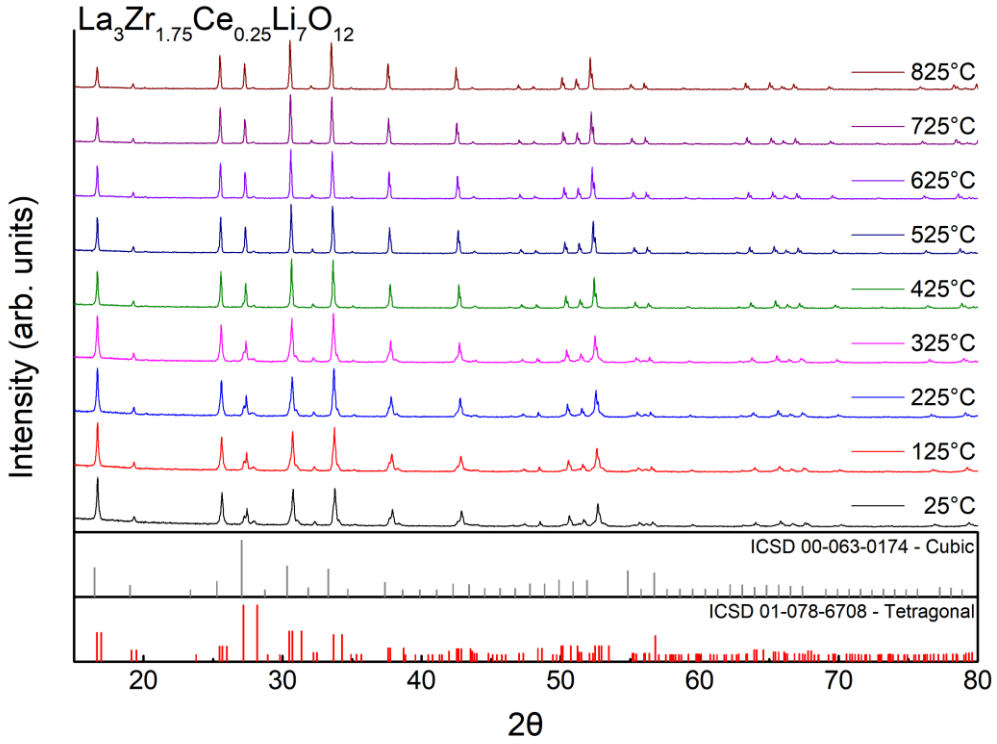

Figure S5. VTPXRD of $La_3Zr_{1.75}Ce_{0.25}Li_7O_{12}$.

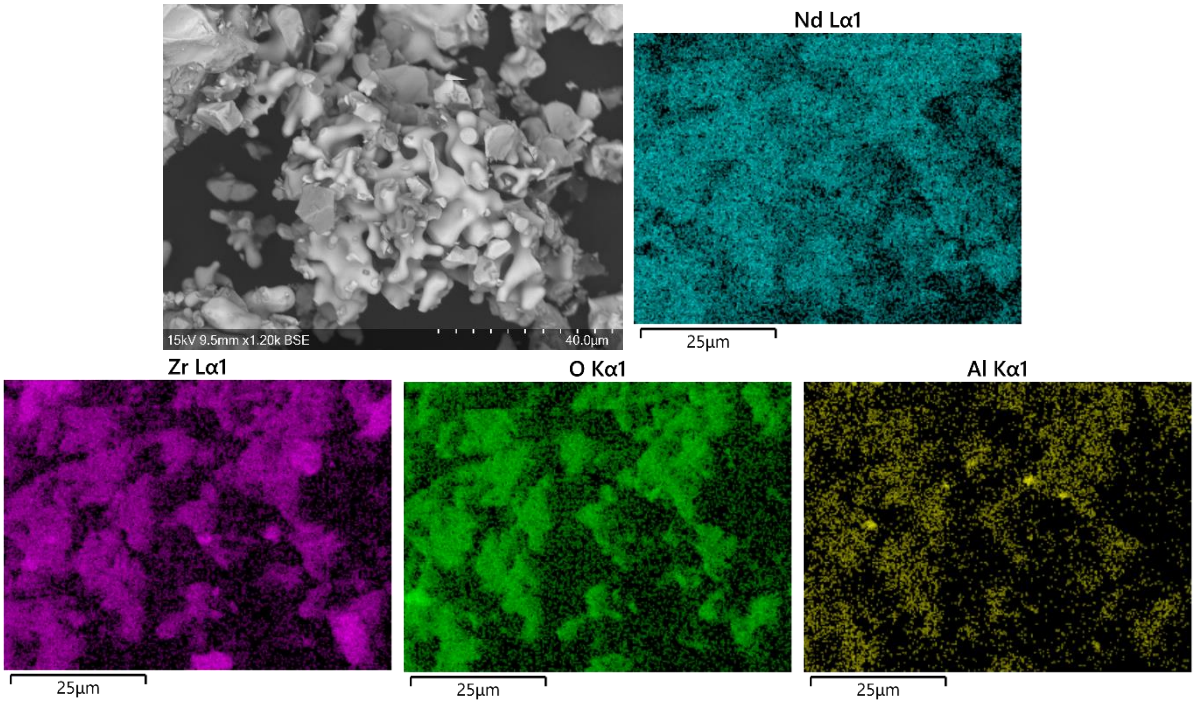

Figure S6. SEM/EDX of ground powder after pellet sanding, illustrating small amounts of Al contamination. $Nd_3Zr_2Li_7O_{12}$ is the example shown.

12.7. APPENDIX 7 -- SUPPLEMENTARY INFORMATION FOR CHAPTER 9.

12.7.1 High entropy lithium garnets – Testing the compositional flexibility of the lithium garnet system.

Mark P. Stockham[1*], Bo Dong[1], Peter R. Slater[1*]

[1]School of Chemistry, University of Birmingham, Birmingham B15 2TT. UK

Correspondence to

M. P. Stockham/P. R. Slater

School of Chemistry, University of Birmingham, Birmingham B15 2TT. UK

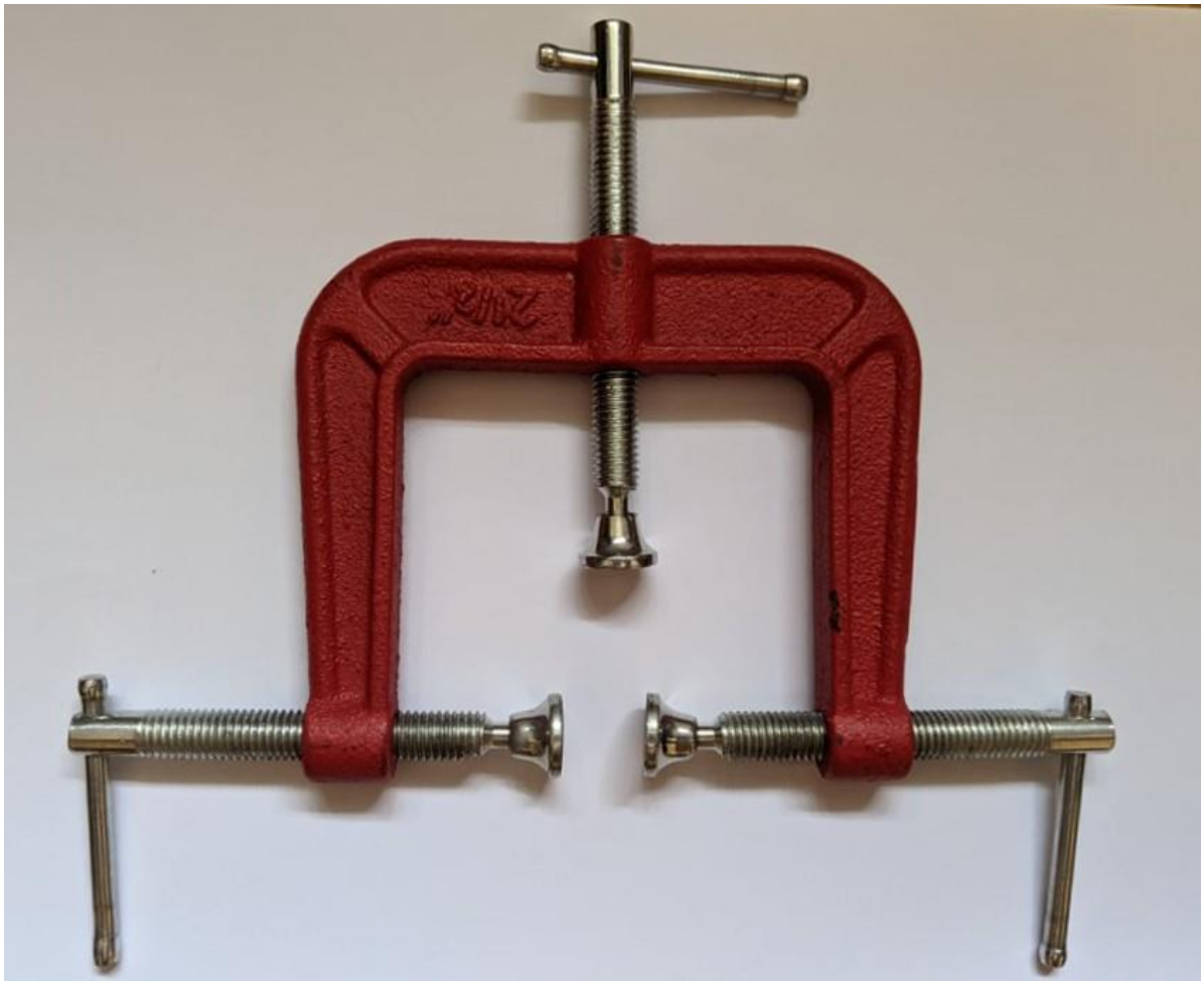

Figure S1. 2½ inch 3-way G-clamp used to form Li symmetry cells under pressure at 175°C (Cu foil was used to cover the contact area to prevent cell adhering to the clamp).

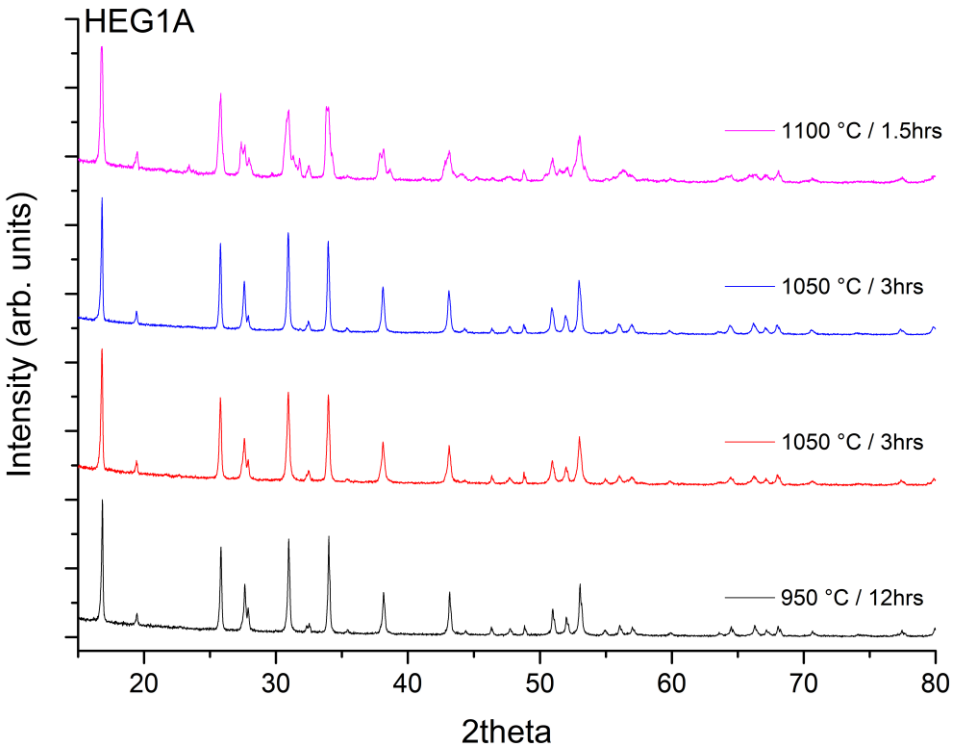

Figure S2. PXRD of HEG1A, whereupon Ga content was reduced to 0.15 to prepare $Ga_{0.2}Li_{5.75}La_{2.5}Nd_{0.5}Nb_{0.65}Ce_{0.1}Zr_1Ti_{0.25}O_{12,}$ with numerous unknown impurity phases which were unable to be removed. 950°C was the first heating step and the remaining are attempted purification steps on the same sample.

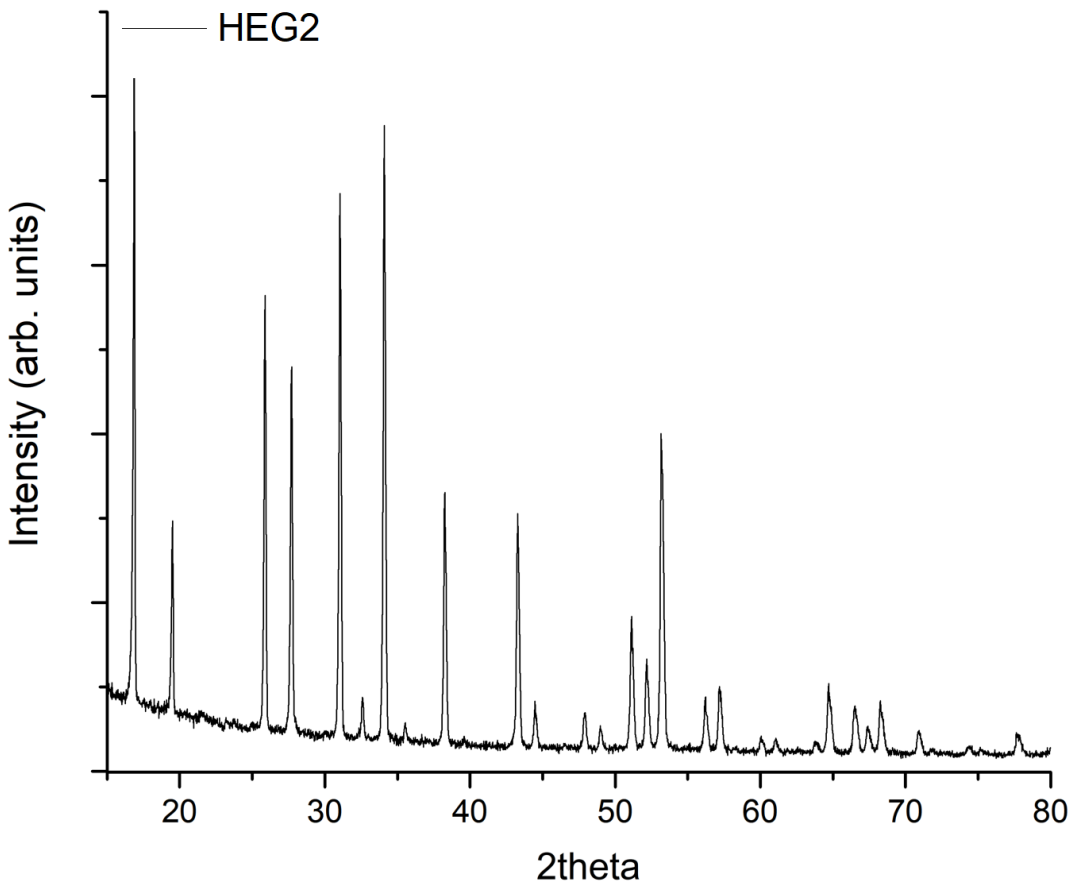

Figure S3. PXRD of HEG2 sintered for 14 hrs (rather than 12hrs), showing complete removal of background peaks ascribed to unreacted Li_2CO_3 in the main article.

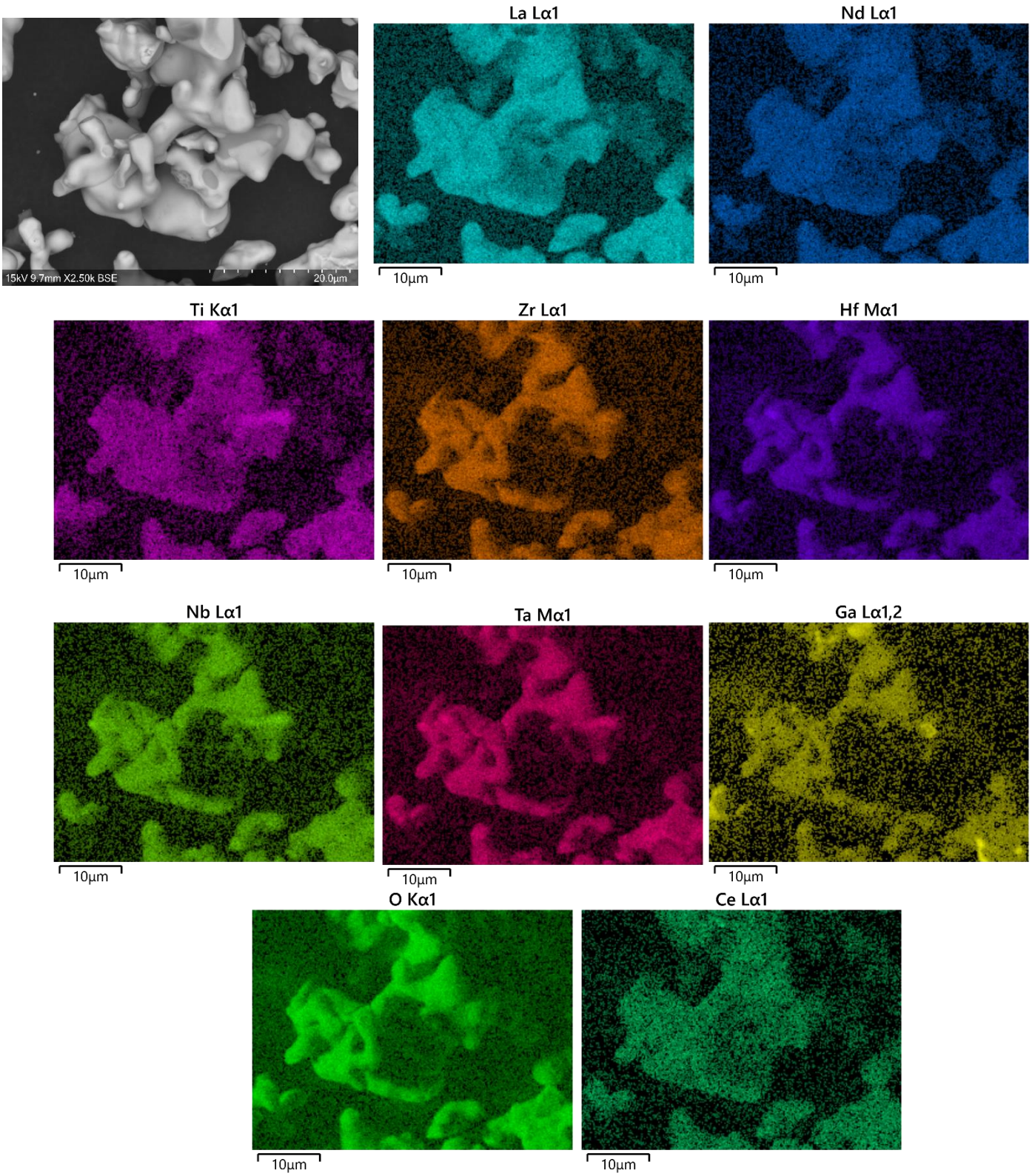

Figure S4. SEM and EDX of HEG2 powder, showing a relatively homogenous elemental distribution of HEG2 with some areas of higher elemental concentrations, particularly Ga.

12.7.2 Impedance calculations

Conductivity values for HEG1 and HEG2 were extracted from the high frequency semi-circle/s in the Nyquist plots and converted to S cm^{-1} by equation 1:

$$\sigma = \frac{l}{RA} \quad 1$$

Where l is the electrolyte thickness, R the high intercept of semi-circle on the *x* axis and A the electrode area. Capacitance is then calculated via the constant phase element fit (CPE) thus:

$$Z_{cpe} = \frac{1}{Q(i\omega)^n} \quad 2$$

Where, ω is the angular frequency, n is the description of non-ideality, Q is the non-ideal capacitance. C is found from Eq. 3

$$C = (R^{1-n}Q)^{1/n} \quad 3$$

This allows calculation of relative permittivity via equation 4.

$$\varepsilon_r = \frac{C}{\varepsilon_0} \quad 4$$

Where ε_0 is vacuum permittivity (8.854 x 10^{-14} F/cm). The related exponents can be found in table S1.

	HEG1	***HEG2***
R_{bulk} *(Ω)*	1109	1122
R_{gb}*(Ω)*	1248	n/a
σ_{total} *(S cm^{-1})*	1x10^{-4}	2x10^{-4}
CPE (F s^{n-1})$_{bulk}$ (Q)	7.8 x10^{-11}	7.7 x10^{-11}
n_{bulk}	0.920	0.926
C_{bulk} *(F)*	2.0 x10^{-11}	2.1 x10^{-11}
C_{bulk}**l/A (F/cm)*	5.2 x10^{-12}	4.7 x 10^{-12}
ε_r	59	53

Table S1. Fitted impedance data from HEG1 and HEG2, with exponents used to calculate capacitance values.

13. Publications

13.1. First Author

1. Stockham, M. P.; Dong, B.; Ding, Y.; Li, Y.; Slater, P. R., Evaluation of the effect of site substitution of Pr doping in the lithium garnet system Li5La3Nb2O12. Dalton Transactions 2020, 49 (30), 10349-10359.

2. Stockham, M. P.; Dong, B.; James, M. S.; Li, Y.; Ding, Y.; Kendrick, E.; Slater, P. R., Evaluation of Ga0.2Li6.4Nd3Zr2O12 garnets: exploiting dopant instability to create a mixed conductive interface to reduce interfacial resistance for all solid state batteries. Dalton Transactions 2021, 50 (39), 13786-13800.

3. Stockham, M. P.; Dong, B.; James, M. S.; Li, Y.; Ding, Y.; Slater, P. R., Water based synthesis of highly conductive GaxLi7−3xLa3Hf2O12 garnets with comparable critical current density to analogous GaxLi7−3xLa3Zr2O12 systems. Dalton Transactions 2021, 50 (7), 2364-2374.

4. Stockham, M. P.; Dong, B.; Slater, P. R., High entropy lithium garnets – Testing the compositional flexibility of the lithium garnet system. Journal of Solid State Chemistry 2022, 308, 122944.

5. Stockham, M. P.; Griffiths, A.; Dong, B.; Slater, P. R., Assessing the Importance of Cation Size in the Tetragonal-Cubic Phase Transition in Lithium-Garnet Electrolytes**. Chemistry – A European Journal 2022, 28 (6), e202103442.

6. Stockham, M. P.; Dong, B.; M.S. James; Slater, P., Reactive sintering of Li6.5La3Zr1Nb0.5Ce0.25Ti0.25O12 for high density lithium garnet electrolytes with anti-dendritic healing properties. – In final Stages

13.2. Contributing Author

1. Dong, B.; Driscoll, L. L.; Stockham, M. P.; Kendrick, E.; Slater, P. R., Low temperature synthesis of garnet solid state electrolytes: Implications on aluminium incorporation in Li7La3Zr2O12. Solid State Ion. 2020, 350, 115317.

2. Dong, B.; Stockham, M. P.; Chater, P. A.; Slater, P. R., X-ray pair distribution function analysis and electrical and electrochemical properties of cerium doped Li5La3Nb2O12 garnet solid-state electrolyte. Dalton Transactions 2020, 49 (33), 11727-11735.

3. Dong, B.; Stockham, M. P.; Li, L.; Tao, X.; Ding, Y.; Li, Y.; Li, C.; Slater, P. R. In Enhanced Densification and Conduction Properties of Li5+xLa3Nb2-xZrxO12 Garnet Solid-State Electrolytes Through Zn Doping on the Nb/Zr Site, 2020.

4. Thomas, S. W.; James, M. S.; Stockham, M. P.; Deakin, J.; Jarvis, A.; Slater, P. R., Synthesis of Borate Doped La10Ge6O27: Confirming the Presence of a Secondary Conducting Pathway. ECS Transactions 2021, 103 (1), 1885-1897.

5. Dong, Bo; Haworth, Abby; Yeandel, Stephen; Stockham, Mark; James, Matthew; Xiu, Jingwei; Wang, Dawei; Goddard, Pooja; Johnston, Karen; Slater, Peter, P. R., Halogenation of Li7La3Zr2O12

Solid Electrolytes: A Combined Solid-State NMR, Computational and Electrochemical Study. Accepted, Journal of Materials Chemistry A

6. Dong, B.; Stockham, M. P.; Goddard, Pooja; Peter, P. R., Carbon incorporation in the Li7La3Zr2O12 garnet framework. - In final preparation stages